UNIVERSITÀ DEGLI STUDI DI PAVIA

# SCIENTIFICA ACTA

## QUADERNI DEL DOTTORATO

VOLUME XIII ANNO XIII NUMERO 2

15 MAGGIO 1998

IV International Workshop on

## RESISTIVE PLATE CHAMBERS AND RELATED DETECTORS

Castel dell'Ovo, Napoli Oct 15-16 1997

Ed SERGIO P. RATTI, RICCARDO DE ASMUNDIS

CENTRO STAMPA - DIPARTIMENTI FISICI
Via Bassi, 6 27100 Pavia

## FOREWORD

On behalf of the Department of Physical Science of the Naples University, of the director of the Naples Section of INFN and of the Organizing Committee, I am glad to welcome you to the IV Workshop on RPC and related detectors.
The first meeting on RPC was held in Lecce in January 1991, the second in Rome in February 1993, the third in Pavia in October 1995. In this period these detectors have gained the attention of the international scientific community for their capability of giving good space and excellent time information at "low" price and therefore are ideal for experiments which have to detect charged particles, mainly muons, on large areas such as cosmic rays experiments or to instrument muon detectors both for reconstruction and triggering purposes.
What seemed to be initially a limitation for RPC to properly work in a high rate environment has been overcome by their use in a different operating regime, avalanche instead of streamer. RPCs have been definitely accepted as the muon trigger detectors for LHC experiments and one of the main points of this workshop will be the comparison of different techniques which are being studied to optimize both performances and large scale productions needed for these experiments.
Beside the R&D program carried out by the LHC groups, since the time of the Pavia meeting, the CP violation experiments at Slac and Kek, BaBar and Belle, have equipped their detectors with RPCs gaining much experience in the construction, testing and installation of large scale systems. On the other hand we are now in the fourth year of running of a large RPC system as the forward-backward muon detector of L3.
A new fixed target experiment at Fermilab has used RPCs for muon trigger and identification and in a very short time we will have the first installation of these detectors at very high altitudes for cosmic ray physics. We will hear about new ideas for future experiments and new interesting developments on the detectors itself as the multigap chamber. Finally the great effort put into the development of new electronics for the detector will be presented. I finally hope that some contributions to this workshop will let us gain some deeper insight on the detector itself and open the way for reliable montecarlo simulations.

Sergio Patricelli
Chairman of the Local
Organizing Committee

# INDEX

# RPC: PRESENT STATUS OF THE ART

R. Santonico
*Università di Roma "Tor Vergata" and INFN Sezione di Roma 2*
*Via della Ricerca Scientifica 1, 00133 Roma*

ABSTRACT

The evolution of ideas on RPCs since the time of the Pavia workshop is presented. Wide gap and multigap RPCs are discussed together with the streamer suppression effects observed for some new gases. The studies on electrode surface and detector ageing are briefly presented.

## 1. Introduction

This report describes the evolution of ideas on RPCs since the time of the Pavia workshop with the main purpose of fixing a starting point for the present 1997 workshop. The main emphasis will be put on the avalanche mode operation which is characterized by a smaller delivered charge with respect to the streamer mode and is therefore much more adequate for rate capability, power consumption and detector ageing, to the working conditions imposed by LHC.

Nevertheless it should be stressed that the RPCs operated in streamer mode have still important applications to cosmic ray and accelerator experiments according to several talks announced in the present workshop.

## 2. Pure avalanche operation of RPCs

The central problem of the avalanche operation of RPCs is that of

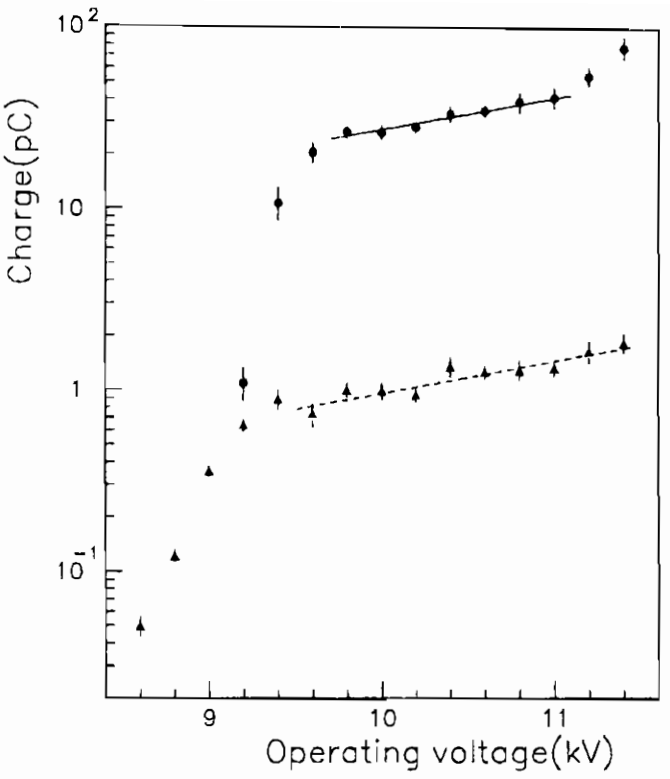


Figure 1: Avalanche precursor signal charge (triangles) and total charge (circles) vs. operating voltage for a gas mixture $Ar/C_2H_2F_4/n\text{-}C_4H_{10}$ = 10/83/7.

achieving a "comfortable" operating point in a large voltage range. It can be focused, just to fix the ideas, using the plot shown in Fig. 1 [1] which represents the RPC signal charge vs. the operating voltage for a gas mixture $Ar/C_2H_2F_4/n\text{-}C_4H_{10}$ = 10/83/7. Here the charge of the avalanche precursor signal is plotted separately from the total charge which is dominated by the streamer at voltages above the streamer threshold.

The plot in Fig. 1 shows a region characterized by a rapid increase of the avalanche charge as a function of the operating voltage followed by a saturation region where the gas amplification is much less voltage dependent. Moreover the charge distribution looks peakless with most events accumulated around zero below the saturation, and exhibits a peak at voltages above saturation [2].

The RPC operation in the avalanche saturation region would offer the advantage of a weak dependence of the working features with respect to the applied voltage. Unfortunately the saturation point is not far from the streamer threshold, as shown in Fig. 1, so that the saturated avalanche operation without streamers is possible only in a modest voltage range. The possibility of extending this range has been investigated following several ideas that are discussed in the following sections.

## 3. The wide gap RPC

The basic idea of the wide gap RPC [3] is that an increased gas gap (3-8 mm) gives two advantages with respect to the "traditional" 2 mm gap:

- an increased ionization which improves the primary cluster statistics;
- a better gas gap uniformity based on the fact that, assuming a given distortion $\Delta g$ for the electrode plates, the relative gap disuniformity $\Delta g/g$ decreases for increasing g.

These considerations suggest that a wide gap RPC could offer an increased voltage plateau with respect to the more usual case of a 2 mm gap, a statement which is interesting to check experimentally even in spite of a number of disadvantages of the wide gap RPCs like the higher operating voltage and the worse time resolution [3].

The comparison of 2 and 3 mm gap RPCs, using a gas mixture $C_2H_2F_4$/i-$C_4H_{10}$=97/3 [4], is shown in Fig. 2 where the detection efficiency vs. the operating field is given for both avalanche and streamer mode operation.

The choice of the electric field instead of the voltage is justified by the fact that the field is much less gap dependent than the voltage. Indeed, for a given gas the field fixes the value of the Townsend coefficient $\alpha$ independently on the gap; nevertheless the operating field is expected to be lower for a wider gap RPC, the gas amplification being given by the product $\alpha g$.

A significant shift to a lower operating field for the avalanche mode operation is indeed observed for the 3 mm gap, but an even larger shift is observed for the streamer mode operation, so that the overall separation

between the avalanche and the streamer working modes is smaller rather than larger in comparison with the 2 mm gap RPC.

With the purpose of making this argument more quantitative, we take the difference of the operating fields of the avalanche and the streamer mode respectively at 50% efficiency as a measurement of the avalanche-streamer separation.

For RPCs, the voltage can be assumed, to a good approximation, to be the same everywhere in the chamber area. In this case, the field disuniformity is given by the gap disuniformity caused by mechanical distorsions of the plates: $\Delta E/E = \Delta g/g$.

For a pure avalanche mode operation, $\Delta E/E$ must be small with respect to the avalanche-streamer separation, defined as the relative difference between the streamer and the avalanche operating fields, $E_{str}$ and $E_{av}$ respectively. Fig. 2 shows that $(E_{str}\text{-}E_{av})/E_{av}$ is 8.3% for the 3 mm and 13.9% for the 2 mm gap, indicating that the gas gap of 2 mm gives a better streamer separation, given by the ratio 13.9/8.3=1.67 even accounting for the gap uniformity, which is a factor 1.5 worse than for the gas gap of 3 mm.

We conclude that at least for heavy gases as $C_2H_2F_4$ the idea that a wide gap RPC has a better avalanche-streamer separation with respect to the standard 2 mm gap is not supported by experimental data.

Finally it should be mentioned that the 3 mm gap RPCs exhibit much larger streamer signal charges than the 2 mm gap RPCs [4].

## 4. The multigap RPC

Another approach to the problem of getting a more favorable charge distribution in avalanche mode is the multigap RPC. This is an RPC in which the same electrodes pick up the charge induced by several gas gaps. Depending on the type of multigap (see below), the signal is the sum or the average of the signals produced by the individual gaps with an obvious reduction of statistical fluctuations. This is shown in Fig. 3 where the charge distributions of a single and a double gap RPC are compared [5]. The latter one exhibits a charge peak that is not visible in the former, indicating a statistical increase in the primary ionization.

Two types of multigap RPCs, schematically represented in Fig. 4, have been developed. In the type *a* [6] (Fig. 4*a*) there is one gas gap on each side of the pick up electrodes, whereas in the type *b* [7] (see Fig.

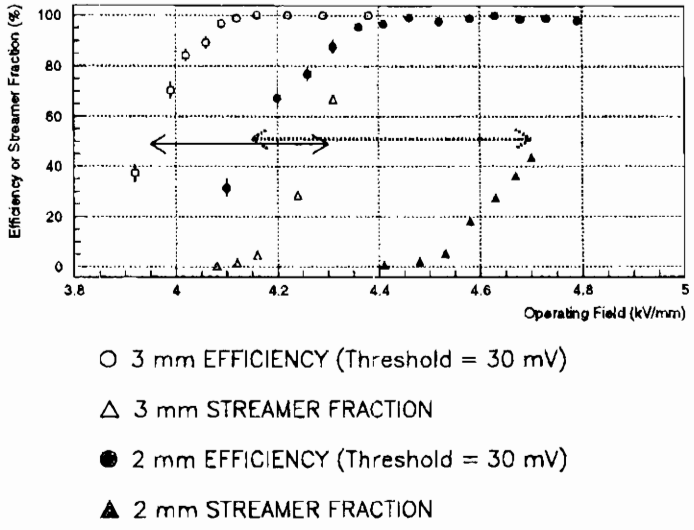


Figure 2: Detection efficiency (30 mV threshold) and streamer fraction vs. operating electric field for 2 mm and 3 mm gap RPCs. The horizontal arrows indicate the difference $E_{str}$-$E_{av}$ for 2 mm (dotted line) and 3 mm (full line) gas gaps.

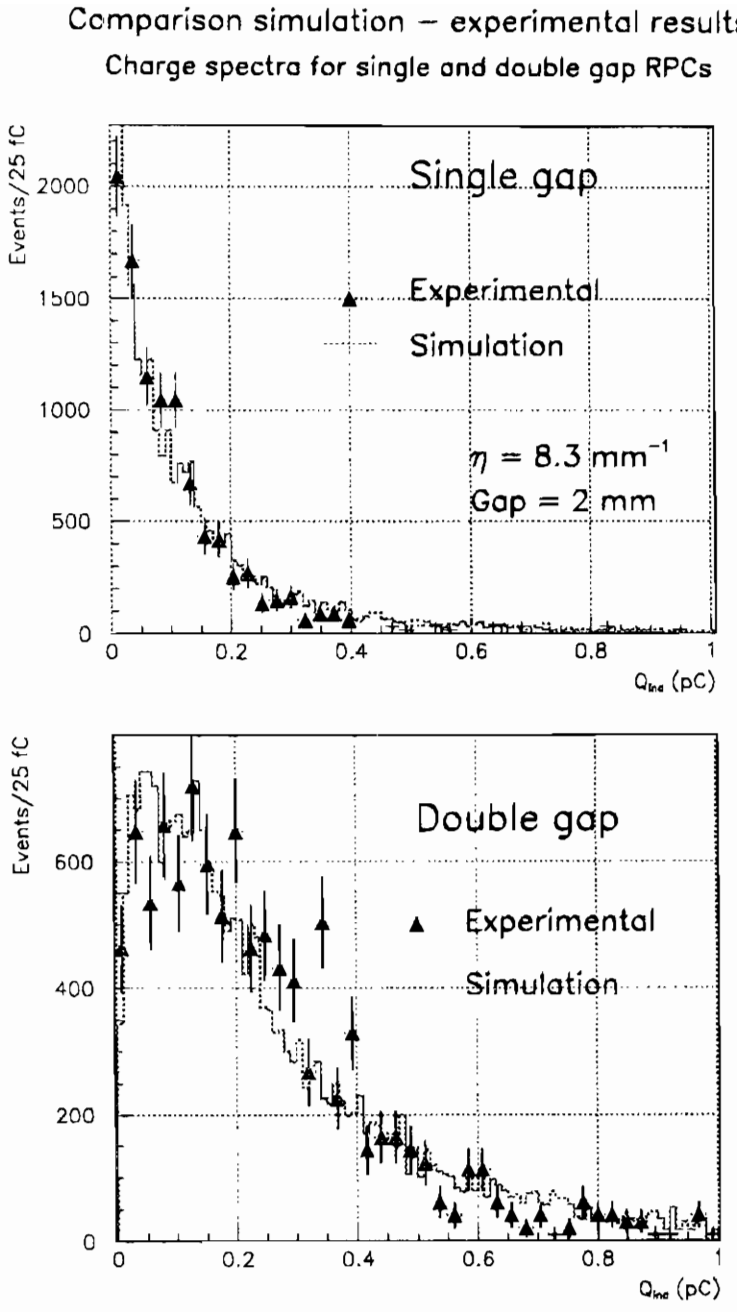


Figure 3: Charge distributions for single and double gap RPCs.

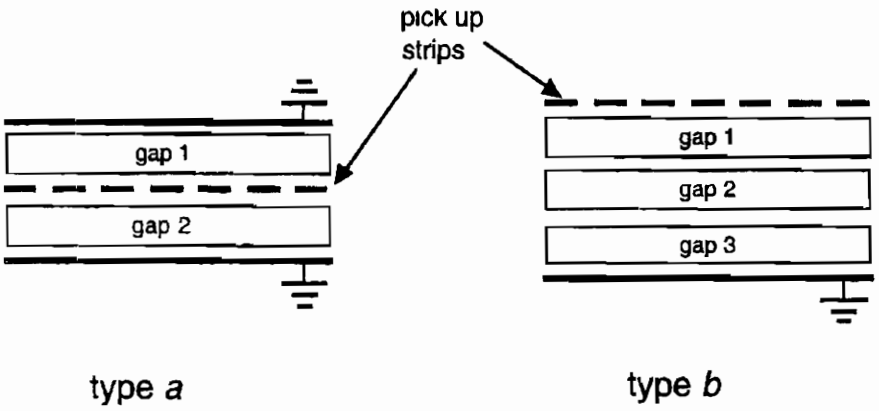


Figure 4: Sketch of the two types of multigap RPCs.

4*b*) there are many gaps on the same side of the pick up electrodes.

The type *b* has the advantage of allowing any number of gaps in comparison to type *a* which allows only two gaps. On the other hand, type *a* has a completely symmetrical pick up for the two gaps. This symmetry does not exist in the case *b* because the size of the induced charge spot depends on the distance from the pick up plane which is different for different gas gaps. This means for example that the cluster size could depend on the gap producing the discharge. This is particularly important when the signal is dominated by the contribution of one gap only which is also the case in which the multigap RPC gives the maximum advantage.

Finally, another difference between the two types is related to the fact that in case *b* the electrons of an avalanche occurring in a given gap run a maximum length of only 1/n of the distance between the strip and the corresponding ground plane. This makes a reduction of the induced charge by the same factor. The comparison of the two types of multigap RPCs is summarized in table 1.

## 5. Streamerless gases

The problem of the pure avalanche mode RPC operation can also be faced from the point of view of the proper choice of the gas.

Does a "streamerless gas" exist?

Two new gases have been tested. The pentafluoroethane, $C_2HF_5$,

Table 1: Comparison of the two types of multigap RPCs

| | Type *a* | Type *b* |
|---|---|---|
| Possible number of gas gaps | 2 | any number |
| Operating voltage | the same as for monogap RPCs | n times higher than monogap RPCs |
| Pick up symmetry with respect to the gaps | symmetrical | non symmetrical |
| Fast signal charge to delivered energy ratio | the same as for monogap RPCs | 1/n of the monogap RPCs |

mixed to 5% $C_4H_{10}$ gave, according to ref. [8], a better voltage plateau with respect to the more usual gases based on tetrafluoroethane.

The second gas tested was $SF_6$ which proved to be an extremely efficient streamer suppressor even when used in very small amounts [9]. The addition of about 1% $SF_6$ to the baseline RPC gas in ATLAS ($C_2H_2F_4/C_4H_{10}$) gave about 1 kV streamerless operating voltage plateau. Fig. 5 shows the detection efficiency and the streamer probability for a gas mixture containing 1%, 2%, 5% $SF_6$ respectively in addition to the binary mixture $C_2H_2F_4/C_4H_{10} = 97/3$.

## 6. Surface treatment of the resistive electrodes

One of the most important features of the electrode surface faced to the gas gap is the smoothness, which presumably determines the electric field on a microscopic scale very near to the surface.

A long experience has been accumulated so far in improving the surface smoothness with paints, like linseed oil, which produce a thin solid layer coating the natural surface of the electrode plates.

Recently bakelite plates with improved surface smoothness have become industrially available. This could allow a good RPC operation even if non coated electrode plates are used. Indeed encouraging results have been obtained by the Pavia group [10] with RPCs using non oiled plates with very smooth surface.

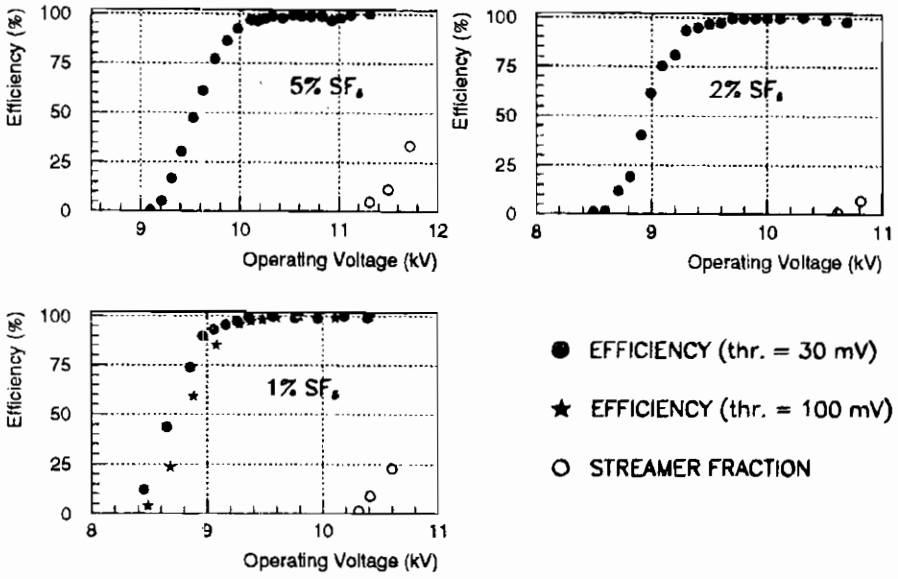


Figure 5: Detection efficiency and streamer probability vs. operating voltage for 5%, 2% and 1% $SF_6$ concentrations.

Nevertheless two basic points concerning these RPCs have to be carefully studied: the noise level which should not exceed the one achievable with coated electrodes and the long term stability which is still completely unknown for RPCs with non coated plates. The testing activity in this field should therefore proceed accordingly.

## 7. Ageing effects

RPCs operating under irradiation of intense sources show, after a long working time, a gradual reduction of their rate capability which should be presumably explained as an effect due to a parallel increase of the electrode plate resistivity. This ageing effects have been proven to be negligible [11] for the RPC applications that are presently foreseen at the LHC. Nevertheless an intense R&D activity is in progress to improve the knowledge and the understanding of ageing effects.

1. R. Cardarelli, V. Makeev, R. Santonico; Nucl. Instr. and Meth. **A 382** (1996) 470.
2. M. G. Alviggi et al.; "*Resistive Plate Chambers in ATLAS*", ATLAS internal note MUON-NO-131, 1 October 1996.
3. E. Cerron Zeballos et al.; Nucl. Instr. and Meth. **A 360** (1995) 512.
4. P. Camarri et al.; "*Latest results on RPCs for the ATLAS LVL1 muon trigger*", poster presentation at the 7th Pisa Meeting "Frontier Detectors for Frontier Physics" (Elba Island, May 25-31, 1997), to be published in Nucl. Instr. and Meth. A.
5. M. Abbrescia et al.; "*Resistive Plate Chambers in avalanche mode: a comparison between model predictions and experimental results*", presented at the 7th Pisa Meeting "Frontier Detectors for Frontier Physics" (Elba Island, May 25-31, 1997), to be published in Nucl. Instr. and Meth. A.
6. T. Moers et al.; "*Measurement of the efficiency and time resolution of double-gap resistive plate chambers*", Nucl. Instr. and Meth. **A 345** (1994) 474.
7. E. Cerron Zeballos et al.; Nucl. Instr. and Meth. **A 374** (1996) 132.
8. E. Cerron Zeballos et al.; Nucl. Instr. and Meth. **A 396** (1997) 93.
9. P. Camarri's talk in this workshop.
10. M. Abbrescia et al.; Nucl. Instr. and Meth. **A 394** (1997) 13.
11. ATLAS Collaboration; "*ATLAS Muon Spectrometer Technical Design Report*", CERN/LHCC/97-22, 31 May 1997.

# INFLUENCE OF RESISTIVE ELECTRODES ON DETECTOR PERFORMANCE

M. MARGARIDA FRAGA *
*LIP-Coimbra, Departamento de Física, Universidade de Coimbra.*

February 9, 1998

ABSTRACT

Most papers on RPCs consider the dependence of their efficiency on rate and call the attention to the voltage drop on the dielectrics, although not supported by quantitative measurements. Two regimes may be considered in such studies: low rate (few Hz/cm$^2$), where "event-per-event" effects can play a role, and higher rates, for which the "mean effect" due to consecutive events result on a "current dependent" behaviour. Experimental data for the study of this latter regime allow for direct computation of the voltage drop across the dielectric, and unequivocally prove that the detector performance is only dependent on the voltage difference across the gas gap. Transient behaviour of the detectors under fast rate change show that, in first approximation, the associated time constant is of the order of $\rho\epsilon$. Furthermore, the possible use of internal floating electrodes, a solution that changes the effective resistance but not the parameter $\rho\epsilon$, is also discussed.

## 1. Introduction

The effect of the counting rate on the performance of resistive de-

*co authors R. Ferreira Marques, E. P . de Lima, A. J. P. L. Policarpo *Laboratório de Instrumentação e Física Experimental de Partículas, LIP - Coimbra Departamento de Física, Universidade de Coimbra, 3000 Coimbra, Portugal*; Carmen C. Bueno, Josemary A. C. Gonçalves and M. Damy de S. Santos *Instituto de Pesquisas Energéticas e Nucleares - Comissão Nacional de Energia Nuclear 05508-900 - Caixa Postal 11049 - São Paulo - Brasil Departamento de Física, Pontifícia Universidade Católica de São Paulo 01303-050, São Paulo, Brasil*

tectors has been investigated by several groups (e.g., [1] and [2]) and it is normally attributed to the voltage drop across the resistive electrodes, although in a rather qualitative way. Here, without loss of generality of the results obtained, rate effects are studied with a classical cylindrical counter geometry. Advantages of this approach are the inherently good energy resolution (good measurements of charge and current) and clear definition of the working regime. The interpretation of the results is based on a rather simple model and relies on the direct comparison of the data measured with the resistive detector with those measured with a metallic one of identical geometry, operated under the same conditions. This technique allows a direct measurement of the voltage across the glass and the errors introduced are small. Due to the finite conductivity of the glass, for a given applied voltage and in the absence of irradiation, the voltage across the glass wall tends to zero once equilibrium is reached. If irradiation starts at $t = 0$, a current $I$ begins to flow, the voltage across the glass increases, causing a decrease of the voltage across the gas. The gain and consequently the current will then also decrease until the stationary regime is regained. In this work we present data that, in a quantitative way, contributes to the clarification of the transient behaviour of resistive detectors.

## 2. Experimental set-up

A cylindrical tube made of glass ($\phi_i$ = 12.7 mm, glass wall thickness = 1.1 mm) with the anode wire (tungsten, 127 $\mu$m $\phi$, or stainless steel, 50 $\mu$m $\phi$) stretched along its axis was used. Its schematic drawing is shown in Fig. 1. This tube is divided into two sections: one of them was covered externally with a thin grounded layer of Aquadag, forming a simple resistive detector, referred to below as RD, while the other was covered internally by the same layer. In a small region of the part painted internally, conductive painting was also applied externally for a length $L$ of 30 mm and connected to ground. When the internal electrode is grounded the tube behaves as a conventional metallic proportional detector and will be designated MD. The internal cathode can also be floating, i.e., it is not connected externally to any passive or active electronics, and we designate it as the floating electrode resistive detector, FERD. The resistivity of the glass was measured to be $6.5 \times 10^{12}$ $\Omega$.cm and its specific dielectric constant is 5, as given by the manufacturer.

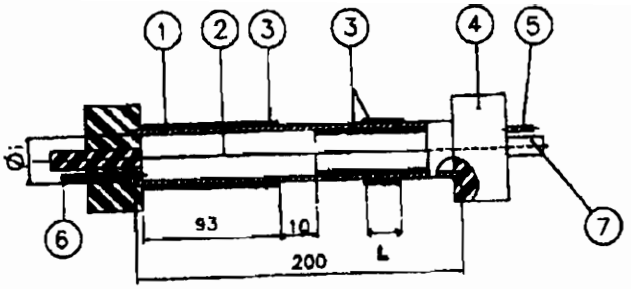


1-GLASS
2-ANODE WIRE
3-ACQUADAG
4-LUCITE CAP
5-GAS INLET
6-GAS OUTLET
7-DELRIN INSULATOR

L = 30 mm

Fig. 1. Schematic drawing of the detector.

The gas mixture, Ar+10%$CH_4$ (P10) at atmospheric pressure, flows continuously through the detector. X-rays from a $^{109}$Cd source (22 keV) irradiate the detector through its glass wall. The apparent length of the detector cylinder irradiated (4 to 16 mm) is limited by Pb plates positioned symmetrically in respect to the source. The counting rate is changed by interposing between the source and the detector Al plates of appropriate thickness (0.5 to 4 mm). The charge spectra were measured using a conventional charge amplifier electronic system and a multichannel analyzer, calibrated with a standard pulse generator. The effect of the amplifier RC shaping networks on the charge pulses was taken into account in order to obtain the total mean charge per avalanche. For the study of the transient effects the signals from the amplifier are fed to a CAMAC ADC, and the control software permits to record the pulse amplitude and time of each event.

## 3. Results and analysis

### *3.1. "Current dependent" behaviour*

The effect of counting rate on the gain of a resistive detector was

studied [3], for a stationary regime, for two electric field geometries and for a wide range of gains ($G = 10^2 - 7 \times 10^4$). The ratio between the gains measured with the resistive and the metallic detectors, for the same applied voltage, is represented in Fig. 2, both as a function of the applied voltage (a) and the current (b). When the detector is irradiated, a cur-

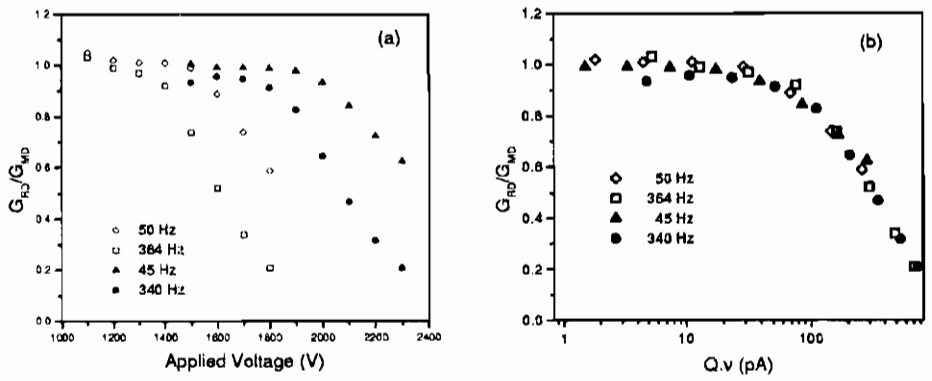


Fig. 2. Gain ratios ($G_{RD}/G_{MD}$) as a function of the applied voltage (a) and of the current (b). Open symbols: 50 $\mu$m SS wire; full symbols: 127 $\mu$m tungsten wire.

rent flows through the gas and a potential drop $\Delta V = RI$ is established between the internal and external surfaces of the tube ($I$ being the current that flows through the gas, when the equilibrium state is reached, and $R$ the resistance of the irradiated part of the tube). This voltage drop can be computed by comparing the charge peak amplitudes measured with the resistive and metallic detectors of the same geometry. The effective potential across the gas is then given by $V_{eff} = V_0 - \Delta V$ and the reduced electric field at the anode by $E_a/P = V_{eff} / \left[ r_a P \ln(\frac{r_i}{r_a}) \right]$ where $V_0$ is the applied voltage and $r_a$ and $r_i$ the radii of the anode and the internal surface of the tube, respectively. If we represent the ratio between the gains measured with the resistive detector and the metallic one, for the same reduced electric field at the anode, as a function of $E_a/P$, we find that it is approximately constant over the $E_a/P$ range investigated (Fig. 3). This proves unequivocally that the detector performance is only dependent on the voltage difference across the gas. A similar behaviour was observed with the resistive detector which has an internal floating cathode (FERD). The advantage of using the FERD is that in this case the resistance can be accurately computed

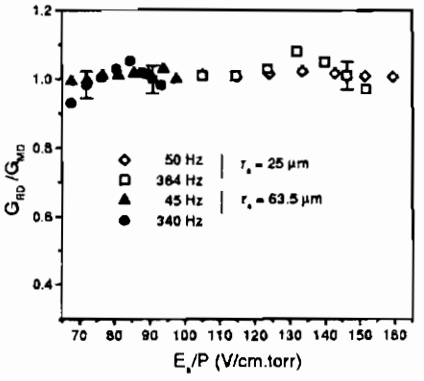


Fig. 3. Gain ratio as a function of the reduced electric field at the anode.

as $R = \rho \ln(\frac{r_e}{r_i})/(2\pi h)$, where $\rho$ is the resistivity, $r_e$ is the external radius of the tube and $h$ is the length of the tube through which the current flows. For the FERD $h$ is the length of the external aquadag layer (see Fig. 1) and does not depend on the irradiation conditions. By increasing this length we can decrease the overall counting rate effect on the gain of the detector.

### *3.2. Transient behaviour*

A simple model was developed to describe the transient response of our resistive detector, which is valid under the following assumptions: i) space charge effects in the multiplication region and surface currents on the glass can be neglected; ii) a "mean effect" due to consecutive events results on a "current dependent" behaviour; iii) the glass has a permittivity which does not depend on time.

Applying the Maxwell equations to our problem, we obtain the following differential equation

$$\frac{dV_{eff}}{dt} = -\frac{1}{C}i(t) + \frac{C_1}{C}\frac{1}{\tau}V_0 - \frac{C_1}{C}\frac{1}{\tau}V_{eff} \qquad (1)$$

where $C = C_1 + C_0$, $\tau = \rho\epsilon$, $C_1$ is the capacity of the glass tube, $C_0$ is the capacity of the corresponding metallic detector, and $i(t) = Q_0.\nu.G(t)$, $\nu$ being the irradiation rate. The variation of the gain with time results from the variation of the voltage across the gas. For the

range of variation of $V_{eff}$ (from $t = 0$ until equilibrium is reached), we can approximate the gain by an exponential function $G = e^{aV_{eff}}$, where $a$ and $G_0$ are parameters obtained by fitting the gain versus applied voltage for a metallic detector of the same geometry. An example of this variation is shown in Fig. 4.

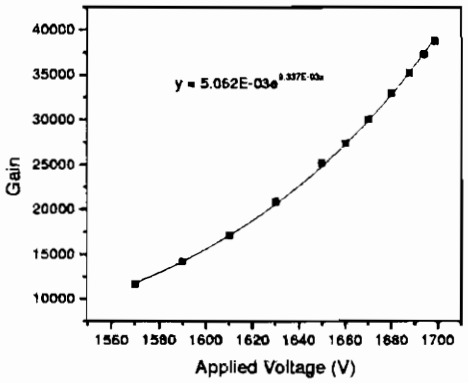


**Fig. 4. Variation of the gain as a function of the applied voltage, for the P-10 gas mixture, as measured for the metallic detector.**

The differential equation for $V_{eff}$ implies that the glass can be considered electrically equivalent to a capacitor of capacity $C_1$ in parallel with a resistor. Upon numerical integration it was found that the resulting curves $G(t)$ could be fitted by either one exponential decay plus a constant term or by a sum of two exponentials plus the constant term, depending on the irradiation conditions. As an example, we present in Fig. 5 the calculated variation of the gain with time for an applied voltage of 1700 V and a counting rate of 1014 Hz ($I_0 = 4$ nA). It is worth noting that both time decay constants are smaller than the $\rho\epsilon$ value of the glass (2.9 s) calculated with the dielectric constant given by the manufacturer. Measurements of the transient response of the resistive and floating electrode resistive detectors were performed for currents from 4 up to 4000 pA. Similar results are obtained for both of detectors. Namely, it was found, as predicted by our model, that for the lower currents the data can be fitted by the sum of a single exponential and a constant term (Fig. 6) while for higher currents a sum of two exponentials plus the constant term is needed (Figs. 7 and 8). However, the time decay constants are approximately one order of magnitude larger than those predicted by our model on the assumption that $k_{glass} = 5$.

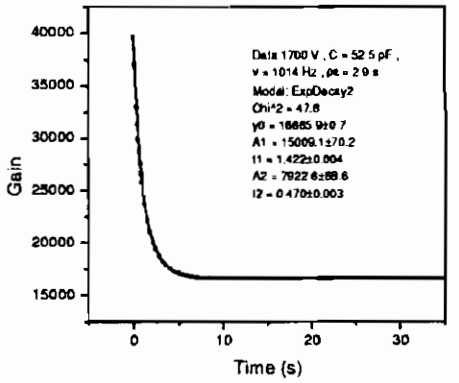


Fig. 5. Variation of the gain with the time, as predicted by calculations.

Therefore, we must use a capacity ten times larger to reproduce our data. The equilibrium value of the gain is also in agreement with the one obtained from the integration of equation (1).

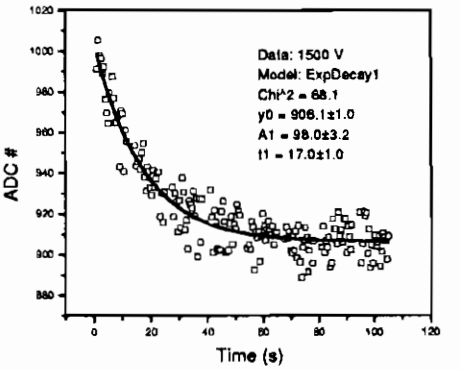


Fig. 6. Pulse height as a function of time ($I_0 = 300$ pA).

However, the time decay constants are approximately one order of magnitude larger than those predicted by our model on the assumption that $k_{glass} = 5$. Therefore, we must use a capacity ten times larger to reproduce our data.

The dependence of the time constants on the current was also investigated. The model described above predicts a decrease of the time

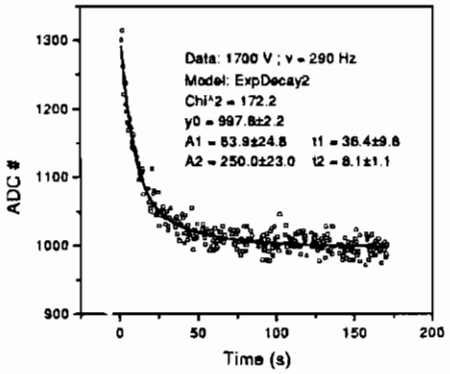


Fig. 7. Dependence with time of the amplitude of the charge signals, for the FERD ($I_0 = 1000$ pA).

constants with increasing current (see table I). Experimentally we found the same behaviour. As it can be seen from Fig. 9, the time constant decrease as we increase either the applied voltage or the counting rate, i.e., the current.

Table 1. Time decay constants.

| $I_0$ (pA) | $t_1$ (s) | $t_2$ (s) |
|---|---|---|
| 1770 | $6.4 \pm 0.2$ | $17.5 \pm 0.1$ |
| 4000 | $4.8 \pm 0.1$ | $14.4 \pm 0.1$ |

The dependence of the time constant on the counting rate was further investigated, for the FERD, for an applied voltage of 1700 V ($G \sim 4 \times 10^4$). In this case, and for rates above 200 Hz ($I_0 > 600$ pA), a sum of two exponentials and a constant term is needed to fit the experimental data. In Fig. 10, the variation of the two time constants are plotted as a function of counting rate, the two sets of data corresponding to measurements in two different days.

## 4. Conclusions

From the experimental data we conclude that the time evolution of the amplitude of the charge signals (or the current) in the resistive detector can be described by a single exponential decay, for low counting rates and/or low gains (low currents), and by a two exponential decay

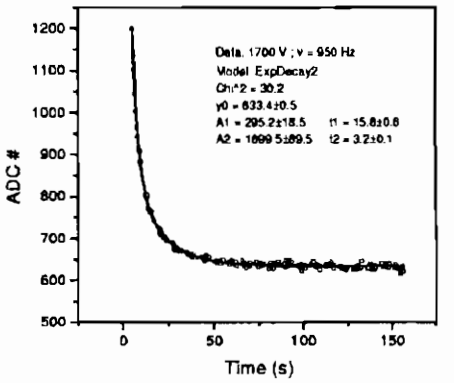


Fig. 8. Dependence with time of the amplitude of the charge signals, for the FERD ($I_0 = 3300$ pA).

for higher currents. The time decay constants decrease with the current increase and are higher (up to a factor of 10) or of the order of the assumed $\rho\epsilon$ value.

Our simplified model implies the correct gain drop for a given applied voltage and a given counting rate, and a time dependence of the charge gain that can be described by one or two exponential decays, depending on the current flowing through the gas. It is also found that the decay time constants decrease with the current. However, it does not reproduce the measured decay constant values. Although we do not know precisely the $\epsilon$ value of our glass (measurements of glass samples are under way), we do not expect it to be more than two or three times larger than the value used. The established model is very simple and it does not take into account, for example, the fact that glass is not polarised instantaneously. More complicated circuits, e.g. with the addition of other branches (consisting of a capacitor in series with a resistor) in parallel with the $C_1$, can be used to describe the behaviour of the glass [4]. A complete study of the electric properties of the glass used are under way and a comparison will then be performed with the relaxation of the dielectric under irradiation conditions.

## 5. Acknowledgements

This work was supported in Portugal by JNICT (contract CERN/CA/1102/96), and in Brasil by FAPESP and CNPq.

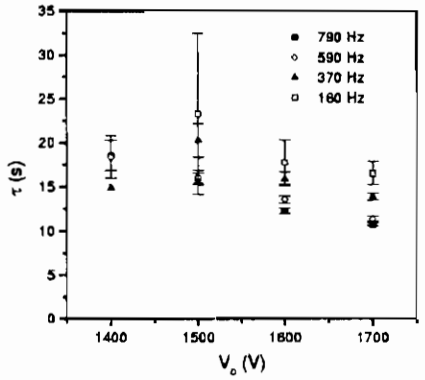


Fig. 9. Decay constant (for one single exponential plus a constant fit) as a function of the applied voltage, for several counting rates, for the Resistive Detector.

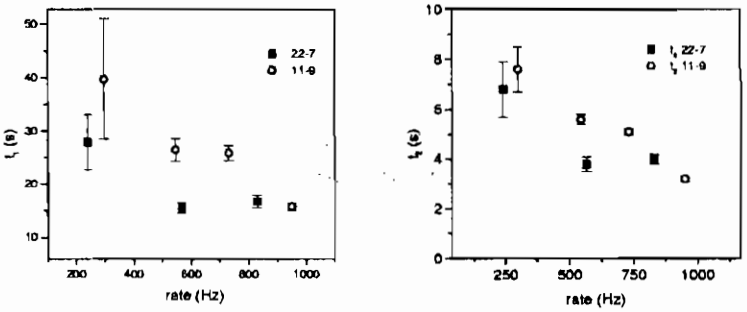


Fig. 10. Variation of the decay constants as a function of the counting rate, for the Floating Electrode Resistive Detector, for an applied voltage of 1700 V.

1. C. Bacci, C. Bencze, R. Cardarelli, F. Ceradine, G. Chiapetti, A. Di Ciaccio, F. Lacava, A. Nizati, D. Orestano, L. Pontecorvo, E. Radermacher, R. Santonico, C. Seez, F. Szonso, S. Veneziano, M. Verzocchi, G. Walzel, G. Wrochna, C.E. Wultz, L. Zanello, *Nucl. Instr. and Meth.* **A 352** (1995) 552.
2. E. Cerron Zeballos, I. Crotty, D. Hatzifotiadou, J. Lamas Valverde, S. Neupane, S. Singh, M.C.S. Williams and A. Zichichi, *Nucl. Instr. and Meth.* **A 367** (1995) 388.
3. Carmen C. Bueno, M.M. Fraga, Josemary A.C. Gonalves, R. Ferreira Marques, A.J.P.L. Policarpo and M. Damy de S. Santos, submitted to *Nucl. Instr. and Meth.* A.
4. V. V. Daniel, *Dielectric Relaxation*, (Academic Press, New York, 1967).

# A NEW MATERIAL FOR EXTREMELY HIGH COUNTING RATE PROPORTIONAL-MODE RPCs

P. FONTE*
*LIP, Dep. de Física, Univ. de Coimbra, Portugal*
*ISEC, Quinta da Nora, Coimbra, Portugal*

ABSTRACT

A new custom-made medium resistivity material was used for the anode plate of an asymmetric, wire-mesh cathode, Resistive Plate Chamber. The anode plate resistivity could be controlled from $2\times10^7$ to $3\times10^{12}$ Ω cm, allowing for a large flexibility in the chamber counting characteristics.

Proportional counting rates up to $10^5$ Hz/mm$^2$ were achieved at gains above $10^4$. The energy resolution at 5.9 keV was 20% FWHM. The observed gain-rate trade-off is well described by a simple ohmic model and further improvements may be expected by lowering the resistivity of the anode material.

Eventual discharges were quenched by the resistive anode and constrained to the glow discharge phase of the sparking process. The discharge affected the detector only locally and the charge released was limited to a few nC.

## 1. Introduction

Parallel geometry chambers are used in three main configurations: Parallel Plate Chambers (PPCs), with two metalic electrodes, Resistive Plate Chambers (RPCs), with two resistive electrodes and Parallel Mesh Chambers (PMCs), with multiple wire-mesh electrodes.

Common features of these detectors when operated in proportional mode are the good timing characteristics [1], good position resolution [2], ease of production in large areas and large gain. The maximum gain is limited to the point where individual avalanches reach a charge around $10^8$ electrons, triggering the formation of streamers [3] that subsequently evolve to higher

* Co authors:
**N.Carolino**, **Y.Ivaniouchenkov** *LIP, Dep. de Física, Univ. de Coimbra, Portugal.*
**V.Peskov** *NASA, Marshall Space Flight Center, Huntsville, Alabama USA.*

current discharges [4]. Recently a new rate-induced breakdown mode was identified in PMCs [5].

In chambers with metallic electrodes (PPCs, PMCs) the discharge progresses until fully formed sparks appear. Although the sparks don't seem to affect the detector in a permanent way [6], the phenomenon causes unacceptable dead times and may compromise the integrity of the readout electronics.

When the electrodes are highly resistive (RPCs) the discharge is quenched at an earlier stage, affecting the detector only locally and being harmless to the readout electronics. It is even possible to operate the RPCs in a saturated gain "streamer mode", featuring very large and fast signals, up to a few hundred pC [7].

The advantage of RPCs in terms of sparkless operation is offset by a severe counting rate limitation of a few kHz/cm$^2$, while PPCs and PMCs can reach counting rates at least up to $10^7$ Hz/cm$^2$ [5, 8] without any decrease of the pulse-height, suggesting their use as high-rate detectors.

It is attractive to attempt to combine the "protectiveness" of RPCs with the large counting rate capability of the metallic chambers. Earlier attempts [9] were focused on an asymmetric RPC with wire-mesh electrodes except for a resistive anode made of Pestov glass. However due to a lack of anode materials with lower resistivity, the counting rate of the device didn't exceed a few tens of kHz/cm$^2$.

In the present work we introduce a new custom-made medium resistivity material whose resistivity can be controlled from $2\times10^7$ to $3\times10^{12}$ $\Omega$ cm allowing for a large flexibility in the chamber counting characteristics, while keeping essentially the same hybrid configuration described above.

The resulting detector actually combined the high counting-rate capability of PMCs ($10^5$ Hz/mm$^2$) while keeping the extreme robustness and "protectiveness" of RPCs.

## 2. Experimental Setup

A schematic drawing of the experimental set-up can be seen in figure 1.

The detector was constituted by a drift region followed by an amplifying gap. The drift region was 15 mm long and delimited by two wire meshes. The amplifying gap, 3.5 mm long, was delimited by the lower drift mesh

(cathode) and by a resistive plate (anode). The meshes were made of stainless steel wires of 50 μm diameter placed at a pitch of 0.5 mm. The detector had an active diameter of 4 cm.

The primary charges were created by a collimated X-ray beam produced by a sharp-focus (0.1 mm) X-ray tube having a Fe anode. The tube produces a bremstrahlung photon energy distribution peaked at 5.5 keV with a maximum energy of 10 keV. The beam was filtered by a nickel foil to absorb the lowest energy photons and delimited by a flat ring collimator placed 4 cm from the tube anode, with selectable openings of 2 and 5 mm diameter. The collimator was placed over the mylar entrance window, 1 mm from the upper drift mesh. It is estimated that the 5.5 keV photons will generate 200 primary electrons, and this was the value used for all calculations.

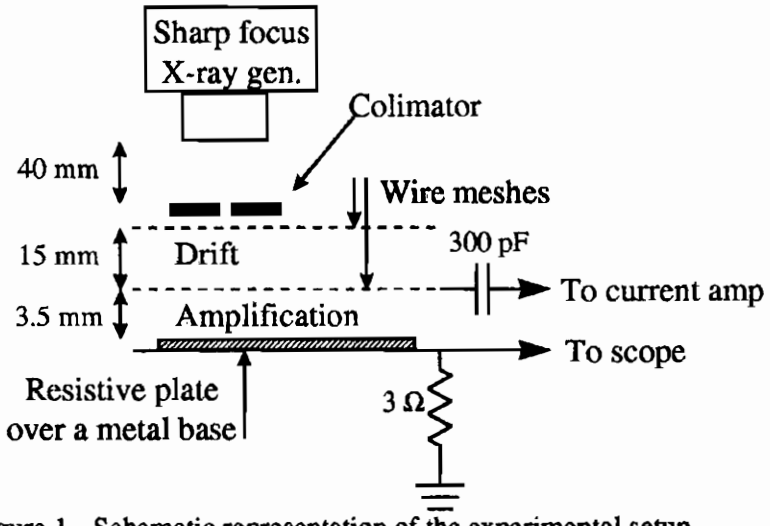


Figure 1 - Schematic representation of the experimental setup.

The resistive plate was deposited over a flat metal plate that provided mechanical support and an uniform electrical connection to the plate. The metal plate was grounded through a 3 Ω resistor and the current signal from discharges could be recorded directly on a scope connected in parallel with the grounding resistor.

The cathode signal was readout through a capacitor by a current amplifier with a 30 ns rise time. Since the rise time of the amplifier was actually longer than the signal width, the pulse height at the amplifier output was related to the avalanche charge and not to the gap current. It was found that

the observed pulse shape at the amplifier output was well reproduced by injecting in parallel with the amplifying gap a square current pulse of 10 ns width and 160 μA amplitude, corresponding to a charge of $10^7$ electrons or 1.6 pC, thus providing a charge calibration of the readout system.

The peak noise level at the amplifier output was around 25 fC and the discriminating threshold for all measurements was placed at 80 fC. This relatively high level was forced by a noisy X-ray tube power supply.

The equivalent electrical circuit from the signal source point of view is shown in figure 2. It can be calculated that the gap capacity per unit area is $C_{gap}=0.25\ pF/cm^2$ and that the plate capacity per unit area is around $C_{plate}=2.6\ pF/cm^2$ (assuming $\varepsilon_r=3$ and a plate thickness of 1 mm). The total capacities can be estimated by multiplying those values by the plate area of 25 $cm^2$. The value if the readout capacitor is $C_{readout}=300\ pF$.

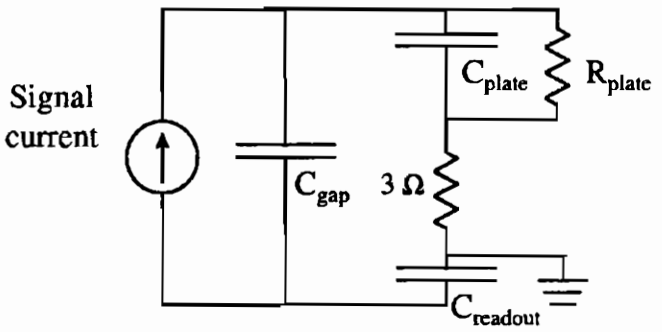


Figure 2 - Equivalent electrical circuit from the signal source (avalanche or streamer) point of view.

The gas mixture was constituted by Ar + 20 % $C_2H_6$ + methanol. The mixture was 50% saturated with the methanol vapours.

## 3. Resistive material

The anodic resistive plate was made from a mixture of epoxy[1] and ink[2], that yields a black rubber-like material.

[1] Araldite.

[2] MOLIN, ball-point pen black ink.

The resistivity can be varied from $2\times10^{7}$ to $3\times10^{12}$ Ω cm by varying the ink concentration (figure 3). Successive measurements taken at two weeks intervals suggest a good stability of the bulk resistivity.

The material shows an ohmic behaviour up to an applied voltage of 1 kV (figure 4) and, although there is some relaxation effect, the short term histeresis cycle is quite narrow (figure 5).

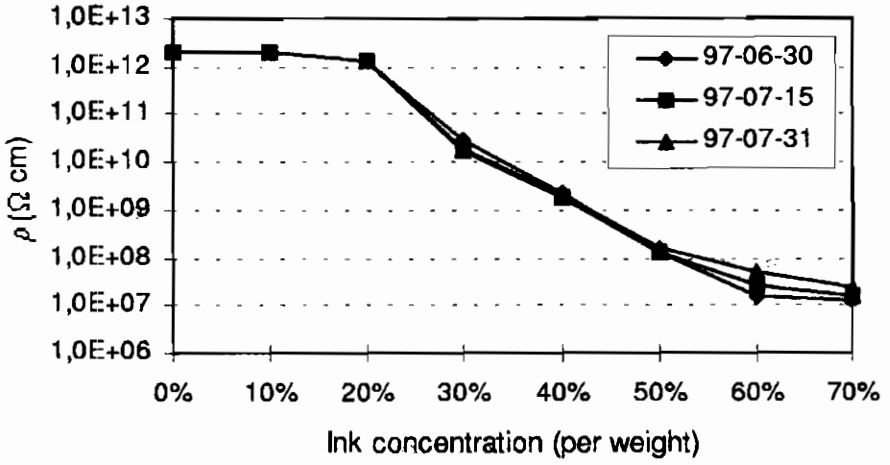


Figure 3 - The anodic material resistivity can be controlled by the amount of ink and varied from $2\times10^{7}$ to $3\times10^{12}$ Ω cm. Successive measurements taken at two weeks intervals suggest a good stability of the bulk resistivity.

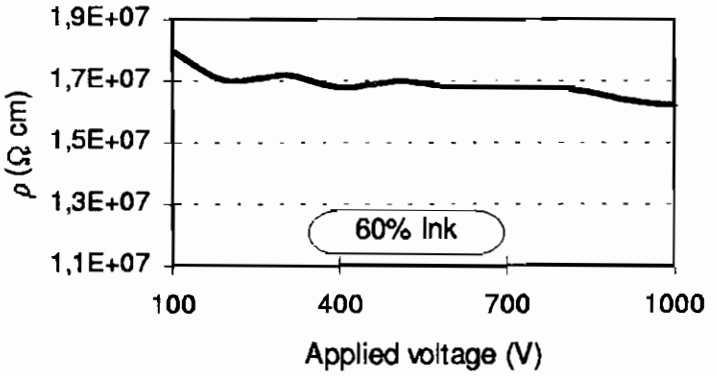


Figure 4 - The resistivity is largely independent from the applied voltage, indicating an ohmic behaviour.

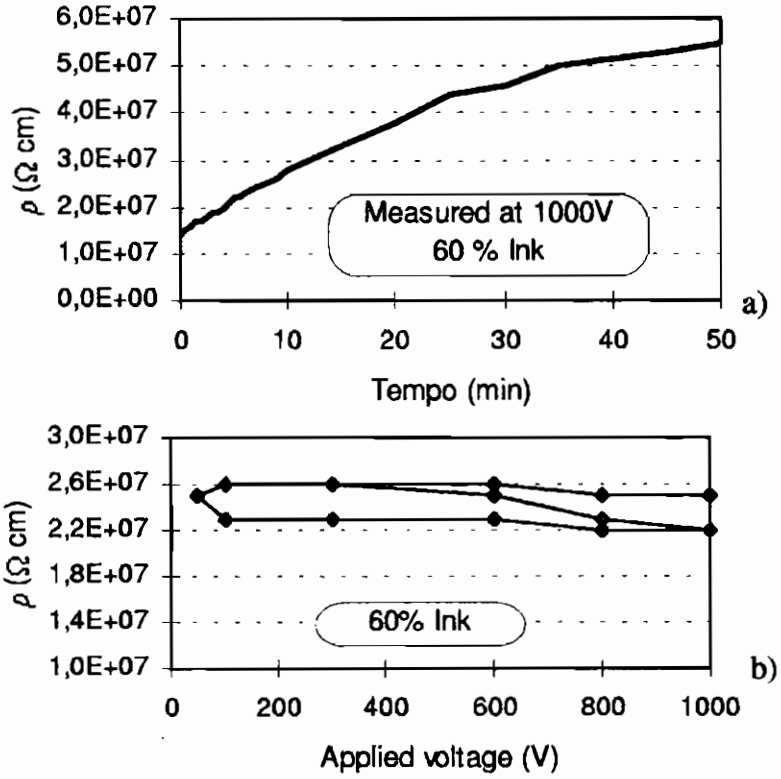


Figure 5 - Although the material shows a marked relaxation effect with a characteristic time of about 30 minutes (a), the fast cycling (1 minute per point) through large voltage excursions results on a relatively narrow histeresis plot (b).

## 4. Results and Discussion

### *4.1 Counting Characteristics*

The detector shows a reasonable energy resolution of 20 % FWHM (figure 6) while the best results for metallic PPCs are typically around 14 % FWHM [10]. In principle there is no reason why the present detector cannot achieve similar resolution values, so we attribute the observed reduced resolution to the deficient parallelism of the gap and to edge effects arising from the relatively small diameter of the active area.

A large counting plateau of more than one order of magnitude in gain was observed when the detector was illuminated by 5.9 keV X-rays (figure 7). The corresponding dark current is negligible and sparks appear only at gains

in excess of $10^6$. The dark current was found to be extremely sensitive to the presence of dust particles, requiring the detector to be assembled in a clean environment.

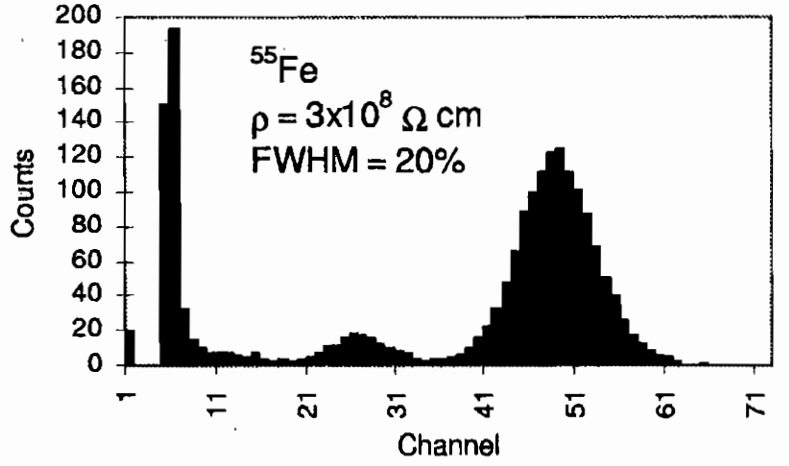


Figure 6 - A 20 % FWHM energy resolution was observed when the detector was illuminated by a $^{55}$Fe radioactive source emitting 5.9 keV X-rays.

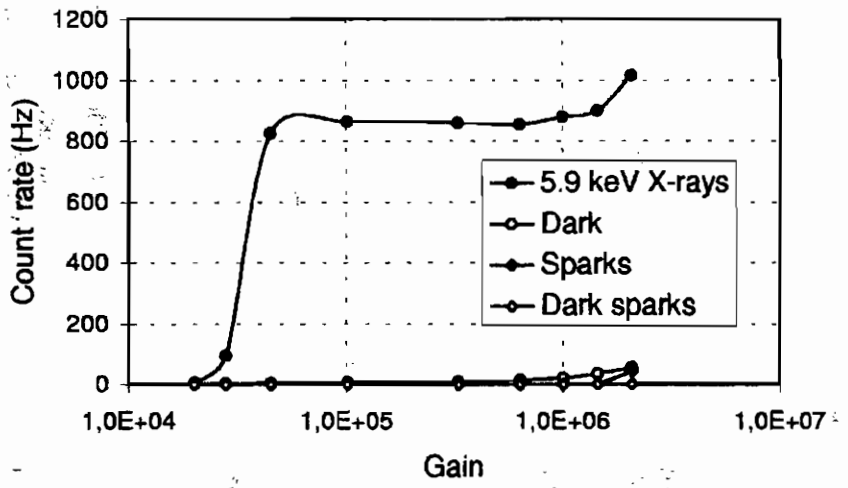


Figure 7 - A large counting plateau of more than one order of magnitude in gain was observed when the detector was illuminated by 5.9 keV X-rays. The corresponding dark current is negligible and sparks appear only at gains in excess of $10^6$.

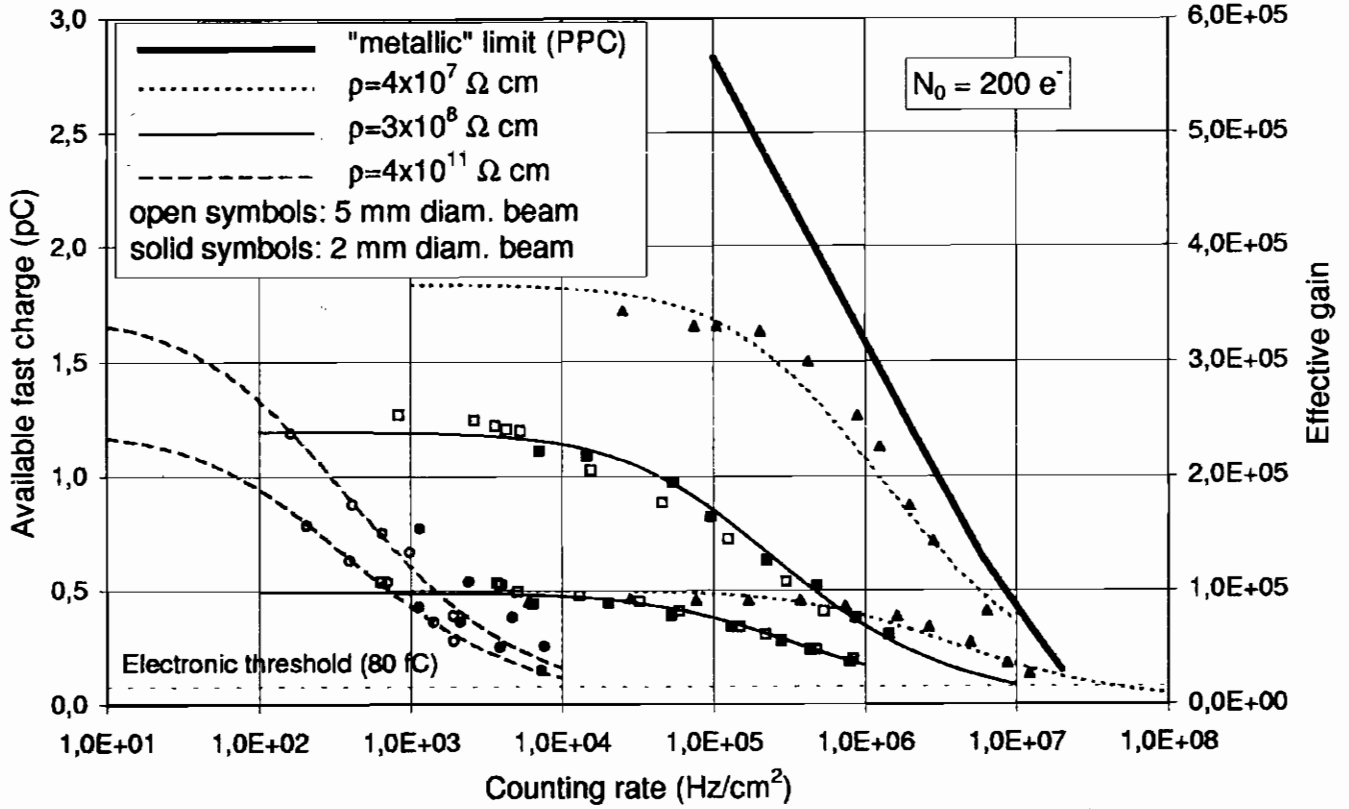


Figure 8 - Gain-rate characteristics of the detector for several values of the anode plate resistivity and beam diameters of 2 and 5 mm. For the lower resistivity studied a counting rate of $10^7$ Hz/cm$^2$ was achieved at a gain in excess of $10^4$. The thin lines were adjusted according to the ohmic model described in the text and the thick solid line marks the intrinsic counting rate limitations of a similarly built all-metallic PMC [5].

The gain-rate characteristics of the detector were studied for several combinations of operating voltages, plate materials and beam diameters, being the detector illuminated with X photons generated by the tube described in section 2. The results are shown in figure 8.

For all plate materials, with resistivity ranging from $4\times10^{7}\ \Omega$ cm to $4\times10^{11}\ \Omega$ cm, a reduction in gain was observed above a certain rate threshold. The threshold rate is different for each plate, but seems to be relatively unaffected by the operating voltage or by the beam diameter.

For the lower resistivity studied a counting rate of $10^{7}$ Hz/cm$^{2}$ was achieved at a gain in excess of $10^{4}$. This value is close to the intrinsic rate limitation that was found in similarly built PMCs [5], indicating that the optimum anode resistivity, that would not limit the chamber performance, should be about a few times $10^{6}\ \Omega$ cm.

*4.2 A Model of the Rate-Gain Dependence*

The simplest assumption one can make about the origin of the rate-gain dependence is that it is caused by a reduction of the effective gap electric field owing to an ohmic voltage drop across the anode plate when crossed by the avalanche current.

Mathematically the model can be expressed by the equations:

$$V = V_0 - R\,I(V)\,,$$

$$R = \rho\frac{L}{S}, \qquad I(V) = f\,e\,N_0\,G(V)\,,$$

$$\frac{ln\ G(V)}{d} = A\ exp\left(-\frac{B}{E}\right), \qquad E = \frac{V}{d}, \qquad (1)$$

where $V$ is the effective voltage across the gap, $V_0$ is the applied voltage, $I(V)$ is the gap current, $R$ is the resistance seen by the gap current, $\rho$ is the plate resistivity, $L$ is the plate thickness, $S$ is the beam cross-section, $f$ is the counting rate, $e\,N_0$ is the primary charge, $G(V)$ is the effective gain written in the Korff approximation and $d$ is the gap length. The parameters $A$ and $B$ were determined experimentally for the gas mixture used.

The available fast charge ($N_e$) shown in figure 8 is related to the remaining quantities by the usual relation

$$N_e = N_0 \, G / ln \, G \, .$$

The model relates the effective gap voltage $V$ (as an implicit function) to the other quantities. Since the plate resistivity under the actual operating conditions is the most uncertain parameter of the model (actually immeasurable directly) it was chosen as a free parameter to be adjusted to the data.

The predicted rate-gain dependence was plotted figure 8 (thin lines). It can be seen that the model describes reasonably well the observed behaviour. Additionally, in table 1 the adjusted values of the plate resistivity are show for each curve and compared to the externally measured DC resistivity. The values agree within a factor of 2, seeming to validate the model when we consider that the range of resistivities covers 4 orders of magnitude and that the model doesn't take into account the beam-edge effects or the material's non-ohmic behaviour.

| | Externally measured | Adjusted | |
|---|---|---|---|
| | | $V_{01}$ | $V_{02}$ |
| ρ (Ω cm) | $4{,}0\times10^{7}$ | $5{,}8\times10^{7}$ | $3{,}8\times10^{7}$ |
| | $3{,}8\times10^{8}$ | $3{,}5\times10^{8}$ | $1{,}8\times10^{8}$ |
| | $4{,}1\times10^{11}$ | $8{,}7\times10^{11}$ | $6{,}1\times10^{11}$ |

Table 1 - Comparison between the values of the plate resistivity ($\rho$) measured externally and the values estimated from the model after a least-squares adjustment to the data points show in figure 8. The values agree within a factor of 2, seeming to validate the model.

### *4.3 Streamer charge*

Discharges were triggered by streamers when the gain exceeded $10^6$, that is, when the avalanche charge exceeded $2\times10^8$ electrons. Since the limit for rate-induced breakdown [5] was not crossed (thick line in figure 8) this type of breakdown was not observed.

As described in section 2 the discharge current could be observed directly on an oscilloscope, being a few typical oscilograms show in figure 9. The characteristics listed to the left of the oscilograms are: plate DC resistivity ($\rho$), plate thickness ($L$), observed discharge charge ($Q_{discharge}$) and charge stored in the plate capacitor per unit area ($Q_{stored}$). The discharge charge was estimated by integrating the area under the leftmost oscilogram for each plate and $Q_{stored}$ was calculated from $C_{plate}$ (see section 2) assuming a typical applied voltage of 4 kV.

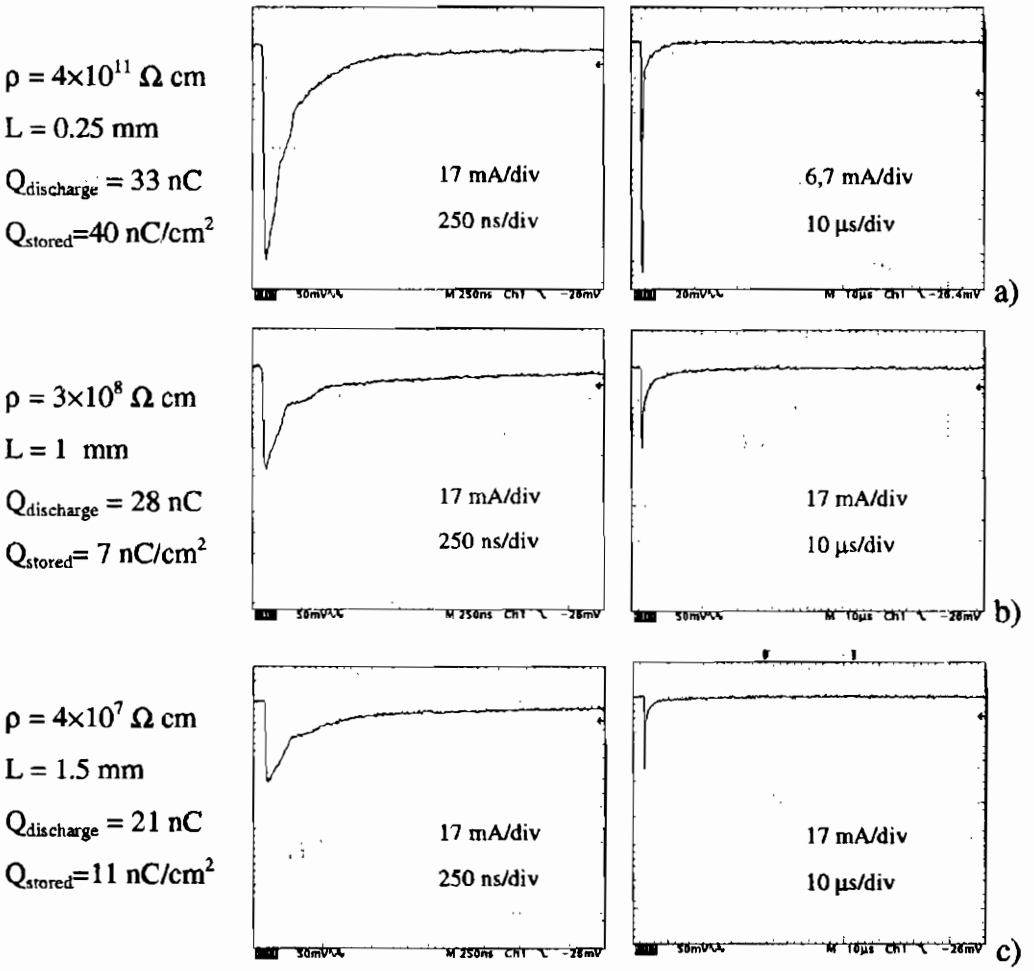


Figure 9 - Typical oscilograms of the discharge current for the anode plates studied in 2 different time scales. The quantities listed to the left of the oscilograms are: plate DC resistivity ($\rho$), plate thickness ($L$), observed discharge charge ($Q_{discharge}$) and charge stored in the plate capacitor per unit area ($Q_{stored}$).

From the values given in section 2 one can conclude that $C_{readout} >> C_{plate} >> C_{gap}$ and from figure 2 it can be seen that, from the capacitive point of view, the ratio between the charge transferred across the gap and the corresponding voltage change is dominated by $C_{plate}$.

For figure 9 a) ($\rho = 4 \times 10^{11}\ \Omega\ cm$), $Q_{discharge}$ is lower than $Q_{stored}$, corresponding to the release of the charge stored in a fraction of a $cm^2$ of the plate surface.

For figure 9 b) and c) $Q_{discharge}$ is larger than $Q_{stored}$ by a factor 2 to 3, suggesting that the conduction of current across the plate during the duration of the discharge is able to feed the discharge with an amount of charge at least comparable to the charge released from the plate surface.

Interestingly, the contribution to $Q_{discharge}$ from conduction across the plate is not proportional to the measured DC plate resistivity ($\rho$). This may be attributed to the fact that the discharge occurs in a short time (~1μs), corresponding to a high-frequency voltage pulse applied to the plate, whose high-frequency resistivity may be completely different from the DC value.

### *4.4 Type of Discharge*

According to [4] the development of violent sparks in parallel geometry is preceded by a sequence of intermediate stages comprising the following discharge types: avalanche, streamer, glow discharge, filamentary discharge and spark.

In the present case the discharges were visually identified as being of the glow-discharge type, featuring a bright cathode spot at the apex of a faint conic-shaped glow region that extends up to the anode. It seems that the current restriction imposed by the anode material prevented the process to evolve beyond the glow-discharge stage.

For the lower resistivity material ($\rho = 4 \times 10^{7}\ \Omega\ cm$) sometimes the glow discharge would be unquenched, fed by the conduction current across the plate. An increase in the amount of quencher ($C_2H_6$) in the gas mixture strongly reduced the frequency of this phenomenon, without completely avoiding it. However it seems probable that the use of more efficient quenchers like isobutane or DME would further alleviate the problem.

## 5. Conclusions

We built and tested an asymmetric Resistive Plate Chamber able to achieve proportional counting rates up to $10^5$ Hz/mm$^2$ at gains above $10^4$. The energy resolution at 5.9 keV was 20% FWHM.

The chamber was constituted by an amplifying gap delimited by a resistive plate anode and a wire mesh cathode, preceded by a drift region. A new custom-made medium resistivity material was used for the anode plate, whose resistivity could be controlled from $2\times10^7$ to $3\times10^{12}$ $\Omega$ cm.

Eventual discharges were quenched by the current limitation imposed by the resistive anode and constrained to the glow discharge phase of the sparking process. The discharge affected the detector only locally and the charge released was limited to a few nC, independently of the plate DC resistivity. This feature is attributed to the dependency of the resistivity with frequency.

The observed gain-rate trade-off is well described by a simple ohmic model and further improvements may be expected by lowering the resistivity of the anode material.

Being the characteristic relaxation time of anodic plate ($\rho\varepsilon$) of the order of a few $\mu$s, the electric transparency of the anode plate is preserved for the fast (<100 ns) electron signal. This will, in principle, allow a bidimensional strip readout to be place below the anodic plate, with typical position resolutions of 100 to 200 $\mu$m [2].

Finally, the spark protection concept presented here may be also useful when applied to other similar high-rate detectors like MICROMEGAS.

## 6. Acknowledgements

The authors gratefully acknowledge Crispin Williams and the LAA Project for lending some of the necessary hardware.

One of us (Y.Ivaniouchenkov) received financial support through the grant ERBCHBGCT920209 from the E.C. "Human Capital and Mobility" program.

This work was done in the framework of the project JNICT-CERN/P/FAE/1143/97.

## 7. References


[1] E. Ceron Zebalos, *Sci. Acta* XI-1, pp.317, 1996
A.Arefiev et al., *Sci. Acta* XI-1, pp.359, 1996
M.Angelone et al, *Nucl. Instrum. Meth.* A355, pp. 359, 1995.

[2] A. Peisert et al, *Nucl. Instrum. Meth.* A247, pp. 435, 1986
E. Ceron Zebalos, *Nucl. Instrum. Meth.* A392, pp.150, 1997.

[3] H.Raether, *Electron Avalanches and Breakdown in Gases* (London, Butterworths, 1964).
J.M.Meek, in *Electrical Breakdown of Gases*, ed. J.A.Rees (London, MacMillan, 1973)
P.Fonte et al., *Nucl. Instrum. Meth.* A310, pp.140, 1991
P.Fonte, *IEEE Trans. Nucl. Sci.* vol.43, pp.2135, 1996.

[4] S.C.Haydon, in *Electrical Breakdown of Gases*, ed. J.A.Rees (London, MacMillan, 1973).

[5] Y.Ivaniouchenkov at al, "*The high rate behaviour of Parallel Mesh Chambers*", presented at the 1997 IEEE Nuclear Science Symposium, 9-15 November, Albuquerque, New Mexico, USA, submitted to IEEE Transactions in Nuclear Science.

[6] A.Arefiev et al., *Sci. Acta* XI-1, pp.359, 1996

[7] I.Duerdoth et al, *Nucl. Instrum. Meth.* A348, pp.303, 1994
R.Cardarelli et al, *Sci. Acta* XI-1, pp.11, 1996
P.Fonte, *Sci. Acta* XI-1, pp.25, 1996

[8] A.Peisert, *Nucl. Instrum. Meth.* 217, pp.229, 1983.
J.Hendrix et al., *Nucl. Instrum. Meth.* A252, pp.246, 1986

[9] V.Peskov et al, FERMILAB TM-1838, 1993
D.F. Anderson et al, *Nucl. Instrum. Meth.* A348, pp.324, 1994

[10] B.D.Ramsey et al, *Nucl. Instrum. Meth.* A248, pp.550, 1986

# Measurement of drift velocity and amplification coefficient in $C_2H_2F_4$-Isobutane mixtures for avalanche operated RPC

Edoardo Gorini *
*Dipartimento di Fisica Universitá di Lecce, Via Arnesano, 73100 Lecce, Italy*

December 13, 1997

ABSTRACT

The knowledge of transport and amplification parameters (drift velocity, first Townsend and attachment coefficients) of the gas mixtures used for avalanche operated Resistive Plate Counters gives the possibility of better understanding the underlying physical processes of these detectors and to develop Montecarlo simulations of their behaviour. We present here a measurement of the drift velocity $v_d$ and of the amplification coefficient $\eta$ in $C_2H_2F_4$-Isobutane mixtures. The ionization in the gas, contained in a 6×22 cm$^2$, 2 mm gap RPC, was obtained by using a pulsed $N_2$ laser, through double photon processes. Results are presented for $v_d$ and $\eta$ as a function of the applied electric field.

## 1. Introduction

Resistive Plate Counters [1], because of their time resolution and rate capability when used in avalanche mode, have been chosen as trigger detectors in two LHC experiments, ATLAS [2] and CMS [3]. Much work has been done, recently, to understand the physics of these detectors when operated in avalanche mode. Even though the RPC are very

*co authors: A. Colucci *Dip. di Fisica Univ. di Lecce*, F. Grancagnolo *INFN Sezione di Lecce*, M.Primavera *INFN Sezione di Lecce*.

simple devices from the point of view of the field configuration a detailed simulation of the signal generation is still at a very early stage [4]. Important ingredients for the understanding of the detector are some physical parameters like the drift velocity $v_d$, the first Townsend coefficient $\alpha$ and the attachment coefficient $\beta$ in the operating gas mixture.

We measured the "effective" amplification $\eta = \alpha - \beta$ and the drift velocity, in the two $C_2H_2F_4$-Isobutane gas mixtures, "candidate" for the the RPC in ATLAS and CMS, respectively 97%/3% and 90%/10%, using a nitrogen laser to ionize the gas in a well localized point of the RPC gap.

## 2. Experimental Setup

A schematic view of the experimental setup is shown in Fig. 1. The RPC is a 2 mm gap, 22×6 $cm^2$ size, detector, equipped with a single copper strip 3 cm wide and 22 cm long. Given the reduced size of the detector no spacers are needed to keep apart the two bakelite planes. Two holes, located at the center of the frame longer side, allow the passage of the laser beam, parallel to the bakelite plates.

The RPC is aligned and contained in a gas tight plexiglas box (40×15×15 $cm^3$ size). The gas mixture is flushed directly into the RPC through its gas inlet and fills the entire volume of the plexiglas box. Quartz windows are provided for the entrance of the UV light in corrispondence of the frame holes. The whole box is covered with grounded aluminium to act as a Faraday cage.

The gas mixture is set by means of mass flowmeters (MKS, Mod. 1559A) and monitored by a flow controller (MKS, Mod. 147C). The gas is continuously circulated through the box volume at a rate of 20 scc/min. The accuracy on the gas composition is estimated to be 0.1%. The absolute and relative internal gas pressures are monitored by a MKS BARATRON system within an accuracy of 0.1 torr, while the gas temperature is measured within 0.1 °C.

High voltage is supplied with a CAEN SY127 system. The applied voltages for both the investigated mixtures ranges from 8.6 to 9.4 kV and accuracy of the system is about 40 V.

A system of three stepping motors, equipped with an electronic motion controller, allows for micrometric motions of the box (and of the RPC) and of the laser beam. The RPC can be moved along the parallel and transverse directions to the laser beam (respectively x and y axes

in Fig. 1) with an accuracy of about 3 $\mu$m. The laser beam can be translated along the z axis by means of a periscope. A converging lens, 10 cm focal length, is mounted solidal to the periscope. The focalized laser beam can then be moved with an accuracy of about 3 $\mu$m.

The alignment of the sistem is performed using a He-Neon laser, mirrors and calibrated pinholes. Two of these pinholes are positioned on the gas box just in front and behind the quartz windows. The parallelism of the RPC with respect to the laser beam has been accurately established.

Ionization is induced in the RPC by a $N_2$ laser (LTB, Mod. PNL-200) emitting at 337 nm. The laser has a 300 ps pulse duration, 40 $\mu J$ pulse energy output and operates at a maximum repetition rate of 20 Hz. A series optical absorbers is positioned before the periscope to reduce beam intensity in order to achieve a "single electron" ionization regime. The beam waist, after the converging lens, is about 15 $\mu m$ as measured with a slit, and the ionization region even smaller (about 7 $\mu m$), since the ionization probability depends quadratically on the UV intensity. A fraction of the laser beam is reflected from a quartz beam splitter before the periscope and directed towards a fast phototube (Hamamatsu, Mod. R1328U-52, 60 ps risetime), whose signal is used as a start for the drift time measurement.

The RPC signal is fed to two Phillips 6955 voltage amplifiers. The data acquisition is performed with a digital scope with 2 GHz sampling rate and 500 MHz bandwidth (Textronix TDS6409A). Both photomultiplier and RPC signal are readout and digitized. They are acquired via GPIB interface on a Macintosh 7100/66, equipped with LabView 3.2 analysis software. The start time from the photomultiplier is taken at, very low, fixed threshold. The stop time from the RPC is taken at the voltage peak. Time difference of the two signals and RPC voltage amplitude at peak are then recorded and stored for further offline analysis.

## 3. Measurements

At the laser focus, the UV light produces electron clusters essentially by ionizing impurities in the gas via double-photon absorption processes. These electrons, drifting through the uniform field region, produce the charge by induction on the strip.

The beam intensity is filtered down by means of optical absorbers in

order to reduce as much as possible the longitudinal ionization region, and to ensure a "single electron" regime with a final ionization rate of about one signal each ten laser pulses.

Fig. 2 shows $\Delta t$ distribution obtained at: 9.2 kV and 1.6 mm from anode, 9.0 kV and 1.0 mm and 8.6 kV and 0.6 mm for the 97%/3% gas mixture. It is worthwhile noticing that the time distributions are almost perfectly gaussian, without tails. Time resolution is mainly due to laser pulse duration, PM resolution and electronics (130-200 ps).

The differences $\Delta t$ between each mean arrival time and that corresponding to point nearest to the strip side have been plotted versus the differences $\Delta l$ between the respective drift paths given by the laser translation (in steps of 200$\mu$m). The drift velocity $v_d$, for any given value of the drift field, has been obtained as the slope of the fitted straight line of the $\Delta l$ values versus the different $\Delta t$. A set of 5 position has been used in the measure and fit, ranging from a distance of 0.6 to 1.6 mm from the strip side. In Fig. 3 is shown one of these fits for the 90%/10% mixture at 9.2 kV.

It must be stressed that this method, based on a computation of differences in space and time, cancels out indeterminations due to field uncertainties , non linear effects in the gain of the preamplifier, time resolution of the detector and, primarely, uncertainties on the absolute positions of the laser spot in the RPC gap.

Fig. 4 shows the corresponding signal pulse height peak, which are again gaussian. It is very interesting to notice the good amplitude resolution (about 20 %).

The amplitude, at different positions, has been plotted versus the differences $\Delta l$ between the corresponding drift paths. The amplitude behaviour is exponential, as expected, and is shown in Fig. 5 for 3% isobutane content gas mixture. The amplification coefficent $\eta$ has been extracted from the exponential term. The same arguments used for the time measurements apply here for the error sources.

## 4. Results

The obtained results are reported in Table 1 and Table 2 respectively for drift velocity $v_d$ and the "effective" amplification coefficient $\eta$ and shown in Fig. 6 and Fig. 7 for the two investigated mixtures versus the reduced field.

Space uncertainties coming from the spot size, the translation along

Table 1. Drift velocities (cm/$\mu s$) for the investigated gas mixtures.

| E (kV) | 10% isobutane | 3% isobutane |
|---|---|---|
| 8.6 | $8.99 \pm 0.21$ | $8.85 \pm 0.17$ |
| 8.8 | $9.99 \pm 0.20$ | $9.51 \pm 0.17$ |
| 9.0 | $11.58 \pm 0.21$ | $10.13 \pm 0.17$ |
| 9.2 | $12.97 \pm 0.21$ | $10.67 \pm 0.17$ |
| 9.4 | $13.47 \pm 0.20$ | $10.86 \pm 0.16$ |

Table 2. amplification coefficient $\eta$ in $cm^{-1}$ for the investigated gas mixtures.

| E (kV) | 10% isobutane | 3% isobutane |
|---|---|---|
| 8.6 | $60.52 \pm 0.02$ | $60.12 \pm 0.06$ |
| 8.8 | $67.38 \pm 0.03$ | $66.74 \pm 0.04$ |
| 9.0 | $74.89 \pm 0.06$ | $72.89 \pm 0.07$ |
| 9.2 | $82.22 \pm 0.05$ | $80.46 \pm 0.05$ |
| 9.4 | $91.35 \pm 0.05$ | $89.24 \pm 0.05$ |

the gap, time uncertainties from the fit to the $\Delta t$ distribution and small pressure and temperature fluctuations during a single measurement contribute to the total error on the drift velocity value at the level 1%, while uncertainties on the electric field given by the power supply are estimated to be at most of the order of 1%. Uncertainties due to the misalignment of the optical system with respect to the chamber are negligible. All measurements have been performed at room temperatures and corrected for small pressure variation.

In Fig. 6 one can notice that with lower isobutane content in the mixture the drift velocity tend to saturate earlier, which means a better stability of operation especially at high particle fluxes. The same behaviour is observed for drift velocity measurements in drift chamber [5]. As is shown in Fig. 6, the drift velocity in the RPC, as expected, is higher than in other gaseous detectors because of very high fields, main reason of the very good time resolution of those detectors.

Fig. 7 shows the behaviour of the "effective" amplification coefficient $\eta$ versus the inverse of the reduced field. The fit in figure is performed with the empirical formula by Korff [6]

$$\frac{\eta}{P} = Aexp^{(-\frac{BP}{E})} . \qquad (1)$$

where we have used $\eta$ instead of the first Townsend coefficient to take into account the attachment which is not negligible for these gas

mixtures. The resulting value for constant A and B are listed in figure for both mixtures. Data show to be still consistent with this simple parametrization, even at these high fields. Data are also consistent with the Raether limit $\eta d < 20$, where $d$ is the gap size.

## 5. Conclusions

Drift velocity and "effective" amplification measurements have been performed in two TetraFluoroEthane based gas mixtures over a limited range of RPC high voltages. This range is limited by the request of operating in avalanche mode: above 9.4 kV the streamer region, which gives a quite different behaviour to the detector starts. The setup has been then proven to work, with the possibility of investigating and measuring the transport parameters of any mixture and of furnishing also experimental inputs for the development and understanding of the physics underlying these detectors [4].

## 6. Acknowledgements

We would like to thank Dr. V.Golovatyuk for many helpful discussions and suggestion in designing the setup. Also we are indebted to our technical staff, Mr. G.Fiore, Mr. R.Gerardi and Mr C.Pinto, for their highly qualified technical assistance.

## 7. References

1. R.Cardarelli et al., *N.I.M.* **A333** (1993) 399.
2. Atlas Technical Proposal *CERN/LHCC/94-43.*
3. CMS Technical Proposal *CERN/LHCC 94-38.*
4. M.Abbrescia et al., *N.I.M.* **A398** (1997) 173-179.
5. P.Bernardini et al., *N.I.M.* **A355** (1995) 428.
6. S.A. Korff, *Electron and Nuclear Counters* (Van Nostrand New York 1946).

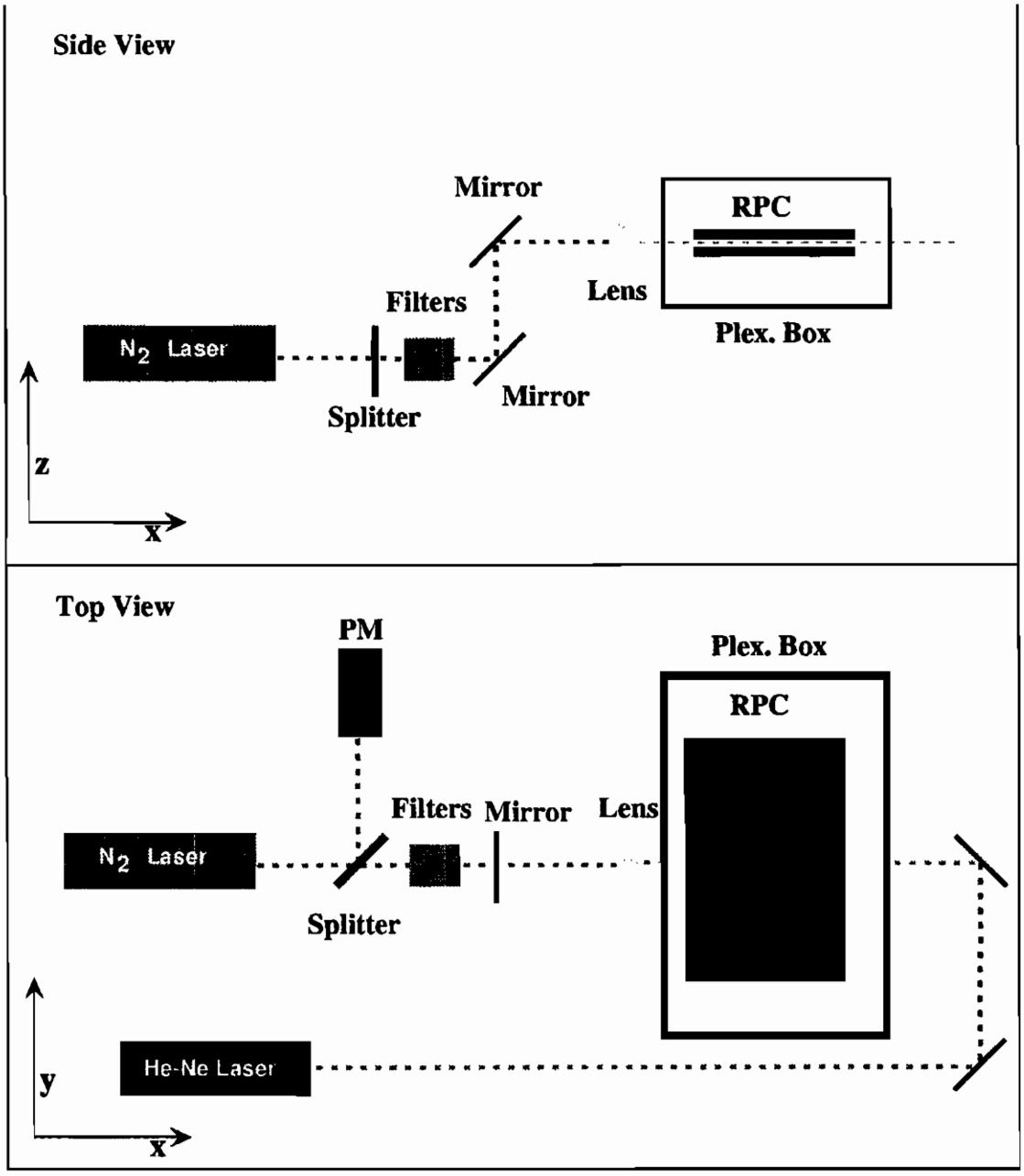


Figure 1: Schematic views of the experimental setup.

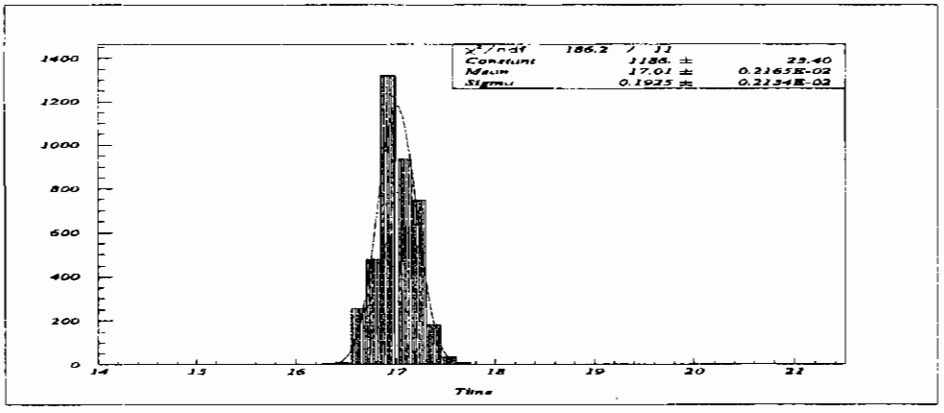


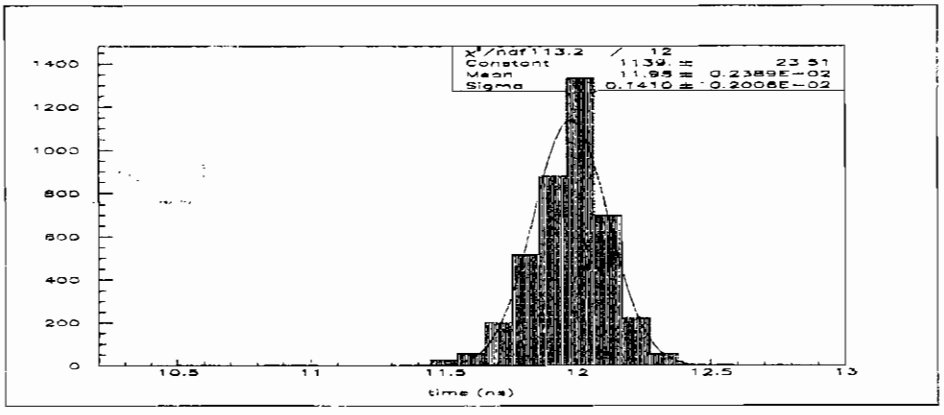


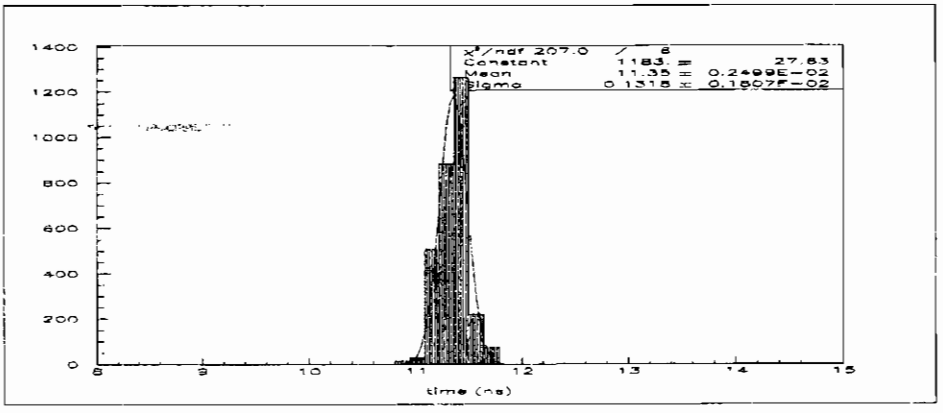


Figure 2: Distribution of the arrival time of the RPC signal at different voltages and distances from the strip inside the gap for the 97%/3% mixture: 9.2 kV (top), 1.6 mm 9.0 kV 1 mm (middle), 8.6 kV 0.6 mm (bottom)

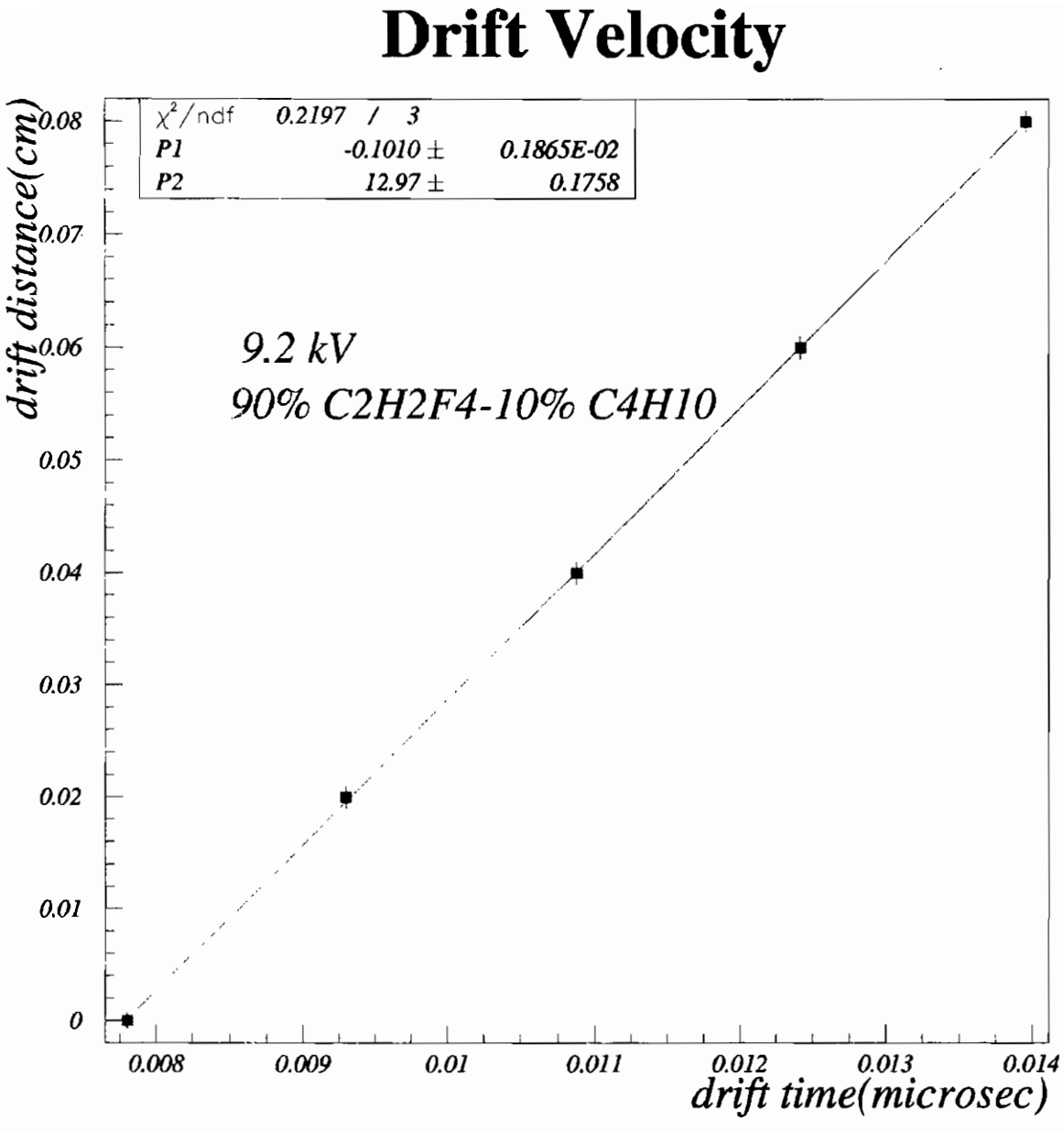


Figure 3: Drift velocity relation for the 90%/10% mixture at 9.2 kV. The errors on position are due to beam spot size and to laser-RPC relative positioning uncertainties. The superimposed fit is performed with a straight line.

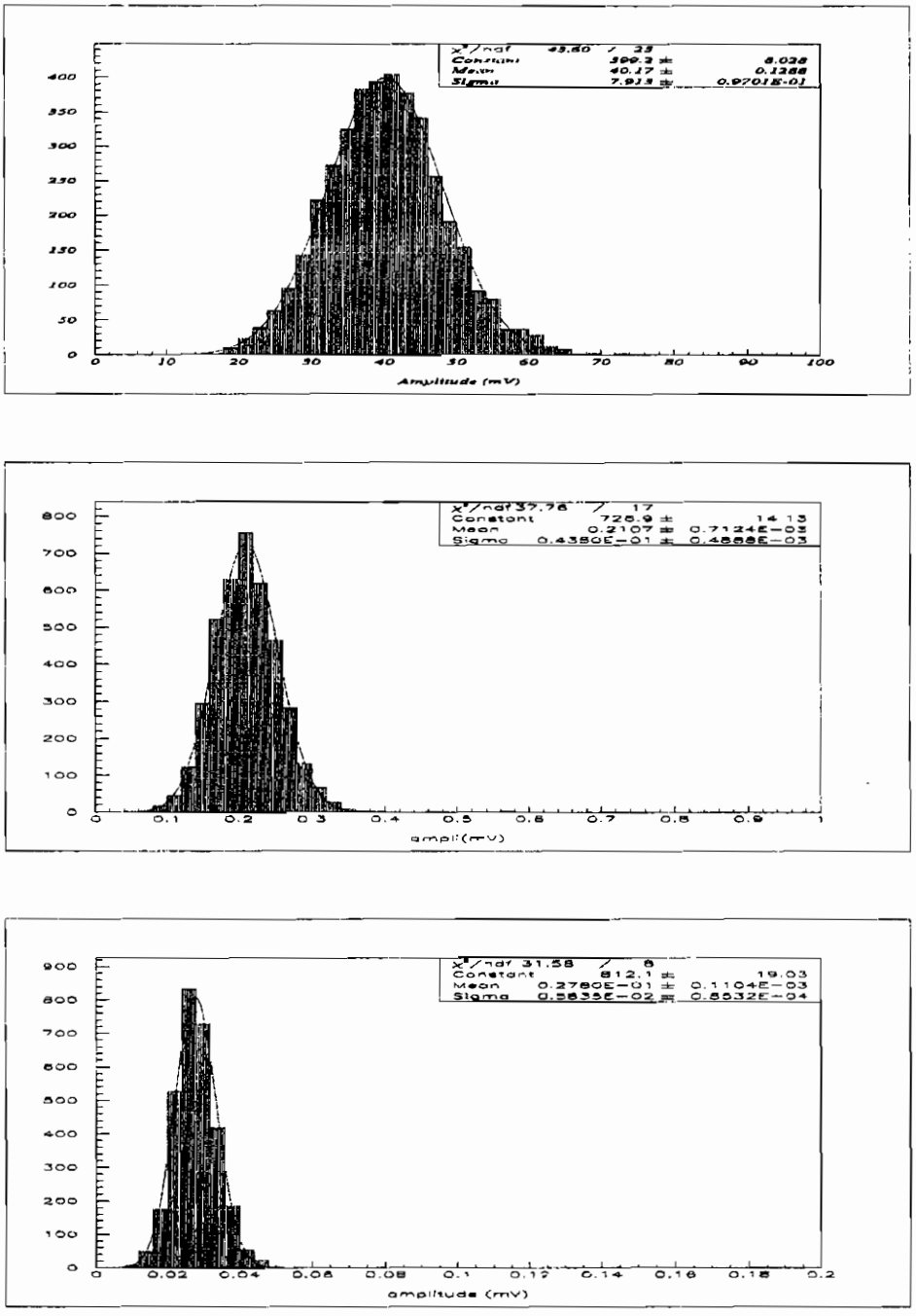


Figure 4: Distribution of amplitude of RPC signal at different voltages and distances from the strip inside the gap for the 97%/3% mixture: 9.2 kV 1.6 mm (top), 9.0 kV 1 mm (middle), 8.6 kV 0.6 mm (bottom)

# Effective amplification coefficient $\eta$

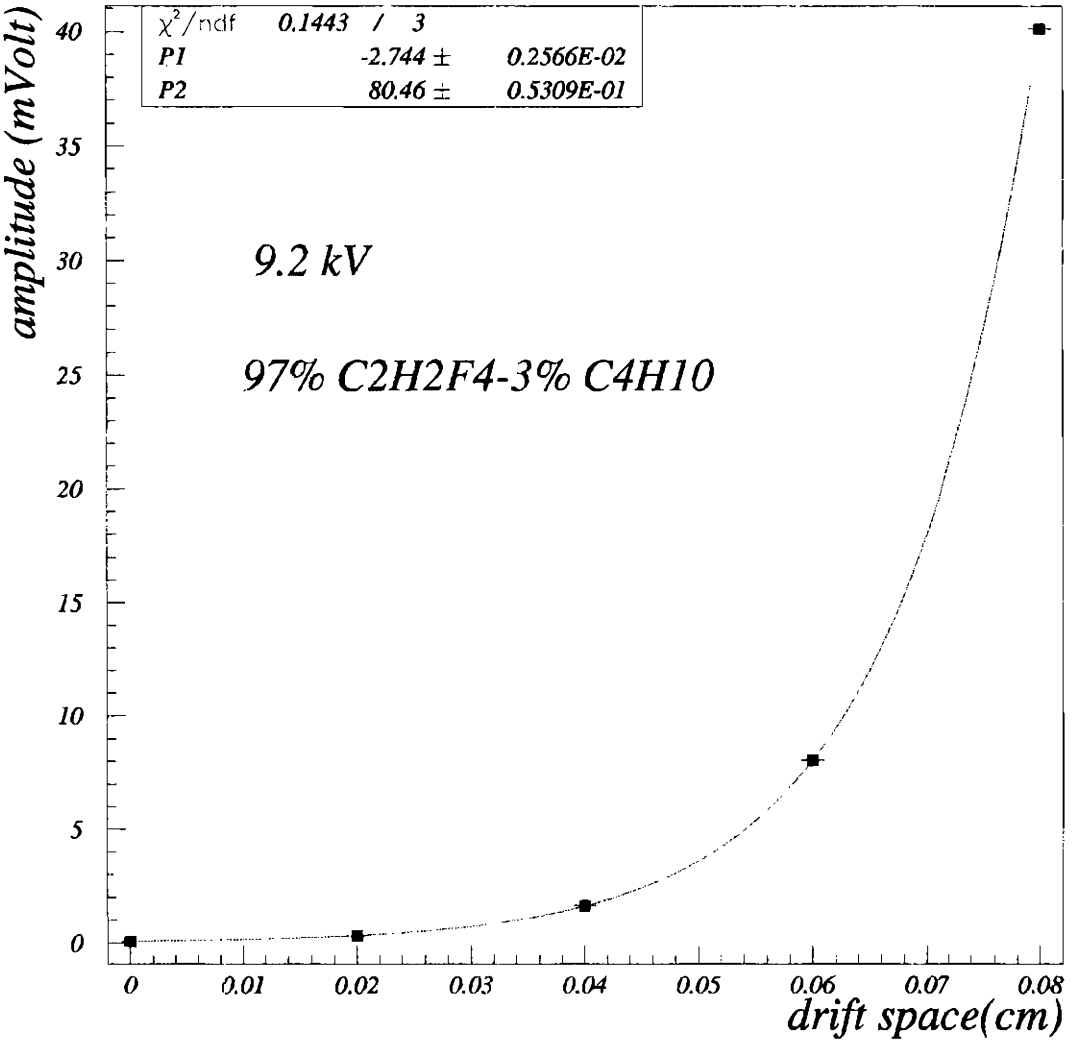


Figure 5: Amplitude vs position inside the RPC gap for the 97%/3% mixture at 9.2 kV. The errors on position are only due to beam spot size and to laser-RPC relative positioning uncertainties. The superimposed fit is performed with an exponential.

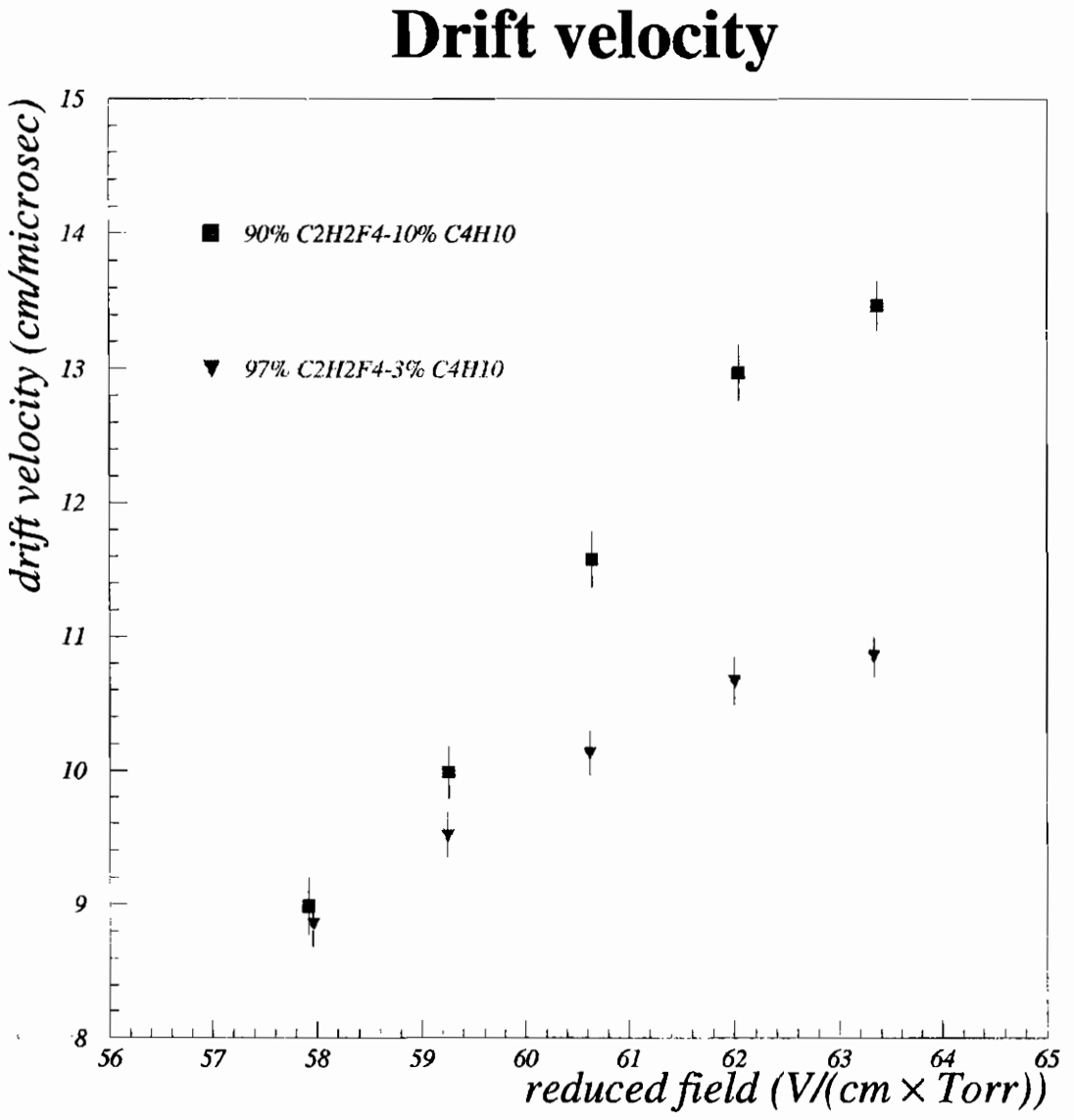


Figure 6: Drift velocity vs reduced field for both investigated mixtures.

# Effective amplification coefficient η

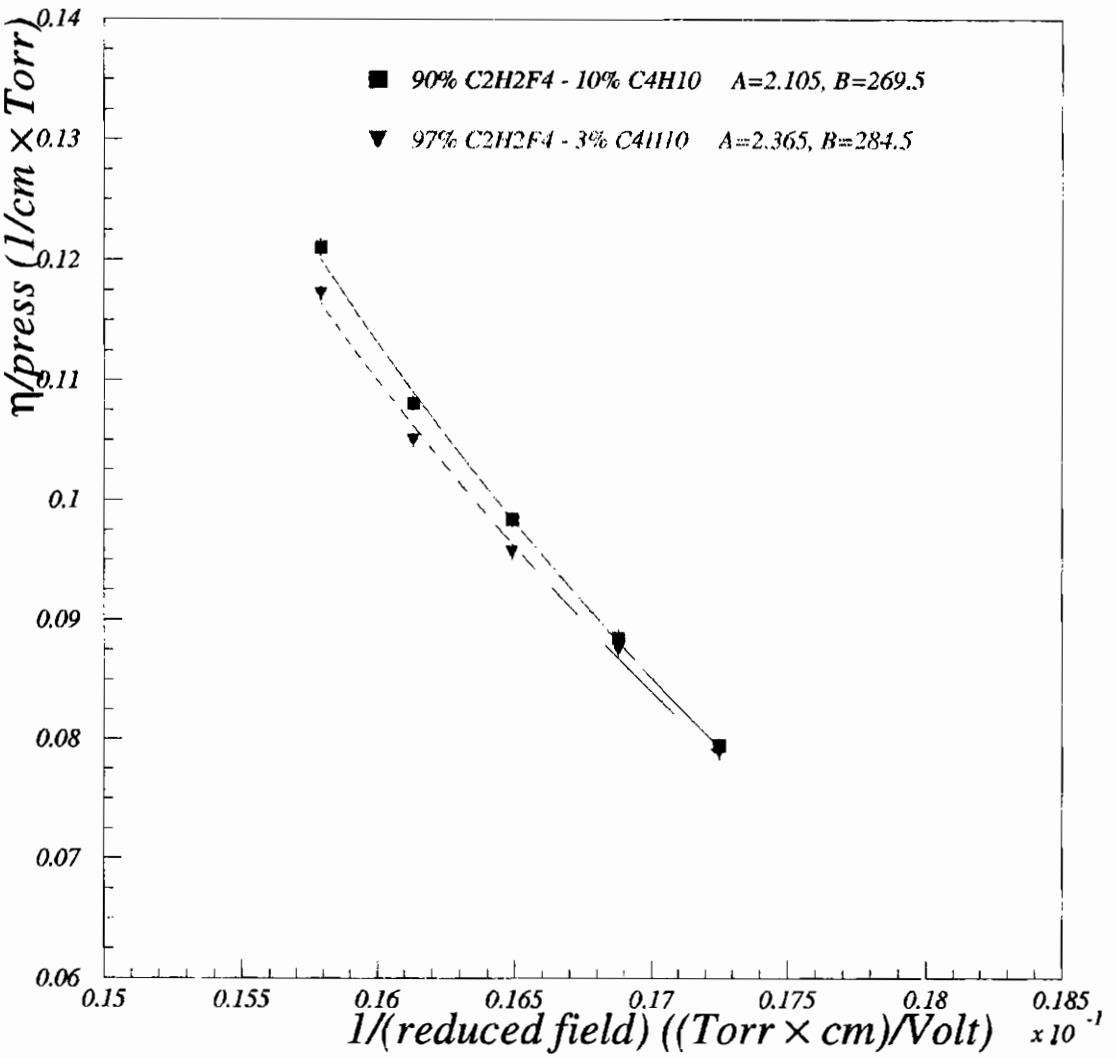


Figure 7: $\eta$/pressure vs inverse of reduced field. The fit is performed with the function described in the text.

# THE DEVELOPMENT OF THE MULTIGAP RESISTIVE PLATE CHAMBER

E. Cerron-Zeballos[1,2], J. Lamas-Valverde[1,2], D. Hatzifotiadou[2,3], M.C.S. Williams[2,3] and A. Zichichi[1,3,4].

[1] *World Laboratory, Lausanne, Switzerland*
[2] *PPE Division, CERN, Geneva, Switzerland*
[3] *INFN, Bologna, Italy*
[4] *University of Bologna, Bologna, Italy*

ABSTRACT

Some of the inspiration for the Multigap Resistive Plate Chamber came from the 3rd International Workshop on RPCs held at Pavia in 1995. In this paper we outline the development of this device; we first examine some basic problems with resistive plate chambers. We then discuss the solution offered by the multigap design. We will conclude with the current status of the development of the multigap RPC.

## 1. Introduction

The inspiration for the development of the 'multigap' RPC came from the last International Conference on RPCs at Pavia in October 1995. At that conference we presented an RPC known as the 'wide gap' RPC [1,2]. We showed that by increasing the size of the gap transitions from avalanche to streamer were supressed; thus we could work in pure avalanche mode. In a comparison between a 2 mm gap RPC filled with freon 13B1 (now banned by the Montreal convention) with an 8 mm gap RPC filled with a mixture containing a large fraction of Argon, we made the following observations: at the knee of the

efficiency plateau the wide gap had a smaller fast charge; thus smaller total charge, which gives a better rate capability and lower power dissipation in the gas. In addition, the wide gap also had a more relaxed mechanical tolerance on the size of the gas gap. However the timing of the narrow (2 mm) RPC was significantly better with a FWHM of 4 ns, compared to the 7.5 ns for the wide gap (8 mm) RPC. We were, thus, motivated to find a way to improve the time resolution of the wide gap, while keeping the other good properties.

Further input for the multigap RPC was provided by the presentation of Santonico at the Pavia conference[3]. He explained an important difference in signal generation between proportional counters and parallel plate chambers. For the proportional tube, individual clusters of electrons drift to the high field region around the wire. As there is only gas gain close to the wire, the signal comprises of a series of pulses, since the drift time of each cluster of electrons is different. However for the parallel plate chamber, there is a uniform high electric field in all the gas volume; thus the growth of all avalanches happens at the same time - the effect is that the avalanches act in parallel. In figure 1, we reproduce a schematic representation of the parallel plate chamber that illustrates this idea. However, it can easily be seen that avalanches act in parallel only if there is some mechanism to 'terminate' the growth of the avalanche. A gas gain of $\sim 10^6$ is needed to produce an avalanche sufficient to produce a detectable signal. Thus if all the small avalanches shown in figure 1 were to act in parallel, the total gain across the total gas gap would have to be incredibly high ($\sim 10^{54}$). In reality, in avalanche mode operation, only avalanches that originate close to the cathode grow sufficiently large to contribute to the signal production. However if one could find a way of 'terminating' the avalanches in the middle of the gap - then one would indeed be able to have a signal produced by many avalanches acting in parallel. This would lead to an improvement in the performance of the RPC.

The third item that triggered the development of the multigap RPC was the description given by Teramoto et al.[4] of the RPCs for the BELLE experiment. Here a single 'RPC device' has the outer

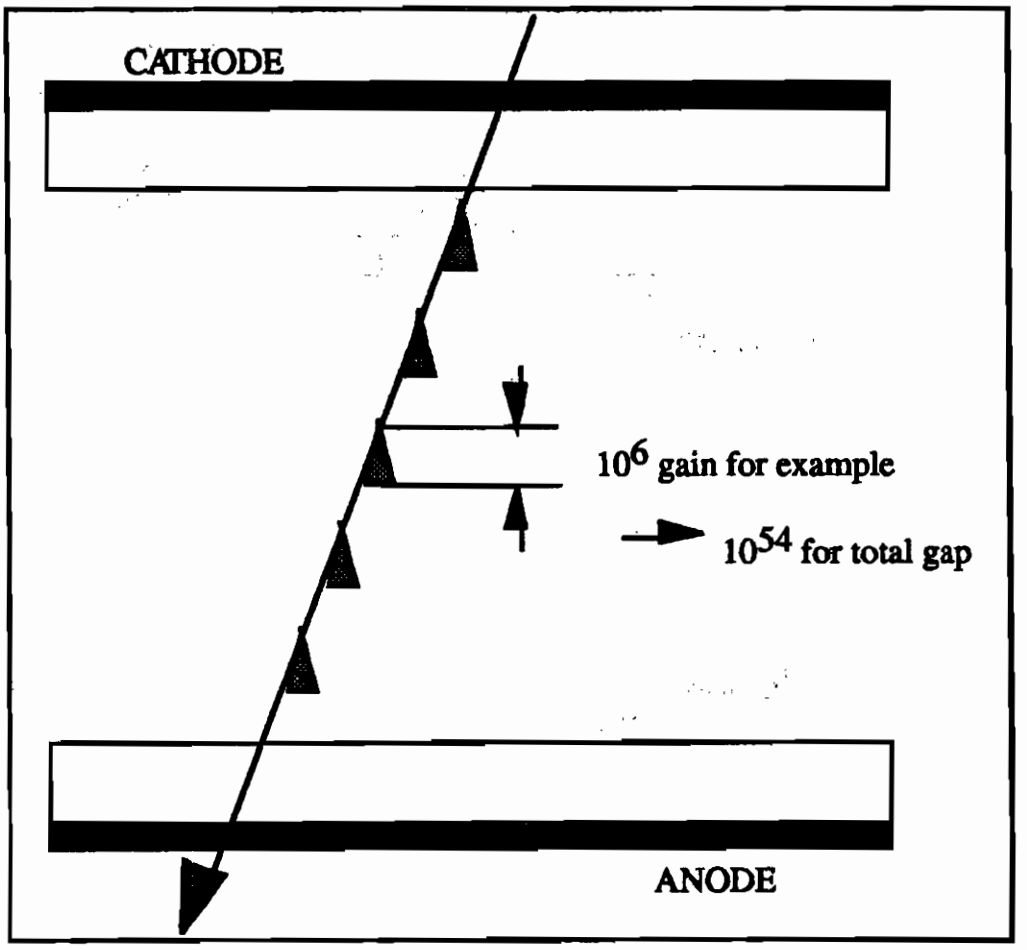


Figure 1: Avalanches from clusters of electrons produced by a through-going charged particle start growing at the same time.

surfaces equipped with theta and phi readout strips. The 'RPC device' consists of a two gap RPC with the electric field in both gaps in the same direction. The electrodes are made from high resistivity graphite layers and the two gaps insulated from each other. This is shown schematically in figure 2. The electrodes, the resistive plates and the various insulating layers are all transparent to the induced signal; thus the signal on the external pickup strips is the sum of the streamers produced in the two gaps.

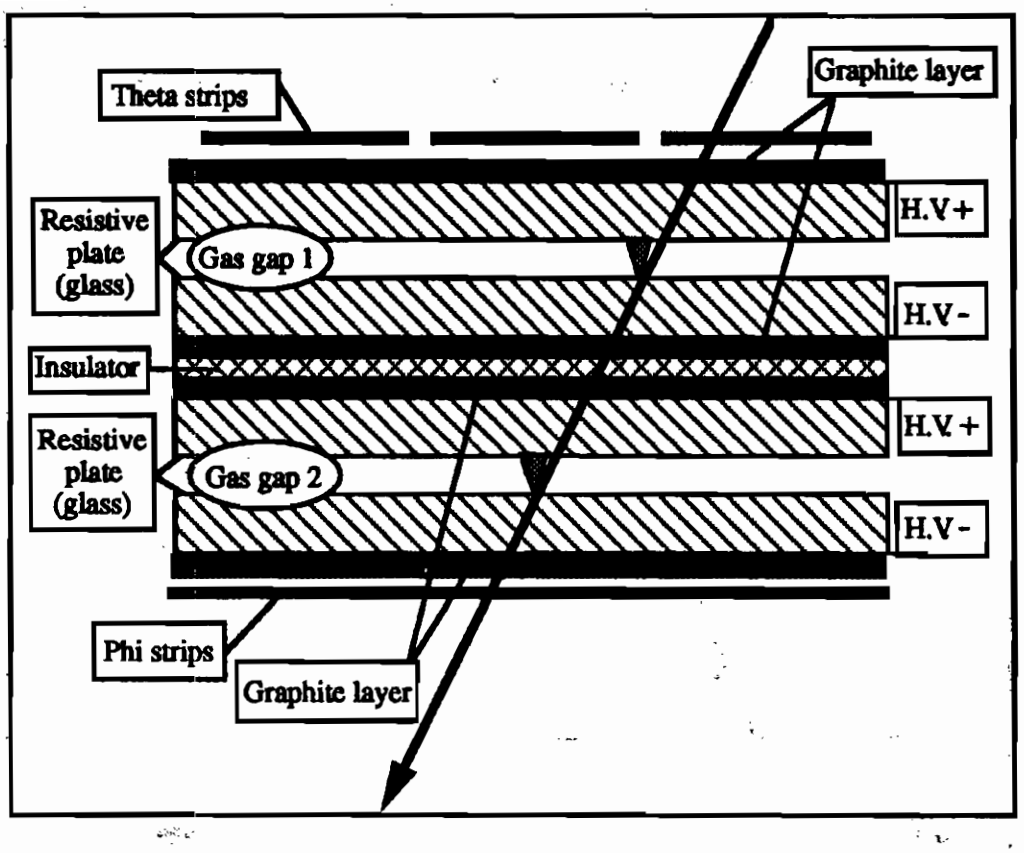


Figure 2. Schematic cross section of RPCs designed for the BELLE experiment at KEK. The streamers in the two gaps act together to generate the signals on the theta and phi pick-up strips.

We thus wanted to design an RPC which had all the good properties of the wide gap RPC but with improved timing. We also recieved the idea from Santonico that if we could make many avalanches act in parallel one would certainly enhance the performance of the RPC. Teramoto had a practical example of this; however his design was somewhat complex.

## 2. Problems with Avalanche Mode in the Wide Gap RPC

If the gas gap of an RPC is increased to enhance the streamer-free range of operating voltage, the time resolution is degraded. The reason for the time jitter is that the production of primary ionisation is a

statistical process. On an individual event basis one does not know where the clusters of ionisation will occur, or the exact number of electrons in a cluster. We need to set the gas gain such that detectable avalanches are produced from any ionisation cluster within some distance close to the cathode. For the wide gap RPC filled with an Argon based gas mixture, there are 3 clusters of ionisation produced per millimetre on average; thus there is a 4% probability that there are no clusters. Therefore one has to consider ionisation clusters anywhere within the closest 1 to 1.5 mm to the cathode. Since the drift velocity of electrons at these electric fields is ~10 ns/mm, it is easy to conclude that a time resolution of the order ~15 ns is attainable. In general, as the gap size is increased, one works at lower electric fields, therefore the drift velocity is slower. In addition the change in gain with distance is lower, so detectable avalanches can be initiated further from the cathode. These two effects increase the time jitter of the avalanche signal. However the basic problem is that a finite distance is needed for the production of primary ionisation.

There is another basic problem for the RPC which is especially apparent in the wide gap version. The number of electrons, N, created in an avalanche is given by the formula: $N=N_o e^{\alpha D}$; where $\alpha$ is the Townsend coefficient, D is the distance the avalanche avalanches and $N_o$ is the initial number of electrons. However, this is just the average number; there are fluctuations on this size which are exponential in nature. We have studied this effect by simulating the charge spectrum obtained from various RPCs[5]. Our finding is that in a single gap of an RPC, the avalanches from individual clusters of ionisation 'merge'; thus one is dominated by fluctuations. These fluctuations have a very bad effect on the charge spectrum; the most probable value is peaked at zero and there is a very long tail of large sized avalanches. This is the worse possible distribution of pulse sizes for a detector, as one needs to work at the lowest possible threshold but also contend with very large avalanches (these also can provoke the formation of a streamer). A possible mechanism of this 'merging' is as follows: close to the anode the avalanches are large; thus an avalanche can be affected by the tail of

positive ions from a preceding avalanche. Either there can be recombination, or a reduction in growth of the avalanche due to the reduced electric field.

Thus the two basic problems of operating wide gap RPCs in avalanche mode are: (a) there is only one 'merged' avalanche in a single gap RPC; the size of this avalanche is dominated by avalanche fluctuations; (b) one needs a finite distance (close to the cathode) in order that clusters of ionisation are produced; the statistical nature of ionisation within this distance generates a time jitter.

## 3. Solutions

In the top two diagrams of fig. 3 we show a schematic cross section of (a) 9 mm monogap RPC and (b) double gap (2 x 4.5 mm) RPC. For the double gap, the 1 mm region needed for creation of primary ionisation clusters can be divided into two regions of 0.5 mm. Operating these devices at the appropiate voltage for full efficiency, one finds that the maximum gain, across the 9 mm gap of the monogap RPC, is the same as the maximum gain across the 4.5 mm in the double gap case. In the case of the double gap, we find that the characteristic distance close to the cathode for production of the primary ionisation is reduced by a factor 2; thus one may expect a similar reduction in time jitter. In addition we now have two independent gaps, thus two independent avalanches. Therefore there will be an averaging of the avalanche fluctuations. Thus the double gap RPC is a big improvement compared to the mono-gap concerning the two fundamental problems of the RPC discussed in the previous section. However this solution has its drawbacks. The gas gap is half the size of the monogap chamber; therefore the tolerance on the gap size needs to be a factor of two smaller. The chamber can be read-out with a single plane of read-out strips, however they are sandwiched between the two RPC planes. This constrains the segmentation of the read-out.

In the bottom graphic of fig. 3, we show (c) a multigap RPC. The construction is similar to the 9 mm monogap shown in figure 3(a).

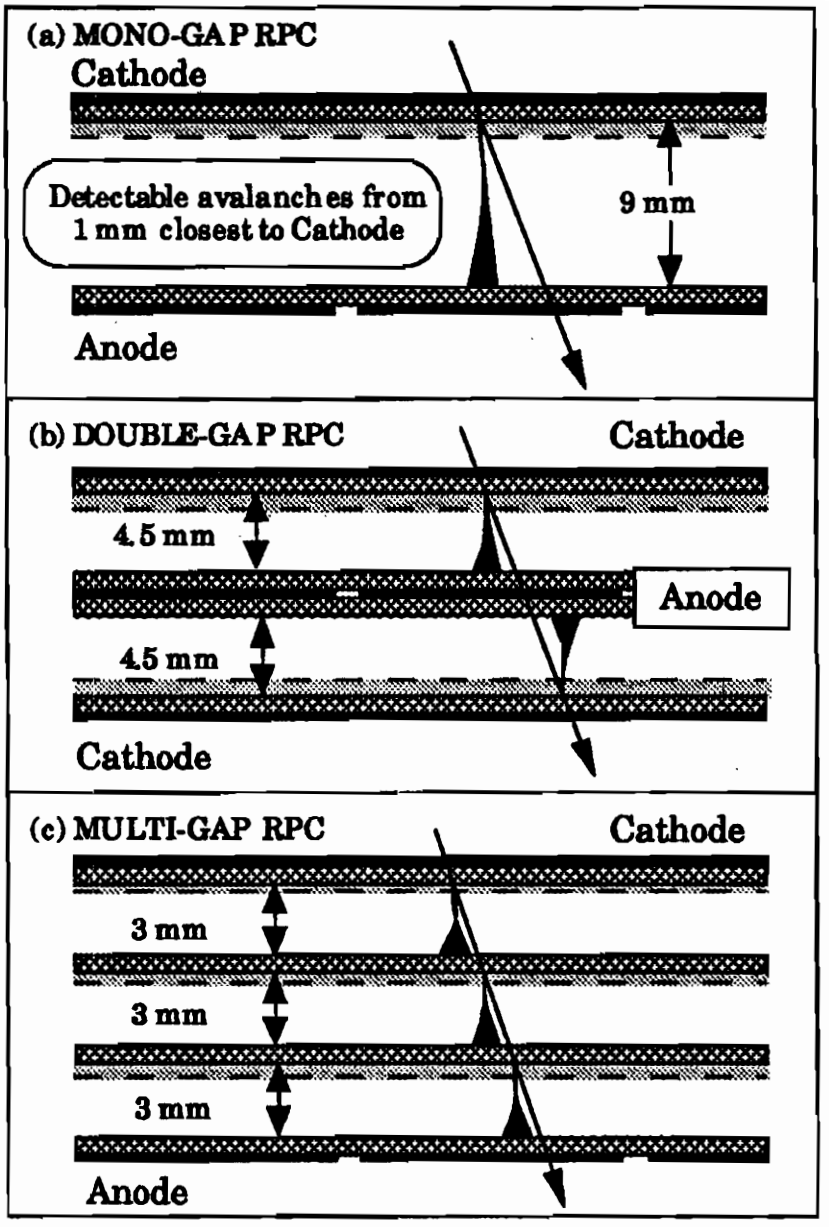


Figure 3. Schematic representation of a monogap RPC (top); a double gap RPC (middle) and a multigap RPC (bottom).

except that two extra resistive plates have been added, dividing the single gap into 3 sub-gaps of 3 mm each. The electrodes, to apply the voltage and to pick-up the induced signals, are mounted on the external

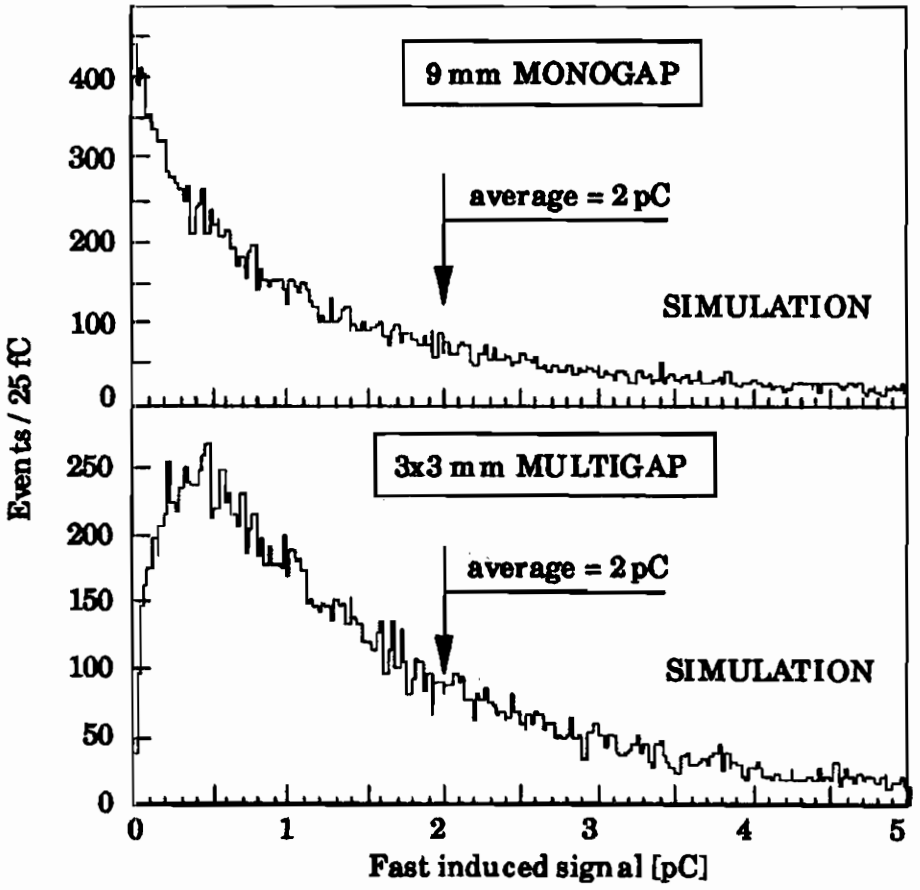


Figure 4. Comparison of simulated charge spectra for a 9 mm monogap and 3x3 mm multigap RPC. In both cases the average charge is set at 2 pC.

resistive plates. No electrical connections are made to the internal plates; they are allowed to take the voltage given by electrostatics. Each sub-gap is independent. The resistive plates act as dielectrics for the fast induced signal from the avalanches, thus the pick-up electrodes sum over avalanches in all three sub-gaps. The intermediate plates have electrons fed into them from one sub-gap, and positive ions from the other sub-gap; thus the net charge is zero. If the voltage does vary on one of the plates, the gains of the sub-gaps change. This results in a net flow of charge into the intermediate plate which adjusts the voltage such that the gas gain in all sub-gaps is equal. We have built many

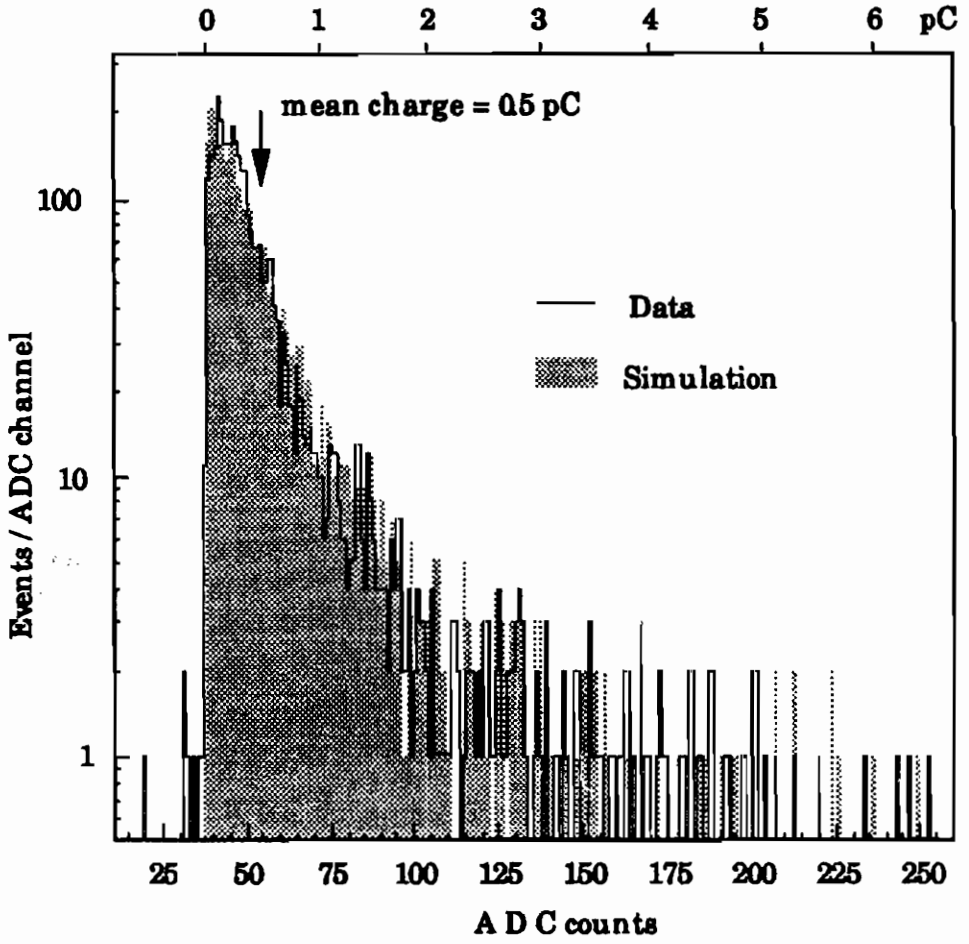


Figure 5. Measured and simulated charge distribution for 3x3 mm multigap

multigap chambers and have measured efficiency plateau curves many times in a pulsed-beam environment at various fluxes. In all our tests we have never observed any sign of instability.

For the multigap RPC, the 1 mm sensitive region of the monogap chamber is divided into 3 regions of 0.3 mm, thus bringing about a corresponding improvement of the time resolution. There are now three independent avalanches, thus the 'built-in' averaging mechanism will bring about a big improvement of the shape of the pulse height spectrum. In fig. 4 we show the simulated charge spectrum for a 9 mm monogap RPC and a 3x3 mm multigap; in both cases the average charge was set to 2 pC. In figure 5 we show the measured

charge spectrum from a 3x3 mm multigap compared to simulation; in this case the average charge is 0.5 pC.

## 4. Highlights of R&D with the multigap RPC

At the start of 1996, the multigap was a newcomer in the family of resistive plate chambers. The goal of the R&D was to gain experience with this design in order to fully understand the operation. To facilitate this understanding we have built and tested 3 variants of this chamber - (a) 2 gaps of 4 mm each (2*4 mm) (b) 3 gaps of 3 mm (3*3 mm) and (c) 4 gaps of 2 mm (4*2 mm). All three chambers were extensively tested in the T9 test beam at CERN, where many parameters were measured as a function of voltage and rate. One satisfying outcome was the very good agreement between the simulated and the measured charge spectra shown in figure 5. This has been fully discussed elsewhere[5]. This accurate simulation can be used as a tool; we have used it to investigate constructional aspects of the chamber, such as the effect of spacers and the effect of gap tolerance.

### *4.1 Results from the test beam*

Efficiency plateau curves at various fluxes for the three types of chamber are shown in fig. 6. We also show the dark current, which is very low and decreases with the number of gaps. We have noticed previously that the dark current starts to rapidly increase with over-voltage; the cause is the production of a large number of 'random' streamers; low dark current is an indication of low number of 'background' streamers. One can also see that there is a step decrease of efficiency at elevated voltages and at high rates. This is caused by 'dead areas' in the RPC created by streamers (initiated by previous through-going particles). Of course this is a region where one does not want to operate the chamber; thus there is a streamer free plateau of ~500 V for the 3*3 mm multigap and ~400 V for the 4*2 mm multigap.

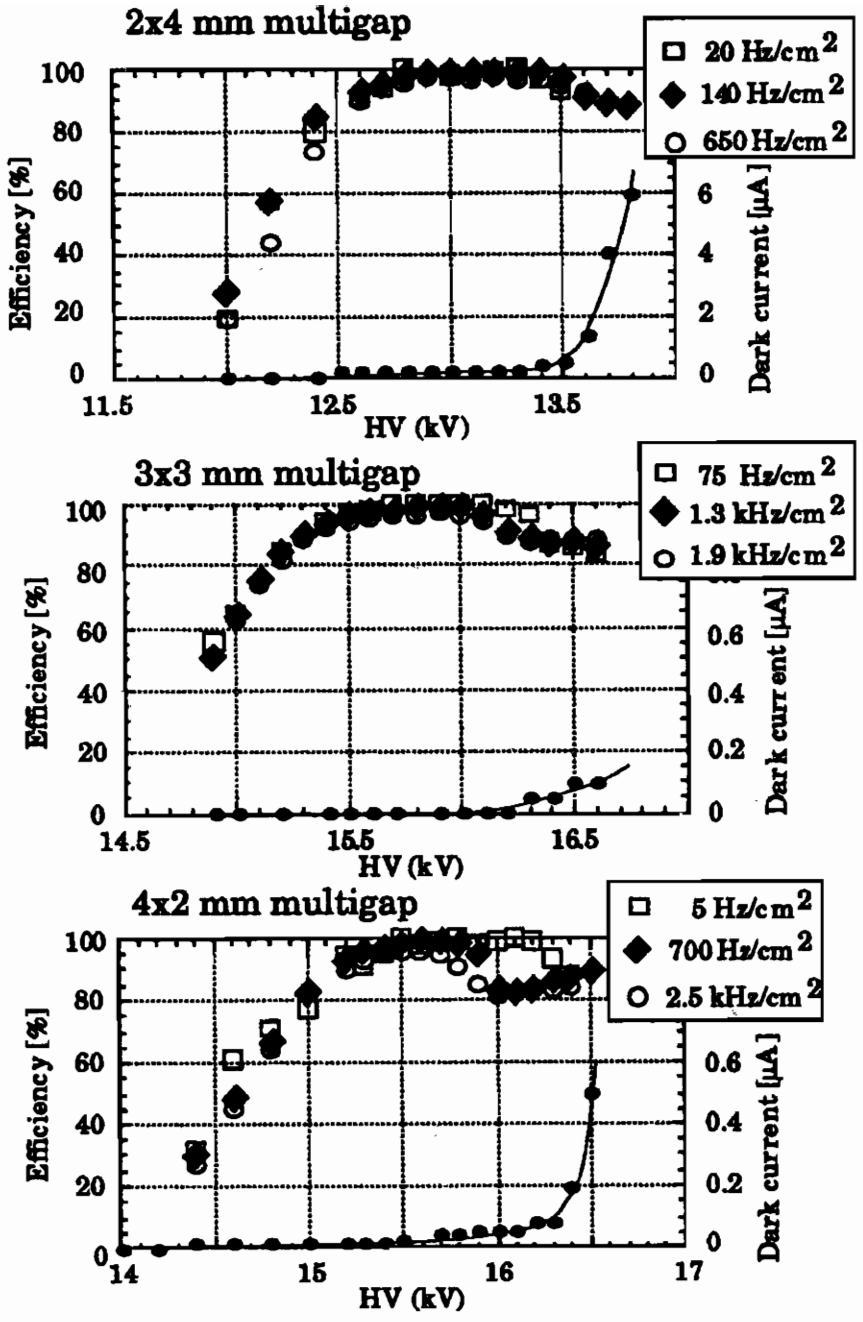


Figure 6. Efficiency versus voltage for 3 versions of the multigap RPC for various fluxes (flood illumination). The dark current corresponds to a chamber of 24x24 $cm^2$ active area. The gas mixture used was 80% Argon, 15% $CO_2$, 4% iso-$C_4H_{10}$, 0.5% $C_4F_{10}$.

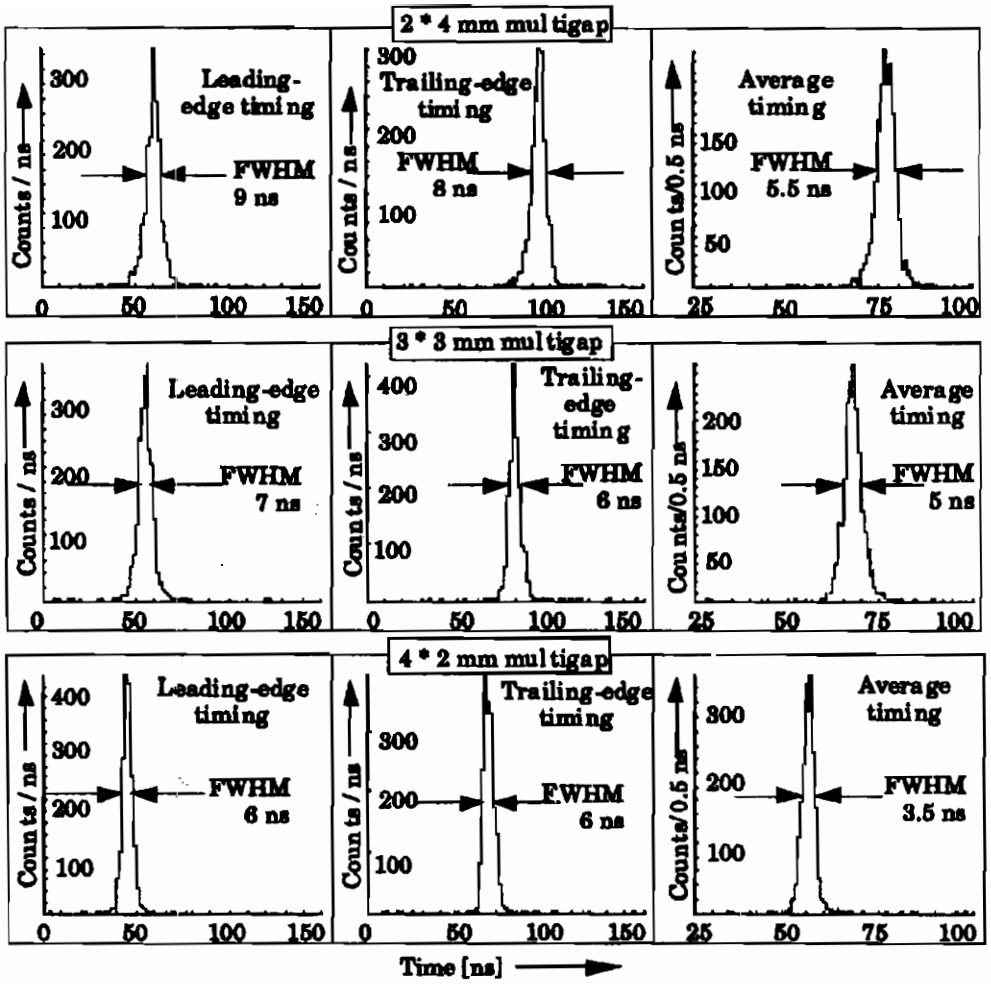


Figure 7. Time spectra for 3 different versions of the multigap RPC. A time-over-threshold discriminator is employed and the time of the leading edge, the trailing edge and the average on an event-by-event basis is shown. The histograms of the leading and trailing edge have 1 ns/bin; the 'average' histogram has 0.5 ns/bin.

In fig. 7 we show the time spectra of these three chambers. We are using a fast current amplifier followed by a time-over-threshold discriminator. We can thus measure the time of the leading edge, the trailing edge and form an average of the two on an event by event basis. This average is the first order slewing correction, and gives an indication of what we may expect from a constant fraction (or similar) discriminator. The binning is 1 ns per bin for the leading and trailing

edge histograms, and 0.5 ns per bin for the average. One can make various observations. All time spectra shift to earlier times as the gap width decreases; this decrease corresponds to a drift speed for the avalanching electrons of 10 ns/mm. The time resolution improves with an increasing number of sub-gaps as expected. Another important aspect of RPC time resolution is the time walk with voltage and rate. We will have to vary the voltage to follow atmospheric conditions; additionally, different regions of the RPC may be on different parts of the plateau curve due to variation in gap dimensions or due to a difference in rate. The mean of the time spectra is shown in fig. 8 for the 4*2 mm multigap (similar curves are obtainable from the two other chambers). It is clear that as the voltage is increased the avalanche signal becomes larger; thus the leading edge becomes earlier and the trailing edge later; however the average (i.e. slewing corrected) spectrum has a time walk of only 1 ns over a 600 Volt variation. A similar behaviour can be observed for the variation with rate. It is clear that the front-end electronics needs to have some slewing correction built-in if we are going to fully exploit the time resolution of the RPC system.

*4.2 Using the simulation as a tool*

One obvious advantage of the multigap is the installation of the spacers (necessary to fix the size of the sub-gap). These are staggered from sub-gap to sub-gap such that a through-going particle only traverses at most a single spacer. Thus, in the other two sub-gaps (in the case of a 3x3 mm multigap RPC avalanches are produced and give a signal. Additionally since the spacer has a dielectric constant greater than the gas filled gap, the electrostatic coupling between the avalanches and the pick-up strips will increase. There is yet another effect; if there is a leakage current across the spacer, the field around the spacer will be reduced; however there will be a corresponding increase of electric field in the other two gaps. We can compute the effect of having 3 sub-gaps and also the case of 2 sub-gaps (with increased electrostatic coupling).

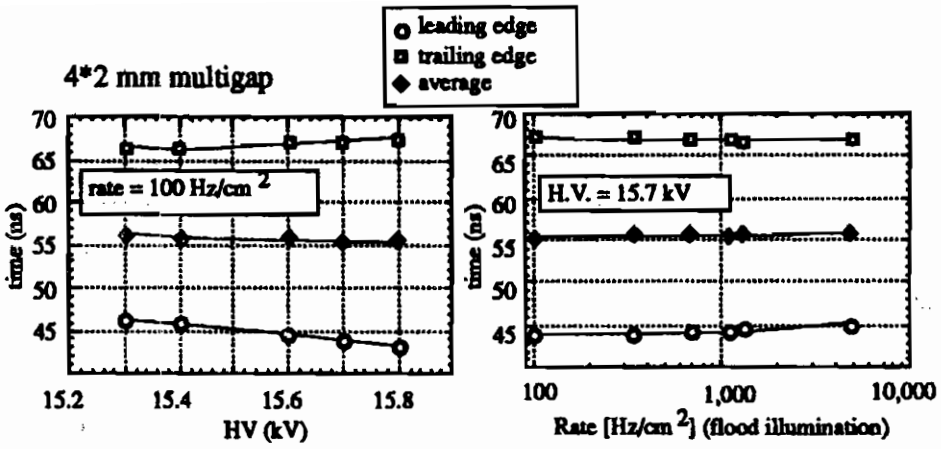


Figure 8. Mean of time spectra for the leading edge, trailing edge and the average versus high voltage and rate.

This is shown in fig. 9, where the efficiency versus threshold is shown for these two cases. If one worked at a 15 fC threshold and covered 20% of the active area with spacers, the global efficiency would fall from 99.5% to 98.7%. To compute the effect of leakage current is not possible; however we scanned over a spacer bar with a very defined beam. We observed a small rise in efficiency leading us to believe that the leakage current balances the drop of efficiency by increasing the electric field in the two sub-gaps that are without spacers at that point.

Another important advantage of the multigap is that the electric field is defined by the voltage applied across the three gaps. The field in the individual sub-gaps is the same for each. We can compute the effect of a change in the total gap dimension. For example if we consider the case of a 3x3 mm multigap, there are 9 mm of gas. If we increase this gap to 9.3 mm keeping the applied voltage the same, there will be a lowering of the electric field; thus a lower gas gain. However the avalanche has now an increased distance to develop in, which can partially compensate the drop in gas gain. In fig. 10 we show in the upper plot our measurement of the Townsend coefficient $\alpha$, versus applied voltage for the 3x3 mm multigap. In the lower plot we show efficiency versus threshold for 4 cases. The top curve is the 3x3 mm

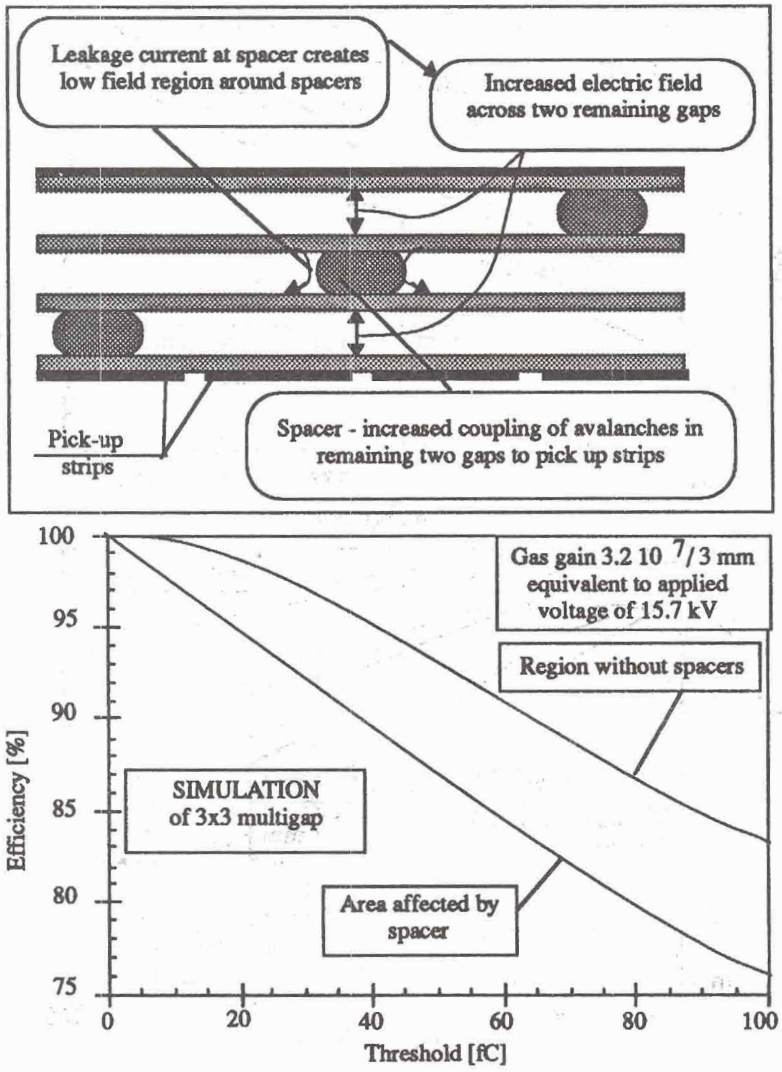


Figure 9. Effect of spacers in a multigap RPC. Leakage current across the spacer leads to a higher field in the two remaining sub-gaps. This effect has not been simulated.

multigap with an applied voltage of 15.9 kV. The lowest curve corresponds to an electric field obtained by increasing the gas gap to 9.3 mm, but keeping the individual sub-gaps to 3 mm in size. The

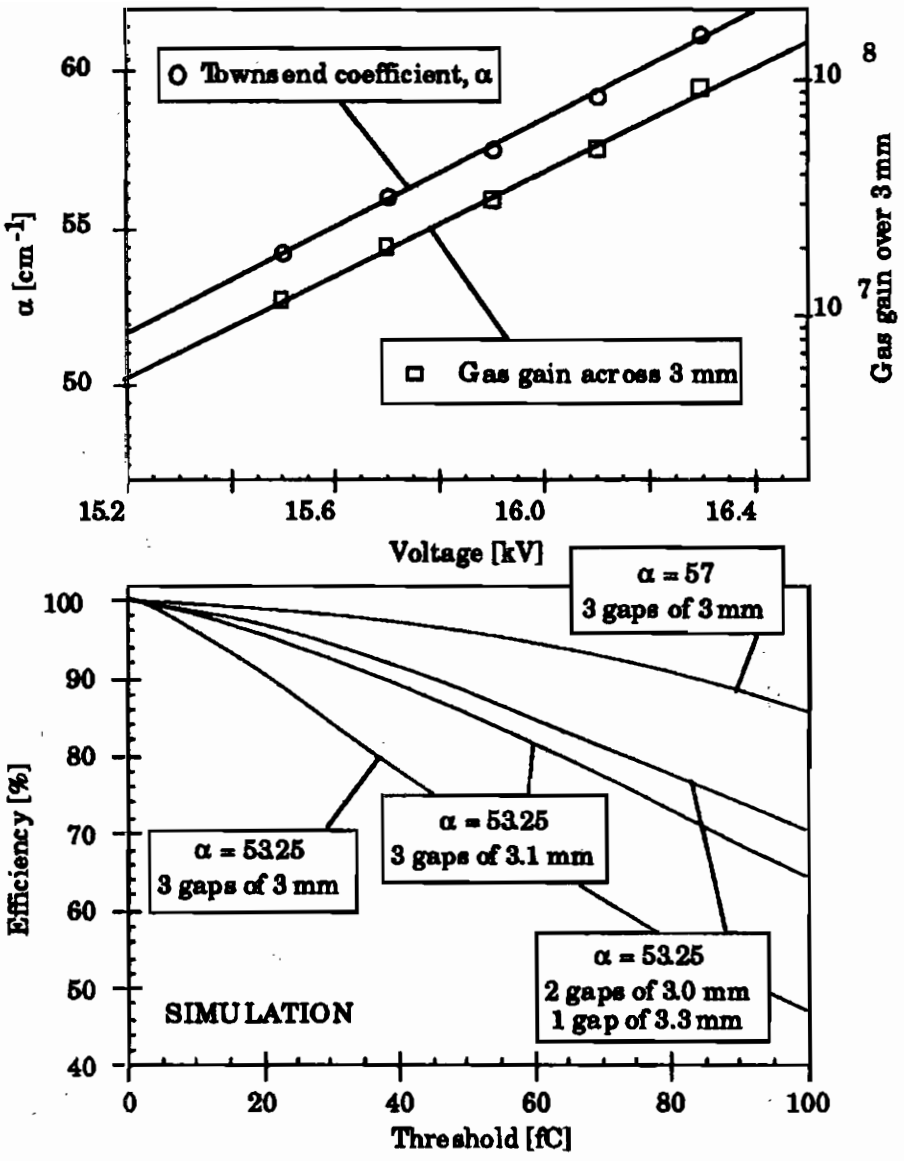


Figure 10. Simulating the increase of the total gap width from 9.0 to 9.3 mm. See text for details.

two intermediate curves correspond to two cases: either the 300 μm is applied to only one sub-gap, or each sub-gap is increased by 100 μm. One can see that there is a compensation effect; the reduction in field caused by the increase of gap size is partially compensated by the additional distance that the avalanche has to develop in. This

compensation is about a factor 2. Whether there is a compensation effect or not depends on the variation of gas gain with electric field, and the variation of field with gap dimension. Since the voltage applied to the multigap is across the full 9 mm, the change in field with gap size is much smaller than for conventional narrow gap RPCs. We can calculate the tolerance for the construction of the multigap RPC; this is (500V/15500V)*9000 μm *2 = 580 μm (i.e. $\sigma = 580/\sqrt{12} = 170$ μm).

## 6. Conclusions

We have discussed the problems associated with operating resistive plate chambers in avalanche mode. We show that the multigap design alleviates these problems. In addition the multigap RPC satisfies the requirement for a muon trigger device for the LHC collider.

## References


1. What have we learned from a comparison between the Wide Gap and Narrow Gap Resistive Plate Chamber, E. Cerron Zeballos, I. Crotty, D. Hatzifotiadou, J. Lamas Valverde, S. Neupane, V. Peskov, S. Singh, M.C.S. Williams and A. Zichichi, Proceedings of the Third International Workshop on Resisitve Plate Chambers and Related Detectors, Scientifica Acta Vol XI, Anno XI, Numero 1, page 295
2. Latest Results on the performance of the wide gap RPC, E. Cerron Zeballos, I. Crotty, D. Hatzifotiadou, J. Lamas Valverde, S. Neupane, V. Peskov, S. Singh, M.C.S. Williams and A. Zichichi, Proceedings of the Third International Workshop on Resistive Plate Chambers and Related Detectors, Scientifica Acta Vol XI, Anno XI, No 1 (1996) page 317
3. Topics in Resistive Plate Chambers, R. Santonico, Proceedings of the Third International Workshop on Resistive Plate Chambers and Related Detectors. Scientifica Acta Vol XI, Anno XI, No. 1, (1996) page 1.
4. R&D of Glass RPCs for the BELLE Detector, Y. Teramoto, A. Yamaguchi and Y. Hoshi, Proceedings of the Third International Workshop on Resistive Plate Chambers and Related Detectors. Scientifica Acta Vol XI, Anno XI, No. 1 (1996) page 401.
5. Avalanche Fluctuations within the Multigap Resistive Plate Chamber. E. Cerron-Zeballos, I. Crotty, D. Hatzifotiadou, J. Lamas-Valverde, R.J. Veenhof, M.C.S. Williams and A. Zichichi; Nucl. Inst. and Meth. A 381 (1996) 569

# THE MICRO-GAP RESISTIVE PLATE CHAMBER

E. Cerron Zeballos[1,2], D. Hatzifotiadou[1,4] J. Lamas Valverde[1,2], E. Platner[5], J. Roberts[5], M.C.S. Williams[1,4] and A. Zichichi[1,3,4]

[1]*PPE Division, CERN, Geneva, Switzerland*
[2]*World Laboratory, Lausanne, Switzerland*
[3]*University of Bologna, Bologna, Italy*
[4]*INFN, Bologna, Italy*
[5]*Bonner Lab, Rice University, U.S.A.*

ABSTRACT

Previously we have found that the freon $C_2F_5H$ has very good properties when used in a resistive plate chamber (RPC) with a single gap of 2 mm. In this paper we report on the performance of a multigap RPC consisting of 4 gaps of 0.8 mm filled with a gas mixture containing this freon.

## 1. Introduction

Previously, we tested [1] two freons in a single 2 mm gap RPC. The first freon was $C_2F_4H_2$ favoured by both ATLAS and CMS LHC experiments; the second freon was $C_2F_5H$. We found that the streamer-free efficiency plateau could be extended from 50 V to 500 V if $C_2F_5H$ is used in place of $C_2F_4H_2$. Additionally we showed that if a streamer was produced in $C_2F_5H$, it was less violent (more quenched) than in $C_2F_4H_2$ and 'prompt' in time, while streamers in $C_2F_4H_2$ are produced after a characteristic delay [2].

At this workshop, we have already reported on a type of RPC that has good time resolution, low time walk and good rate capability;

this type of RPC is known as the multigap RPC [3,4,5]. The details of this device can be found elesewhere in these proceedings[3]. Since the total gas gap in these devices was 9 to 10 mm, we could not use a gas mixture with a high fraction of freon as this would require an extremely high voltage.

However we know that this freon, $C_2F_5H$, has beneficial properties for a single 2 mm gap RPC; the question is: what can we achieve with a series of narrow gaps? In this paper we report the results from testing a 4*0.8 mm multigap RPC filled with a gas mixture mostly consisting of $C_2F_5H$. This version of multigap we call the microgap, since each of the gaps that make the series is less than one millimetre in size. It should be noted that Ammosov et al. [6] have already obtained encouraging results with a 3*1 mm and 3*1.5 mm filled with a gas mixture containing $C_2F_4H_2$.

## 2. Construction of the chamber

We have built two microgap chambers; the first was rectangular with a size of 35x45 $cm^2$; the second was a wedged shaped chamber of dimensions 2.5x1.2 $m^2$. Both chambers shared a similar construction technique. We will discuss some details of the construction of the large wedged shaped chamber. The size of this large chamber was constrained by the size of honeycomb panels we had on hand (2500 x 1250 x 6 $mm^3$) and the size of our flat table (2500 x 1500 $mm^2$). We chose a non-rectangular shape for the chamber in order to learn about problems related to large detectors of arbitrary shape; we selected this particular wedge shaped geometry since it matches the geometry of typical endcap detectors at LHC.

The cross section of the chamber is shown in figure 1. It consists of four 800 μm wide gas gaps. To ensure the relative uniformity of the gas gaps, 1 cm wide spacer bars, were placed every 5 cm in each gap; these were offset from gap to gap so that a through-going particle would only pass through 1 spacer bar. It should be noted that due to the high density of spacer bars, in general only 3 of

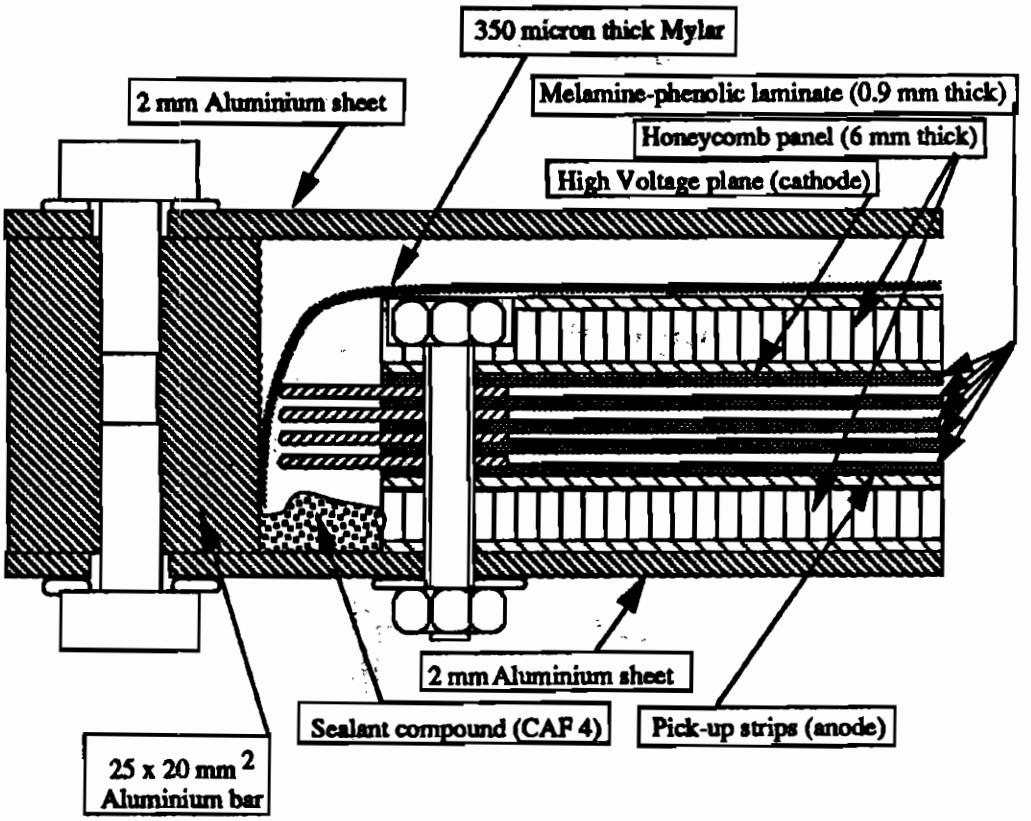


Figure 1: Cross section of microgap RPC showing detail at edge.

the 4 gas gaps are active for a through-going particle. The spacer bars were made of Bakelite sheet cut into strips (Bakelite was chosen due to availability in the CERN stores). The nominal thickness was 0.5 mm, but varied between 0.48 and 0.54 mm for the various sheets we used; the thickness of the spacer bar was increased to 0.8 mm by applying a layer of double-sided adhesive tape on each surface. Similar spacer bars were used around the perimeter; however these were 2 cm wide and 12 cm long. Holes were drilled every 10 cm around the perimeter and nylon bolts inserted. These bolts served two purposes; the first to provide a more secure system to hold the chamber together (in addition to the double sided tape); the second purpose is to attach the chamber to the aluminium plate, which serves as the main support element for the

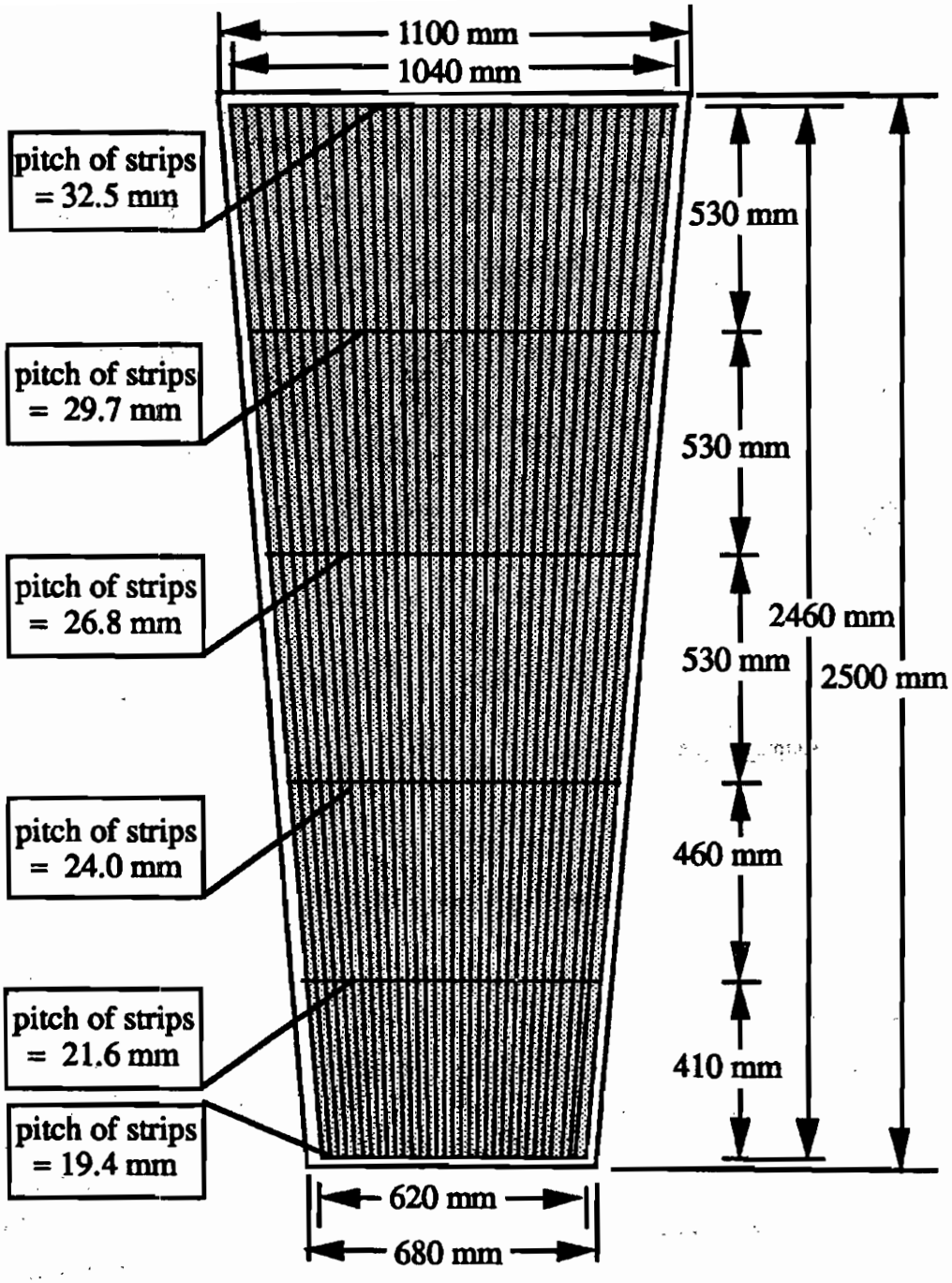


Figure 2: Layout of pickup strips for the large chamber. The inter-strip gap was 1.5 mm.

chamber. We did not want to glue the aluminium to the honeycomb panel since a change in temperature would lead to stresses that would cause the chamber to warp. The perimeter spacers were placed such that after each 12 cm spacer there was an 8 cm gap. The position of this gap alternated from layer to layer. The existence of this gap allowed gas to freely enter the gas gaps of the detector. There were additionally 15 nylon bolts inserted through the active region of the chamber. These were aligned with an internal spacer bar in the gas gap closest to the high voltage plane; spacer washers of diameter 16 mm were used for the other gas gaps.

The layout of the pickup strips is shown in figure 2. The design consists of 32 wedge-shaped strips divided into 5 regions. We used aluminium-coated melamine-phenolic laminate to construct the read out strip plane. We supplied a roll of aluminium foil (25 μm thick) to the manufacturer* of the melamine-phenolic laminate. The aluminium foil was applied to the phenolic surface at the time when the boards were being pressed; the phenolic layer itself is used to adhere the aluminium. We etched this aluminium into strips for the small chamber using conventional printed-circuit production techniques. The pickup strips for the large chamber were cut by hand with a scalpel; obviously this operation would be performed by some industrial technique if mass production of this type of chamber is envisioned. The high voltage plane was constructed from a similar aluminium-coated melamine-phenolic panel. In both planes we removed the aluminium layer in a 2 cm diameter region around the internal spacer/bolts.

We cut 16 mm holes through the outer aluminium sheet; this was aligned with 19 mm diameter holes through the honeycomb panel. These holes allowed us to make an electric connection to the pickup strips (and thus to read out the strips). These holes were positioned at the intersection of four pickup strips.

---

* Argolite S.A. CH-6130 Willisau

A large sheet of mylar (350 μm thick) was used to isolate the aluminium cover from the high voltage plane. This was cut slightly larger than needed so that the excess could curve down and provide high voltage protection for the chamber from the aluminium side bars. A silicon based sealant (CAF-4) was liberally used to seal the aluminium sheets to the aluminium frame. The honeycomb was also sealed to the aluminium sheet on the pick-up strip side. Additionally all nylon bolts were coated with this sealant.

## 3. Results of tests

We tested both these chambers in the T9 test beam in the East Hall. The tests were mostly performed with a negative 8 GeV/c pion beam; the flat-top of the spill lasted 0.25 s and we had one, two or sometimes three spills every 15 s. Initially we used a gas mixture of 95% $C_2F_5H$ with 5% iso-$C_4H_{10}$ bubbled through a water reservoir at 10°C (gas mixture A). The addition of 1% water vapour was to keep the resistivity of the melamine-phenolic plates at a low value, ~$10^{11}$ Ωcm. The knee of the efficiency plateau with this gas mixture was at 17 kV; using a different mixture of 85% $C_2F_5H$, 10% Ar and 5% iso-$C_4H_{10}$ also bubbled through water at 10°C (gas mixture B) the knee was at the lower voltage of 16.2 kV. The large chamber was only tested with mixture B.

### *3.1 Efficiency and rate capability*

This large chamber was sealed one day before our beam test, which lasted only 3 days. The performance of the chamber improved over these 3 days, in particular the dark current dropped by a factor 2 each day. The dark current plotted in figure 3 is the result obtained after flowing gas for 3 days. This value is about a factor 2 higher thanwe would expect if we just scaled up with the area from the small chamber. The data was obtained with a defocused beam where the

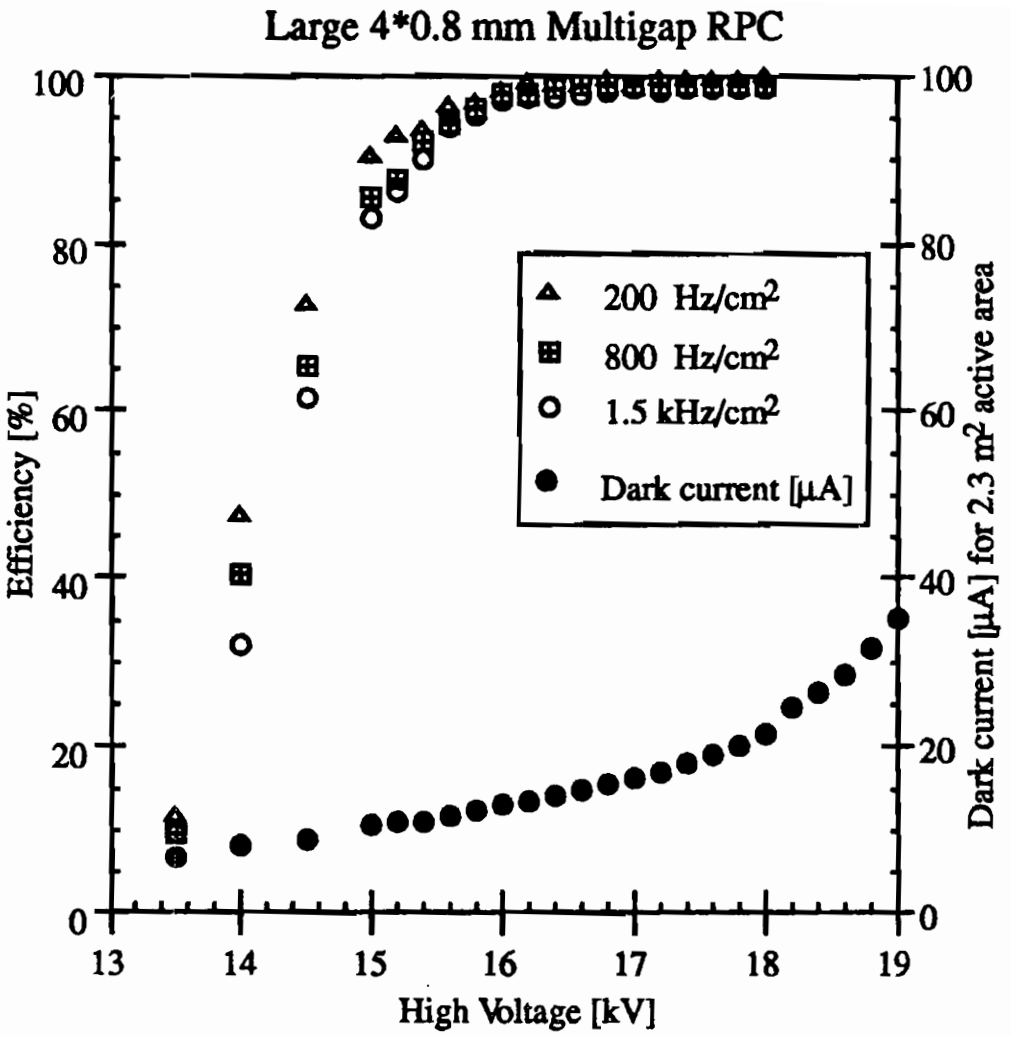


Figure 3: Efficiency versus voltage for various particle fluxes (large area illumination). The dark current is also shown. The gas mixture was 85% $C_2F_5H$, 10% Ar and 5% iso-$C_4H_{10}$ bubbled through water to add 1% water vapour.

beam was uniform over a 30 cm diameter area. The central 4x4 $cm^2$ region was selected with a scintillator.

We show in figure 4 the efficiency versus rate for the small (35x45 $cm^2$) chamber for the two gas mixtures at a voltage just above the knee of the efficiency plateau. It appears that the gas mixture B has slightly improved rate capability; this is consistent with a reduction in the charge (see section 3.4).

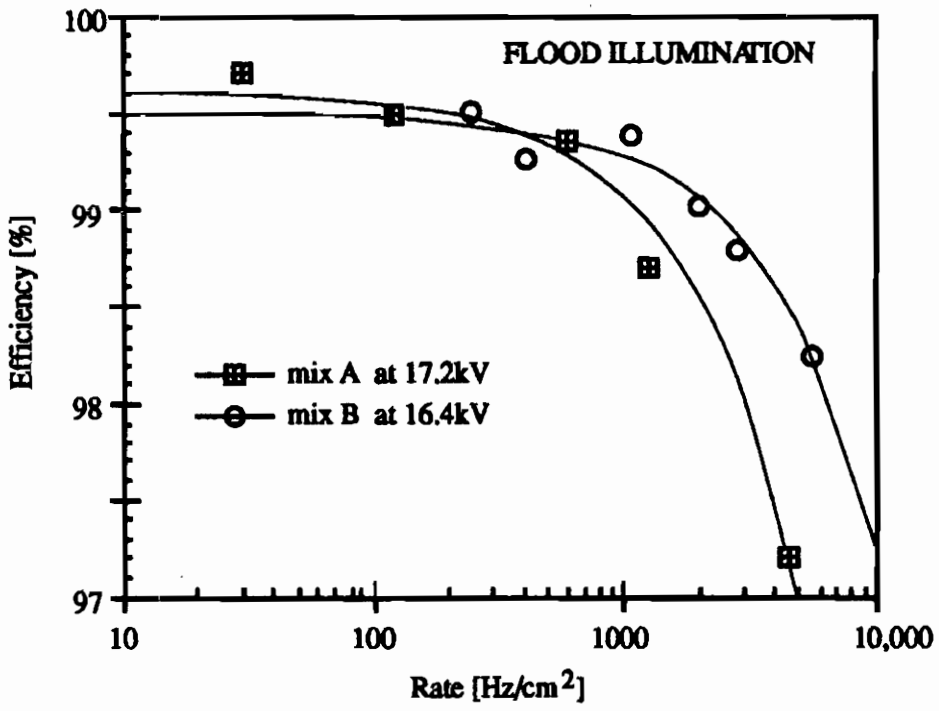


Figure 4: Efficiency versus rate for the two gas mixtures. The beam was defocused and illuminated the complete active area of the chamber.

### *3.3 Time resolution and time-walk*

The time resolution is excellent with this type of chamber. The signals are amplified with a current amplifier with a peaking time of ~5 ns and then discriminated with a simple leading edge discriminator. Our threshold is ~10 fC. In general a 4x4 $cm^2$ scintillator selected 3 strips; we select one strip (the strip with the highest rate) for this study. No corrections have been made for time slewing or for the jitter of the scintillator. The time spectra for six voltages between 16 kV and 18 kV with a flux of 75 $Hz/cm^2$ are shown in figure 5.

To achieve good time resolution in a large experiment, which may contain many thousands of square metres of RPC detector, it is important to have low time-walk in addition to a good intrinsic time

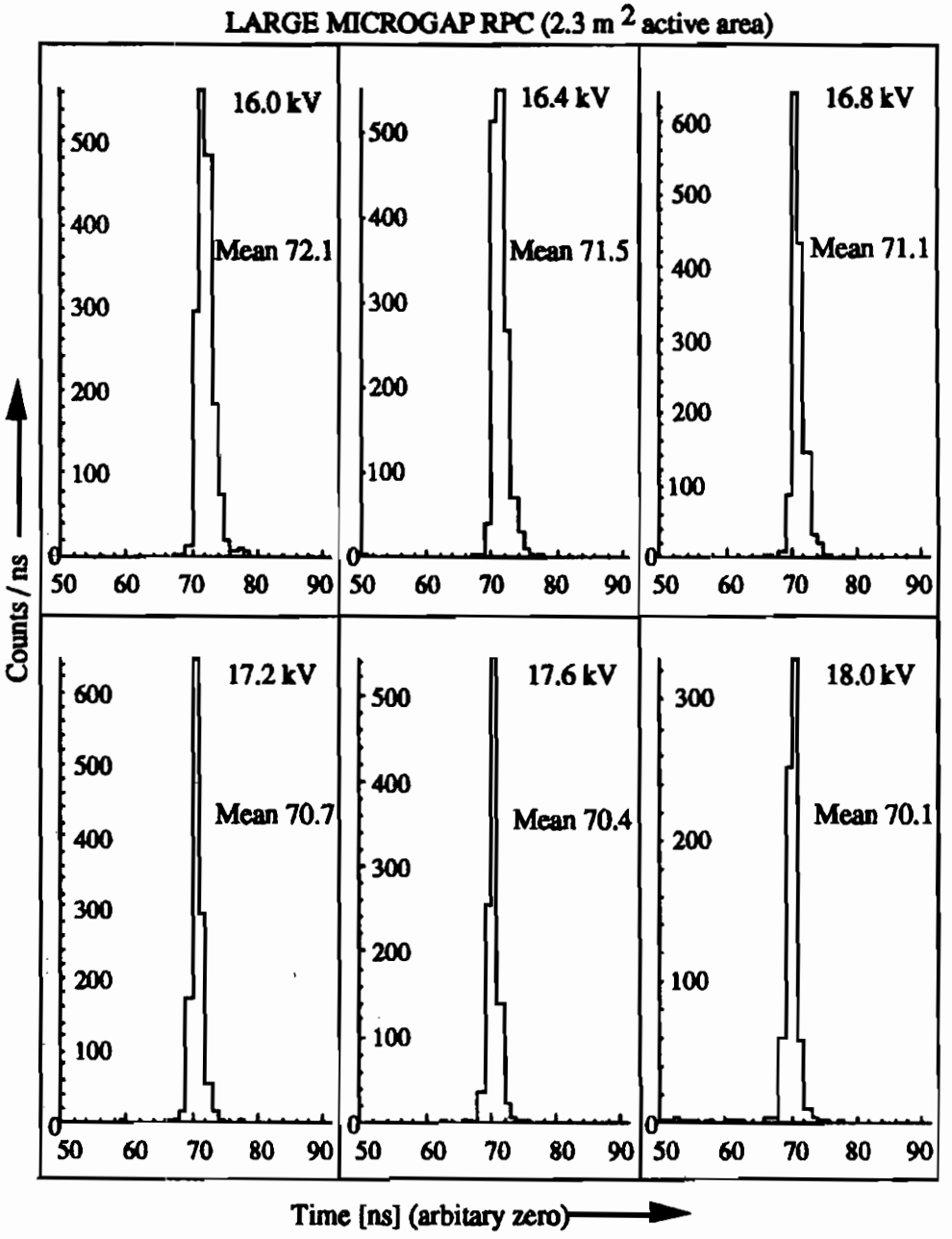


Figure 5: Typical time spectra obtained with the large wedged shaped chamber for voltages between 16 and 18 kV (Gas mixture B was in use). The beam was defocused with a flux of 75 Hz/cm$^2$.

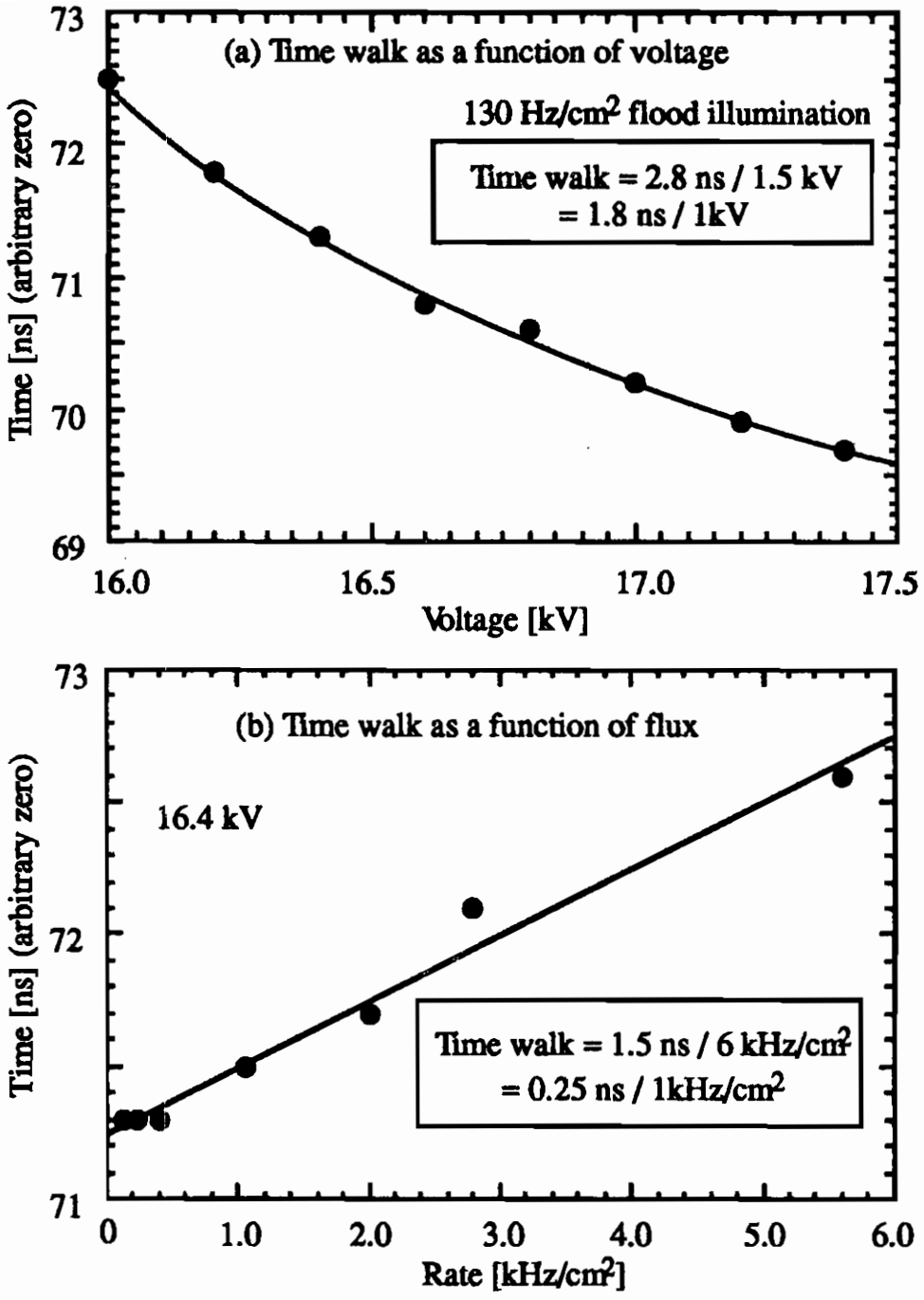


Figure 6: Time walk (a) as a function of voltage (b) as a function of rate for the small chamber. Gas mixture B was in use.

resolution. The voltage corresponding to the knee of the efficiency plateau will follow atmospheric pressure; this will result in a shift in the time of the signal if there is a large time-walk with voltage. There will be variations in the electric field due to unavoidable variations of the size of the gas gap; thus a large time-walk will result in timing differences from one area of the chamber to another. Additionally it is likely that the flux will vary over the surface of the detector and the absolute flux may vary with time. The time walk versus voltage is shown in figure 6a and time walk versus rate in 6b. These time-walks are much smaller than we measured with a single 2 mm gap chamber [1], and gives us confidence that the excellent time resolution ($\sigma \sim 1$ ns) of the microgap can be utilised.

### *3.4 Charge spectrum, strip multiplicity*

Using the small chamber, we measured the total charge of the 'fast' signal by using the cathode signal. We read out the cathode plane through a 1 nF capacitor; this signal was amplified, inverted and then fed to a LRS 2249A ADC (the large chamber was not fitted with this capacitor, therefore the cathode could not be read-out). The gate width was 100 ns, the peak of the fast avalanche signal occurred 30 ns from the start of the ADC strobe. We show in figure 7 charge spectra for the two gas mixtures at 18.6 kV for mixture A and 17.4 kV for mixture B. (These voltages correspond to 25% streamer probability for these two gases; see figure 9). The charge spectrum for the avalanches is Landau in shape, however one can clearly see a second peak at 8 pC for gas mixture B and yet another peak at 16 pC. We equate these two peaks with the production of one and two streamers. The exponential drop of the spectra for the low charge part of distribution (pure avalanches) has a different slope for the two gas mixtures (see figure 7). The streamer charge is larger and has a bigger variation for gas mixture A.

It is interesting to note that the fast charge produced by the streamer is somewhat independent of the applied voltage. In figure 8

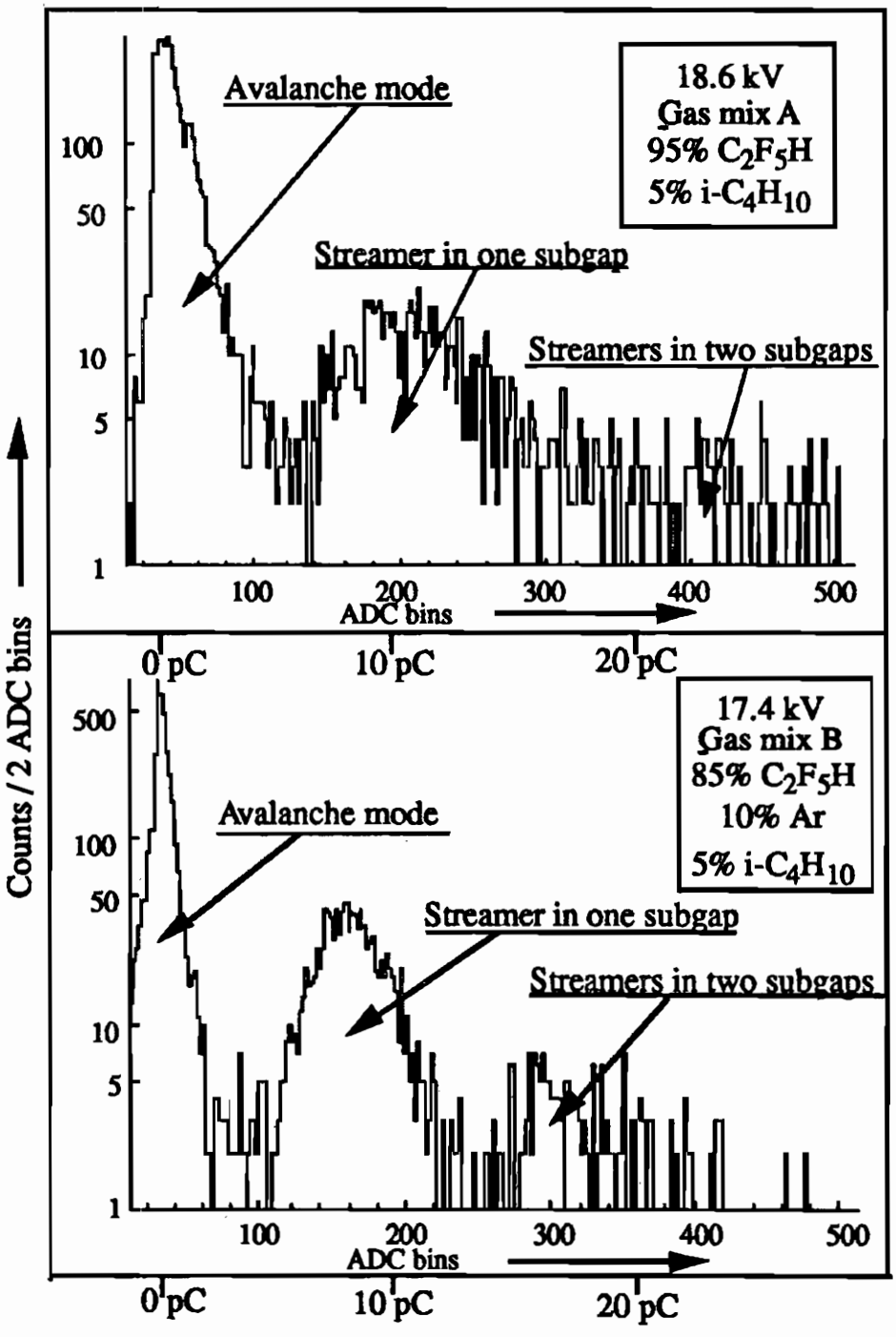


Figure 7: Charge spectra for small chamber at 1000 V above knee of efficiency plateau for two gas mixtures.

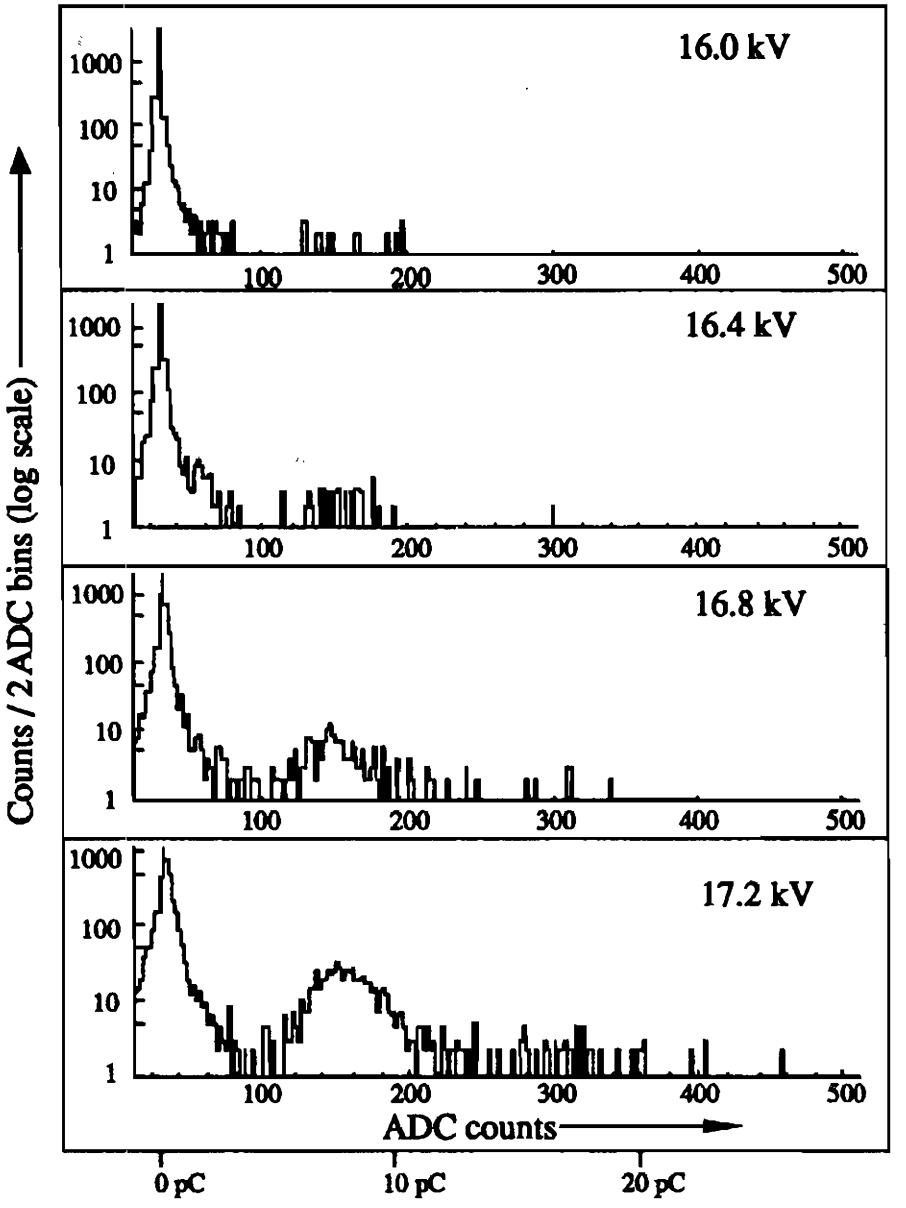


Figure 8 Charge spectra for the small chamber at 4 different voltages (gas mixture B).

we show the charge spectra (again on a log scale) for four voltages over a 1.2 kV range. Clearly the fraction of streamers increases with voltage, but the charge remains constant. The log scale emphasises the fact that there are events with a charge below the pedestal value; this is an

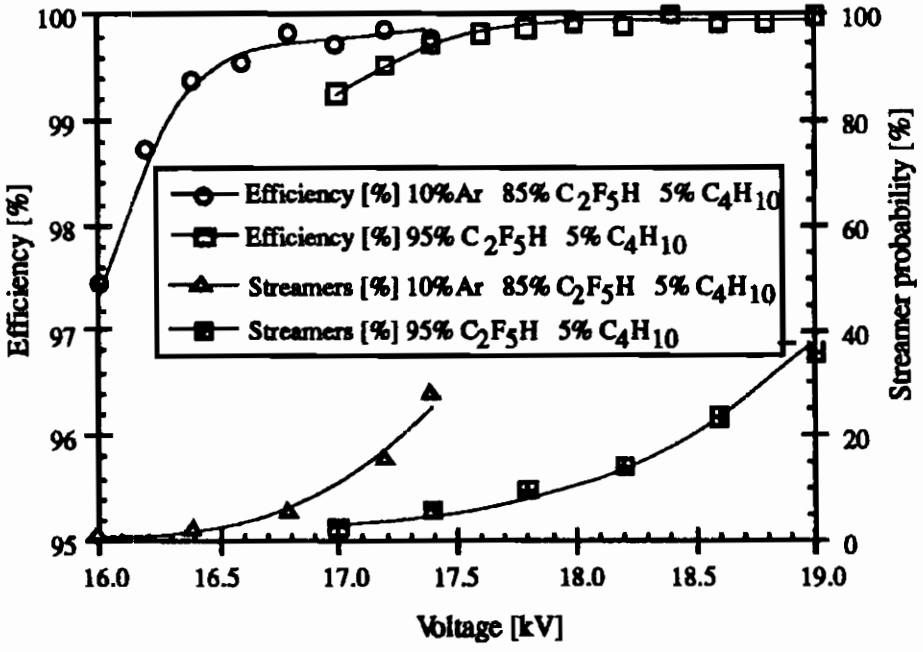


Figure 9: Efficiency and streamer probability for two gas mixtures.

unfortunate aspect of the ADC we were using. Large signals applied to the input cause a shift in the pedestal value for some milliseconds. This did not allow a precise measurement of the charge spectrum for low values of charge. However the spectra is obviously sufficient to tag the occurrence of streamers; we put a cut at 100 ADC counts and plot the fraction of streamers versus voltage for the two gas mixtures. This is shown in figure 9.

It is clear that there will be a certain fraction of streamers with this chamber even at the voltage corresponding to the knee of the efficiency plateau. It is relevant to ask whether we can operate in this mixed mode of operation: one major worry is that the cluster of hits may dramatically increase when there is a streamer. Our cluster algorithm is the following: each readout strip is connected to a multihit TDC; we start searching for a hit 100 ns before we expect a hit from the chamber and select the earliest hit. We then open a time window and

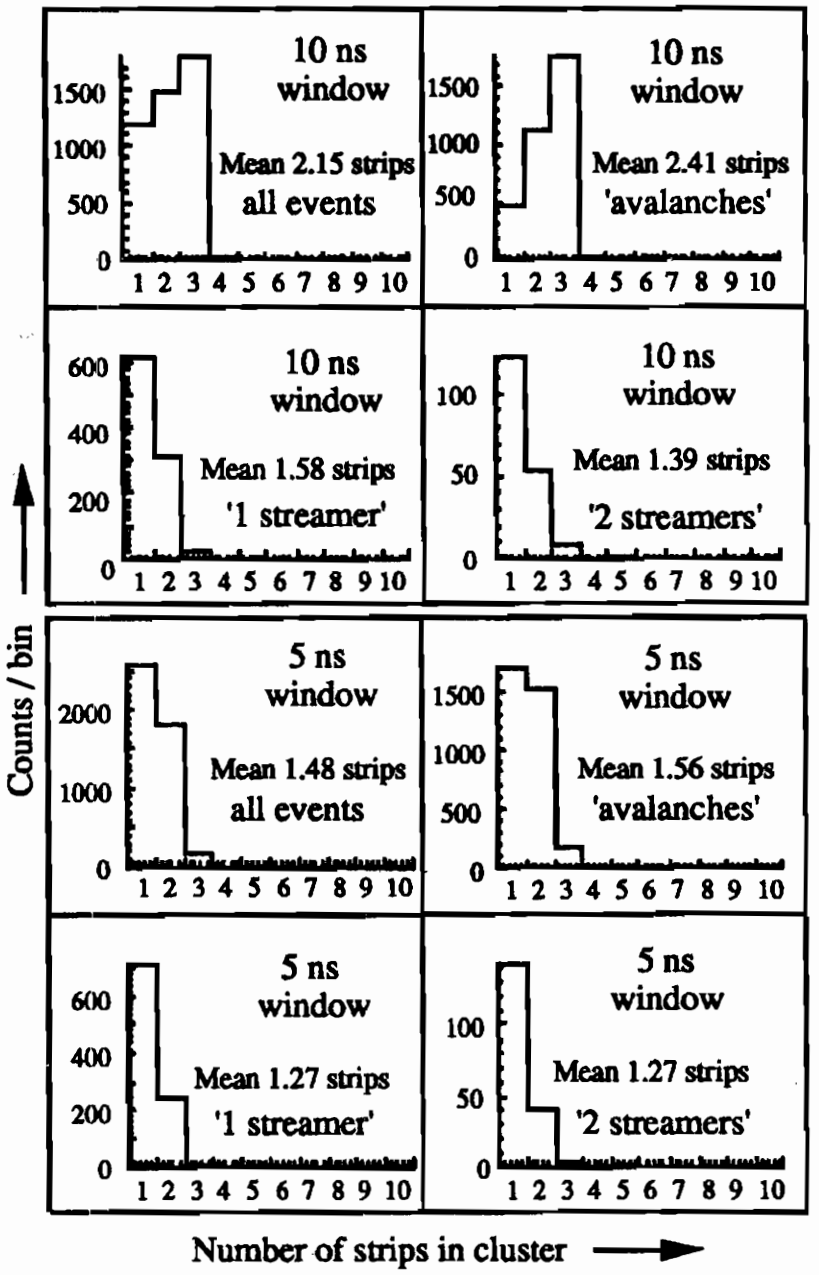


Figure 10: Cluster sizes for avalanche, one streamer and two streamer events for two time windows. See text for details of cluster algorithm.

look at all other strips for hits within this window. If the resultant hit strips are all neighbours (i.e. no unhit strip within the cluster) we define it as a single cluster. This cluster may contain between 1 and 16 strips; the maximum 16 is given by the maximum of 16 channels that we had instrumented at a given moment. Events with more than one cluster are rejected. Initially we use a 10 ns window and the results are shown in figure 10a for the three cases of avalanche, one streamer or two streamers (using the boundaries of 100 and 250 ADC bins on the plot shown in figure 7). Surprisingly the cluster multiplicity reduces when there is a streamer. If we use a 5 ns window (shown in figure 10b) we find a substantial reduction of cluster size for avalanches, whereas the cluster size for streamers remains unchanged. There are several effects which may contribute to this result: most of the cluster width for the

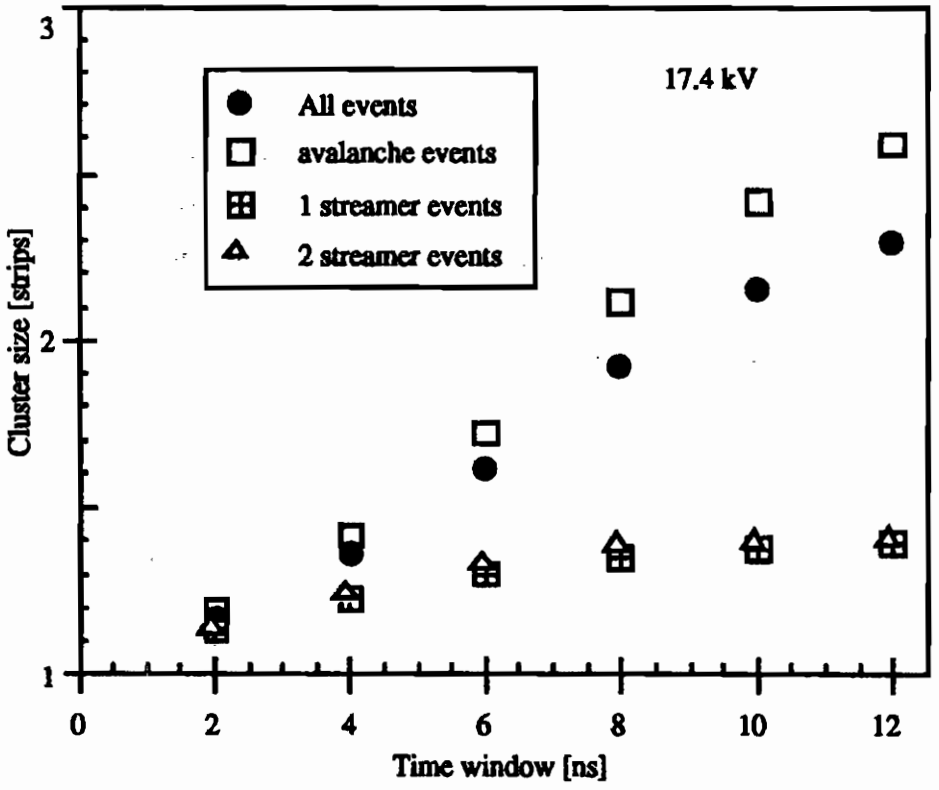


Figure 11: Cluster size versus time window for three types of signal: avalanche, single streamer and double streamer.

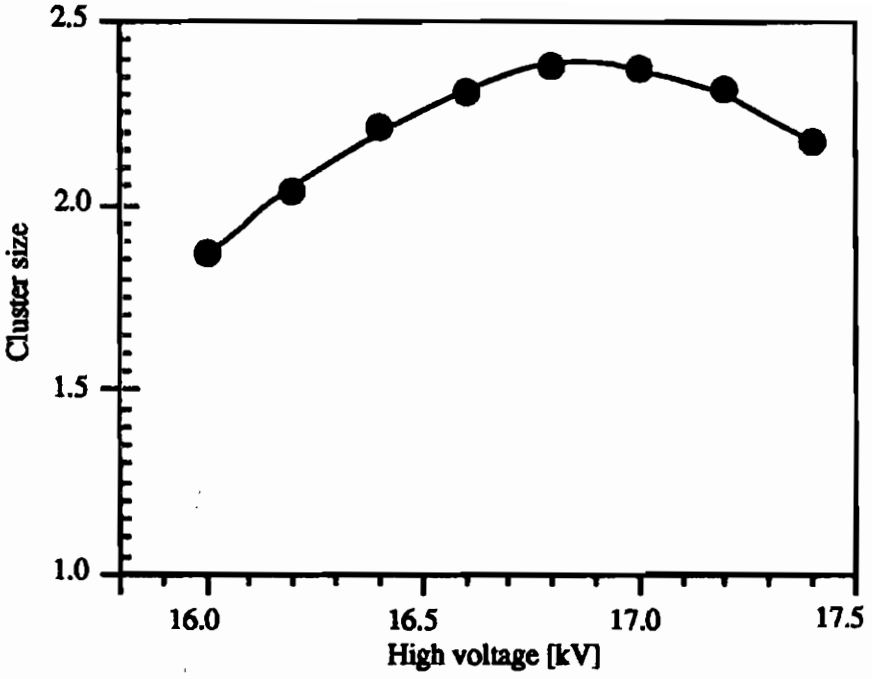


Figure 12: Cluster size versus voltage. Gas mixture B was in use.

low pulseheight events is caused by cross talk in the front-end electronics. Our amplifiers are built on small boards; each board has 4 channels of amplifiers. We have found that neighbouring strips on two different boards have far less cross talk than neighbours on the same amplifier board leading us to believe that the cross talk between amplifier channels is a major contributor to the cluster size. In general we have not been studying cluster width, since there are various groups within the CMS and ATLAS LHC collaborations designing front-end electronics; it seemed premature to study this aspect in depth if there will be new improved front-end electronics available in the short-term future. However in this instance we have started to look at cluster size in order to assess how disruptive streamers may be. In figure 11 we plot cluster size as a function of the time window. For the avalanche events the cluster size increases for a larger time window; however when the signal is large (a streamer) it seems as if the neighbouring channels are switched off for some time (at least 12 ns according to

figure 11). There is a well known electrostatic effect which generates inverted signals on neighbouring strips [6], however this is only true if the avalanche (or streamer in this case) is close to the anode pickup strip [7]. Thus this effect is not large for the multigap design, since the induced signals on the pick-up strips are generated from avalanches/streamers produced in all sub-gaps. Another mechanism that can produce signals of opposite polarity on the neighbouring strips is via the capacitive coupling of the anode strips to the cathode. There

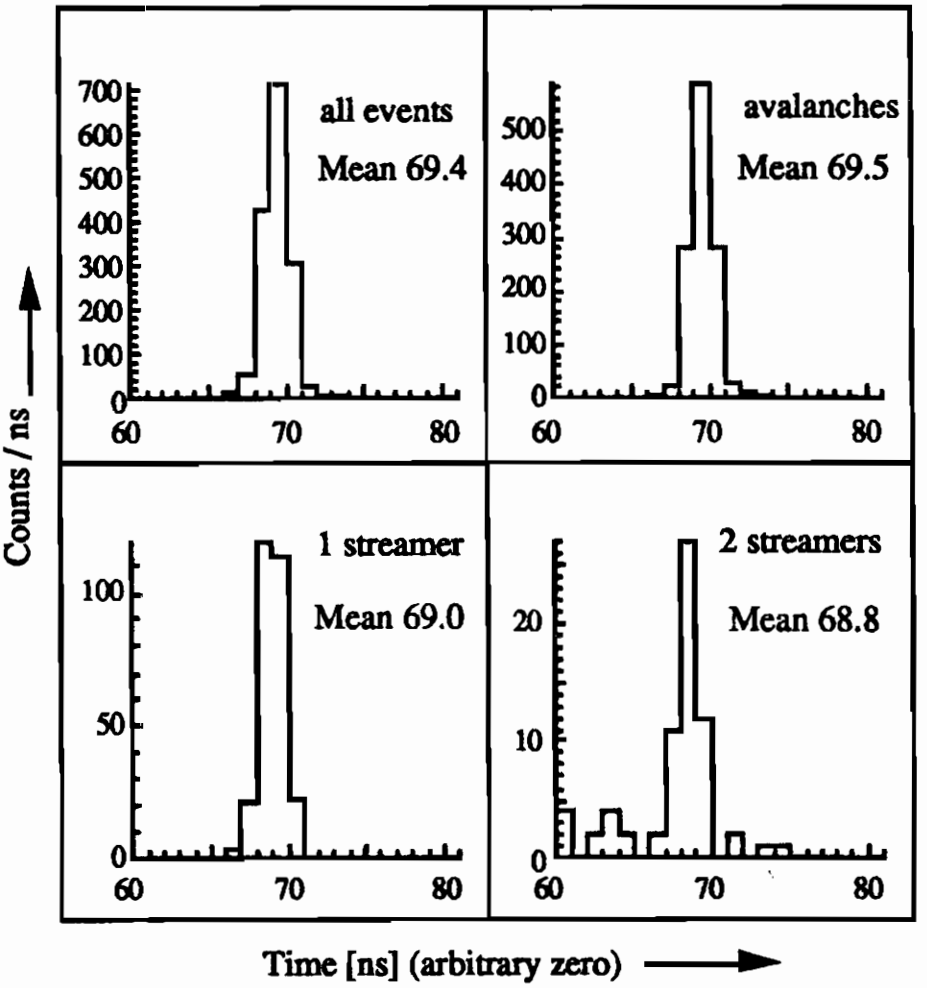


Figure 13: Time spectra for avalanche, single streamer and two streamer events for the small RPC. The voltage was 17.4 kV; gas mixture B was in use.

is a positive-going signal generated on the cathode plane; thus (via capacitive coupling) there will also be positive signals produced on the anode strips. The strip closest to the avalanche will of course have a large negative signal from the avalanche/streamer itself; but all other strips will just have the positive going signal from capacitive coupling to the cathode. We can not fully investigate this phenomenon since our amplifiers are followed by a 10 ns differentiator - but no shaping circuit and thus ring. This ringing prevented detailed study; however the bottom line is that the streamers do not seem responsible for large cluster sizes; indeed it appears that there is a phenomenon which injects a negative signal into the neighbouring strips (and thus switches the neighbours off).

We plot in figure 12 the average cluster size versus voltage (10 ns gate) for the small chamber. We see that the cluster size decreases with voltage above 16.8 kV as the fraction of streamers increases. We have never before observed a drop in cluster multiplicity with voltage in our previous studies of multigap RPCs - however this is the first time when these micro-streamers have been a dominant mode of operation.

As a final aspect of these micro-streamers we show the time spectra for these three cases: avalanche, one streamer and two streamers. The results are shown in figure 13. The two streamer sample had a larger accidental background; however it is clear that there is some time slewing, decreasing the average time for larger signals; the one streamer case is 0.5 ns earlier and has smaller tails in the time distribution. This time slewing (already small) can be reduced with faster electronics or with electronics that has some built in slewing correction.

## 5. Tests at the Gamma Irradiation Facility (GIF)

The large chamber was also tested at the Gamma Irradiation Facility (GIF) at CERN. The GIF has a 740 GBq $^{137}Cs$ source and a muon beam. The intensity of the gamma radiation could be controlled

by various filters. Our tests were performed with the chamber mounted 2.2 m from the source. We tested the chamber either with the maximum irradiation (filter factor = 1 in the GIF control system) or with the source off. The counting rate with source on corresponded to a rate of ~ 3 kHz/cm$^2$. The full active area of the chamber was irradiated. With this counting rate we observed a relatively high level of noise. On investigation we found two potential causes which we will eliminate if we build large chambers in future. Both problems were related to the cathode plane, which was a single foil of aluminium. Problem 1: in our previous prototype chambers we had decoupled the cathode to ground with a high voltage capacitor. For this large chamber we had no decoupling capacitor. There was some coupling to ground due to the capacitance between the cathode plane and the external

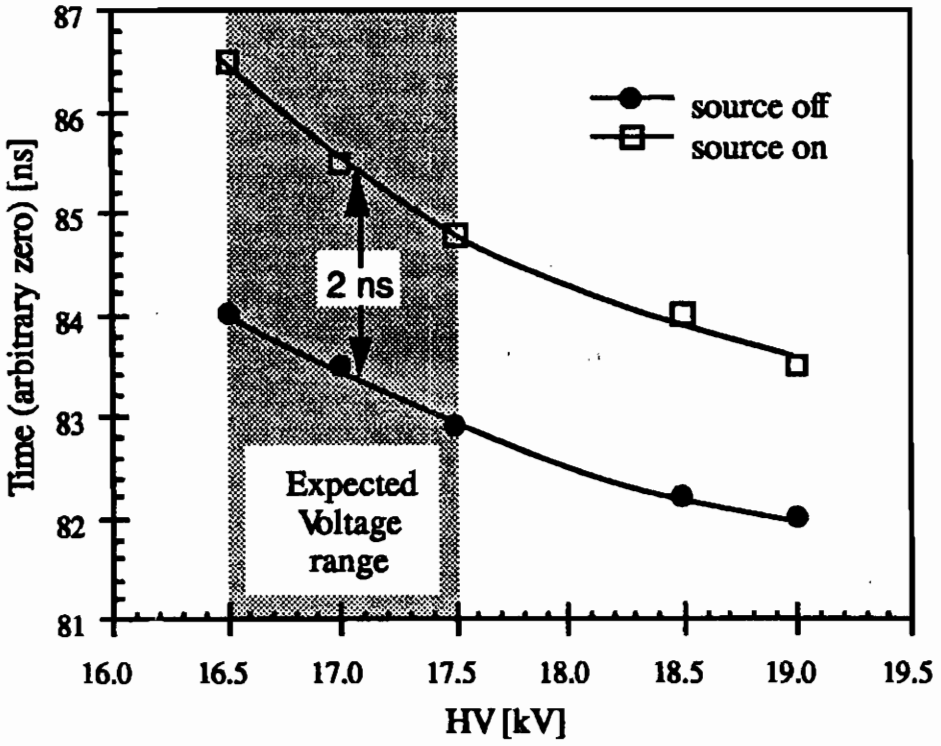


Figure 14: Time walk measured in the GIF facility at CERN. The gas mixture was 85% $C_2F_5H$, 10% Ar and 5% iso-$C_4H_{10}$ bubbled through water to add 1% water vapour.

aluminium box; but there was a much larger capacitance between the cathode and the anode strips. Thus all signals on the cathode were coupled to the anode strips. Problem 2: we had no resistor between the cathode plane and the high voltage cable. Thus signals on the cathode would go up the high voltage cable, get reflected at the high voltage power supply and reappear on the cathode plane 200 ns later. With a small test chamber this reflection would continue for many cycles.

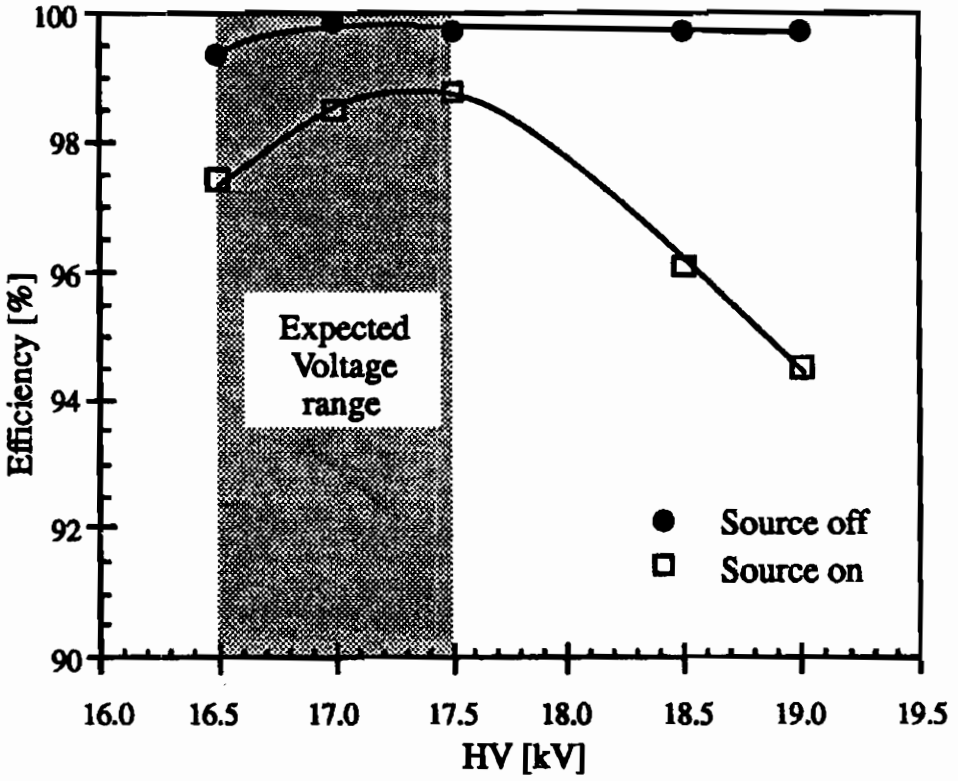


Figure 15: Efficiency measured in the GIF facility at CERN. The gas mixture was 85% $C_2F_5H$, 10% Ar and 5% iso-$C_4H_{10}$ bubbled through water to add 1% water vapour.

Both these problems can be easily solved. We have testsed a small chamber constructed with a ground plane very close to the cathode plane. It would be no problem to do this for large chambers. In addition, we would segment the cathode (and matching ground

planes) to match the anode segmentation. Each cathode area would be coupled resistively to the high voltage supply. The segmented ground would be connected to the ground of the front-end amplifiers, thus providing a good 'signal-return'. In this way even though the chamber would be constructed as one large area, it would act as a mosaic of small independant chambers.

Despite these problems this large chamber behaved well in these GIF tests. In figure 14 we show the time walk for source on and source off. In figure 15 we show the efficiency versus voltage again for source on and source off. The drop in efficiency with source on at very high voltages we attribute to this high level of noise discussed above.

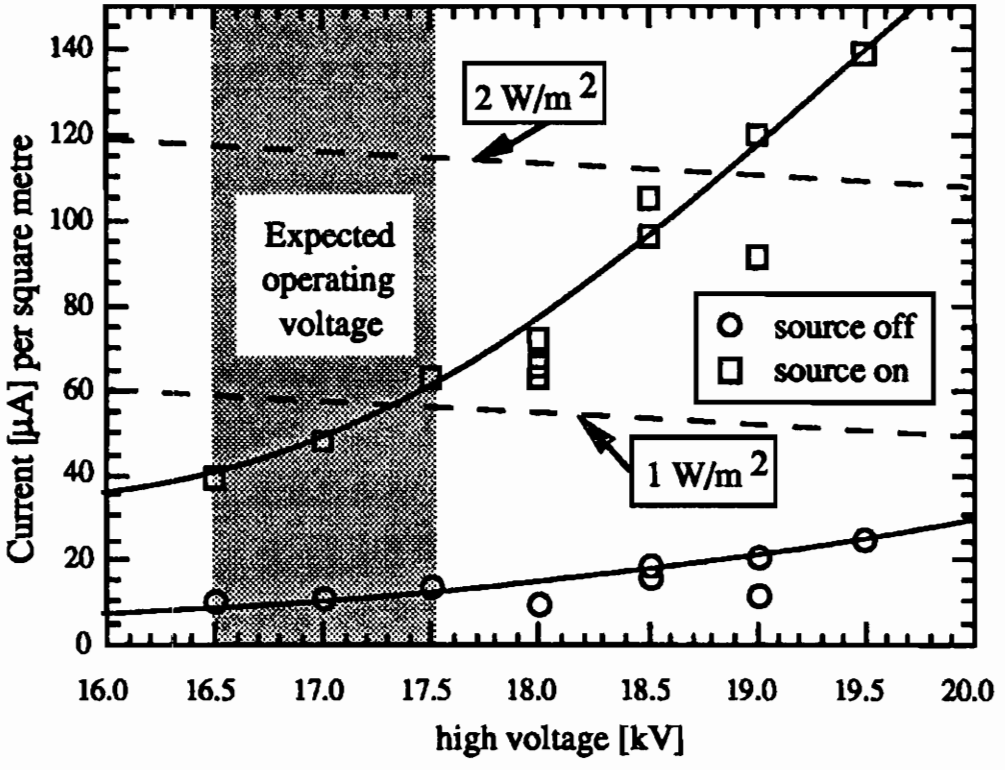


Figure 16: Current measured at the GIF facility at CERN. The gas mixture was 85% $C_2F_5H$, 10% Ar and 5% iso-$C_4H_{10}$ bubbled through water to add 1% water vapour.

An important consideration is the power dissipation in the gas volume. 1 W/m$^2$ would heat up this gas volume by over 300°C in one hour, thus we can not rely on gas flow to remove the heat. Most gaseous chambers have metallic cathodes and the heat is conducted via the cathode to the outside world. In the case of the RPC the gas volume is bounded by these resistive plates, which are not good conductors of heat. In figure 16 we show the current drawn by the chamber with the source on and the source off. If the full source irradiation does correspond to conditions in the endcap of a typical LHC experiment, then we would be able to operate this type of chamber below 1 W/m$^2$ power.

## 6. Discussion

This is the preliminary investigation of a microgap RPC and it is obvious that more study is needed. However it seems clear that it is unlikely that we can operate this device in pure avalanche mode; pure avalanche mode operation was possible with the conventional multigap with typically 3*3 mm geometry. However the small gap size together with this very quenching freon ensures that the streamers are small (micro-streamers). From this study we would conclude that a mixed mode of operation (avalanche and micro-streamer) is feasible. The time spectra and cluster multiplicity appear compatible between the two modes.

The excellent time resolution, small time walk and extremely good rate capability makes this a very interesting device for LHC applications. Further studies, especially of the large chamber, are in progress and will be reported at a later date.

We have long believed that a mixed mode (streamer mixed with avalanche) operation is not desirable for a RPC detector. However in this case we have micro streamers, which produce a signal of comparable charge to that of the avalanche. It may be possible to operate this type of chamber in a pure micro-streamer mode (maybe at the expense of some rate capability); this would simplify the design of the front-end electronics.

## Acknowledgements

We have enjoyed technical help with the design and the drawings of the large microgap RPC from the group at Wisconsin University; this was due to the interest and enthusiasm of Prof. Richard Loveless and Farshid Feyzi. The mechanical workshop at CERN produced the aluminium box at very short notice; in particular we thank M. Masson. It is always a pleasure to use the test beams at CERN, and we thank all those who keep the East Hall test beams running in such an excellent manner.

## References

[1] Streamer free Operation of a 2 mm Gap Resistive Plate Chamber with $C_2F_5H$, E. Cerron Zeballos, I. Crotty, D. Hatzifotiadou, J. Lamas Valverde, M.C.S. Williams and A. Zichichi, Presented at the 4th International Conference on Resistive Plate Chambers, Napoli, Oct. 1997.

[2] R. Cardarelli, R. Santonico and V. Makeev, The avalanche to Streamer transition in RPC's, 3rd International Workshop on Resistive Plate Chambers and Related Detectors, Pavia, Oct. 1995. Scientifica Acta Anno XI, Vol. XI, Numero 1 (1995)11.

[3] The Development of the Multigap Resistive Plate Chamber, E. Cerron Zeballos, D. Hatzifotiadou, J. Lamas Valverde, M.C.S. Williams and A. Zichichi, Presented at the 4th International Conference on Resistive Plate Chambers, Napoli, Oct. 1997.

[4] E. Cerron Zeballos, I. Crotty, D. Hatzifotiadou, J. Lamas Valverde, S. Neupane, M.C.S. Williams and A. Zichichi, Nucl. Instr. and Meth A 374(1996)132.

[5] E. Cerron Zeballos, I. Crotty, D. Hatzifotiadou, J. Lamas Valverde, M.C.S. Williams and A. Zichichi, Nucl. Instr. and Meth A 392(1997)145.

[5] V.V. Ammosov, V.A. Gapienko, V.F. Konstantinov, Yu.M. Sviridov, V.G. Zaets, Bean Study of the Charge Properties of some RPC Modifications, ATLAS Internal Note MUON-NO-211 August 1997.

[6] V. Radeka, Ann. Rev. Part. Sci. 38(1988)217.

[7] I. Crotty et al. Nucl. Instr. and Meth. A 360(1995)512.

# STREAMER FREE OPERATION OF A 2 mm GAP RESISTIVE PLATE CHAMBER WITH $C_2F_5H$

E. Cerron Zeballos[1,2], I. Crotty[1], D. Hatzifotiadou[1,4], J. Lamas Valverde[1,2], M.C.S. Williams[1,4] and A. Zichichi[1,3,4]

[1]*PPE Division, CERN, Geneva, Switzerland*
[2]*World Laboratory, Lausanne, Switzerland*
[3]*University of Bologna, Bologna, Italy*
[4]*INFN, Bologna, Italy*

ABSTRACT

It is necessary to operate the resistive plate chamber (RPC) in avalanche mode to obtain high efficiency at elevated particle fluxes. We examine this mode of operation with a 2 mm gap RPC using gas mixtures containing $C_2F_4H_2$ and $C_2F_5H$. In order to explain the data we propose that the avalanche growth is strongly limited by space charge effects.

## 1. Introduction

Resistive plate chambers (RPC) have been in use in various experiments since the 1980's; however in all cases the flux of particles has been rather low. In the original Letters of Intent for experiments at LHC, the prime candidate for implementation of the muon trigger is the RPC. The proposed type of RPC has a 2 mm gas gap bounded by 2 mm thick (linseed-oil treated) Bakelite plates. In order to operate at the expected flux of particles at the LHC experiments, both ATLAS and CMS [1,2] proposed operating these devices in 'low-gas gain' mode (nowadays this mode is usually referred to as avalanche mode). There has been an extended study to find a suitable gas mixture; the

proponents [3,4,5] of this type of RPC have proposed mixtures containing a high fraction of $C_2F_4H_2$ (an ecologically acceptable freon). The basic problem is to operate the RPC in avalanche mode with high efficiency and with only a very low contamination of streamers (i.e. pure avalanche mode).

Data from various groups show a variety of charge spectra measured from this device. Abbrescia *et al.* [3] show an exponential shape, Ammosov *et al.* [5] show a 'Landau-shaped' distribution; while Alviggi *et al.* [5] show a Gaussian shaped distribution. The ease of operation of this detector depends on the exact shape of these spectra; thus we started a series of measurements in order to understand these apparent differences between various groups.

We have simulated the charge spectrum using the program described in ref. [6]. We assume that the number of primary ionisation clusters is 75/cm (obtained by scaling up by the atomic number of the molecule $C_2F_4H_2$ from data for Argon) and have set the gas gain such that the average fast signal is 1 pC (assuming that fast/total charge is $1/\alpha D$ and the attachment coefficient is zero; $\alpha$ is the Townsend coefficient and D the size of the gas gap). We show the result in figure 1 for three cases; (a) no avalanche fluctuations; (b) exponential fluctuations are applied to individual avalanches formed from each cluster of primary ionisation; (c) exponential fluctuation applied to single merged avalanche. In all cases the shape is exponential with a long tail of high values of fast charge. For the wide gap RPC and multigap RPC [6] there were marked differences in the spectra when the fluctuations described above were applied; in that study we found that case (c) best described the measured charge spectrum. Transition to streamer production should begin when the avalanche produces more than $10^8$ positive ions (i.e. for fast signals greater than 1 pC); however this limit may be higher in the presence of a strong quencher such as the freons used in this study. This exponential shaped charge spectrum (as generated by the simulation) indicates that (a) a very low threshold discriminator is needed and (b) already there is a significant number of large avalanches, which could trigger a transition to a streamer.

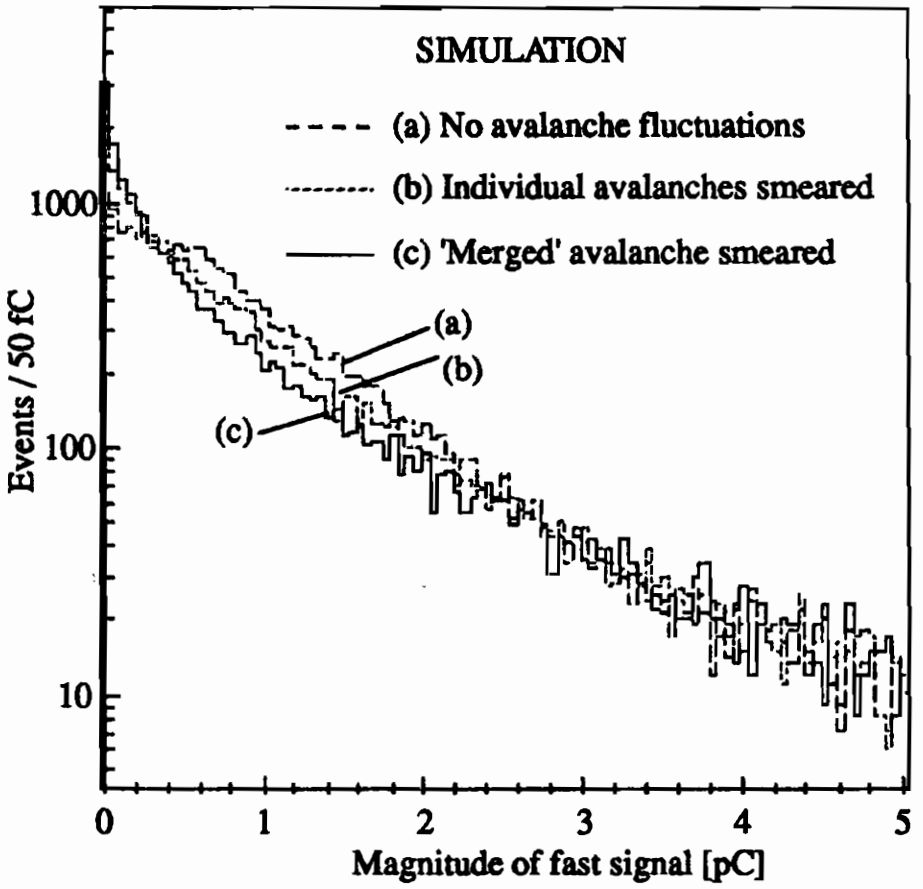


Figure 1. Simulation of charge spectrum produced by a 2 mm gap RPC filled with $C_2F_4H_2$. Three cases are shown; (a) no avalanche fluctuations applied; (b) each cluster of primary ionisation creates an independent avalanche, the size of which is smeared by an exponential fluctuation; (c) all individual avalanches are merged into a single avalanche, which is then smeared by the exponential avalanche fluctuations.

However this simulation does not agree with data presented by various groups, where they show that pure avalanche mode operation is possible; also the shape of our simulated charge spectrum is only consistent with data obtained by Abbrescia et al.

## 2. Experimental Set-up

The resistive plate chamber used in this study was constructed with resistive plates made from 0.8 mm thick melamine-phenolic

laminate sheets of 32 x 32 $cm^2$. The smooth melamine surface faced the gas, while the outer phenolic surfaces were painted with conductive paint (Nickel paint with surface resistivity 1-2 $\Omega/\square$) to form pad electrodes of 24 x 24 $cm^2$. The gas gap was bounded by a 2 cm wide and 2 mm thick PVC spacer around the perimeter. A layer of glue attached the resistive plates to these spacers, thus creating a gas gap between 2.1 and 2.2 mm. One electrode, the cathode, was connected with a 1 M$\Omega$ resistor to a high voltage power supply; the signal developed on the cathode was read out through a 1 nF capacitor. This signal was fed into a fast current amplifier, the output of which was inverted and split between an ADC and a discriminator. The other electrode was connected to ground either through the 1 M$\Omega$ input impedance of the oscilloscope or to an ADC with input impedance of 50 $\Omega$. The exact set-up is described below where the measurements are discussed.

We triggered on through-going cosmic rays with a series of scintillator counters selecting a 10 x 10 $cm^2$ area in the centre of the RPC. We performed two series of tests; for the first we used a gas mixture of 3% iso-$C_4H_{10}$ and 97% $C_2F_4H_2$. Normally we add 1% water vapour to our gas mixtures to keep the resistivity of our melamine-phenolic plates at a low value [7]. For the tests with this gas mixture we did not add water vapour. The voltage needed to reach the knee of the efficiency plateau slowly increased from 10.5 to 11.2 kV over the several week period of the tests. We attribute this rise to an increase in resistivity, thus generating an increasing voltage drop across the resistive plates. We have ignored this effect except to note that various plots will be labelled with voltage relative to the knee of the efficiency plateau so that comparisons can be made. For the second series of tests we used a gas mixture of 95% $C_2F_5H$ (also ecologically friendly) and 5% iso-$C_4H_{10}$ bubbled through a water reservoir at 10°C in order to add 1% water vapour. For these tests the working voltage was more constant.

## 3. Measurement Technique

There are various types of measurements made with this chamber. We have measured the charge spectrum of the fast signal derived from the cathode pad. We have measured the time spectrum with the threshold of the discriminator set at 10 fC. We also measured the total charge produced by the avalanche or streamer. For this measurement we connected an oscilloscope directly to the anode, using the high impedance of the oscilloscope to connect the anode to ground potential. A typical oscilloscope display is shown in figure 2. The step is due to the movement of the electrons towards the anode; the long ramp is due to the drift of the positive ions toward the cathode. Eventually the voltage levels off when all the ions have been collected. The total voltage deviation can be converted to charge, as we have measured the total capacitance of the anode to ground. In this case it is 0.7 nF. We are interested in the ratio of fast charge/total charge, i.e. the size of the initial step to the total deviation. This is clearly visible for the event shown in figure 2; however we are also interested in small avalanches, where the total deviation due to the collection of positive ions is several mV. Obviously the sensitivity and noise of the system would make it difficult to measure the step directly. We, thus, also monitored the fast signal measured by a fast current amplifier attached to the cathode, having first calibrated the output of this amplifier to the step observed for large avalanches. However it should be noted that this step is not always a clean step for calibration. An example is shown in figure 3. Here one can observe the fast signal due to the electrons, a fast ramp that could be caused by the drift of negative ions (since the gas is electronegative) finally followed by the slow ramp as the positive ions drift to the cathode. On a slow time scale (shown in figure 2) one can not distinguish between the ramp of the negative ions and the fast electron signal; however it is only the electron signal that produces the observed fast signal of the avalanche. Another factor that we have to take into account is the coupling between the cathode and anode. A positive going signal is generated on the cathode and negative

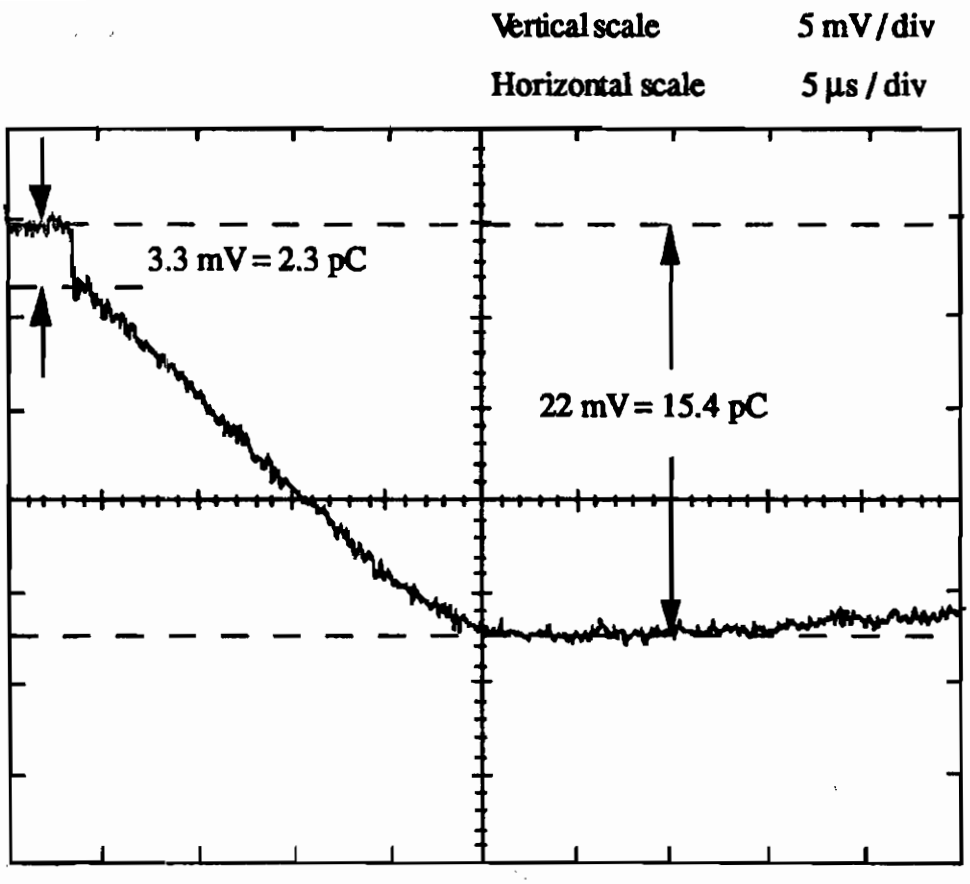


Figure 2. Typical avalanche signal observed by an oscilloscope directly attached to the anode with a 1 MΩ input impedance.

on the anode; thus any capacitive coupling between the two plates will lead to a reduction of the signal. This reduction will depend on how each electrode is decoupled to ground. Additionally there is capacitive coupling between the electrode and ground which will allow part of the signal to be lost rather than fed into the amplifier. Thus we cross-check our calibration by (a) knowing the gain of the amplifier attached to the cathode and (b) measuring the change of the mean of the charge spectrum obtained from the cathode when the anode is either coupled to ground through a 50 Ω or 1 MΩ resistor. Even after this calibration procedure the uncertainty in the exact charge we estimate to be ~ 20%.

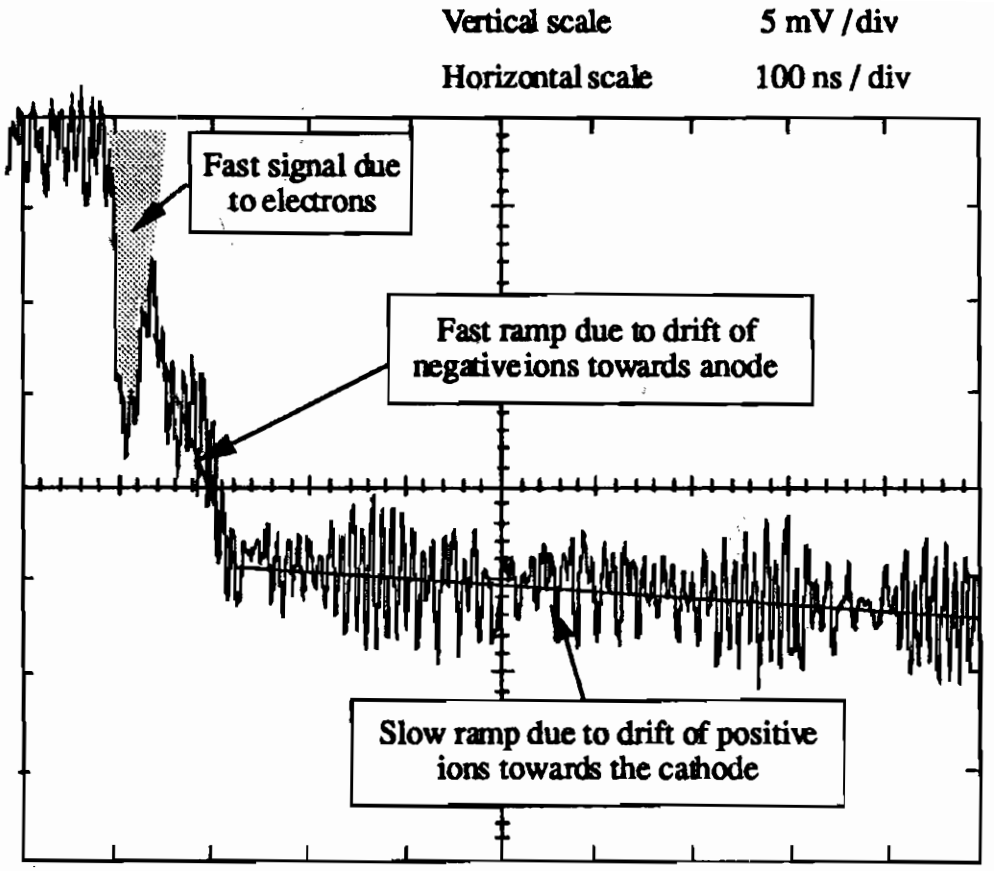


Figure 3. Avalanche signal on expanded time scale. We attribute the first fast signal to the movement of the electrons, the fast ramp to the movement of the negative ions and the slow ramp (almost flat on this time scale) to the drift of the positive ions.

## 4. Results

In figure 4 we show the efficiency plot of the RPC with the two gases under test. We also show the probability of producing a streamer. In the upper plot we show two curves; one is for 'prompt' streamer and the other for 'any' streamer. By 'prompt' streamer we mean that there has been more than 5 pC of charge within 50 ns of the original avalanche. The probability for 'any' streamer is obtained by inspecting the output from the RPC for some microseconds with the

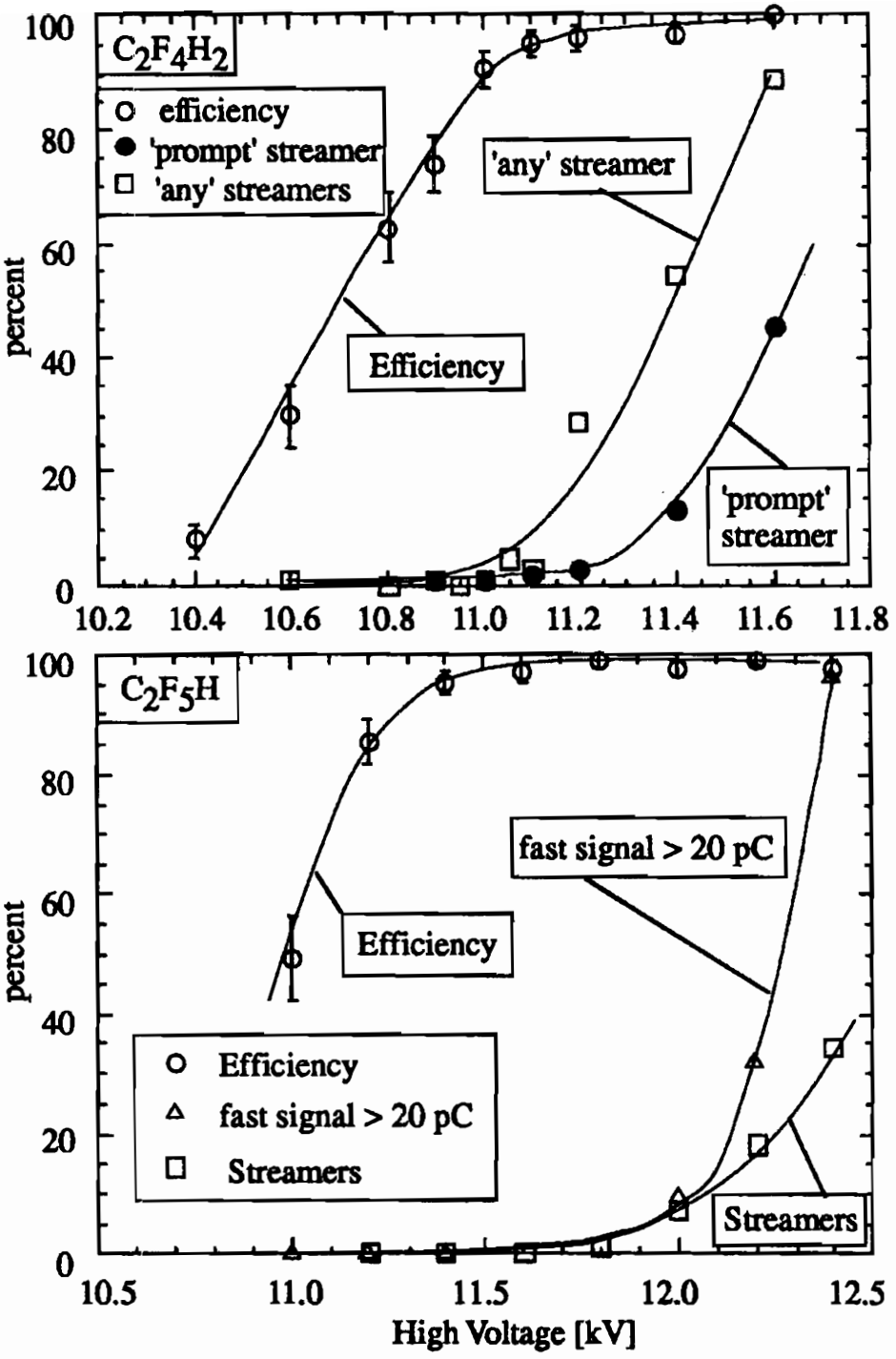


**Figure 4. Efficiency versus voltage for the two gas mixtures. We also show the probability of a streamer.**

oscilloscope. The lower plot refers to the $C_2F_5H$ gas mixture. With this gas, the streamer was always 'prompt'; it does not have this characteristic delay between the avalanche and streamer as first observed by Cardarelli et al. [8]. Also, as discussed more fully below, $C_2F_5H$ is more 'quenching' than $C_2F_4H_2$; thus any streamer produced is less violent and the transition between avalanche and streamer happens for a higher avalanche charge. Thus we do not distinguish between 'prompt' and 'any' streamer for the lower plot. However we also plot the occurrence of a signal > 20 pC within our 50 ns gate; this is a mixture of streamers and large avalanches.

In figure 5 we show the ratio of 'fast signal/total signal' plotted as a function of fast charge. Ideally this should be $1/\alpha D$ (where $\alpha$ is the Townsend coefficient and D the size of the gas gap) if the attachment coefficient is zero. This is shown as a dotted line superimposed on the figure. Obviously this ratio is well below this

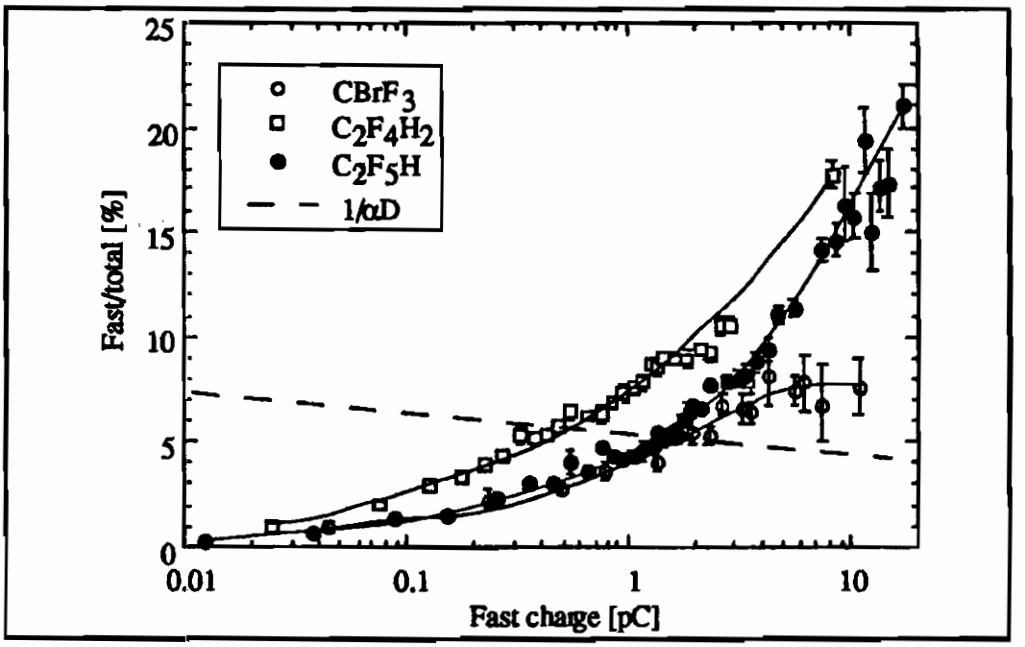


Figure 5. Ratio of fast signal to total signal plotted as a function of fast charge for the two gas mixtures. We also show the theoretical value of $1/\alpha D$. Additionally we show a measurement made previously with a mixture containing $CBrF_3$ [9].

$1/\alpha D$ value for small avalanches. We assume the cause is that the 'electronegative' freons have a non-zero attachment coefficient. When the attachment coefficient is non-zero, we expect a ratio of fast/total signal to be $(\alpha'/\alpha).(1/\alpha' D)$ where $\alpha' = \alpha - \eta$ and $\eta$ is the attachment coefficient. There is a clear rise of the ratio of fast/total for increasing avalanche size; we attribute this to space charge effects. The electric field experienced by the electrons at the head of the avalanche is affected by the positive ions produced during the growth of the avalanche. These positive ions reduce the electric field and thus limit the growth of the avalanche. This will effectively move the centre of gravity of the electrons in the avalanche away from the anode, thus leading to an increase of this ratio of fast/total charge. As a comparison, we also include a measurement of this ratio for freon 13B1 that we have made previously [9]. Even though the systematic uncertainty is different between the two measurements, it is instructive

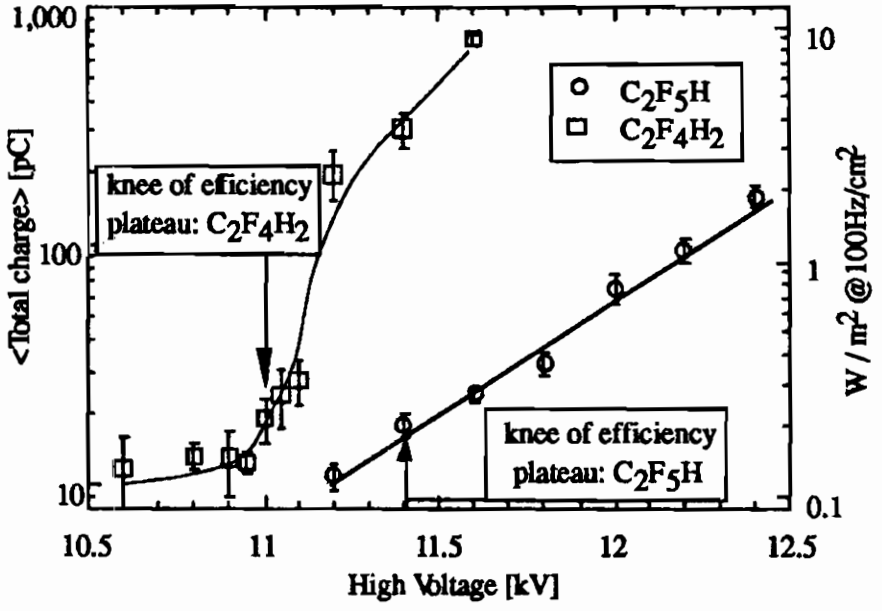


Figure 6. Total charge produced in the gas gap by a single through-going cosmic ray plotted as a function of applied voltage for the two gas mixtures under test. The right hand axis is marked with power dissipated in the gas gap per square metre assuming a flux of 100 Hz/cm$^2$.

to see an increase of the ratio of fast/total charge. It should be noted that only events producing single avalanches in the chamber are used for this measurement. Events that have an after-pulse or streamer have been eliminated; thus the large number of data points corresponding to a fast signal in the range 10 to 20 pC with the $C_2F_5H$ gas mixture indicates that large and clean avalanches can be produced with this mixture (i.e. no transition to streamers and after-pulses).

In figure 6 we show the total charge produced by a single through-going cosmic ray as a function of voltage for the two gases. It is clear that for the $C_2F_4H_2$ mixture, the total charge is dominated by the production of streamers above the knee of the efficiency plateau. The lower probability of streamer and the lower intensity of the streamer discharge with the $C_2F_5H$ gas mixture leads to a large reduction in the amount of charge in the gas gap. Knowing the total charge, we can calculate the power dissipation in the gas gap assuming

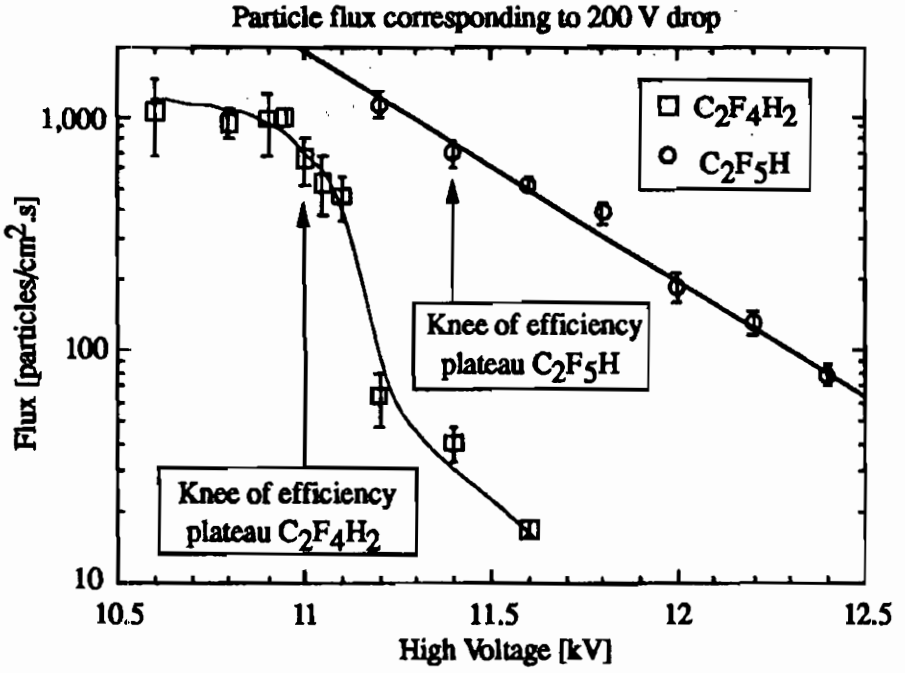


Figure 7. Rate needed to produce a 200 V drop across the resistive plates assuming a resistivity of 4 $10^{10}$ Ωcm and a plate thickness of 2 mm for each electrode.

a flux of 100 Hz/cm$^2$ over a 1 m$^2$ area. This is marked on the right hand axis. Although 1 W/m$^2$ does not seem a large source of power, it will heat the gas contained in this 2 mm thick volume by over 300°C in one hour. Since the resistive plates are not good thermal conductors, some thought has to be given to the extraction of the heat even at this relatively low flux of 100 Hz/cm$^2$. One can also estimate the rate capability, knowing the amount of charge produced and the resistivity of the plates. We show, in figure 7, the rate necessary to produce a 200 V drop, assuming a resistivity of 4 $10^{10}$ Ω.cm and a plate thickness of 2 mm for both electrodes. Obviously the rapid change in efficiency with voltage as shown in figure 4 would make a 200 V drop excessive unless one is working above the knee of the efficiency plateau. The high fraction and large charge produced by streamers in the $C_2F_4H_2$ gas mixtures would result in a rate capability ~50 Hz/cm$^2$. The $C_2F_5H$ mixture, however, is capable of being operated at ~500 Hz/cm$^2$.

In figure 8 we show the time spectrum obtained with a discriminator set with a ~10 fC threshold for the $C_2F_5H$ gas mixture for four voltages(11.3, 11.5, 11.9 and 12.3 kV). On this figure we also show the Full Width at Base (FWAB), which is a window that contains 99% of all the events. It is clear that for optimal timing one has to work with the voltage set well above the knee of the efficiency plateau. Similar results were obtained with the $C_2F_4H_2$ gas mixture (i.e. one has to work at 400 V above the knee of the efficiency plateau to obtain a FWHM of 4 ns). In figure 9 we show the time walk with voltage. This large time walk (~2.5 ns/100 V) will be of concern in critical timing applications.

In figure 10 we show the charge spectrum at four voltages 11.3 kV, 11.5 kV, 11.9 kV and 12.3 kV (i.e. 200 V below the knee, the knee, 400 and 800 V above) for the $C_2F_5H$ gas mixture. Similar results were obtained with the $C_2F_4H_2$ gas mixture. The principal effect is the change from the exponential shape for low voltages to a Landau shaped distribution at the knee and then to the apparent gaussian shape 800 V above the 'knee' voltage; however it should be

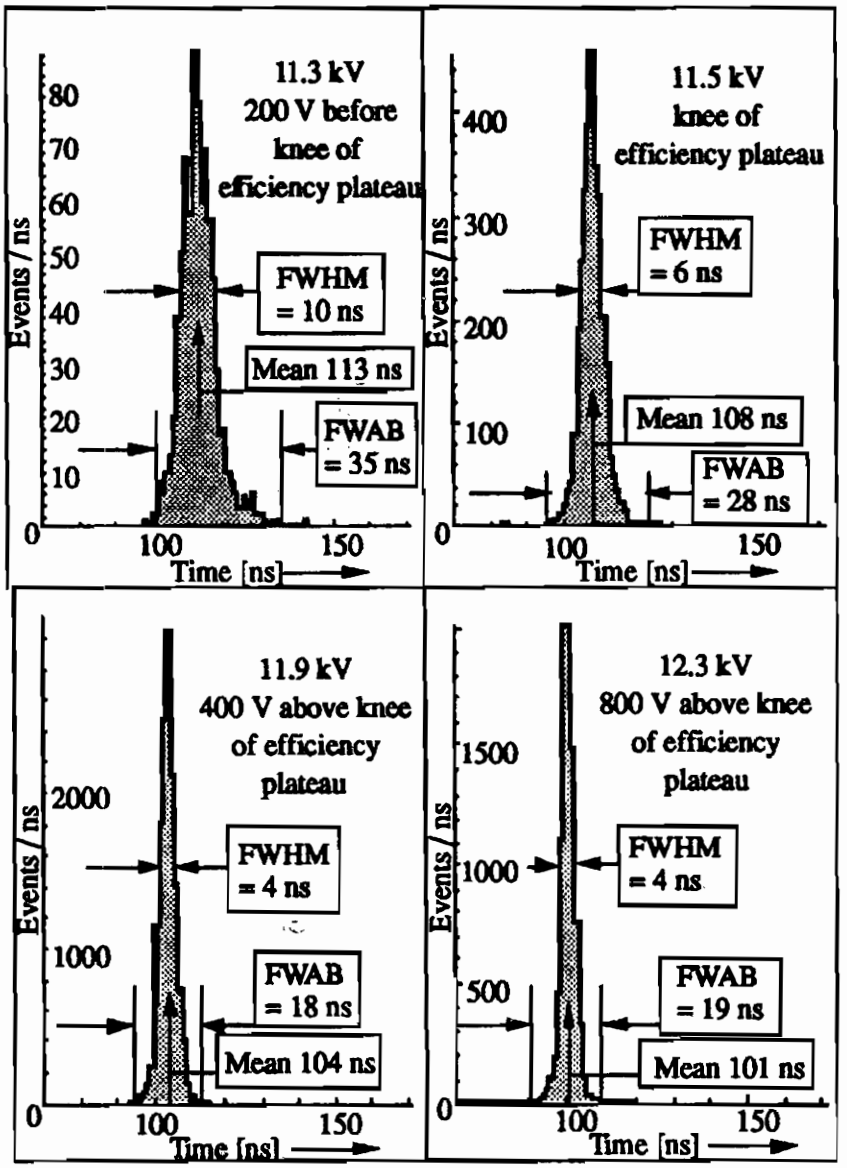


Figure 8. Time spectra measured with the $C_2F_5H$ gas mixture for four voltages. The full width half maximum (FWHM) is shown and the window necessary to contain 99% of the total events. (FWAB).

noted that the histogram corresponding to 12.3 kV only contains 10% of all events. There is a long tail containing the other 90%; thus in reality it is not gaussian. The change from exponential to the Landau

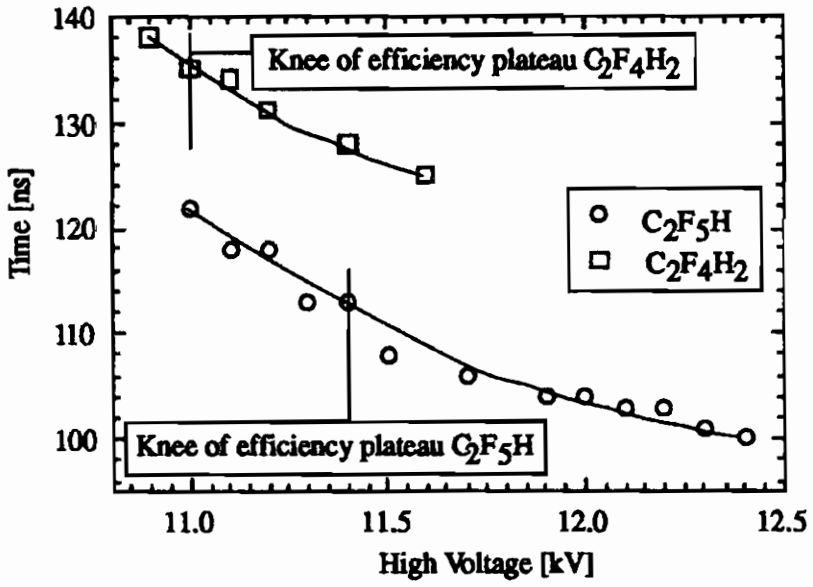


Figure 9. Time walk with voltage for two gas mixtures.

shape is due to this strong limitation in the growth of large avalanches due to space charge effects.

## 5. Results of Test Beam

All the tests described above were performed with cosmic rays. We have also tested the same 2 mm gap RPC in the T9 test beam at CERN. This beam was defocused to covered the active area of the RPC with a uniform flux. It was set at negative 8 GeV/c and consisted mainly of pions. The spills had a flat top of 250 ms and occurred every 15 to 20 s.

In figure 11 we show the efficiency versus voltage for various fluxes. 1 % water vapour is added to both gas mixtures in this case. It is clear that the efficiency starts to drop as soon as the voltage is raised above the knee of the plateau even at the modest flux of 30 Hz/cm$^2$ for the $C_2F_4H_2$ mixture. The $C_2F_5H$ mixture does have a true plateau although there is a reduction in efficiency at the knee voltage for high fluxes. We also measured the time walk with the $C_2F_5H$ mixture. This

is shown in figure 12. It is clear that this time walk will be a problem if the RPC is used in some critical timing application.

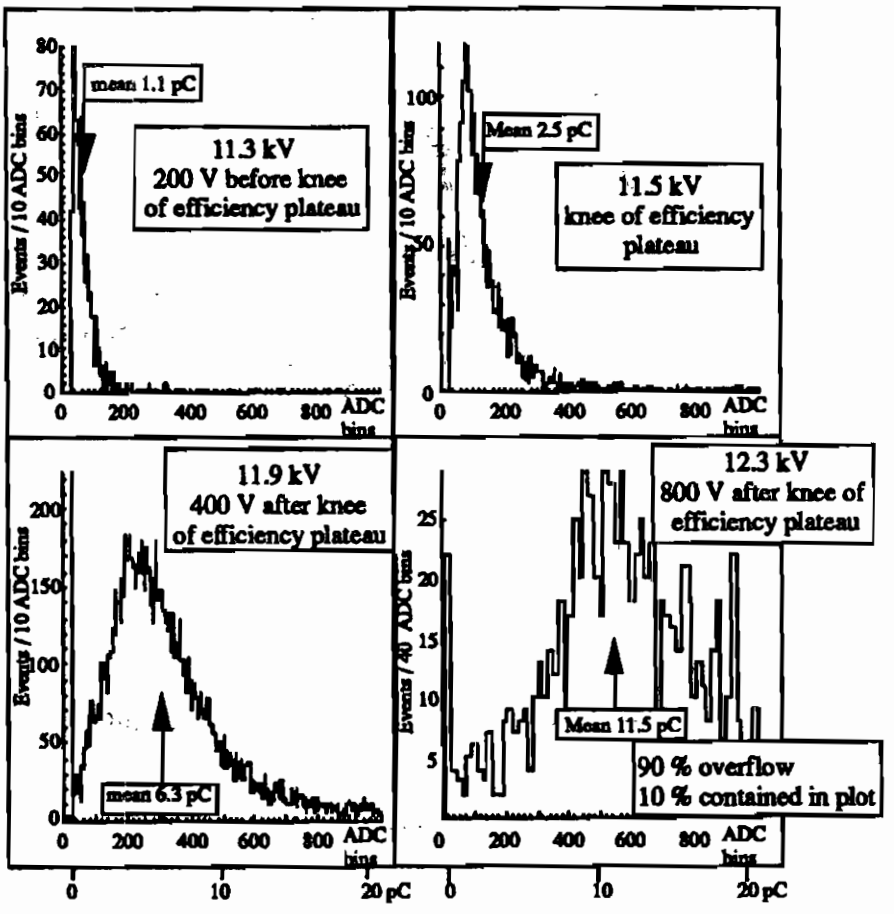


Figure 10. Charge spectra from a 2 mm gap RPC with the $C_2F_5H$ gas mixture.

## 6. Discussion

Our initial interest was to understand the differences in the shape of the charge spectra obtained by various groups working with a 2 mm gap RPC with $C_2F_4H_2$. We find that the shape changes as one varies the applied voltage. Thus the different shapes presented by various groups

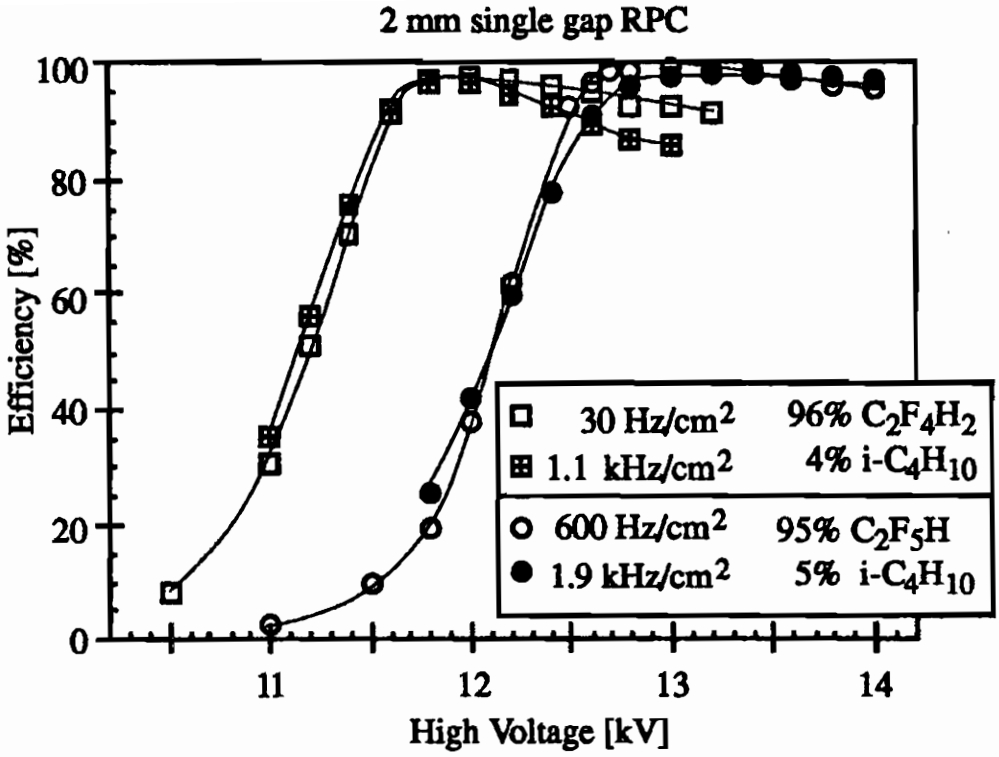


Figure 11: Efficiency versus voltage for various fluxes for two different freon mixtures.

iare a reflection of operating the RPC at a different gas gain. The mechanism that we believe is responsible for this change in shape is the space charge of the positive ions created as the avalanche grows. This could also explain our measured rise in this ratio fast/total signal. Reducing the voltage produces an exponential shaped charge spectrum. It is very difficult to work with this exponential shaped spectrum since it requires an ever lower discriminator threshold.

In order to move away from this exponential shaped charge spectrum, we are forced to operate the RPC in a mode where the gas gain of large avalanches is limited by space charge (luckily there exists this space charge limitation; otherwise these avalanches would all grow to a size that would trigger a transition to a streamer). In this mode of

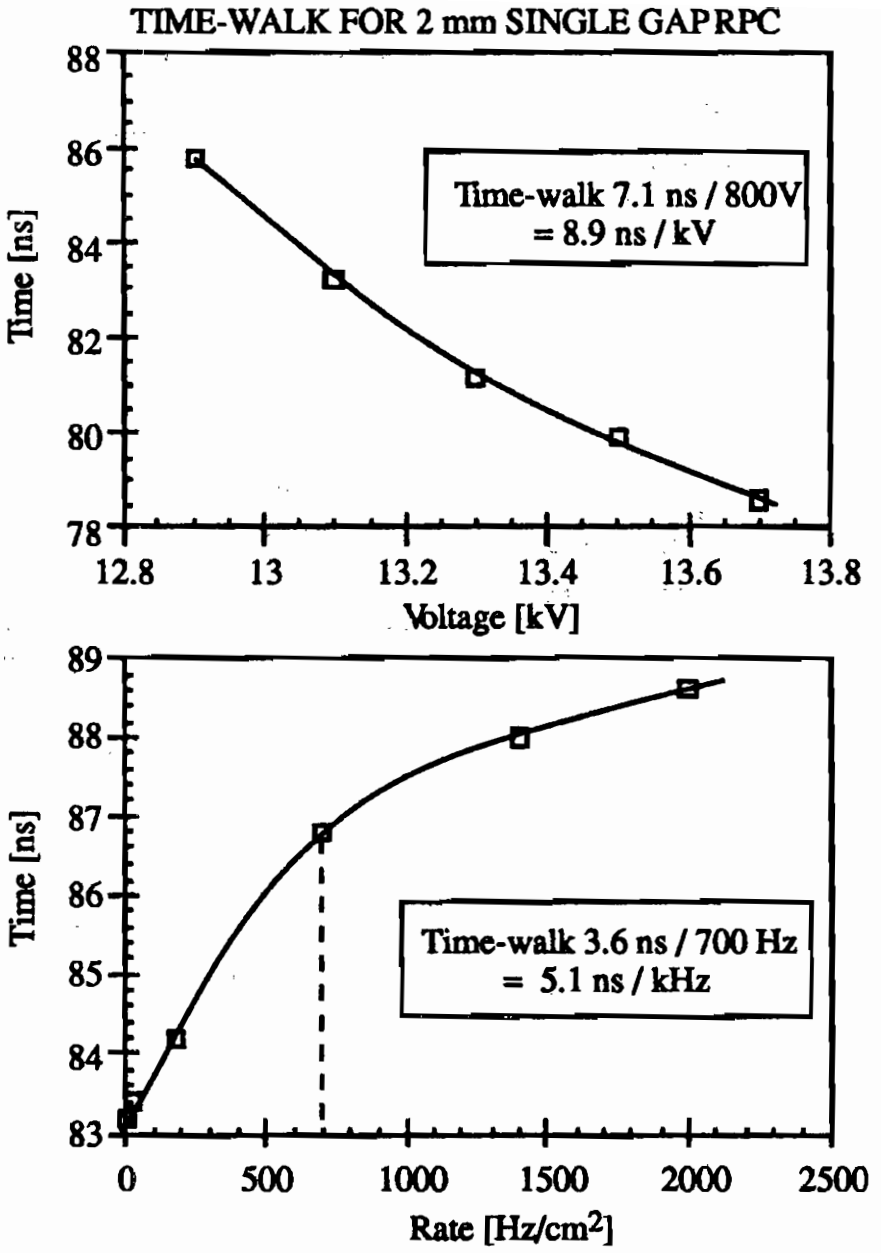


Figure 12: Time walk for single 2 mm gap RPC. The gas mixture containing $C_2F_5H$ was in use.

space-charge-limited avalanches, we do not expect an increase in the window of safe operating voltage (range of voltage at full efficiency with ~0 % probability of streamer) by increasing the gas gap (to 3 mm

for example). In fact, one may find a reduction in the window of safe operation, since the density of positive ions in an avalanche for a 3 mm gap RPC will be less than a 2 mm gap RPC. It is the density of ions that give rise to space charge effects, which plays the all important role of limiting the avalanche growth.

$C_2F_5H$ is a more suitable gas than $C_2F_4H_2$; it is denser and has one less hydrogen per molecule - which could be important in environments where there is a high background of neutrons. It is more quenching, thus the transition to streamer occurs at larger avalanche size. Additionally any streamer produced has a much lower total charge. However it appears to have a larger attachment coefficient, thus working at very low gas gains would be difficult.

For an effective mechanism to limit the growth of large avalanches, the gas gain has to vary rapidly with a change in electric field, otherwise the gas gain will not be modified by space charge of the positive ions. (It should be noted that the efficiency of the $C_2F_5H$ gas mixture does rise more quickly with voltage than the $C_2F_4H_2$ mixture, thus the gas gain does vary more rapidly with voltage). However the rapid change of gain with a small change in the electric field has adverse side effects; the gas gain will vary rapidly with a small change in the gap dimension; the probability of streamers will increase rapidly with applied voltage (once the threshold for streamer production has been passed). One may enhance the window of safe operation if one can find a gas mixture that allows one to operate the RPC at a low applied voltage. It is the interplay between the field due to space charge and the electric field across the gas gap that leads to the reduction in the growth of the avalanche. However a gas mixture that operates at a lower electric field may also have a slower drift velocity of the electrons; thus the time resolution could be degraded. The time resolution together with our measurement of time walk indicates that the use of a single gap RPC may have marginal timing properties for LHC experiments.

The fact that the streamers are delayed for the $C_2F_4H_2$ allows one to operate slightly above the threshold for streamer production. One can use the preceding (and clean) avalanche signal to generate the

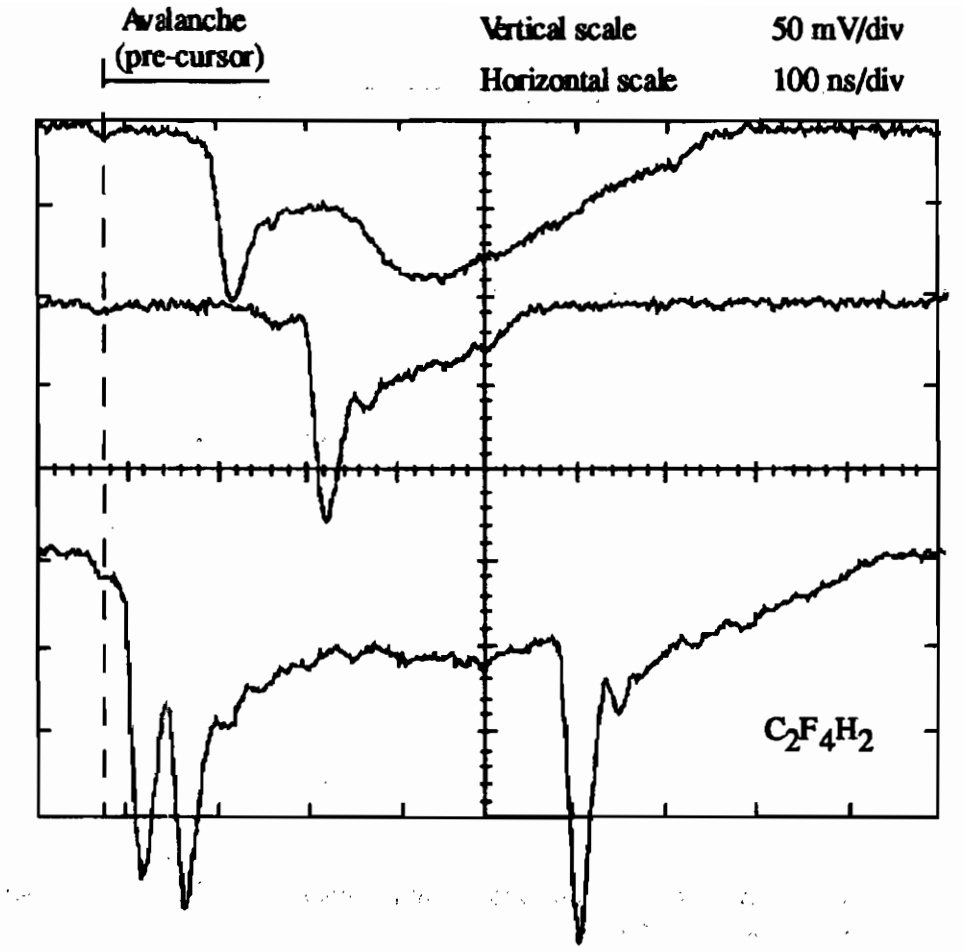


Figure 13. Typical streamer signals with $C_2F_4H_2$ gas mixture. The anode was directly connected to the oscilloscope with input termination of 50 Ω. Voltage set at 300 V above 'knee' of efficiency plateau.

trigger signal. The large cluster of hit strips associated to the streamer occurs later. Nonetheless there may be problems due to the large amount of produced charge (i.e. limited rate capability) and the extra noise in the system. It is instructive to question why this gas ($C_2F_4H_2$) has delayed streamer production, while other gas mixtures do not.

The transition between avalanche and streamer is initiated by the high electric field around the cloud of positive ions[10]. This high field

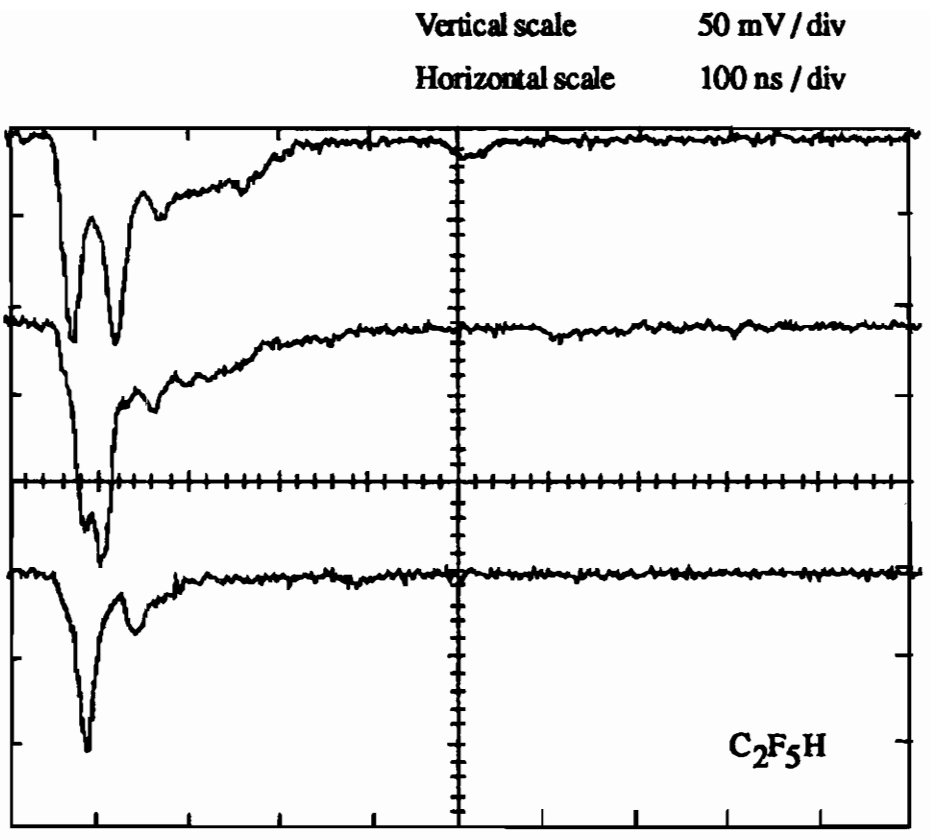


Figure 14. Typical streamer signals with $C_2F_5H$ gas mixture. The anode was directly connected to the oscilloscope with input termination of 50 Ω. Voltage set at 1400 V above 'knee' of efficiency plateau.

can directly ionise the gas triggering the production of a streamer. The field around the positive ions is partially negated by the electrons at the head of the avalanche; however these electrons disappear when they enter the anode plate; this leads to a sudden increase in field around the positive ions. Since these gases are electronegative there are also negative ions generated in the avalanche which are interspersed among the positive ions. These will slowly drift out towards the anode leading to a further increase in field around the positive ions. On reaching the anode, the extra electron carried by the negative ions should jump across onto the anode (and disappear) allowing the neutralised ion to drift off. However it is not clear how instantaneous this process is and

how long the negative ions may sit on the surface of the anode. Thus, we have two processes which depend on the species of negative ions (thus can be gas dependent); the drift speed of the negative ions and the speed that the negative ions are discharged on reaching the anode. As shown in figure 3, we have a signal that we associate with the drift of the negative ions with the $C_2F_4H_2$ gas.

Finally we show some typical oscilloscope traces of streamers in the two gases. For this measurement we directly connect the anode to the oscilloscope; the input of the oscilloscope is terminated by 50 Ω. For the $C_2F_4H_2$ mixture shown in figure 13 we are operating at 300 V above the knee of the efficiency plateau; figure 14 shows streamers in $C_2F_5H$ at a voltage 1400 V above the knee of the efficiency plateau. It is clear that the streamers in $C_2F_5H$ are more heavily quenched.

The LHC experiments plan on building many thousand of square metres of RPC, with each chamber being of some square metres in size. One of the critical parameters for the mass production of these chambers will be the tolerance of the gas gap. A change in the dimension of this gap causes a change in electric field. Thus, if 'streamer-free' and high efficiency operation can be achieved for a 200 V range with an applied voltage of 10 kV, this corresponds to change of 40 micron in the 2 mm gap (i.e. the chambers have to be constructed with a tolerance of $\sigma \sim 12$ μm). However, there is a correction to be made since a wider gap indeed has a lower field, but the avalanche has some extra distance to develop. We can estimate this correction since Ammosov et al.[4] compare the operating voltage of a 2 mm and 3.5 mm chamber filled with 97% $C_2F_4H_2$ and 3 % iso-$C_4H_{10}$. They report that the operating voltage increases from 8 kV to 13 kV for this increase of gap width; thus the required tolerance is 60 microns (i.e. $\sigma \sim 60/\sqrt{12} = 17$ μm). This is still a very tight tolerance!

## 6. Conclusions

We have tested a 2 mm gap RPC with two types of freon. For both we find an increase in fast/total charge for increasing avalanche

magnitude; this leads us to speculate that the growth of large avalanches is limited by space charge. We believe that this mechanism is also responsible for the change in shape of the charge spectrum. The shape changes from an exponential at low gas gain to a 'Landau shaped' spectrum at high gas gain.

We find that the gas $C_2F_5H$ has a larger voltage window of 'safe operation' (full efficiency with negligible streamers) and thus is a more suitable gas for use in narrow gap RPCs. Additionally we find that any streamers produced in $C_2F_5H$ are 'prompt' but less violent than in $C_2F_4H_2$.

We have measured a large time-walk with voltage, which could limit the time resolution for large RPC systems. Additionally one needs to operate above the knee of the efficiency plateau to obtain a time resolution acceptable for LHC applications; however at this elevated voltage we measure a drop in efficiency already at a flux in the order of tens of $Hz/cm^2$ for the $C_2F_4H_2$ gas mixture. However it appears one will be able to work up to some $kHz/cm^2$ flux for the $C_2F_5H$ gas mixture. One should not overlook the power dissipation in the gas volume at these elevated fluxes. Finally, the cost of $C_2F_5H$ is a factor ~ 3 more than $C_2F_4H_2$; this could also be a critical constraint for large systems.

## References


1. ATLAS Technical proposal, CERN/LHCC/94-43, LHCC/P2 (1994).
2. The CMS technical proposal, CERN/LHCC/94-38, LHCC/P1 (1994).
3. Performances of a Resistive Plate Chamber operated in avalanche mode under $^{137}Cs$ irradiation , M. Abbrescia et al., CMS note 97/003 and submitted to Nucl. Inst. Meth A.
4. Comparison between 2 mm and 3.5 mm gap RPCs operated at Low Gas Gain. V.V. Ammosov, V.A. Gapienko, V.A. Sen'ko, E.A. Usenko, I.L. Vasiliev, V.A. Zaets, September 1996, Protvino, Russia. Unpublished report.

5. Resistive Plate Chambers in ATLAS, M.G. Alviggi, P. Bagnaia, P. Camarri, R. Cardarelli, P. Creti, R. de Asmundis, A. Di Ciaccio, E. Gorini, M. Primavera, L. Pontecorvo, P. Oberson, R. Santonico and S. Veneziano. ATLAS Internal Note, MUON-NO-131, October 1, 1996.

6. E. Cerron Zeballos et al. Nucl. Inst. and Meth. A 381(1996)569.

7. I. Crotty et al. Nucl. Inst. Meth A 360(1995)512

8. R. Cardarelli, V. Makeev and R. Santonico; Nucl. Instr. and Meth. A382(1996)470

9. E. Cerron Zeballos et al. Nucl. Inst. and Meth A373(1996)35.

10. A Model of Avalanche to Streamer Transition in PPC/RPC Detectors, P. Fonte, talk given at 3rd Int. Workshop on Resistive Plate Chambers, Pavia, October 1995, Scientifica Acta, Vol XI (1996)25.

# 8-CHANNELS GAAS IC FRONT-END DISCRIMINATOR FOR RPC PARTICLE DETECTORS

R.Cardarelli[1], S.Ciorciolini[2], V.Chiostri[1], G.Orengo[2]
*1) Dipartim. di Fisica & INFN - Università "Tor Vergata" - via della Ricerca Scientifica - 00133 Roma - Italy*
*2) Dipartim. di Ingegneria Elettronica - Università "Tor Vergata" - via Tor Vergata - 00133 Roma - Italy*

ABSTRACT

A front-end discriminator for application in readout electronics of RPC particle detectors, composed of a high-gain pulse amplifier integrated with a variable threshold comparator and an ECL buffer, has been designed. An 8-channels full custom chip has been fabricated in GaAs technology by GIGA foundry. The chip turns out to be very stable, featuring high voltage gain (>1000), gain-bandwidth product ($10^{11}$) and sensitivity ($\sim 50\mu V$), fast rise time (1.5ns), high trigger time resolution (1ns), and 25mW per channel of power consumption.

## 1. Front-end outlines

A resistive plate chamber (RPC) detector operating in avalanche mode produces typically a single signal of 5ns FWHM and 1.5ns time jitter, while the pick-up propagation time is 15ns. The input stage of the front-end is a voltage amplifier; the good time performance of the RPC detectors, utilized for the bunch crossing identification, imposes the amplifier rise time of the order of the RPC jitter time, because the large fluctuation in signal amplitude of the detector ($100\mu V$ to 0.5V ) generates a jitter time at the threshold crossing of the order of the pulse rise time.
The amplifier frequency response is optimized for typical time structure of the avalanche signal according to the following conditions: 1) same risetime for the amplifier and input signals, which is nearly 1.5 ns; 2) minimum return-to-zero time for the output signal. The resulting frequency response has a maximum at 100MHz and a 3dB bandwidth of 160MHz. The amplifier output is bipolar shaped, as shown in Fig.3, giv-

ing zero integrated charge thus avoiding a possible dependence of steady output voltage on the counting rate.
The high input impedance $R_I$ of the amplifier should be matched to the low impedance $R_S$ of the pick-up strip. Teaming this amplifier with a simple transformer input coupling yields the voltage amplification to be multiplied by a factor $n(R_S+R_I)/(n^2R_S+R_I)$, which reaches the maximum for $n^2=R_i/R_S$, if n is the turns ratio of the transformer. This means an increase in the discriminator sensitivity until the noise is one order of degree below. Moreover it has been demonstrated that an input transformer coupling can reduce the amplifier's noise figure when the equivalent input noise voltage is much greater than the noise voltage generated by the input noise current through the source impedance. Coaxial air-coupled spiral inductances seem to be a suitable choice, since ferrite materials cannot be used in the high intensity magnetic fields of the high energy physics experimental apparatuses. Conversely lossless LC impedance matching network with the same amplifier bandwidth feature high complexity.

## 2. 8-channel prototype realization

A two-channel full custom prototype chip of the front-end circuit has been already realized in GaAs technology [1] (die size lxl.25 $mm^2$). This chip was a preliminary step before the 8-channel final version, which has been realized and tested on a full-custom board. The schematic and the monolithic layout of the 8-channel chip are reported in Fig.1 and Fig.2 respectively (die size 1.5x2.3 $mm^2$). Two channels have independent bias lines for testing.
The MESFET process employed is the Triquint-GIGA D1SS type with 0.6$\mu$m of gate length. 2OGHz cutoff frequency MESFETs have been chosen for their intrinsic high gain-bandwidth product. Moreover, working at frequencies above the 1/f corner, the GaAs MESFET features the minimum serial-parallel noise at the given frequency band.
The amplifier is composed of three ac coupled gain stages. The comparator is ac coupled to the amplifying section and composed of three stages connected in differential mode. It outputs a positive or negative squared pulse from a bipolar one, with 450ps rise and fall time. The threshold value can be regulated a bit over the noise level. An ECL output buffer is capable of driving a few metre long 100 ohm flat cable

connecting the front-end to the local trigger logic.
The circuit turned out to be very robust versus both temperature, power supply and processing variations. Cross talk between channels and oscillations could easily be the result of parasitic couplings between circuit elements as well as package and bonding wires. Stage supplies are separated inside the monolithic area, and strongly filtered on the board before connection. Ground is the same except for the output ECL driver, to avoid the feedback propagation of spurious spikes generated by output rise/fall transitions.

## 3. Experimental results

All measurements have been performed on an 8-channel test board by mean of a TEK-TDS684B digital oscilloscope. A summary of channel characterization is presented. The amplifier output pulse shape for an avalanche-like input pulse is shown in Fig.3. A preliminary measurement of the front-end sensitivity is reported in Fig.4, where an input pulse of 200$\mu$V amplitude has been discriminated, with a 1:3 turns ratio of the transformer. The overall voltage gain is approximately 1500 with a 100MHz bandwidth, resulting a gain-bandwidth product GBWP$>10^5$; better results can be achieved with higher turns ratios. The threshold has been set at a minimum value of 200mV, because the RF noise level is rather high in the measurement setup environment. The comparator has been also characterised and the results are plotted in Fig. 5 and Fig. 6, where the output jitter time can be seen for a variation of input pulse width and amplitude respectively. The autoshaping capability of the circuit has been demonstrated. The maximum skew time between channels on the test board can be seen in Fig.7; as it can be seen, the channel paths are well equalised. The absence of cross-talk interference between adjacent board channels is shown in Fig.8. Finally, the measured power consumption per channel is 25mW.

## 4. References


1. G.Orengo, R.Cardarelli, V.Chiostri, E.Johansen, "Multichannels GaAs MMIC front-ends for gas chamber particle detectors", *Proceed. of 5th European Gallium Arsenide Applications Symposium GAAS 97*, pp.341-344, Bologna, September 1997.

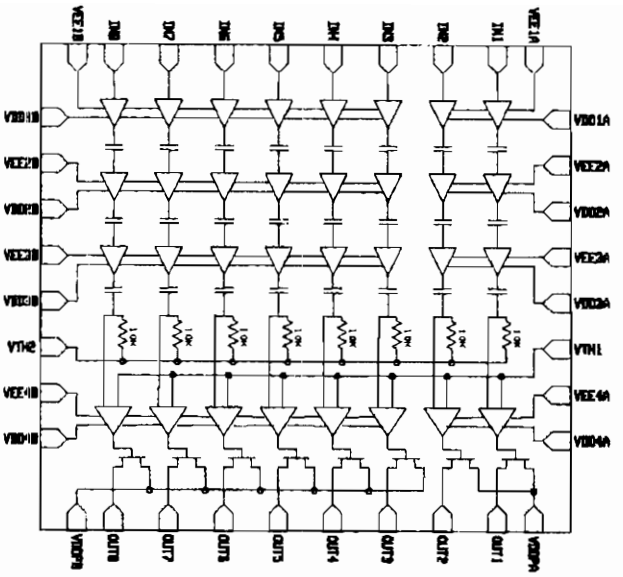

Figure 1: Schematic layout of the 8-channel front-end

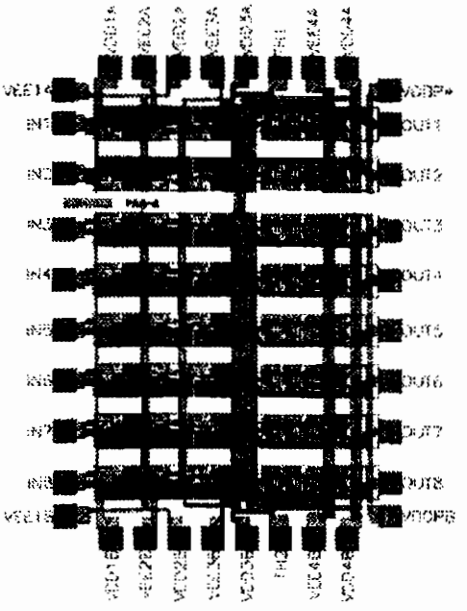

Figure 2: Monolithic layout of the GaAs IC 8-channel front-end (die-size 1.5x2.3mm $^2$)

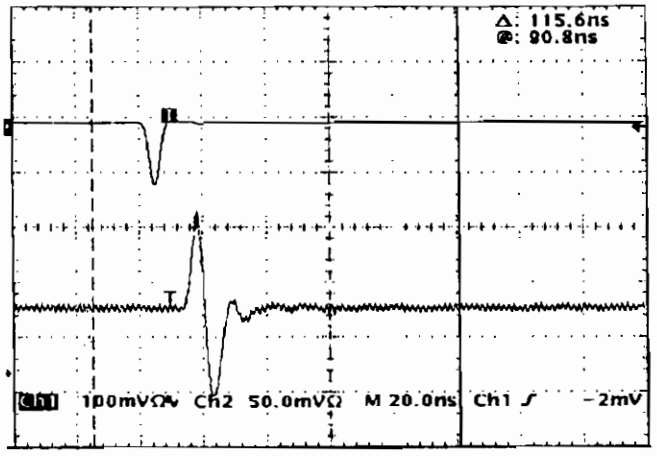


Figure 3: Amplifier output pulse shaping for a triangular-shaped input signal

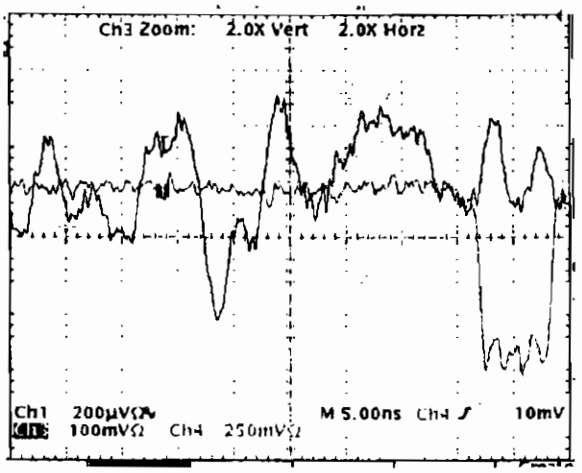


Figure 4: Sensitivity ($200\mu$V). The voltage gain is 1500 (trasformer impedance ratio 1:9)

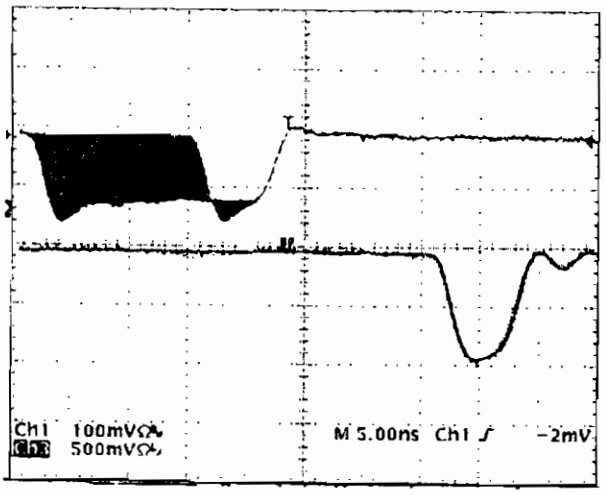


Figure 5: Output jitter (on the fall) vs input pulse width (6-20ns)

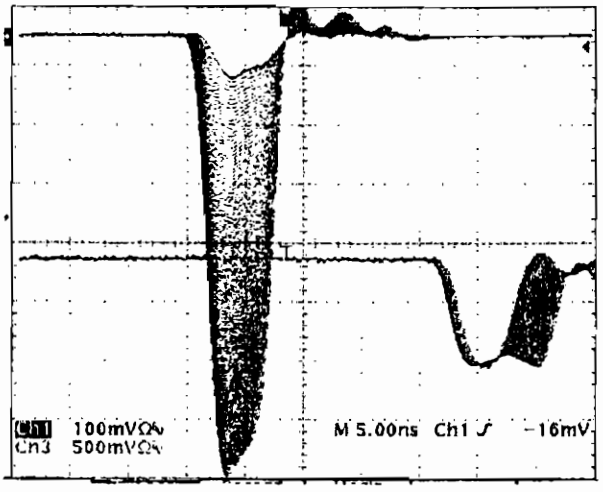


Figure 6: Output jitter (on the fall) vs input pulse width (50-700mV less 30dB attenuation)

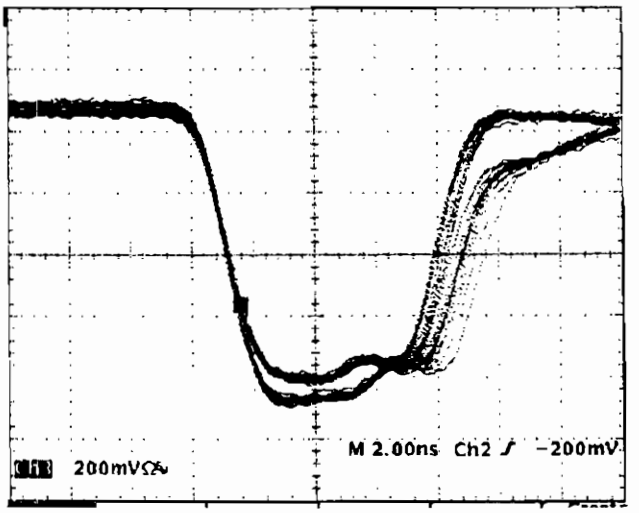


Figure 7: Maximum skew (on the fall) of the board channels

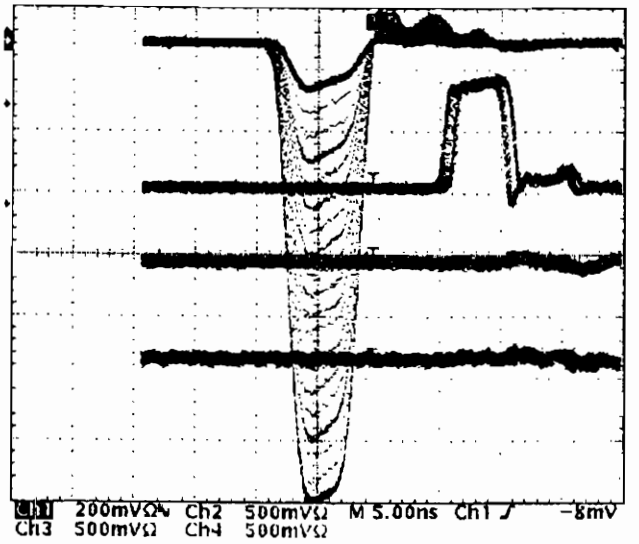


Figure 8: Cross-talk between adjacent channels

# FRONT END ELECTRONICS FOR RPC DETECTOR OF CMS

F. LODDO *
*Dipartimento Interateneo di Fisica and Sezione INFN, Bari, Italy*

December 15, 1997

ABSTRACT

A prototype front-end amplifier-discriminator-monostable circuit for Resistive Plate Chamber detectors is presented. It has been designed and manufactured using the Maxim-SHPI bipolar technology. The aim of the circuit is to amplify a delta-like current signal ranging from 20 fC to 20 pC and to generate a fast output pulse.

## 1. Introduction

The RPC detectors will be used in CMS experiment for the muon trigger system [1]. The aim of this circuit is to amplify a current signal coming from a Resistive Plate Chamber (RPC) detector for timing measurement purpose. The input dynamic range is 20 fC $< Qin <$ 20 pC. The amplifier must provide an output pulse having rise time as fast as possible. The shape of the current signal, induced by a single cluster, is described by the function $I(t) = I_0 \exp(t/\tau)$; $0 \leq t \leq 15$ ns, for $C_2H_2F_4$-based gas mixtures having electron drift speed in the order of 130 $\mu$m/ns and $\tau$ (gas time constant) $\sim$ 1 ns at the nominal working point of the detector. This can also be considered a good approxima-

*co authors : M. Abbrescia, G. Bruno, A. Colaleo, G. Iaselli, G. Lamanna, M. Maggi, B. Marangelli, S. Natali, S. Nuzzo, G. Pugliese, A. Ranieri, F. Romano *Dipartimento Interateneo di Fisica and Sezione INFN, Bari, Italy*; S. Altieri, V. Arena, G. Bonomi, G. Gianini, M. Merlo, S. P. Ratti, C. Riccardi, L. Viola, P. Vitulo *Dipartimento di Fisica Nucleare e Teorica and Sezione INFN, Pavia, Italy*

tion of the real signal, since almost the whole induced current originates from the first two clusters. For RPCs that will be operated in the barrel region of CMS, the current signal comes from a strip-line 1.3 m long whose characteristic resistance $R_0$, for an RPC with 2-mm double-gap geometry and a strip width ranging from 2 to 4 cm, ranges from 40 to 15 $\Omega$, respectively. The corresponding strip capacitance ranges between $\sim$ 160 pF and $\sim$ 420 pF. The propagation delay is $\sim$ 5.5 ns/m.

## 2. Design constraints

The rise time of the induced signal ($\sim$ 1 ns) is shorter than the propagation delay along the strip, therefore this one must be treated as a transmission line and properly terminated at both ends. In fact, reflected signals increase occupancy and, if the termination resistance is $> R_0$, a fraction of input charge is reflected and lost, that is the effective threshold is increased. The strip is terminated on one end by the input resistance of the preamplifier and on the other end by an ohmic termination, that is less expensive and power consuming than active terminations, in front of a small increase of noise.

Since the termination resistance has a small and variable value, an AC coupling between strip and amplifier is required. Simulations and past experience show that, setting the threshold around 20 fC, the detector is fully efficient with low streamer probability. This means that a $\sigma_{noise} < 4$ fC could be tolerated.

The excellent timing information of the input signal must be preserved by the amplifier. This purpose is easily satisfied by an amplifier having a single dominant pole at relatively low frequency and the next high frequency pole as far as possible. The output pulse will have nearly the same fast rise as the input and a long tail. Since in the barrel the expected single rate is less than 200 kHz/channel (with the maximum strip area of $130 \times 4$ cm$^2$), a tail length below 50 ns would allow a negligible pile-up probability. The fast peaking time and the slow tail tend to affect the series and the parallel noise, respectively. This consideration has been kept into account, in order to not exceed the required noise limit.

In a RPC working in avalanche mode, the avalanche pulse is often followed by an after-pulse with a delay ranging from 0 to some tens of ns: the possible second trigger must be masked. Therefore, the discriminator must be followed by a one-shot and the pulse length set to a value that

is a trade-off between the possible second trigger and the dead time. A length of 100 ns, giving a dead time of 2%, has been considered a good compromise.

## 3. Technology

The front-end asic has been made in semi-custom bipolar technology SHPI by Maxim. This process has been already used in many high energy physics experiments. In fact, silicon bipolar technologies offer a good trade-off in speed, power, low intrinsic noise and reliability. These properties make them ideal for fast, low power and low noise designs. Moreover, its radiation hardness was considered adequate even at the highest radiation levels of LHC [2].

The Maxim SHPI technology consists of vertical npn transistors, lateral pnp and jfet transistors, active base and implanted resistors, MOS capacitors and Schottky diodes. The unity gain-bandwidth product of the npn transistor peaks at 9 GHz with 500 $\mu$A of collector current for a minimum area device. The claimed typical on chip matching of the base-emitter voltage is 1 mV or less, while adjacent resistors match better than 1 %. The *semi-custom-Quicktile* approach for fabrication was chosen: groups of devices are placed within predefined layout areas called tiles. All device layers, except the interconnect metal layers, are placed by the manufacturer: the designer proceeds with the layout of the metal layers.

## 4. The circuit

The circuit is made of six identical channels, each one consisting of an amplifier, a discriminator-monostable and a differential 110 $\Omega$ line driver. The requested power supplies are +3V and -2V; the overall power consumption is about 30 mW/channel. The package is quad-flat-pack, 64 pins.

### *4.1. The amplifier*

The preamplifier (Fig.2) is made of a common emitter transresistance stage, to match the characteristic impedance of the strip. In this technology, a common emitter stage is fast enough, so no cascode was

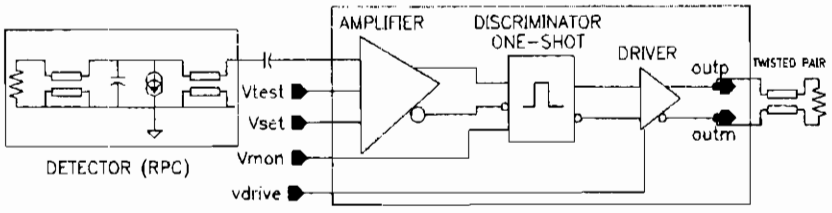


Fig. 1. Single channel block diagram

required. The expression of the input impedance is:

$$Z_i(s) = R_{feed}\frac{s + \frac{1}{R_L C}}{s + \frac{g_m}{C}} \tag{1}$$

where $R_{feed}$ is the feedback resistance, $g_m$ is the transconductance and the parallel of $R_L$ and $C$ is the internal load across which the voltage gain is produced. The zero of the above expression is at 100 MHz. At low frequencies, the value of $Z_i$ is about 20 $\Omega$, while it is about 30 $\Omega$ at the signal frequencies (around 100 MHz). The input transistor $Q_{in}$ has a very low base resistance ($\sim$ 10 $\Omega$) and it does not give an important contribution to the series noise. The current in $Q_{in}$ is about 700 $\mu$A and $R_L$ is 2 K$\Omega$. The resultant open loop gain is 55, while the dominant pole of the preamplifier is about 180 MHz. A dummy input preamplifier was required to balance the DC output variations of the real input first stage. The transresistance stage is followed by a gain stage that introduces a dominant pole at 18 MHz, giving a tail length of $\sim$ 30 ns. The charge sensitivity is $\sim$ 1.6 mV/fC, on the basis of past experience on the detector. The typical simulated responses of preamplifier and gain stage are shown in Fig.3. The differential output of the amplifier is then DC-coupled to the threshold circuit. It is made of a couple of emitter followers, $Q_{efl}$ and $Q_{efr}$ and resistors $R_3$ and $R_4$, which provide a suitable level shift to the two outputs. These two emitter followers are fed by the differential amplifier $Q_{thl}$ and $Q_{thr}$. The threshold input, $V_{set}$, is attenuated by a factor four and used to set a voltage difference between $Q_{thl}$ and $Q_{thr}$ and, therefore, a current difference through $R_3$ and $R_4$. In such a way, the initially balanced preamplifier outputs are now unbalanced, providing a threshold condition at discriminator input. In the linear operating region, the voltage shift is about

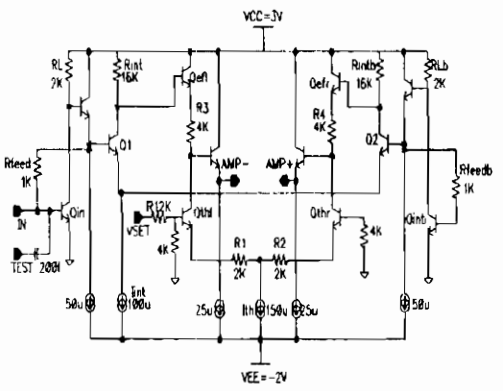


Fig. 2. Schematic diagram of amplifier

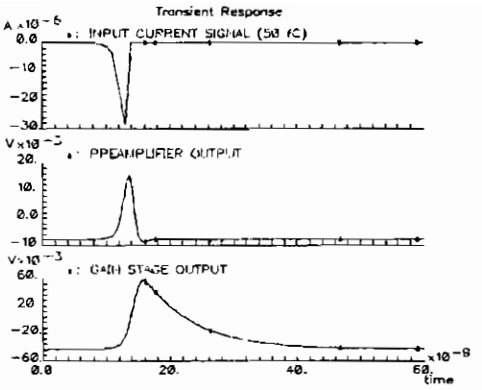


Fig. 3. Typical transient amplifier response.

$$\Delta V \approx \frac{V_{set}}{4}\frac{R_3}{R_1} \tag{2}$$

In order to keep the ratio $R_1/R_3$ constant over process and temperature variations, resistors $R_1$ and $R_3$ should be of the same type (active base resistors). In such a way, $\Delta V \sim V_{set}/2$ and depends only upon the external voltage control. The current through the threshold differential amplifier, $I_{th}$, has been set to 150 $\mu$A in order to allow a linear behavior of such a circuit in the requested wide threshold range, between 10 fC and 300 fC. The power consumption is 7 mW.

### *4.2. Noise calculation*

The equivalent circuit of detector and amplifier for noise analysis is shown in Fig.4 [3]. The parallel noise is dominated by the thermal noise of the termination resistance at the far end of the strip and can be represented by an equivalent noise current generator with power density $i_n^2(A^2/\mathrm{Hz})$ in parallel to the termination resistor, supposed noiseless. The series noise is represented by an equivalent noise voltage generator with power density $e_n^2(V^2/\mathrm{Hz})$ in series with the input [4].

$$i_n^2 = \frac{4KT}{R_0} \sim 1.1 \times 10^{-21} \quad \mathrm{A}^2/\mathrm{Hz} \tag{3}$$

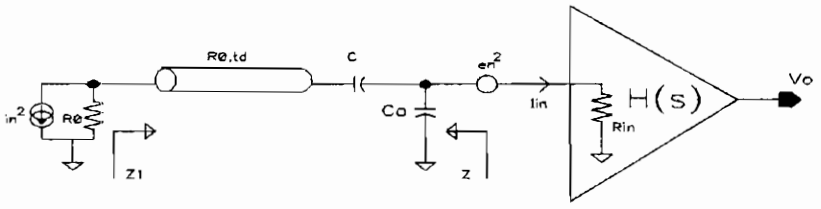


Fig. 4. Equivalent circuit of detector and amplifier for noise analysis

$$e_n^2 = 4KT(\frac{0.5}{g_m} + R_{BB'}) \sim 4.6 \times 10^{-19} \quad \mathrm{V^2/Hz} \tag{4}$$

$$H(s) = \frac{V(s)}{I(s)} \approx \frac{A}{1 + s\tau_L} \tag{5}$$

$\tau_L$ being the time constant of the dominant pole and $A$ the gain.

The preamplifier being current sensitive, it is convenient to transform the noise voltage generator into an equivalent current noise generator with power spectrum

$$i_{ns}^2 = \frac{e_n^2}{|R_{in} + Z|^2} \tag{6}$$

where $Z$ is the impedance shown in Fig.4 and $R_{in}$ is the input resistance of the preamplifier. For simplicity, in this analysis $R_{in}$ is supposed to be equal to the strip characteristic impedance.

$$Z = (R_0 + \frac{1}{sC})//\frac{1}{sC_a} \Rightarrow Z = \frac{1 + sR_0C}{s[sR_0CC_a + C + C_a]} \tag{7}$$

where $C$ is the AC-coupling capacitance between the strip and the preamplifier and $C_a$ the total capacitance on the preamplifier input. Being $C \gg C_a$,

$$Z \approx \frac{1}{sC}\frac{1 + sR_0C}{1 + sR_0C_a} \tag{8}$$

$$i_{ns}^2 = \frac{e_n^2}{\left|R_0 + \frac{1}{sC}\frac{1+sR_0C}{1+sR_0C_a}\right|^2} \tag{9}$$

The rms noise at the output is found by integration of the noise current through $R_0$ multiplied by the square of the magnitude of the transfer function of the amplifier:

$$V_{ns}^2 = \int_0^\infty i_{ns}^2 \, |H(j\omega)|^2 \, df \sim 1.9 \quad \text{mV rms} \tag{10}$$

in the worst case of $R_0 = 15\Omega$. This integral is calculated numerically.

Assuming the line to be ideal, the impedance seen at the far end is:

$$Z_1 = R_0 \frac{Z_i + R_0 tanh(st_d)}{R_0 + Z_i tanh(st_d)} \tag{11}$$

where $Z_i = 1/sC + R_0$ and $t_d \sim 7$ ns is the propagation delay.

Then, the parallel noise current flowing into the preamplifier is (being $1/sC_a \gg R_{in}$)

$$i_{np}^2 = i_n^2 \left| \frac{R_0}{R_0 + Z_1} \right|^2 \tag{12}$$

and, again, the rms noise at the output is:

$$V_{np}^2 = \int_0^\infty i_{np}^2 \, |H(j\omega)|^2 \, df \sim 1.3 \quad \text{mV rms} \tag{13}$$

in the case of $R_0 = 15\Omega$.

Finally the total output noise will be $V_n = \sqrt{V_{ns}^2 + V_{np}^2} \sim 2.3$ mV rms.

Simulation of the circuit, including all the noise sources, shows a total output noise $\sim 2.7$ mV, corresponding to an $ENC \sim 1.7$ fC, fully satisfying the noise limit of 4 fC.

### *4.3. The discriminator-monostable*

The discriminator (Fig.5) is made of a two stage differential amplifier (Q1,Q2) and (Q3,Q4). The first one operates with 80 $\mu$A current, the second with 40 $\mu$A current giving, with the intermediate buffers, a total power consumption $< 1$ mW. This circuit provides a 160 mV digital pulse even at the minimum level threshold (10 fC). The discriminator is followed by a one-shot circuit, that gives a pulse shaped at 100 ns. The monostable is another differential amplifier (QML,QMR), driven

on one branch by the discriminator output (vb1), on the other by the AC coupling with the first branch output (vb2). The required tuning of the pulse width is made by means of a tunable positive feedback circuit: once the monostable output goes up, the differential amplifier (QFL, QFR), driven by the outputs (mon+, mon-), injects the tunable current I_WIDTH into the resistor $R_{shift}$, therefore adding a proper level shift to the signal vb2. This shift acts as an hysteresis, making the state transition faster, preventing the circuit from repetitive triggering due to the noise and, depending on its value, it sets the chosen pulse width. The power consumption of the discriminator + monostable is 7 mW.

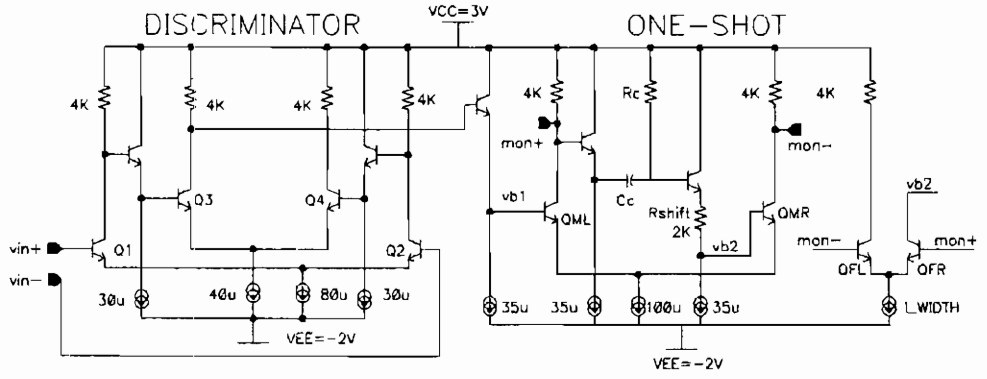


Fig. 5. Schematic diagram of discriminator and monostable

### *4.4. Timing performances*

Computer simulations and experimental results of the time slewing introduced by the front-end channel as a function of charge overdrive are shown in Fig.6. The amplitude contribution is due to the time the signal takes to reach the threshold. The additional walk introduced by the discriminator is due to the finite gain-bandwidth product of the circuit and is negligible for overdrives > 1 fC. This slewing could be reduced by a constant- fraction discriminator or other slewing correction techniques. Fig.7 shows the time distribution, obtained by weighting the time slewing with the probability of occurrence of each charge value given by the charge spectrum. The timing error due to these 2 factors is $\sigma_{t\_el} \sim 0.7$ ns. The noise contribution to the time resolution is:

$$\sigma_{t\_n} = \frac{\sigma_n}{(dV/dt)} \tag{14}$$

where $\sigma_n < 3$ mV is the rms noise and $dV/dt$ is the slew rate of amplifier output at the crossing of discriminator threshold. It is 20 mV/ns on average. Then, $\sigma_{t\_n} < 0.2$ ns $\Rightarrow \sigma_{tot\_el} < 0.7$ ns. Compared to the experimental total error ($1.8 \div 2$ ns), the walk contribution appears negligible. All these considerations convinced us that the timing characteristics of the comparator were fully satisfied and a constant-fraction discriminator was not necessary.

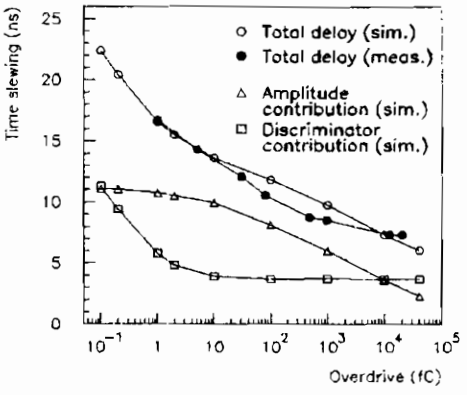


Fig. 6. Time slewing vs charge overdrive

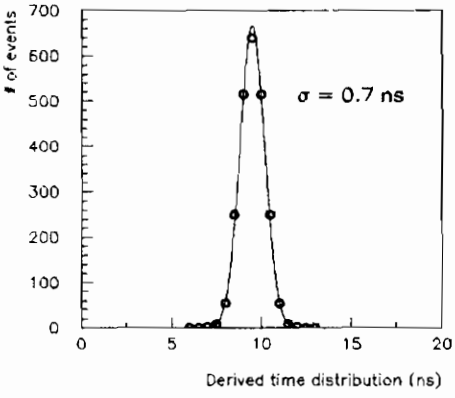


Fig. 7. Time distribution

### *4.5. The output driver*

The driver (Fig.8) has to feed a twisted pair cable with a signal level of 300 mV on 110 Ω, as required by LVDS receivers. The corresponding power consumption is $\sim$ 18 mW. We are also considering the possibility of housing part of the readout electronics on the same front-end PCB. This solution would make the cable not necessary, and the driver power could be decreased down to 5 mW. For this purpose, the chip has the possibility of reducing the driver output current.

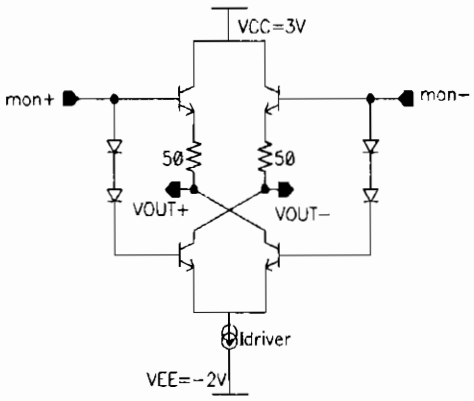


Fig. 8. Schematic diagram of output driver

## 5. Measurements

The first experimental test on prototypes has been performed on the test bench. The input charge was provided by a 50 Ω pulse generator (Le Croy 9210) through a 2 pF capacitor. The basic design parameters, such as charge sensitivity, power consumption, noise and timing performances have shown good agreement with simulations and design parameters. Moreover, no cross-talk was observed up to 10 pC input. The threshold uniformity has resulted not satisfactory: in fact, in front of an expected value $\sim$ 3 fC rms, the measured one was $\sim$ 6 fC rms. In the summer 1997, a large RPC has been instrumented with this front-end chip and exposed to the H2 muon beam. The circuit worked fine and, compared to the old hybrid front-end electronics, it showed a drastic reduction of cross-talk between channels [5].

### *5.1. Noise measurement*

Noise measurements have been performed using the following technique [6]: an input charge $Q_{in}$ at frequency $f_{in}$ is provided to the circuit. With the superposition of the noise, the signal amplitude has gaussian distribution; we set two different thresholds, $V_{th1}$ and $V_{th2}$ in order to have the output signal with frequency $f_{out1} = 0.117 f_{in}$ and

$f_{out2} = 0.883 f_{in}$. Then, $V_{th1} - V_{th2} = 2.35\sigma_n = 5.2$ mV rms, corresponding to an $ENC \sim 1.4$ fC. This value is less than the simulated one ($\sim 1.7$ fC), because it does not include the noise contribution of the passive termination.

## 6. Conclusions

We have designed and prototyped a bipolar front-end asic for the RPC detector of CMS. Measurements of the performance of the prototypes agree with the design constraints and with Spice simulations. Further improvements of the coupling between amplifier and discriminator in order to decrease the threshold disuniformity will be done in the next run. Moreover, we will try to decrease the input impedance of amplifier down to 15 Ω.

## 7. References


1. CMS Muon Technical Design Report (1997)
2. P. Giubellino et al. Nucl. Phys. B (Proc. Suppl.) 32 (1993), 540.
3. R.L.Chase et al., *Transmission line connections between detector and front end electronics in liquid argon calorimetry*, Nucl. Instr. & Meth. **A330** (1993) 228-24
4. V. Radeka, *Low noise Techniques in Detectors*, Ann. Rev. of Nucl. and Part. Science, **Vol.38** (1988)
5. G. Pugliese et al., *Performances of a large double gap RPC*, Proceedings of the IV International Workshop on Resistive Plate Chambers and Related Detectors, Napoli, Italy, 15-16 October 1997.
6. P. Jarron et al., *A fast current sensitive preamplifier (MSD2) for the silicon microstrip detector*, Nucl. Instr. & Meth. **226** (1984) 156-162

# Performance of RPCs operated with various gas mixtures

P. Camarri, R. Cardarelli, A. Di Ciaccio, L. Di Stante, R. Santonico
*INFN Sezione di Roma 2, Via della Ricerca Scientifica 1, 00133 Roma, Italia*

March 25, 1998

ABSTRACT

The performances of 1.5, 2 and 3 mm gap RPCs operated with the "reference" ATLAS gas mixture ($C_2H_2F_4/C_4H_{10}$=97/3) were compared in cosmic ray tests. The effects of small additions of a strongly electronegative gas ($SF_6$) were also studied.

## 1. Introduction

The avalanche and streamer operating modes in Resistive Plate Chambers can be characterized in the plot showing the charge pulse, in logarithmic scale, vs. the operating voltage [1]. For an avalanche discharge this plot is characterized by a linear region typical of the Townsend exponential discharge where the gas gain is very strongly dependent on the operating voltage, followed by a relatively flat region with a much weaker gas gain dependence on the operating voltage, indicating a saturation of the avalanche possibly due to space charge effects.

For most gases, including the one of Ref. [1], the voltage range in which an RPC can be operated in avalanche mode is limited by the appearance of the streamer. This is normally a non wanted phenomenon which, in addition of increasing drastically the delivered charge, also produces high pick-up strip multiplicities as expected from the very low

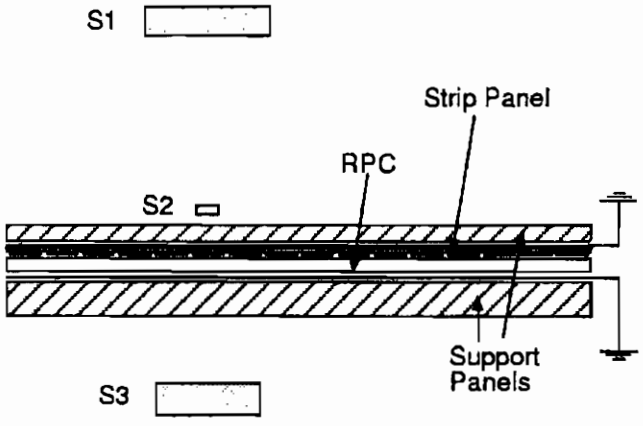


Figure 1: Experimental layout: scintillator telescope and details of the test RPC; digital oscilloscope and DAQ system.

discrimination threshold that is required by the avalanche operation.

## 2. Experimental setup

This paper describes a cosmic ray test made in the INFN laboratories of Roma 2 by means of an experimental set up similar to the one already described in Ref. [1]. A set of three scintillators S1, S2 and S3 are used to select a cosmic ray beam intersecting the RPC under test. Two scintillators, S1 and S3, have relatively large sizes, $60 \times 10$ cm$^2$ and $50 \times 8.5$ cm$^2$, with respect to the RPC pick up strips, while the third one is a "finger" of $2 \times 30$ cm$^2$, 1 cm thick. The RPC of $50 \times 50$ cm$^2$ sensitive area, has a 2 mm gap between 2 mm bakelite plates, according to the scheme of the ATLAS Muon TDR [2].

The read out is made of 16 aluminum strips glued on a plate of expanded polystyrene 3 mm thick which has a grounded aluminum foil glued on the opposite face. Thin grounded copper wires are inserted between contiguous strips. The strips, which have an impedance of 25 $\Omega$, are terminated at both ends. At the end where the signal is read out the termination is realized by a 50 $\Omega$ resistor in parallel with a 50 $\Omega$ cable feeding 1/2 of the signal current into the amplifier. The experimental setup and the RPC lay out are sketched in Fig. 1.

## 3. Study of the performances of 1.5, 2 and 3 mm gap RPCs

This test is also described in Ref. [3]. We measured the RPC detection efficiency using the RPC front-end electronics that has been developed for ATLAS. This frontend circuit [4] consists of a voltage amplifier coupled to a discriminator. The amplifier has a frequency bandwidth of 160 MHz with a gain of 300 at 100 MHz and an input impedance of 50 Ω. The amplified signal is fed into a standard discriminator with threshold adjustable from 30 mV to 1 V. This frontend circuit, already used in many beam tests of RPCs [5], is made with standard commercial components. This circuit will be integrated in a GaAs chip [6] but this one was not used in the present test.

The front-end board was fixed at one end of the strip plane, on the opposite side of the end connected to the oscilloscope. Also in this case the 25 Ω impedance of the pick up strip was matched using a 50 Ω resistor in parallel with the amplifier input.

The detection efficiency was measured by the direct counting, via NIM scalers, of the coincidences between the fast-OR of 5 RPC strips and the trigger signal of the scintillator telescope. The streamer fraction was evaluated by measuring the integrated charge with a CAMAC LeCroy 2249W ADC module; the integration gate (400 ns wide) was started by the cosmic ray trigger, so the strip signals had to be delayed (about 100 ns) before the integration: no electronic amplification was needed for this measurement, due to the large amplitude of streamers with respect to avalanche pulses.

We tested 1.5, 2 and 3 mm gap RPCs operated with the binary gas mixture $C_2H_2F_4/C_4H_{10}$=97/3. With the purpose of accounting for the temperature and pressure variations during several weeks data taking, we rescaled the applied voltage $V_a$ according to the relationship $V = V_a \times (P_0/P) \times (T/T_0)$ where $T$ is the laboratory absolute temperature, $P$ the atmospheric pressure and $T_0 = 293$ K, $P_0 = 1010$ mbar are arbitrarily defined temperature and pressure reference values [7]. The above formula is based on the hypothesis that gas discharge related phenomena are invariant for any change of $V$, $T$, $P$ which leaves the ratio of the voltage to the gas density unchanged. The relevance of the rescaling is shown in Fig. 2 where the efficiency vs. voltage is given for the binary gas $C_2H_2F_4/C_4H_{10}$ =97/3 at two different pressures (Fig. 2(a)). The

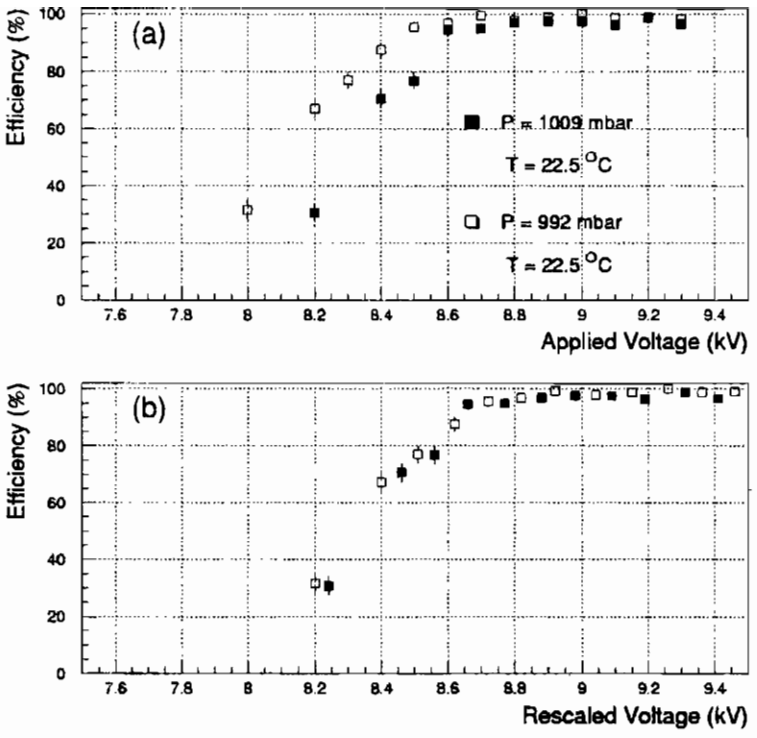


Figure 2: (a) Detection efficiency vs. the applied voltage for the binary gas mixture, at two different values of the atmospheric pressure. (b) Detection efficiency vs. rescaled voltage for the experimental points shown in (a): the voltage was rescaled using reference values for the atmospheric pressure and temperature, 1010 mbar and 20 °C respectively.

200 V shift observed between the operating voltages corresponding to the different pressures disappears when the data are plotted vs. the rescaled voltage (Fig. 2(b)). In the following of this paper all the quoted voltages are normalized with respect to temperature and pressure according to the above formula.

In Fig. 3 (a), (b), (c) the efficiency and the streamer fraction as a function of the operating voltage are shown, for the 1.5, 2 and 3 mm gap respectively.

In Fig. 4 the efficiency (30 mV threshold) and the streamer fraction as a function of the operating electric field are shown, for 2 mm and 3 mm gap; we see that the avalanche-streamer separation is narrower for the 3 mm gap. In Fig. 5 the average streamer charge vs. the operating electric field is shown for the three different gaps; this charge is much larger in the 3 mm gap, where we could also observe streamer afterpulses appearing up to 2 $\mu$s after the primary avalanche pulse.

## 4. Study of new gas mixtures

The data taking of the test was made using a 4 channel digital oscilloscope of 1 GHz analog bandwidth which sampled 500 points per signal at a sampling speed up to 5 Gsample/sec. The oscilloscope was triggered on throughgoing cosmic rays using the triple coincidence signal of the scintillator telescope and for each trigger the signal waveforms of three consecutive pick up strips were recorded. The scintillator finger was centered over the middle strip. Due to the geometrical acceptance of the telescope, the cosmic ray trajectory intersected sometimes the region between two contiguous strips and the signal was shared between them.

The data acquisition was managed by a personal computer which recorded the waveforms of the three strips.

The gas was the mixture $C_2H_2F_4/C_4H_{10}$=97/3, with the addition of a small amount of $SF_6$. We tried 5%, 2% and 1% of $SF_6$; the binary mixture without $SF_6$ was also tested for reference.

For each gas we scanned a voltage range of at least 2 kV. At operating voltages below the streamer threshold the oscilloscope horizontal scale was set at 10 ns/cm and a typical avalanche signal was measured by about 40 sample points. Above the streamer threshold the time scale was set at 50 ns/cm so that delayed streamers up to about 500 ns were detectable. The corresponding sampling frequency was only 1 Gsam-

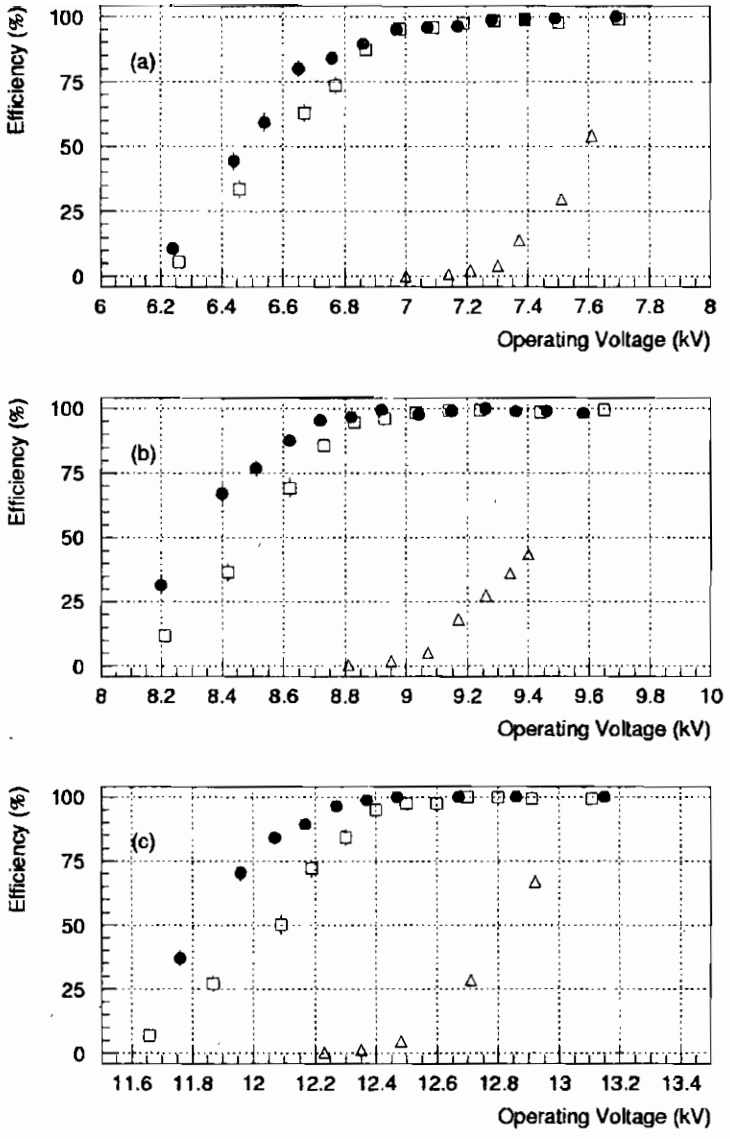


Figure 3: Efficiency (30 mV and 100 mV threshold) and streamer fraction as a function of the operating voltage for 1.5 mm (a), 2 mm (b) and 3 mm (c) gap.

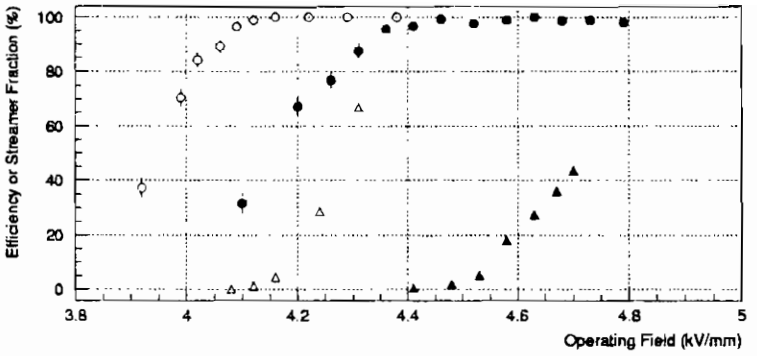


○ 3 mm EFFICIENCY (Threshold = 30 mV)

△ 3 mm STREAMER FRACTION

● 2 mm EFFICIENCY (Threshold = 30 mV)

▲ 2 mm STREAMER FRACTION

Figure 4: Efficiency (30 mV threshold) and streamer fraction as a function of the operating electric field for 2 mm and 3 mm gap.

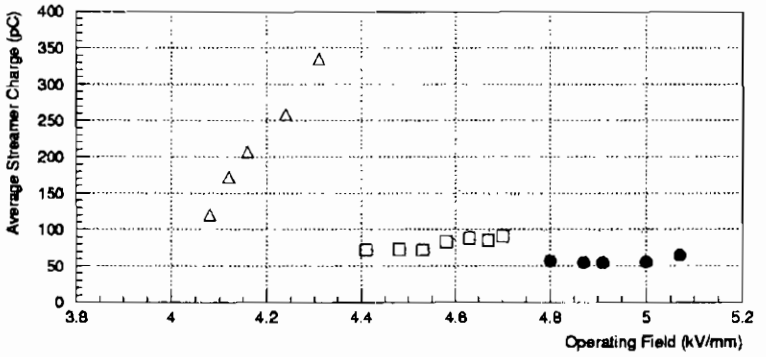


△ 3 mm

□ 2 mm

● 1.5 mm

Figure 5: Average streamer charge as a function of the operating electric field for 1.5, 2 and 3 mm gap.

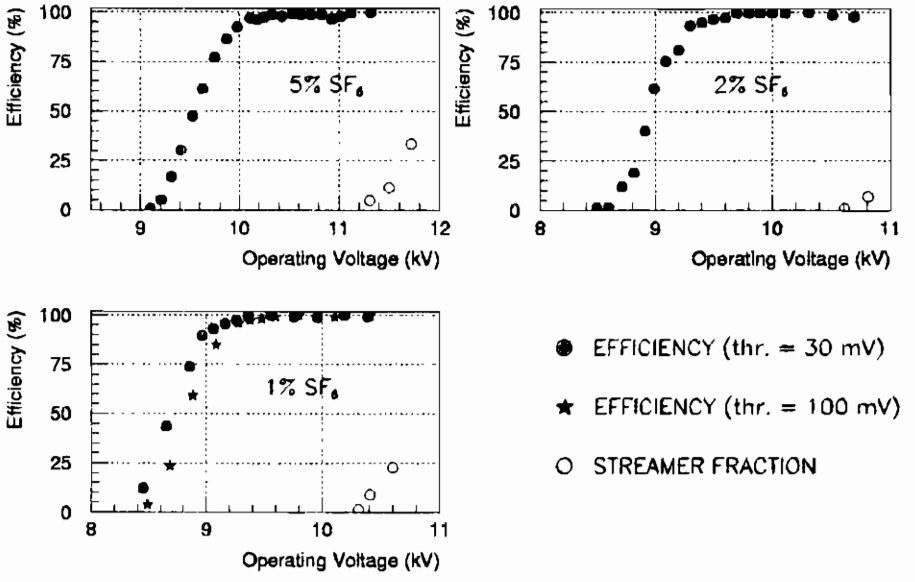


Figure 6: Detection efficiency and streamer probability vs. operating voltage for 5%, 2%, 1% $SF_6$ concentrations.

ple/s and a typical avalanche signal was measured with only about 8 sample points, a rather modest number that made the avalanche measurements obtained in these conditions significantly poorer. The fraction of streamers expected after 500 ns was completely negligible for all the tested gases.

The signals of the three strips were amplified using a voltage amplifier of gain 25, frequency bandwidth 500 MHz, input impedance 50 Ω and equivalent noise of 6 dB. At very low voltage, where the signal amplitude was only a fraction of a millivolt, two cascaded amplifier stages were used, whereas above the streamer threshold no amplifier was used to avoid saturation effects due to large signals.

In Fig. 6 the detection efficiency (measured using the ordinary counting technique) and the streamer fraction vs. the operating voltage are shown for the tested mixtures; the avalanche-streamer separation is about 1 kV in all cases.

In Fig. 7 a typical avalanche signal at 9.4 kV (a) and an avalanche signal followed by a streamer afterpulse at 10.65 kV (b) are shown, for the mixture containing 1% $SF_6$.

The signal charge distributions were studied for all $SF_6$ concentra-

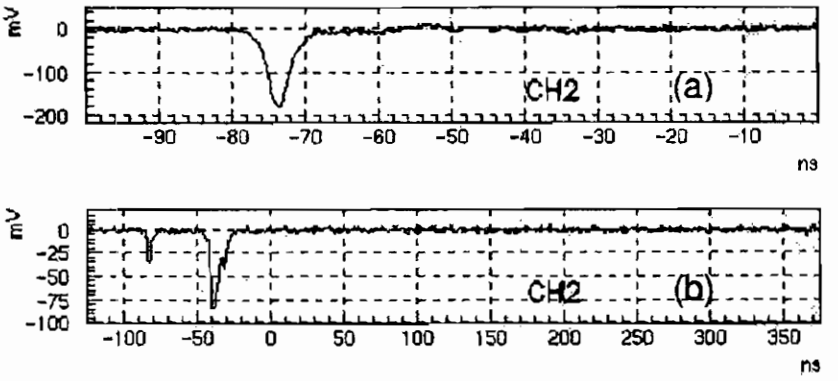


Figure 7: Waveform samples: (a) avalanche signal at 9.50 kV observed with an amplifier gain of 25; (b) avalanche followed by afterpulses at 10.65 kV (no amplification). The $SF_6$ concentration is 1%.

tions and operating voltages. As an example we show in Fig. 8 the distributions for 2% $SF_6$ in the range 9.21-10.14 kV. A drastic change in the shape of the distributions for increasing voltage is clearly visible: at low voltage, e.g. 9.21 kV, most of the events are accumulated in the lowest channels and no peak is visible whereas, at 9.68 kV and above, the distributions look peak shaped.

The average avalanche charge value $\langle q \rangle$ versus the operating voltage is shown in Fig. 9. For each gas there is an interval where $\ln\langle q \rangle$ increases linearly with the voltage, followed by a region of gradual saturation. The full detection efficiency is reached at the same charge, about .6 pC, for all the gases, including the one without $SF_6$. On the contrary, at the streamer threshold, the charge is 3 pC for all three gases containing $SF_6$ and only 1 pC for the binary mixture without $SF_6$. Above the streamer threshold the total signal charge, which is dominated by the streamer, is also plotted in Fig. 9 in addition to the avalanche precursor charge.

In Fig. 10 the cluster size distributions at four different values of the operating voltage are shown. The cluster size is defined as the number of contiguous strips in which the signal amplitude is greater than a certain voltage threshold, and was measured by reading 5 contiguous strips with

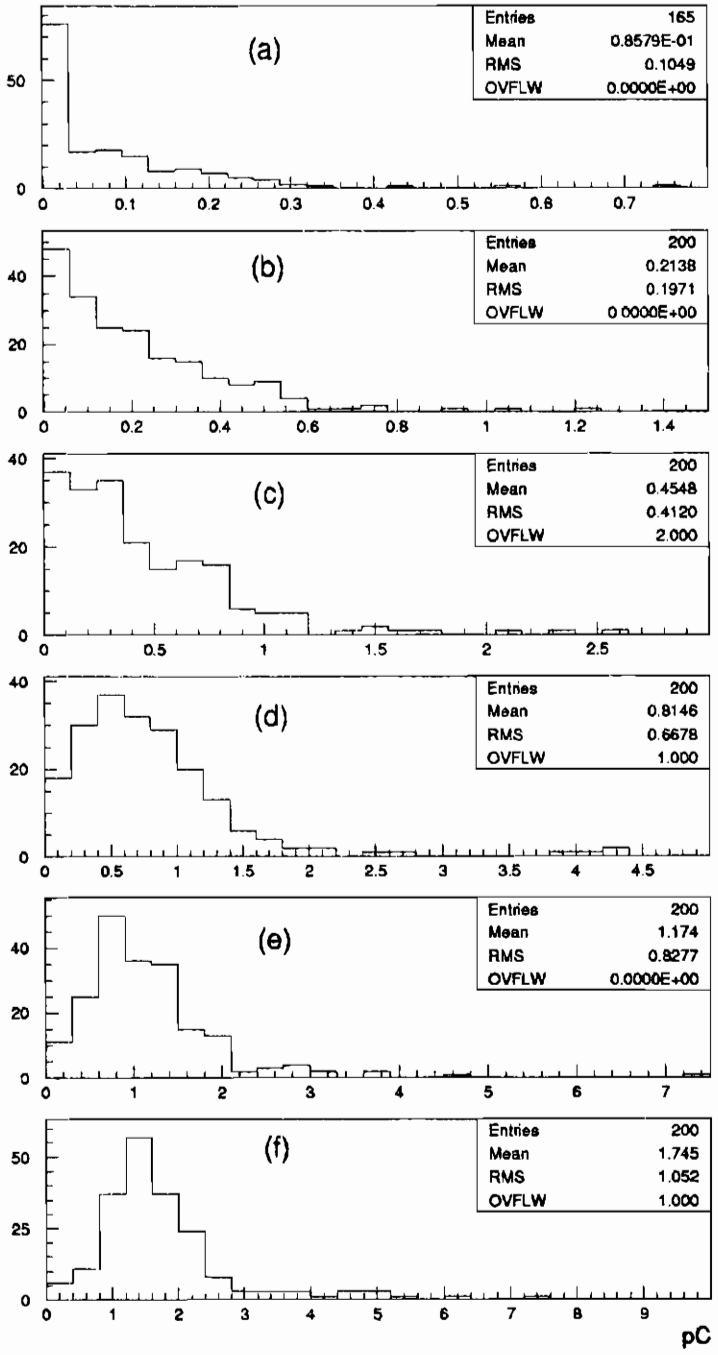


Figure 8: Avalanche charge distributions for 2% $SF_6$ and (a) 9.21 kV, (b) 9.37 kV, (c) 9.55 kV, (d) 9.68 kV, (e) 9.90 kV and (f) 10.14 kV.

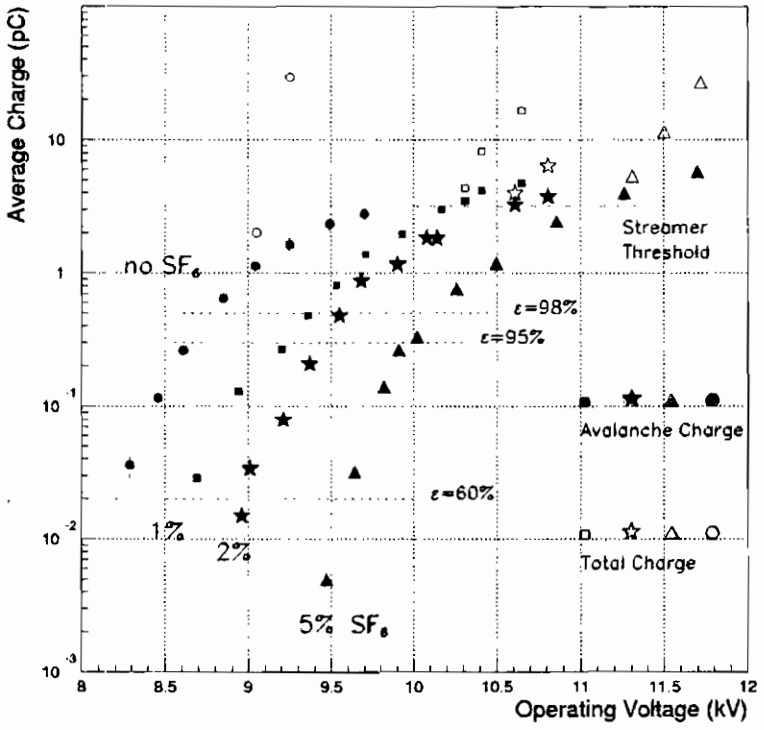


Figure 9: Average avalanche and total signal charge vs. the operating voltage for the four gases tested.

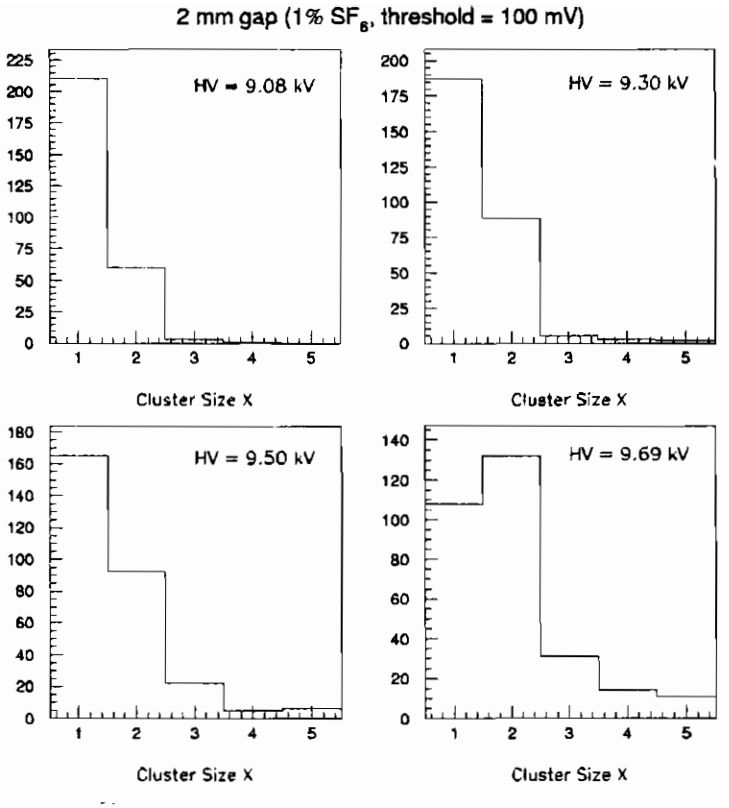


Figure 10: Cluster size distributions at different operating voltages (1% $SF_6$ and 100 mV threshold).

a CAMAC TDC module. Choosing the mixture with 1% $SF_6$ and a 100 mV threshold, we observe an average cluster size smaller than 2 up to 9.7 kV (that is 500 V above the plateau knee.

In our search for streamer suppressing gases we also tested, for completeness, the binary mixture $C_2HF_5/C_4H_{10}$ [8] with 3% and 6% of butane. The observed avalanche-streamer separation (see Fig. 11) is not greater than the one observed with the binary mixture $C_2H_2F_4/C_4H_{10}$.

## 5. Conclusions

The measurements described above show that:

- the use of 3 mm (and wider) gap, with respect to 2 mm gap,

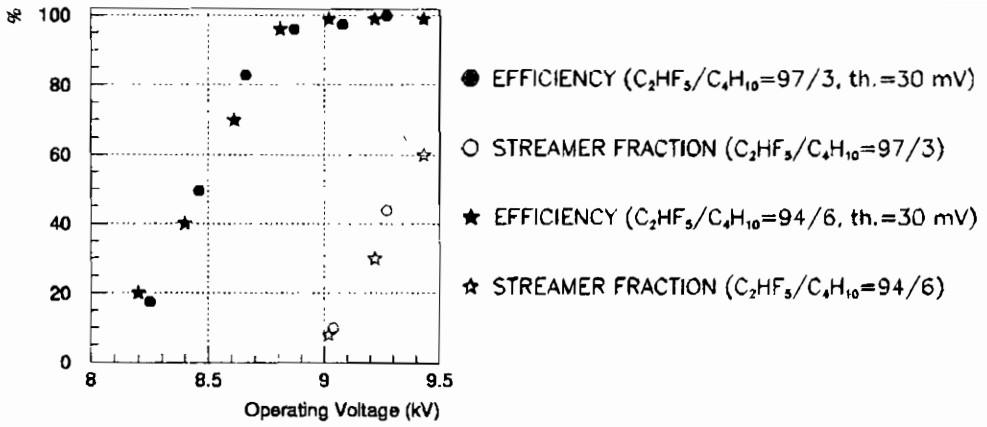


Figure 11: Detection efficiency (discriminating threshold = 30 mV) and streamer probability for the binary gas mixtures $C_2HF_5/C_4H_{10}$=97/3 and 94/6.

RPCs is not encouraged in connection with the reference ATLAS RPC gas mixture ($C_2H_2F_4/C_4H_{10}$ = 97/3), due to the narrower avalanche-streamer separation observed, and the very high charge associated to streamers;

- after adding small amounts of $SF_6$ to the reference mixture, we observed a remarkable improvement of the RPC performances: 2 mm gap RPCs can be operated in pure avalanche mode with a 1 kV streamer free efficiency plateau. Moreover our experimental results confirm that the induced charge distributions are peak shaped as the RPC reaches its maximum efficiency: this is due to space charge effects, since the predictions based on the simple Townsend exponential gain lead only to distributions in which most of the events are accumulated in the lowest channels: actually, this can only be observed at low operating voltages (below the efficiency knee).

1. R. Cardarelli, V. Makeev, R. Santonico; Nucl. Instr. and Meth. **A 382** (1996) 470.
2. "*ATLAS Muon Spectrometer Technical Design Report*", CERN/LHCC/97-22.
3. P. Camarri et al.; "*Latest Results on RPCs for the ATLAS LVL1 Muon Trigger*", Proc. of the 7th Pisa Meeting on Advanced

Detectors (Isola d'Elba, May 25-31, 1997), to be published in Nucl. Instr. and Meth.
4. R. Cardarelli; "*Gli RPC come rivelatore di trigger muonico a LHC*", invited talk at the "LXXXII Congresso Nazionale della Società Italiana di Fisica", Verona, 23-28 settembre 1996.
5. C. Bacci et al.; Nucl. Instr. and Meth. **A 352** (1995) 552. M. Abbrescia et al.; Nucl. Phys. **B 44** (1995) 218 (Proc. Suppl.). M. G. Alviggi et al.; "*Resistive Plate Chambers in ATLAS*", ATLAS internal note MUON-NO-131, 1 October 1996.
6. R. Cardarelli et al.; "*RPC Front-End Electronics for the ATLAS LVL1 Trigger Detector*", Proc. of the 7th Pisa Meeting on Advanced Detectors (Isola d'Elba, May 25-31, 1997), to be published in Nucl. Instr. and Meth.
7. For rescaling with respect to temperature only, see also: M. Abbrescia et al.; Nucl. Instr. and Meth. **A 359** (1995) 603.
8. E. Cerron Zeballos et al.; CERN/LAA-MC 97-01.

# Preliminary results on double gap RPC in a high background environment

Marcello Maggi *
*Dipartimento Interateneo di Fisica and Sezione INFN, Bari, Italy*

February 27, 1998

ABSTRACT

A double gap Resistive Plate Chamber was tested in a muon beam under high intensity photon flux. Results on the efficiency and time resolution are given. The chamber was successfully operated at the highest available photon flux corresponding to an effective counting rate of $\approx 1$ kHz/cm$^2$. These results show that such a chamber can reliably be used as muon trigger device for LHC experiments.

## 1. Introduction

The Gamma Irradiation Facility (GIF) created at CERN allows the study of the detector performance in a background environment similar to the one expected in the Large Hadron Collider (LHC) environment.

A double gap Resistive Plate Chamber (RPC) was exposed to a photon flux producing an effective counting rate up to $\sim 1$ kHz/cm$^2$ per each gap. Since RPCs are proposed as trigger devices in LHC experiments,

*co authors: M. Abbrescia, A. Colaleo, G. Iaselli, F. Loddo, B. Marangelli, S. Natali, S. Nuzzo, G. Pugliese, A. Ranieri, F. Romano *Dipartimento Interateneo di Fisica and Sezione INFN, Bari, Italy* ; S. Sergueev *Joint Institute For Nuclear Research, Dubna, Russia* ; L. Gorn *University of Florida, Gainesville, USA* ; S. Altieri, V. Arena, G. Belli, G. Bonomi, G. Gianini, M. Merlo, S.P. Ratti, C. Riccardi, L. Viola, P. Vitulo *Dipartimento di Fisica Nucleare e Teorica and Sezione INFN, Pavia, Italy.*

they must have high efficiency and good time resolution for bunch identification up to the highest rates. Here, for the first time, measurements of efficiency and time resolution in such a conditions are shown.

## 2. The test set-up

The GIF area was built downstream the CERN X5 muon beam line and it is shown schematically in Figure 1. The photon flux is provided by a 20 Ci $^{137}Cs$ source. A system of moving filters allows the modulation of photon radiation level investing the chamber. The chamber was located at a distance of 1.8 m perpendicular to the irradiation cone and aligned to the muon beam. A system of scintillators was used to trigger the beam particles.

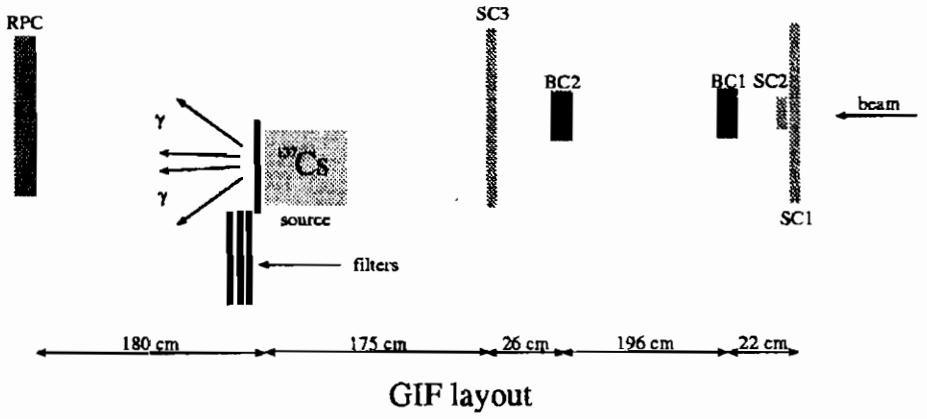


Fig. 1. Schematic view of the GIF facility.

The RPC under test was a double gap chamber, having $50 \times 50$ cm$^2$ area and 3 mm gap width. The resistive bakelite electrodes have been produced with improved surface so as to avoid the traditional linseed oil treatment. The resistivity of the bakelite plates was $10^{11}$–$10^{12}$ $\Omega$cm. The chamber was operated with a 90% $C_2H_2F_4$, 10% $i$-$C_4H_{10}$ gas mixture.

The alluminum read-out strips were 1.3 cm wide with 1.5 cm pitch. Each strip was 25 cm long and the full length of the chamber was covered by two consecutive strips that were read-out at the two opposite sides of the chamber. Figure 2 shows a schematic view from the top and a cross section of the chamber. A set of cylindrical 8-mm diameter spacers were located in a grid of 10 cm pitch. In the present design the spacers were

aligned in two gaps so that they give arise to an effective dead area of about 1%.

The chamber was equipped with hybrid front-end preamplifiers, with input impedance of $\approx 40\ \Omega$ and bandwidth of 10 MHz. The RPC signals were discriminated with 40 mV thresholds before feeding a multi–hit common-stop Time–to–Digital Converter (TDC) with a 64 $\mu$s gate and a 1 ns sensitivity.

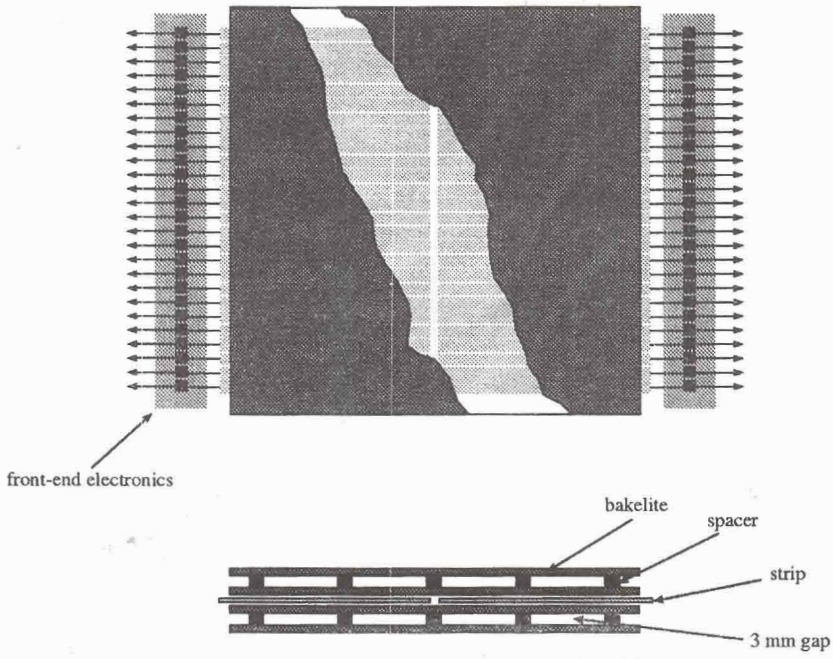


Fig. 2. Schematic view of the RPC.

## 3. Experimental results

The data coming from the TDC were used in order to determine the

observed rate, the time resolution and the efficiency.

### *3.1. Observed rate*

The measured effective rate is due to Compton electrons mainly emerging from the interactions of the photons into the bakelite layers close to the gas volume. A single electron could fired more than one strip, mainly due to cross-talk and the scattering angle of the electron. Since secondary signals produced by those effects might be delayed due to electronic layout and time slewing, every hits within 250 ns time window was combined into clusters. The measurement of the observed rate was performed with the following method.

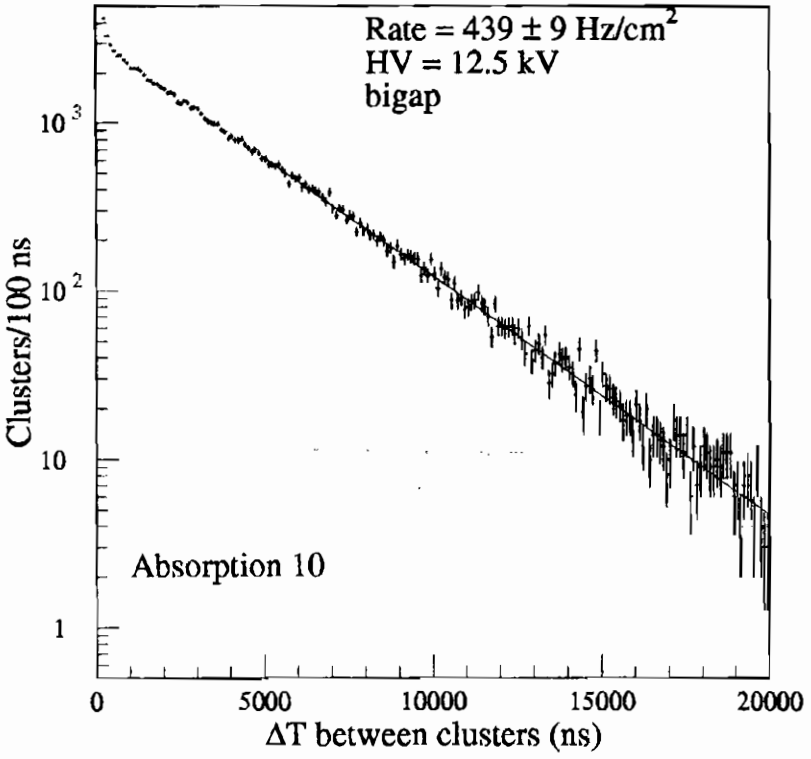


Fig. 3. Distribution of the time difference between two consecutive clusters generated by photons.

The signals coming from the RPC read-out channels were first or-

dered in time and then clusters are searched for. In fact strips that see more charge are fastest because of time slewing. Hits from adjacent strips within a cluster gate of 250 ns from the fastest strip are included in one cluster. One event consists of all signals in the 64 $\mu$s TDC gate and contains more clusters. The time difference between two consecutive cluster follows the exponential law, whose slope gives directly the observed rate of clusters.

Figure 3 shows an example of such a measurement performed with a photon flux filtered with an absorption factor of 10 and for an operating voltage, HV, of 12.5 kV. Only clusters with the fastest strip in the central 10 strips were considered, in order to define a fiducial area well inside the active chamber. The peak at small time difference is due to systematic effect in the clustering procedure but it do not affect the rate measurement that is extracted from larger time differences.

In Table 1 the results obtained for the various absorption factors are summarised. The errors associated to the observed rate are dominated by systematics studied by varying the cluster gate time, the HV of the chamber and the fiducial area of the chamber used.

Table 1. Observed rate as a function of the absorption factor of the filters.

| Absorption factor | rate (Hz/cm$^2$/gap) |
|---|---|
| 1 | 1100±100 |
| 2 | 700±50 |
| 5 | 375±30 |
| 10 | 225±25 |
| 100 | 50±10 |

Absorption 1 means that no filters are used. As Table 1 shows, the effective rate reached is well beyond what it is expected in LHC environment and represents a safe margin on the rate capability requirement. For example, the highest hit rate foreseen, in the Compact Muon Solenoid (CMS) [1] experiment at LHC, at the maximum rapidity region ($\eta = 2.1$) where Resistive Plate Chambers are foreseen to be installed, is $\approx 300$ Hz/cm$^2$.

### *3.2. Timing*

The timing of the RPC response to the beam particles with respect to the time of the trigger system, ($T_0$), was anticipated of $\approx 200$ ns. The

timing of the RPC, $T_{RPC}$, was then defined as the time of the fastest strip within 200 ns around the nominal RPC average timing. In Figure 4 the $T_{RPC} - T_0$ distribution is shown, at 12.5 kV and for an absorption factor of 10.

The distributions have contributions also from signals coming from photons hitting the chamber before the muon signals. This effect produces a tail on the right of the distributions and it is parametrised with a polynomial function that is cross-checked in a time window and in a region of the chamber where beam particles are not present. A fit to the distributions from different HV and different absorption factors are performed using for the beam particle response a double Gaussian parametrisation.

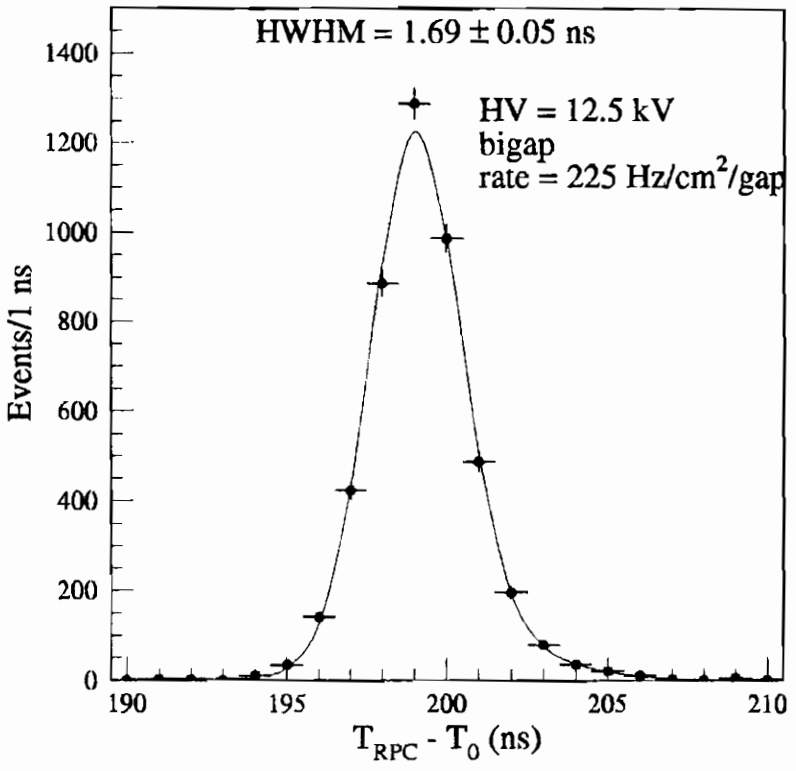


Fig. 4. Distribution of the time difference between the RPC response and the trigger signal.

In Figure 5 the Half Width Half Maximum (HWHM) is shown as a

function of the HV. The full squares represent the resolution obtained without source; the best time resolution is achieved at 12.5 kV and it is 1.5 ns. The full down(up)–triangles are the results at absorption 10(5), the best resolution at 13 kV being 1.6 ns. The full circles are obtained at absorption 2, the HWHM at 13.5 kV is 1.8 ns. Finally the open squares, representing the data taken with no filters (maximum rate), show a resolution that at the best (13.75 kV) is 2.3 ns.

The time resolution should be compared with the time difference between two consecutive bunch crossing expected at LHC $\approx$ 25 ns. The results obtained then fulfil the timing requirement for an efficient bunch crossing identification as pointed out in Reference [2].

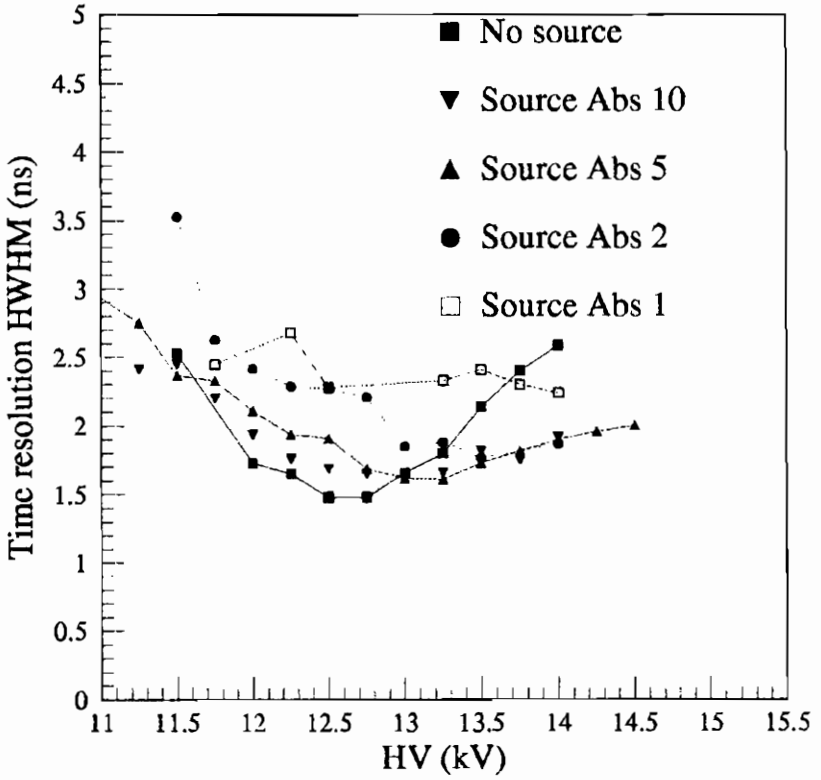


Fig. 5. Time resolution of the RPC as a function of the applied HV and at different absorption factor.

The average time response of the RPC depends [3] on the product of the first effective Townsend coefficient (where the attachment coefficient

is subtracted) and the drift velocity. As shown in [4] both the quantities depend on the operating voltage of the chamber, so that a time–walk as a function of the applied HV is expected.

The effective voltage across the gap is reduced with respect to the nominal setting because of the current passing through the bakelite plates. The current is proportional to the rate of ionising particle so the voltage drop. One expects that a time–walk appears also as a function of the rate once the applied HV is fixed.

Figure 6 shows the average time response of the RPC as a function of the rate for three values of the applied HV: 13, 13.5 and 14 kV.

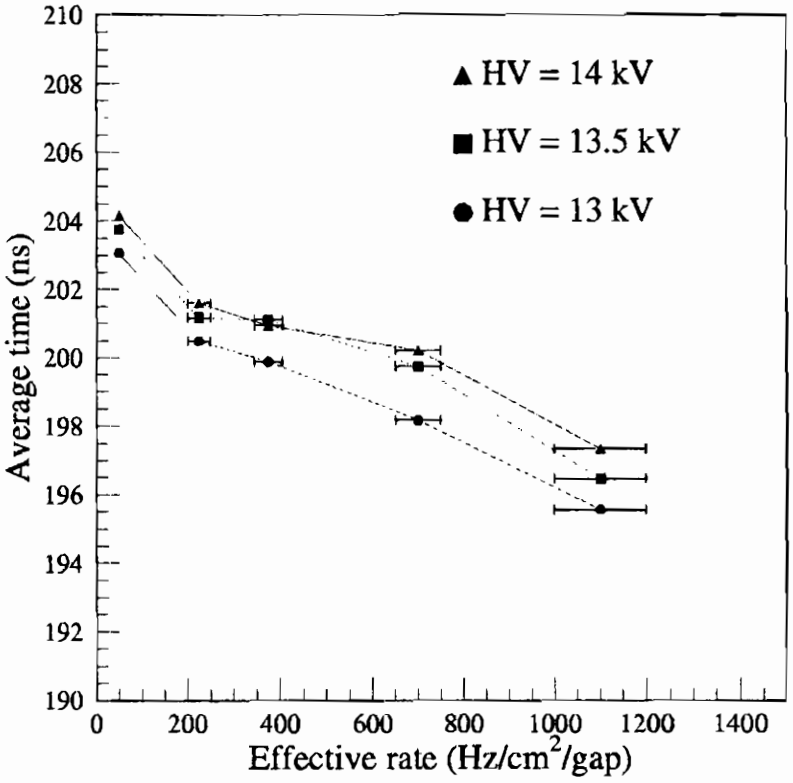


Fig. 6. Average time response of RPC as a function of the rate and at different applied HV.

This effect contributes to the worsening of the time resolution once the chamber is immersed in a non uniform background condition. However, the observed differences are very well contained within the 25 ns

of the expected bunch crossing period at LHC.

### *3.3. Efficiency*

The number of observed events $N_{obs}$ in a given time window, taking into account the probability $P_s$ that a spurious hit appears on the chamber, is:

$$N_{obs} = \epsilon N_{trig} + P_s (1 - \epsilon) N_{trig} , \quad (1)$$

where $\epsilon$ is the efficiency to determine. So, the events where the chamber registered both a spurious hit and a hit coming from the beam particle are counted only once and subtracted in the spurious events ($P_s \epsilon N_{trig}$). The observed efficiency is $\epsilon_{obs} = N_{obs}/N_{trig}$, and the following relation holds:

$$\epsilon_{obs} = \epsilon + P_s (1 - \epsilon) , \quad (2)$$

so that

$$\epsilon = \frac{\epsilon_{obs} - P_s}{(1 - P_s)} . \quad (3)$$

Therefore two quantities are needed, the observed efficiency, $\epsilon_{obs}$, and $P_s$ that is determined by measuring the number of times the chamber is hit in the same time window but out of time (500 ns before the trigger signal).

In the following two time windows are considered: 200 ns, to collect all the signals coming from the chamber, to measure the intrinsic efficiency of the RPC; 20 ns, to emulate the gate at LHC, and that represents the efficiency for a correct bunch identification.

In Figure 7 the efficiency plateau of the chamber is shown for various filter settings. Without source the RPC reaches $\approx 99\%$ efficiency at 11.7 kV. The inefficiency is mainly due the dead area given by the spacers. At the highest effective rates the maximum efficiency is reached slowly at higher applied voltage (13 kV). Moreover no efficiency drop are presents at the maximum applied voltage used, so that efficiency plateaus are suitably large.

Figure 8 shows the efficiencies curves at various absorption factors in 20 ns gate time. As expected from the measured time resolutions at low effective rates the loss in efficiency due to poor time measurements are small ($< 0.1\%$). At the highest effective rates the efficiency loss due to poor time measurements reaches at maximum $\approx 0.8\%$.

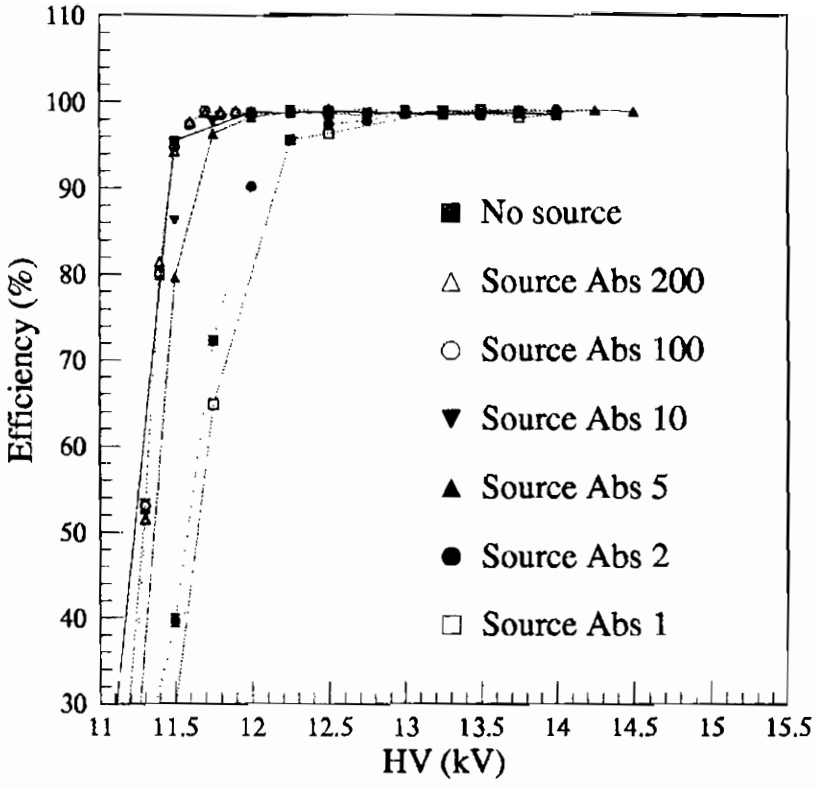


Fig. 7. Efficiency curves as a function of the applied HV, for different absorption factors.

These results show that double gap RPCs can reach a bunch identification efficiency of $\approx 98\%$ at an effective rate of 1 kHz.

## 4. Discussion and conclusions

A double gap Resistive Plate Chamber was tested with a muon beam under a high rate photon flux at the Gamma Irradiation Facility at CERN. A time resolution better than 2.5 ns was measured. Efficiency of $\approx 99\%$ is reached. The effect of the time resolution and tails of the time measurements on the bunch identification efficiency, expected at LHC, was also studied by computing the efficiency in a 20 ns time window. The measured efficiency loss was only 0.8% at the highest effective rate of 1 kHz/cm$^2$ in each gap.

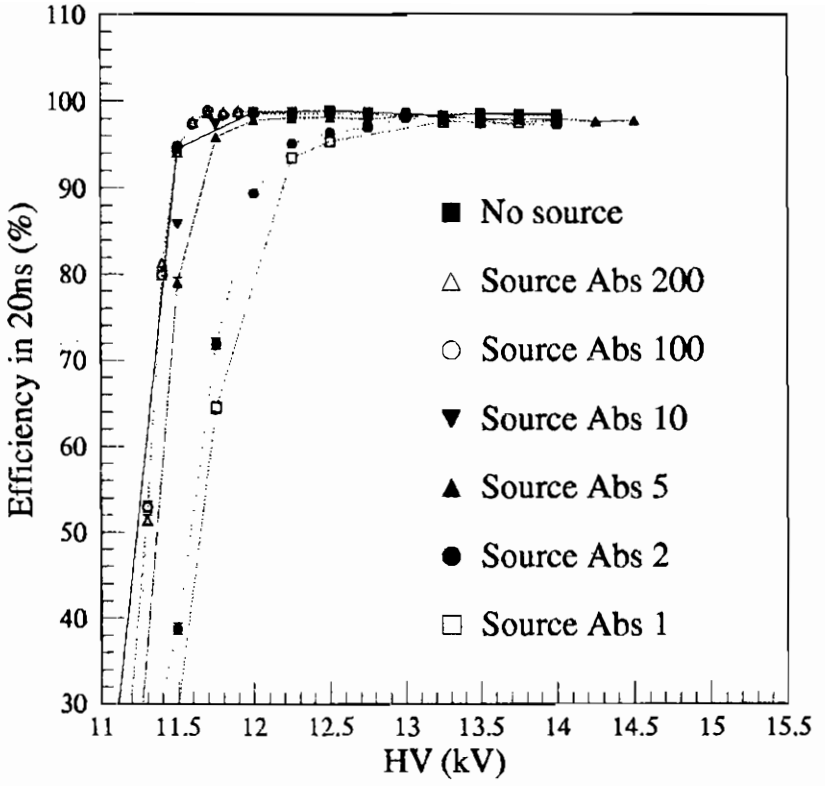


Fig. 8. Efficiency curves as a function of the applied HV, for different absorption factors. The efficiency is computed in a time window of 20 ns

The high rate background induces the RPC to draw large currents. The drop voltage on the resistive bakelite plates can be as high as hundreds volts. The knee of the efficiency plateau is then reached for higher nominal setting of the applied voltage at increasing effective rate.

The effect is simply due to the fact that the average time between two ionisation processes in the same area is less than the time constant of the re-charging process, so not all the charge is supplied before the second ionisation takes place. So, the actual voltage across the gas gap, found by the beam particle, undergoes fluctuations around the average, due to two competing effects, the re-charging of the external supply and the ionisation of the background hits. This explains the deterioration of the time resolution for higher rates, since drift velocity and effective

Townsend coefficient depend on the voltage across the gas gap.

The dependence of the drift velocity and of the effective Townsend coefficient on the voltage produces a time–walk of the RPC response. This translates to a time–walk as a function of the background rate, because of the voltage drop on the resistive plates. This effect can lead to worse bunch identification efficiency at LHC for chambers exposed to an environment whose background conditions differ in the chamber area. The average time response of the RPC under test had difference of 3–4 ns for effective hit rates going from 200 to 1000 Hz/cm$^2$/gap or from 50 to 200 Hz/cm$^2$/gap. A correct determination of the efficiency loss for bunch identification requires a detailed simulation of the background condition expected at LHC. Nevertheless the result obtained are very promising.

## 5. Acknowledgement

We would like to acknowledge the helpful support of I. Crotty at the GIF. We are also grateful to the technical staff of the Bari and Pavia groups for their excellent work.

## 6. References

1. *CMSM Technical Proposal*, CERN/LHCC/94–38
2. M. Abbrescia et al., *Beam Test Results on Resistive Plate Chambers for the CMS experiment*, CMS Note 1997/062 (1997).
3. M. Abbrescia et al., *The simulation of Resistive Plate Chambers in avalanche mode*, Contribution to this Workshop.
4. E. Gorini et al., *Measurements of drift velocity and effective ionisation coefficient in $C_2H_2F_4$-iso-butane mixture for avalanche operated RPC*, Contribution to this Workshop.

# Performance of large double gap Resistive Plate Chambers

G. Pugliese *
*Dipartimento Interateneo di Fisica and Sezione INFN, Bari, Italy*

March 10, 1998

ABSTRACT

Two double gap Resistive Plate Chambers, with 2 and 3 mm gap width, operated in avalanche mode, were tested in the CMS-H2 muon beam. Efficiency, time resolution and cluster size have been measured both in the central region of the chambers and averaged over a large surface. In addition, a test with a prototype VLSI version of the front-end amplifier has been performed.

## 1. Introduction

Resistive Plate Chambers (RPCs) operated in avalanche mode have recently been considered as detectors for the muon trigger at the future Large Hadron Collider (LHC) [1].
The response uniformity over a large surface of an RPC is a crucial issue for its operation. Variations of the gap width, due to mechanical tolerances, may result in local non uniformity of the chamber efficiency, time resolution, etc. It is therefore necessary to measure the average performance over large surfaces, by illuminating with a muon beam different portions of the chamber.

*co authors : M. Abbrescia, G. Bruno, A. Colaleo, G. Iaselli, G. Lamanna, F. Loddo M. Maggi, B. Marangelli, S. Natali, S. Nuzzo, A. Ranieri, F. Romano *Dipartimento Interateneo di Fisica and Sezione INFN, Bari, Italy*; S. Altieri, V. Arena, G. Bonomi, G. Gianini, M. Merlo, S. P. Ratti, C. Riccardi, L. Viola, P. Vitulo *Dipartimento di Fisica Nucleare e Teorica and Sezione INFN, Pavia, Italy* ; Serguei Sergueev *Joint Institute For Nuclear Research, Dubna, Russia*

We report about the performance of double-gap RPCs developed in the context of the CMS R&D project.

## 2. Experimental set-up

Two large double gap RPCs (1.3×1.2 $m^2$), with 2 and 3 mm gap width, have been exposed to the CMS-H2 beam line at CERN SPS during the summer 1997. The test setup is shown schematically in Fig. 1. The bakelite resistivity was $\simeq 2 \times 10^{11} \Omega$cm (no linseed oil treatment).

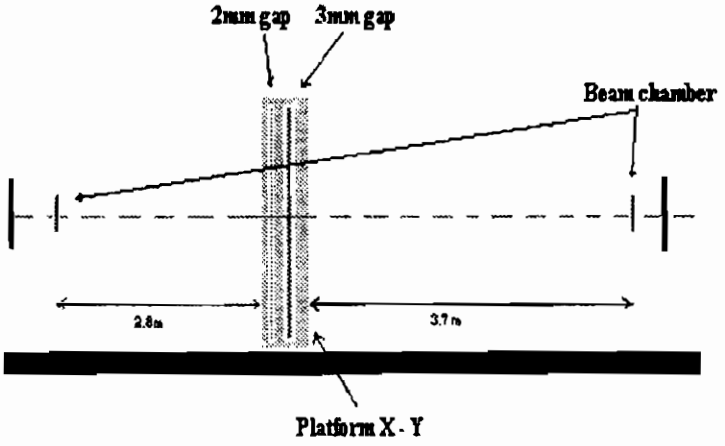


Fig. 1. Schematic view of the CMS-H2 beam line.

A grid of spacers (10 cm in pitch) insures the uniformity of the gap width. In the present design the spacers of the two gaps are aligned [2]. The signals were read-out by means of aluminum strips (3.5 × 130 $cm^2$, the typical dimentions of the barrel strips in CMS [1]) located between the two gaps. The chambers were both filled with a 90% $C_2H_2F_4$ and 10% i-$C_4H_{10}$ gas mixture.
In a first period of measurements a hybrid front-end preamplifier, characterized by a 40 Ω input impedance and 10 MHz bandwidth, was used; later the 2 mm chamber was equipped with a VLSI version of the amplifier with also a discriminator and a monostable circuit; this has been

extensively described elsewhere [3].
A low intensity 220 GeV/c muon beam was used for this test. The flux intensity, measured with a set of scintillators covering a $2 \times 2$ cm$^2$ area, was about 200 Hz/cm$^2$. The trigger was given by another set of scintillators defining a $10 \times 10$ cm$^2$ area.
The signals were discriminated with a 30 mV threshold (equivalent to $\approx$ 20 fC) in both sets of measurements, before feeding a common stop multihit TDC (mod. LeCroy 2277A) with a time window of 500 ns and a sensivity of 0.5 ns.
To measure efficiency, time resolution and cluster size, the strip with the minimum arrival time ("the fastest") was chosen and only a 3 strip wide neighbour region it was considered. The efficiency was defined as the ratio between the signal counting rate and the trigger rate, within a 60 ns window.

## 3. Experimental results

### *3.1. Local performance*

In this section we report the performance obtained when the beam was centered on the $10 \times 10$ cm$^2$ central region of each chamber. The position is chosen so that the maximum of the beam profile was away from the spacers (Fig. 8). In Figs. 2-3, the efficiencies of the two chambers vs. the applied high voltage (HV) are shown; the in-spill drawn current (after subtraction of the off-spill current) is also given. As expected a higher voltage was required for the 3 mm gap RPC with respect to the 2 mm one.
The average cluster size as a function of the applied HV is shown in Figs. 4-5; it is computed around the fastest fired strip by counting the number of adjacent strips hit within different time windows (10 ns, 50 ns and 250 ns).
The increase, shown in the figures, might be due both to the increase of the charge produced in the chamber, and to the fact that larger signals produce a larger cross-talk between adjacent strips. It has been observed, by means of test bench measurements, that cross talk signals arrive delayed by few tens of ns, due to the electronic layout of the chamber [3]. This effect could explain the large increase of the cluster multiplicity when a larger gate window is considered.

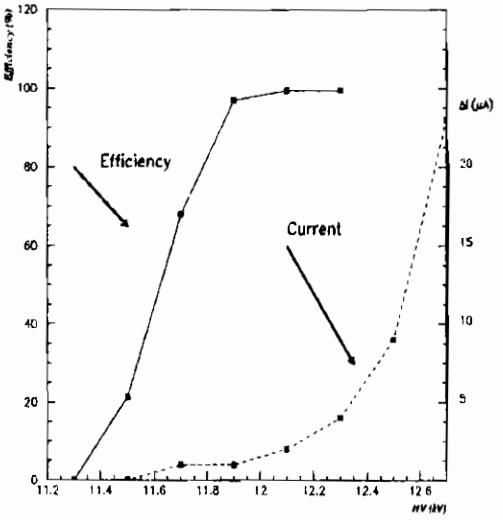


Fig. 2. Efficiency vs. HV for 3 mm gap RPC.

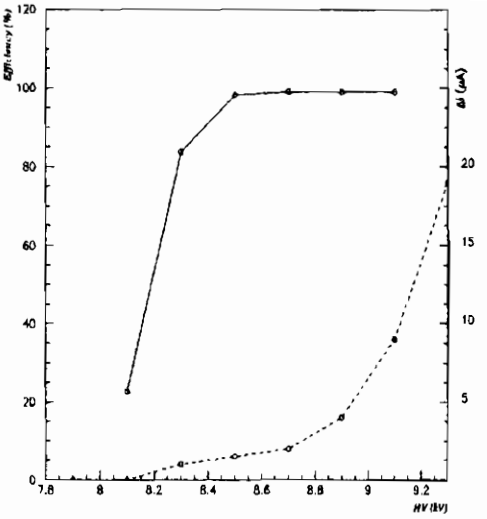


Fig. 3. Efficiency vs. HV for 2 mm gap RPC.

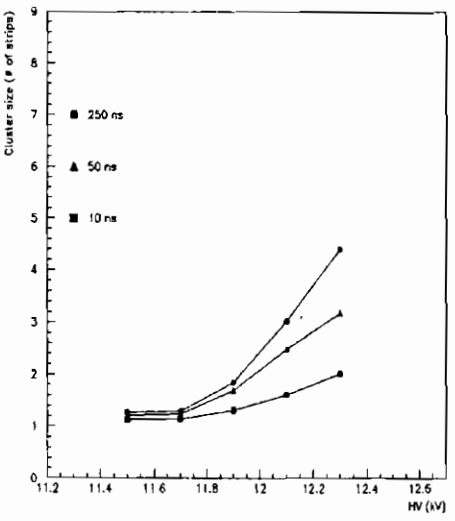


Fig. 4. Average Cluster size for 3 mm RPC in the central region.

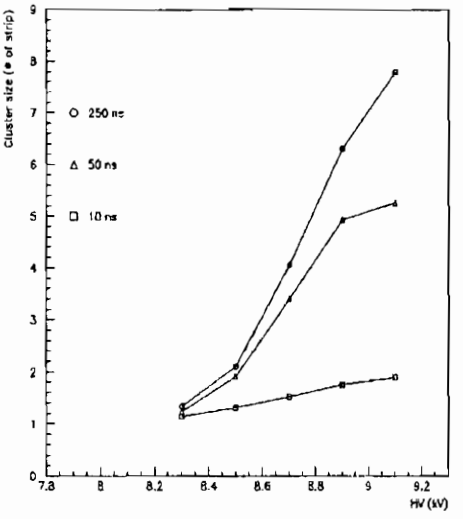


Fig. 5. Average Cluster size for 2 mm RPC in the central region.

Time distributions for 3 and 2 mm chambers are shown in Fig. 6; as expected the narrow gap RPC gives better timing. In Fig. 7 the sigma values (which refer to a Gaussian fit relative to the central part of the distributions) are reported vs. the $HV$ for the two chambers. The curves are characterized by an improve of the timing performance.

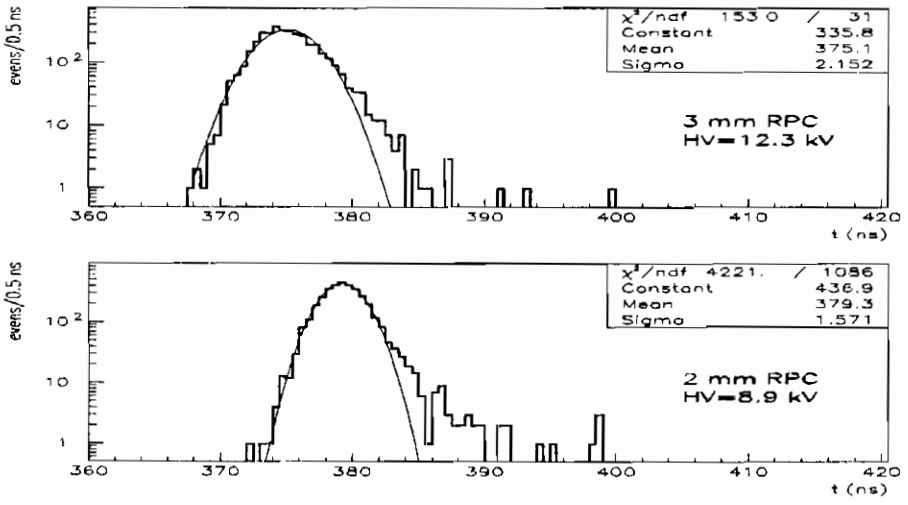


Fig. 6. Time distributions for 2 mm and 3 mm RPCs.

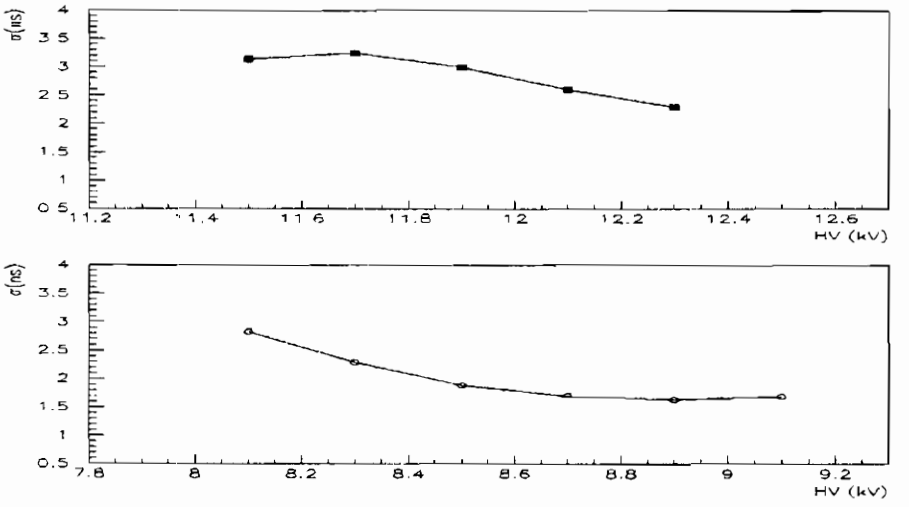


Fig. 7. Time resolution of 3 mm and 2 mm RPCs as a function of the applied HV

*3.2. Average performance*

It is important to study the response uniformity of a chamber over a large surface. In order to have different regions illuminated by ionizing particles, the chambers were displaced in steps of 10 cm in the plane perpendicular to the beam.
Here we report the results obtained in 18 different regions: 9 regions along the vertical direction (perpendicular to the strip direction) and 9 regions along the horizontal direction (parallel to the strip direction), each $10 \times 10$ cm$^2$ large, 10 cm away from the previous one and located along the central axes of the chamber (Fig. 8).

Figs. 9-10 report, for the two chambers, the efficiencies as a function

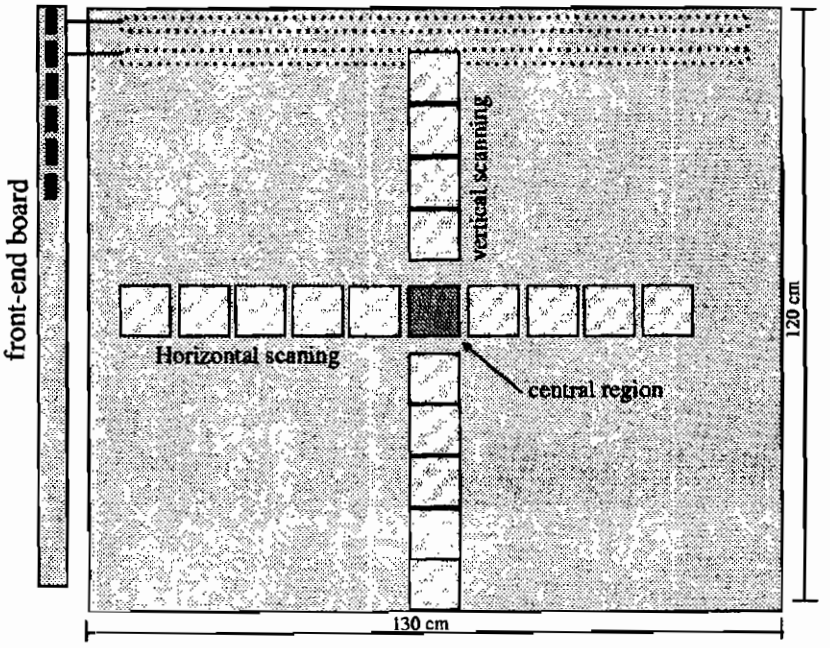


Fig. 8. Schematic view of the RPC.

of the position (along the direction orthogonal to the strips), at several high voltages. It can be seen that, at increasing voltages the point to point fluctuations tend to become smaller, and eventually negligible at

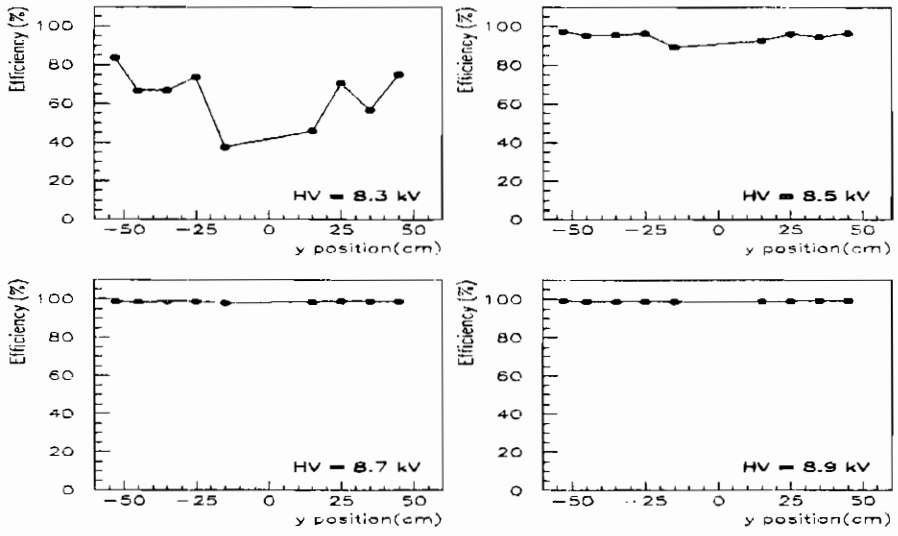


Fig. 9. Efficiencies along the direction orthogonal to the strips for the 2 mm RPC.

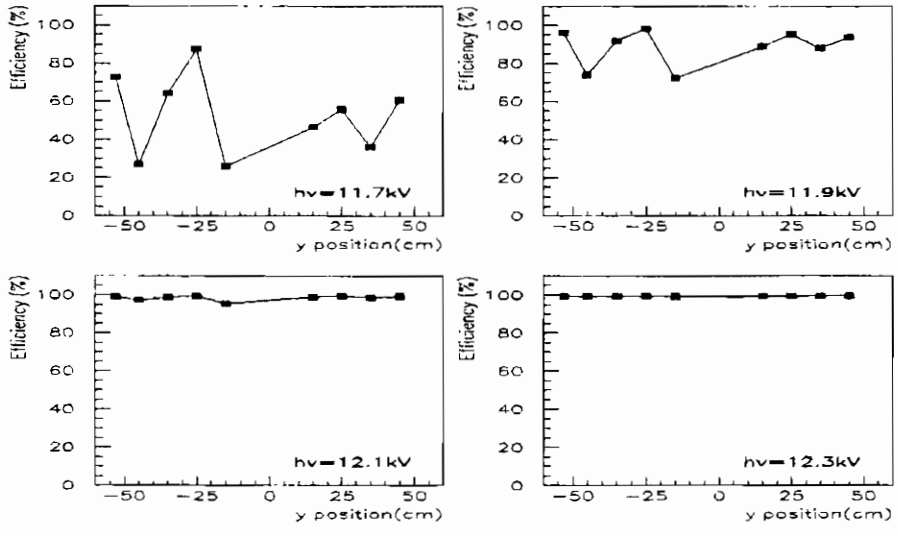


Fig. 10. Efficiencies along the direction orthogonal to the strips for the 3 mm RPC.

the detector working voltage.
The same behavior is observed for the average signal arrival time and its jitter. Both quantities are also computed at the different positions as a function of the high voltages.
In Fig. 11 the values of the signal arrival times and of the time resolution, averaged over the different positions, are given as a function of the high voltage. The dashed lines select a 1 RMS region around these values. The two chambers show a good uniform response over the whole surface also for the time related quantities.

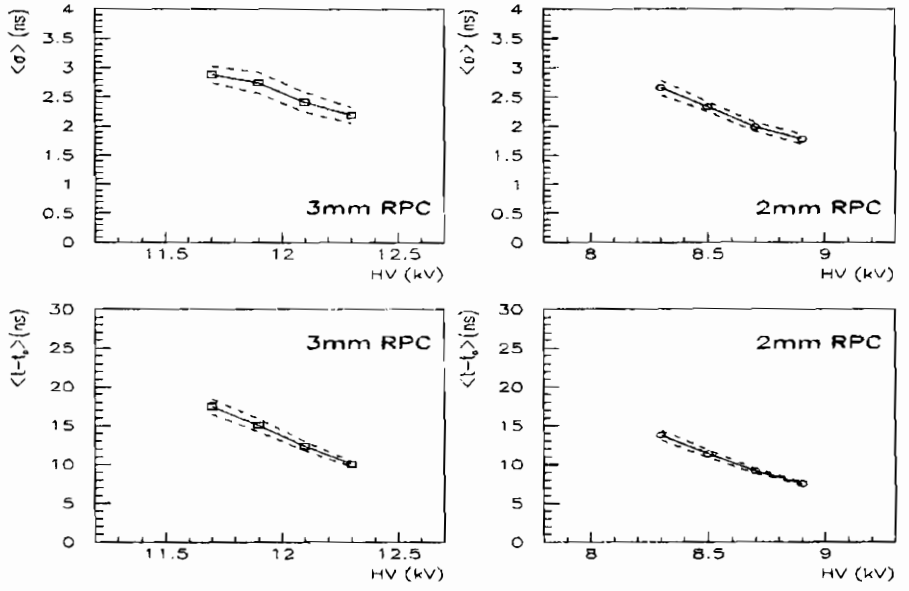


Fig. 11. Average time resolution (up) and average arrival time(down) vs. the high voltage.

### *3.3. Cluster size measurements*

A second period of measurements was devoted to study the performance of the 2 mm gap chamber equipped with the prototype VLSI version of the front-end amplifier. While the hybrid version provides a single ended output analog signal, the VLSI front-end gives a differential

analog signal which could allow a reduction of the cross talk between adjacent channels and eventually end in a better cluster size.
Fig. 12 shows the cluster size distribution (computed in a 250 ns window) of the 2 mm RPC at HV=8.7 kV in the efficiency plateau; the

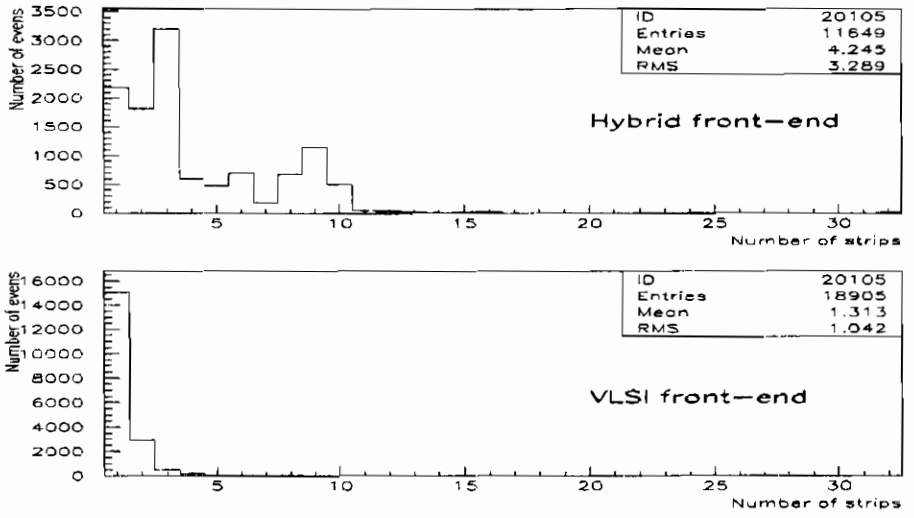


Fig. 12. Distribution of number of strips per cluster.

two curves correspond to the data obtained with the hybrid front-end electronics and to the VLSI version. It is clear the drastic reduction of the cluster size.

## 4. Conclusions

Two large double gap Resistive Plate Chambers, with 2 mm and 3 mm gap widths, were tested in the CMS-H2 muon beam line.
The comparison between the two RPCs shows that the 3 mm is characterized by a worse overall time resolution, as expected, with respect to the 2 mm one. Efficiency and cluster size, are compatible.
The average performance over a large surface was measured; the efficiency averaged over the entire scanning area is $\approx$ 99% for both chambers.
The results obtained with the 2 mm RPC instrumented with VLSI chip are very promising expecially for the drastic reduction of the cluster size.

## 5. References


1. CMS Collaboration, *Technical Design Report*, CERN/LHCC/94-38
   ATLAS Collaboration, *Technical Design Report.*
2. M. Maggi et al., *Preliminary results on double gap RPC in a high background environment* Contribution to this Workshop.
3. F. Loddo et al., *Front end electronics for RPC detector of CMS*, Contribution to this Workshop.

# Beam test results of Inverted Double Gap RPCs with high counting rate capability for the CMS experiment

H. Czyrkowski, R. Dąbrowski, M. Ćwiok, W. Dominik,
J. Królikowski, P. Majewski
*Institute of Experimental Physics, Warsaw University,*
*ul. Hoża 69, PL-00 681 Warsaw, Poland*

M. Górski
*Soltan Institute of Nuclear Studies,*
*ul. Hoża 69, PL-00 681 Warsaw, Poland*

December 15, 1997

ABSTRACT

Two medium size prototypes of Inverted Double Gap RPC were tested in H2 SPS beam at CERN in the intensity range up to 7 kHz/cm$^2$. The detectors having identical construction, but made out of bakelite with the volume resistivity different by three orders of magnitude allowed the study of the impact of the electrode material conductivity on the RPC operation characteristics. The RPC made out of bakelite with $5 \cdot 10^8$ Ωcm volume resistivity exhibits stable operation in the whole range of beam intensities with full efficiency and good timing properties.

## 1. Introduction

A gas detector in which the primary ionization signal is amplified in gas in uniform electric field has served since the beginning of the century for studying the avalanche processes [1]. Detection of single impacts of radiation [2] became possible with introduction of charge sensitive amplifier. The use of Parallel Plate Avalanche Chambers (PPAC) in which electric field is formed by potential difference between two flat and parallel metallic planes, was, however, limited to experiments with heavy ionizing charged particles requiring small active surfaces. PPAC normally operates close to the limit of the proportional multiplication with Townsend mechanism to provide efficient detection of minimum ionizing particles at large capacitance of a read-out electrode. With fluctuating ionization in the gas gap, an avalanche may turn into discharge. Violent sparking damages the surface of the electrodes (mostly the cathode), thus degrading the operation of the counter. Both, the energy of a discharge and the dead-time of the detector increase with discharging capacitance that is proportional to the area of the electrodes. It prevents from using large PPAC in particle physics experiments.

The use of thick semiconductive glass with the volume resistivity in the range of $10^9$ $\Omega$cm as anode of PPAC allowed operation of the detector in limited discharge mode at moderate rate profiting from intrinsically good time resolution of the device [3].

The detector called "Resistive Plate Chamber" [4] is based on the same principle as the one developed by Pestov. However, because of the use of a cheap commercial material (bakelite plates) for electrodes, large area detection systems were aimed [5]. The use of high resistivity electrodes' material allows to consider the detector plane as a dense matrix of small independent detection cells. This approach has, however, an obvious drawback: the standard RPC may suffer from the severe rate limitation. Avalanche current in the gas gap provokes the voltage drop across the thick electrode; this changes dynamically the charge amplifying field. The amplitude of the signal and the timing of the detector response may become rate dependent even at moderate rates of avalanches. Operating the detector at the moderate mean charge gain improves its rate capability [6,7] for the price of using sensitive amplifiers for readout.

When the operation of large area RPC in high rate environment is required, the material on the electrodes should be selected in such a way that the avalanche current in the gap causes negligible voltage drop on the electrodes. Significance of the field variations in the gap is obviously related to the steepness of the gain versus field dependence at the working voltage.

Maximum current that may flow across the gas gap is set by the resistance of the electrodes, thus setting the limit of the product of the avalanche charge and the avalanche rate. With increasing radiation rate, the charge gain (avalanche charge) shall automatically decrease resulting in loss of the detection efficiency. The loss of efficiency is enhanced due to an exponential-like pulse height distribution.

An obvious way to improve the rate capability of a RPC is, therefore, to increase the limit of the avalanche current flowing across the gas gap. The limit is set by the high resistivity of the electrode material. Using a material with lower resistivity should improve the rate capability of a RPC. However, if the conductivity of the electrodes becomes too high the operation of the detector should possibly suffer from the limitations related to the PPAC configuration.

The possible beneficial use of low resistivity materials for the RPC operation has been suggested earlier in [8]. An improvement in the detection efficiency when using plates of lower resistivity - $\rho \sim 4 \cdot 10^{10}\ \Omega$cm instead of $\rho \sim 2 \cdot 10^{11}\ \Omega$cm, is reported in [9]. The good efficiency has been obtained for radiation intensity up to about $50\,\mathrm{Hz/cm^2}$ only in the streamer mode of operation of the detector. In spite of this limitation, the quoted measurements confirm that the volume resistivity of the electrode material is a crucial parameter for stable operation of a RPC.

It is very difficult to establish precisely, on the basis of the results existing in the literature, a correlation between the performance of a RPC and the actual conductivity of the electrodes.
There are three main reasons for this:

- the initial resistivity of the materials used for the construction lies in a narrow band around the $10^{11}\ \Omega$cm,

- the volume resistivity of standard bakelite plates depends strongly on the water content [8]; the resistivity increases by orders of magnitude after few weeks in the dry gas atmosphere [10], and it drops again if the plate is exposed to humid air [11],

- a practical method that allows to monitor the resistivity of the electrodes after a RPC is assembled does not exist; the only signature of the gradual increase of the resistivity is the shift of the working voltage towards higher value during long term operation of the detector.

Results of the test of a RPC made out of low resistivity material and designed for continuous operation in radiation fluxes larger than $1\,kHz/cm^2$ are presented in this paper.

The study of impact of the electrodes' conductivity on the performance of the RPC operated in avalanche mode is extended to low resistivity materials in this work. On the basis of a simple RC circuit considerations one can estimate that the proper resistivity should be in the range of $10^9\,\Omega cm$ for stable operation at rates exceeding $1\,kHz/cm^2$. The question can be raised whether a detector with parallel electrodes of moderate volume resistivity will have the features of a Resistive Plate Chamber - independence of operation of neighboring areas.

## 2. Experimental set-up. Description of the chambers and tests

Two double gap RPC modules were built in a similar way, but using electrode material with nominal volume resistivity different by about three orders of magnitude. Both detectors were assembled in the Inverted Double Gap RPC structure (Fig. 1). We shall call the high and low resistivity chambers RPC1 and RPC2, respectively.

Sensitive areas of RPC1 and RPC2 have dimensions, respectively, $50\,cm \times 50\,cm$ and $24\,cm \times 24\,cm$.

An IDG RPC is essentially a stack of two identical single gap RPCs each equipped with its own strip readout plane. The readout planes are placed on the external faces of the double RPC structure. A thin metallic plate on ground potential, sandwiched between two independent RPC planes, serves for electric screening of the subunits; the plane is separated electrically from the electrodes. The two RPCs are pressed together (put in tight contact) in the single mechanical structure. The module is assembled between two flat and rigid honeycomb planes which assure good mechanical contact of all elements and the flatness of the structure.

The readout electrodes were made of 1.5 mm thick G-10 plates with copper foils on two sides. The strip pattern was etched on the plane facing the gas gap; the other plane was connected to the ground thus

assuring shielding of the module. The strips were 10 mm wide with 2 mm spacing. The double gap RPCs were assembled in such a way to have strips in both planes in the same direction. Pairs of corresponding strips of the double gap module were connected together at one end, thus forming a common readout structure. Other ends of strips were individually terminated on 1 kΩ. Analog sum of signals induced by avalanches from two gaps, picked-up on the readout electrodes, forms the final signal.

The single gap RPC was build with two parallel plates of bakelite of about 2 mm thickness. The fixed distance over the whole surface of the two plates - the width of the sensitive gas volume, was assured by the frame inserted along the edges and by small disks (spacers) forming a matrix of 100 mm pitch. The spacers were first glued to the plates with an adhesive film in order to avoid the leak of the glue to the gas volume. After the module was assembled, some glue was injected through small holes drilled in the spacers' axes through the plates; this technique reinforces junction of spacers to the electrode surface that may be problematic when the standard fixation procedure is used, especially if the inner surface of the plates is covered with melamine. This simple technological operation allows one to control the surrounding of the spacers and it increases the safety level for breaking caused by accidental pressurization of the gap. This disks having 10 mm in diameter and the external frame were made out of bakelite with about $10^{12}$ Ωcm volume resistivity; edges exposed to the gas and high electric field were carefully polished.

The width of the gas gaps of RPC1 and RPC2 were 2.2 mm and 2.0 mm, respectively. Slightly wider gap of the RPC1 was due to technical reasons only. Operation of a RPC - detection efficiency and timing properties, should not depend significantly on the gap width in this range [12]. The RPCs forming IDG RPC structure were positioned in such way as to have the spacers in the same location in the detection plane; no special care was taken to achieve precise positioning.

The outer surfaces of the RPC units that face the central shielding plate were coated with a graphite solution providing low surface resistivity of about 100 Ω/□. The outer surfaces on the readout side had higher surface resistivity; in the case of the RPC1 subunits the surface resistivity due to graphite varnish coating was about 200 kΩ/□ and in the case of the RPC2 it was set to 25 kΩ/□ during the bakelite production by integration of a sheet of carbon paper (the conductivity of the surface was probably too high for the efficient pick-up of signals [13]).

Conductive surfaces of each single gap RPC were protected with 200 $\mu$m thick PVC foil. The detector may be powered by applying difference of electric potentials to the conductive surfaces; in our case, the surfaces facing strip planes were grounded and a negative high voltage was applied to the surfaces facing the central shielding plane. Due to the individual connections of the subunits of the double gap modules to the power supplies, the single gap operation of the detector could be studied.

The RPC1 was made out of 2 mm thick bakelite plates cladded with thin melamine film[1] having the volume resistivity of about $6 \cdot 10^{11}$ $\Omega$cm. The surfaces of the plates were smooth and shiny due to the cladding as well as because of using very refined tools in the production procedure [14]. It has been demonstrated by others that RPC made out of sufficiently good surface quality material do not need oiling for acceptable operation with low spurious noise [14]. Therefore, inner surface of this RPC was not treated with linseed oil. The resistivity of the surface was about $1.5 \cdot 10^{11}$ $\Omega/\Box$.

For the construction of the RPC2 the special bakelite with low volume resistivity has been developed[2] according to our specification; the volume resistivity of 1.9 mm thick plates was $5 \cdot 10^{8}$ $\Omega$cm. The developmental samples were used for electrodes. Because of rather poor quality of surfaces that face the gas volume, the modules of the RPC2 were "oiled" after the chamber assembly. The importance of the surface smoothing by linseed oil treatment for a RPC operation is documented in the literature [15]. The modules of the RPC2, however, were not tested before the treatment. For the surface treatment a standard linseed oil with 1 % additive of hardener was used. The hardener, containing salts of manganese and lead, accelerates hardening of a thin film of liquid and assures uniform hardening in the volume in presence of air. The resistivity of the surface before treatment was about $2 \cdot 10^{10}$ $\Omega/\Box$.

Mechanical and electrical parameters of the modules are summarized in Table 1.

During the beam tests, 14 central strips of each IDG RPC module were equipped with front-end preamplifiers[3] having 10 MHz bandwidth and charge sensitivity about 1.5 mV/fC. The outputs of the amplifiers were fed to discriminators via 10 meter long coaxial cables. The ampli-

[1] Courtesy of the INFN group from Bari.

[2] IZO-ERG S.A., Gliwice, Poland.

[3] Courtesy of the INFN group from Bari; more infomation about the amplifiers can be found in [14].

Table 1. Mechanical and electrical characteristics of the RPCs

| | RPC 1 | RPC 2 |
|---|---|---|
| dimensions of the active area [$cm^2$] | 50 × 50 | 24 × 24 |
| gap width [mm] | 2.2 | 2.0 |
| thickness of the bakelite plates [mm] | 2.0 | 1.9 |
| volume resistivity of the electrodes [$\Omega$cm] | $6 \cdot 10^{11}$ | $5 \cdot 10^{8}$ |
| inner surface resistivity [$\Omega/\Box$] | $1.5 \cdot 10^{11}$ | $2 \cdot 10^{10}$ * |
| outer surface resistivity (readout side) [k$\Omega/\Box$] | 200 | 25 |
| strip width / pitch [mm] | 10 / 12 | 10 / 12 |
| strip length [mm] | 528 | 306 |
| oiling | no | yes |

* before oiling.

fied signals were discriminated at 30 mV. The width of discriminated pulses was set to 50 ns. Discriminated signals converted to differential ECL standard were connected to the multihit TDC module in CAMAC (LeCroy 2277 of 1 ns time resolution operated in a common start mode with 1 $\mu$s time range). Thus the arrival time of leading edges of avalanche pulses could be recorded during 1 $\mu$s after the trigger from the set of scintillator counters.

The data reported in this paper were taken with the chambers filled with a gas mixture of 90% $C_2H_2F_4$ and 10% iso-butane. During the same run the gas mixture containing $C_2HF_5$ as a main carrier has also been tested; the results will be published separately.

The hodoscope formed by RPC1 and RPC2 was installed in the H2/SPS beam at CERN and tested during the period of September 1997. The set of scintillator counters defined the trigger selecting particles traversing 10 × 10 $cm^2$ area in the plane of the hodoscope. Two 10 × 10 $cm^2$ drift chambers, placed upstream and downstream allow particle tracking. The hadron beam has been defocused in order to illuminate a largest possible area of the hodoscope, however the hadron beam spot was still slightly smaller than the one for the muon beam. The high rate capability studies of the IDG RPCs were performed with the hadron beam. The time structure of the SPS beam is 2.5 s long periodical

extraction with the period of 14 s.

## 3. Measurements and results

The measurement reported here were performed for the central position of the RPCs - the axis of the beam coincide with the center of the grid of spacers.

In Figure 2 the detection efficiency of the two modules tested is shown as a function of the applied voltage for different particle rates. The efficiency is averaged over 2.5 seconds of the spill duration.

The low resistivity RPC2 module exhibits full efficiency with plateau width of 500 V for the highest applied rates. Slight effect of the particle rate appears only for highest rates. The shift of 100 V observed for the beam intensity of 7 kHz/cm$^2$ remains small with respect to the width of the plateau. The shift may be partially due to the variation of the ambient temperature during one week period of tests. However, the influence of the ambient temperature on the working voltage has been observed, a quantitative analysis of this effect has not been done; this important item is currently under study. The slopes of all curves characterizing the RPC2 are sharp and nearly independent of the radiation rate. This hints that the avalanche charge distribution (not measured separately during this test) has a peaked shape and it preserves the shape for the whole range of intensities applied.

The rate limitation clearly appears in the case of the high resistivity RPC1 module. The avalanche current lowers dynamically the electric field in the gas gap due to high resistivity of the electrodes. Already at 3 kHz/cm$^2$ the 95 % level of efficiency is barely achieved at highest voltages.

The study of the evolution of the detection efficiency during the particle spill reveals better the possible effects of continuous operation at intense radiation fluxes. In the measurements shown in Figure 3, the working points for both RPCs were chosen 300 V above the voltage at which the efficiency was 95 % at 640 Hz/cm$^2$.

The detection efficiency of the RPC1 decreases dramatically with the irradiation time during the spill for the highest rates; the clear tendency is visible already at 1400 Hz/cm$^2$. In the case of the RPC2 the full efficiency is maintained during the beam spill for all intensities. It is important to point out that during first 0.5 s of spill the high resistivity RPC1 operates with full efficiency, thus measurements with periodic

irradiation of few hundred milliseconds duration may give misleading results. It is clear that continuous irradiation periods much longer than seconds are necessary for correct evaluation of a RPC operation.

The avalanche arrival time as a function of the time in the spill is shown in Figure 4. The delay of the avalanche increases with the rate which can be explained by the dynamic drop of the amplification field in the gap. In the case of the RPC2 the shift is of the order of 2 ns between 640 and 7000 Hz/cm$^2$. The shift is much more pronounced for the RPC1; even at moderate rate of 640 Hz/cm$^2$ the RPC1 begins to loose its time properties 1.5 s after the beginning of the irradiation. The time walk shows tendency to saturate when an equilibrium is reached; one can estimate that the maximum time walk related to variations of the radiation rate is about 2 ns and 9 ns for, respectively, low and high resistivity RPCs operated at the given working point. Again, during first few hundred milliseconds of the irradiation both detectors exhibit time walk smaller than 0.5 ns. The phenomenon of the rate dependence of the time walk, observed for the high resistivity RPC, is a severe limitation when the radiation intensity varies either with time or within area of the detector.

Timing characteristics of the RPC2 show very small dependence on rate (fig. 5). Time resolution as a function of rate remains constant at the level of 2.2 ns up to rates as high as 3000 Hz/cm$^2$; the width of the time distribution increases by about 0.5 ns at 7000 Hz/cm$^2$. The full width at the base (at the level of 2 %) of the time distribution is about 13 ns as it is shown in Figure 6 for the rate of 640 Hz/cm$^2$. An increase in the charge amplification results in fastest arrival time of the avalanches with more narrow time spread.

The cluster multiplicity measured, taking into account strips fired within 10 ns after the fastest one, is shown in Figure 7. The criterion on the time window for cluster reconstruction was introduced in [14] and justified by the delayed cross-talk in the read-out electronics then observed, which could lead to apparent enlargement of the cluster size. Measurements were performed for both RPCs in the same point of the efficiency curves corresponding to the radiation intensity of 640 Hz/cm$^2$. The cluster multiplicity measured for the low resistivity RPC2 has narrow distribution with the mean of 1.8 strip; the high multiplicity tail (multiplicity larger than 4) is much less pronounced for the RPC2 than it is in the case of the RPC1. This demonstrates that the amplification process is well localized in the RPC made out of the material with vo-

lume resistivity about $5 \cdot 10^8\,\Omega$cm. The abundance of the events with multiplicity 1, observed for the RPC1, may be explained as resulting from the smaller avalanche charge for the RPC with high resistivity electrodes.

## 4. Discussion and conclusions

The results obtained for the low resistivity RPC2 module confirm that Resistive Plate Chamber has intrinsic capability of high rate operation. The volume resistivity of the electrodes should be selected to match the required performance. Electrical characteristics of the electrodes are crucial for stable operation of a RPC in the wide range of the radiation rates.

The fluctuations of the avalanche process, due to the dynamic behavior of the chamber, are less pronounced for the detector with low resistivity electrodes. The stable operation up to rates around $7000\,\mathrm{Hz/cm^2}$ has been achieved with the efficiency plateau broader than 500 V.

Due to low resistivity the RPC2 module has excellent time characteristics; time resolution of $\sigma \sim 2.2$ ns has been measured up to rates of $3000\,\mathrm{Hz/cm^2}$. The total width at the base of the distribution is about 13 ns.

Exposure times of the detector to a continuous radiation flux shorter than 1 s do not allow to reveal the time characteristics of a RPC.

The avalanches in the RPC with the electrodes having the volume resistivity of $5 \cdot 10^8\,\Omega$cm are well localized; the average cluster size is 1.8 strip of 12 mm pitch.

The performance of the RPC2 module matches well the severe requirements imposed on the muon trigger detector for the CMS experiment. Double gap RPCs with electrodes of low resistivity can operate in the hottest regions of the CMS detector, where the radiation background at the level exceeding $1\,\mathrm{kHz/cm^2}$ may be expected.

As it has been already mentioned, the resistivity of the surfaces facing the strip planes in the RPC2 was probably too low for the efficient pick-up of signals. It might result in narrowing of the efficiency curve for the chamber as well as in the broadening of the detected cluster size. The effect of the surface resistivity on the signal transmission to the external pick-up electrode has been simulated and confirmed experimentally for the plastic tubes operated in streamer mode [13]. The full transmission was reached for surface resistivity exceeding $100\,\mathrm{k\Omega/\square}$. One can expect

that for the avalanche mode of operation the threshold surface resistivity for the full transmission should be higher because of lower frequency. Having in mind the high resistivity of the plates, the surface resistivity in the MΩ range should not limit the rate capability of the detector. This item should be systematically studied.

## 5. Acknowledgements

The authors are grateful to Fabrizio Gasparini for encouragement in starting the study and for continuous interest. We are indebted to Giuseppe Iaselli for very fruitful discussions and for providing kindly the amplifiers for read-out. We wish to thank to the INFN groups from Bari and Pavia for pleasant cooperation.

We thank Gyorgy Bencze and Fritz Szoncso for their support during the tests in H2/SPS beam.

This work was partially financed by Polish Committee for Scientific Research under grants KBN 115/E-343/SPUB/P03/119/96 and KBN 115/E-343/SPUB/P03/004/97.

## 6. References

1. L. B. Loeb, *Fundamental Processes of Electrical Discharge in Gases*, (John Wiley and Sons, Inc., New York, 1939).
2. J. Christiansen, *Z. angew. Phys.* **4** (1952) 326.
3. Yu.N. Pestov and G.V. Fedotovich, Preprint IYAF 77-78 (SLAC translation 184 (1978)).
4. R. Santonico and R. Cardarelli, *Nucl. Instr. and Methods* **187** (1981) 377.
5. see for example CMS Technical Proposal, CERN/LHCC/94-38, LHCC/P1 and references to the respective chapter.
6. R. Cardarelli, Proceedings of II International Workshop on the Resistive Plate Chambers in Particle Physics and Astrophysics, Pavia '93, *Scientifica Acta*, **vol. 8**, no. 3. (1993) p.159.
7. H. Czyrkowski et al., Proceedings of the International Workshop on Resistive Plate Chambers and Related Detectors, Pavia '95, *Scientifica Acta*, **vol. 11**, no. 1. (1995) p.197.
8. W. Dominik "Resistivity of commercially available materials for RPC electrodes", CMS NOTE 1997/23.

9. Gy. Bencze et al., *Nucl. Instr. and Methods* **A340** (1994) 466.
10. I. Crotty et al., *Nucl. Instr. and Methods* **A360** (1995) 512.
11. I. Crotty et al. "Further studies of avalanche mode operation of resistive parallel plate chambers", CERN PPE/94-39, CERN/LAA-MC 94-12.
12. M. Abbrescia et al. "Recent results and developments on double gap RPC for CMS", presented at the 7th Meeting on Advanced Detectors, La Biodola, 25-31 May, 1997.
13. G. Battistoni et al., *Nucl. Instr. and Methods* **202** (1982) 459.
14. M. Abbrescia et al. "Beam Test Results on Resistive Plate Chambers for the CMS Experiment", CMS NOTE 1997/062.
15. M. Abbrescia et al., *Nucl. Instr. and Methods* **A394** (1997) 13.

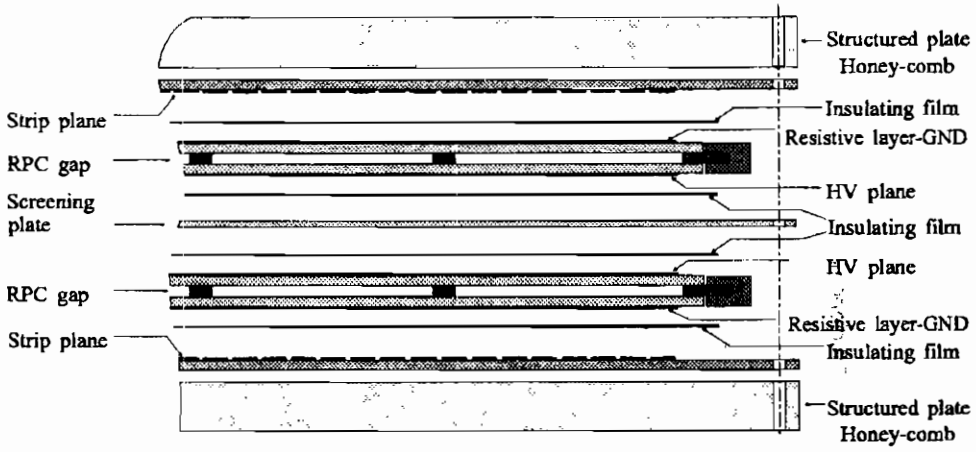


Fig. 1. Cross section of an Inverted Double Gap RPC used in our tests; expanded view.

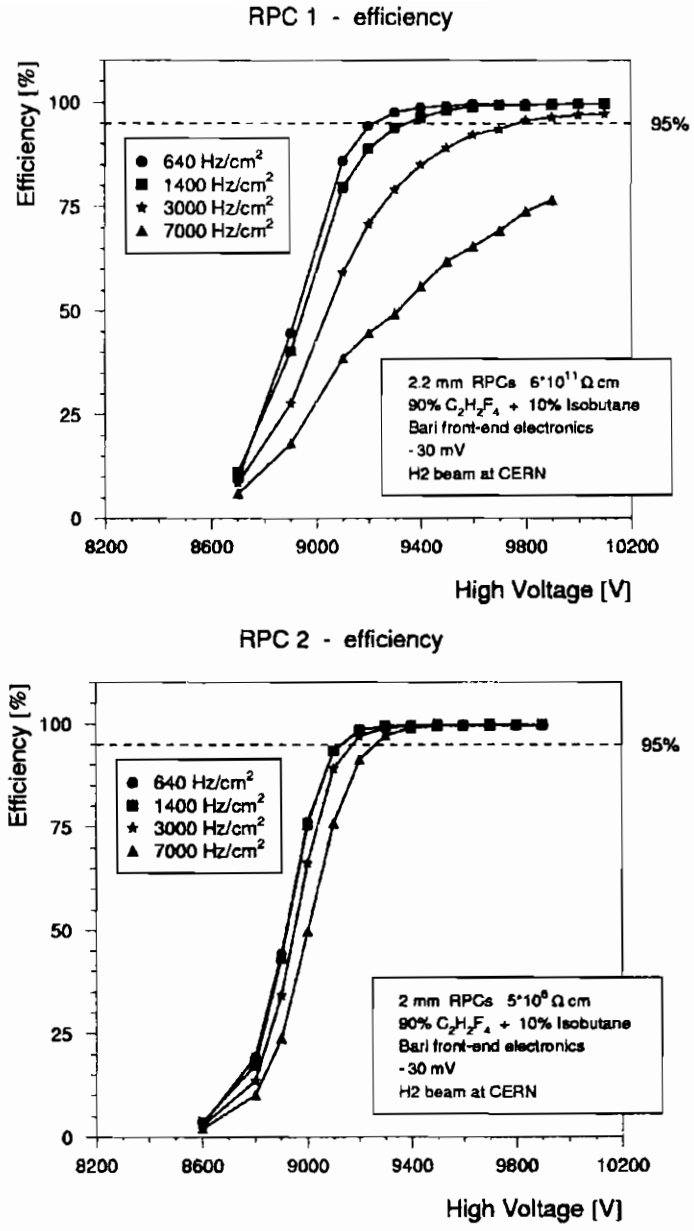


Fig. 2. Detection efficiency averaged over 2.5 s beam extraction cycle for high resistivity RPC1 and low resistivity RPC2 modules as a function of the supply voltage for several particle fluxes. Signal discrimination threshold was −30 mV in all measurements.

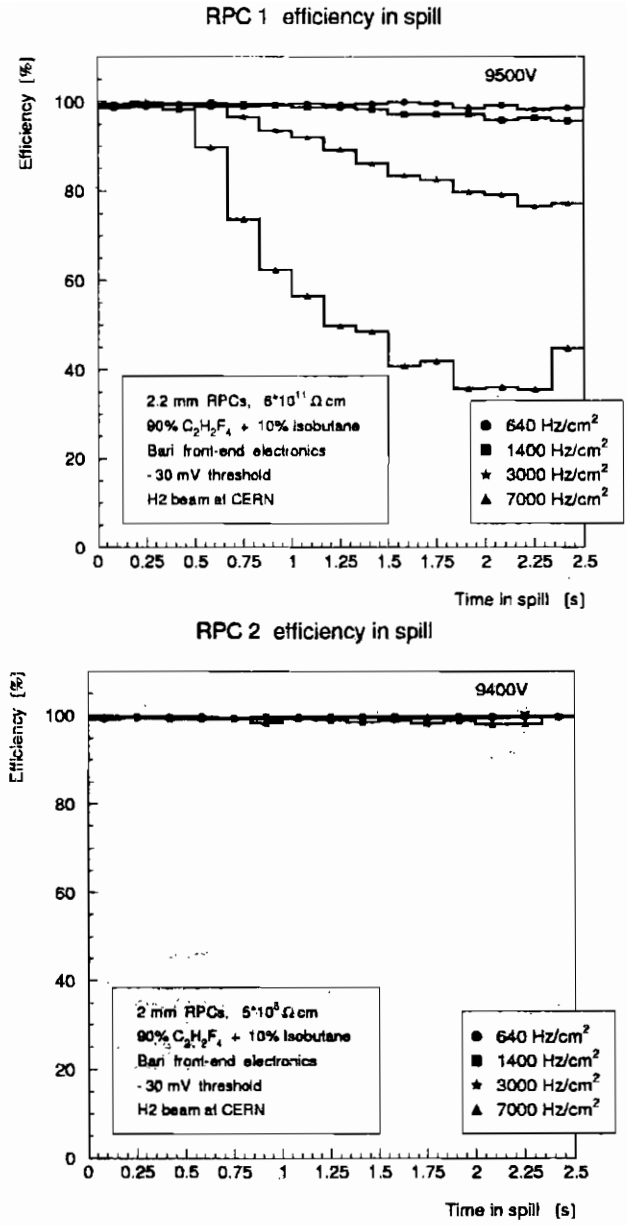


Fig. 3. Detection efficiency of RPC1 and RPC2 as a function of time during the extraction cycle of the beam for various fluxes. Signal discrimination threshold was $-30\,\mathrm{mV}$ in all measurements.

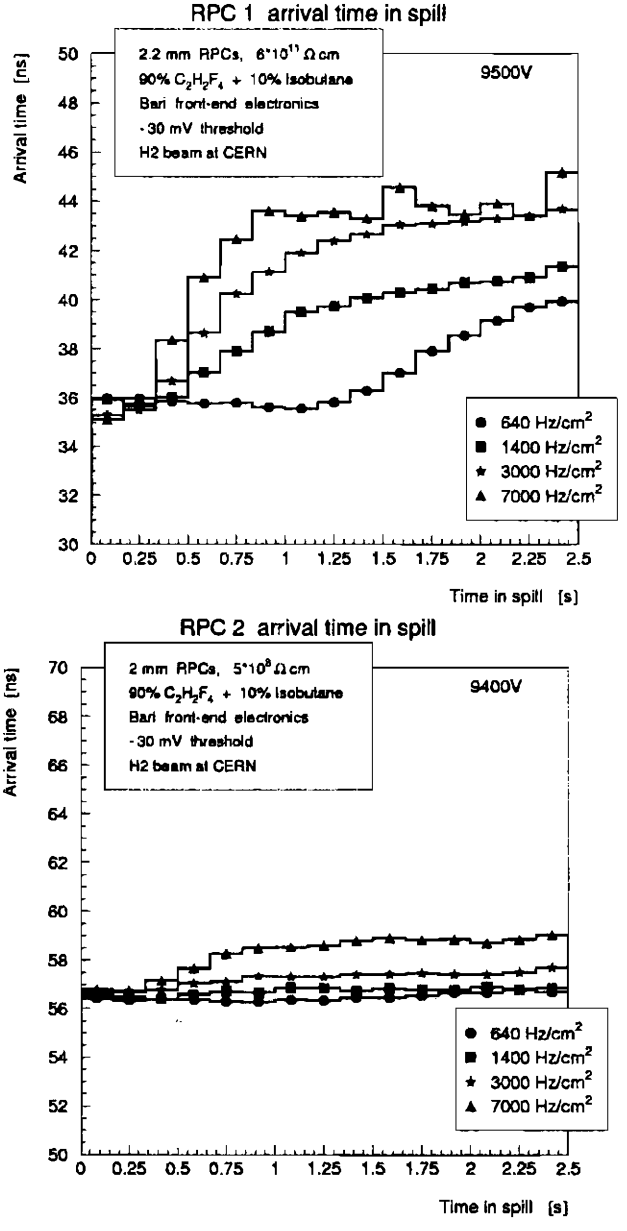


Fig. 4. Signal arrival time, measured for RPC1 and RPC2, as a function of time during the extraction cycle of the beam for various fluxes.

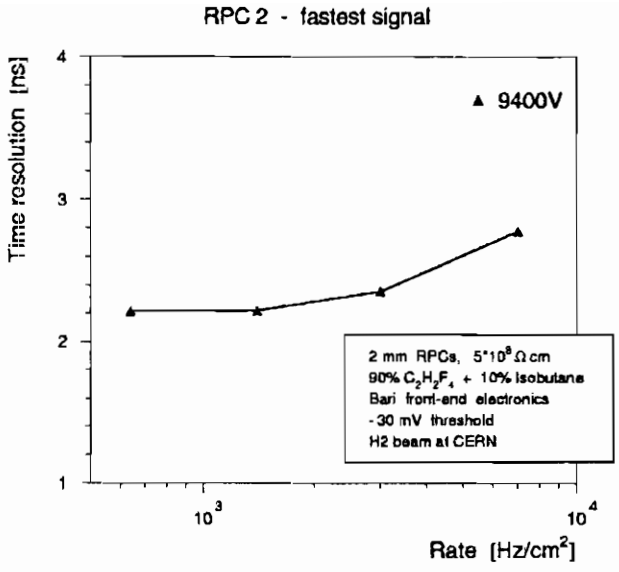


Fig. 5. Time resolution of the low resistivity RPC2 module, operated at the high voltage 200 V above the knee of the efficiency plateau, as a function of the particle flux.

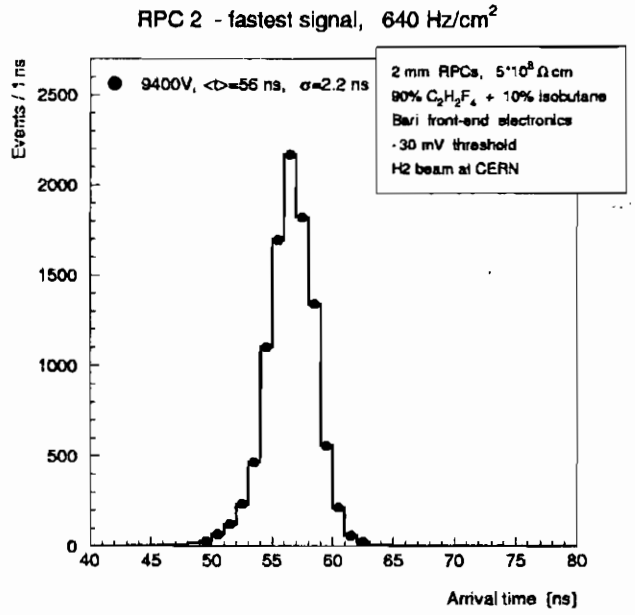


Fig. 6. Distribution of the avalanche arrival time with respect to the trigger defined by the beam counters for radiation flux of 640 Hz/cm$^2$. The value of the voltage applied to the RPC2 module was 200 V above the knee of the efficiency plateau.

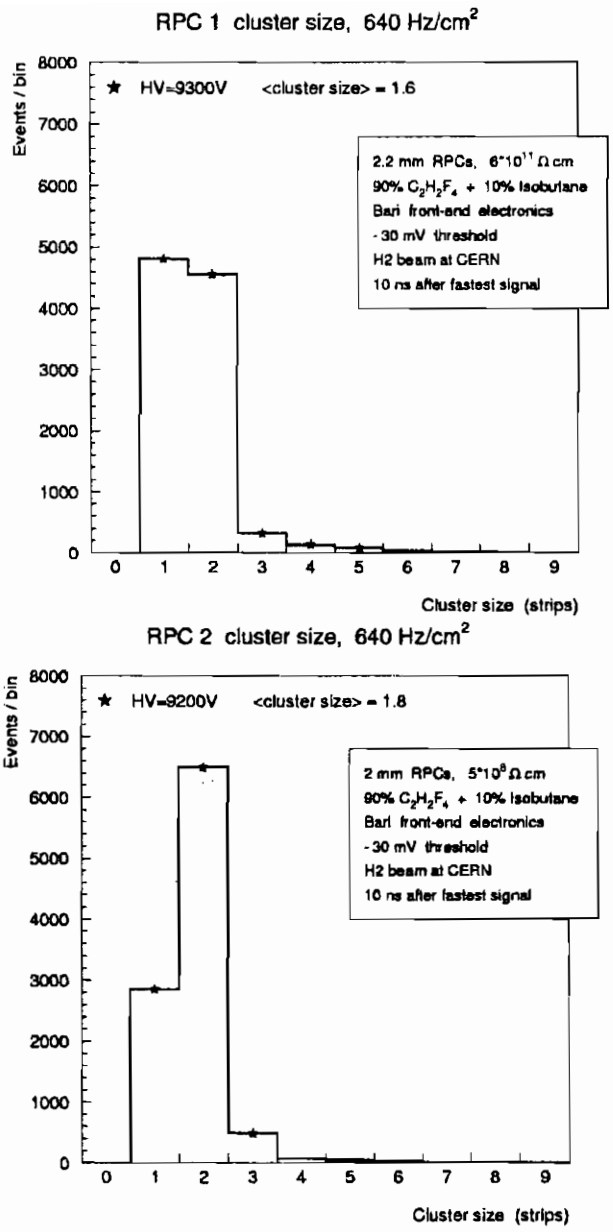


Fig. 7. Cluster size measured in RPC1 and RPC2 at the particle flux of 640 Hz/cm$^2$; the cluster is defined by signals arriving within 10 ns after the fastest one.

# RPCs for the ATLAS Level-1 muon trigger : Test-beam results

P.Camarri[a], R.Cardarelli[a], P.Creti[b], R.de Asmundis[c], A.Di Ciaccio[a], M.Donatacci[d], V.Gapienko[e], E.Gorini[b], A.Leo[d], V.Konstatinov[e], A.Paoloni[a], M.Primavera[b], R.Santonico[a], Y.Sviridov[e], I.Vassiliev[e,†], S.Veneziano[d], E.Usenko[e], Y.Xie[f] and V.Zaets[e].

[a] *University of Roma "Tor Vergata" and sezione INFN, Italy*
[b] *University of Lecce and sezione INFN, Italy*
[c] *University of Napoli and sezione INFN, Italy*
[d] *University of Roma "La Sapienza" and sezione INFN , Italy*
[e] *IHEP, Protvino, Russia*
[f] *Institute of High Energy Physics, Academia Sinica, Beijing, The People's Republic of China*
[†] *deceased*

presented by

Anna Di Ciaccio

ABSTRACT

A full-size ($270 \times 90$ $cm^2$) and a small-size ($50 \times 50$ $cm^2$) RPC trigger tower prototype have been tested at the ATLAS H8 beam facility at CERN. Results on the basic performance of the full-size chambers, operated in avalanche mode, are presented. Dedicated studies have been done on the small-size chambers to measure the collected charge and the streamer probability as a function of the applied voltage and to optimise the front-end amplifier threshold.

## 1. Introduction

To exploit the Large Hadron Collider (LHC) discovery potential, the ATLAS Collaboration[1] has designed a high resolution muon spectrometer, based on three large superconducting air-core toroid magnets, covering the pseudo-rapidity range $|\eta| \leq 2.7$[2]. It is instrumented with stand-alone triggering and momentum measurement capability.

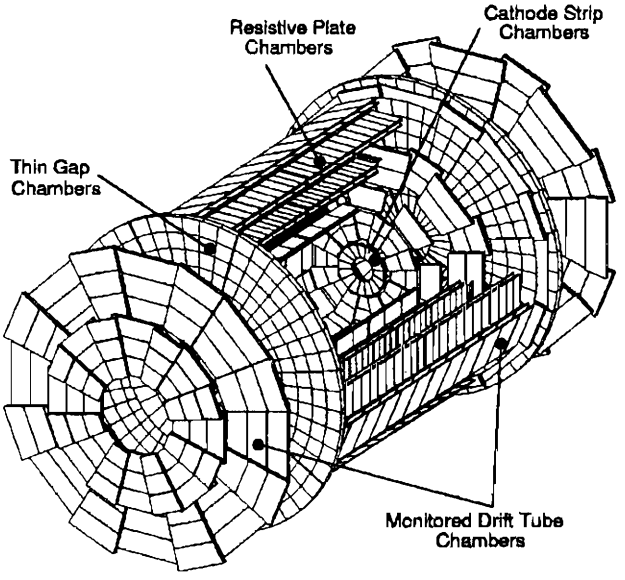


Figure 1: 3-D view of the ATLAS muon system.

High pressure drift tubes (MDTs) in the central region and Cathode Strip Chambers (CSCs) at high rapidity provide a precise measurement of the muon track coordinates in the bending direction. The trigger sys-

tem consists also of two different technologies: Resistive Plate Chambers (RPCs) in the barrel region and Thin Gap Chambers (TGCs) in the end-cap regions and extends over a total pseudo-rapidity range $|\eta| \leq 2.4$ (see Figure 1).

## 2. The RPC trigger scheme

The trigger system in the barrel consists of three stations of RPCs: the first two are located on both sides of the middle MDT chambers and provide the low $p_t$ ($p_t \geq 6\ GeV$) trigger, the third station is adjacent to the outer MDT chambers. The coincidence of all three stations allows to increase the $p_t$ threshold to 20 GeV. The trigger logic requires three out of four layers in the middle station for the low $p_t$ trigger and in addition, one of the two outer layers for the high $p_t$ trigger (see Figure 2). Due to the high level of low energy particles background, the trigger scheme is implemented in two projections.

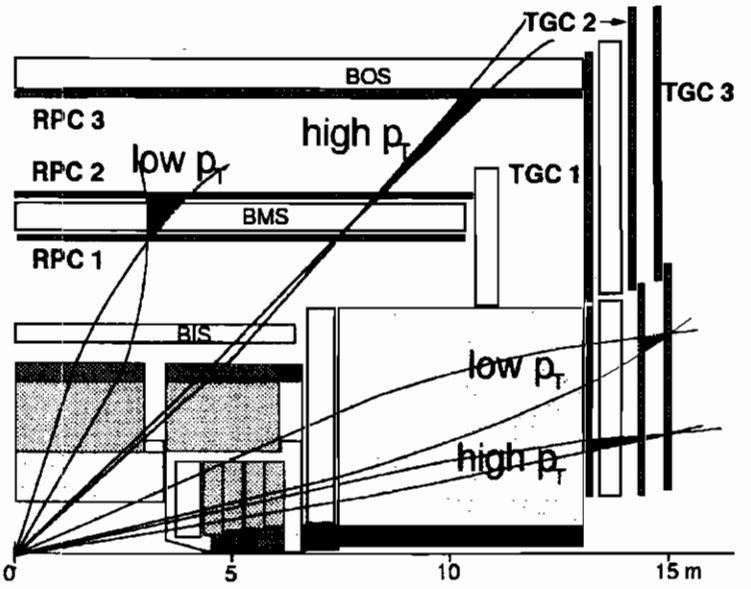


Figure 2: Schematic representation of the triggering scheme.

The ATLAS RPCs chambers cover an area of about 3650 $m^2$ and extend over a pseudo-rapidity range $|\eta| \leq 1$. The chambers must satisfy

three basic requirements:

- bunch-crossing identification (the time between two adjacent bunch-crossings is 25 ns);
- well-defined pt cut-off in moderate magnetic field with a spacial granularity of the order of a cm;
- measurement of the second coordinate in the direction orthogonal to the one measured by the precision chambers with a spacial resolution better than 1 cm.

## 3. Resistive Plate Chambers

The RPC is a gaseous detectors providing a typical space-time resolution of 1 cm×1 ns with digital read-out. The basic RPC unit is a narrow gas gap (2 mm) formed by two parallel resistive bakelite plates, separated by insulator spacers. The primary ionisation electrons are multiplied into avalanches by a high, uniform electric field of typically 4.5 kV/mm. For avalanche operation a non-flammable and environmentally safe gas, tetrafluoretane ($C_2H_2F_4$) has been used[3].

The signal is read-out via capacitive coupling by metallic strips on both sides of the detector. A trigger chamber is made of two detector units, namely two gas gaps, each one read-out by two orthogonal planes of pick-up strips: the $\eta$ strips are parallel to the MDTs wire and provide the bending view of the trigger detector; the $\phi$ strips, orthogonal to the MDTs wires, provide the second coordinate measurements. A scheme of a trigger chamber is shown in Figure 3.

## 4. RPCs experimental set-up at H8

An intensive program of chamber prototype tests has been carried out in 1996 and 1997 at CERN ATLAS H8 test-beam facility in the SPS North Area. The program was driven mainly by two needs:

- to study the basic features of the detector working in avalanche mode;
- to test the performance of full-size chamber prototypes.

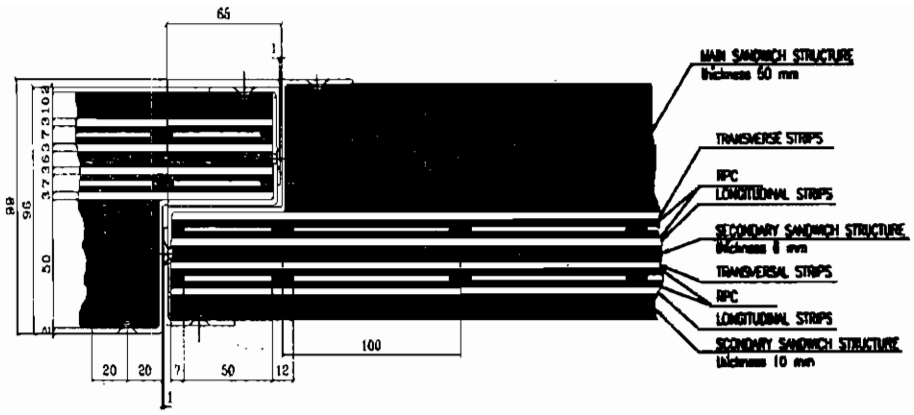


Figure 3: Schematic representation of a trigger station (doublet).

A full-size ($270 \times 90\ cm^2$) and a small-size ($50 \times 50\ cm^2$) trigger tower have been tested with muon and pion beams up to a maximum flux of 900 Hz/cm$^2$. Both towers consisted of six single-gap RPC chambers, arranged in three stations of two chambers each, like it is foreseen in ATLAS. These chamber doublets were located along the beam line, two at a distance of 40 cm from each other and the third 200 cm downstream with respect to the second one in order to simulate the low-$p_t$ and high-$p_t$ first-level muon trigger schemes (see Figure 4).

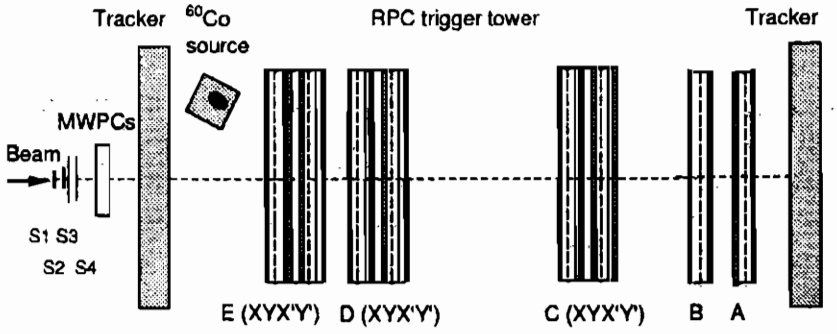


Figure 4: RPC chamber layout in the H8 test-beam facility.

Each gas gap was read out on both sides by 31 mm pitch strips, orthogonal to each other. The front-end electronics consisted of a two-stage voltage amplifier with a gain of about 300 and a bipolar output signal[5]. The amplified strip signals were sent to discriminators with thresholds adjustable between 30 mV and 1 V.

The beam trigger signal was provided by scintillator counters of various dimensions ($2 \times 2, 4 \times 4, 10 \times 10$ $cm^2$). A precise and independent reconstruction of the muon tracks along the horizontal direction was obtained in 1996 by means of two trackers, each made out of two matrices of four by four drift tubes, operated in streamer mode[4] and in the 1997 by a BIL MDT prototype: the Calypso chamber[6].

With the aim of simulating the low-energy LHC background conditions, a 14 mCi $^{60}Co$ source was used to irradiate the upstream RPC with a photon flux producing $\sim$100 Hz/cm$^2$ counting rate spread over most of the detector area.

## 5. Analysis and results of the full-size chambers

The measurement on the full-size chambers concerned the following parameters:

- efficiency;
- time resolution;
- cluster size;
- tracking accuracy.

The chambers were operated with a gas mixture of isobutane (3%) and tetrafluoroetane (97%) at a beam flux of 350 Hz/cm$^2$ distributed over an area of $10 \times 10$ $cm^2$ with the additional flux of the low energy gammas. The amount of isobutane, 3%, was well below the mixture flammability threshold which is about 5.7%. The front-end amplifier threshold was set at 150 mV for all the channels. The discriminator outputs were sent either to input registers for pattern reconstruction or to 1 ns resolution TDCs for time measurements.

In Figure 5 the detection efficiency is plotted as a function of the operating voltage for all the chambers of the three doublets (C, D, E). All chambers reach an efficiency $\geq$ 98% at about 9.0 kV.

The distribution of the time of flight between two RPCs of the tower is shown in Figure 6. From a Gaussian fit of this distribution we extract a $\sigma = 2$ ns, corresponding to a single-layer time resolution of 1.5 ns, well below the 25 ns LHC bunch-crossing time.

Figure 7 shows the average cluster size for the six RPC chambers of the full-size trigger tower (twelve strip planes) at voltages of 8.8, 9.0 and 9.2 kV around the efficiency plateau knee. The average cluster size, namely the number of contiguous hit strips per event, is 1.5 at a voltage of 9.0 kV where the chambers are fully efficient.

Figure 8 shows the distribution of the residuals coming from a straight line fit of all tracks crossing the full-size trigger tower (six RPC chambers in both views). The measured spatial resolution is 6 mm.

## 6. Results of the small-size chamber tests

A set of 50 × 50 $cm^2$ chambers with similar characteristics, was installed at H8 both in 1996 and 1997 to measure the following parameters:

- avalanche charge;
- streamer charge;
- transition from avalanche to streamer and streamer probability;
- rate capability;
- efficiency for different front-end amplifier thresholds;
- response to particles traversing the gas gap at various angles.

The study of the charge distribution is interesting in order to understand the working regime of the RPCs. Increasing the applied voltage, we observe a transition from the avalanche regime to the streamer regime characterised by a much higher collected charge and its almost independence on the primary ionisation.

To study the avalanche and at the same time the streamer-charge distributions, the strips were read out at both ends. The strip signals from one end were directly sent to the input of an ADC module to measure the streamer-charge (it is big enough to require no amplification). The long duration of the gate signal (250 ns) allowed for possible long delays

of the streamers. Instead the signals from the opposite end, were first amplified and then sent to a second ADC module for avalanche-charge measurement. The gate signal in this case was only 70 ns, to exclude possible streamer-signals usually occurring at a much later time.

The avalanche-charge distributions are shown in Figure 9 for operating voltages ranging from 8.6 kV to 9.0 kV in steps of 200 V. They were obtained by summing the charge on the strips that had a 3 $\sigma$ signal above the pedestal. At 8.6 kV the charge distribution shows an exponential shape as expected for proportional mode operation. At 9.0 kV a peak is clearly visible, suggesting saturated avalanche mode operation. The collected charge is about 0.5 pC and is only 1/2 of the signal extracted because the strips are terminated at both ends with their characteristic impedance (25 $\Omega$). The termination is realized by a 50 $\Omega$ cable in parallel with a 50 $\Omega$ resistor.

The streamer-charge distributions, obtained summing the strip signals without amplification, are plotted in Figure 10 for operating voltages of 9.0, 9.4, 9.6 KV. The streamer charge is about 20 pC, a factor 40 higher than the avalanche-charge and it is basically independent from the applied voltage. From these distributions we have extracted the streamer probability for applied voltages above the plateau knee.

In Figure 11 the efficiency and streamer probability are reported as a function of the operating voltage for a chamber doublet at a beam flux of 500 Hz/cm$^2$ and for a front-end threshold of 100 mV for the Y strips and 200 mV for the X strips. The data refer to two different gas mixtures, iso-$C_4H_{10}/C_2H_2F_4$, in ratios of 6%/94% and 1.6%/98.4%. For both mixtures the streamers appear at a voltage about 200 V above the efficiency plateau knee.

We have explored two possible ways, the first in a beam and the second with cosmic-rays in our laboratory in Rome, to increase the high voltage plateau before the appearance of streamers:

- working with a lower amplifier threshold;
- searching for a streamer-less gas mixture[8].

To test the first idea the amplified signals were fed into a standard discriminator module with the threshold adjustable from 30 mV to 1 V. Results on RPCs chamber efficiency and average cluster size versus the operating voltage for 30, 60 and 100 mV thresholds are presented in

Figure 12 and Figure 13. A 30 mV threshold is corresponding to a charge seen by the detector of only 20 fC. At a lower front-end threshold we observe an increase of the high voltage plateau (i.e. at 30 mV the plateau knee occurs already at 8.6 kV) but the cluster size is too high at 9.0 KV. In fact it has been shown that an average strip cluster width greater than two could seriously affect the selectivity of the trigger[9].

With the purpose of correlating the observed cluster size with the track position, we have reconstructed the muon trajectories using a high spacial resolution detector ($\sigma < 100$ $\mu$m), the Calypso chamber[6]. The distribution of the track impact points on a RPC strip plane is presented in Figure 14 for events with cluster size one, two and three and for 30 mV threshold.

The distribution pattern fits the 3 cm strip pitch: events with cluster size two are occurring when the particle hits the detector around the edge of two contiguous strips, while the cluster size is one when the strip is hit around its centre. Events with cluster size three, pretty abundant for the 30 mV threshold, are understood as due to a large induced charge extending over three neighbouring strips.

The comparison of the efficiency at beam fluxes of 500 and 900 Hz/cm$^2$ over a 10×10 cm$^2$ area and in presence of a counting rate of ~100 Hz/cm$^2$ from low energy photons, spread over most of the chamber, is plotted in Figure 15. We conclude that RPCs have a rate capability up to 1 kHz/cm$^2$ with a threshold as high as 100 mV.

Figure 16 shows the efficiency and the streamer probability for particles entering the gas gap at $30^0$, $40^0$, $60^0$ angles. To account for temperature and pressure variation during the data taking we have normalised the operating voltages to arbitrary defined values for the temperature and pressure (T = 293 K and P=1010 mbar). We can remark that an angle is influencing the efficiency response, but not much the streamer probability, suggesting that a $0^0$ angle is less favourable for the avalanche-streamer separation.

## 7. Conclusions

The analysis of the 1996 and 1997 H8-beam data, in parallel with the work in our laboratory, has provided a better knowledge of the avalanche-working mode of the RPCs. We believe that the actual performance of the detector could insure an efficient ATLAS muon LVL1 trigger at LHC.

The still open question, emerging from these data, of a better separation between the avalanche and the streamer regime in the plateau region, has been solved by very recent laboratory test-results. They show that the addition to the 'standard' gas of 1% of sulphur exaflouride ($SF_6$) reduces dramatically the streamer formation[10].

## 8. Acknowledgements

We would like to thank L.Di Stante for the precious help in setting up the RPC chambers.

## 9. References

1. ATLAS Technical Proposal, *CERN/LHCC/94-43* (December 1994).
2. ATLAS Muon Spectrometer Technical Design Report, *CERN/LHCC/97-22* (31 May 1997).
3. R.Cardarelli, V. Makeev, R.Santonico, in *Nucl. Instr. and Meth.*, A382 (1996) 470;
   M.G.Alviggi et al.; *ATLAS Muon Note 131* (1 October 1996).
4. C.Bacci et al, *ATLAS Muon Note 135.*
5. R.Cardarelli et al, in *Proceeding of this Workshop.*
6. P.Creti et al, *ATLAS Muon Note 196* (24 October 1997),
   C.Bini et al, *ATLAS Muon Note 204* (16 July 1997) .
7. R.Cardarelli et al.;, *RPCs Front-End electronics for the ATLAS LVL1 Trigger Detector*, Proc.of the 7th Pisa meeting on Advanced detectors, Isola d'Elba, May 25-31, 1997 to be published in Nucl.Instr. and Meth.
8. P.Camarri et al, in *Proceeding of this Workshop.*
9. L.Luminari, *presentation at the ATLAS Collaboration Meeting*, November 1997.
10. P.Camarri, R.Cardarelli, A.Di Ciaccio, R.Santonico, *Streamer suppression with $SF_6$ in RPCs operated in avalanche mode* (to be published in Nucl.Instr. and Meth.).

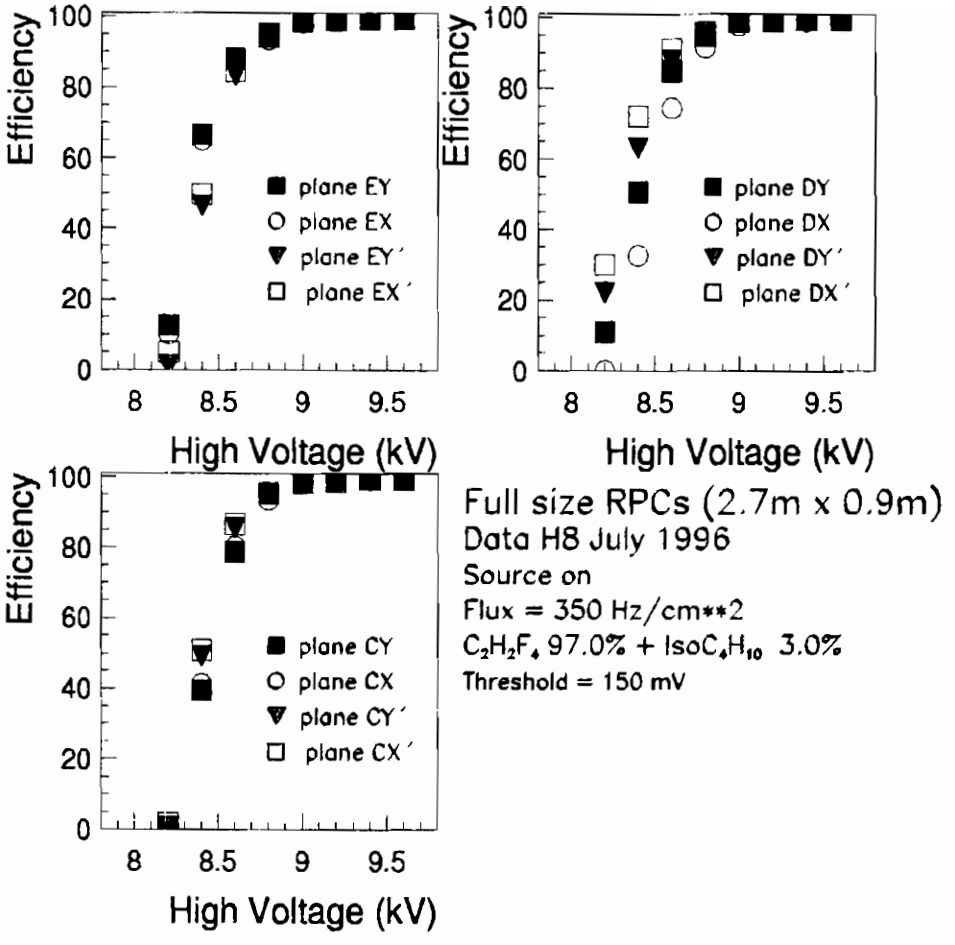


Figure 5: Detection efficiency vs. operating voltage for a full size trigger tower (three chamber doublets).

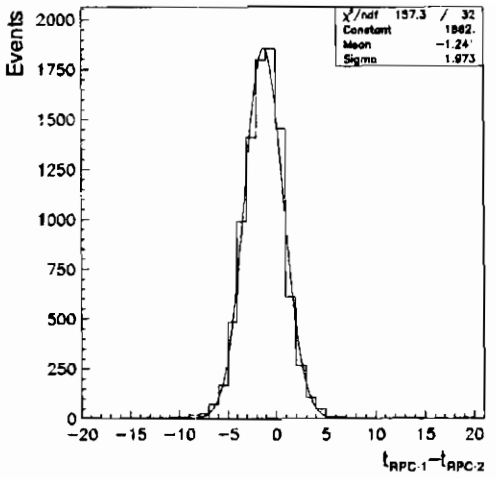


Figure 6: Distribution of time of flight between two RPC chambers.

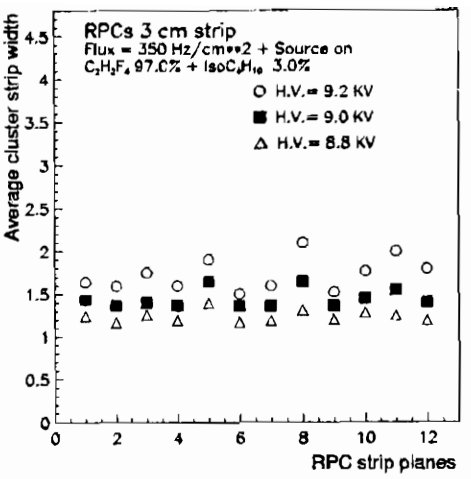


Figure 7: Average cluster size widths for the full size RPCs.

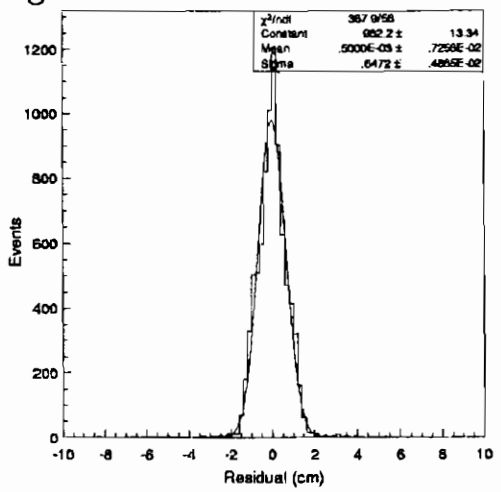


Figure 8: Distribution of RPC residuals with respect to the reconstructed hit positions provided by external trackers.

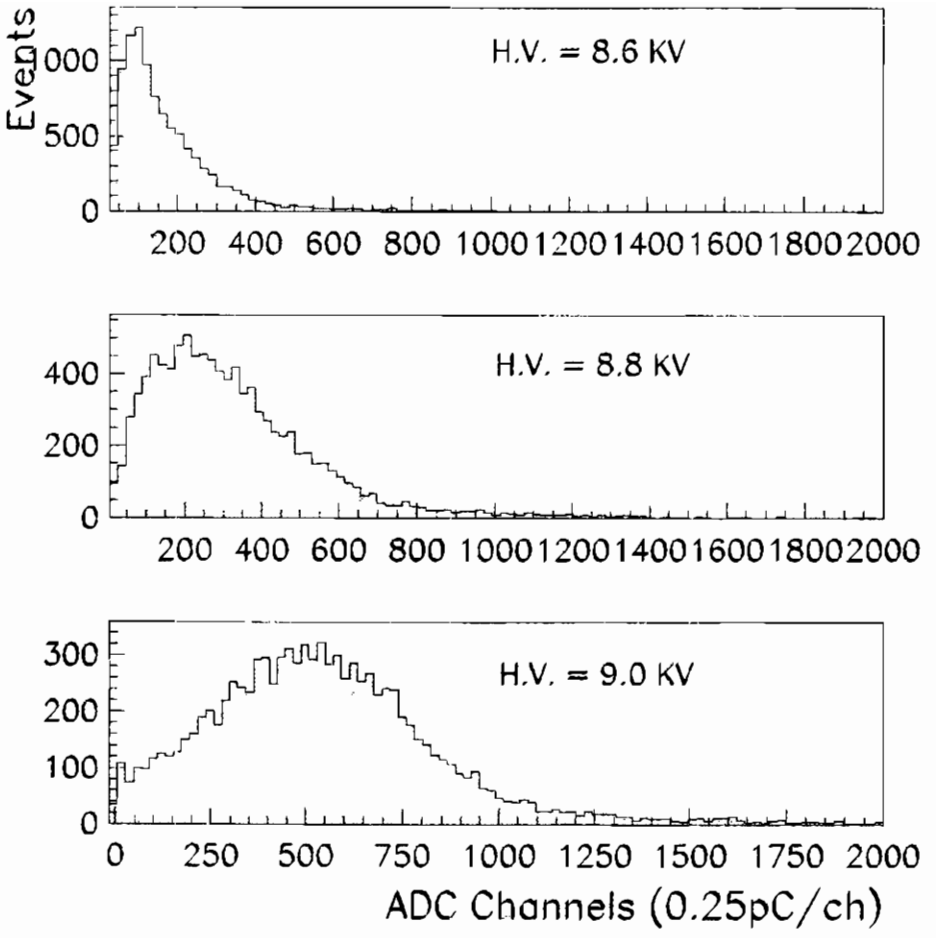


Figure 9: Avalanche charge distributions at various operating voltages around the plateau knee. The distributions are obtained summing the charge on the strips with a signal of 3 $\sigma$ above the pedestal.

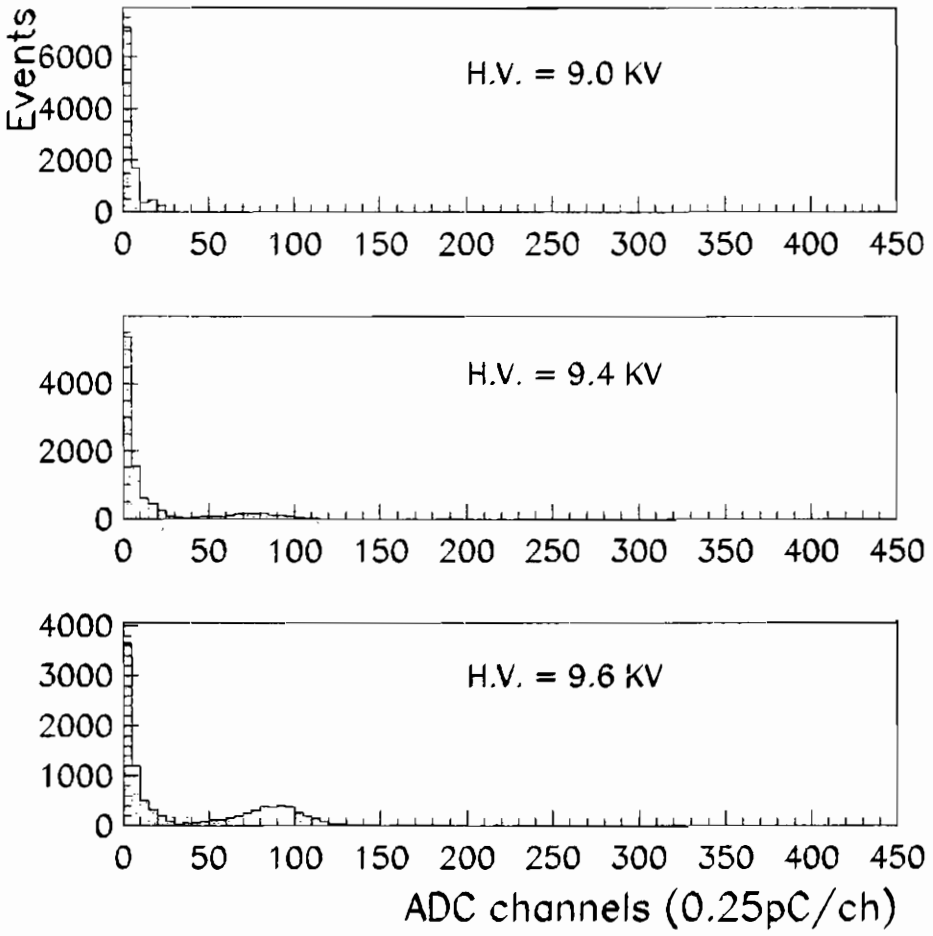


Figure 10: Streamer charge distributions at 9.0, 9.4, 9.6 KV above the plateau knee.

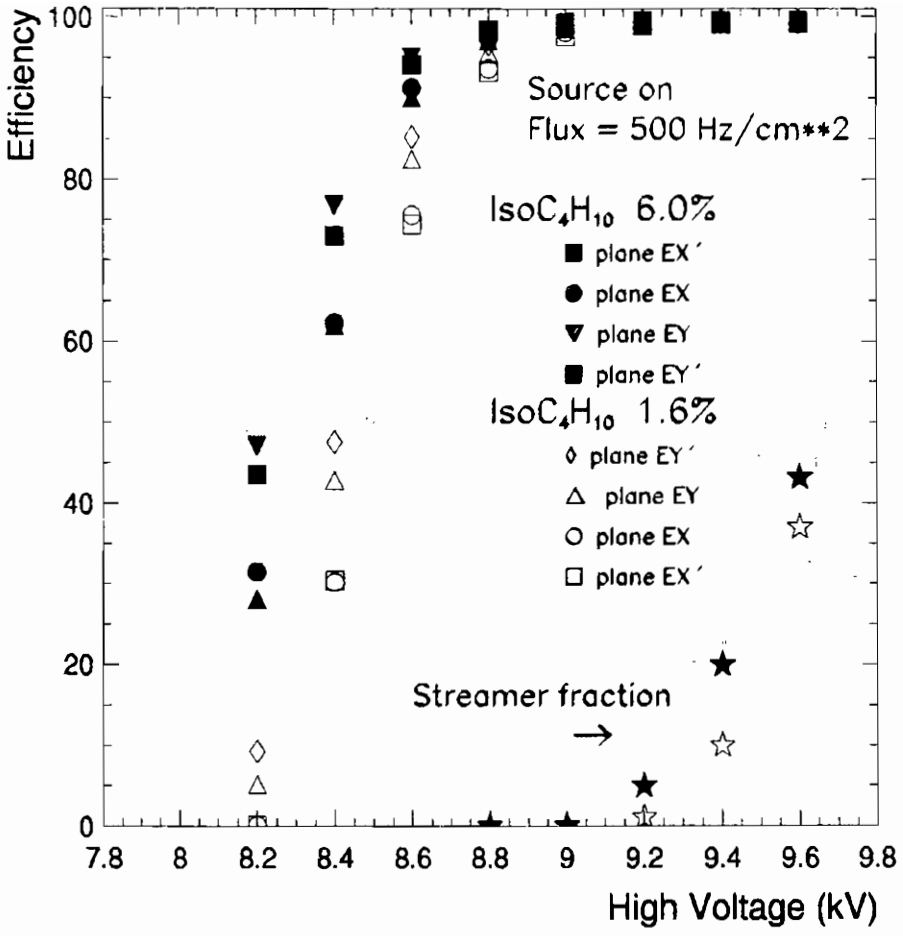


Figure 11: Efficiency curves and streamer probabilities vs. applied voltages for a 50x50 $cm^2$ doublet. Each doublet consists of four strip planes (X,Y,X',Y'). The closed and open symbols refers to 6% iso-$C_4H_{10}$ and to 1.6% iso-$C_4H_{10}$.

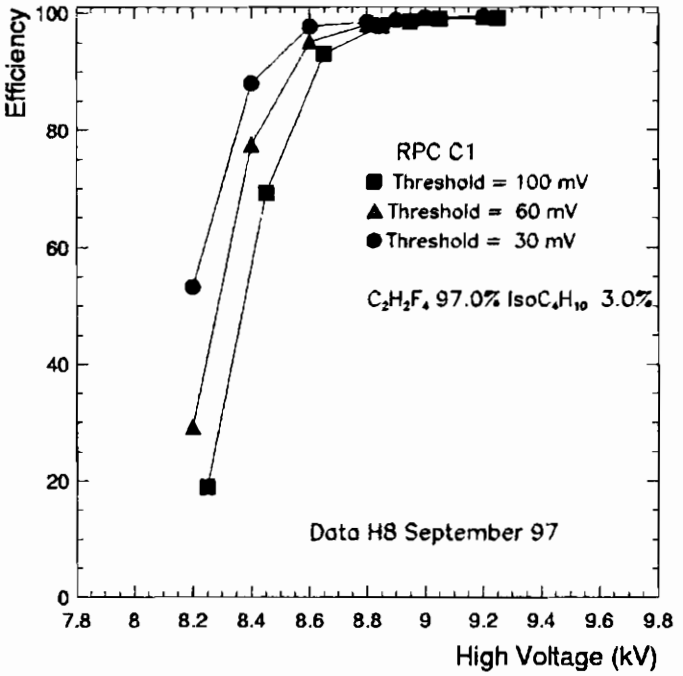


Figure 12: Efficiency curves for 30, 60,100 mV front-end thresholds vs operating voltages.

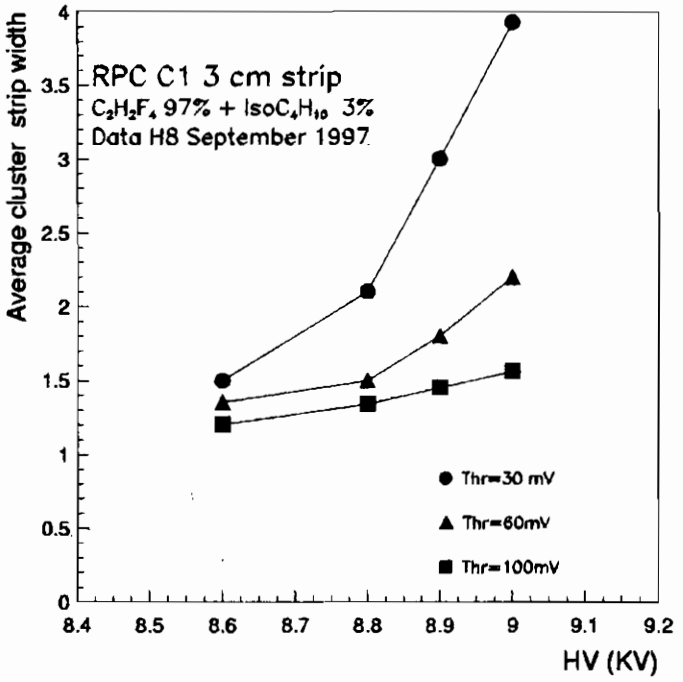


Figure 13: Average cluster size widths vs. operating voltages for 30, 60, 100 mV front-end thresholds.

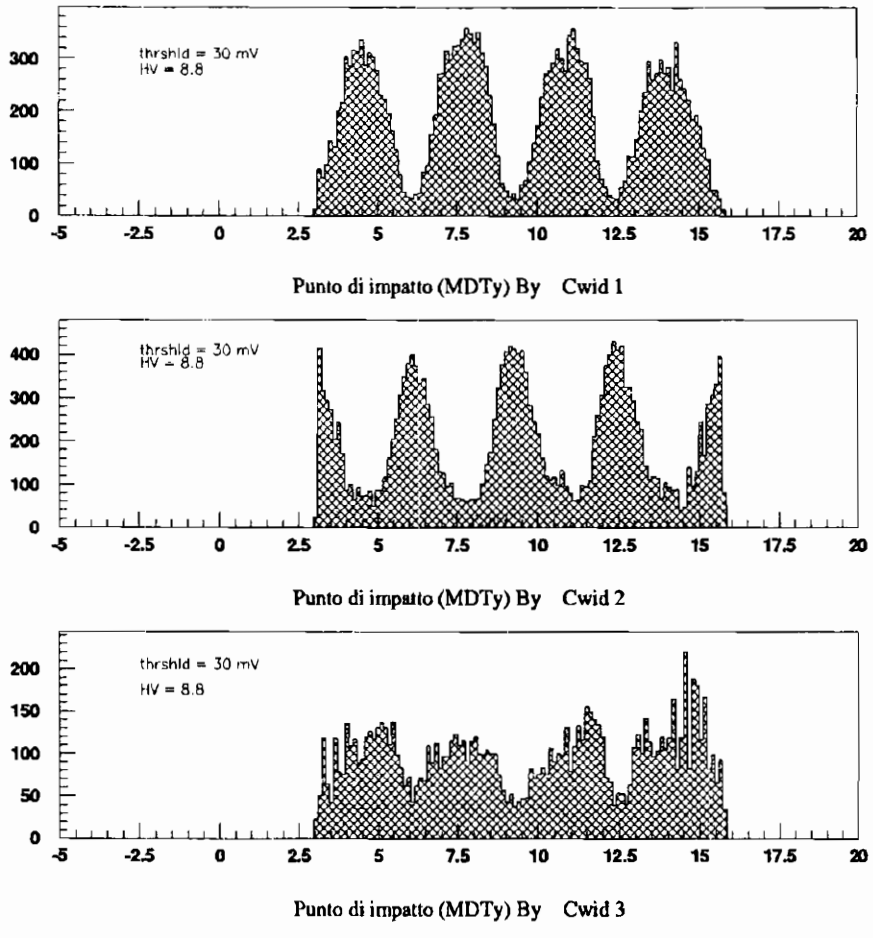


Figure 14: Impact points on a RPC strip plane of the tracks reconstructed with the Calypso chamber for events with cluster size one (top), two (center) and three (bottom).

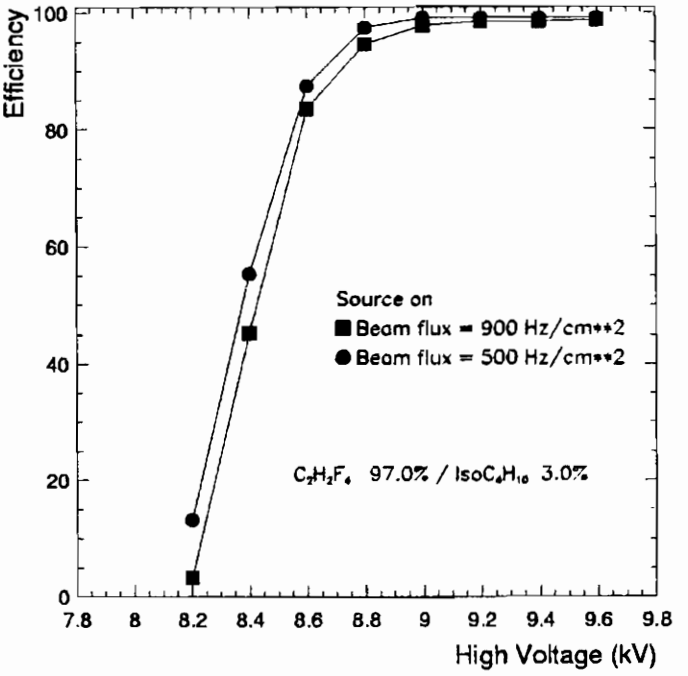


Figure 15: Efficiency curves at beam fluxes of 500 and 900 $Hz/cm^2$.

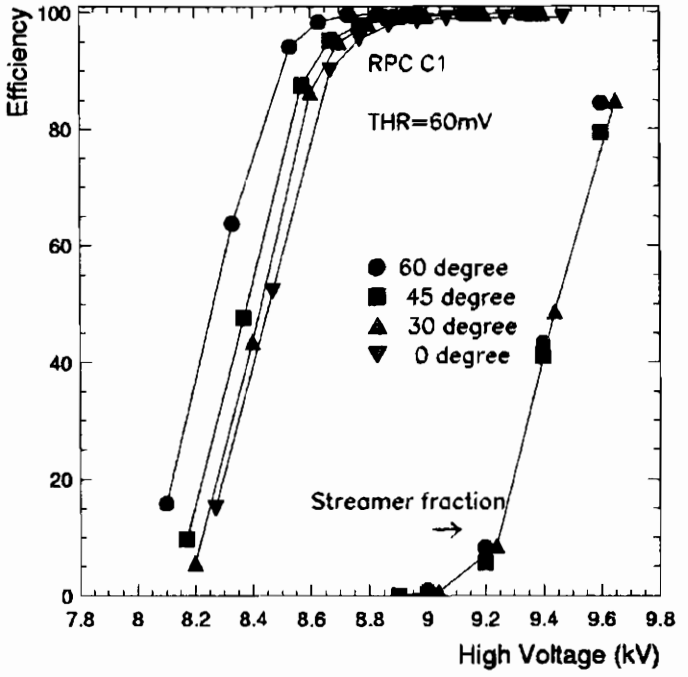


Figure 16: Efficiency curves vs. applied voltage for $0^0$, $30^0$, $45^0$, $60^0$ incidence angle to the RPC. The streamer probabilities vs the applied voltages are also plotted.

# THE SIMULATION OF RESISTIVE PLATE CHAMBERS IN AVALANCHE MODE

MARCELLO ABBRESCIA *
*Dipartimento Interateneo di Fisica e Sezione INFN,*
*v. Amendola 173, 70126 Bari, Italy*

January 16, 1998

ABSTRACT

A model to simulate the avalanche formation process and the induced signal in a Resistive Plate Chamber is presented. A first investigation of the effects of various parameters on the performance of this kind of detector is reported.

## 1. Introduction

Resistive Plate Chambers (RPCs) [1] are detectors for ionizing particles presently used in many different experiments performed both with cosmic rays and at accelerators [2]. They will play a very important role for the first level muon trigger in the future experiments CMS and ATLAS at the planned Large Hadron Collider (LHC).

RPCs were developed at the beginning of 1980s, and have been originally conceived to be operated in streamer mode, meaning that the elec-

*coauthors: G. Bruno, A. Colaleo, G. Iaselli, G. Lamanna, F. Loddo, M. Maggi, B. Marangelli, S. Natali, S. Nuzzo, G. Pugliese, A. Ranieri, F. Romano of *Dipartimento Interateneo di Fisica and Sezione INFN, Bari, Italy* ; S. Altieri, V. Arena, G. Bonomi, G. Gianini, M. Merlo, S. P. Ratti, C. Riccardi, L. Viola, P. Vitulo of *Dipartimento di Fisica Nucleare e Teorica and Sezione INFN, Pavia, Italy*

tric field inside the gas gap is so intense to generate limited discharges localized near the track of an ionizing crossing particle. Because of the large pulses generated, which do not require a sophisticated front-end electronics, this mode of operation is particularly useful when a relatively low flux of particles is involved ($< 200$ Hz/cm$^2$).

However, when the flux of incident particles is higher, RPC efficiency decreases, since, after a discharge has taken place, it is necessary a certain time for the zone of the bakelite plates involved in the discharge process to get charged again.

A possible way to overcome this problem is to operate RPCs in avalanche mode, using a weaker electric field inside the gas gap, and transferring part of the needed amplification from the gas to the front–end electronics. RPCs operated in avalanche mode have shown performances fully adequate to the ones required for the future experiments at LHC [3] [4].

Since the introduction of this mode of operation, a great effort has been made to find out the best possible operating conditions for RPCs in avalanche mode, like the most suitable gas mixtures, electronics, and detector design parameters (gap width, electrode material, etc.). Surprisingly, despite the huge amount of experimental data collected, in various conditions, the understanding of the basic principles of operation of this kind of detector is poor, and a comprehensive theoretical model able to explain and predict the effect of the different structural parameters on the chamber performance is still lacking.

In this paper a Monte–Carlo program, simulating the avalanche growth and the pulse development in RPCs, together with the subsequent electronic signal processing, is presented. This model, based on the usual avalanche Townsend theory, represents just a first attempt to reproduce the main physical processes taking place in an RPC. The program has been used to compute the main physical performances of these chambers (i.e. charge spectra, efficiency and time resolution); the simulation results, moreover, have been compared with the available experimental data. It has also been successfully used to compute the timing performance of another kind of detector, very similar to RPCs, namely Parallel Plate Chamber.

This paper is structured as follows: in the first part the model used is briefly explained, stressing the approximations done and the present limits of the simulation. In the second, a detailed study of charge spectra and efficiency, in various conditions and detector configuration, is

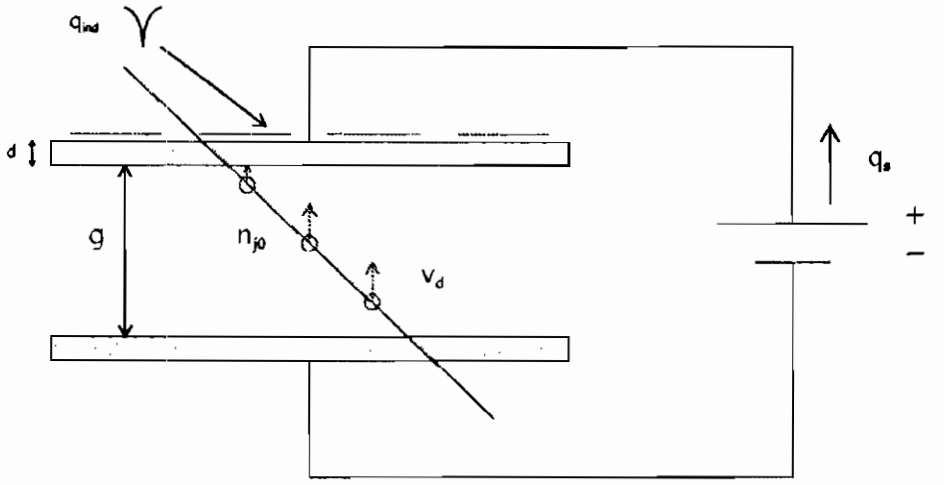


Fig. 1. Signal generation in RPCs

presented. In the third, a similar study is done about time properties.

## 2. The model

Just a short description of the model used in the simulation is reported here. This description, sometimes, for the sake of brevity, oversimplifies the problems underlying the simulation; each one of the following points would require a thorough examination.

The program starts considering an ionizing particle which crosses the RPC gas gap and generates a certain number $n_{clust}$ of primary ion–electron clusters. If the track is perpendicular to the RPC, the probability that $k$ clusters are generated is given by:

$$P(n_{clust} = k) = \frac{(\lambda g)^k}{k!} e^{-\lambda g}$$

where $\lambda$ is the primary cluster density, and $g$ is the gap width. If the azimuthal angle of the incident particle $\theta \neq 0$, then $\lambda$ has to be replaced by its "effective value" $\lambda_{eff} = \frac{\lambda}{\cos\theta}$. The electrons contained in the clusters drift toward the anode and, if the electric field is intense enough, give rise to the corresponding avalanches (Fig. 1). The $j-th$ cluster initial position $f_j(x_0)$ is given by simple Poisson statistics:

$$f_j(x_0) = \frac{\lambda}{(j-1)!}(\lambda x)^{j-1}e^{-\lambda x}, \qquad 0 < x < g$$

For avalanche development the usual exponential law is assumed, so that the charge $q$ at the position $x$ is:

$$q(x) = \sum_{j=1}^{n_{clust}} q_{el} n_{j0} M_j e^{\eta(x-x_0^j)} \tag{1}$$

being $x_0^j$ the initial position of the $j^{th}$ cluster (the first cluster is the closest to the cathode), containing $n_{j0}$ electrons, and $\eta$ the first effective Townsend coefficient (i.e. the Townsend coefficient $\alpha$ minus the attachment coefficient $\beta$), and $q_{el}$ the elementary electron charge.

The factor $M_j$ accounts for possible fluctuations with respect to the exponential growth; these are modeled by means of the Furry's law, which is valid for low values of the reduced electric field $E/p$ ($p$ gas pressure):

$$P(n) = \frac{1}{N}\exp(-\frac{n}{N})$$

or by a Polya distribution (valid for high values of $E/p$):

$$P(n) = \left[\frac{n}{N}(1+\theta)\right]^{\theta} \exp\left[-\frac{n}{N}(1+\theta)\right], \qquad \theta = 0.5$$

where $N = n_0 e^{\eta(g-x_0^j)}$ [5]. Here $P(n)$ represents the probability that the considered avalanche contains, after a path lenght $g - x_0^j$, $n$ electrons; the factor $M_j$ in Eq. (1) is taken randomly from one of these two distributions.

After simulating the drifting avalanches, the program computes the charge $q_{ind}$ induced on the external pick–up electrodes (strip or pads) by the motion of the same avalanches. This is done by a direct application of the Ramo theorem [6]. At first the weighting field $\mathbf{E_w}$ inside the gas gap is computed (in the case of an RPC it has a simple form, being approximately uniform in the gap for pads or strips with dimensions much greater than the gap width); then, in this approximation, the charge induced by one cluster (so the index $j$ can be omitted) is given by:

$$q_{ind} = \frac{q_{el}}{\eta g} n_0 M k \left[ e^{\eta(g-x_0)} - 1 \right] \qquad (2)$$

where the factor:

$$k = \frac{\epsilon_r g}{n_g \epsilon_r g + (n_g + 1)d}$$

takes into account the fact that, as will be pointed out later, not the whole charge can actually be read out by front–end electronics [7]. Here $d$ is the RPC electrode plate thickness, $n_g$ the number of gaps in the detector, and $\epsilon_r$ the bakelite relative dielectric permittivity.

In addition (and more interesting) to the charge induced $q_{ind}$, the program can compute the current $i_{ind}(t)$ induced by the moving avalanches on the external pick–up electrodes, as a function of time; the final result (for one cluster) is:

$$i_{ind} = -Mkq(x)\mathbf{v_d} \cdot \mathbf{E_w}$$

where $\mathbf{v_d}$ is the electron drift velocity in the gas mixture considered. In explicit form (and considering all clusters):

$$i_{ind}(t) = -k\mathbf{v_d} \cdot \mathbf{E_w} q_{el} e^{\eta v_d \Delta t} \sum_{clusters} n_{j0} M_j \qquad (3)$$

Here $\Delta t$ is the time elapsed from the passage of the ionizing particle in the gap, i.e. the time from the generation of the primary clusters. The previous result is useful because, once simulated the current $i_{ind}(t)$, the whole information coming out from an RPC is reproduced. The simulated signals can be input to simulated electronics, pre–amplifiers, discriminators, TDCs, ADCs, etc. For instance, in the case of charge amplifiers, the output voltage (to be input to discriminators) is simply:

$$v_{out} = P_1 \int i_{ind}(t) dt$$

where $P_1$ is the amplifier charge sensitivity.

A few considerations must be done about the validity range (and the limits) of this simulation. In the present state, it does not include any space–charge effect, and so the simulation describes RPCs operated in what is generally called "pure avalanche mode" (for instance, in these conditions, the streamer probability is negligible).

Practically, single gap RPCs operate in pure avalanche mode up to about the knee of their efficiency plateau. This means that the simulation can predict:

1. position and slope of the efficiency curves up to $\sim 90$ %;

2. charge spectra up to the corresponding operating voltage;

3. time properties (essentially time resolution and time walk); this can be done for operating voltages greater than the ones considered in the previous points, since timing is given by the crossing of an electronic threshold which takes place when the avalanche has not fully developed, and so space–charge effects are negligible.

For double and multi–gap RPCs, where each single gap can be operated at lower gain, these limits are pessimistic (in particular the one regarding the efficiency). Beyond these limits, nevertheless, corrections must be applied. However, it is amazing that the experimental values of parameters that should be strongly affected by space–charge effects (i.e. streamer probability) are very close to the simulation results.

## 3. Charge spectra and efficiency

### *3.1. Single gap RPCs*

The simulated spectra of the induced charge $q_{ind}$ for single gap RPCs is shown in Fig. 2. Two cases are considered: a typical "narrow" gap ($g = 2$ mm, Fig. 2a) and a "wide" gap ($g = 9$ mm, Fig. 2b) RPC. The value of the first effective Townsend coefficient $\eta$ (the Townsend coefficient minus the attachment coefficient), has been chosen in such a way that the average values of the two distributions are, more or less, the same. The distributions differ significantly; in the narrow gap case the distribution tends to diverge near the origin, while in the wide gap case it tends to vanish near the origin. This peculiar characteristic has deep implications for what concerns efficiency, but also for rate capability and even time resolution.

It is worth noting that the behavior near the origin can be predicted, under certain approximations (for instance, just considering only the contribution to $q_{ind}$ of the cluster closest to the cathode) by means of simple analytical computations. The final results is:

$$f_1(q_{ind}) = A q_{ind}^{\left(\frac{\lambda}{\eta}-1\right)}$$

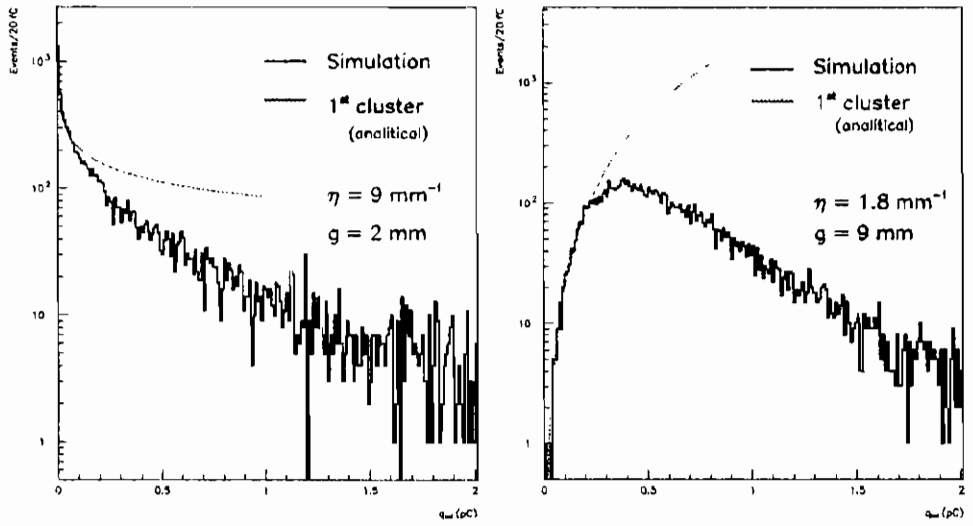


Fig. 2. Comparison between narrow and wide single gap simulated charge spectra

which states that the charge distribution should depend only on the ratio between $\lambda$ (the primary cluster density, i.e. the number of clusters generated per mm by the ionizing particle) and $\eta$. Here $A$ is the renormalization factor. This function is also reported in Fig. 2, and coincides well with the simulation for small values of $q_{ind}$.

The comparison between the simulated and the experimental $q_{ind}$ charge spectra for 2 mm single gap RPCs is shown in Fig. 3. Two different gas mixtures are considered: one currently used in CMS (90 % $C_2H_2F_4$, 10 % iso-$C_4H_10$, considered throughout this paper, unless otherwise specified), the other with a higher Ar content (70 % Ar, 15 % $C_2H_2F_4$, 10 % $CO_2$, 5% iso-$C_4H_10$) [8]. The agreement between the simulation and the experiment is good, in particular in the region where $q_{ind} > 100$ fC. There is a significant difference for $q_{ind}$ between 0 and 100 fC. This is due to the presence of an experimental threshold, which does not allow to reveal events with a charge smaller than a certain value. When an event lies in that region, the relative signal is too low to be detected and the chamber is considered to be not efficient. Therefore, from the behavior of the charge spectra near the origin it is possible to predict chamber efficiency.

The comparison between the simulated and the experimental efficiency for 2 and 3 mm single gap RPCs is shown in Fig. 4 [9]. The

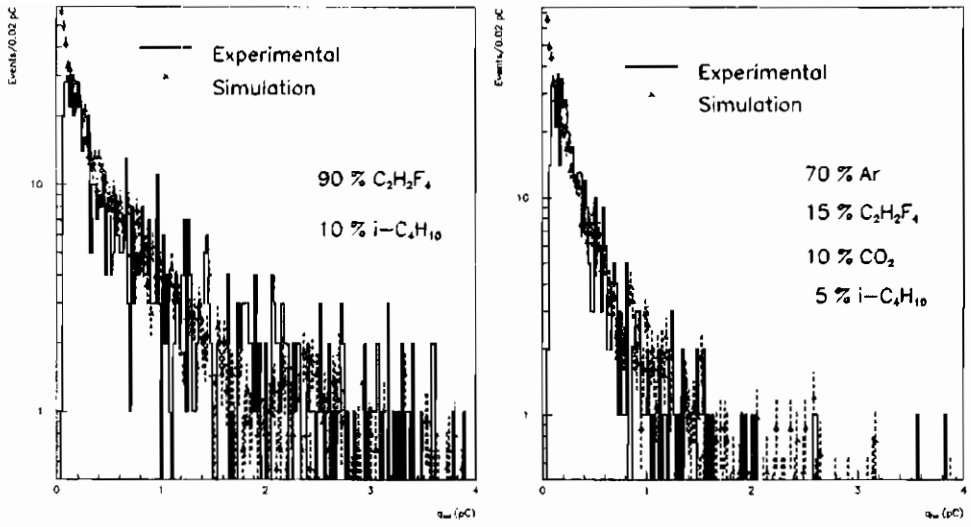


Fig. 3. Comparison between simulated and experimental charge spectra

experimental voltage threshold was about $V_{thr} = -1$ mV (referred to the signal induced on the strip), simulated with a 100 fC charge threshold. The agreement, for the 2 mm, is good, while, for the 3 mm, a shift between the simulated and the experimental curve of about 100 V is present; the relative error is, however, less than 2 %. In the same figure the simulated and experimental streamer probability is reported. The simulated streamer probability has been computed just counting the number of avalanches containing more than $10^8$ electrons. The agreement, even in this case, is fairly good. As pointed out by some authors [10], if space–charge effects are taken into account, the net result would probably be a sort of gas gain saturation effect. This means that the avalanche–streamer transition should take place at higher voltages with respect to the simple model used here; therefore the simulated curve should be shifted toward higher operating voltages, giving a better agreement.

### *3.2. Double and multi–gap RPCs*

A simple layout of single, double and multi–gap RPCs is reported in Fig. 5. In a single gap there is one gas gap, the strips on one side

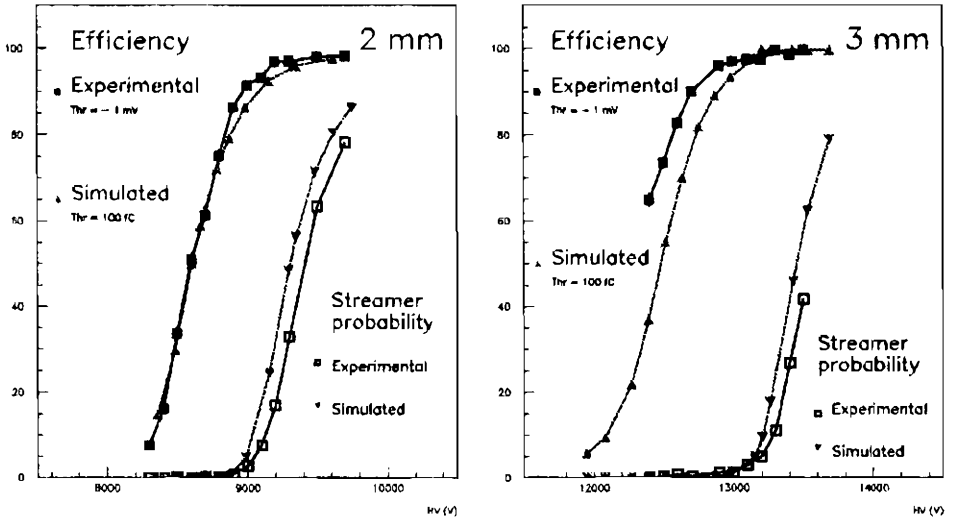


Fig. 4. Comparison between simulated and experimental efficiency

and the ground plate on the other side. In a double gap there are two gaps, the strips in the middle and the ground plates on the outer sides. In this way the sum of the signals coming from the two gaps is obtained on the central strips. In a multi-gap there are three (or more) gaps and, since the strips cannot be placed somewhere in the middle, they are on one side of the whole detector, while the ground plate is on the other side. This could seem trivial, but has deep implications on the signal read-out from pick-up strips. As already pointed out, the signal can be computed by means of the Ramo theorem, which, very roughly, states that the read-out electrode has to be put at 1 V, while the others are grounded. In these conditions the weighting field $\mathbf{E_w}$ is computed. The charge induced $q_{ind}$ is then given by the drifting charge $q_{drift}$ times the voltage drop $\Delta V_w$ (relative to $\mathbf{E_w}$, not to the real operating voltage) inside the gas gap: $q_{ind} = q_{drift}\Delta V_w$. As can be easily deduced from Fig. 5, where the read-out strips are evidenced, in a single gap $\Delta V_w \sim 1$ V. In a double gap, $\Delta V_w \sim 1$ V per gap, while in a multi-gap $\Delta V_w \sim 1/3$ V per gap. This means that, once fixed the charge per gap which is drifting inside the detector, the charge per gap induced on the external pick-up strips is about a factor 3 lower in the multi-gap case, with respect to single and double gaps.

Obviously, corrections must be applied to this simple scheme; for in-

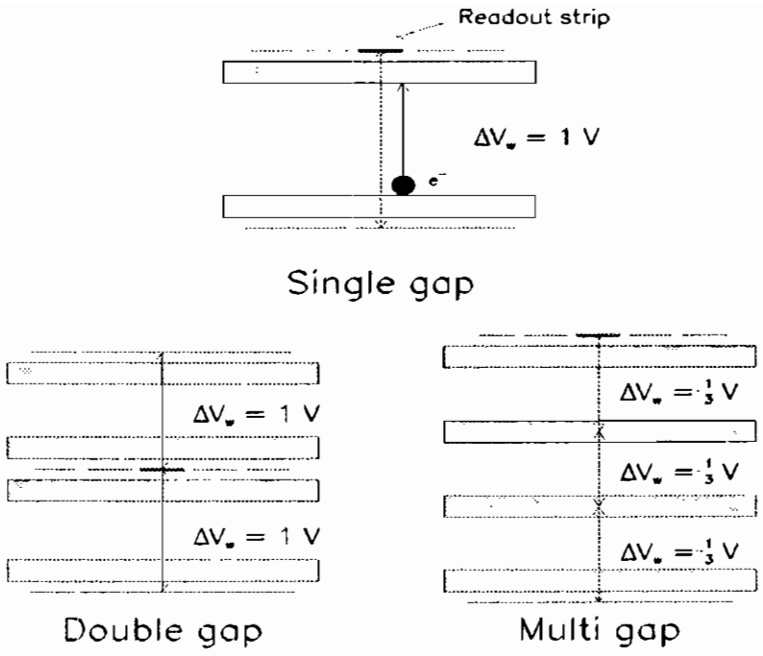


Fig. 5. Simple layout of single, double and multi-gap RPCs, for the Ramo theorem

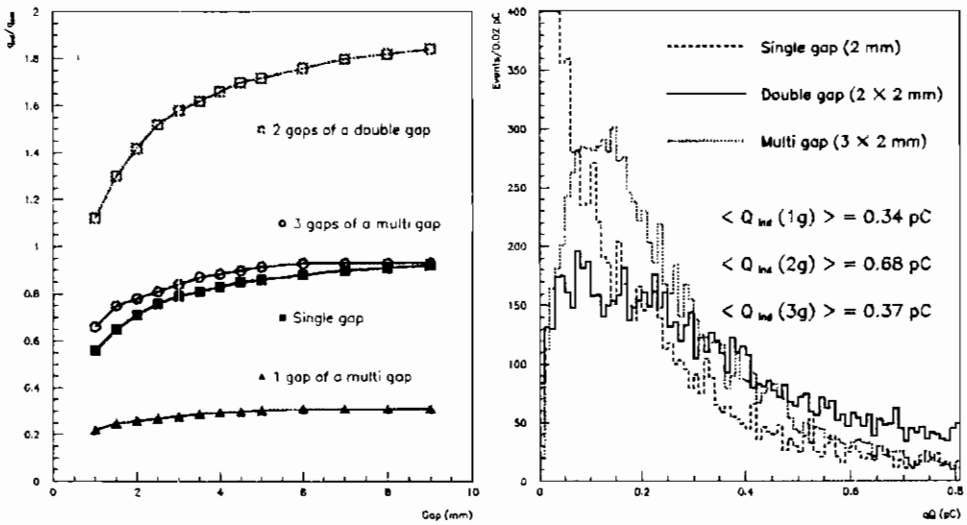


Fig. 6. a. Ratio between induced charge and drifting charge in single, double and multi-gap RPCs; b. simulated charge spectra of single, double and multi-gap RPCs

stance, the bakelite electrode thickness and permettivity must be taken into account (the bakelite is considered here as a perfect dielectric material). The final result (already cited in the description of the model), is the factor $k$ of Eq. (1); it can also be obtained using the generalized Ramo theorem [11].

There is a simple way to look at the effects of this phenomenon. Let us consider an RPC where, for instance, a charge $q_{drift} = 1$ pC is drifting in each gap (so that the total drifting charge $q_{drift(tot)}$ will be about 2 pC in a double gap and 3 pC in a multi-gap). The ratio between $q_{ind}$ and $q_{drift}$, which is directly related to the factor $k$ above computed, is reported in Fig. 6a, for different detector configurations and versus the gap width. In a single 2 mm gap RPC $\frac{q_{ind}}{q_{drift}} \sim 0.7$, in a double gap $\frac{q_{ind}}{q_{drift}} \sim 1.4$, in a multi-gap about $\frac{q_{ind}}{q_{drift}} \sim 0.8$. Apparently this could mean that either a higher electronic threshold can be used in the double gap case (with respect to single and multi-gap), or the same threshold can be used and the double gap RPCs could be operated with a drifting charge which is about a factor 2 smaller. Obviously, lower drifting charge per gap $q_{drift}$ means higher rate capability.

However, there is another effect which takes place passing from single to double and multi-gap, and this effect compensates the disadvantage of a lower $k$ for multi-gap. The point is that, again, the charge spectra shape changes. This is just a statistical effect, due to the fact that double and multi-gap spectra are the convolutions of two, or three single gap spectra. The comparison among the $q_{ind}$ charge distributions for the three types of RPCs considered is reported in Fig. 6b. The single gap spectra exhibits the usual monotonically decreasing shape, the double and the multi-gap a sort of Landau shape. Even if the multi-gap spectra has half the average value, with respect to double gap, it is more detached from the origin.

The comparison between simulated and experimental charge spectra for single and double 2 mm gap RPCs is shown in Fig. 7 [12]. The single gap spectra was actually obtained with a double gap RPC having a gap turned off. The agreement between simulation and experimental data is very good and, in particular, the change of the spectra shapes is verified. As already pointed out, this change has implications for what concerns the efficiency achievable with this type of detector.

This effect is evidenced in Fig. 8 where the predicted efficiencies for 2 or 3 mm single, double and multi-gap RPCs are reported versus the value of the electronic charge threshold $q_{thr}$. In the region of interest

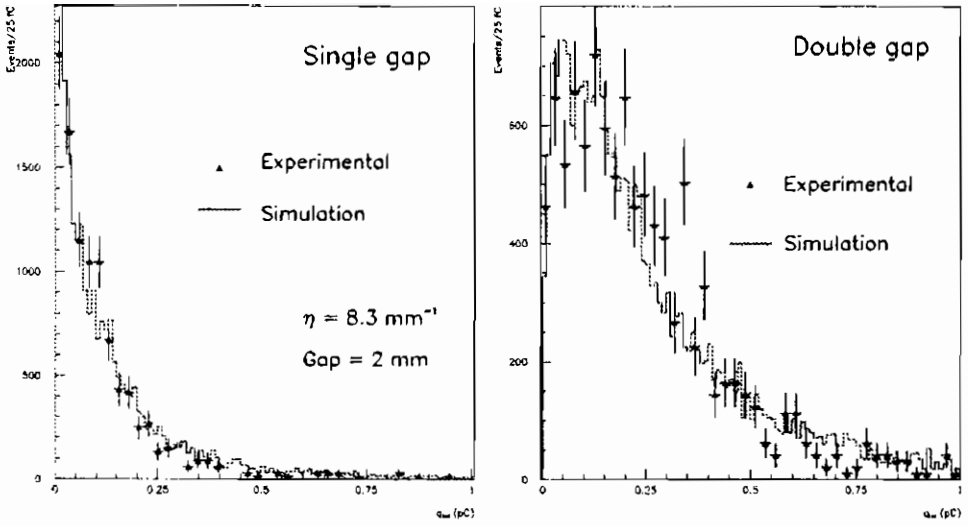


Fig. 7. Comparison between simulated and experimental charge spectra of single and double gap RPCs

(typically between 0 and 100 fC) the performance of double and of multi–gaps is essentially the same, while single gaps seem to be disadvantaged.

The average value of the charge $q_{ind}$ induced on pick-up electrodes, again in the three cases of single, double and multi–gap is shown in Fig. 9. In Fig. 9a the gap width is changed, keeping constant and equal to 18 the so–called "total gain" of the chamber, i.e. the product between $\eta$ and $g$. The average value of $q_{ind}$ in the case of double gap is about twice the value for single and multi–gap, as already explained. In addition the average value of $q_{ind}$ increases as the gap increases. In Fig. 9b and 9c the gap width is fixed, at 2 or 3 mm, and $\eta$ (that means the operating voltage) is changed. As the operating voltage increases, so the charge does.

## 4. Timing properties

### *4.1. The sources of signal fluctuation*

Another important item that can be dealed with this model is the

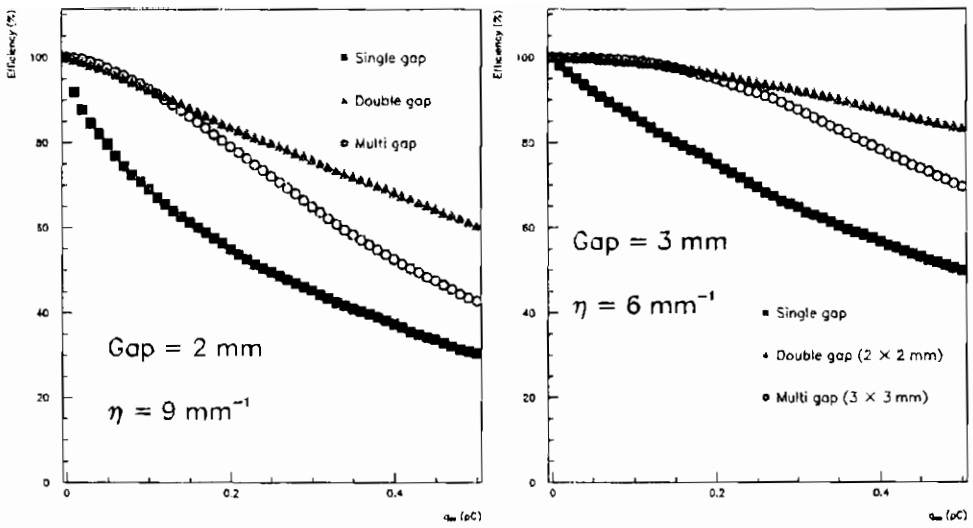


Fig. 8. Efficiency versus electronic threshold

simulation of the timing properties of RPCs. Time resolution, for instance, can be computed quite easily; it is enough to take the expression of the current $i_{ind}(t)$, let this current evolve with time (there is an exponential growth up to the moment of the electron collection at the anode), and measure the time when this current, or the corresponding induced charge $q_{ind}$, if charge amplifiers are used, becomes greater than a certain electronic threshold. This is the time the chamber has given a useful response.

Let us consider what are the variables changing from event to event, that cause this crossing time to vary. In the expression of $i_{ind}(t)$ (Eq. (3)), the term $-k\mathbf{v_d} \cdot \mathbf{E_w} q_{el} e^{\eta v_d \Delta t}$ is constant, once the operating conditions and the time $t$ are fixed, since it contains fixed quantities like the drift velocity $\mathbf{v_d}$, the weighting field $\mathbf{E_w}$ and the first effective Townsend coefficient $\eta$.

What, in general, changes from event to event, is the last term $\sum_{j=1}^{n_{clust}} n_{j0} M_j$, containing the number $n_{clust}$ of clusters per event, the number $n_{j0}$ of electrons in each cluster and the avalanche gain fluctuation factor $M_j$ (the last two terms, in general, change from avalanche to avalanche in the same event). This three factors are the main responsible of the observed time resolution.

It is important, therefore, to study the distributions of these factors.

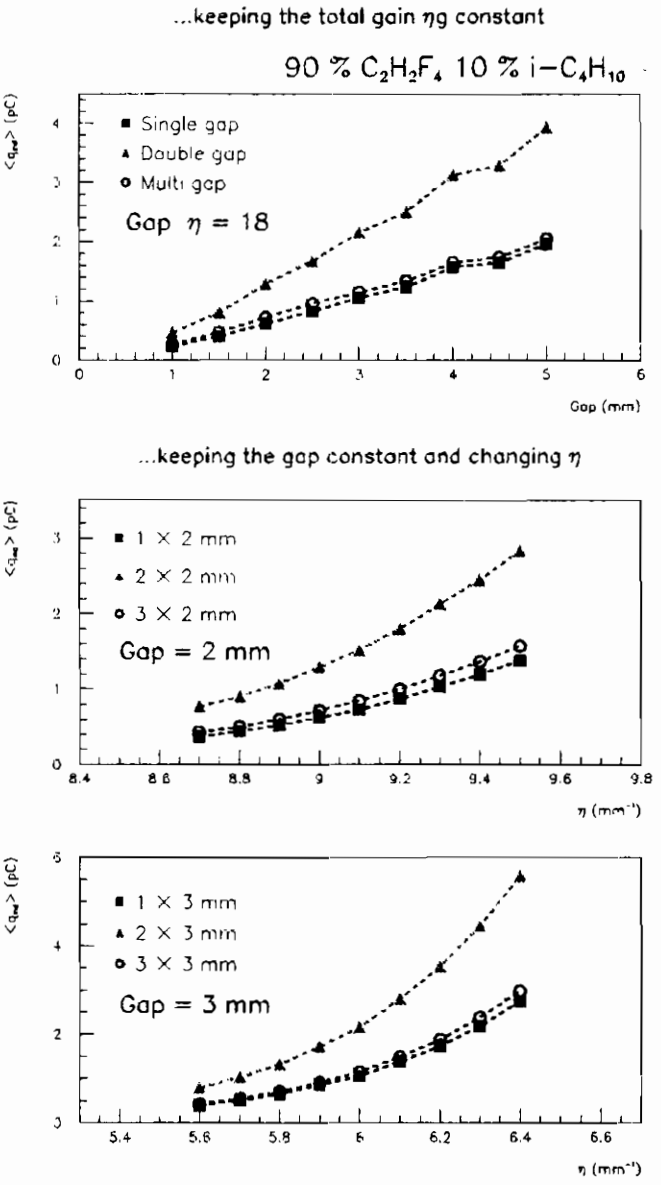


Fig. 9. Simulated charge average values for single, double and multi-gap RPCs

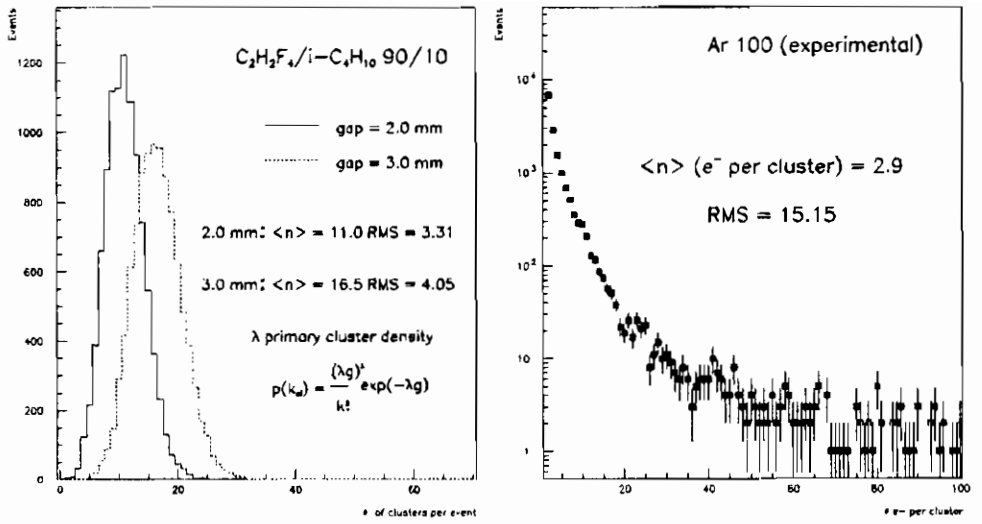


Fig. 10. a. Simulated number of clusters per event; b. cluster size distribution in Ar (experimental), from Ref. 13

The distributions of the number of cluster per event $n_{clust}$, in the case of 2 and 3 mm single gap RPCs is reported in Fig. 10a. They follow Poisson statistics with average $\lambda g$, marked in the figure together with the RMS. The RMS values (obviously given by $\sqrt{\lambda g}$) are important because they are, more or less, proportional to the time resolution that would be observed if only this source of signal fluctuation would be present and all the others would be, somehow, switched off.

The distribution of the number of electrons per cluster (i.e. the cluster size) for pure Ar is reported in Fig. 10b. It is characterized by an average value of about 3, and a long tail toward the right, so the corresponding RMS is $\sim$ 15; the events with about or more than 100 electrons are mostly due to delta rays. The distribution shown in Fig. 10b is one of the very few cluster size distributions measured experimentally [13] (the others are relative to He, $CO_2$, and some hydrocarbons); for all the others theoretical predictions must be used [14] [15].

The convolution of $n_{clust}$ and the cluster size gives the distribution of the total number of electrons per event, which is reported in Fig. 11a, in the case of 2 and 3 mm single gap RPC. The fact that the RMS of the 3 mm distribution is greater than the 2 mm one, allows to conclude

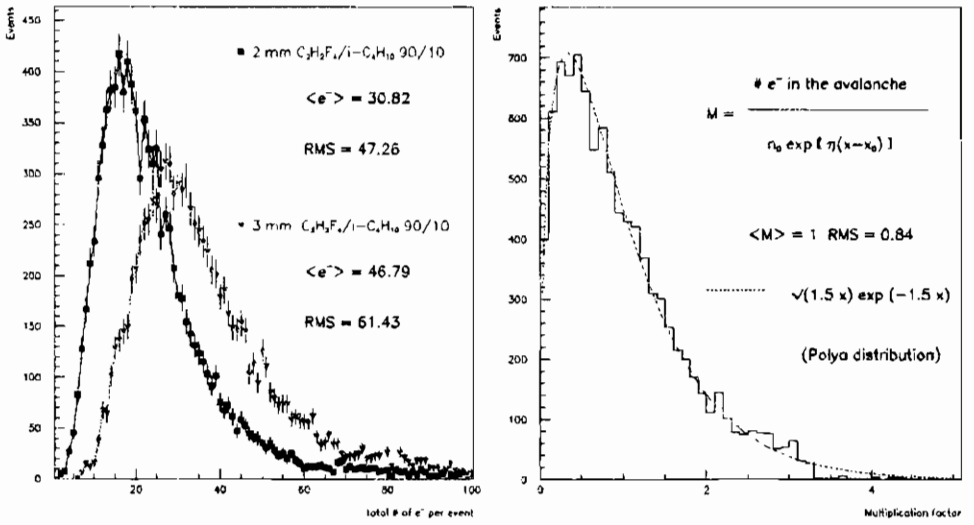


Fig. 11. a. Simulated total number of electrons per event; b. gain fluctuation factor

that the time resolution of 3 mm chambers will be worse than the 2 mm (at the same operating conditions). This is not trivial, and follows from the statistics of the basic processes taking place in RPCs.

Finally, the last source of signal fluctuation in RPCs is the fluctuation in the avalanche gain. The average number of electrons at the end of an avalanche of length $x$ is given by $n(x) = n_0 e^{\eta x}$. However, since an avalanche is a statistical process, sometimes more and sometimes less electrons will be present. As already pointed out, the ratio $M_j$ between the actual number of electrons and the expected value follows (in the case of high values of the reduced electric field $E/p$, which is the typical case of RPCs) a Polya distribution, as plotted in Fig. 11b, superimposed to the simulated distribution of $M_j$.

### *4.2. Results*

The simulated chamber time responses, in the case of 1 mm single gap RPCs filled with Ar/iso-$C_4H_{10}$ 70/30 are reported in Fig. 12a, for three different values of the effective first effective Townsend coefficient. They are very well gaussian shaped. As the operating voltage is increased (equivalent, in the simulation, to an increase of the first

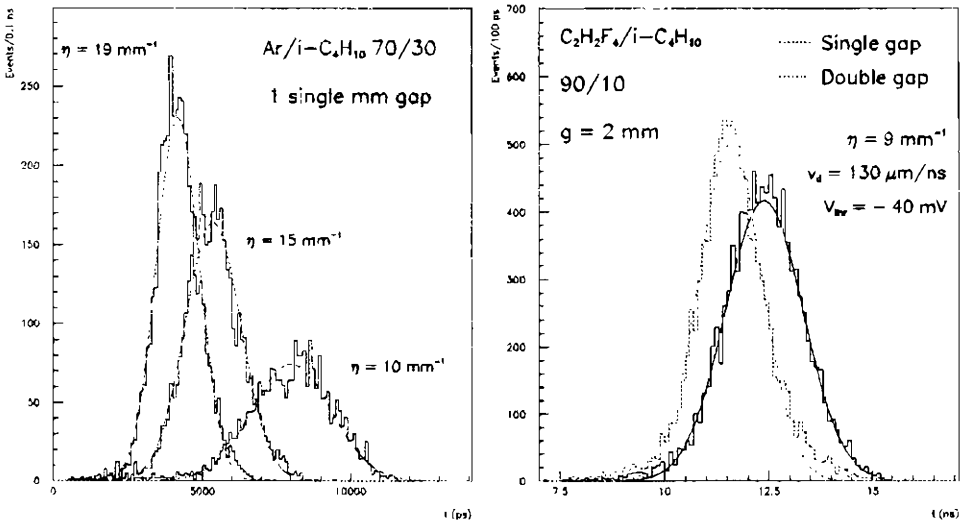


Fig. 12. a. Simulated chamber time responses for single gap 1 mm RPC; b comparison between the simulated chamber time reponses of single and double gap RPCs

Townsend coefficient), the chamber becomes faster and faster (the distributions shift toward the left where, at $t = 0$ there is the passage of the particle), and more and more precise (the distributions are narrower and narrower). From a qualitative point of view, the same effect takes place passing from single to double gaps (or multi-gaps); the simulated chamber time response for single and double 2 mm chambers are reported in Fig. 12b, where it is evident, again, that the double gap chamber is faster (the distribution is shifted toward the left) and more precise (the distribution is narrower). Moreover, the double gap distribution in Fig. 12b is not symmetric, being characterized by a longer tail toward the right, corresponding to a delayed chamber response. This is a well known effect, experimentally verified several times. It is of statistical origin: it follows from the fact that the double gap distribution is obtained by taking the fastest of two signals gaussianly distributed themselves.

Time resolution can be directly computed starting from the distributions just shown. The simulated time resolution $\sigma_t$ for single and double gap RPCs, as a function of the gap width is reported in Fig. 13. Again the total gain $\eta g$ is fixed equal to 18. In Fig. 13 the effect that a change of the drift velocity $\mathbf{v_d}$ in the chosen gas mixture has on the numerical

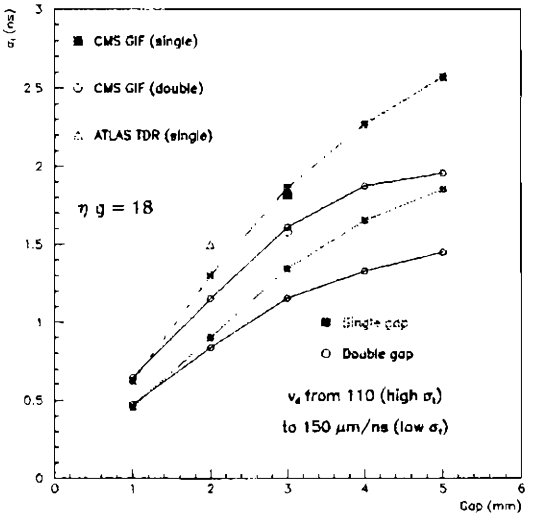


Fig. 13. Simulated chamber time resolution for single a double gap RPCs

value of $\sigma_t$ is put in evidence; this is the most important parameter to this respect.

At the time this simulation has been developed, the electron drift velocity for mixtures containing $C_2H_2F_4$ had not been experimentally measured; the first experimental results about this quantity have just been presented in this workshop [16]. So the results are plotted in Fig. 13, by changing $\mathbf{v_d}$ in a reasonable range, i.e. from 110 $\mu$m/ns to 150 $\mu$m/ns; the actual values, at the typical operating voltages, are around 130 $\mu$m/ns. In the figure the curves corresponding to this minimum and maximum values are evidenced (both for single and double gap). In Fig. 13 some experimental data are also reported, both from CMS and ATLAS. The agreement again is quite good; in the 3 mm case, the experimental value, measured at CERN Gamma Irradiation Facility [17], is about 1.7 ns for the single gap and 1.5 ns for the double gap, against simulated values of about 1.5 and 1.3 ns respectively. In the 2 mm case it is about 1.5 ns for the single gap [18] against a predicted value of 1.3 ns. There is a systematic difference between the predicted values and the experimental ones, which are greater of about 200 ps. This is expected, since there are many minor sources of time jitter which is not feasible to include in the simulation; for instance small differences among the thresholds of various electronic channels, electron diffusion,

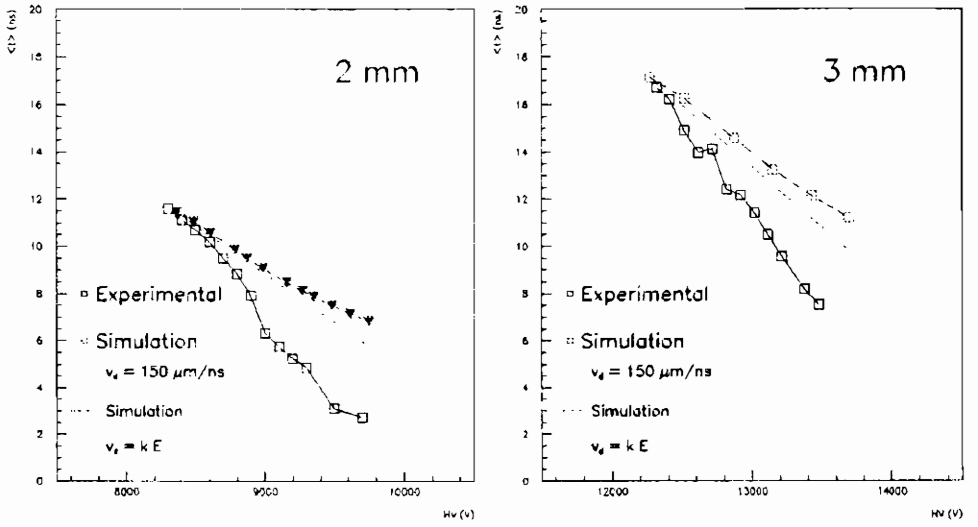


Fig. 14. Comparison between simulated and experimental time walk for single gap RPCs

possible disuniformities in the gas gap, etc.

Another important parameter characterizing RPCs performance is time walk, i.e. the variation of the threshold crossing time with respect to the passage of the particle (as a function, for instance, of the operating voltage). The comparison between the simulated and the experimental time walk for single 2 and 3 mm gap RPCs is reported in Fig. 14. Since the absolute chamber time response (that means the signal delay with respect to the passage of the particle) is not measured experimentally, the comparison has to be done just taking into account the slope of the relative curves. In the 2 mm case the simulation result is about 5 ns/kV, while experimental values range from 6 ns/kV [9] to about 10 ns/kV [19]. There is a great spread in the experimental results. For what concerns the simulation it has to be pointed out that the drift velocity $\mathbf{v_d}$ has been assumed to be constant with respect the electric field. This is surely not the case, and when the appropriate corrections will be introduced, the resulting value will be greater and probabily somewhere in the experimental range. The same happens, more or less, in the 3 mm case.

The simulated time resolution $\sigma_t$ for single, double and multi-gap

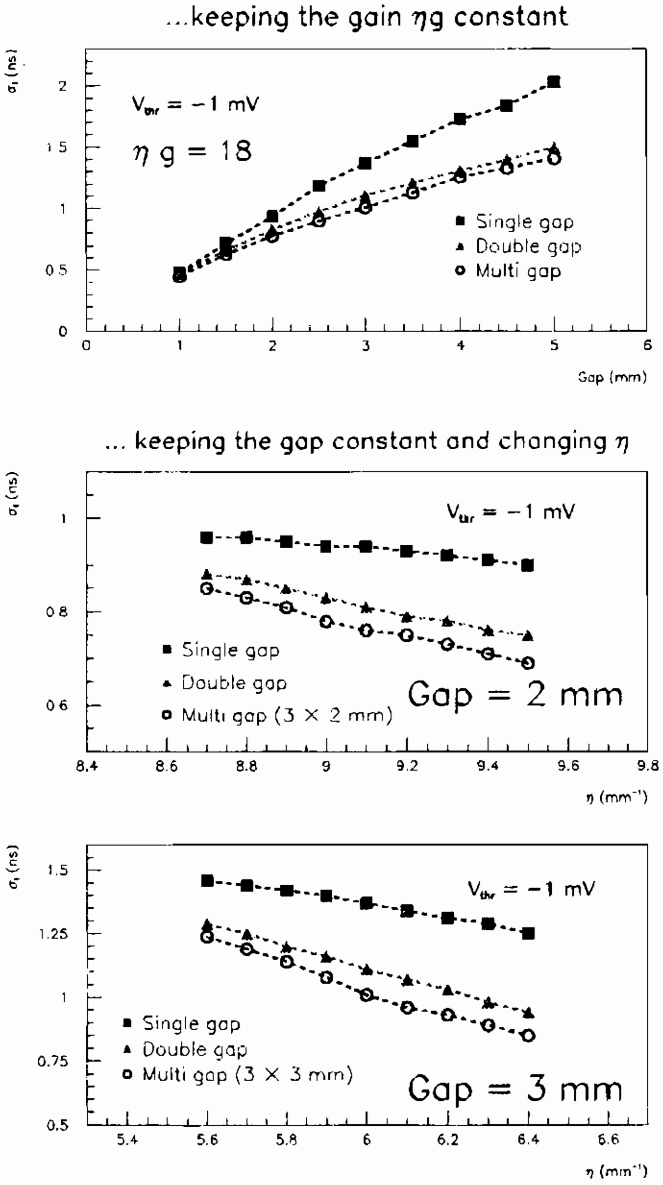


Fig. 15. Simulated time resolution for single, double and multi-gap RPCs

RPCs is shown in Fig. 15. In Fig. 15a the gap width has been changed, keeping constant the total gain of the chamber, while in Fig. 15b and 15c the gap width is fixed and the first effective Townsend coefficient (i.e. the operating voltage) is varied. The first effect to be noted is that the wider the gap, the worse the time resolution, which was expected from the statistical considerations done before; in addition, $\sigma_t$(double gap) $\sim$ $\sigma_t$(multi gap), while single gap RPCs are strongly disadvantaged.

## 5. Conclusions

A model describing the basic processes taking place in Resistive Plate Chambers in avalanche mode has been developed. The model has been used to reproduce the available experimental data, and explains most results, obtained in many different operating conditions and with different kinds of chambers (single, double and multi-gap). The agreement between the simulation and the real data is good (in the validity range of the hypothesys explained in Sec. 2) for what concerns charge distribution and efficiency. The simulation reproduces also fairly well the time performance of the chamber.

The model can be used to choose among different RPC types, depending on the required performance; for instance:

1. wide gap RPCs could be better than narrow gaps for what concerns efficiency (and rate capability); the opposite is true for what concerns time resolution

2. multi-gap RPCs do not show any significant improvement with respect to double gap RPCs.

Obviously, the simulation can be improved. It would be easy to write down a list of physical effects that have not been included, because negligible in first approximation or just because too difficult to be taken into account.

At the moment there is a great effort being made to include some of missing effects in the model. For instance, there is some experimental evidence that space-charge effects could be responsible for a change in the charge spectra shapes (for high values of $q_{ind}$), as the operating voltage is increased beyond the values characteristic of the "pure avalanche" mode operation [9] [20] [21] [18] [22]. To take into account this effect a more refined calculation of the effective electric field (i.e. the exter-

nal field plus the field generated by the electrons and the ions of the avalanches) is needed and is being developed.

Other important items have already been included, even if the corresponding results have not been reported here; this is the case of the effects of possible deformations in the gas gap (or due to the presence of the spacers). Another, easy in principle to include but difficult from a computational point of view, is the prediction of the number of strips fired per event, i.e. the strip multiplicity.

However, by far the most interesting of these problems, at the moment only partially investigated, is the simulation of the dynamical behavior of RPCs, when the flux of incident particles is not negligible. In this situation a delicate balance between the process of electrode discharge (due to the electron avalanche collection) and charging–up (thanks to the external power supply) is present. This is, in fact, a primary issue to be studied in the future, since, at LHC, RPCs will operate in a high background environment and, in general, with a high detection rate.

## 6. References


1. R. Santonico et al., *Development of Resistive Plate Chambers*, Nucl. Instr, & Meth. **187** (1981) 377-380
2. G. Bressi et al., Nucl. Instr, & Meth. **A 261** (1987) 449
   E. Petrolo et al., Nucl. Instr, & Meth. **A 315** (1992) 44
   L. Antoniazzi et al., Nucl. Instr, & Meth. **A 315** (1992) 92
   C. Bacci et al., Nucl. Instr, & Meth. **A 315** (1992) 102
   A. Antonelli et al., Nucl. Instr, & Meth. **A 337** (1993) 34
   M. Abbrescia et al., Nucl. Instr, & Meth. **A 336** (1993) 322
   M. Ambrosio et al., Nucl. Instr, & Meth. **A 344** (1994) 350
3. *CMS Technical Proposal*, CERN/LHCC/94-38
4. *ATLAS Technical Proposal*, CERN/LHCC/94-43
5. H. Genz, *Single electron detection in proportional gas counters*, Nucl. Instr. & Meth **112** (1973), 83-90
6. S. Ramo, **Proc. IRE** 27 (1939) 584
7. M. Abbrescia et al., *Properties of $C_2H_2F_4$ based gas mixture for avalanche mode operation of Resistive Plate Chambers*, Nucl. Instr. & Meth. **A 398** (1997), 173-179
8. M. Abbrescia et al., *Performance of a Resistive Plate Chamber*

*operated in avalanche mode under $^{137}Cs$ irradiation*, Nucl. Instr. & Meth. **A 392** (1997), 155-160
9. M. Abbrescia at al., *Results on charge, efficiency and timing of a small single gap Resistive Plate Chamber*, talk given at the CMS Muon group, CERN, March 16, 1997
10. W. Blum and G. Rolandi, *Particle detection with drift chambers*, Ed. Springer–Verlag (1993)
11. E. Gatti et al., *Signal evaluation in multielectrode radiation detectors by means of a time dependent weighting vector*, Nucl. Instr. & Meth. **193** (1982), 651-673
12. M. Abbrescia et al., *Beam–test results on double gap Resistive Plate Chambers proposed for the CMS experiment*, submitted to NIM, CMS Note/1997–062
13. H. Fischle et al., *Experimental determination of ionization cluster size distributions in counting gases*, Nucl. Instr. & Meth. **A301** (1991) 202-214.
14. F. Lapique and F. Piuz, *Simulation of the measurements by primary cluster counting of the energy lost by a relativistic ionizing particle in argon*, Nucl. Instr. & Meth. **174** (1980) 297-318.
15. I. Smirnov, *HEED, an ionisation loss simulation program, User's guide, Version 1.01*, CERN Program Library
16. E. Gorini et al., *Measurements of drift velocity and effective ionization coefficient in $C_2H_2F_4$–Isobutane mixtures for avalanche operated RPC*, Contribution to this Worksop
17. M. Maggi et al., *Beam test results on large double gap RPC in a high background environment*, Contribtion to this Workshop
18. *ATLAS Technical Design Report*, CERN/LHCC/97-22
19. R. Cardarelli et al., *The avalanche to streamer transition in RPC's*, talk given by V. Makeev, proceedings of the III International Workshop on Resistive Plate Chambers and related detectors, in Scientifica Acta, Vol. XI (1996), n. 1
20. P. Camarri et al., *Performace of RPCs operated with various gas mixtures*, Contribution to this workshop
21. A. Di Ciaccio et al., *Latest ATLAS RPC test–beam results*, contribution to this workshop
22. E. Cerron Zeballos et al., *Pure avalanche mode operation of a 2 mm gap Resistive Plate Chambers*, Nucl. Instr. & Meth. **A 396** (1997) 93-102.

# Optical Observation of RPC's Streamer

Y. Teramoto *
*Institute for Cosmic Ray Physics, Faculty of Science,*
Osaka City University,
3-3-138 Sugimoto, Sumiyoshi, Osaka 558, Japan

November 18, 1997

ABSTRACT

Visual images of streamers inside a glass RPC were measured using an image intensifier and a CCD camera in the view looking into the glass electrode. The shapes of the signals are circular with approximately 1mm diameter. Electrically induced signals were also measured simultaneously, which showed good correspondences with the optical measurements. For the events with afterpulses, the average distance between each streamer is approximately 3mm for the gas: $Ar/C_4H_{10}/C_2H_2F_4/ = 25/25/50$. In addition, avalanche signals were optically measured using a photomultiplier, which is intrinsically free from electrical noise.

## 1. Introduction

Bakelite electrodes are used in most of the RPCs since the development of RPCs by R. Santonico and R. Cardarelli [1]. Recently, glass plates have been also used for the RPC's electrodes by several groups [2] [3] [4]. Particularly, glass RPCs are used for the $K^0_L$-and-$\mu$(KLM) sub-detector [5] [6] for the BELLE experiment [7] at KEKB. Those glass RPCs, however, use carbon-based conductive sheet or paint for providing bias-voltages on the glass electrodes, hence non-transparent. We built

*co authors: Y. Inoue, I. Kitayama, H. Miyoshi, Y. Muranishi, E. Nakano, H. Sakai, T. Takahashi

RPCs by using transparent conductive paint, ET-680 [8], for the bias-voltage supplying planes and transparent conductive sheet, IDIXO [9], for the signal pickup planes. By making those planes transparent, we could visually observe the gas amplification processes inside the RPC. In the previous report [10], the observations were done by eye. In this report, we present visual images of RPC's signals taken by a combination of an image intensifier and a CCD camera. In addition, waveform of avalanche signals measured by a photomultiplier( PMT ) will be briefly mentioned. The test was done with cosmic-rays.

## 2. Visual Image Measurement

### *2.1. RPC*

Fig. 1 illustrates the cross-sectional view of the used RPC. Float glass with 1.7mm thickness was used for the electrodes. Its surface and volume resistivity are $\sigma = 6 \times 10^{12}\Omega/\square$ and $\rho = 5 \times 10^{12}\Omega \cdot \mathrm{cm}$, respectively.

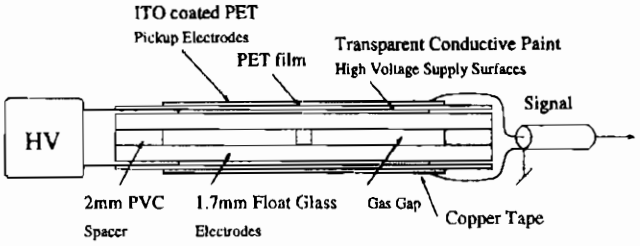


Fig. 1. Schematic drawing of the glass RPC.

For the frame and the spacer of the RPC, we used 2mm-thick PVC, which provides a 2mm gas gap. On the outer surfaces of the glass electrodes, we painted conductive paint, Oshar Coat ET-680, which is made of metal-chelated acrylic resin. The measured surface resistivity of the paint on the glass was $\sigma \sim 10^8\Omega/\square$. For the pickup electrodes, we used a pair of IDIXO sheets. The IDIXO sheet is made of 100$\mu$m PET coated with 0.4$\mu$m ITO conductive film on its one side. The measured surface resistivity of the ITO surface was $30\Omega/\square$. This resistivity is relatively high compared with the $50\Omega$ impedance of the coaxial cable, which was used to send the induced signals from the pickup electrodes to

the scope. To reduce the effective resistivity of the electrode, we placed 1cm-wide copper tape along the four sides of the 18×18 $cm^2$ electrode. To avoid a closed-loop of copper tape to be formed, we cut the tape in one place. For an extra high-voltage insulation, 70$\mu$m PET sheet was placed in between the Oshar Coat surface and the IDIXO sheet.

### *2.2. Setup and Measurements*

The setup for the measurement is shown in Fig. 2. The RPC was housed in a light-shielded box and viewed by an image intensifier, Hamamatsu II-100U.

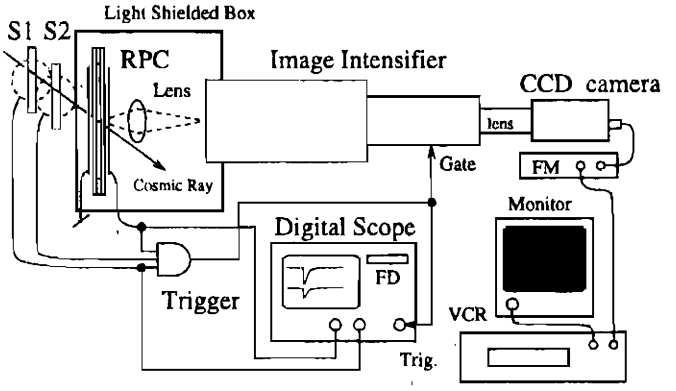


Fig. 2. Block diagram of the setup for the visual image measurements.

For simplicity of supporting the image intensifier, we put the image intensifier in the horizontal direction. In order for the image intensifier to see the inside the RPC through its electrode with simple optics, we put the RPC in the vertical position with the cathode plane facing to the image intensifier. A Nikon 63mm F2.8N lens was use to project the images of the RPC's streamers on the input surface of the image intensifier. In most of the data, the magnification was set to ×3. Because the diameter of the image intensifier's photo-sensitive surface is 10cm$\phi$, the viewing window was 3.3cm$\phi$ for ×3 magnification. We also took events with ×7 magnification. Focusing was adjusted by putting a sheet of label with scale patterns on the surface of the pickup plane and projecting the scale patterns on the input surface of the image intensifier. Then, a small correction was done for the thickness of the RPC and the final adjustments were done by watching the images of real events on the TV

screen. The used image intensifier consists of three stages; approximately 10 % quantum efficiency for each stage. The second stage( MCP ) has a function of retaining its optical images with $T_{half} = 7\mu$sec. Then, gates can be applied to the third stage( MCP ), so that the retained images of the second stage are amplified and formed on the output screen of the image intensifier. This delayed-gate function was crucial to our measurement. The output screen of the image intensifier was viewed by a CCD camera, then recorded by a VCR with the VHS format. The images were also monitored by a TV screen.

Triggers were made of 3-fold coincidence of signals from two 10×10 $cm^2$ scintillation counters and the electrically induced signals of the RPC. Triggers were provided to both the image intensifier and the digital scope; opening the gate of the image intensifier, and triggering the digital scope to record the waveform of both the RPC's pickup signals and the outer scintillator's signals. The pulse heights of the outer scintillator's signals were monitored to reject the events with showers. For the triggered events that have at least one light-spot on the video screen, we recorded the time of the events and save the scope's waveform on the floppy disk. The frequency of such events was once in a few minutes for ×3 magnification. Then later in the offline analysis, we made matches of the video data and the scope data.

For the recorded events, we have mainly analyzed the events with afterpulses. It is one of the advantages of optical measurement that one can accurately determine the locations of multiple streamers in the afterpulses by their visual images. Multiple light-spots, observed in the events with afterpulses, are considered to be caused by multiple avalanches due to the emissions of photons. The used gas mixture [11] was $Ar/C_4H_{10}/C_2H_2F_4/ = 25/25/50$. The RPC was operated at 8.8kV, which is 200V above the knee of the efficiency plateau. For this operating condition, more than 90 % of the events have single streamer, i.e. one light-spot.

### *2.3. Shapes and Sizes*

Examples of the events with ×3 magnification were shown in Fig. 3. Shapes of light-spots observed near the center are circular. Shapes of light-spots, however, are triangular, when they were observed in the peripheral region of the viewing window with ×3 magnification. They had tails pointing to the center of the viewing window. By flipping the

anode and cathode of the RPC, there was no significant change neither in their shapes nor in their tail directions. Hence, we conclude that triangular shapes are caused by the optical effects of glass electrodes.

(a)

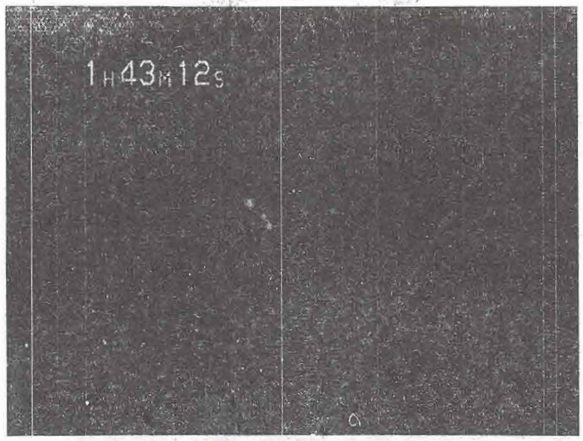


(b)

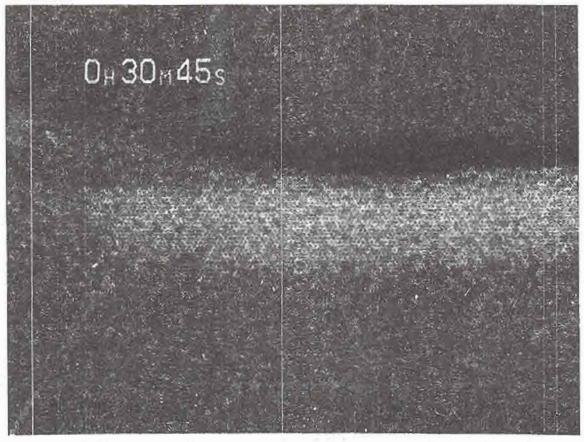


Fig. 3. Examples of the events with ×3 magnification: (a) triple-light-spot event near the center, (b) double-light-spot event in the peripheral region. The viewing window is 3.3cm(V) × 4.3cm(H).

With ×7 magnification, all the observed events had circular shapes. Fig. 4 shows a typical event with ×7 magnification. The size of each light-spot is approximately constant and it is 1mm. Each light spot has

its halo of a size of approximately 2mm. Though the exact reason of this halo is not known to us, it is plausible that halo is simply caused by reflections of light by the glass electrodes.

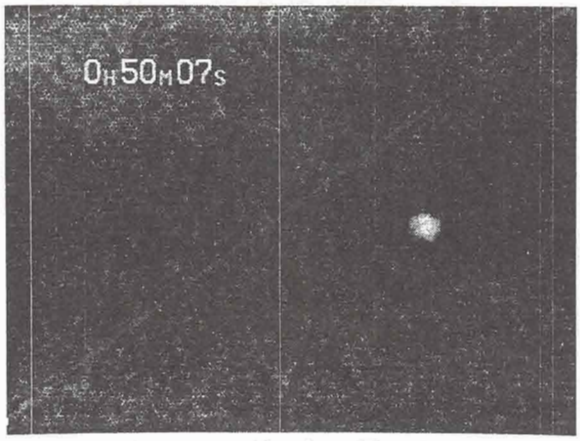


Fig. 4. A typical event with ×7 magnification. The viewing window is 1.4cm(V) × 1.8cm(H).

*2.4. Multi-Spot Events*

Though the signals with afterpulses are considered as events with multiple streamers, this explanation has not been clearly demonstrated. Since visual images can detect the existences and the locations of multiple streamers, we examined the correspondences of light-spots in the video pictures and the waveform of the electrically induced signals for multiple streamer events. Fig. 5 shows three examples of double-light-spot events. As seen in these examples, there's one-to-one correspondence between the number of light-spots and the number of pulse peaks in approximately 60 % of the events. For the reset of the events without match, it is consistent that those events are caused by two reasons; either two pulses are overlapped in timing or a part of the light-spot's cluster is outside the viewing window.

As seen in Fig. 5, there's also a correlation between the distance between the light-spots and the time interval between the pulse peaks.

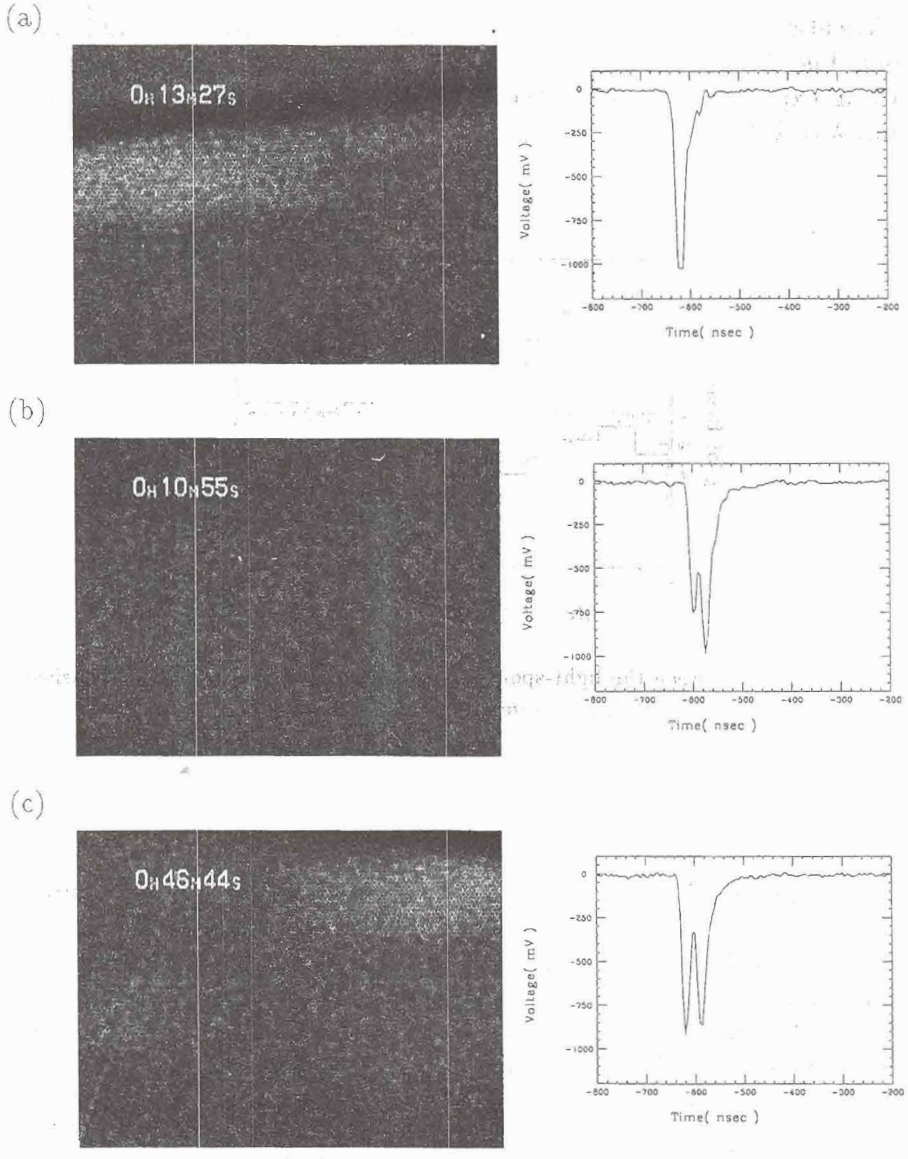


Fig. 5. Examples of double-light-spot events( left ) with scope waveform( right ) for different distance of separation. The waveform in (a) is saturated at -1.024V. The magnification is ×3 and the size of the viewing window is 3.3cm(V) × 4.3cm(H).

We also measured the distances, $D$, between the closest pair of light-spots. Fig. 6 shows the distance distribution. If we fit the distribution with an $\exp(-D/\lambda)$ form for the data with the distances greater than 1mm, $\lambda = 2.9$mm.

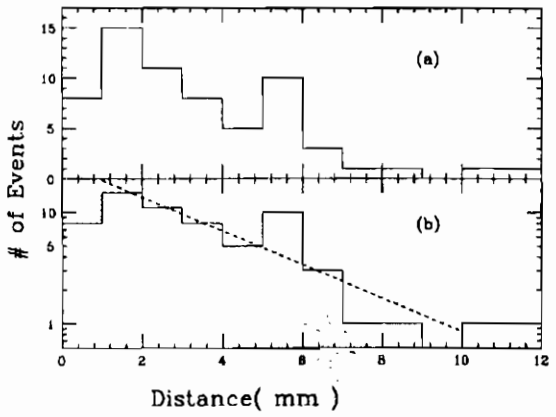


Fig. 6. Distance between the light-spots; (a) linear scale, (b) log scale. The dashed line shows $\exp(-D/\lambda)$ with $\lambda = 2.9$mm.

## 3. Waveform Measurement

Time developments of optical and electrical signals were measured by a setup shown in Fig. 7. Cosmic rays were triggered by 2-fold coincidences of scintillation counters placed under a transparent RPC. Optical signals were measured by a photomultiplier( PMT ) located at the top of the RPC. The electrical signals were picked-up by a set of transparent electrode( top side ) and a copper electrode( bottom side ). The setup was housed in a light-shielded box. We used the same gas mixture as the visual image measurement. The RPC was operated at 9.8kV, which is 800V above the knee of the plateau for this RPC. The used PMT was Hamamatsu H1161 operating at 1.7kV. Fig. 8 shows a typical example of a set of electrical and optical signals with afterpulses.

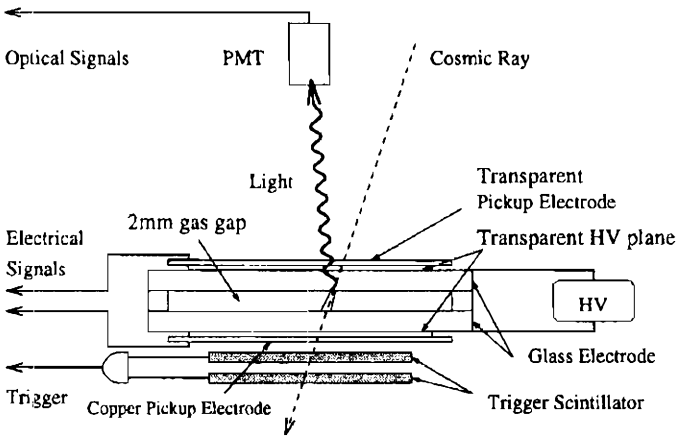


Fig. 7. Schematic drawing of the setup for the waveform measurements.

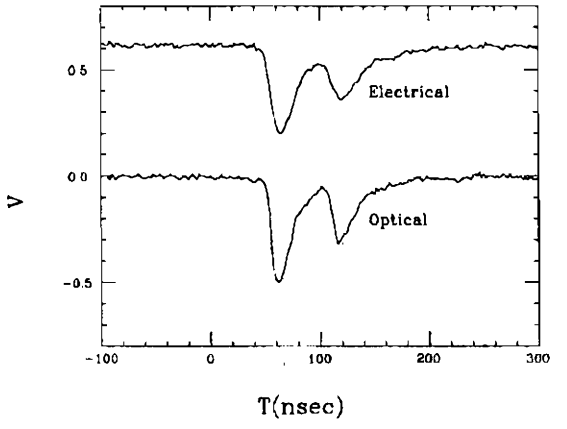


Fig. 8. Waveforms of optical and electrical signals with afterpulse.

As seen in this example, two waveforms have good correspondences in each other. By reducing the operating voltage to 9.2kV, we could see both the streamer and avalanche signals at the same time, as shown in Fig. 9. As seen in Fig. 9, optical signals have better signal-to-noise ratios than electrically induced signals. This is due to the reason that electrical noise does not affect on the optical measurement and also the low noise characteristics of PMT.

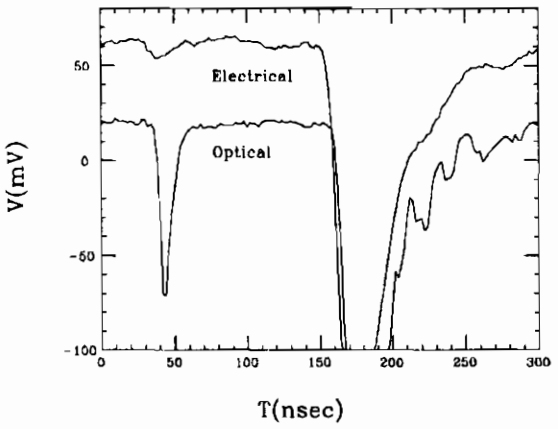


Fig. 9. Avalanche and streamer mode signals. The peaks near $T = 40$ns are avalanche mode signals. The peaks near 180ns are streamer mode signals.

## 4. Discussions and Summary

In our previous report [10] based on the observation by eye, the majority of the observed events have triangular shapes. In addition, we also observed linear shapes. In this measurement, we observed triangular shapes. But it was shown that the triangular shapes are caused by the optical effect of glass electrodes and they are not the shape of the streamers themselves. Also, we have not observed linear shapes in this measurement. The reason for not observing linear shapes is under investigation. One possible reason for this difference was that the gas mixtures for the two measurements were different. As mentioned in the previous report, linear shapes were only seen with the "R116 mixture": $Ar/C_4H_{10}/C_2F_6/ = 52/37/11$. So, we recently took data with the "R116 mixture". Though the analysis has not been completed at the time of writing this report, we haven't seen the linear shapes with this gas mixture yet.

As a summary, the measured shapes of the visual images are circular. Their diameter is approximately 1mm. For the events with multiple streamers, we observed the existences of afterpulses in the electrical

measurement. The averaged distance between the streamers is 3mm for the multiple streamer events. We also measured the time development of optical signals using a PMT. With a PMT, we could measure the avalanche mode signals with a good signal-to-noise ratio, since optical measurement is intrinsically free from electrical noise.

## 5. Acknowledgements

This study is being done as one of the extended R&D work for the BELLE KLM subdetector. The authors thank all the members of the KLM subdetector group for the various supports on this work and many useful discussions on this subject. The KLM subdetector group is a collaboration of the following institutes: Aomori Univ., KEK, Osaka City Univ., Princeton Univ., Tohoku Univ., Tohoku Gakuin Univ. and Virginia Poly Tech.. We also thank Dr. T. Iijima and Dr. T. Sumiyoshi of KEK for allowing us to use their image intensifier and other equipments which was crucial to this measurement.

## 6. References

1. R. Santonico, R. Cardarelli, *Nucl. Instr. and Meth.* **187** (1981) 377.
2. G. Bencivenni, M. D'Incecco, G. Felici, C. Gustavino, E. Iacuessa, *Nucl. Instr. and Meth.* **A345** (1994) 456.
3. D. G. Michael, D. R. Relyea, *Nucl. Instr. and Meth.* **A373** (1996) 30.
4. P. O. Mazur, *Proc. 3rd. Int. Workshop on Resistive Plate Chambers and Related Detectors*, ed. Sergio P. Ratti, Marco Merlo (1996) Pavia, p. 331.
5. N. Morgan, *Proc. 3rd. Int. Workshop on Resistive Plate Chambers and Related Detectors*, ed. Sergio P. Ratti, Marco Merlo (1996) Pavia, p. 101.
6. Y. Teramoto, A. Yamaguchi and Y. Hoshi, *Proc. 3rd. Int. Workshop on Resistive Plate Chambers and Related Detectors*, ed. Sergio P. Ratti, Marco Merlo (1996) Pavia, p. 401.
7. The BELLE Collaboration, "Technical Design Report", *KEK Proceedings, 1995-1.*
8. *Oshar Coat ET-680*, Time Chemical Corporation Ltd., 4-7-7 Hi-

rai, Edogawa, Tokyo 132, Japan.
9. *IDIXO*, Idemitsu Kosan Corporation Ltd., 1280 Kamiizumi, Sodegaura-shi, Chiba, Japan.
10. Y. Inoue, I. Kitayama, H. Miyoshi, Y. Muranishi, E. Nakano, T. Takahashi, Y. Teramoto, *Nucl. Instr. and Meth.* **A394** (1997) 65.
11. M. Sanpei *et al.*, *IEEE Trans. Nucl. Sci., Vol. 44, No. 3* (1997) 752.

# PROPERTIES OF THE LINSEED OIL AND PROPERTIES OF THE BAKELITE SURFACES

Paolo Vitulo *
*Dipartimento di Fisica Nucleare e Teorica*
and Sezione INFN,
via Bassi 6, Pavia, I-27100, Italy

April 2, 1998

ABSTRACT

We present a study of some properties of the bakelite electrodes used for the construction of Resistive Plate Chambers (RPCs). Advantages and drawbacks of the treatment are summarized in terms of surfaces omogeneity, neutron activation and absorbance properties. Roughness of different types of bakelite and resistivity measurements are also reported on and related to the bakelite production stage.

## 1. Introduction

One of the most disputed topics on bakelite Resistive Plate Chambers (RPCs) has been the use of the linseed oil treatment of the internal electrodes. Since their development[1], bakelite RPCs operated in

*co authors :M. Abbrescia,G. Bruno,A. Colaleo, G. Iaselli,G. Lamanna, F. Loddo, B. Marangelli, S. Natali, S. Nuzzo, G. Pugliese, A. Ranieri, F. Romano *Dipartimento Interateneo di Fisica and Sezione INFN, Bari,Italy*; S. Altieri, V. Arena, G. Belli, G. Bonomi, A. Braj, G. Gianini, M. Merlo, S.P. Ratti, C. Riccardi, L. Viola *Dipartimento di Fisica Nucleare e Teorica and Sezione INFN, Pavia, Italy*; L. Rossi, *Dipartimento di Fisica "A. Volta" and INFM, Pavia, Italy*

streamer mode have been largely used with oil treatment both in accelerator and non accelerator experiments. In recent years a new mode of operation[2] (avalanche mode) has been proven to give excellent results in terms of increased rate capability.

Bakelite RPCs are at present part of the approved trigger detector baseline both for the CMS and the ATLAS projects. While some of the main detector parameters (electrode material, thickness, resistivity, electronics) have been substantially chosen for the final design of both experiments, two different technological approches are foreseen: ATLAS will use $2\,mm$ mono-gap[3] standard oiled bakelite RPCs while CMS will use double gap bakelite RPCs and is considering and testing the use of both not-oiled electrodes and $3\,mm$ gas gap.

Encouraging results[4] on the performance of RPCs in such a configuration (wider gas gap and bakelite electrodes of improved surface roughness) might push the final decision towards the elimination of the linseed oil treatment.

Nonetheless, since the foreseen environmental conditions into which the detectors will operate are equivalent for ATLAS and CMS, the question is proper of which the best configuration for the muon detector will be .

Part of the answer might be attributed to the role played by the linseed oil both in the process of the gas discharge and in the electrical and mechanical properties of the bakelite onto which it is deposited.

In the following we try to characterize and to summarize the properties of such a compound as well as the advantages and drawbacks of its use in conjunction with the properties of the bakelite plates and with some performances of the whole RPC. It is also worth of note the description of the industrial processing of the bakelite plates as it sets some important electrical properties of the final product.

## 2. Linseed Oil

Crude Linseed Oil[5] is an organic mixture of linolenic, linoleic and oleic acids. After heating refining and the adding of desiccative metals to guarantee the drying process, it is used in many commercial products for paints and coatings. In particular, for traditional RPCs, pentane is added as a solvent to the linseed oil. The treatment of the electrodes is done by filling the entire gas volume of a fully assembled RPC with linseed oil that is then slowly taken away. A subsequent process of

polymerization of the oil is done by fluxing the emptied gas volume with dry air. The resulting effect[6] is the deposition of a thin layer (about 40 $\mu m$) of oil on both bakelite surfaces facing the gas volume.

### *2.1. Surface homogeneity*

It is easy to guess that the linseed oil layer deposited onto the electrode surfaces could prevent microdischarges due to the surface irregularities. This has been already proven[6] for RPCs operated in streamer mode. The presence of linseed oil accounts for a drastic reduction in single rate (one order of magnitude) and dark current.

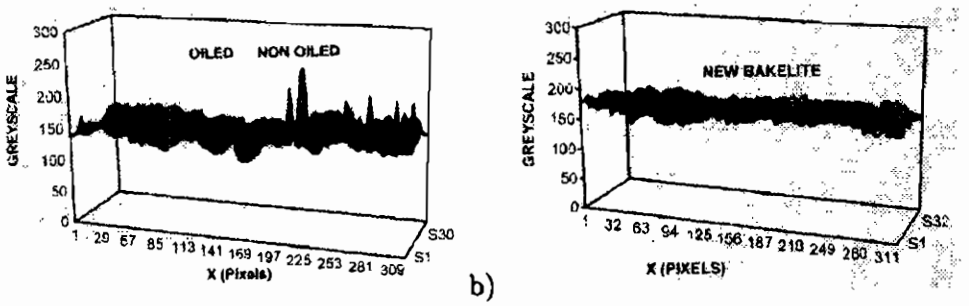


a) b)

Figure 1: Matrix pixel greyscale (A.U.) for a- a standard bakelite sample in which a layer of linseed oil has been deposited on a limited region b- a new bakelite sample (oiless) with improved surface treatment.

To visually verify the effect of the linseed oil we took a sample of standard bakelite and deposited, on a limitated region, a layer of commercial available linseed oil. We took then a X160 magnification picture of the entire surface and plotted its pixel matrix greyscale, as shown in Fig. 1a. From it one can appreciate the contribution of the linseed oil to the improvement of the surface (lefthand part of the picture). For comparison Fig. 1b shows a similar plot, on the same scale, for the new bakelite used in the proposed RPCs for CMS. Already from these figures one can appreciate the significant improvement of the surface quality of the electrodes. In section *3.2* a useful variable, the average roughness, will be introduced as a quantitative parameter to evaluate the quality

of the electrodes surfaces.

### *2.2. Activation by thermal neutrons*

A major concerns is the material damage due to the neutron flux and dose rate in the experimental areas at LHC.

Depending upon the energy of the incoming neutrons, different processes can take place in organic materials such as those used in RPCs. However, despite the different mechanisms and the different secondary radiation production for fast and slow neutrons, the equivalence in damage for equivalent energy absorption (and hence dose) is a rather good approximation for covalent materials such Linseed Oil. The expected dose rate in the CMS barrel region will not exceed $1\,Gy/year$[7]; a factor 100 more is foreseen in the forward region.

The dose rate of $1\,Gy/year$ is consistent with what one expects from a particle dosage of fast neutrons ($> 1\,MeV$) equivalent to some $10^{10} n/cm^2$ depending on the exposed material[8].

We are here interested in the thermal component of such a background because thermal neutrons might induce activation in the RPCs. We have used the 250 kW Triga Mark II research reactor located in Pavia to irradiate a small quantity of linseed oil to detect, by activation analysis, any kind of beta radioisotope that might induce additional noise into the detector. The gamma spectra, obtained by a gamma-spectroscopy analysis, in the range $13\,KeV \div 2\,MeV$, show the activation of $^{59}Co$ and hence the presence of $^{60}Co$.

The resulting specific activation was about $30\,Bq/gr$ in one exposure (about $10^{14}$ thermal $n/cm^2$). A negligible content of $^{82}Br$ was also measured ($3\,Bq/gr$). Obviously this numbers depend on the thermal neutron fluence and have to be roughly scaled by the ratio of the expected thermal neutron fluence in the CMS barrel and forward regions to the fluence we have used in this measurements. On the other hand the fluence of thermal neutrons to give the equivalent above dosages is a factor 100 more than the fast neutron fluence.

The observed activation of linseed oil seems not to prevent the RPC operation in the CMS neutron background.

### *2.3. Absorbance measurements*

We have performed absorbance measurements to investigate any ad-

ditional property of the linseed oil that might somehow make its use imperative in the RPCs construction process. During the gas discharge, especially close to the transition phase between avalanche and streamer formation, UV photons are created by recombination. The idea might be considered of using the linseed oil as a quencher for such a photons.

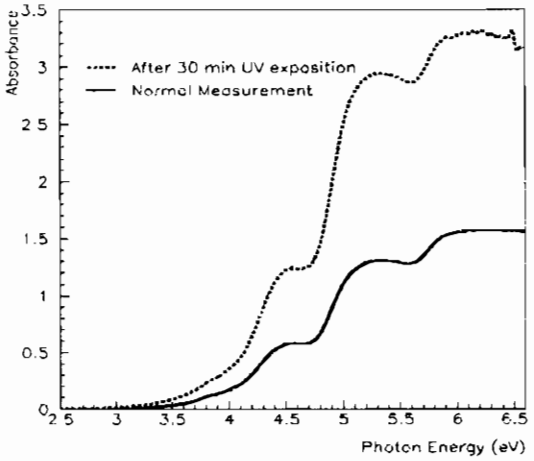


Figure 2: Absorbance curve for linseed oil before (solid) and after (dashed) exposure to a UV lamp.

We have measured the transmission of a light beam across a linseed oil sample. The beam energy spectrum range was between 2.2 and 6.6 $eV$. The energy upper bound was limited by the fact that after 6.6 $eV$ the substrate (the material that physically sustains the sample) begins to absorb all incoming light. To obtain the final curve for the linseed oil it is necessary to subtract the absorption due to the substrate (obtained in a calibration test) from that of the overall absorption curve. The result is shown in Fig. 2 (solid line) where the absorbance $(-log(I/I_0))$ is plotted versus the energy of the incoming light of intensity $I_0$, being $I$ the intensity of the transmitted beam. The effect of the linseed oil polymerization is shown as a superimposed curve (dashed line) after having illuminated the sample with a UV lamp for 30 minutes. As one can see, above 3.5 $eV$ the linseed oil begins to absorb UV photons. However

there is no detectable evidence in the data[6] of such a quenching effect.

*2.4. Effect on the surface resistivity*

It has been suggested[9] that the RPC rate capability could be explained through the ratio of the bulk to surface resistivity of the electrodes.

As it has been pointed out, the surface resistivity of the bakelite electrodes is mainly due to the outer layer of the electrode facing the gas. In the case of standard RPCs the last layer is that of the linseed oil while for the new type of electrodes (improved surface with no oil) the melammine layer should be considered. The authors show that a uniform high voltage distribution over the electrode surfaces can be reached if the surface resistivity of the electrodes is high compared to their bulk resistivity. Moreover their two dimensional resistor network model predicts that the spread area $A$ of the signal on the inner surfaces of the electrodes can be written as $A_0(1+F/d)d^2$ , with $d$ the electrode thickness, $A_0$ a correction factor of the order of 1-2 and $F = \rho/\sigma$ the ratio of bulk to surface resistivity.

The rate capability $R$ is expected to be proportional to $1/A$ so it is a function of the ratio $\rho/\sigma$. According to that the lower resistivity of the linseed oil might account for a lower rate capability.

We have measured bulk and surface resistivity of the standard bakelite with linseed oil and of the new bakelite with improved surface. While the bulk resistivities are of the same order ( $\rho \sim 10^{11}\,\Omega cm$) the surface resistivities were respectively $\sigma \sim 4.3\ 10^{11}\Omega/\Box$ and $\sigma \sim 1.3\ 10^{13}\Omega/\Box$. These values have to be considered within an error of 10%-20%.

According to the above model, a bigger area $A$ and a lower rate capability is expected for a standard oiled RPC.

In Fig. 3[10] data on rate capability for an oiled and a non oiled $2\,mm$ gap RPC are compared. The efficiency of the two chambers is plotted versus the particle flux and the HV set to a value for which, at low rate ($\sim 250\,Hz/cm^2$), each RPC was at the beginning of its efficiency plateau. Two curves are also shown in the figure and represent the fit function $f = E_0(1-r/R)$ for different values of the fit parameter $R$, the rate capability (defined as the flux at which the chamber efficiency is 0.7); $r$ is the particles flux and $E_0$ the chamber efficiency when $r << R$.

The resulting values for the two rate capability $R$ (oiled RPC) and $R'$ (non oiled RPC) were about 4.4 $kHz/cm^2$ and 7.1 $kHz/cm^2$ respec-

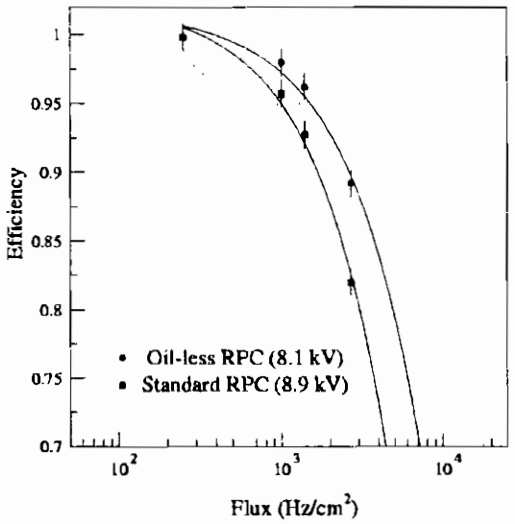


Figure 3: Comparison of efficiency vs particle flux for standard oiled (full squares) and non-oiled CMS like $2\,mm$ gap RPC (full squares). HV set to a value corresponding to the knee of the efficiency plateau at $250\,Hz/cm^2$. Fit curves (solid lines) are described in the text.

tively. For the same flux the non oiled RPC mantains higher efficiency than the standard one. The ratio $R/R' \sim 0.6$ is far from unity, the only difference between the two chambers being the electrode treatment. The linseed oil might be one of the reasons.

On the other side if we calculate the same ratio using the above model we obtain $R/R' \sim 0.5$, in qualitative agreement with what found by the fit.

## 3. Bakelite electrodes

### *3.1. Bakelite production*

The bakelite foils used in the standard RPCs are made of several compressed layers of ordinary paper that are processed into a resin bath, heated and cut to the proper size. The bath is made of a mixture of a phenolic and melammine resins in different percentages according to the desired bulk resistivity. The top and the bottom layer of the final

product are substituted with a more refined paper layer that has been processed with either a melammine or a phenolic bath only.

This part of the production is crucial as it fixes the surface resistivity of the electrodes and hence the rate capability of the RPCs. It is worth of mention also the very final process of the production in which all the paper layers are heated and compressed. The heating sets the water content of the bulk and hence contributes to its resistivity. The compression is achieved by means of two stainless steel plates, the roughness of which is transferred to the RPCs electrodes.

Clearly, the resin mixture (as well as its water content) accounts for the initial bulk resistivity of the electrodes while their outside layers modify the surface resistivity. Such surface treatment contibutes also to the bulk resistivity, the phenolic one being used to obtain low resistivity. Finally the roughness of the steel plates accounts for the surface roughness. These three parameters play a decisive role to set the rate capability and the noise level of the final detector.

### *3.2. Surface Wrinkledness*

In section *2.1* we have shown a qualitative way to estimate the electrode surface quality. In this section a quantitative parameter is introduced to quantify the goodness of a surface. After selecting a total sampling length $l_s$ we measured the *average roughness* $R_a$ defined as :

$$R_a = \frac{1}{l_s} \int_0^{l_s} |y| dx,$$

where $y$ is the vertical profile displacement from the *average line of the profile*, defined by the relation $\int_0^{l_s} y dx = 0$.

Let be $\lambda$ the minimum sampling length ($cut - off$). We set $\lambda = 0.8\,mm$ in all our measurements and $l_s = 5\,\lambda$. The used roughness-meter is schematically shown in Fig. 4a: the vertical displacement of a surface exploring diamond pick-up is transferred by means of a hinge to an illuminated slit. Two photocells (located behind it) measure the light flux through the slit. The unbalance, positive or negative, of the two fluxes is proportional to the analyzed geometrical profile.

The average roughness of different bakelite sheets, used for the RPCs electrodes, is shown in Fig. 4b which summarizes the results in terms of $R_a$ (in $\mu m$) measured at different positions on the sample surfaces. For each point $R_a$ represents the average value of four measurements.

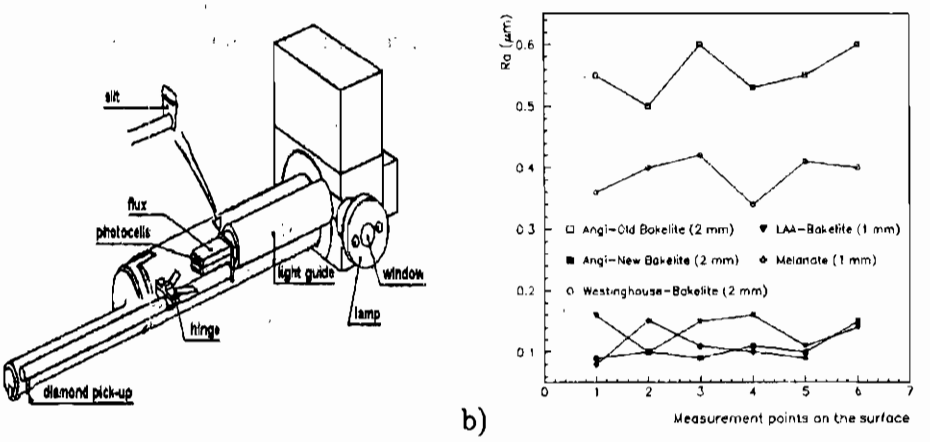


Figure 4: a- Schematic view of the roughness-meter used for the electrode surface measurements; b- Average roughness $R_a$ (in $\mu m$) of electrode surface for planes of different bakelite. Measurements are taken on different points on the sample surface

Data are shown for a standard bakelite (as used in L3, Babar and ATLAS), a new improved one (proposed for CMS), a bakelite used by the LAA group and a sample manufactured by Westinghouse. Values for a Melanate sheet are also reported.

The comparison between standard bakelite (open squares) and new bakelite (full squares) used by CMS, shows the significant improvement (about a factor five) on the surface quality.

This can be directly obtained at the production stage. However, as already pointed out in section *2.1*, the linseed oil treatment on the standard bakelite produces a uniform layer onto the electrode surface. Its $R_a$ value is of the order of $0.2\,\mu m$, being actually only a factor two worse than the surface roughness of the new bakelite.

### *3.3. Electrodes Resistivity*

The bulk resistivity ($\rho$) of the bakelite is another important factor to be considered in view of the use of RPCs at the Large Hadron Collider (LHC). Recent results[11] show that low resistivity RPCs perform very well in a high particle bakground, maintaining a very good efficiency up to about 7 $kHz/cm^2$. The bakelite resistivity is still an important subject of discussion mainly related to the possible variation of the nom-

inal value with time and with the environmental conditions of LHC, i.e. gamma and neutron background.

To have an insight into the matter, we continuously monitored the value of the resistivity of a (new improved) bakelite sample over a period of over 400 hours. The result is summarized in Fig. 5a where also the temperature variations during the test are quoted.

In resistivity measurements the electrical contact between meter and surface is a delicate issue; approximately every 100 hours the measurement setup was stopped to restore a good electrical contact (by mean of a conductive gel) and then restarted again. The outcome of this procedure on the measured values is marked, in Fig. 5a, by four vertical lines.

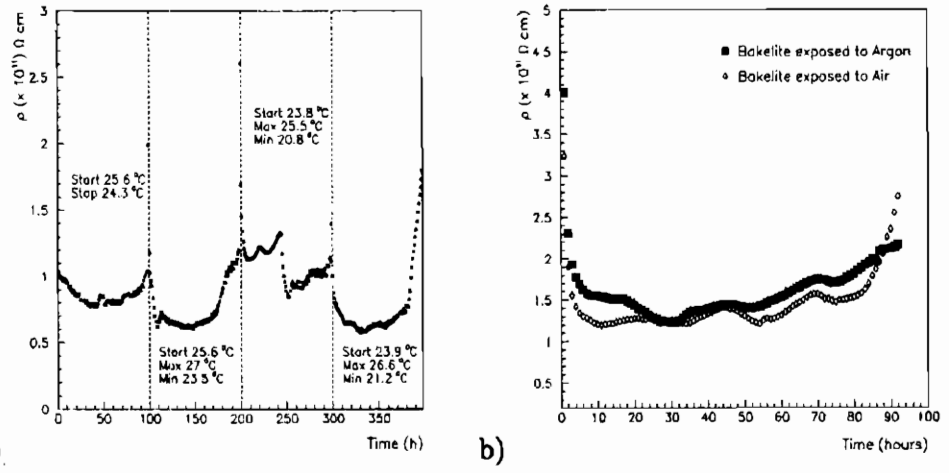


Figure 5: a- Bulk resistivity $\rho$ ($\Omega\, cm$) vs time ($h$) for a new improved bakelite sample. Every 100 hours the measuring setup is stopped to restore a good electrical contact between the electrodes (as explained in the text): the solid lines have been inserted to mark this effect onto the measured values. b- Bulk resistivity $\rho$ ($\Omega\, cm$) vs time ($h$) for a new improved bakelite sample in an argon saturated environment (full squares). For comparison the $\rho$ values of the same sample measured in standard condition are superimposed.

As expected, the bulk resistivity is a function of the temperature and may easily andergo a variation of as much as a factor 2 in 100 hours. Additional question refers to the behaviour of the resistivity in a very dry environment. We have compared the measured bulk resistivity for a bakelite sample placed in an argon saturated volume and in air (at

the same temperature). The data are shown in Fig. 5b as usual plot of resistivity $\rho$ versus time. The bulk resistivity in argon seems to be systematically larger than the value in air by as much as 20 %. However the effect is of the same order of magnitude of the error on the resistivity measurements ($\pm$ 10%). The rise at the end of the time range in Fig. 5b, is due, as previously stated, to the effect of the drying up of the conductive gel layer on the measuring electrodes surfaces. This effect, however, might be due only to a larger leakeage current in air during the measurements and has still to be investigated in more detail.

The effect of neutron irradiation on the bakelite resistivity has been evaluated in static conditions where the resistivity of a sample has been measured before ($\rho$) and after ($\rho'$) heavy irradiation. The difference $\rho - \rho'$ vs time has been found to range within a factor two.

Dynamic measurements, where $\rho$ is monitored under continuous irradiation, will certainly help in understanding the expected behaviour of the RPCs at LHC.

## 4. Conclusion

Either the use of a linseed oil layer or the use of low roughness foils for the electrode surface treatment of bakelite RPCs, appear both valid to meet the expected background rates at LHC. If the function of the linseed oil layer is only noise reduction through the smoothing of the underlying surface, we can probably avoid a step in the production by substituting it with an improved surface bakelite. This solution seems to provide a better rate capability.

The possibility that the linseed oil implies a quenching effect should also be considered more in detail. The data seem not to show a clear evidence of such effect. The linseed oil can be $^{60}Co$ activated, but disturbing effects of the induced ($\beta$) rate ($\sim kHz/RPC$) might be possible only with a thermal neutron fluence of $\sim 10^{14}\, cm^{-2}$.

Finally, since the linseed oil treatment is done after the chamber assembling, the strongest assumption on the benefit of the linseed oil solution is the recovering of a rather good surface independently of any accidents that might have happened to the bakelite foils after the production stage. In this view, the use of linseed oil treatment for the RPCs could be considered a conservative choice.

## 5. References


1. R. Santonico, R. Cardarelli, Nucl. Instr. and Method 187 (1991) 377-380
2. - P. Fonte, Scientifica Acta XI (1996) 25.
   - R. Cardarelli, R. Santonico, V. Makeev, Scientifica Acta XI (1996) 11.
   - I. Duerdoth et al, Nucl. Instr. and Meth. **A348** (1994) 303.
   - I. Crotty et al., Nucl. Instr. and Meth. **A337** (1994) 370.
3. ATLAS *Muon Technical Design Report*, CERN/LHCC/97-22
4. -M.Abbrescia et. al., *Beam Test results on RPCs for the CMS experiment* CMS Note 1997/062 (To appear in Nucl. Instr. and Method)
   -M. Maggi et al., contribution to this Workshop
5. Ullmann's Encyclopedia of Industrial Chemistry A 10 (1994) 227
6. M. Abbrescia et al., Nucl. Instr. and Method **A 394** (1997) 13-20
7. CMS *Technical Proposal*, CERN/LHCC/94-38, pg 123
   CMS *Muon Technical Design Report*, CERN/LHCC/97-32
8. Nuclear Engineering Handbook, H. Etherington Editor, McGraw-Hill (1958)
9. Y. Inoue et al., Nucl. Instr. and Method **A 372** (1996) 39-44
10. G. Lamanna, *Prestazioni di RPC con differenti caratteristiche fisiche e di funzionamento per l'esperimento CMS*, Thesis (Unpublished)
11. W. Dominik et al., contribution to this Workshop

# Measurement of EAS Thickness for Individual Events with RPC in the GREX/COVER_PLASTEX Experiment

M. AMBROSIO *
*INFN, Sezione di Napoli, Italy*

January 12, 1998

ABSTRACT

Extensive Air Showers detected by GREX array have been sampled by means of highly segmented 8 $m^2$ bakelite RPC in the GREX/COVER_PLASTEX experiment. Delay distributions of particles in EAS front at PeV energies with respect to the first arriving particle have been analysed for individual events. The use of RPCs allowed for the first time a measurement of arrival time of individual particles in individual events in a core distance range 0-100 m, where the high density of particles in the shower front requires the use of detectors with a large dynamic range. With this technique an estimation of RPC linearity has been possible by comparing the expected particle density estimated from array scintillators with the density detected by RPC detectors. Results indicate no saturation effects up to hundred particles/$m^2$.

## 1. Introduction

The use of bakelite Resistive Plate Counters (RPC) [1] in Extensive Air Shower (EAS) apparatus for cosmic ray physics in the energy range $10^{14}$-$10^{17}$ eV was first attempted in the GREX/COVER_PLASTEX

*co authors : C.Aramo[1,2], L.Colesanti[3], A.D.Erlykin[4];
[1]INFN, Sezione di Catania, Italy
[2]Dipartimento di Fisica - Università di Catania, Italy
[3]INFN, Sezione di Napoli, Italy
[4]P.N.Lebedev Physical Institute, Moscow, Russia

(G/C_P) experiment [2][3]. The possibility to obtain a precise arrival time measurement of particles crossing the detector area and to segment the pick-up in small pads allowed a precise definition of space-time characteristics of the shower front, whose curvature and thickness were measured in a core distance range of 0-100 m [4].

In fact the use of large area, highly segmented RPCs, embedded in a EAS array, makes possible to obtain arrival time distribution of particles in the shower front for individual events and to study correlations between time distributions, core distance and primary energy. This approach can give an additional information for the multivariate analysis with another information from the array in order to obtain the more precise estimate of the primary mass composition in so called *"knee"* energy region ($\sim 3 \times 10^{15}$ eV), where change of the slope of the primary cosmic ray energy spectrum is not yet understood.

On the other hand the comparison between RPC detectors and scintillators in a EAS array permits the investigation of such RPC characteristics not allowed otherwise, as the detector linearity in terms of the number of particles/$m^2$ that can be detected at the same time. In fact the shower front invests a surface detector with a number of particles ranging from 1/$m^2$ to hundreds or thousands/$m^2$, depending on the primary energy, observation level and shower core distance, in a more or less uniform way. By the density distribution in the array detectors it is possible to estimate the number of particles crossing the RPC and correlate it with the detector response: the appearence of saturation effects gives the limit to the RPC linearity.

For this purpose individual EAS events collected by the G/C_P experiment have been analysed with the aim to obtain the individual arrival time distribution of particles in the shower front and to compare the number of particles estimated from the array density distribution with the number of pads fired in a 1x2 $m^2$ RPC equipped with 6x6 $cm^2$ pads. Results show that RPC linearity extends up to hundred of particles/$m^2$.

## 2. The GREX/COVER_PLASTEX experiment

The G/C_P experiment (Fig. 1), was located at Haverah Park, near Leeds (U.K.). It was based on a conventional scintillator array named

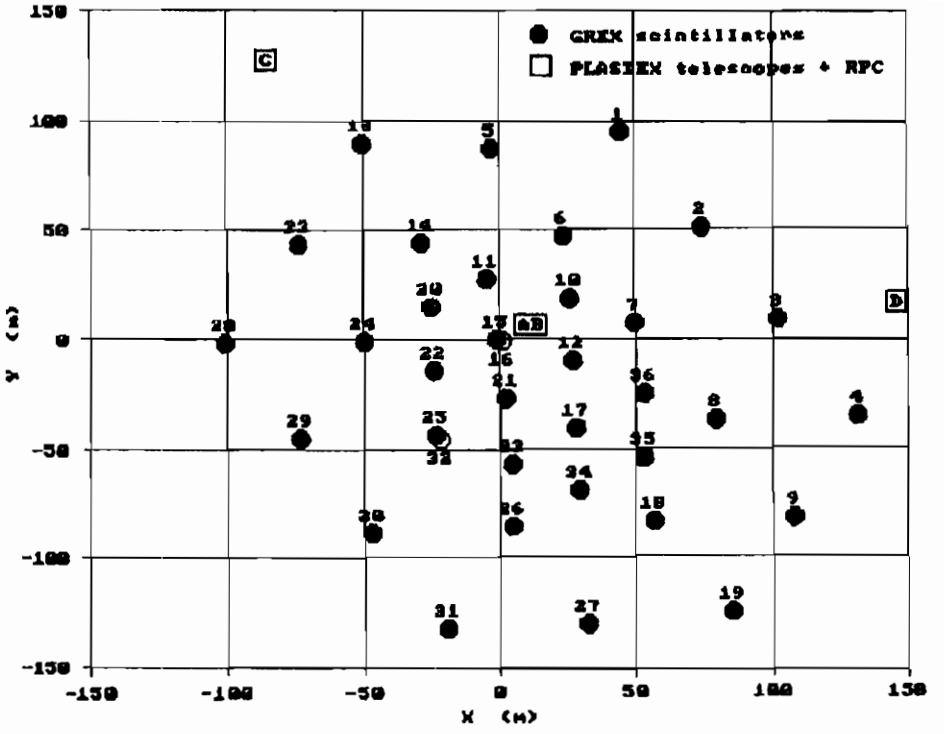


Figure 1: The layout of the GREX/COVER_PLASTEX array.

GREX [5], in which the limited streamer tubes (LST) telescope subarray, named PLASTEX [6], was embedded. Four 4 $m^2$ RPC layers equipped with 24x24 $cm^2$ copper pads were installed on the top of the four LST telescopes (Fig. 2). Pads were read by the front-end timing electronics ensuring a 2 ns time resolution for each channel. Two layers, named A & B, were installed side by side in the array center and other two, named C & D, at the array periphery, 150 m from the center and 260 m from each other. For each 4 $m^2$ detector layer, 64 independent time measurements were allowed, permitting simultaneous observation and arrival time measurement of up to 256 individual particles in the EAS shower front.

### *2.1. Large area highly segmented RPCs*

In the G/C_P experiment bakelite single gap RPCs, 1x2 $m^2$ sized, $10^{12}$ $\Omega$ $cm^2$ resistivity, have been used with a gas mixture of 68% Argon, 28% Isobuthane, 4% Freon, covering the total area of 16 $m^2$ (8 $m^2$ in the

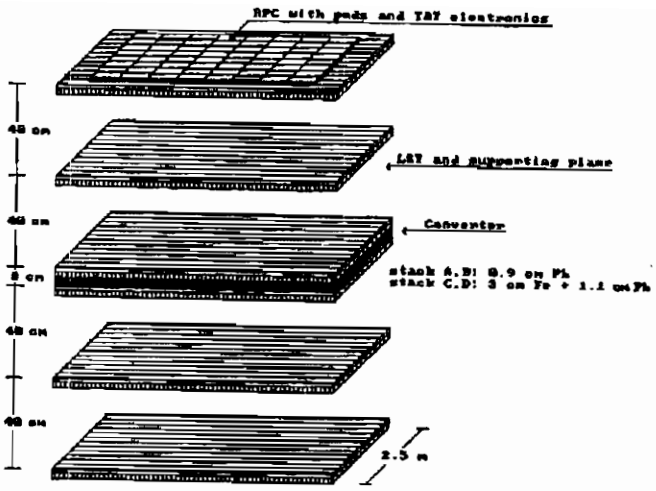


Figure 2: Layout of the COVER_PLASTEX telescope.

array center, 4 + 4 $m^2$ at the array periphery). The signal pick-up was obtained by means of 12x12 $cm^2$ copper pads, small enough to avoid the time jitter due to the signal propagation. In order to reduce the number of pick-up readout channels, 4 pads was ORed toghether by means of a pure resistive $OR_4$. In total 4x64 = 256 timing channels, 128 in the array center and 64 + 64 at the array periphery, were installed, so allowing detection of up to 16 individual particles/$m^2$ in 16 $m^2$. If operated in connection with tracking LST telescopes, RPCs allow a separate measurement of the arrival time of electrons and muons in the shower front.

### *2.2. The readout electronics*

While RPC signals arrive after few ns, the array trigger arrives with a delay of about 600-800 ns due to the distance between scintillators and to the shower axis inclination. Hence electronics readout boards must work in a free running mode. For this purpose a new front-end electronics, named **T&T** (Tracking & Timing), was developed [7][8]. This electronics allows a local signal processing and acquisition independent from the array trigger: a 16 bit cyclic memory continuously shifting stores the input image also in the absence of signal, with a 32 ns frequency. The cycle is stopped by the trigger signal, also stored in a T&T memory. By this way the arrival time of a signal with respect to the array trigger in each channel can be evaluated simply by counting the

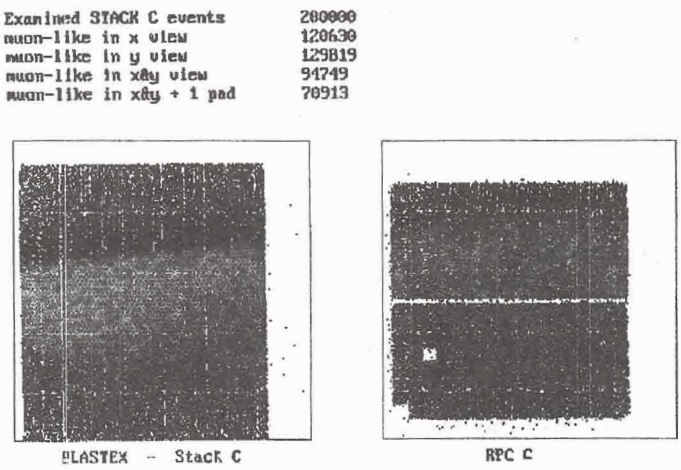


Figure 3: LST and RPC image from autotrigger run.

number of bits between the signal image and the trigger image with a 2 ns accuracy (1 bit = 2 ns). The acquisition program scans a 1.5 $\mu$s memory depth only for fired channels.

*2.3. RPC characteristics*

Calibration runs were made periodically using LST tracking telescopes: a coincidence between the upper and lower planes (Fig. 2) selected atmospheric muons crossing the telescope. Fig. 3 shows result of a run with 200.000 events from which dead LST wires and dead pads can be easily identified and RPC efficiency and position can be estimated. By this way detector characteristics were continuously monitored [9][10], in particular for what concerns single counting rate, plateau, efficiency, cross talk and after pulses. Signal threshold was set to 120 mV at 7200 V. Temperature and pressure effects were found to be negligible.

## 3. Time structure of individual events

Thanks to the RPC performance the G/C_P experiment permitted the study of shower front space-time structure in the energy range of $4x10^{14}$ - $10^{17}$ eV and in the core distance range of 0-100 m [4]. In addition accurate arrival time measurements of individual particles in individual EAS have been obtained and permitted the event by event

determination of shower front parameters.

### *3.1. Experimental information*

For each event the GREX array provides:

- Estimate of primary energy;
- Determination of shower axis ($\leq 1°$ accuracy);
- Core position estimate ($\sim$6 m accuracy).

From each RPC layer the following information is obtained for the same event:

- Number of fired pads (pad multiplicity);
- Arrival time of each pad signal (particle) with respect to the array trigger.

Finally from each LST telescope the information is obtained on:

- Number of strips fired in each plane;
- Track reconstruction for particles crossing telescopes and identification of muons among electrons.

Fig. 4 shows an event with the primary energy of 1632 TeV, axis inclination $\theta_x$,$\theta_y$ = -13.46°, 8.57°, core distance 22.52 m. In this event the RPC layers A and B in the array center ( 4 $m^2$ and 64 pads each ) detect 74 particles measuring the arrival time for each of them with respect to the array trigger. Then times are referred to the first arriving signal (zero time = arrival time of first detected signal) and arrival time distribution of all particles is easily obtained, as shown in the small graph in fig. 4, as well as its mean $\langle t \rangle$ = 8 ns and RMS sig = 7.58 ns. Small boxes in this picture indicate pick-up pads, while numbers inside them indicate the measured arrival time of particle crossing pad, referred to the first detected. Note that all times are even, due to the T&T electronics limit of 2 ns time resolution.

### *3.2. Event selection and analysis criteria*

Data analysis has been restricted to the events detected only by two RPC layers (A & B) in the array center, where up to 128 independent

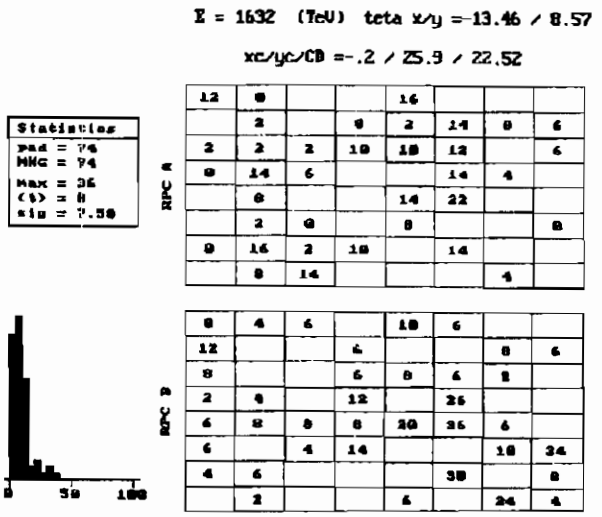


Figure 4: Display of an individual event.

arrival times in a single event can be measured. A lower limit of 13 fired pads ($\geq$2 particles/m$^2$) cuts events with poor individual statistics, and an upper limit of 60 fired pads ($\leq$7 particles/m$^2$) reduces the probability of more than 1 particle hitting a pad. In addition analysis has been restricted to only events which core position was inside the inner part of the array, i.e. no more than 100 m from the inner RPC layers. The average time window for arrival times has been set to 600 ns. A total of $\sim$190000 events surviving cuts have been analysed.

Each event is then characterized by:

- multiplicity n ($13 \leq n \leq 60$);
- time measurements $t_i$, i = 1,...n;
- N = n-1 delays $\tau_i$=$t_i$-$t_1$ with respect to the first (earliest) particle arriving in the RPC detectors.

Then for each $k$ event a delay distribution with respect to the first arriving particle is obtained. Average delay $\langle \tau_i^k \rangle$ and standard deviation $\sigma^k$ of individual distributions have been estimated as:

$$\langle \tau_i^k \rangle = \sum_{i=1}^{N} \tau_i^k / N$$

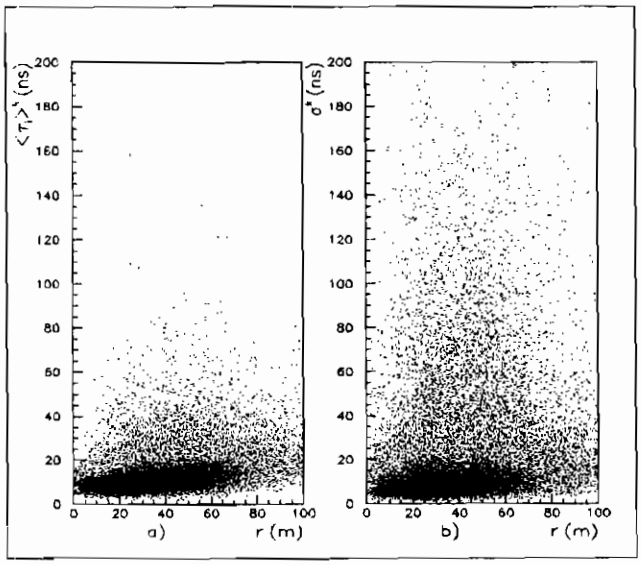


Figure 5: Particles average arrival time $\langle \tau_i^k \rangle$ (a) and shower front thickness $\sigma^k$ (b) vs core distance r.

$$\sigma^k = \sqrt{\sum_{i=1}^{N} (\tau_i^k - \langle \tau_i^k \rangle)^2 / (N-1)}$$

and cumulated in histograms according to the core distance r.

### *3.3. Analysis results*

Fig. 5a shows the correlation between $\langle \tau_i^k \rangle$ and core distance r, while the correlation between $\sigma^k$ and r is shown in Fig. 5b. It can be seen that events with the particle mean arrival time $\langle \tau_i^k \rangle$ of more than 40 ns and thickness $\sigma^k$ of more than 40 ns have been detected at all core distances, making evident the large arrival time fluctuations in the EAS front.

In Fig. 6a and 6b the dependence on r of T - mean value of $\langle \tau_i^k \rangle$ and $\Sigma$ - mean value of $\sigma^k$ is shown. It can be seen that the mean arrival time T derived from individual events increases from 9 to 22 ns in the selected core distance range of 0-100 m, with the corresponding mean thickness $\Sigma$ ranging from 8 to 25 ns.

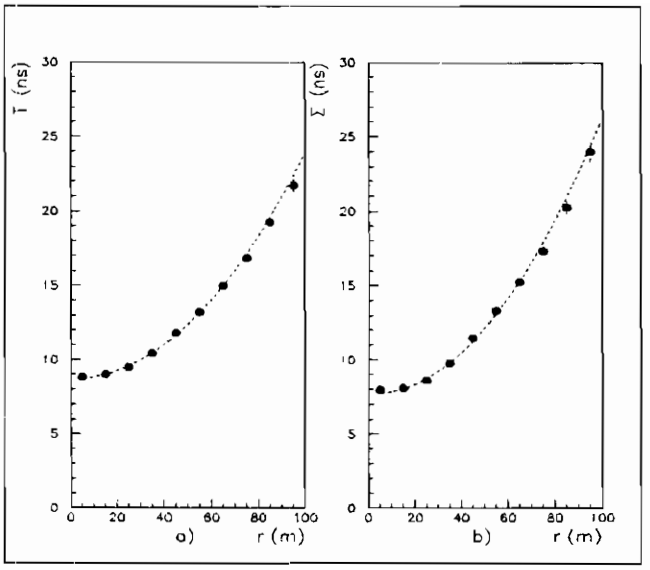


Figure 6: Mean of $\langle \tau_i^k \rangle$ values T (a) and mean of $\sigma^k$ values $\Sigma$ (b) vs core distance r.

## 4. RPC linearity estimation

In order to estimate the RPC linearity as the number of particles/$m^2$ detected individually at the same time, a 2 $m^2$ RPC was installed on the second plane of LST telescope B. The detector was equipped with 6x6 $cm^2$ copper pads read by a digital readout electronics recording the number of fired pads. By this way 512 pick-up channels were available, opening the possibility to detect up to 256 particles/$m^2$.

### *4.1. Comparison with streamer tubes*

A first estimate of RPC linearity can be obtained simply by comparing the number of fired pads with the number of fired strips in the LST plane supporting the RPC detector. LST strips are 1.2 cm sized, allowing detection of maximum 76 particles/$m^2$. Fig. 7 shows this correlation. It can be seen that up to 76 particles/$m^2$ the correlation is very good, and the number of fired pads corresponds to the number of fired strips within the expected fluctuations.

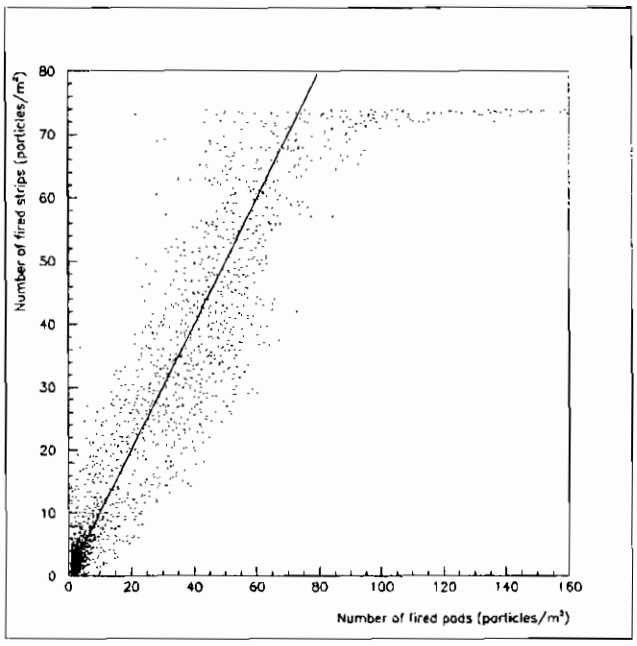


Figure 7: Pad - strip correlation.

*4.2. Comparison with NKG*

The number of particles crossing a 1 $m^2$ detector invested by an EAS can be estimated using the Nishimura-Kamata-Greisen (NKG) formula:

$$\rho_{NKG} = \frac{N_e}{R_0^2} c(s) \left[\frac{r}{R_0}\right]^{s-2} \left[1 + \frac{r}{R_0}\right]^{s-4.5}$$

where:
$N_e = 10^6 \left(\frac{E}{10^{16}}\right)^{1.18}$
$s = 1.3$
$c(s) = 0.45$
$R_0 = 79$ m

With the NKG formula the number of particles crossing the RPC 6x6 $cm^2$ layer can be estimated using the primary energy E and the core position r provided by GREX array. Fig. 8 shows the correlation between particle density in the RPC layer and density estimated by means of NKG formula. It can be seen that, taking into account natural fluctuations of EAS development and the accuracy of the primary energy $E_p$ and core distance $r$ determination, there is a satisfactory correlation

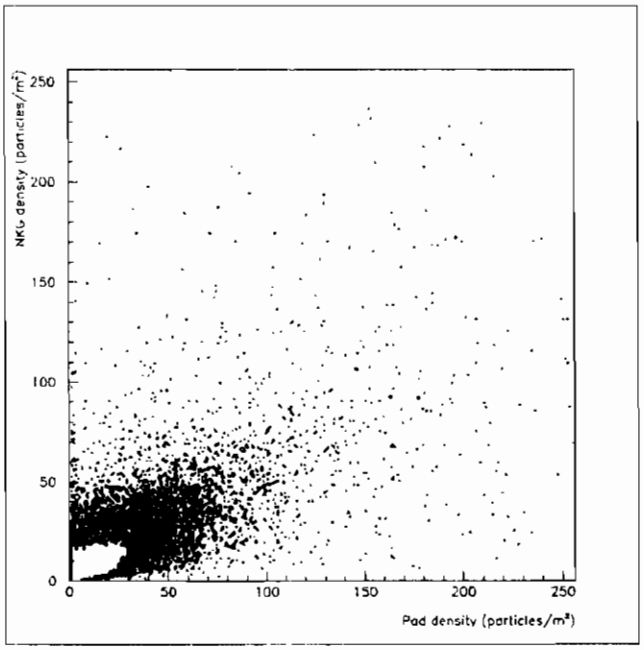


Figure 8: Particle density estimated with NKG formula vs RPC pad density (contour plot).

between particle density (fired pads) measured by RPC and particle density estimated by NKG formula.

## 5. Conclusion

The use of highly segmented RPCs embedded in the GREX array permitted the study of the fine time structure of the EAS front in individual events at core distances of 0-100 m. The presence of events with the large average arrival time and the large front thickness has been observed.

Due to the wide range of primary energies and core distances EAS provide the wide range of particle densities in the array distributed more or less uniformly in the detector area, then allowing the estimate of detector linearity. By this way the linearity of RPC detectors has been estimated both by comparison with streamer tubes equipped with thin strips and by comparison with the particle density in the nearby scintillators. It has been found that RPCs have the linearity up to hundred of particles/$m^2$.

The performance of RPCs in G/C_P experiment demonstrated that the use of such detectors in EAS physics can be very fruitfull and can give the precise information on shower front characteristics, allowing a

detailed study of extensive air shower phenomena.

## 6. Acknowledgments

Authors are grateful to the Leeds group of Prof. A.A.Watson for the array disponibility and maintenance, and to the Palermo group of Prof. L. Scarsi for the PLASTEX and RPC operation.

## 7. Bibliography

1. R. Santonico & R. Cardarelli, *Nucl. Instr. and Meth.*, **187** (1981) 377.
   R. Santonico & R. Cardarelli, *Nucl. Instr. and Meth.*, **A236** (1988) 20.
2. G. Agnetta et al., *Proc. XXIII IVCRC, Calgary*, **4** (1993) 270.
3. G. Agnetta et al., *Nucl. Instr. and Meth.*, **A359** (1995) 596.
4. G. Agnetta et al., *Astroparticle Physics* **6** (1997) 301.
5. G. Brooke et al., *Proc. XIX ICRC, La Jolla, U.S.A.*, **3** (1985) 426.
6. G. Agnetta et al., *Il Nuovo Cimento*, **13C** (1990) 391.
7. G. Agnetta et al., *Nucl. Instr. and Meth.*, **A315** (1992) 415.
8. G. Agnetta et al., *Nucl. Instr. and Meth.*, **A337** (1994) 521.
9. L. Colesanti et al., *Proc. RPC 1995, Pavia* (1995) 157.
10. G. Agnetta et al., *Nucl. Instr. and Meth.*, **A381** (1996) 64.

# Arrival Time Measurement of Muons in Extensive Air Shower with Bakelite RPC

C. ARAMO *
*Dipartimento di Fisica, Università di Catania*
*INFN, Sezione di Catania, Italy*

January 21, 1998

ABSTRACT

In high energy cosmic ray physics, the detection with surface array of muons produced along the shower development in the Earth atmosphere is particularly important for the study of primary mass composition. The combined use of muon production height along the shower axis evaluated from muon direction and from muon arrival time selects high energy muons not significantly scattered in the atmosphere nor deviated in the geomagnetic field. This allows the reconstruction of Extensive Air Shower (EAS) longitudinal development in the energy region $10^{15}$ - $10^{16}$ eV. A test of this technique, called TTC (Time-Track Complementarity), is in progress in the EAS-TOP experiment: 40 $m^2$ of bakelite RPCs have been installed under the hadron calorimeter with the purpose to obtain accurate measurement of muon arrival time respect to the shower core.

*co authors: M. Ambrosio[1], G. Battistoni[2], A. Candela[3], F. Cassese[1], A. Chiavassa[4], B. D'Aquino[1], M. De Deo[3], M. D'Incecco[3], R. Fonte[5], P.L. Ghia[6], G. Giuliani [7], A. Grillo[3], M. Lindozzi[3], C. Morello[6], G. Navarra[4], R. Rocco[1];
[1]INFN, Sezione di Napoli, Italy
[2]LNF dell'INFN e INFN, Sezione di Milano, Italy
[3]LNGS dell'INFN, Italy
[4]Dipartimento di Fisica, Università di Torino e INFN, Sezione di Torino, Italy
[5]INFN, Sezione di Catania, Italy e Università del New Mexico - Albuquerque (USA)
[6]Istituto di Cosmo-Geofisica del CNR e INFN, Sezione di Torino, Italy
[7]Istituto di Cosmo-Geofisica del CNR e LNGS dell'INFN, Italy

## 1. Introduction

At primary energies above $10^{14}$ eV the cosmic ray primary flux becomes too low to measure the primary spectrum and composition through the direct calorimetric experiments operating on balloons or satellites. Measurements have therefore to be performed with large ground based arrays detecting Extensive Air Showers (EAS) produced in primary cosmic ray interactions with Earth atmosphere. Surface arrays are usually built with scintillator or Cerenkov detectors, the energy threshold and energy range depending from observation level, array dimension and detector spacing. Primary energy can be estimated by the energy deposit in the array detectors, while the shower axis inclination can be reconstructed measuring delay between signals in the fired detectors.

Actually one of major challenge in the EAS physics is the understanding of the origin of so called *"knee"*, the slope change in the cosmic ray differential flux at primary energy of about $3 \cdot 10^{15}$ eV. Some hypothesis on the *"knee"* origin connect the slope change with a variation of primary mass composition [1]-[5]. Then the primary mass estimation in the *"knee"* energy region is the most important objective of some modern arrays [6]-[14]. Unfortunately the primary mass estimation is masked by the Earth atmosphere that prevents direct detection of cosmic rays: at the Earth surface only interaction products of primary particle with air nuclei can be detected. In addition it is impossible to measure energy and nature of individual particles in the shower front and fluctuations in the shower development reduce more and more the correlation between the primary mass and measured informations. The sum of described circumstances makes possible only a statistical estimate of primary mass composition using a multivariate analysis of as many as possible parameters and informations in the shower front detection.

One of possible new information that can be used is the longitudinal development of EAS hadron component which depends both from nature and energy of the primary particle and from its interactions with the air nuclei. The carriers of this information are muons emitted in decays of parent pions and kaons detected as penetrating particles in shielded detectors or in tracking telescopes. Muons have never been used up to

now to reconstruct the hadron longitudinal development of EAS because they are not produced directly in the shower axis. In addition they are deviated by the geomagnetic field and by the multiple coulomb scattering in the atmosphere and the eventual detector shielding changes their direction. Nevertheless the reconstruction of muon longitudinal development may be a powerful tool for primary mass measurement and for the study of high energy hadron interactions with the atmosphere nuclei in the *knee* energy region with high efficiency (duty cycle 100 %) [15][16].

In this paper we describe the possibility to reconstruct the muon production profile at PeV energies by the combination of tracking and timing measurements as provided by a large area tracking and timing telescope now available in the EAS-TOP experiment [10][17][18] where 40 $m^2$ of bakelite RPCs [19][20] have been installed under the existing muon-hadron detector with the purpose to obtain accurate measurement of muon arrival time respect to the shower core.

## 2. The TTC technique

The muon production height can be reconstructed using an array providing information on the shower core position ($X_0$, $Y_0$), axis direction ($\theta_0$, $\varphi_0$) and arrival time of the shower front in the core ($t_0$) operating jointly with a tracking and timing telescope which for each muon detected gives the position ($X_\mu$, $Y_\mu$), the direction ($\theta_\mu$, $\varphi_\mu$) and the arrival time respect to the shower core ($\tau_\mu = t_\mu - t_0$).

The muon tracking requires thick absorbers to reduce contribution of low energy electrons more abundant than muons and a good tracking accuracy over a large and highly segmented area. Furthermore muons are subject to large fluctuations and, being charged particles, are subject to multiple coulomb scattering and deviation in the geomagnetic field. Then the use of only tracking for the reconstruction of apparent muon height of production ($h_\mu^{track}$) is unsatisfactory [15][16]. Also the time measurements alone are difficult to be interpreted in terms of apparent muon height of production ($h_\mu^{time}$), being dominated by arrival time fluctuations and non-relativistic effects [15][16]. The combined use of timing and tracking (TTC, Time-Track Complementarity) informations selects muons whose apparent height of production ($h_\mu^{TTC}$) is consistent for both measurements. In particular as TTC coherence criterium can be

used the requirement that the absolute value of difference between muon production height reconstructed by tracking and by timing is smaller than the corresponding error, i.e.:

$$ABS(H) \leq \Delta H \tag{1}$$

where:

$$H = h_\mu^{track} - h_\mu^{time}$$

$$\Delta H = \sqrt{(\Delta h_\mu^{track})^2 + (\Delta h_\mu^{time})^2}$$

with $\Delta h_\mu^{track}$ and $\Delta h_\mu^{time}$ errors of $h_\mu^{track}$ and $h_\mu^{time}$ respectively.

The production depth in this approach can be calculated as:

$$Z_\mu^{TTC} = \frac{Z_\mu^{track} + Z_\mu^{time}}{2} \tag{2}$$

It has been demonstrated [16] that the combined use of muon production height from tracking and timing selects high energy muons not significantly scattered in the atmosphere and not deviated in the geomagnetic field. The efficiency of this selection is about 30 %.

Simulation results* obtained applying this criterium are shown in fig. 1, where the average production depth (2) is compared with the muon production depth for proton and iron induced showers. It can be seen that difference between the reconstructed longitudinal development of proton and iron induced showers remains significant and can be used as an additional parameter for the mass composition study. It is therefore important to check the feasibility of an experiment concerning the consistency of the two measurements (i. e. the possibility of their combination), the effective final measurement errors, and the reproducibility of the selection procedures by a simulation in a real experiment.

Moreover, the required accuracies for a satisfactory reconstruction must be $\leq 5$ m on the core position estimate, $\leq 3$ ns for $\tau_\mu$ measurement, $\leq 1°$ for shower axis determination and $\leq 5$ mrad on muon track.

*100 vertical proton and 100 vertical iron induced showers with energy of $10^{15}$ eV have been simulated by means of the CORSIKA code [21] with VENUS + GHEISHA version of the hadron interaction model.

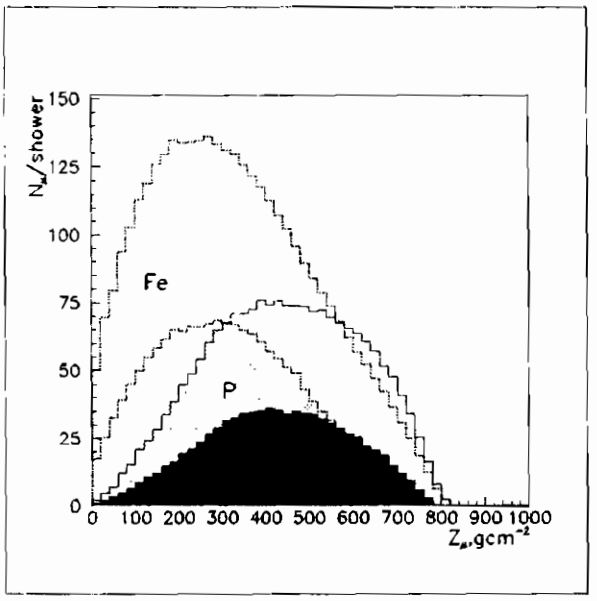


Figure 1: Reconstruction of the production depth distribution by means of TTC-approach for muons, detected at core distances R > 120 m in proton (full lines) and iron (dotted lines) induced shower. Not hatched histograms - distributions of all muons in the shower at R > 120 m reduced by a factor 3, hatched histograms - reconstructed distributions for TTC selected muons.

## 3. Experimental layout

The EAS-TOP array is located at Campo Imperatore (2005 m a.s.l., 810 g/cm$^2$ atmospheric depth), above the underground Gran Sasso Laboratories, and include detectors of electromagnetic, muon, hadron and atmospheric Cerenkov light components (fig. 2).

The e.m. detector [22] is made of 35 plastic scintillator modules (10 m$^2$ each, 4 cm thick, divided into 16 individual units), distributed over an area of $\sim$ $10^5$ m$^2$ and organized in circles (of 50-88 m radii) interconnected with each other, for trigger and data taking organization. The triggering energy loss threshold in each module is of 3 MeV (0.3 of a minimum ionizing particle m.i.p.) The EAS arrival direction is obtained through the times of flight among the different detectors, measured with 0.5 ns sensitivity, and the resolution obtained is 0.83°(0.5° for $N_e$ > $10^5$). The shower size $N_e$ and the core location are obtained from the fit to the recorded particle densities and the resolutions are calculated using

a Monte Carlo simulation and the GEANT code obtaining $\sigma_{N_e}/N_e \sim 0.1$ and $\sigma_{cd} \sim 5$ m for $N_e > 10^5$.

The muon-hadron detector [23], located at the edges of the scintillator array (fig. 2), is a tracking module consisting of a 9 active planes, 30 cm away from each other, interleaved with iron absorbers 13 cm thick, the total height is about 280 cm, the surface is 12x12 $m^2$. Each plane is made of two layers of streamer tubes (3x3 $cm^2$ section, 12 m length) for muon tracking and one layer of tube operating in "quasi-proportional" regime for hadron calorimetry. The tracks X coordinates are obtained by the signals of the anode wires (368 in a layer), the Y ones by the induced signals on strips (3 cm width) placed orthogonally to the wires. The muon tracking is performed by 16 layers of streamer tubes: a muon track is defined from the alignment of at least 6 hits (wires) in different layers of tubes. The muon energy threshold is $E_\mu \sim 1$ GeV for vertical incidence, the resolution (i.e. the difference between the numbers of visible and reconstructed muons with at least 6 wires and strips fired) is less than 4.3 % up to 30 reconstructed muons and the angular resolution is $\sim 0.6°$. Since the core is located by the e.m. array, by using the theoretical l.d.f. (Nishimura-Kamata-Greisen, NKG formula) [24], the total muon number $N_\mu$ can be obtained; the accuracy is $\sim 20\%$ at $N_e \sim 10^6$. The effective muon sensitive area is increased by 10 $m^2$ scintillator detectors positioned below 13 e.m. modules, each shielded by 30 cm of iron.

In September 1997 a layer of 20 bakelite single gap RPCs, 1x2 $m^2$ sized, $10^{12}$ $\Omega$ $cm^2$ resistivity, has been installed under the muon hadron detector (fig. 3), covering a total area of 40 $m^2$, grouped in 5 strips each with 4 detectors. The pick-up is obtained by means of 12x12 $cm^2$ copper pads (128 pads for each RPC) to avoid the time jitter due to the signal propagation. In order to reduce the number of pick-up readout channels, 4 pads are ORed together by means of a pure resistive $OR_4$. Each signal $OR_4$ is read by an electronic readout board with 32 input channels and a FAST-OR which is the output signal of 2 $m^2$ RPC. The 4 FAST-OR of each strip are ORed together and sent to a COMMON START of a TDC Lecroy 2228A with 2.5 ns/ch resolution. The COMMON STOPS of 5 TDC, related with 5 RPC strips, are obtained using 7 EAS-TOP triggers corresponding to different scintillator counters of the array. RPC acquisition is operated separately from the array acquisition and the

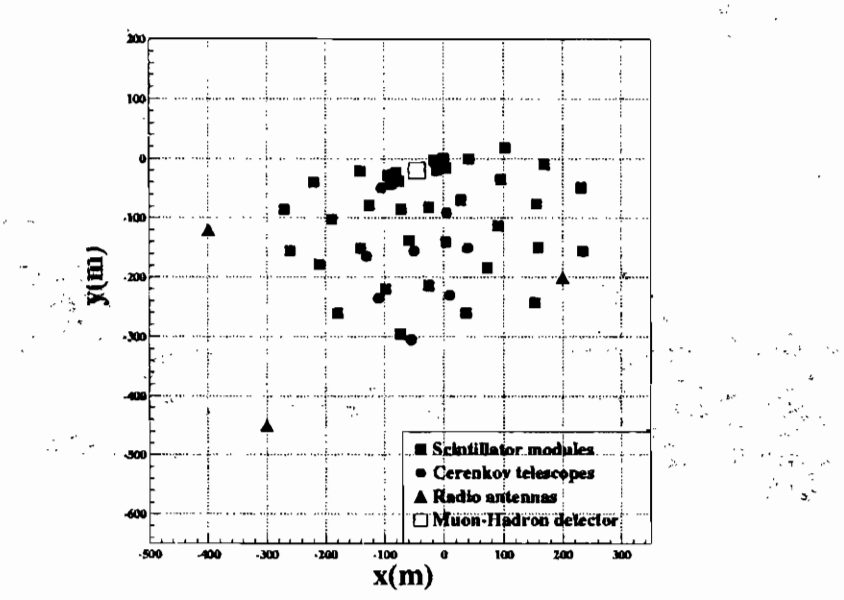


Figure 2: The EAS-TOP array.

event building is made possible by reading an atomic clock time on the occurrence of a trigger. Then an event is characterized by the presence of a START signal on almost one TDC, 1 or more TDC STOP signals and the coincidence, within 1 $\mu$s, between the absolute time related with RPC and absolute time related with EAS-TOP experiment.

In this way each event is characterized by:

- arrival direction of shower axis;
- core location;
- electromagnetic size, $N_e$;
- number of muons, $N_\mu$;
- track reconstruction of muons crossing the muon-hadron detector;
- arrival time of muons crossing the 40 $m^2$ RPC layer with respect to the EAS core.

## 4. Performance of bakelite RPC detectors

Before the RPC installation under the muon-hadron detector, each detector has been tested at Gran Sasso Laboratory (1000 m a.s.l.). Then

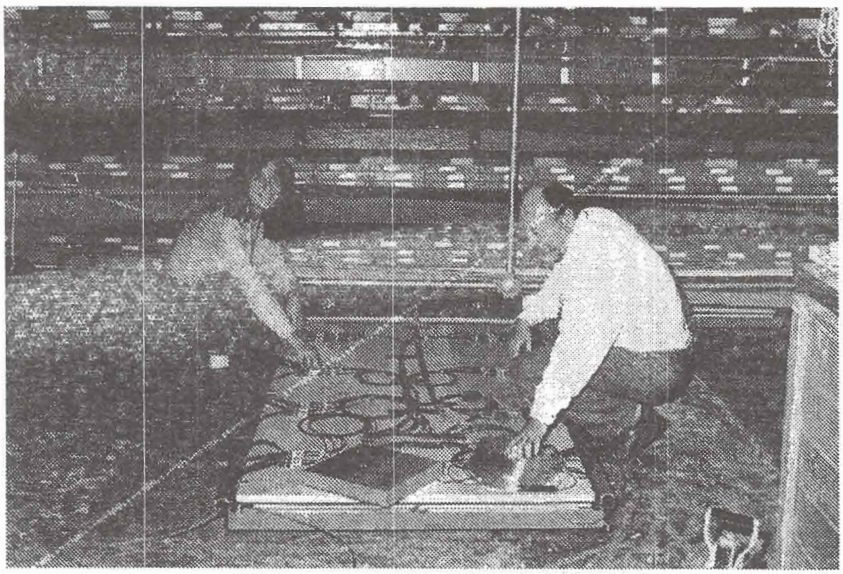

Figure 3: Installation of RPC under the muon-hadron detector.

RPCs have been tested again after their installation at EAS-TOP level (fig. 3).

The used RPCs are the same previously used in the GREX/COVER_PLASTEX experiment [25] from April '93 to June '95. On the basis of this previous experience, the same running conditions have been chosen [26][27], i.e. a gas mixture of 68% Argon, 28% Isobuthane, 4% Freon, a 7 kV high voltage and a 120 mV input threshold of the readout front-end electronics.

The average DC current versus HV supply of 2 RPCs is shown in fig. 4 (left plot) at laboratory level and EAS-TOP level (under the muon-hadron detector). Right plot shows instead the single counting rate of the same 2 RPCs for laboratory and EAS-TOP level. The lower single counting rate at EAS-TOP level is due to the presence of muon-hadron detector above the RPC layer imposing a 1 GeV threshold on muons and absorbing low energy particles.

The RPC efficiency at laboratory level is reported in fig. 5 (left plot) making evident a wide plateau indicating a very high and stable efficiency value of about 95%.

A time resolution better than 1 ns can be easily and directly achieved using pads of a few $cm^2$ size [28]. The use of a non fast readout electronics with 2.5 ns per bin TDCs produces a time resolution not better

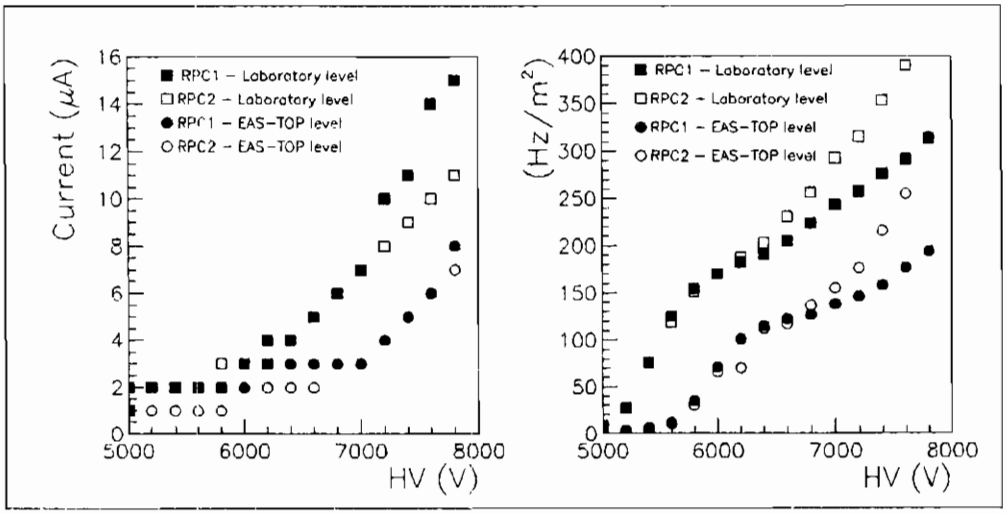


Figure 4: Current input (left plot) and single counting rate (right plot) as a function of HV supply.

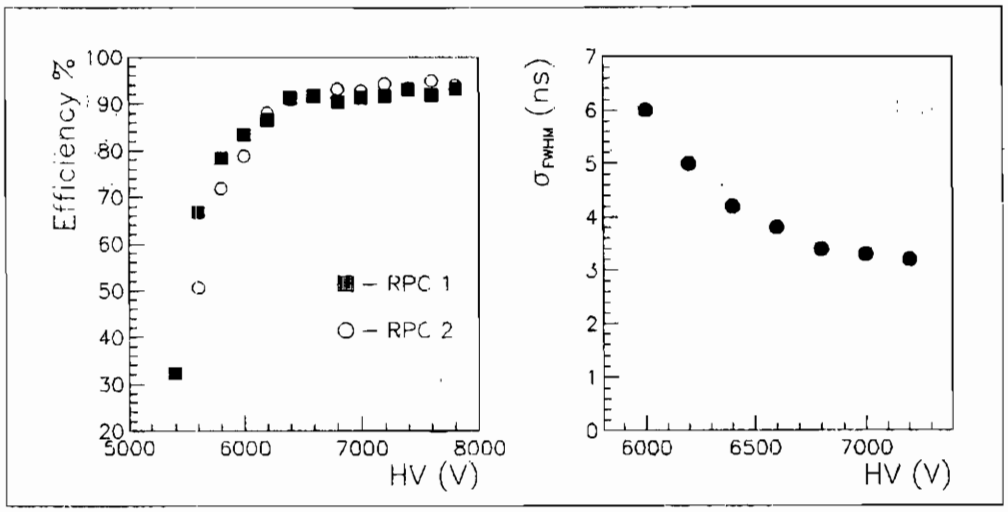


Figure 5: Efficiency (left plot) and time resolution of RPC + readout electronics (right plot) as a function of HV supply.

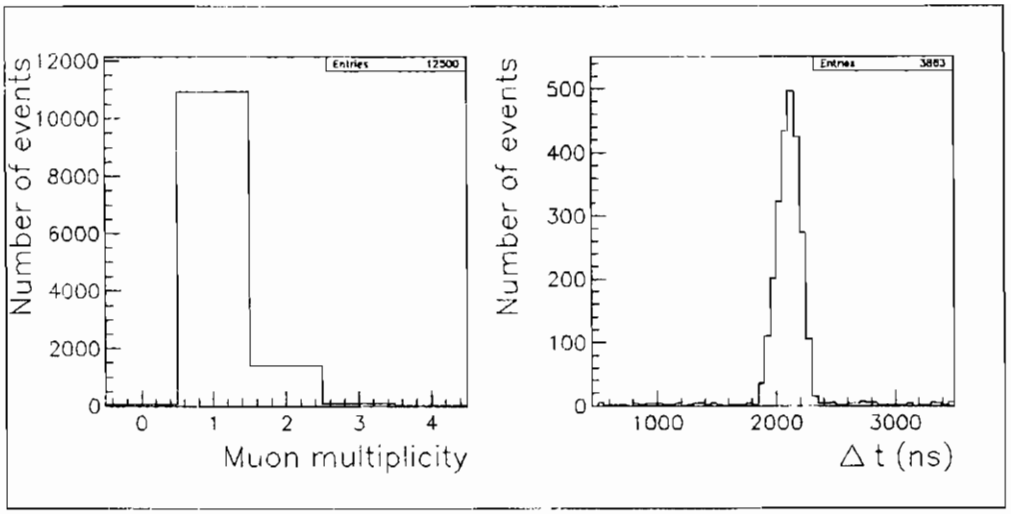


Figure 6: Muon multiplicity detected by RPCs (left plot) and raw delay distribution of 1 EAS-TOP trigger respect to muon arrival time (right plot).

than 3 ns, achievable at 7 kV as shown in fig. 5 (right plot).

## 5. First results

Data taking with the RPCs layer started in the middle of October and first data have been used to perform the apparatus debug. In fig. 6 (left plot) the muon multiplicity distribution detected with RPCs is shown for 12500 events. It can be seen how most of events present only 1 muon, but a significant fraction can permit the study of multimuon events. At the moment no correlation between arrival times has yet been possible.

Fig. 6 (right plot) shows a raw delay distribution of an EAS-TOP trigger with respect to the muon arrival time. Since the muon arrival times are not yet correlated with the arrival time of the shower front in the core, the $\sigma$ of shown delay distribution is due to the different core position and axis inclination of analysed event in the array. The value $\sigma = 92$ ns is coherent with the expected one for the core position spread and for shower inclination.

## 6. Conclusion

The use of a layer of highly segmented RPC under the muon-hadron detector in the EAS-TOP array permits measurement of muon arrival time that, combined with the muon tracking, allows the possibily to reconstruct the EAS hadron longitudinal development in the *knee* energy region. RPCs allow accurate time measurement on large area also in presence of high particle multiplicity. Operating conditions appear to be stable also at high mountain level and in the presence of storm and snow. The success of the described test can open the possibility to apply the TTC technique in modern arrays for a better estimation of cosmic ray primary composition in the *knee* energy region.

## 7. Acknowledgments

Authors are gratefull to A. Lauro, F. Pagano, A. Parmentola, C. Gustavino, S. Parlati, EAS-TOP collaboration and all the technicians of mechanical service of LNGS.

## 8. Bibliography

1. Kulikov G.V. and Khristiansen, *JETP*, **35** (1958) 635.
2. Peters B., *Nuovo Cimento*, **14** (1961) 436.
3. Hillas A.M., *16th ICRC, Kyoto*, **8** (1979) 7.
4. Biermann P.L., *23th ICRC, Calgary*, Inv. Rap. High. Papers (1993) 45.
5. Erlykin A.D., *Nucl. Phys. B (Proc. Suppl.)*, **39A** (1995) 215.
6. Klages H.O. et al.,*25th ICRC, Durban*, **HE 2.1.1** (1997) 141.
7. Borione et al., *24th ICRC, Rome*, **2** (1995) 76.
8. Bird D.J. et al., *24th ICRC, Rome*, **3** (1995) 504.
9. Boothby K. et al., *24th ICRC, Rome*, **3** (1995) 444.
10. Aglietta M. et al. (EAS-TOP Coll.), *IL Nuovo Cimento*, **9C** (1986) 262.
11. Aharonian F. et al., *23th ICRC, Calgary*, **4** (1993) 291.
12. Miller T.C. et al., *24th ICRC, Rome*, **2** (1995) 768.

13. Allen G.E. et al., *24th ICRC, Rome*, **1** (1995) 942.
14. Aglietta M. et al. (EAS-TOP and MACRO Coll.), *25th ICRC, Durban*, 4 (1997) 41.
15. Danilova T.V. et al., *J. Phys. G.: Nucl. Part. Phys.* **20** (1994) 961.
16. M. Ambrosio et al., *J. Phys. G: Nucl. Part. Phys.* **23** (1997) 219.
17. Aglietta M. et al (EAS-TOP Coll), *25th ICRC, Durban*, 4 (1997) 13.
18. Aglietta M. et al (EAS-TOP Coll), *25th ICRC, Durban*, 4 (1997) 125.
19. R. Santonico & R. Cardarelli, *Nucl. Instr. and Meth.*, **187** (1981) 377.
20. R. Santonico & R. Cardarelli, *Nucl. Instr. and Meth.*, A**236** (1988) 20.
21. Knapp J., Heck D. 1995, Extensive Air Shower Simulation with CORSIKA: A User's Guide ( Version 4.50 ), Forschungszentrum Karlsruhe.
22. Aglietta M. et al. (EAS-TOP Coll.), *Nucl. Instr. and Meth.*, **A336** (1993) 310.
23. Aglietta M. et al. (EAS-TOP Coll.), *Proc. 22th ICRC, Dublin*, **HE 3.6.31** (1991) 708.
24. Kamata K. et al., *Supp. Prog. Theo. Phys.*, **6** (1958) 93.
25. G. Agnetta et al., *Nucl. Instr. and Meth.*, **A359** (1995) 596.
26. L. Colesanti et al., *Proc. RPC 1995, Pavia* (1995) 157.
27. A. Agnetta et al., *Nucl. Instr. and Meth.*, **A381** (1996) 64.
28. M. Ambrosio et al., *Nucl. Instr. and Meth.*, **A344** (1994) 350.

# The RPC trigger system of L3: history and current status

Gianpaolo Carlino *
*INFN, Sezione di Napoli.*
*Pad. 20 Mostra d' Oltremare*
*I-80125 Napoli, Italy*

March 12, 1998

ABSTRACT

The L3 RPC forward-backward trigger system consists of 192 RPC bigap modules of trapezoidal shape, and associated readout and trigger electronics. One half of the system has being in use since Spring 1994 while the whole system since Spring 1995. So the system has being working for 4 years of LEP runs. Some major changes have been introduced starting from 1995, like gas mixture and consequently High Voltage set points. History of the system will be presented together with the performances, reliability and RPC modules status

## 1. Introduction

The RPC trigger system of the L3 experiment at LEP [1] provides the specific trigger capability for the Forward–Backward (F/B) spectrometer [2]. This spectrometer has been installed because the higher energies of LEP2 require a more complete coverage for muon detection since the existing L3 barrel detector covers, with full resolution, only polar angle between 44° and 136°. The F/B detector adds muon accep-

*co authors : A. Aloisio, M.G. Alviggi, N. Cavallo, R de Asmundis, V. Innocente, L.Lista, P. Paolucci, S. Patricelli, D. Piccolo, C. Sciacca

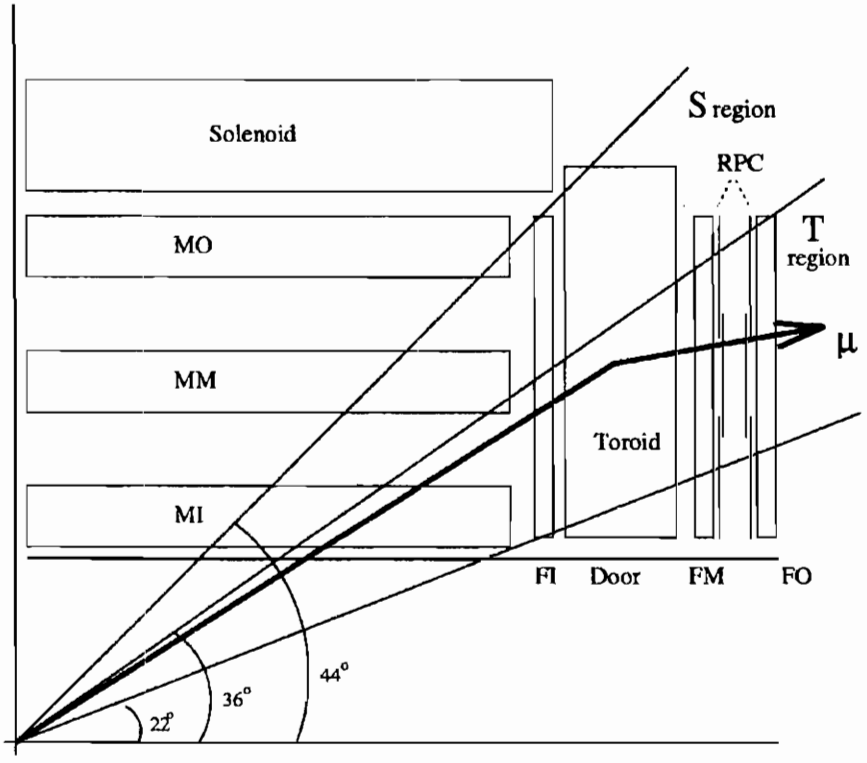


Figure 1: Side view of the F/B spectrometer of L3, with inner (FI), middle (FM), outer (FO) drift chambers and RPC's for triggering

tance in the polar angle range $44° \leq \theta \leq 22°$ (Fig. 1). The measured solid angle coverage is increased to 92% of $4\pi$.

The first half of the detector has been installed in the 1994 LEP winter shut–down. In the next year shut–down the installation has been completed.

The F/B detector consists of 96 precise drift chambers of trapezoidal shape mounted in three layers (FI, FM, FO) on either side of the two magnet doors which are toroidally magnetised. As figure 1 shows, there are two complementary regions, S and T; in each region a different method to measure the muon momenta is used.

In the S region the muons are analysed by measuring the helical bend in the 0.5 T solenoid field with the central drift chambers MI, MM and the new forward chamber FI. In the T region the deflection by the

1.24 T toroidal field in the 0.9 m iron doors is used to measure muon momenta.

## 2. The RPC system

Outside the magnet door, between the FM and FO drift chambers, two planes of Resistive Plate Counters (RPC) are placed in order to generate a fast level-1 trigger for particles coming from the interaction vertex. The use of RPCs in the F/B spectrometer is the first large scale application for chambers completely built and assembled by industry. The total system consists of 192 double-gap RPCs of trapezoidal shape, in three different sizes, covering a total area of more than 300 $m^2$.

A single-gap RPC is made of two bakelite plates (two mm thick, $\rho \simeq 2 \cdot 10^{11}$ $\Omega$ cm) kept at a constant distance of 2 mm by a 10 cm pitch grid of round PVC spacers ($\phi \simeq 1$ cm). The gap between the two bakelite plates has been filled, in the first years of operation, with a gas mixture of argon, isobutane and freon (58:38:4). In the beginning of the 1996 LEP operation the gas mixture has been modified replacing freon with $C_2H_2F_4$ (57:37:6). The outer surfaces of the bakelite plates are painted with a graphite solution in order to apply the high voltage.

A double-gap RPC (Fig. 2) consists in two of this units, staggered by 5 cm so that the spacers do not overlap. The readout plane, placed between the two single-gaps, is segmented in 32 strips with 3.1 cm pitch (6144 total readout electrodes).

Both sides of the readout electrodes are equipped with front-end electronic boards accepting inputs from 16 adjacent strips. Signals are amplified, discriminated ($\simeq$ 60 mV) and converted to shaped (200 ns) TTL differential outputs. A fast signal made on each board with the OR of 16 strips is also generated with a threefold fan–out: one output is fed to an 1875 LeCroy TDC for the measurement, one is used for monitoring purposes and the last one is used to generate a Super–OR signals for the 96 strips of each FM or FO planes.

The RPCs performances have been deeply studied in a dedicated test station in Naples laboratories with a drift chamber system for cosmic tracks reconstruction. All the counters, before being mounted in the L3 experiment, have been tested in a cosmic ray stand at CERN in order to check the performances of all electronics and to measure the efficiency plateau of each detector. The operating point of the chambers

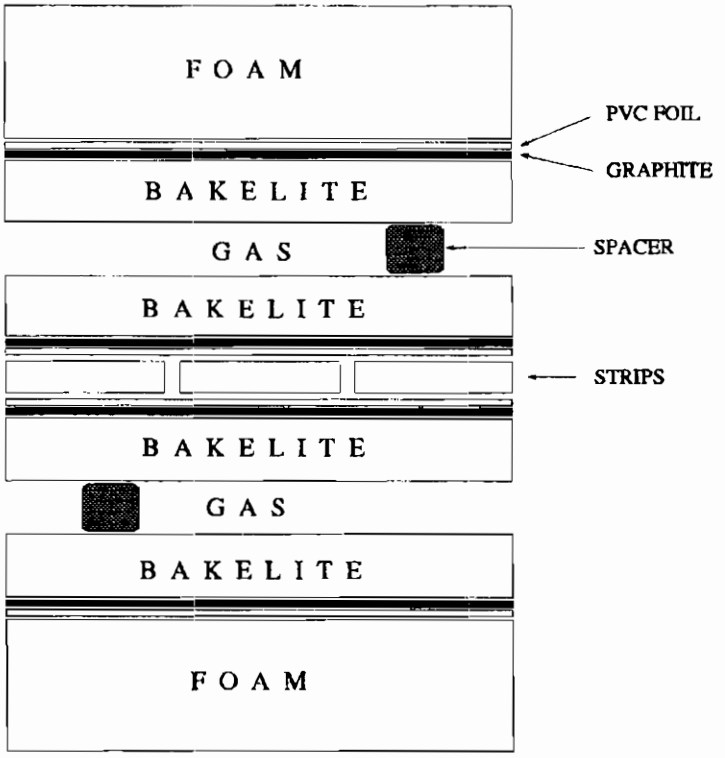


Figure 2: Cross section of a double gap RPC (not to scale)

has been chosen, with the old gas mixture, at about 7600 V. With the new mixture the operating point has been moved to about 7200 V.

## 3. Trigger generation

The RPC trigger system provides a fast identification of muons coming from the interaction vertex. The strips signals are sent to the Zero Suppressor modules [3] (96 inputs corresponding to one RPC plane) and their status is latched when a strobe pulse is present (Fig. 3). The input pattern is processed in a typical time of 1 $\mu s$ (2 strips fired) and the addresses of the hit strips are transferred to a Track Finder module.

The strobe pulse to the Zero Suppressor can be chosen between two possibilities: a signal synchronous with the beam crossing or a coincidence between the beam crossing and the coincidence between the two Super–OR signals (FM–FO planes) of any of the 32 "half octants". The second mode of operation is used in the bunch train mode LEP runs,

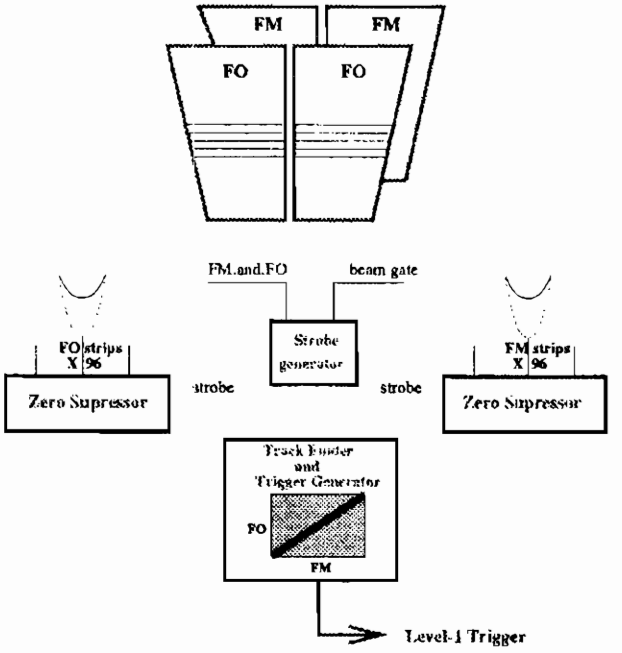


Figure 3: Trigger logic

when each beam consists of 4 trains with 2 to 4 bunchlets, in order to allow the bunchlet where the physical interaction occurs.

The Track Finder unit searches for coincidences in a 96 x 96 programmable Trigger Matrix filled cell by cell by all possible muon roads pointing to the interaction vertex. Each cell of the Trigger Matrix is mapped into one of the 96x96 locations of a four bit RAM. The pattern of the roads depends on the muon polar angle of production, momentum, magnetic deflection and multiple scattering in 1 $m$ thick iron door and has been simulated using Monte Carlo techniques (Fig. 4).

Maximum search time of the unit is $(200 + 50 \cdot N_i \cdot N_j)$ ns, where $N_i$ and $N_j$ are the numbers of hit strips in the first ('FM') and second ('FO') plane, while typical search time is 0.5 $\mu s$ (2 x 2 strips fired). Since the track finding starts only when the encoding is terminated, the typical total trigger time is 1.5 $\mu s$.

When a coincidence is found in the programmed pattern, a trigger signal is generated and together with the informations coming from other detectors produces a level-1 muon trigger for the Forward-Backward

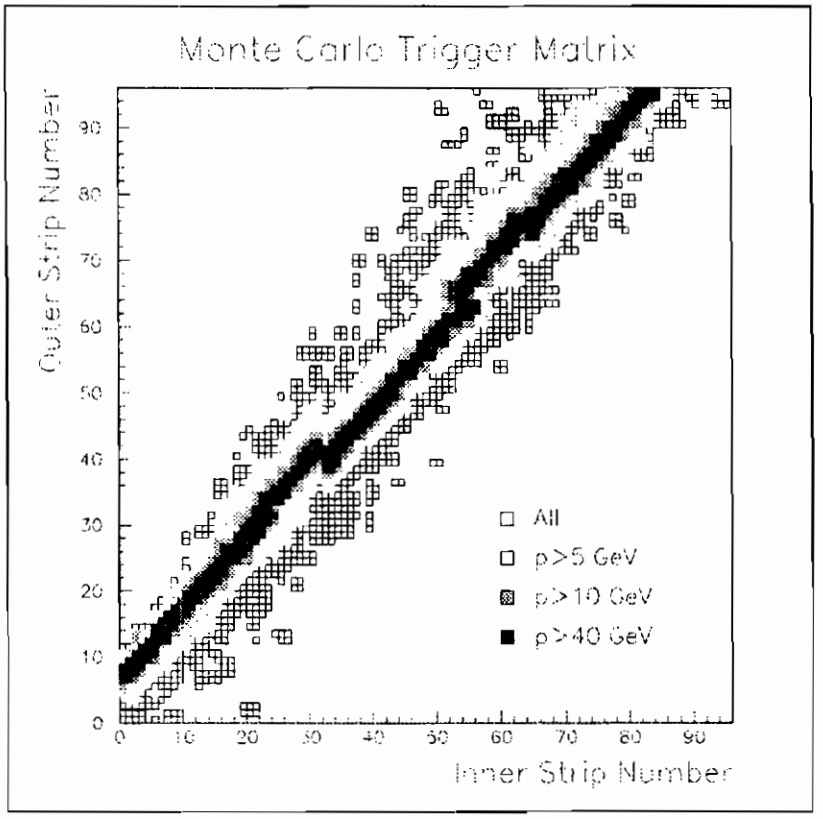


Figure 4: Monte Carlo simulation of the Trigger Matrix for muons with different momenta.

region.

The complete trigger system is composed of 16 sub-systems, each formed by two Zero Suppressor units and one Track Finder unit.

Data words containing the addresses of hit strips in the event are kept in a memory in the Track Finder modules and are transferred, via an ECL differential asynchronous bus, to Fastbus for data acquisition when a general L3 level-1 trigger is present.

## 4. Performances

The RPC performances have been studied using samples of dimuon $Z$ decays: $Z \rightarrow \mu^+\mu^-$, for which good track reconstruction in provided both in the L3 central tracking detector and in the muon spectrometer. Details can be found in [4].

From 1996, due to the higher LEP energies, the dimuon cross section is drastically reduced and we have also to use samples of single muon

events, with lower momenta.

### *4.1. Space Resolution and Detector Efficiency*

When a charged particle crosses an RPC, the discharge in the gas volume induces signals on the strips, in a region few millimetres wide. Discharges in the two separate gas volumes read by the same electronics and the slope of the particle track broaden this charge distribution. A signal can therefore be induced on more than one strip. At the reconstruction level adjacent strips are joined to form a 'cluster', described through the 'centre of gravity' of the fired strips, the multiplicity i.e. the number of fired strips and two times corresponding to the TDC readouts on both ends of the strips. The cluster multiplicity increases with the high voltage applied to the RPCs electrodes.

In 1994 and 1995 LEP runs we obtained an average cluster multiplicity of $\mu = 2.10 \pm 0.02$. With the new gas mixture the multiplicity increased to $\mu = 3.08 \pm 0.03$

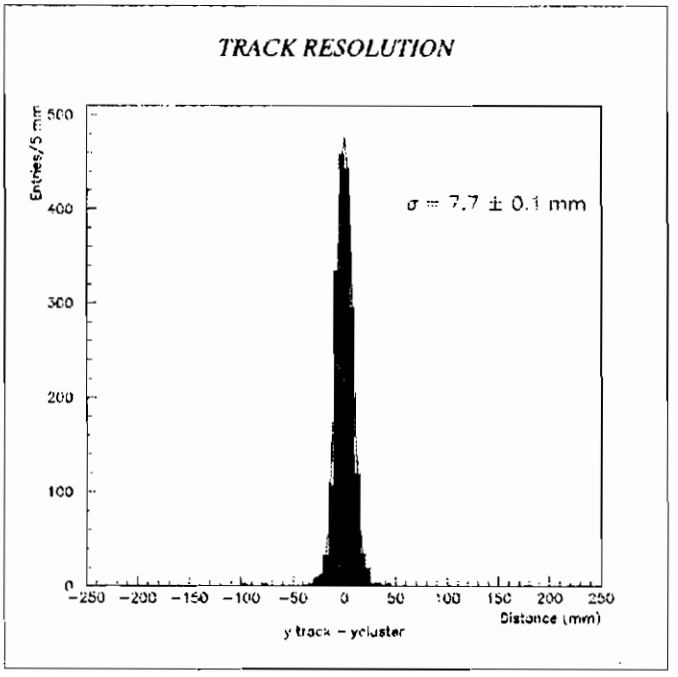


Figure 5: Space resolution of the RPCs.

Comparing the position (y-coordinate in fig. 5) of the cluster centroid with the expected position reconstructed using the F/B drift chambers, we obtain a global space resolution of $\sigma_y = 7.7 \pm 0.1$ mm.

In case of full detector efficiency, at least one cluster should be found for each FM-FO plane. It is also possible to find more than one cluster in a plane because of the overlap between the Middle RPC and the other two (Large and Small). Therefore, the number of events for which no cluster was found or in the FM or in the FO plane allows an estimate of the overall detector efficiency resulting in $\epsilon = 99.5 \pm 0.1$ %.

Both the space resolution and the detector efficiency have been measured in the years giving stable results.

### *4.2. Time Resolution and bunchlet identification*

To measure the event timing, the time measured by the RPCs needs to be corrected mainly for three effects:

- different cable lengths and electronic response among channels,
- time of flights of the muons,
- time of propagation of the induced signal along the strips.

The first effect is corrected using the T0 calibration. It consists of pulsing every timing readout channel (Fast-OR of 16 strips) on the front end boards and reading the obtained mean time, 'T0', at the end of the read-out chain i.e. on the TDCs. The obtained T0s can differ also of several ns and have to be subtracted to the data read time.

The time of flight of the muon can be calculated with enough precision using the impact point on the RPCs extrapolated from the chambers reconstructed tracks. To calculate the correction due to the propagation time of the induced signal along the strip we also use the information coming from the F/B tracks, since the RPCs cannot provide a precise enough measurement of this coordinate. The length of the strips goes from 96 to 216 cm corresponding to a time spread of $\sim$ 5-10 ns with a propagation velocity of $1/v_p = 4.8$ ns/m as estimated from data.

After having taken into account all these corrections the time resolutions we measured are: $\sigma = 2.16 \pm 0.05$ ns in 1994,$\sigma = 2.4 \pm 0.1$ ns in 1995 (Fig. 6) and $\sigma = 2.6 \pm 0.2$ ns in 1996. The increase of the time

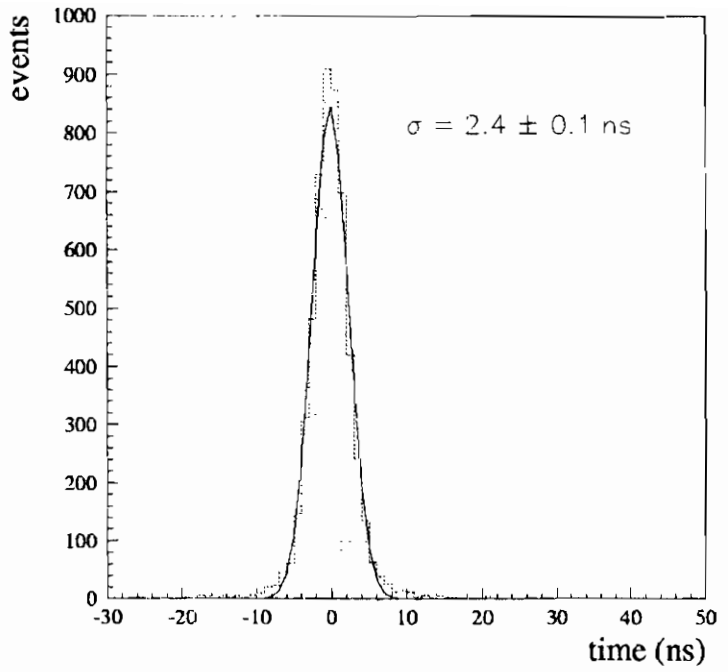


Figure 6: Time resolution of the RPCs.

resolution from 1995 is due to the widening of the TDC dynamical range because of the LEP bunch train mode operation.

The RPCs provide also the bunchlet identification, i.e. in which bunchlet the event occurred, recognising when the coincidence between the Beam Gate and the two Super OR (FM and FO planes) coincidence took place. This can of course be checked with respect to other bunchlet identifications given by different detectors and with respect to the time of the RPC event. Figure 7 shows the RPCs time distribution, without subtracting the inter-bunchlet time, versus the bunchlet number identified by the RPCs strobe logic. The RPCs bunchlet number identification is found to be always in agreement with the same determination made from other detectors.

*4.3. F/B Trigger efficiency*

The trigger system in the F/B region is based not only on RPCs but also on the F/B chambers and on two planes of endcap scintillators (on

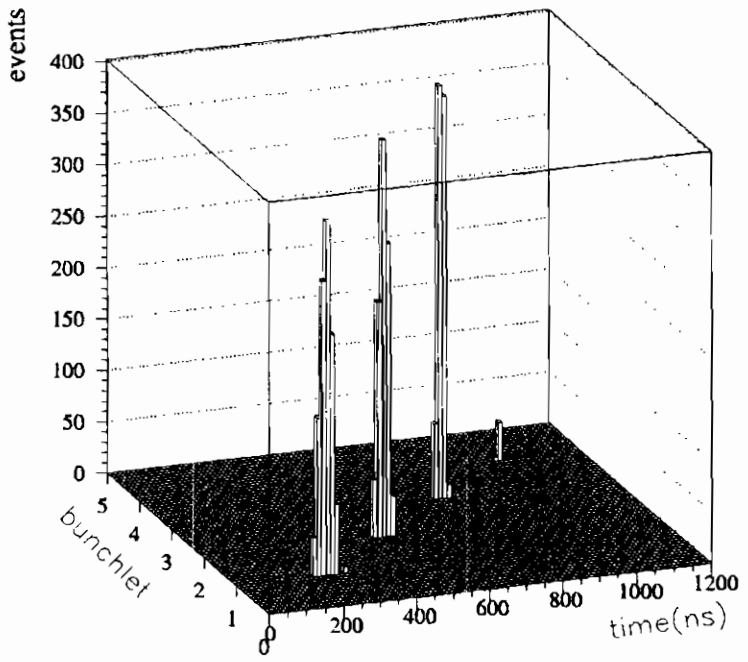


Figure 7: RPCs time distribution versus bunchlet number.

the Master and Slave sides) in order to have some redundancy and to reduce the rate due to the beam background outside the magnet, where the RPCs are placed. There is also an angular region in which the barrel spectrometer contributes to generate a trigger but we will not take it into account here.

The trigger logic is divided into a dimuon trigger and a single muon trigger, each of them made of three sub-triggers.

The dimuon trigger consists of:

- the RPC-RPC sub-trigger, requiring the presence in two opposite octants of the RPCs trigger;
- the RPC-ESCI/FB sub-trigger, requiring the RPCs trigger in one octant and the combined Endcap scintillators-F/B chambers trigger in the opposite octant;
- the ESCI/FB-ESCI/FB sub-trigger, requiring the presence in two opposite octants of the combined Endcap scintillators-F/B chambers trigger;

the two octants are considered 'opposite' within a tolerance of $\pm 1$ octant.

The single muon trigger consists of the following sub-triggers:

- the RPC-FB sub-trigger, requiring both the RPCs and the F/B chambers triggers in the same octant;
- the RPC-ESCI sub-trigger, requiring both the RPCs and the endcap scintillators triggers in the same octant;
- the FB-ESCI sub-trigger, requiring both the F/B chambers and the endcap scintillators triggers in the same octant.

The trigger efficiency has been studied using events with at least a trigger different from the FB trigger in such a way to allow an unbiased evaluation.

We obtain a dimuon trigger efficiency of $\epsilon_{dimuon} = 99.8 \pm 0.4$ % and a single muon trigger efficiency of $\epsilon_{single} = 98.7 \pm 0.5$ %.

## 5. Detector stability

The L3 RPC system is a large system both for number of units and total area covered and requires a continuous monitoring and maintenance. In particular the dark rate averaged on the whole system is used to monitor the noise of the detector. Figure 8 shows the singles behaviour of the RPCs in the 1994, 1995 and 1996 runs. The plot shows a reduction of the noise after the first year of operation.

## 6. Bibliography


1. B. Adeva *et al.* N.I.M. 298 (1990) 35.
2. A. Adams *et al.* N.I.M. A383 (1996) 342.
3. A.Aloïsio et al., IEEE Transactions on Nuclear Science VOl. 41, No. 1, February 1994.
4. G.Carlino *et al.*, Proc. of the "4th International Conference on Advanced Technology and Particle Physics", Como 1994; Nucl. Phys. B 44 (1995) 417-422;
   D.Piccolo *et al.*, Proc. of the "6th Pisa meeting on Advanced detectors", Isola d'Elba 94, Nucl. Instr. and Meth. A360 (1995)

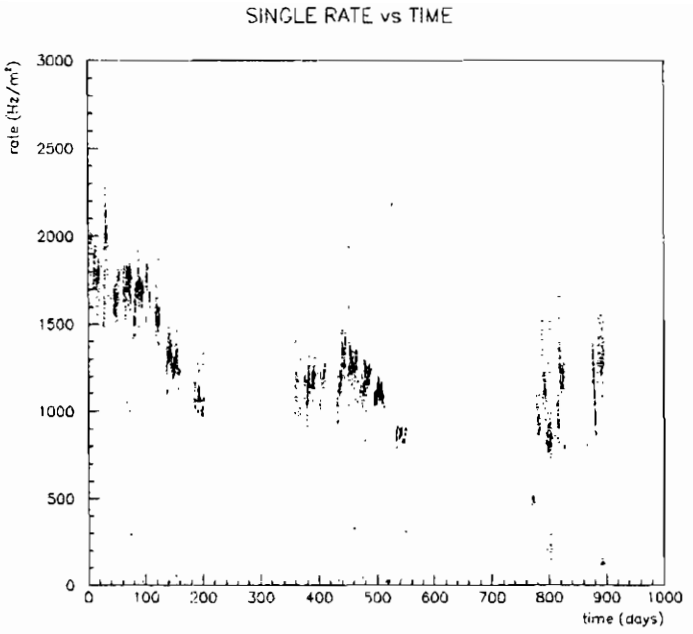


Figure 8: Averaged value of RPCs dark activity.

340-344;
P. Paolucci *et al.* Proc. of the "3rd International Workshop on the RPC in Particle Physics and Astrophysics", Rome 1993, Scientifica Acta, XI, (1995) 129;
R. de Asmundis *et al.* Proc. of the "3rd International Workshop on the RPC in Particle Physics and Astrophysics", Rome 1993, Scientifica Acta, XI, (1995) 139;
A. Aloisio *et al.*, N.I.M. A379 (1996) 552.

# Glass RPC Module for BELLE Endcap $K_L/\mu$ Detector

K. Abe[1], K. Abe[2], H. Hanada[2], H. Haitani[3], Y. Hoshi[3], Y. Inoue[5], N. Kawamura[6], I. Kitayama[5], T. Nagamine[2], M. Nakajima[2], T. Nakajima[2], E. Nakano[5], S. Narita[2], K. Neichi[4], H. Sakai[5], M. Sanpei[3], T. Takahashi[5], T. Takayama[2], Y. Teramoto[5], M. Ueki[2], M. Yamada[2], M. Yamaga[2], A. Yamaguchi[2], H. Yuta[6]

[1] *KEK, Tukuba 305 JAPAN*
[2] *Department of Physics, Tohoku University, Sendai 980-77 JAPAN*
[3] *Department of Applied Physics, Tohoku-Gakuin University, Tagajo 985 JAPAN*
[4] *Department of Commerce, Tohoku-Gakuin University, Sendai 980 JAPAN*
[5] *Department of Physics, Osaka City University, Osaka 558 JAPAN*
[6] *Department of Engineering, Aomori University, Aomori 030 JAPAN*

December 15, 1997

ABSTRACT

We constructed the glass RPCs for the subsystem of $K^0_L/\mu$ detection in BELLE experiment at KEK-B factory. The structure of a endcap RPC module with a double gap superlayer is described. The performance of the endcap glass RPCs in streamer mode is also described together with nonflammable gas mixture study.

## 1. Introduction

The BELLE experiment at KEK-B factory in Japan is designed for a study of CP violation and physics related with b-quark decay.[1] The

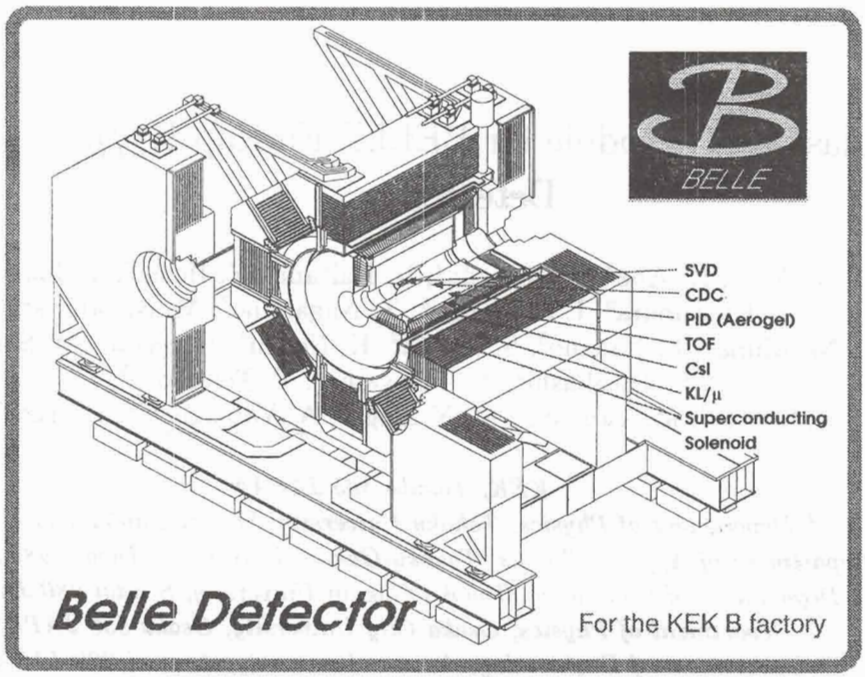


Fig. 1. Schematic of BELLE detector at KEK B factory.

KEK-B factory produces an order of $10^8$ $\Upsilon(4S)$ resonances decaying into $B\bar{B}$. As the accelerator provides an asymmetric collision of $8.0GeV$ electrons and $3.5GeV$ positrons, B and $\bar{B}$ are having a different energy, and it makes possible to measure the time difference of B lifetime for CP violation study.

The $B^0 \to J/\psi\ K^0$ is the most important decay mode for measuring one of unitarity triangle angles. Many of B decay channels involve muons in the final state. The $K^0_L$ and muon detection is an important part in this experiment.

Fig.1 shows the BELLE detector which consists of vertex detector, tracking chamber, aerogel PID, TOF, CsI calorimeter, and $K^0_L/\mu$ detector, so called KLM. The KLM subsystem is designed to detect neutral kaons and muons with momenta $\geq$ 600MeV/c.

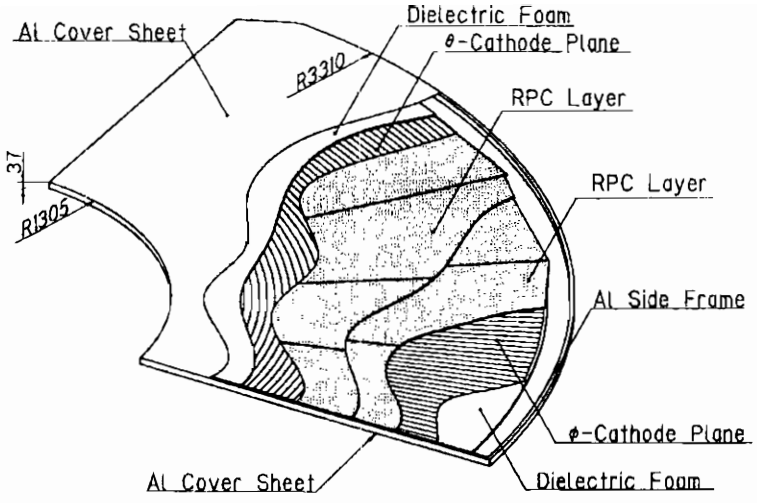


Fig. 2. Cutaway view of Endcap RPC module.

## 2. Endcap KLM Module

The KLM detector consists of an octagonal barrel and two endcaps. They are composed of sandwich of fifteen $47mm$ absorber iron plates and fourteen $44(\pm 5)mm$ instrumented gaps. The endcap KLM module has been designed to fit to the guaranteed $39mm$ gaps and to be a fun-shaped quadrant.[2] There are a total of 112 quadrant modules in the two endcaps. Glass RPC were identified as the most attractive counters for KLM. Though the glass RPCs died by water vapour of 200ppm or more in the RPC gas,[3] they have not failed over year in long-term test without water vapour in the gas. PVC/ABS RPCs without the linseed oil dropped to less than 50% efficiency in 20 weeks.

Fig.2 shows a cutaway view of endcap RPC module. Each endcap quadrant is designed as a double gap superlayer having two independent RPC layers (top and bottom). Each layer comprises five wedge-shaped RPCs: four large RPCs and one small one. The top and bottom RPCs are arranged to stagger each other to avoid overlapping of the dead regions near the RPC edge spacers. The RPC cathode readout of each module has an orthogonal pattern of theta($\theta$) and phi($\phi$) strips. The theta strip is $36mm$ wide and $2mm$ gap spacing, and its length varies from $2m$ at the inner radius to $5m$ at the outer radius. The phi strip

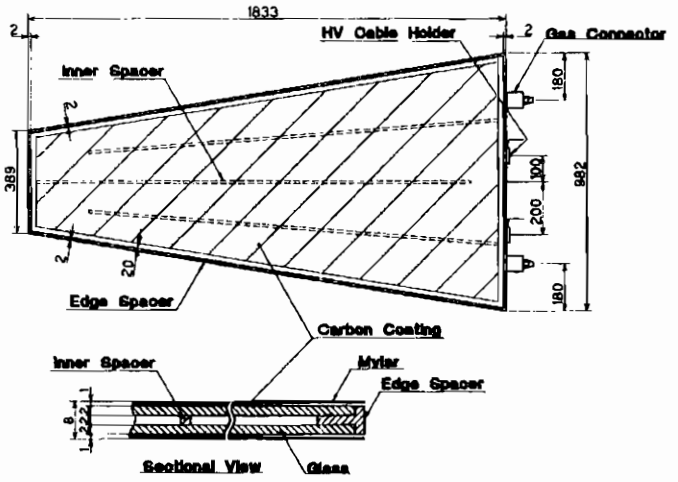


Fig. 3. Endcap RPC.

is $1.83m$ long, and wedging from $19mm$ to $47mm$ width and $2mm$ gap spacing. Each module has 48 theta strips and 96 phi strips. The total number of readout strips in two endcaps is 16128 channels. High voltage (HV) is distributed separately to each RPC, but gas flows serially through the top layer RPCs and through the bottom, separately.

Fig.3 shows a view of one large RPC in the endcap module. The material of RPC electrode is $2mm$ thick float glass with the volume resistivity of $\sim 5 \times 10^{12} \Omega cm$. instrumented The two glass electrodes are maintained the $2mm$ gas gap spacing by Noryl inner spacers and tee-shaped edge spacers, and glued by 3M DP460 epoxy. The tee-shaped spacer provides a good gas seal at the perimeter. The carbon tape, SHINTRON STR-9140 with a surface resistivity of $10^7 \sim 10^8 \Omega/sq$, is pasted on the outer glass surface for distributing the high voltage. The HV and gas connectors are placed at the outer edge of RPC to reduce the dead space at the inner radius of the module.

Fig.4 shows a schematic view of the superlayer structure of double gap RPC in the module. The HV is supplied to the same direction for two RPC layers. The readout cathode planes of theta and phi are located at the outer surface of the superlayer RPCs. The number of readout channels and the module thickness are made possible to reduce by this superlayer structure.

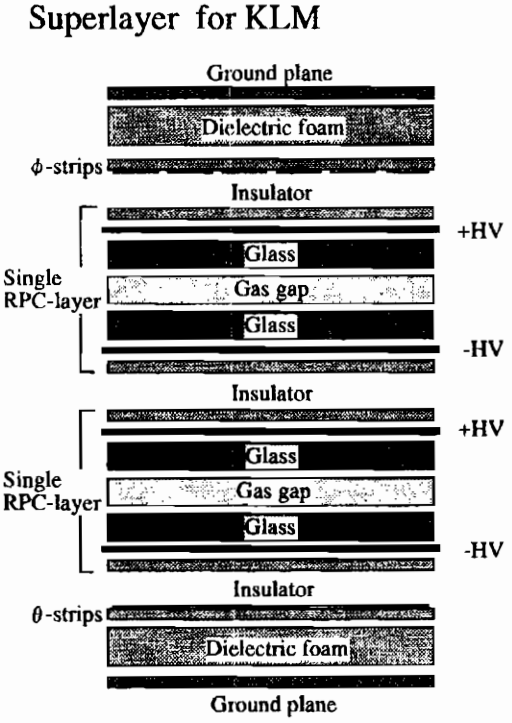


Fig. 4. Cross-section of superlayer RPC.

## 3. Endcap Module Test

A preliminary test of the modules is performed by using cosmic-rays. Fig.5 shows a schematic view of experimental setup and the readout electronics for the module test. A set of the eight modules is used at the standing position for the test, and three for a cosmic-ray trigger. The gas mixture used for the test consists of 25% Argon, 25% Butane-silver and 50% HFC134a, which we call it a standerd gas.[4] The readout boards consist of 6U VME modules. Signals from the cathode pickup strips fed into the discriminators of MAX908 comparators, then fed into LeCroy 1877 multi-hit TDCs. Hit channels are obtained by decoding the time delay of the signals from the common stop signal.

The module efficiency has been measured by using cosmic-ray tracks reconstructed by hits in all of trigger modules. Fig.6-a (-b) shows the

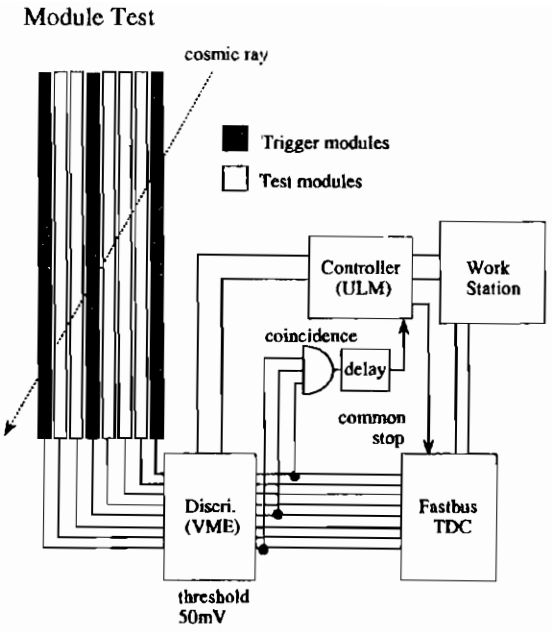


Fig. 5. Schematic of experimental setup and the readout electronics

efficiency plateau of 5 individual RPCs of top (bottom) single layer in a typical module. The efficiency of the RPC itself is better than 90% at an operating high voltage $4.3kV/mm$ and a discriminator threshold of $50mV$. The individual RPCs have almost same performance, so that we consider the module efficiency of the single layer or superlayer. Fig.6-c shows the efficiency plateau of top, bottom and superlayer. The efficiency at the plateau is more than 98% in superlayer operation.

The efficiency maps of the single layers and the superlayer of a typical module are shown in Fig.7-a, -b and -c. In Fig.7, the box display is proportional to the efficiency of higher than 80%, and its maximum size equals with a overlap size of $\theta$ and $\phi$ strip. The efficiency map shows to be uniform in the whole area of RPC module. The superlayer efficiency which is effectively the logical OR of two RPCs having $\geq$90% efficiency is consistently better than 98% for all modules constructed.

The readout strips are multi-hitted sometimes by cross-talk and/or afterpulse causing from a larger streamer discharge. The hit mulitiplicity of responding strips is crucially important for a reconstruction of $K_L^0/\mu$. Multiple hit strip distribution of the modules is shown in Fig.8-a and

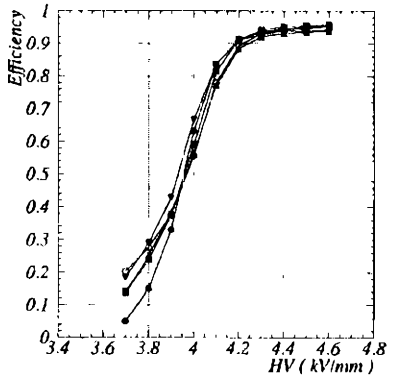


Fig.6-a. Efficiency plateau for 5 RPCs of top layer.

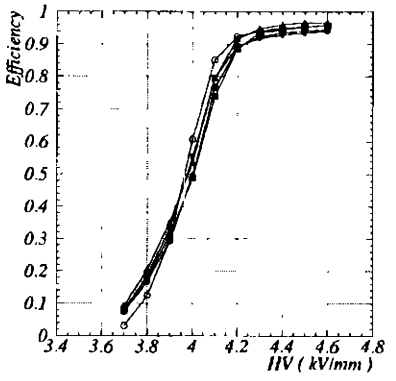


Fig.6-b. Efficiency plateu for 5 RPCs of bottom-layer.

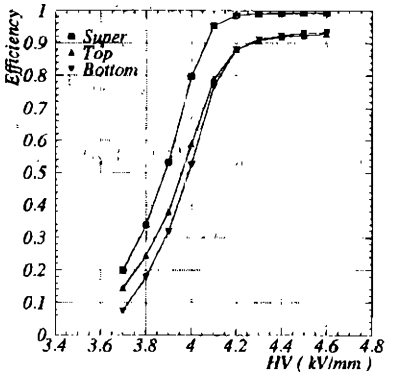


Fig.6-c. Efficiency plateau for top, bottom, superlayer.

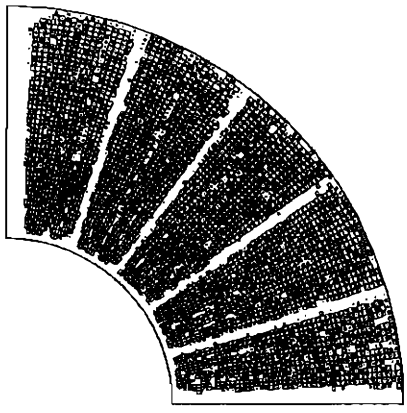

Fig.7-a. Efficiency map of top layer in endcap quadrant.

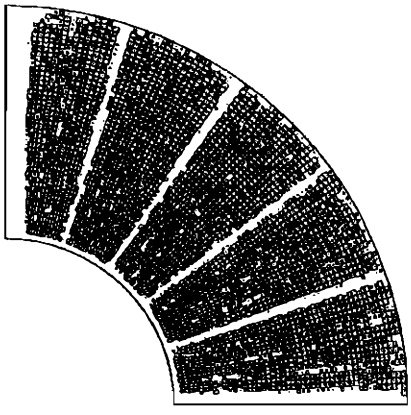

Fig.7-b. Efficiency map of bottom layer in endcap quadrant.

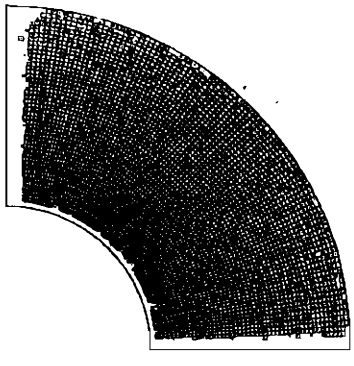

Fig.7-c. Efficiency map of superlayer in endcap quadrant.

-b for theta and phi cathode, respectively. The first, second, and third column from the left of Figs. show the distribution of an average hitted-strip in superlayer, top, and bottom layer operation. The first, second, third, and fourth row from the top show for all modules, modules with $10^7\Omega/sq$ HV conducting graphite, with $10^5\Omega/sq$, with $10^6\Omega/sq$. Multiple hit of strips depends on the surface resistivity of HV conducting material and the distance between the readout cathode and RPC. The hitted-strip multiplicity on the theta and phi readout cathode are 1.4 and 1.6 for single layer, and 2.5 and 3.1 for superlayer on the average, respectively. We have examined these multiplicities are reduced without any efficiency reduction by increasing the discriminator threshold to about 80-100$mV$. We need to optimaize the threshold in order to have good overall RPC efficiency and good tracking of $K^0_L/\mu$.

## 4. Nonflammable Gas Study

We have been using the gas mixture of 25% argon, 25% butane and 50% HFC-134a for testing RPC modules. The butane concentration of nonflamable limit is about 12% at the mixing ratio of Ar:HFC134a = 1:1.[5] To decrease the butane concentration might increase afterpulses, because the butane prevents the second discharges by absorbing photons. The gas mixture we studied is 16 combination of butane concentration of 4%, 8%, 12% and 25% and argon 20%, 25%, 30% and 35%, and HFC-134a is adjusted to be 100% in total. The RPC performance is compared at the plateau HV difined as a 200V/mm above the knee[6] of efficiency plateau curve.

Fig.9 shows the efficiency plateau curves for 16 gas mixtures: (a) butane 25%, (b) 12%, (c) 8% and (d)4% including Ar 20% to 35%. A plateau curve for gas mixture of Ar 25%, butane 25% and HFC-134a 50% is drawn by solid circles in Fig.9 for a comparison. Plateau HV decreases from $4.4kV/mm$ to $4.0kV/mm$ as increaseing Ar from 20% to 35% and does not depend on butane concentration.

Fig.10 shows (a) efficiency(%), (b) dark currnt($\mu A/m^2$), (c) single count rate($Hz/cm^2$) and (d) sigma($ns$) of TDC distribution at the plateau HV vs. Ar concentration of 20% to 35%, including butane 4% to 25%. The difference of RPC performance between framable and nonflammable gas mixture is very small. Nonflamable gas mixture of butane 8% is usable for the glass RPC.

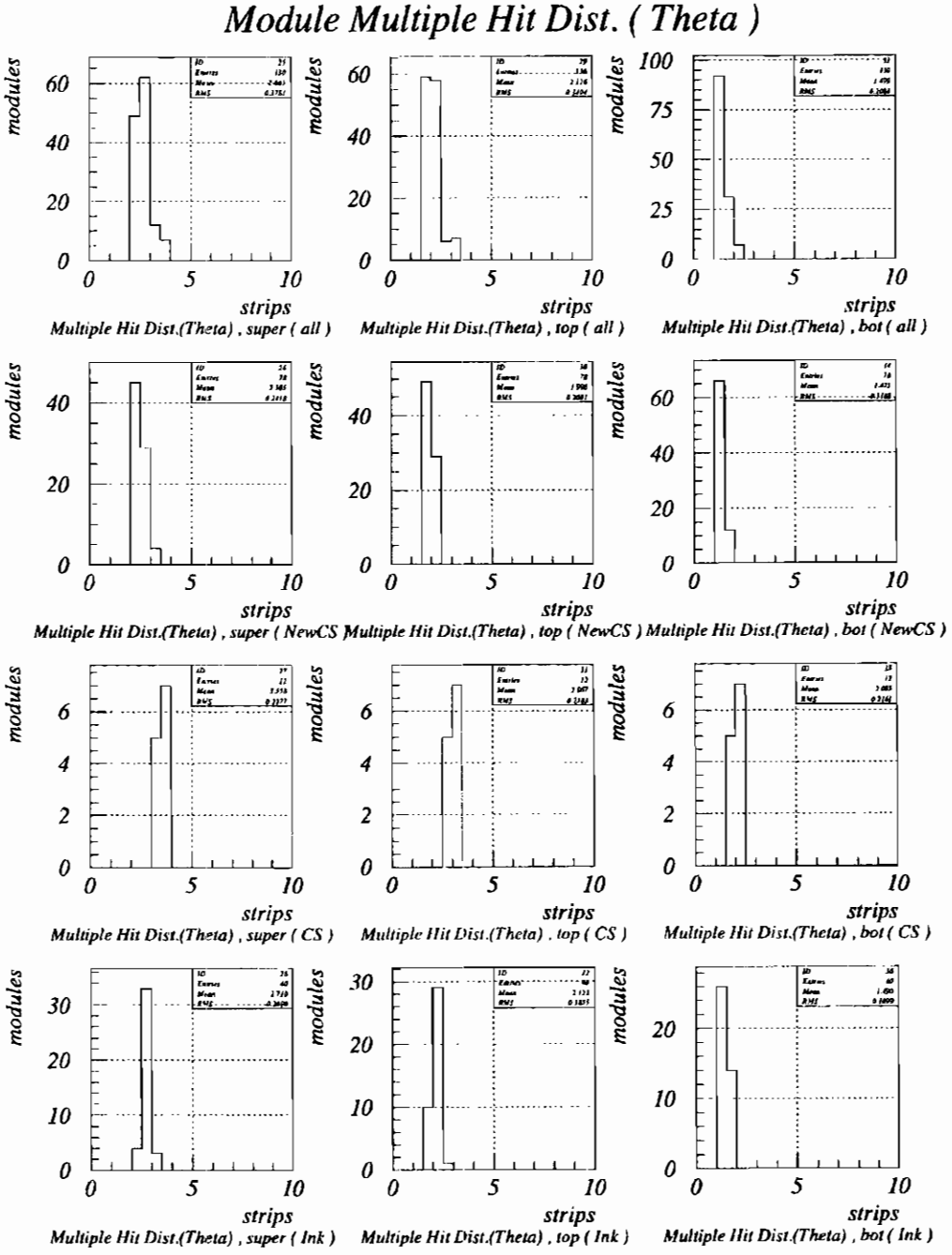


Fig.8-a. Multiple hit strip distribution for $\theta$ cathode readout.

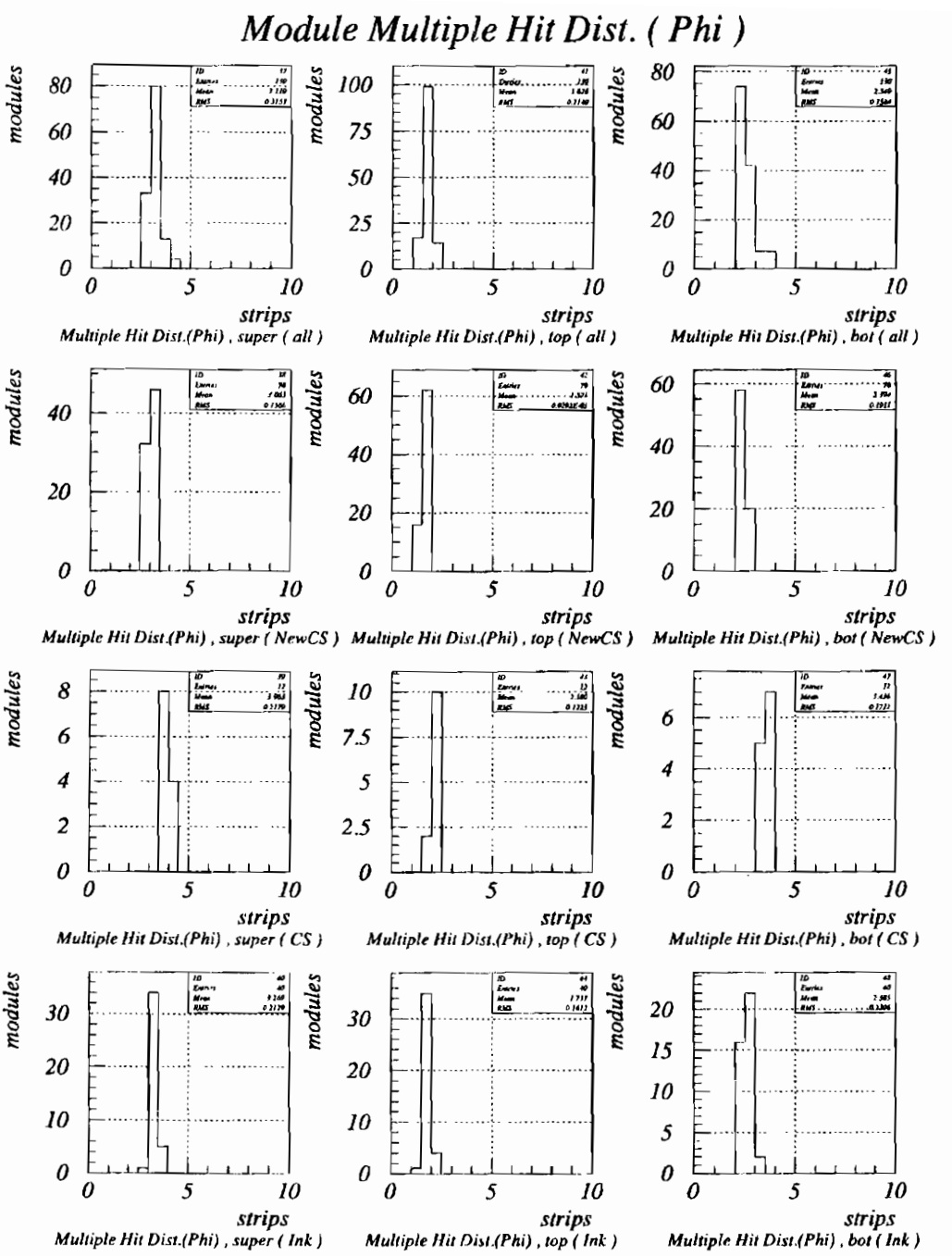


Fig.8-b. Multiple hit strip distribution for $\phi$ cathode readout.

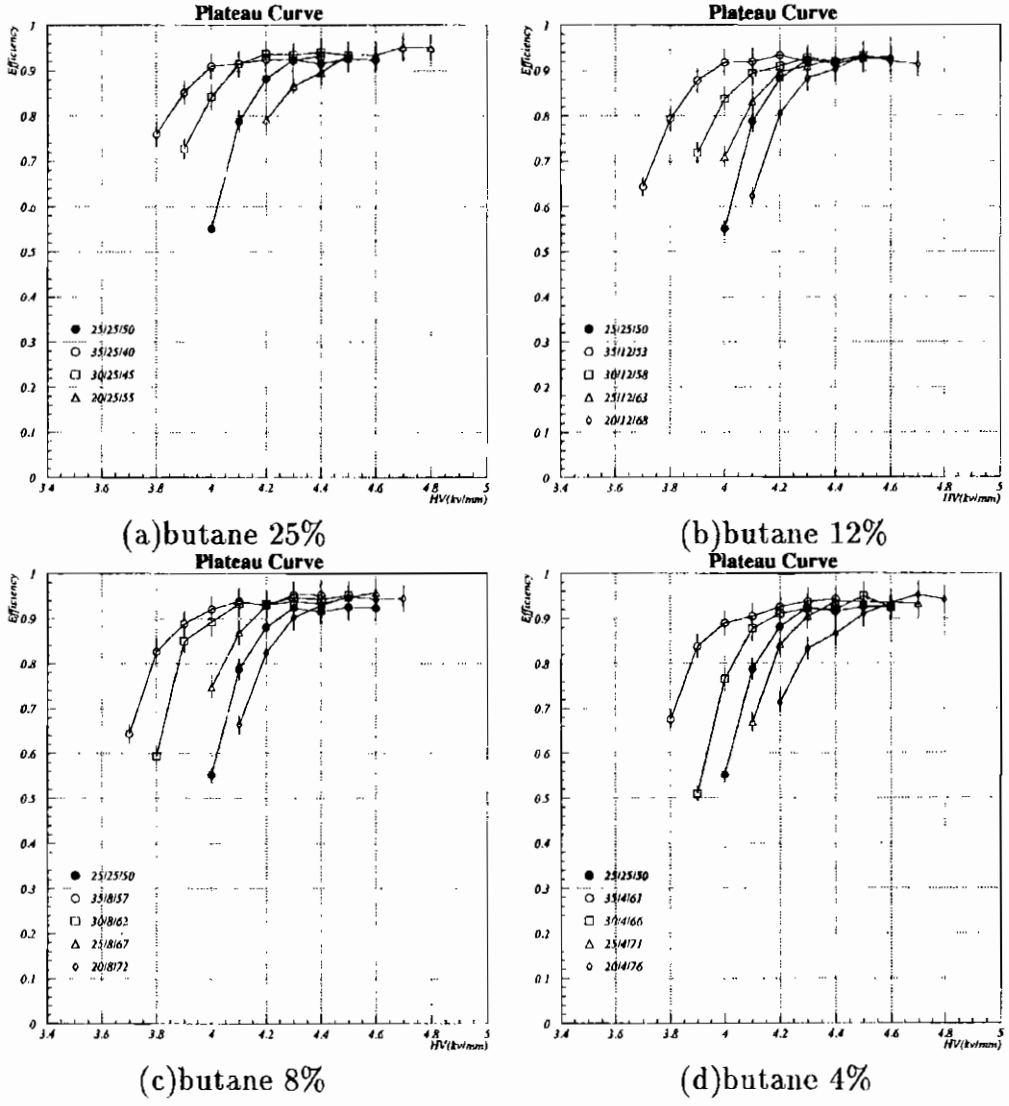


Fig.9. Plateau curves for 16 combinations of gas mixture: (a) butane 25%, (b) 12%, (c) 8% and (d) 4%. Solid circles show for standard gas (Ar 25/Butane 25/Freon 50).

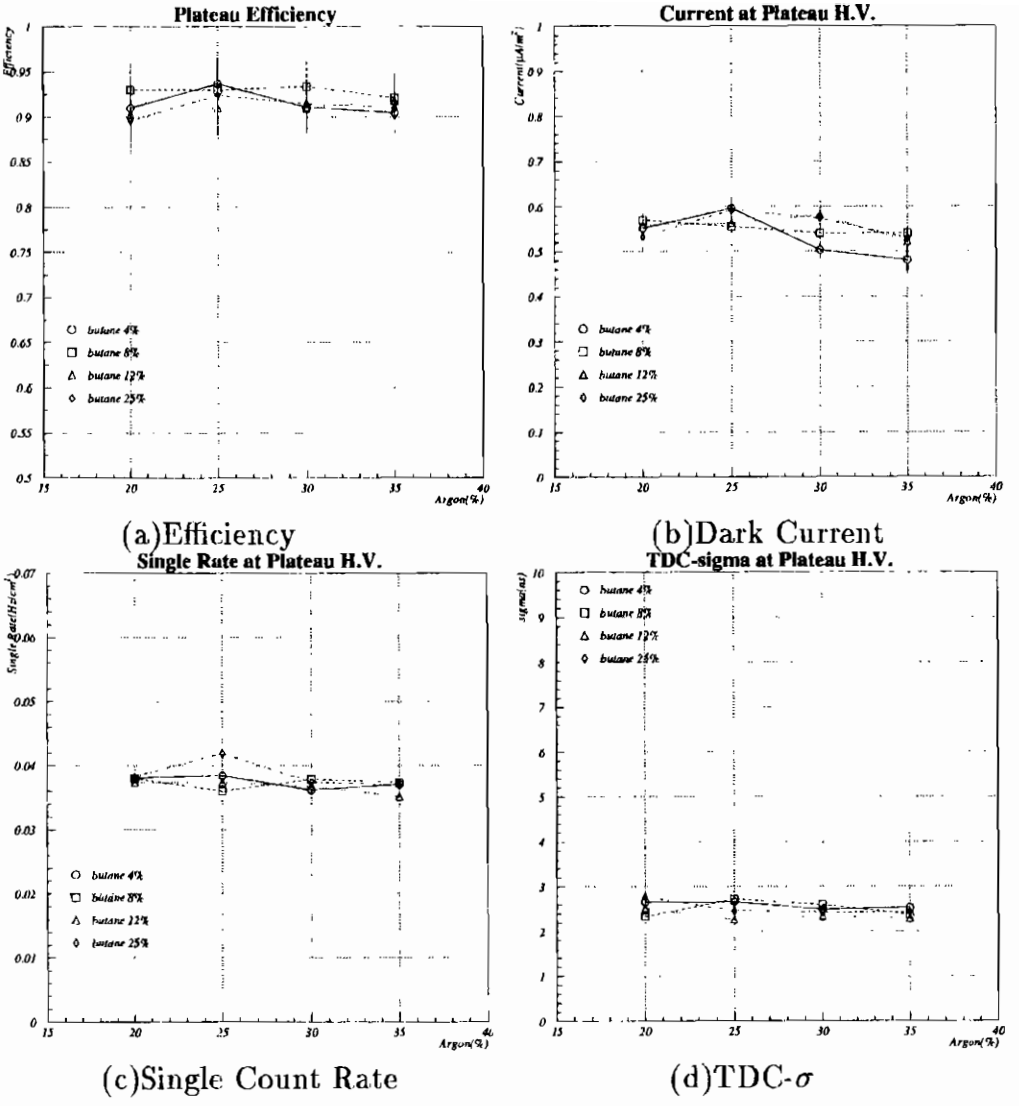


Fig.10. (a) efficiency, (b) dark Current, (c) single count rate, and (d) TDC-$\sigma$ at plateau HV vs. Ar 20% to 35%, including butane 4% to 25%.

## 5. Summary

No glass RPCs have failed in long-term test by means of streamer mode over 600 days so far. The long-term operation of glass RPCs is continuing. The cosmic ray test of the endcap glass RPC modules with the superlayer schem of double gap and double readout cathode has demonstrated the greater than 98% efficiency, the uniform efficiency map, the single rate of less than $1kHz/m^2$, and the average hitted-strip of about 3 at $50mV$ threshold in superlayer operation. The strip multiplicity reduces to less than 2 at 80-$100mV$ threshold without any efficiency reduction. HV conducting graphite with a resistivity of more than $\sim 10^7 \Omega/sq$ is better for less multiple hit of readout strips. Non-flammable gas mixture of 8% butane-silver is usable for glass RPCs. The 3/4 of endcap RPC modules has been installed in BELLE detector so far. BELLE physics run will start in early 1999.

## 6. Acknowledgements

This work is supported in part by a Grand in Aid of Scientific Research, Ministry of Education, Science and Culture, Japan. The KLM subsystem group consists of Princeton University, Virginia Polytechnic Institute and State University in USA and Aomori University, KEK, Osaka City University, Tohoku University and Tohoku Gakuin University in Japan.

## 7. References

1. M.T.Cheng et al.(BELLE collaboration), Technical Design Report, KEK Report 95-1, 1995.
2. M.T.Cheng et al.(BELLE collaboration), KEK Progress Report 96-1, 1996.
3. Y.Teramoto et al., Proc. of the RPC95, Pavia, Oct. 1996, 401.
4. M.Sanpei et al., IEEE Trans. Nucl. Sci. 44-3, 1997, 752.
5. Y.Hoshi et al., KEK BELLE Note No.185, 1997.
6. N.Morgan, Proc. of the RPC95, Pavia, Oct. 1996, 101.

# The IFR detector at BaBar experiment: general overview and construction status

Davide Piccolo *
*INFN, Sezione di Napoli.*
*Complesso Universitario di "Monte S. Angelo"*
*I-80126 Napoli, Italy*

April 7, 1998

ABSTRACT

**The IFR system is a RPC based detector used to identify muons and neutral hadrons in the BaBar experiment. Physical motivations, detector geometry and an overview of the operations since the chamber production up to the installation will be reported.**

co authors : A. Palano INFN Bari, Italy; A. Buzzo, R. Contri, G. Crosetti, M. Lo Vetere, M. Macrì R. Monge, M. Pallavicini, C. Patrignani, E. Robutti, A. Santroni Univ. Genova and INFN Genova, Italy; F. Anulli*, R. Baldini, R. De Sangro, D. Falciai, I. Peruzzi*, M. Piccolo, Z. Yu, A. Zallo, Lab. Naz. Frascati-INFN Frascati, Italy; G. Carlino, N. Cavallo, F. Fabozzi, C. Gatto, L.Lista, P. Paolucci, C. Sciacca, Univ. Napoli and INFN Napoli, Italy; R. Bionta, D. Wright, LLNL; H. Band, J. Johnson, Univ. Wisconsin; * Dip. Fisica, Univ. of Perugia and INFN-LNF;

## 1. Introduction

The BaBar experiment [1] is mainly dedicated to the study of the CP violation in B meson decays. It will be installed at the PEP II machine at SLAC. PEP II is a $e^+e^-$ asymmetric storage ring designed, after an initial luminosity of $3\times10^{33}\ cm^{-2}s^{-1}$, to reach $10^{34}\ cm^{-2}s^{-1}$.

Electron and positron beams will have different energies ($E_{e^-} = 9$ GeV, $E_{e^+} = 3.1$ GeV) producing a center of mass energy at the $\Upsilon(4S)$ resonance. The $\Upsilon(4s)$ resonance decay about 50 % of the times in $B^\circ\bar{B}^\circ$ mesons and by the analysis of the decays products of these particles is possible to clarify the origin of the CP violation.

Fundamental requirements to study the CP mechanism are:

- reconstruction of as many as possible exclusive final states;
- tagging of the B meson flavour;
- time ordering of the meson decays.

In order to fulfill such requirements, a large angular coverage detector has been designed. It's composed basically, going from the innermost up to the outermost, by a silicon vertex detector, fundamental to reconstruct the decay length of the B mesons, a cylindrical drift chamber, a CsI crystal based electromagnetic calorimeter, a particle identification device (DIRC) and an instrumented flux return (IFR) to identify muons and neutral hadrons.

The BaBar experiment will also allow significant progresses in understanding of the B, charm and $\tau$ physics.

## 2. IFR requirements

The IFR system [2] is the outermost detector of the BaBar experiment. It is mainly dedicated to the muons and neutral hadrons identification. Reconstruction of $K^\circ_L$ particle, for example, allows to tag the useful CP channel $B^\circ \rightarrow K^\circ_L J/\psi$.

Resistive Plate chamber (RPC), used as active detecors, are inserted inside the iron gaps of the magnetic flux return. RPCs have been choosen

for their reliability, flexibility to be produced in different shapes and possibility to cover large areas at a relative low cost. Good time resolution, efficiency and high readout granularity make this technology ideal for the IFR needs.

Muons must be identified and discriminated from the pion background. This can be achieved because of the different behavior of these two particles inside the IFR. Muons are penetrating particles and leave a narrow hit distribution along the track; pions on the contrary are absorbed after few layers and exibit a broader hit distribution.

Range measurements, hit distribution shapes, time measurements and other variables are analyzed and a maximum likelihood fit is performed to assign to each track a probability to be either a muon or a pion [3].

## 3. IFR geometry

The IFR system is composed of a barrel and two endcaps. The barrel is divided in six sectors and each endcap in two half-doors. RPC chambers are used as active detectors inside the gap between iron plates used to return the magnetic flux.

Each barrel sector is made of 19 RPC layers and 18 iron plates with graded segmentation. The width of iron plates varies between 2 cm, for the innermost plates, and 10 cm for the outermost. A thinner width for the innermost plates and a coarse segmentation for the outermost ones results in an optimized $\mu/\pi$ discrimination [3]. Table 1 summerizes the iron plates width.

| iron plate | width (cm) |
|---|---|
| 1÷ 9 | 2 |
| 10÷13 | 3 |
| 14÷16 | 5 |
| 17 | 10 |
| 18 | 10 |

Table 1: *Iron plate width in the barrel.*

A single IFR barrel layer is composed of 3 RPC modules of rectangular shape. The smaller side of each module is 125 cm, the other side span between 191 and 312 cm going from the innermost layer up to the

outermost one.

The total number of RPC chambers in the barrel subsystem is 342 (380 chambers produced including spares).

The outermost layer (layer 19) has a different geometry with respect to the previous layers because the iron plates used as mechanical supports for the IFR structure cover part of the useful area. For this reason the RPC modules used for the layer 19 have a special shape.

The endcap doors are composed of 18 RPC layers and 17 iron plates. Each half door layer is physically divided in three units (top, middle, bottom) and each unit in two RPC modules making the chamber. A single RPC module of the endcaps has a trapezoidal shape. Forward middle unit modules have a circular cut in the inner part near the beam pipe and backward middle unit modules exibit two linear cuts on one side in order to leave space for the beam pipe.

Fig. 1 shows a pictorial view of the IFR system.

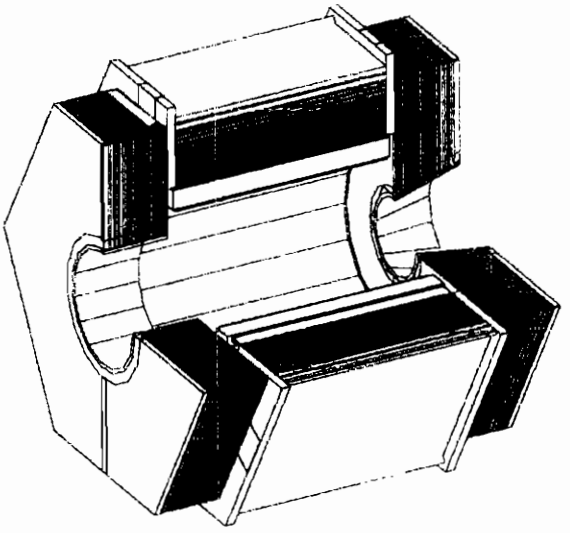


Figure 1: Pictrorial view of the IFR system

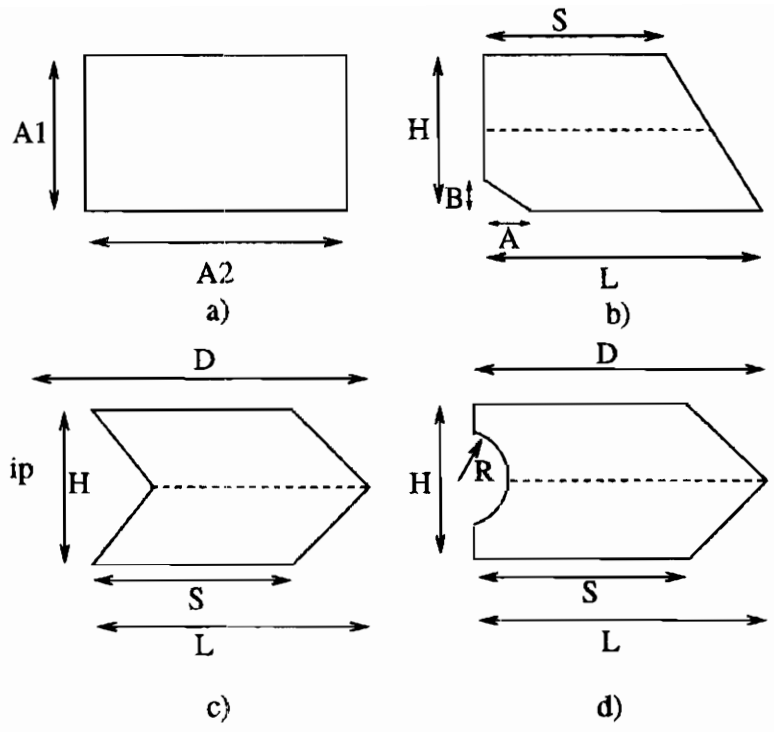


Figure 2: RPC modules geomtery: a) Barrel module, b) top-bottom endcap units, c) middle backward units, d) middle forward units.

Table 2, 3, 4 and 5 report barrel and endcap module sizes. Fig 2 shows the schematic shape of the modules.

More details about the IFR RPCs sizes can be found in [4].

## 4. RPC module design and strip readout

Apart from the shape, each RPC module has the same structure shown in fig. 3.

RPC modules are single gap detectors working in streamer mode, with a double strip plane readout.

The sensitive part of the RPC is a 2 mm wide gap filled with a gas mixture of Argon (48 %), $C_2H_2F_4$ (40 %), Iso-buthane (4 %). This mixture shows optimal performances [5] for what concerns efficiency, dark current, random noise rate and time resolution; at the same time

| layer | A1 | A2 |
|---|---|---|
| 1 | 1243 | 1908 |
| 2 | 1243 | 1966 |
| 3 | 1243 | 2029 |
| 4 | 1243 | 2093 |
| 5 | 1243 | 2156 |
| 6 | 1243 | 2220 |
| 7 | 1243 | 2283 |
| 8 | 1243 | 2347 |
| 9 | 1243 | 2410 |
| 10 | 1243 | 2474 |
| 11 | 1243 | 2549 |
| 12 | 1243 | 2620 |
| 13 | 1243 | 2692 |
| 14 | 1243 | 2763 |
| 15 | 1243 | 2858 |
| 16 | 1243 | 2953 |
| 17 | 1243 | 3017 |
| 18 | 1243 | 3124 |

Table 2: *Barrel modules sizes in mm for the 18 innermost layers.*

the gas mixture used into the RPCs is not flamable due to the low percentage of iso-buthane.

The RPC electrodes consist of high resistivity (about $10^{11}\ \Omega \times cm$) bakelite plates painted with a graphite film for ground and HV distribution.

Two pick-up strip planes are used to read-out the detector information. The pick-up electrodes are placed on both sides of the chamber with strips running in orthogonal directions, thus providing a bi-dimensional readout.

For each barrel layer 96 strips run parallely to the beam direction ($\phi$ strips) and 96 in the orthogonal direction (Z strips). The Z strips pitch is 2.8 cm constant for all barrel layers. The $\phi$ strips pitch span between 2 and 4 cm according to the layer position (tab: 6). This $\phi$ projective geometry preserve a constant number of strips for all layers.

Endcap layers are composed by three chambers (top, middle, bot-

| | Forward | | | | Backward | | | |
|---|---|---|---|---|---|---|---|---|
| layer | S | L | A | B | S | L | A | B |
| 1 | 1517 | 2587 | 0 | 0 | 1254 | 2323 | 0 | 0 |
| 2 | 1517 | 2587 | 0 | 0 | 1284 | 2353 | 0 | 0 |
| 3 | 1517 | 2587 | 0 | 0 | 1314 | 2383 | 0 | 0 |
| 4 | 1577 | 2647 | 0 | 0 | 1344 | 2413 | 0 | 0 |
| 5 | 1577 | 2647 | 0 | 0 | 1374 | 2443 | 0 | 0 |
| 6 | 1577 | 2647 | 0 | 0 | 1404 | 2473 | 0 | 0 |
| 7 | 1577 | 2647 | 0 | 0 | 1434 | 2503 | 26 | 6 |
| 8 | 1577 | 2647 | 0 | 0 | 1464 | 2533 | 57 | 12 |
| 9 | 1577 | 2647 | 0 | 0 | 1494 | 2563 | 90 | 18 |
| 10 | 1577 | 2647 | 0 | 0 | 1517 | 2587 | 117 | 22 |
| 11 | 1577 | 2647 | 0 | 0 | 1517 | 2587 | 117 | 22 |
| 12 | 1577 | 2647 | 0 | 0 | 1517 | 2587 | 117 | 22 |
| 13 | 1577 | 2647 | 0 | 0 | 1517 | 2587 | 117 | 22 |
| 14 | 1577 | 2647 | 0 | 0 | 1517 | 2587 | 117 | 22 |
| 15 | 1577 | 2647 | 0 | 0 | 1517 | 2587 | 117 | 22 |
| 16 | 1577 | 2647 | 142 | 19 | 1517 | 2587 | 117 | 22 |
| 17 | 1577 | 3124 | 272 | 50 | 1517 | 2587 | 117 | 22 |
| 18 | 1577 | 2647 | 707 | 232 | 1517 | 2587 | 413 | 121 |

Table 3: *Endcap top units sizes in mm.*

| | Forward | | | | Backward | | |
|---|---|---|---|---|---|---|---|
| layer | R | D | L | S | D | L | S |
| 1 | 738 | 3295 | 3165 | 2630 | 3295 | 2844 | 2309 |
| 2 | 754 | 3295 | 3165 | 2630 | 3295 | 2844 | 2309 |
| 3 | 770 | 3295 | 3165 | 2630 | 3295 | 2844 | 2309 |
| 4 | 786 | 3295 | 3225 | 2690 | 3295 | 2844 | 2309 |
| 5 | 802 | 3295 | 3225 | 2690 | 3295 | 2844 | 2309 |
| 6 | 818 | 3295 | 3225 | 2690 | 3295 | 2844 | 2309 |
| 7 | 834 | 3295 | 3225 | 2690 | 3295 | 2844 | 2309 |
| 8 | 850 | 3295 | 3225 | 2690 | 3295 | 2844 | 2309 |
| 9 | 867 | 3295 | 3225 | 2690 | 3295 | 2844 | 2309 |
| 10 | 886 | 3295 | 3225 | 2690 | 3295 | 2844 | 2309 |
| 11 | 905 | 3295 | 3225 | 2690 | 3295 | 2844 | 2309 |
| 12 | 924 | 3295 | 3225 | 2690 | 3295 | 2844 | 2309 |
| 13 | 945 | 3295 | 3106 | 2572 | 3295 | 2844 | 2309 |
| 14 | 970 | 3295 | 3006 | 2472 | 3295 | 2844 | 2309 |
| 15 | 996 | 3295 | 2928 | 2394 | 3295 | 2844 | 2309 |
| 16 | 1021 | 3295 | 2865 | 2330 | 3295 | 2844 | 2309 |
| 17 | 1047 | 3295 | 2806 | 2272 | 3295 | 2844 | 2309 |
| 18 | 1194 | 3295 | 2541 | 2007 | 3295 | 2676 | 2141 |

Table 4: *Endcap middle units sizes in mm.*

tom); for each of them 64 strips of 2.8 cm pitch run in the horizontal direction. Vertical strips have a pitch of 3.8 cm and the number of strips is a function both of the chamber and of the layer. Bottom, top and middle backward chambers have 64 strips regardless of the layer position. Middle forward chambers have between 55 and 80 strips according to table 6.

## 5. Front End electronics

The Front-End electronic Card (FEC) [6] collects signals coming from 16 RPC strips and generates two fast-or ECL signals and one serial output concerning the status of the 16 strips at the arrival of a trigger signal.

| | Forward | | | | Backward | | | |
|---|---|---|---|---|---|---|---|---|
| layer | S | L | A | B | S | L | A | B |
| 1 | 1577 | 2647 | 0 | 0 | 1517 | 2587 | 117 | 22 |
| 2 | 1577 | 2647 | 0 | 0 | 1517 | 2587 | 117 | 22 |
| 3 | 1577 | 2647 | 0 | 0 | 1517 | 2587 | 117 | 22 |
| 4 | 1577 | 2647 | 0 | 0 | 1517 | 2587 | 117 | 22 |
| 5 | 1577 | 2647 | 0 | 0 | 1517 | 2587 | 117 | 22 |
| 6 | 1577 | 2647 | 0 | 0 | 1517 | 2587 | 117 | 22 |
| 7 | 1577 | 2647 | 0 | 0 | 1517 | 2587 | 117 | 22 |
| 8 | 1577 | 2647 | 0 | 0 | 1517 | 2587 | 117 | 22 |
| 9 | 1577 | 2647 | 0 | 0 | 1517 | 2587 | 117 | 22 |
| 10 | 1577 | 2647 | 0 | 0 | 1517 | 2587 | 117 | 22 |
| 11 | 1577 | 2647 | 0 | 0 | 1517 | 2587 | 117 | 22 |
| 12 | 1577 | 2647 | 0 | 0 | 1517 | 2587 | 117 | 22 |
| 13 | 1577 | 2647 | 0 | 0 | 1517 | 2587 | 117 | 22 |
| 14 | 1577 | 2647 | 0 | 0 | 1517 | 2587 | 117 | 22 |
| 15 | 1577 | 2647 | 0 | 0 | 1517 | 2587 | 117 | 22 |
| 16 | 1577 | 2647 | 142 | 19 | 1517 | 2587 | 117 | 22 |
| 17 | 1577 | 3124 | 272 | 50 | 1517 | 2587 | 117 | 22 |
| 18 | 1577 | 2647 | 707 | 232 | 1517 | 2587 | 413 | 121 |

Table 5: *Endcap bottom units sizes in mm.*

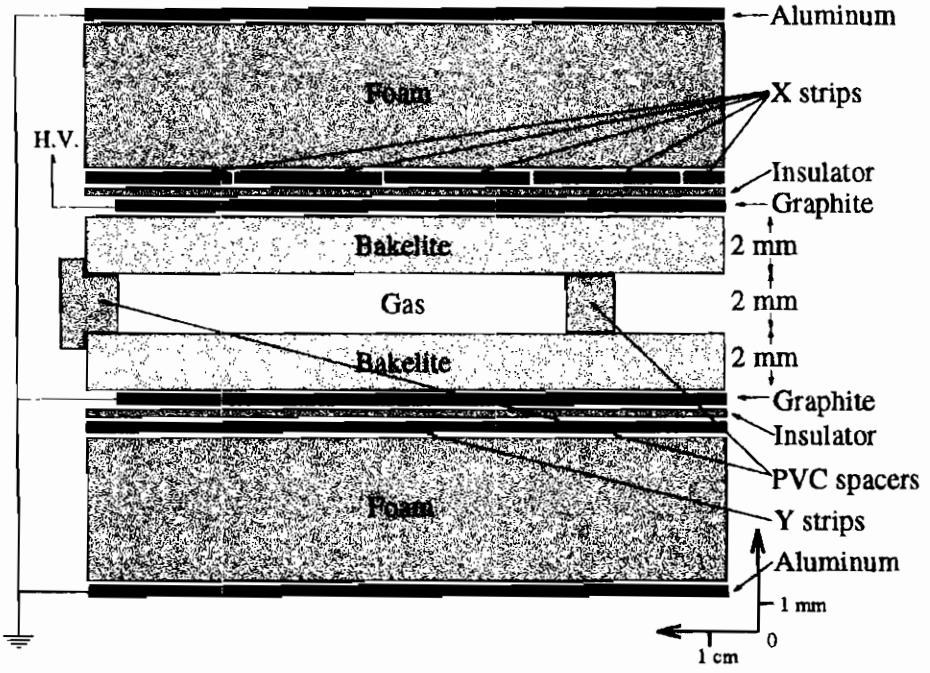


Figure 3: RPC design

The input stage is connected directly to the strip and continously receives and discriminates signals. Whenever a trigger arrives, a snapshot of the 16 strips is taken and two fast-or signals are provided.

One of the fast-or signals is used for time measurement with TDCs, the other one is used to monitor the RPC performances through the counting rate measurement or for trigger purpose.

Serial output is sent to the IFR FIFO board (IFB) used for the front-end electronic readout [7].

Signals coming from strips placed on opposite side of the chamber have opposite polarity, so two different cards, with dedicated input stage, have been designed for both negative and positive signals.

Alternate strips are connected to the same electronic card, this way if one FEC fails, efficiency could be partially recovered for events with multiplicity greater than one by simply increasing a little bit the H.V of the chamber.

Part of the FECs are physically located inside the iron gap attached on the RPC chambers, and part in *ad hoc* crates installed outside the IFR detector.

| layer | $\phi$ strip pitch (mm) | middle forward strips |
|---|---|---|
| 1 | 19.7 | 80 |
| 2 | 20.3 | 80 |
| 3 | 21.0 | 80 |
| 4 | 21.7 | 79 |
| 5 | 22.3 | 78 |
| 6 | 23.0 | 78 |
| 7 | 23.6 | 77 |
| 8 | 24.3 | 77 |
| 9 | 25.0 | 78 |
| 10 | 25.6 | 78 |
| 11 | 26.4 | 78 |
| 12 | 27.1 | 75 |
| 13 | 27.9 | 74 |
| 14 | 28.6 | 68 |
| 15 | 29.6 | 68 |
| 16 | 30.6 | 68 |
| 17 | 31.3 | 68 |
| 18 | 32.4 | 55 |
| 19 | 33.0 | |
| 19(S2/S4) | 35.9 | |

Table 6: *$\phi$ strips pitch and number of vertical strips in middle forward units as a function of the layer position. Layer 19 sector 2 and 4 (S2/S4) have only 88 strips of pitch 35.9 mm.*

Total number of FECs used in the whole IFR system is about 3000.

## 6. RPC production, assembling and test

The IFR system is a very large area detector so a big effort has been realized in terms of RPC production, assembling and test.

The total number of RPC modules produced has been 892 (including spares) for a total area of about 2300 $m^2$. About 45000 electronic channels are handled by about 3000 FECs.

RPC modules are produced at the General Tecnica factory. The first step of the production is the measurement of the bakelite resistivity.

Only plates with a value between 1 and $6\times10^{11}$ $\Omega\times$ cm are used for RPC assembling. The maximum size of the chambers that can be actually produced is $3.2 \times 1.3\ m^2$.

Strips planes are also produced at the same factory and sent in Napoli for cabling.

Two test stations have been prepared to check RPC integrity and performances. The first of them is located in Frascati. Two large area RPCs are used for trigger and up to 4 boxes, each with 12 RPC modules, can be put under test at the same time.

At the arrival in Frascati each module is filled with gas and a little overpressure is produced for the leak test of the chamber and to check the integrity of the spacers that guarantee the fixed distance between the backelite electrodes. If some of the spacers results not perfectly glued the module will exibit a longer time to reach the standard overpressure because it swell in the region of the damage.

Each module is then assembled with longitudinal strips (Z strips for barrel modules, and horizontal for the endcap units) and is ready to be tested with cosmic rays.

Main measurements performed are the following:

- single rate and dark current vs High Voltage;
- efficiency vs High Voltage;
- local efficiency with reconstructed cosmic tracks;
- time resolution.

Performances results can be found in the reference [5].

Accepted RPCs are successively supplied to SLAC where different modules of the same layer (or unit for the endcaps) are joined together and transversal strips ($\phi$ strips for barrel, vertical for endcaps) are glued on the free side of the layer.

After a new test with cosmic rays the chambers are inserted into the iron gaps and mounted on the detector.

## 7. Conclusions

342 Barrel and 432 Endcap RPC modules have been succesfully installed inside the IFR iron gaps. All the front-end electronic cards have

been produced and part of them mounted on the chambers (remaining part of the FECs will be inserted in crates outside the IFR). DAQ electronics will be installed by march 1998 and the IFR system will be ready to be tested with cosmic rays.

Starting of the PEPII operations is expected at the begin of 1999.

## 8. Acknowledgments

We wish to exprime our acknowledgments to P. Parascandolo, L. Parascandolo, S. Minutoli, E. Masone, M. Negri, L. D'Aniello, L. Rocco, F. Cassese, B. D'Aquino and G. Barisone for their important contributions in electronic design and constant help during all the phases of RPCs construction and installation.

## 9. Bibliography

1. BaBar Technical Design Report, BaBar Collaboration, SLAC Report SLAC-R-95-457, march 1995;
2. The muon and $K_L$ Detector for the BaBar Experiment: Physics Requirements, Final Design and Start of Construction, Nucl. Physics B (Proc. Suppl.) 61B (1998) 244-249
3. L.Lista, BaBar-Note 413/98;
4. S. Calcaterra, BaBar Note 309/97
5. S. Calcaterra *et al.*, theese proceedings;
6. Electronic Design of the Front-End for the RPC Muon Detector at BaBar, Nucl.Physics B (Proc. Suppl.) 61B (1998) 545-550, N.Cavallo, F.Fabozzi, P.Paolucci, L.Parascandolo, P.Parascandolo, D.Piccolo;
7. Design of a high throughput FIFO Board, F.Fabozzi, P.Parascandolo.

# Electromagnetic Shower Measurements with RPCs

Douglas Wright*
*Lawrence Livermore National Laboratory,*
*PO Box 808, Livermore, CA 94550, USA*

ABSTRACT

**RPCs can work as well as traditional gas ionization type detectors in a sampling electromagnetic shower calorimeter with iron absorbers. Test beam data from SLAC show good linear response and energy resolution from small-gap RPCs operated in the spark mode in electromagnetic showers.**

## 1. Introduction

The single-particle tracking capability of resistive plate chambers (RPCs) is well known; however, the purpose of this test-beam effort was to determine if RPCs could be used in a sampling iron calorimeter to measure electromagnetic showers. The number of energetic electrons produced in an electromagnetic shower is a good measure of the energy deposited in the shower. If the charge response of an RPC operating in the spark mode is sufficiently narrow, and the occlusion region is not larger than the average spacing of the electrons in a shower, then the sum of the charge produced in the RPC should be proportional to the number of electrons in the shower.

This new application of RPC technology was motivated by our proposal to use RPCs as a robust and inexpensive detector for MINOS, a long-baseline neutrino oscillation experiment at Fermilab. The MINOS

*Ed Hartouni, Richard Bionta, Harlan Olson, Mike Wang

detector [1] must simultaneously detect single muons, electromagnetic and hadronic showers in the GeV energy regime. The detector is a monolithic structure of alternating iron plates and active detector elements with a total active area of approximately 24,000 $m^2$. The iron acts both as a target for the accelerator-produced neutrino beam and as absorber planes for the subsequent particle interactions. Since MINOS is underground (shielded from cosmic rays) and the event rate from the neutrino source is low ($\sim$ 20k events per year), it is ideally suited for conventional RPC technology operating in the spark mode.

In order to measure the calorimetric response of an RPC we generated electromagnetic showers with a high energy electron beam from the SLAC Final Focus Test Beam (FFTB) incident on an iron plate. We placed an RPC and scintillator counter behind the iron plate and measured the response of both detectors simultaneously.

## 2. Chamber construction

The RPC used in the test beam (see the photograph in Figure 1) was of a typical design developed at Lawrence Livermore National Laboratory (LLNL) [2,3]. The detector employed an ABS plastic doped with a conducting polymer as the resistive electrode. The high voltage was applied to a graphite coating on the outside of each ABS electrode. The detector package was insulated with a 0.8 mm layer of resin-coated fiberglass (FR4). The active area of the RPC was approximately 30 cm x 30 cm and the gas gap was 2 mm. Since the insulating plane, ABS electrodes, and adhesive are transparent, one can see the graphite coating and button location (absence of graphite) in the photo. The visible striations are an artifact from the strips of transfer adhesive that bonds the insulating plane to the graphite-coated ABS. The gas lines and HV connector are visible at the top and right sides in the photo. The read-out strips were contained on a small board that was attached to one side of the RPC. A copper ground plane was attached to the other side.

## 3. Chamber performance with cosmic rays

In addition to the test beam experiment, the performance of the chamber was measured with cosmic rays. All tests were conducted with a gas mixture of 60% argon, 39% isobutane, 1% $SF_6$. For the cosmic-ray tests the external read-out had a pitch of 1.6 cm and covered the entire

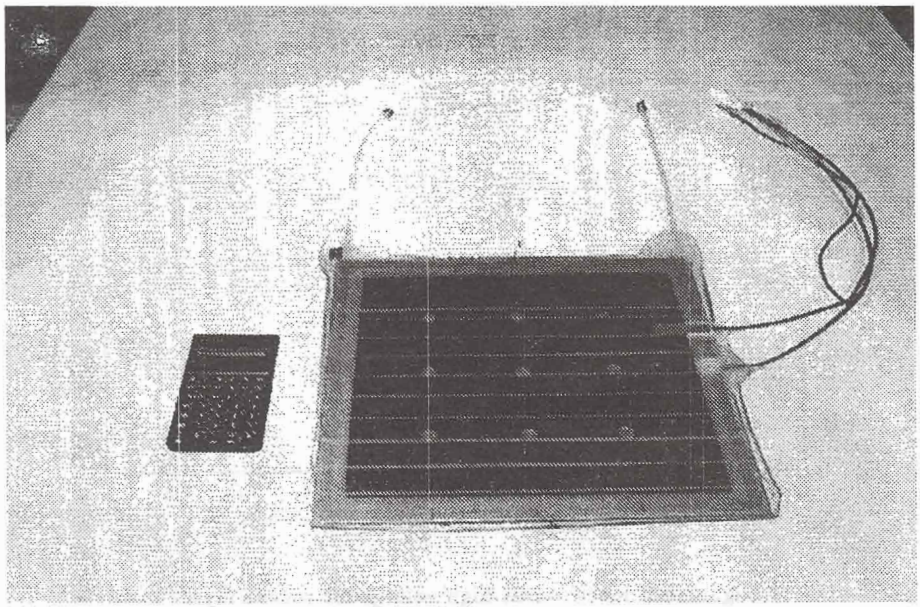

Fig. 1. LLNL RPC used in the test beam.

active area. The efficiency versus high voltage plateau curve is given in Figure 2. The chamber achieved 95% efficiency at 7250 V measured with LeCroy 4413 discriminators set to a 15 mV threshold. The chamber was triggered with a set of scintillator counters that nearly covered the active area of the RPC.

For the cosmic-ray test, the charge on each strip was measured with a LeCroy 1882 (Fastbus ADC) and the total charge was summed off-line. The charge response for two characteristic voltages and two timing gates are given in Figure 3. At 6700 volts the chamber is only partially efficient (42%), but has a narrow charge distribution, which corresponds to a single spark for each incident cosmic ray. As one increases the voltage, the amount of charge in the pulse increases, and the amount of after-pulsing also increases significantly. As was demonstrated for glass-electrode RPCs [4], by decreasing the integration time, the effects of after-pulsing can be reduced. The effective gain is also reduced, since the gate becomes shorter than the decay time of a single RPC pulse; thus part of the primary pulse is thrown away. One must be careful to properly time the beginning of the integration gate, since the time delay resulting from the formation of the streamer changes with high voltage.

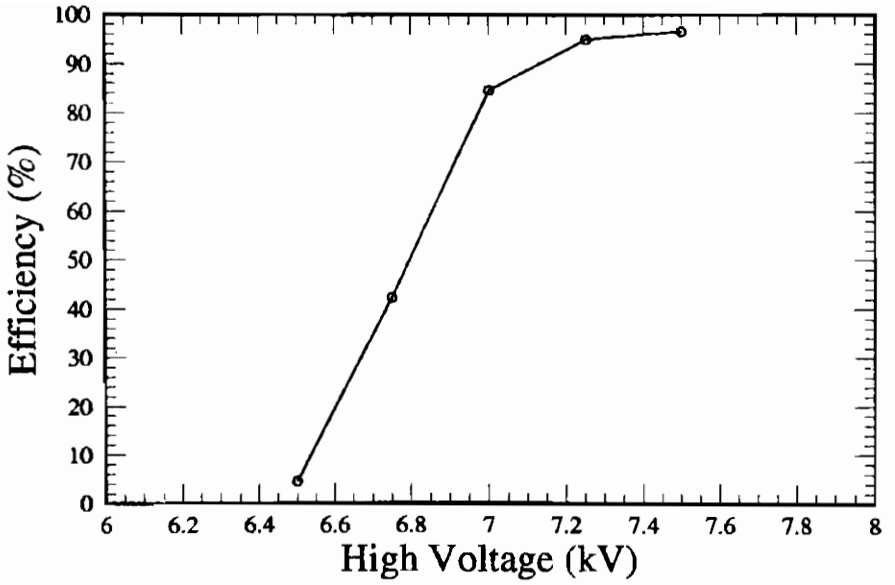


Fig. 2. Efficiency versus high voltage for cosmic rays.

For single particles at 7300 V with an integration gate of 30 ns, the RPC achieves high efficiency, a narrow charge distribution and suitable gain without amplification. If the occlusion length is also small, then it is likely that the RPC will function as a calorimeter.

## 4. Experimental Set-up

The Final Focus Test Beam (FFTB) at SLAC is used primarily for accelerator studies, but is often used for detector experiments. Bremsstrahlung photons produced when the primary electron and positron bunches scrape collimators in the main linac are extracted and directed onto a target where they produce $e^+$ $e^-$ pairs. The secondary electrons are momentum selected and focused by a series of magnets and collimators in the FFTB.

The FFTB can run parasitically to the SLAC Linear Collider (45 GeV in each beam) and produce electron beams in the range of 1-25 GeV. The beam size is small, on the order of 1 mm, and the rate is very low, approximately 120 Hz. No attempt was made to alter the transverse position of the beam, so the detectors in the experiment were consistently

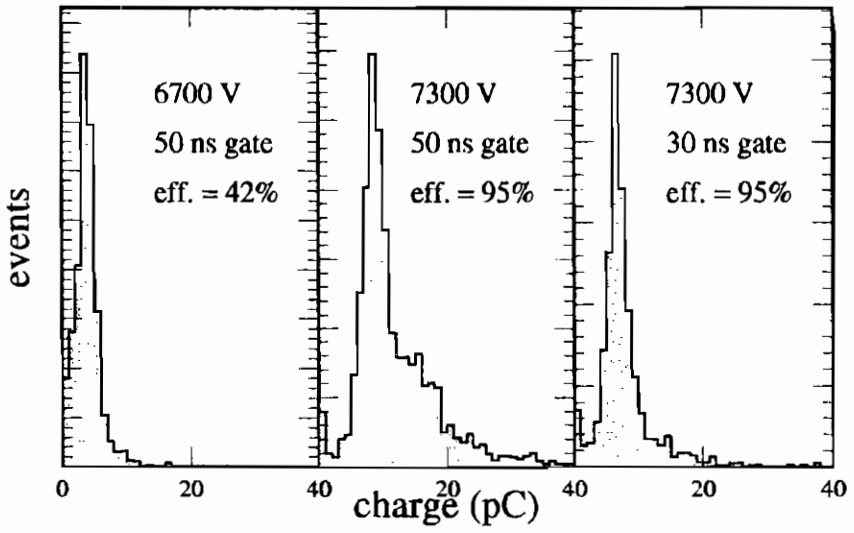


Fig. 3. Charge response of the RPC for cosmic rays. The amount of after-pulsing increases with voltage, but can be reduced by shortening the integration time. The charge calibration in the plots is only approximate.

illuminated in the same spot.

The nominal rate of 120 Hz for the electron beam in the FFTB is set by the frequency of the $e^+$ $e^-$ bunch pairs in the linac. Within a single pair, the $e^+$ and $e^-$ bunches are separated by only 60 ns. The rate in the FFTB can be further reduced by setting the upstream collimators and magnets. Even at an overall low beam rate, it is possible to have electrons separated by only 60 ns (from a photon emitted by both the primary $e^+$ and $e^-$ in a bunch pair).

The experimental set-up, shown in Figure 4, consisted of upstream scintillator counters, steel plates to generate an electromagnetic shower, and a series of detectors to sample the shower. The upstream scintillator counters were used to trigger on the beam, and reject off momentum particles and coincident beam background.

Three steel plates, 2 cm thick and spaced 2 cm apart, were used to generate the showers. The steel spacing was chosen to approximate the average density of the MINOS detector.

A streamer tube array was attached to the last steel plate and was immediately followed by the RPC and two scintillator counters. The RPC should not have significantly altered the shower incident on the

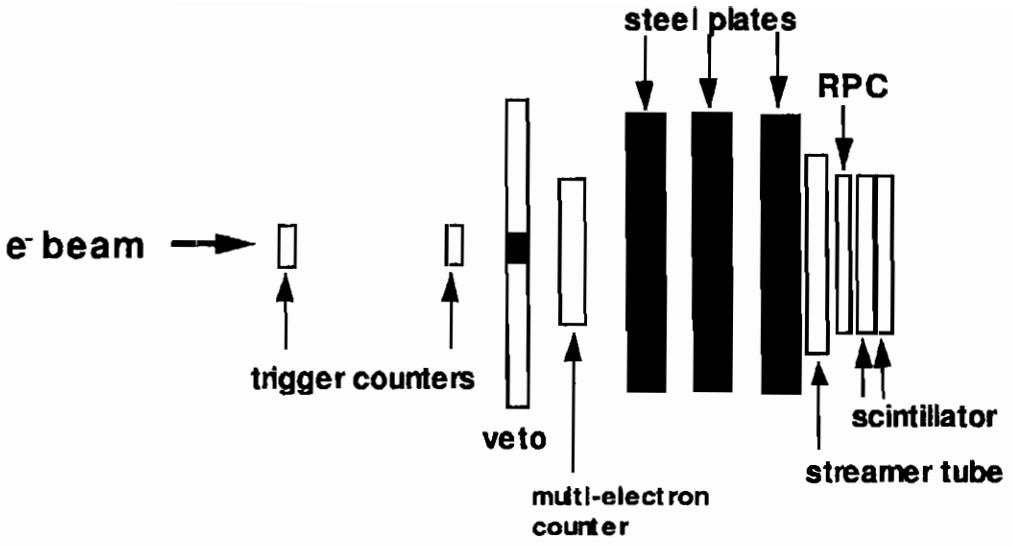


Fig. 4. Experimental set-up at the FFTB.

scintillator, since it was only about 0.1 radiation lengths compared to approximately 3.4 radiation lengths for the steel.

The RPC read-out strips were built on a separate board and were placed against the chamber during the tests. The read-out consisted of 10 strips that were 14 cm long. The central six strips had a pitch of 1 cm, while the outer strips had a pitch of 2 cm. Each strip was connected to an ADC channel of a LeCroy 1449W. No amplification was used (under some voltage settings attenuators were required to prevent the charge integrator on the ADC from saturating). The strips covered the same area as the scintillator of the counters placed behind the RPC.

## 5. Data

The gas used for the test beam was mixed with a different apparatus but was nominally the same as that used for the cosmic-ray test: 60% argon, 39% isobutane, 1% $SF_6$. All the data were collected in one run over a 17-hour period. Since the amount of run-time was limited and there was no time to look at the data during the run period, a more conservative integration gate of 40 ns was used for most of the data.

Data were taken on the high voltage plateau (7300 V), where the chamber is fully efficient for single particles, and well below plateau

(6700 V), where it was only partially efficient. For each voltage setting the appropriate time delay was set so that the start of the integration gate coincided with the beginning of the spark signal from the RPC. Three beam energies were selected: 5, 12, and 20 GeV. Most of the data were taken with beam rates around 2-3 Hz with a few runs at 8 Hz.

## 6. Shower energy measurements

The RPC and scintillator counters were read out simultaneously. For a beam energy of 20 GeV, the pedestal subtracted ADC counts of the scintillator and the sum of the counts from all of the RPC strips are shown in Figure 5. The RPC voltage was set at 7300 V and the

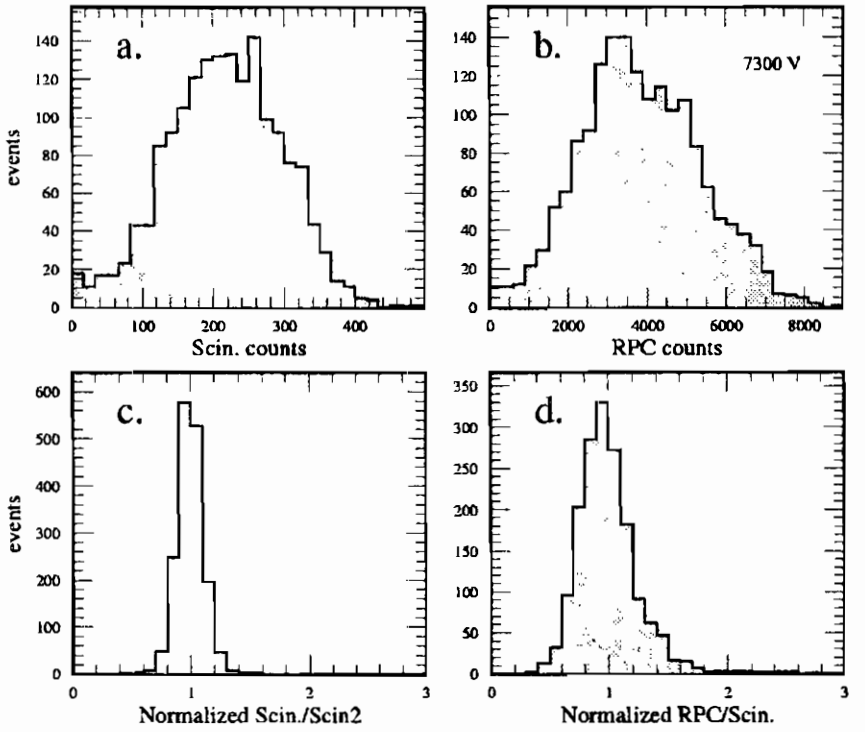


**Fig. 5. Pedestal subtracted ADC counts for scintillators and RPC for 20 GeV incident electrons on 6 cm of steel.**

integration gate was 40 ns. The high gain of the RPC was achieved without external amplification. The observed range of energies are due

to fluctuations in the electromagnetic shower.

The intrinsic resolution of the scintillator can be seen by comparing the signals from the two counters. Figure 5.c shows the ratio of the response of the two scintillator counters. Figure 5.d shows the ratio of the RPC response to the scintillator counters. The RPC has larger intrinsic fluctuations than the scintillator, but still yields a narrow response. The tail in Figure 5.d is presumably due to the RPC after-pulsing. A shorter integration time would reduce this tail further.

Figure 6 shows the scatter-plot and corresponding profile histogram

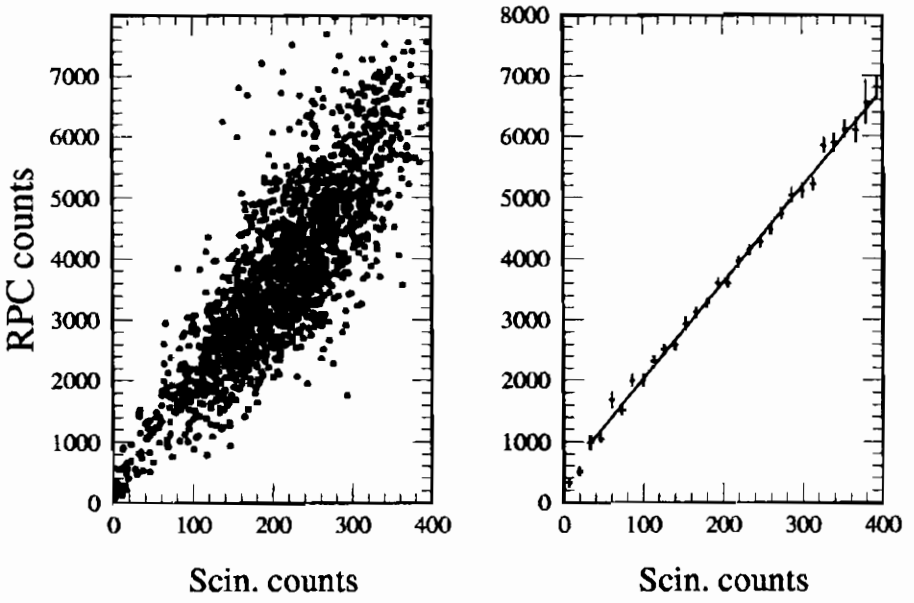


Fig. 6. RPC versus scintillator response. The second plot is a profile histogram of the first plot. The error bars indicate the statistical error of the mean value.

comparing the scintillator and RPC response for the 20 GeV beam energy. The RPC response was linear over a wide range of shower energies. At very low energy the response is quadratic (this was also observed for streamer tube measurements in this test beam).

Similar results were obtained at lower RPC voltages. At 6700 V the RPC is only 47% efficient for single particles; however, it still detects showers with high efficiency. As expected, the effects of after-pulsing were reduced and the gain was much lower. Figure 7 shows the response function for the RPC at both 6700 V and 7300 V.

We also noted that the event rate affected the RPC gain. Data

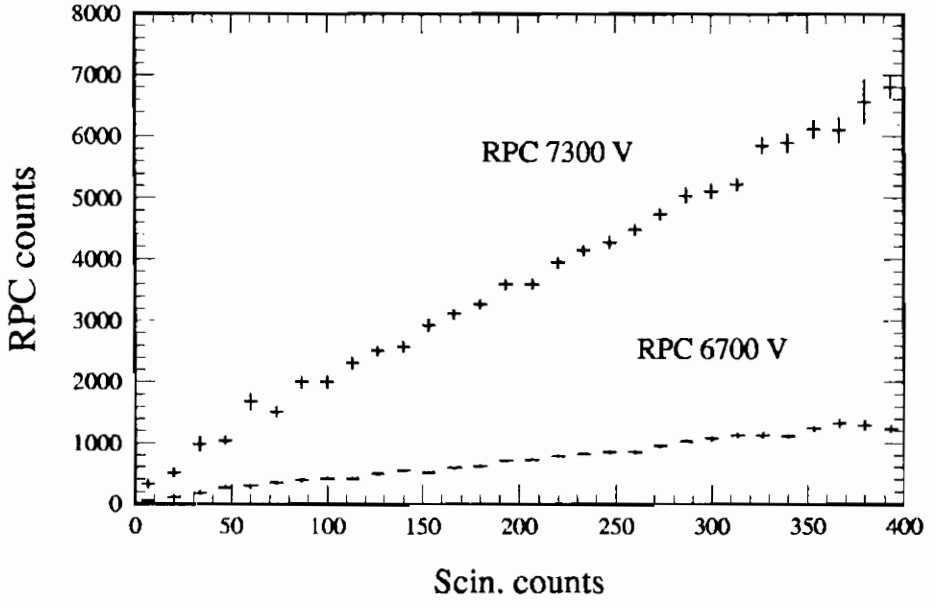


Fig. 7. RPC response at two voltage settings versus scintillator.

were taken at two different beam rates (1.7 Hz and 8 Hz) at a selected beam energy of 5 GeV. The higher rate was created by slightly opening the collimators. An increase in the rate by a factor of 5 resulted in a reduction in the gain by about 1.5. Presumably the increased event rate results in a lower effective voltage on the RPC at it attempts to recharge.

## 7. Conclusions

Test beam data show good linear response and energy resolution for the charge collected from a narrow-gap RPC operating in spark mode in an electromagnetic shower. No external amplification of the RPC signals is necessary. After-pulsing, even with a relatively long integration cgate, does not significantly impair the calorimetric response, but the event rate can significantly affect the gain.

The calorimetric response of the RPC is well matched to the needs of the MINOS experiment and RPC technology provides an alternative

to limited streamer tubes in sampling calorimeters.

## 8. Acknowledgments

I would like to thank Doug Michael for his assistance during the data taking. Thanks also to my colleagues who participated in the test beam effort for a variety of detectors: Richard Cotton, Yuri Gornushkin, Misha Ignatenko, Jonathan Thron, and Maxim Roehrig. We gratefully acknowledge the assistance of the SLAC accelerator operators, without whose help these measurements could not have been made.

## 9. References

1. The MINOS Collaboration, "P-875: A Long-baseline Neutrino Oscillation Experiment at Fermilab," Fermilab Report NuMI-L-63, February 95.
2. C. Wuest, *et al.* , "High Rate Resistive Plate Chambers," Proceedings of the International Industrial Symposium on the Supercollider, San Francisco CA, May 1993.
3. D. Wright, *et al.* , "ABS Plastic RPCs," Proceedings of the Third International Workshop on Resistive Plate Chambers, Pavia, Italy, October 1995.
4. D. Michael and D. Relyea, *Nucl. Inst. and Meth.* **A373** (1996) 30.

# PERFORMANCE OF THE *BABAR* RPC's IN A COSMIC RAY TEST

A. CALCATERRA *
*Laboratori Nazionali di Frascati-INFN, C.P.13, Frascati, I-00044, Italy*

February 7, 1998

ABSTRACT

The IFR group has instrumented the Iron Flux Return of the *BABAR* detector with 800 Resistive Plate Chamber detectors. This note describes the acceptance tests made in Frascati with cosmic rays, and shows performance parameters, efficiency, and time resolution, obtained by means of these tests.

## 1. Introduction

The *BABAR* Experiment at PEP-II is under construction at the Stanford Linear Accelerator Center (SLAC). The IFR group has instrumented the Iron Flux Return of the solenoid of the *BABAR* Detector with Resistive Plate Chambers. More information on the physics program to be studied with *BABAR* will be found in [1], and the overall

*co authors: A. Palano *INFN Bari, Dipartimento di Fisica, via Amendola 173, I-70126 Bari, Italy* ; A. Buzzo, R. Contri, G. Crosetti, M. Lo Vetere, M. Macri', R. Monge, M. Pallavicini, C. Patrignani, M. G. Pia, E. Robutti, A. Santroni *U.Genova, Dipartimento di Fisica, via Dodecanneso 33, I-16146 Genova, Italy* ; F. Anulli, R. Baldini, R. De Sangro, D. Falciai, I. Peruzzi, M. Piccolo, Z. Yu, A. Zallo *Lab.Nazionali di Frascati-INFN, C.P.13, I-00044 Frascati, Italy* ; G. Carlino, N. Cavallo, F. Fabozzi, C. Gatto, L. Lista, P. Paolucci, D. Piccolo, C. Sciacca *U.Napoli, Dipartimento di Fisica, Mostra d'Oltremare, pad.19, I-80125 Napoli, Italy* ;

structure of the IFR subdetector is described in [2].

## 2. The RPC's in *BABAR*

Resistive Plate Chambers represent a well-known and widely used tecnique in high-energy physics experiment [3]. The particular variation of this technique employed in *BABAR* is the one-gap detector shown in Fig.1: the active volume is a 2 mm gap enclosed between 2 Bakelite sheets, also 2 mm thick. The Bakelite sheets are kept apart by plastic spacers/insulators, arranged in a 10 cm by 10 cm regular lattice. The external Bakelite surfaces are graphite-painted, and covered with 100 $\mu$m thick mylar, cut around the HV connection. The non-flammable and environmentally-acceptable gas mixture to be employed in *BABAR* is the 3-component Ar : Freon 134A : Isobutane 48:48:4.

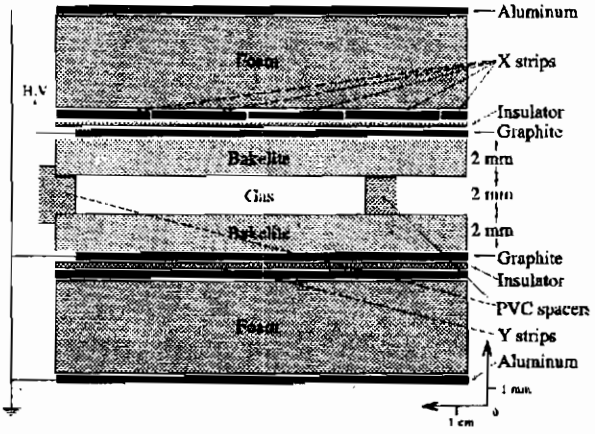


Fig. 1. The RPC's for the *BABAR* experiment at PEP-II.

The external readout electrodes, on both sides, are shaped as two arrays of X and Y-strips, and are made machining two sheets of 100 $\mu$m mylar covered with a 60 $\mu$m layer of Aluminum: 33 knives, held by a rotating bar, scrape the Aluminum over a width of 2 mm, for any desired length, producing a layer of 32 readout strips. This layer, and a continuous Al ground plane, are then glued on opposite sides of a $\sim$ 5 mm thick foam panel. This particular thickness gives adequate stiffness to the readout panel, and at the same time insures a $\sim 33\Omega$ impedance for the readout line, to match the impedance of the twisted-pair cables.

About 800 RPC's have been built and installed in the detector: they have various shapes (most rectangular and trapezoids) and dimensions

ranging from 2 to 7 $m^2$. Before installation, they are assembled in groups of 2 or 3, to form a chamber filling a slot in the Iron. The *BABAR* barrel has been instrumented with 19 layers of RPC's, and both endcaps with 18 layers, covering $\sim 95\%$ of $4\pi$.

## 3. The Cosmic Ray Setup in LNF

After construction at the factory in Colli, Italy, the RPC's are shipped to the INFN facility in Frascati, where they are tested for gas leaks, and one side of pickup external electrodes is glued on. Then, they are re-packed in the same steel boxes already used for the trip to Frascati for the final shipment to SLAC. The finished boxes are placed between two trigger planes, also made with RPC's, and tested with cosmic rays. The separation between the two ($\sim 2$ $m^2$ wide) trigger planes is 150 cm.

### *3.1. Plateau Runs*

The first type of test performed in Frascati is a HV scan, usually in steps of 100 V, from 6 kV up to 9 kV. For every HV setting the DAQ records three numbers for each RPC:

- The current drawn.
- The rate of singles, obtained counting the number of hits for a given number of random triggers, divided by the gate length.
- The number of hits for a given number of coincidence triggers.

The number of triggered hits as a function of HV is then linearly interpolated to obtain values of the HV for which 10%, 50%, and 90% efficiencies are reached. Rate of singles and drawn current for the HV point closest to the 90% efficiency point are also stored, as well as the highest efficiency value measured during the test.

All previous efficiencies are adversely affected both by noise and/or cosmic ray showers, and also by geometric trigger effects.

### *3.2. Tracking Runs*

A second type of test is then run, in which the strips on the trigger modules are individually read out; only events with one strip cluster on the trigger planes are selected, the particle trajectory is calculated, and the efficiency of RPC's can be more correctly measured, as well as

surface-mapped if enough statistics is available. These runs typically last one night and $\sim$ 100,000 events are stored on tape.

## 4. Results from Test Setup

### *4.1. Homogeneity of Detectors*

Some curves from the HV scans have been plotted in Figs.2 and 3, for 5 randomly chosen modules: the efficiency, the rate of singles, and the current drawn. In Fig.2(left) one can see that plateau curves for several different RPC's superpose nicely on each other: the points for 10% and 90% efficiency are the same, as well as the efficiency plateau. Moreover, comparing both sides of Fig.2 it is evident that the rates of singles flatten as expected between 7.5 and 8 kV, where the "knee" of the efficiency curve starts to form.

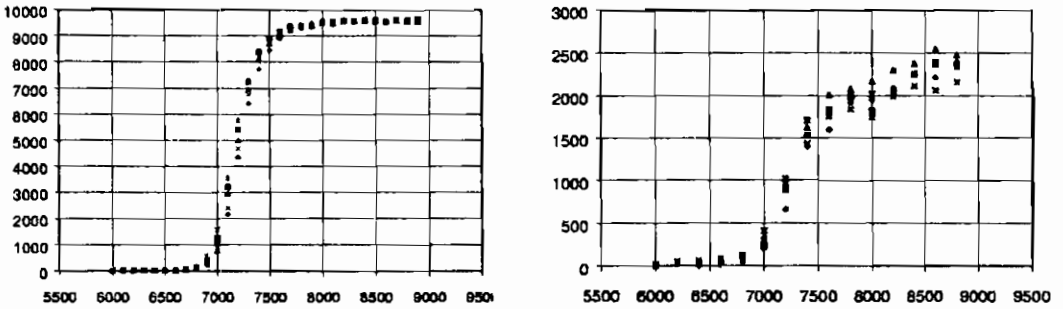


Fig. 2. Counts for 10,000 triggers(left) and single rates(right) *vs.* HV.

On Fig.3 is shown the increment of the dark current for the same RPC's in Fig.2: typically, normal RPCs draw between 4 $\mu$A at 6 kV and less than 20 $\mu$A at 9 kV.

In Fig.4 typical currents at 90% efficiency are histogrammed: the distribution is broadly centered around 9 $\mu$A, and the small peak at 18 $\mu$A is caused by saturation of the ADC reading the current. The current drawn shows some dependency on ambient temperature.

Another check of the similarity of parameters for all plateau curves may be obtained plotting the distributions of points at 90% efficiency, shown in Fig.5(left), and of the difference in HV between the point at

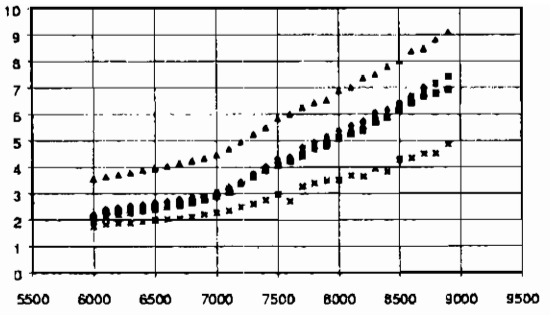


Fig. 3. Dark current ($\mu$A) *vs.* HV.

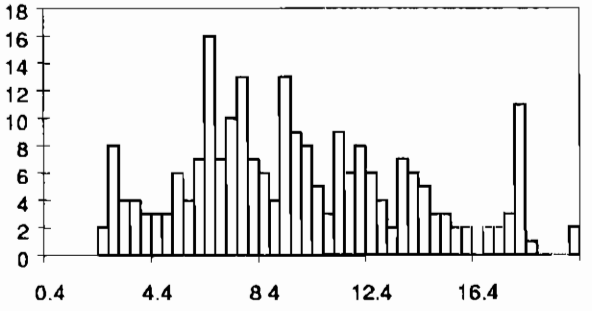


Fig. 4. Current drawn ($\mu$A) at 90% efficiency.

90% and the one at 10%, which gives an indication of the steepness of the plateau curve, in Fig.5(right).

Fig. 5(left) shows a distribution centered around 7.6 kV, with a $\sigma$ of $\sim$ 100 V. Plotting the correlation of this same quantity *vs.* module ID (i.e. *vs.* time) one obtains Fig.6: the greatest part of the 100V $\sigma$ above is due to long-term systematic effects in the experimental setup, either in temperature or in the composition of the gas mixture. In the test setup these effects have been monitored, but not corrected for; in *BABAR* appropriate adjustments will be made.

One may note a greater scatter of the points for 90% efficiency affecting the endcap RPC's, from #500 on: this is because (in the Plateau Runs) trigger geometric effects were not corrected for, and they are more sizable for RPC's with trapezoid shapes.

The width of the $\Delta$V distribution in Fig.5(right) has very little impact on the performance of the detectors: one can see from its correlation with the plateau efficiency, shown in Fig.7, that RPC's which reach the plateau at a higher HV are nevertheless just as efficient as the others; on the other end, equalizing the operating points of all RPC's in the IFR

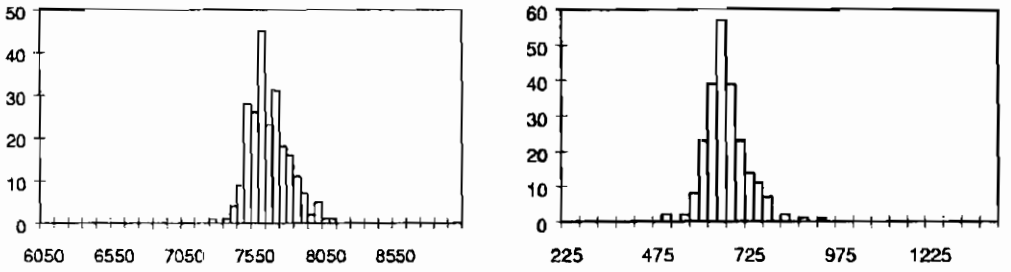


Fig. 5. HV for 90% efficiency(left) and $\Delta$V(90%–10%)(right).

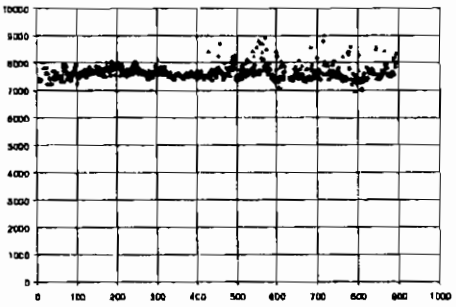

Fig. 6. HV for 90% efficiency *vs.* Module ID (*i.e.* time).

may require increasing somewhat the number of HV channels.

The distribution of rate of singles as a function of time, in Fig.8, shows an increment, due to increase in the size of the RPC's over the construction period of $\sim$ 1 year.

### *4.2. Efficiency from Plateau Runs*

A distribution of plateau efficiencies for barrel RPC's is shown in Fig.9, *vs.* module ID: the average efficiency is of $\sim$ 96.5%, and has been very stable all along the tests. Again, it must be emphasized that this efficiency measurement is biased because the data have not been selected in any way, except than for the trigger requirement.

### *4.3. Efficiency from Tracking Runs*

Much better control over systematics is obtained during the Tracking

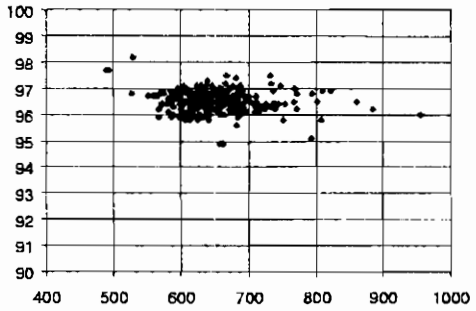


Fig. 7. Efficiency from Plateau Runs *vs.* $\Delta$V(90%-10%).

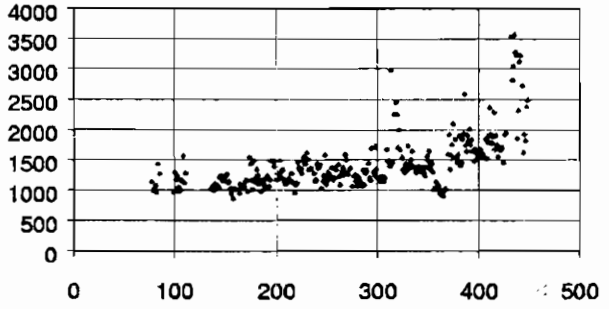


Fig. 8. Singles rate at 90% efficiency *vs.* Module ID.

Runs, in which measures are taken to reject spurious events due to cosmic ray showers, and cuts on the track position are made to ensure that particles cross active regions of all detectors. The result of this study is shown in Fig.10(left), integrated over a typical chamber, and Fig.10(right) plotted against the expected impact point.

The curve in the first picture is approximately gaussian, with an average value of (97.2±0.3)%, but is apparent from the right-hand side that this is an average over the whole RPC, including the regions where the plastic spacers line up, very apparent as dips in the efficiency happening every 10 cm.

If these regions are cut, one obtains the limit efficiency of (98.2±0.1)% shown in Fig.11.

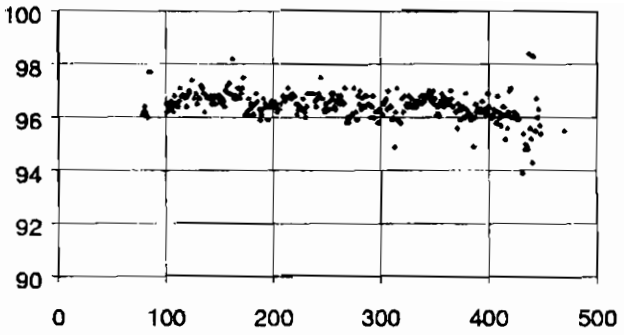


Fig. 9. Efficiency from Plateau Runs *vs.* Module ID.

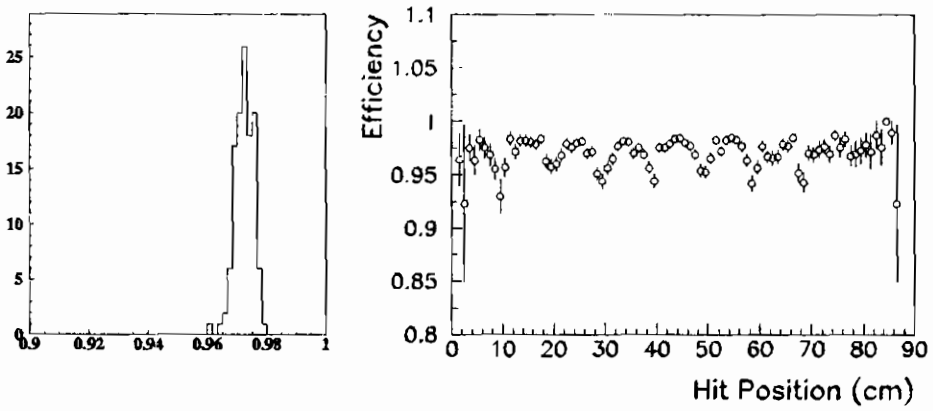


Fig. 10. Efficiency from Tracking Runs, integrated(left) and plotted along chamber edge(right).

### *4.4. Timing Performance*

The intrinsically fast response of RPC's makes then ideally suited for timing measurements: in *BABAR* they will be used not only as an imaging device for $\mu/\pi$ separation and $K_L^0$ identification, but also as a penetrating muon trigger, the readout electronics implementing a FAST-OR of 16 channels [4].

Consequently, a study of time resolution has been made as part of our routine tests, plotting the time difference between hits in adjacent layers, measured from a common START. The results are shown in Fig.12(left):

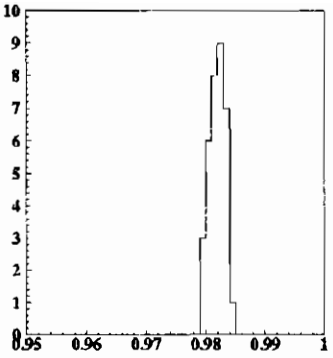


Fig. 11. Limiting efficiency for device.

the peak has been fitted as the sum of two gaussians, the narrow one having $\sigma = (1.86 \pm 0.02)$ns. Taking into account a factor $\sqrt{2}$ because the difference of two measurements is plotted, one ends up with a corrected time resolution of $(1.31 \pm 0.02)$ns.

Furthermore, this time resolution is expected to scale with the charge in the spark, *i.e.* with the applied HV; Fig.12 (right) shows that this is indeed the case.

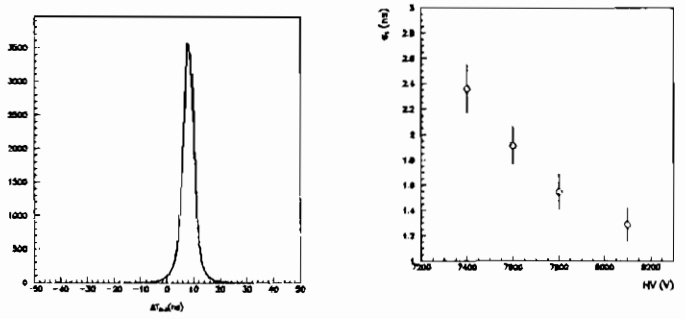


Fig. 12. Time resolution (ns)(left) and its dependency on HV(right).

### *4.5. Dependency on Bakelite Resistivity*

One item of concern has been whether to expect dependency of the behaviour of the RPC's on the resistivity of the Bakelite sheets employed

in the construction: Figs.13 and 14 show that this is not the case: the "noise" parameters like current drawn and rate of singles (Fig.13) do not vary with resistivity values, over a range of 1 to 6 $\times$ $10^{11}\Omega\times$cm.

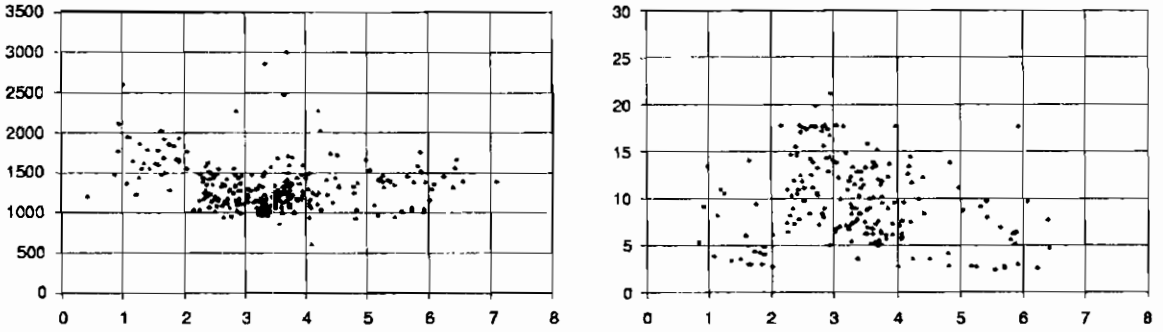


Fig. 13. "noise" parameters *vs.* average Bakelite resistivity ($10^{11}\Omega\times$cm)

Likewise, the three main parameters determining the shape of the plateau curve, $\Delta$V(90%-10%), the midpoint at 50%, and the efficiency from Plateau Runs, this last one shown in Fig.14, are not affected by resistivity variations.

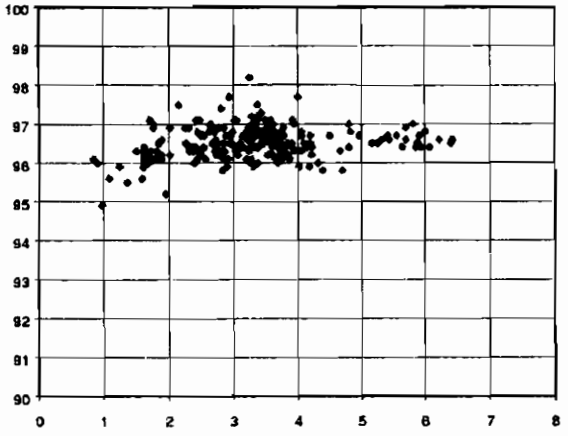


Fig. 14. Efficiency plateau *vs.* average Bakelite resistivity ($10^{11}\Omega\times$cm).

## 5. Conclusions

The IFR group has very satisfactorily terminated construction and installation of a $4\pi$ muon and neutral hadron detector in the flux re-

turn of the *BABAR* detector. First results from cosmic ray runs of the assembled detector are expected in Spring 98.

## 6. Acknowledgements

We are indebted to the competent help and steady dedication of G. Barisone, L. D'Aniello, S. Minutoli, M. Negri and P. Parascandolo. Without their continuous support the IFR construction and installation could not have been completed in time.

## 7. References

1. The *BABAR* Letter of Intent, SLAC-443, Jun 1944; The *BABAR* Technical Design Report, SLAC-R-95-457, Mar 1995.
2. R. Baldini et al., Proc. of the Int. Workshop on the RPC in Part. Phys. and Astrophys., Pavia 1995; P. Paolucci et al., Nucl. Instr. and Meth. A379(1996)472-474; F. Anulli et al., Nucl. Phys. 61B(1998)244-249; see also the contribution by D. Piccolo to these Proceedings.
3. R. Santonico and R. Cardarelli, NIM **A187**,377(1981); R. Santonico and R. Cardarelli, NIM **A263**,20(1988); A. Aloisio et al., NIM**A360**,340(1995); A. Adam et al., NIM**A383**,342(1996).
4. Paper contributed by G. Crosetti to these Proceedings.

# STUDY OF ECOLOGICAL GAS MIXTURES AND SIGNAL SHAPE ON GLASS RPC

Stefano M. Mari *
*Università della Basilicata and I.N.F.N. Roma*

February 12, 1998

ABSTRACT

In the first part of this paper we present the performance of 2 mm and 3 mm gap glass RPC operating in streamer mode. The data show a minimum in the time resolution as a function of the Isobutane/R134A ratio. In the second part we discuss the induced pulse amplitude and shape as a function of detector parameters, by comparing direct measurements with the results of a dedicated simulation program.

## 1. INTRODUCTION

In this paper we present the results obtained in testing the glass electrode RPC known as Glass Spark Counter (GSC) (*G. Bencivenni et. al. 1994*). The advantage of using float glass as electrode material consists of its homogeneity and its excellent surface quality, thus making possible the realization of noiseless detectors without the need of surface treatement. Several tests have already shown the capability of the GSC to work in streamer mode (*C. Gustavino et. al. 1996*) by using a gas mixture of $\sim \frac{2}{3}$ Ar, $\sim \frac{1}{3}$ Isobutane and a few percent of freon R13B1. In our test we replace the no longer allowed R13B1 ($CF_3Br$)

*co authors : Mario De Vincenzi *University of Rome RomaTre and I.N.F.N. Roma* ; Carlo Gustavino, Stanislav Mikeyev *L.N.G.S. Assergi (AQ)* ; Nikita Ogievetsky *Cogitech (New York).*

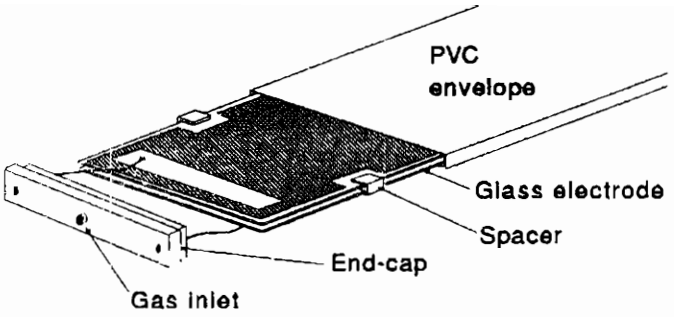


Figure 1: *Sketch of a Glass Spark Counter (GSC).*

with R134A ($C_2H_2F_4$) which is an ecological and non-flammable gas. The time resolution obtained with 2 and 3 mm gap GSC's operating in streamer mode with R134A-based gas mixtures, is presented here.

To further improve the GSC design and to better understand the induction mechanisms on pick-up, we have also studied the induced pulse amplitude and shape as a function of the detector parameters, by comparing test measurements with the results of a dedicated simulation program. The excellent agreement between real data and simulation results demonstrates the capability of the program to predict the behaviour of a detector, whose response can than be predicted and tailored to the experimental requirements.

## 2. GSC MODULE

The GSC module is shown in fig.1. A detailed description can be found in (*C. Gustavino et. al. 1996*). It consists of a pair of float glass electrodes 1 m long, 8 cm wide and 1.85 mm thick. The glass resistivity is $\rho \sim 10^{12}\,\Omega \cdot cm$. The 2 mm and 3 mm gap is obtained by using "E" shaped spacers ensuring a gap tolerance of a few tens of microns. The high voltage is applied to the glass by mean of a water-based graphite coating, with a surface resistivity $\sigma$ in the range of $300 \div 600 K\Omega$/square. The glass electrodes are inserted into a PVC envelope, thus ensuring gas

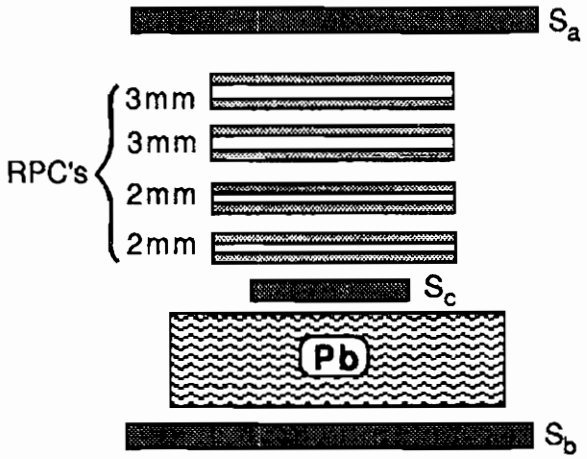


Figure 2: *Schematic view of the cosmic ray telescope used to perform the test.*

containment.

## 3. STUDY OF ECOLOGICAL GAS MIXTURES

The measurements presented in this section have been carried out at the "RomaTre" University using the telescope for cosmic rays sketched in fig.2. This telescope consists of three scintillators and of four layers of GSC's: two layers with 2 mm gap chambers and two layers with 3 mm gap chambers. Each GSC layer is equipped with Al strips 2.6 cm wide and 50 cm long. One 2 mm gap layer and one 3 mm gap layer are read out by electronic cards generating a logical FAST-OR used for timing studies. The scintillator and the FAST-OR signals are sent to a TDC. The analog signals from the remaining two layers of GSC's is directly sent to a charge integrating ADC. A 15 cm thick lead layer is inserted between the middle and bottom scintillators in order to select the penetrating component of cosmic rays. The trigger is generated by the coincidence of the three scintillator signals. For each trigger both the timing of the GSC's and the charge collected by the strips is measured.

The behaviour and the performance of the GSC's operating in streamer mode have been studied using gas mixtures in which the usual freon (R13B1) has been replaced with the non ozone-depleting gas Tetrafluorethane ($C_2H_2F_4$).

The measurements have been performed by using the following gas mixtures:

- Mixture 1: (Ar=15%, Iso=4%, R134A=81%)
- Mixture 2: (Ar=15%, Iso=10%, R134A=75%)
- Mixture 3: (Ar=15%, Iso=42.5%, R134A=42.5%)
- Mixture 4: (Ar=15%, Iso=75%, R134A=10%)

For these mixtures the Iso/R134A ratio is 1/20, 1/7, 1/1, 7/1, respectively. The mixing accuracy has been controlled with a precision of about 1%.

For each gas mixture we have measured the efficiency ($\epsilon$), the current and the single counting rate of the GSC's as a function of the high voltage (HV). The operating HV for each set of measurements has been chosen using the following procedure. We measured the efficiency as a function of the high voltage and we localized the HV at which the efficiency reaches 95% of the plateau level. Then we added 100 V to ensure that the data were taken well inside the full efficiency region:

$$HV = (HV@95\%\epsilon_{plateau} + 100)\ Volt$$

During each run we monitored the room temperature and the atmospheric pressure and we adjusted the HV requiring $VT/p = const$, where $V$ is high voltage, $T$ is the mixture temperature and $p$ is the operating pressure.

Fig.3 shows the charge distributions for the four gas mixtures and for the 2 mm and the 3 mm gap chambers. These distributions show clearly two peaks. The charge of the second peak is approximately two times the charge of the main peak, as expected for double and single streamer pulses. The two sets of plots in fig.3 show that decreasing the amount of R134A increases the charge of the single streamer peak from about 80 (200) pC to about 200 (800) pC for the 2 (3) mm gap GSC layer. This is due to the quenching effect on electrons produced by R134A. These plots show also the increase of the Isobutane fraction in the gas mixture reduces the percentage of double streamer events. As expected, the single streamer charge for the 3 mm gap GSC's is greater than the charge of the 2 mm gap chambers. Fig.4 shows the mean charge and the peak charge as a function of the gas mixtures. These plots show a

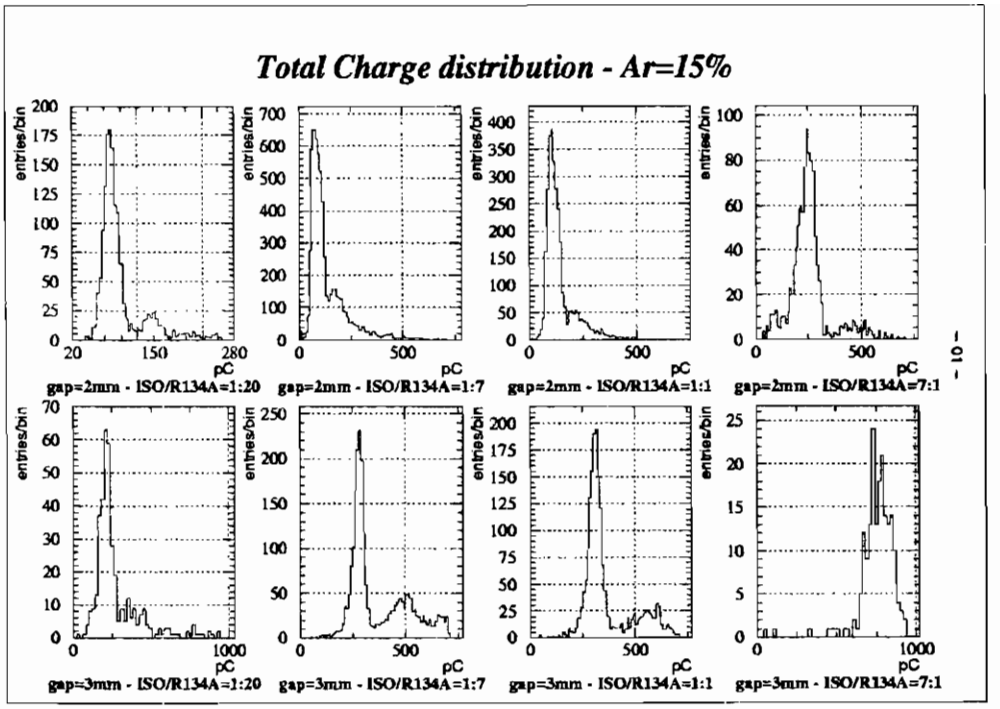


Figure 3: *Charge distribution as a function of the gas mixture used for the two gaps tested.*

quite constant value of the peak and mean charges in the central region of the Iso/R134A ratio, while for the high value of this ratio the (peak and mean) charge increases by a factor $(2 \div 3)$.

Fig.5 shows the time delay between the signals from one scintillator and from the GSC's as a function of the Iso/R134A ratio. The two plots exhibit a minimum in the central region of the Iso/R134A ratio. Fig.6 shows the time resolution of the GSC's as a function of the Iso/R134A ratio. The time resolution of GSC's is defined as the standard deviation of a gaussian curve fitted to the experimental distributions. The time resolution of the 2 mm gap GSC is always better than the one of the 3 mm gap GSC, reflecting its faster streamer generation. These plots show clearly a central region of the Iso/R134A ratio with a minimum for the time resolution. At the limit values of the Iso/R134A ratio range which we used, the time resolution down-grades. The behaviour of the time resolution as a function of the mean value of the total charge is shown in fig.7. The data show that the time resolution is related to

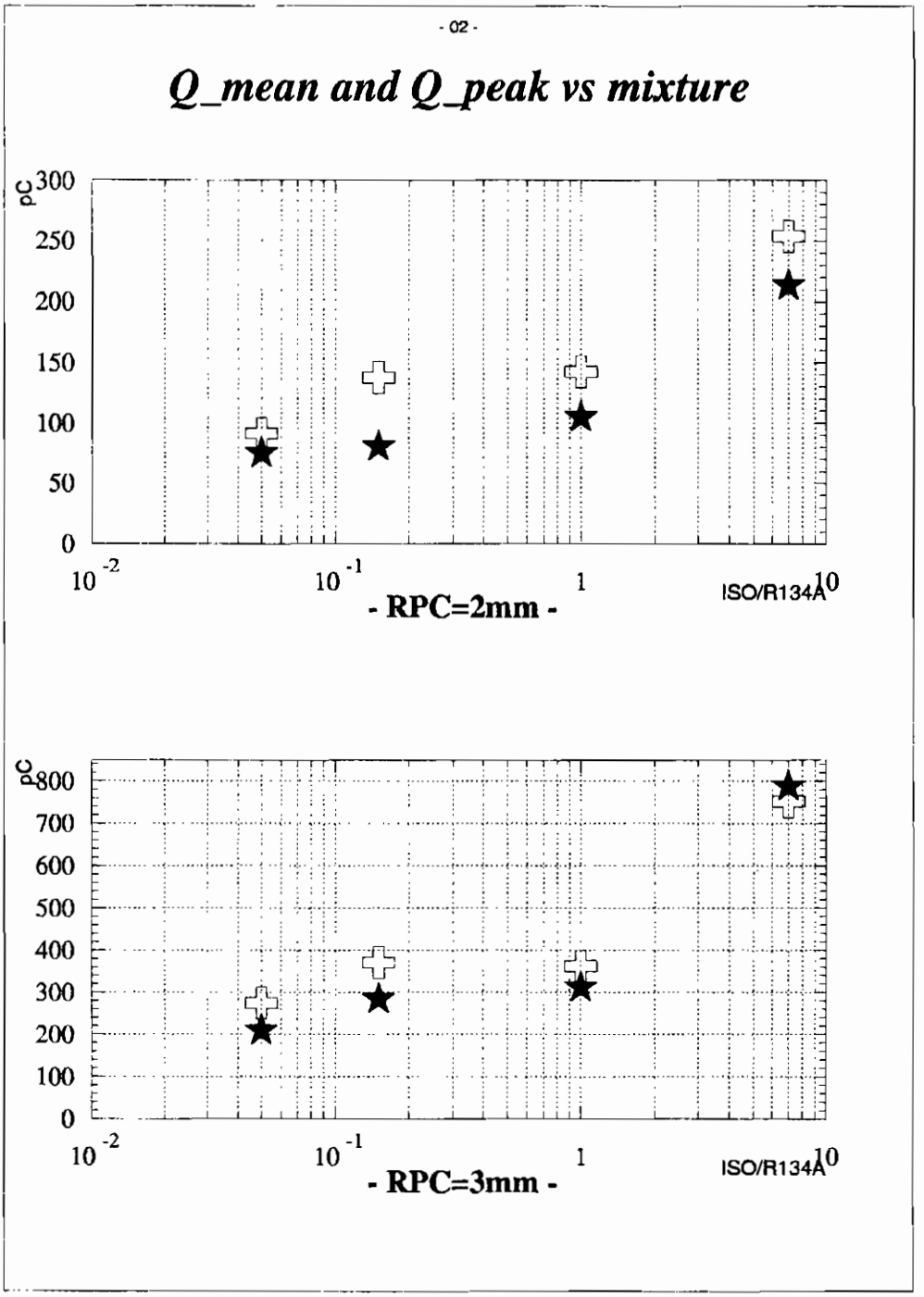


Figure 4: *Average charge (cross) and peak charge (stars) as a function of the ISO/R134A ratio for the two gaps analysed.*

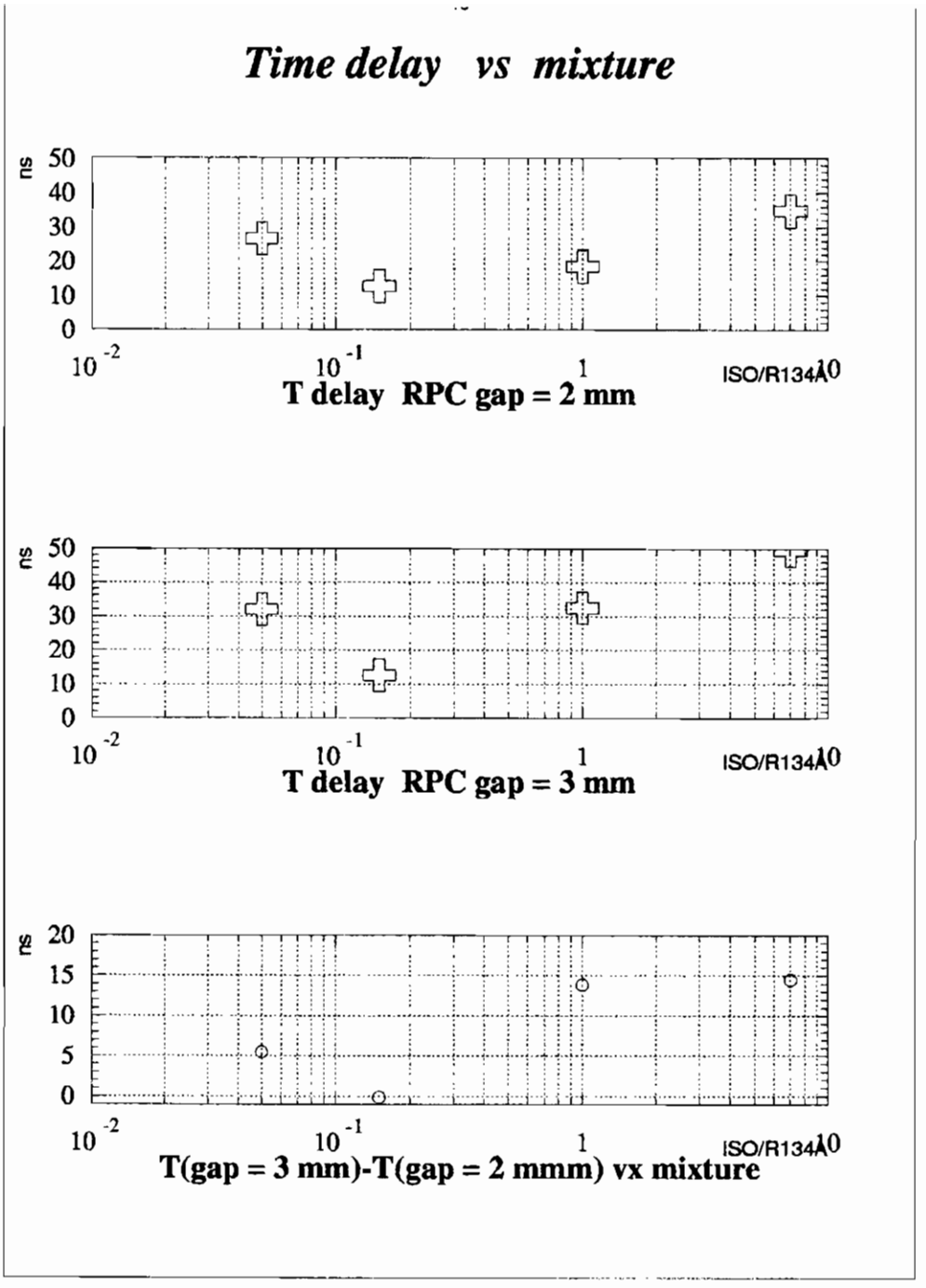


Figure 5: *Time delay between trigger signal and GSC signal as a function of Iso/R134A ratio.*

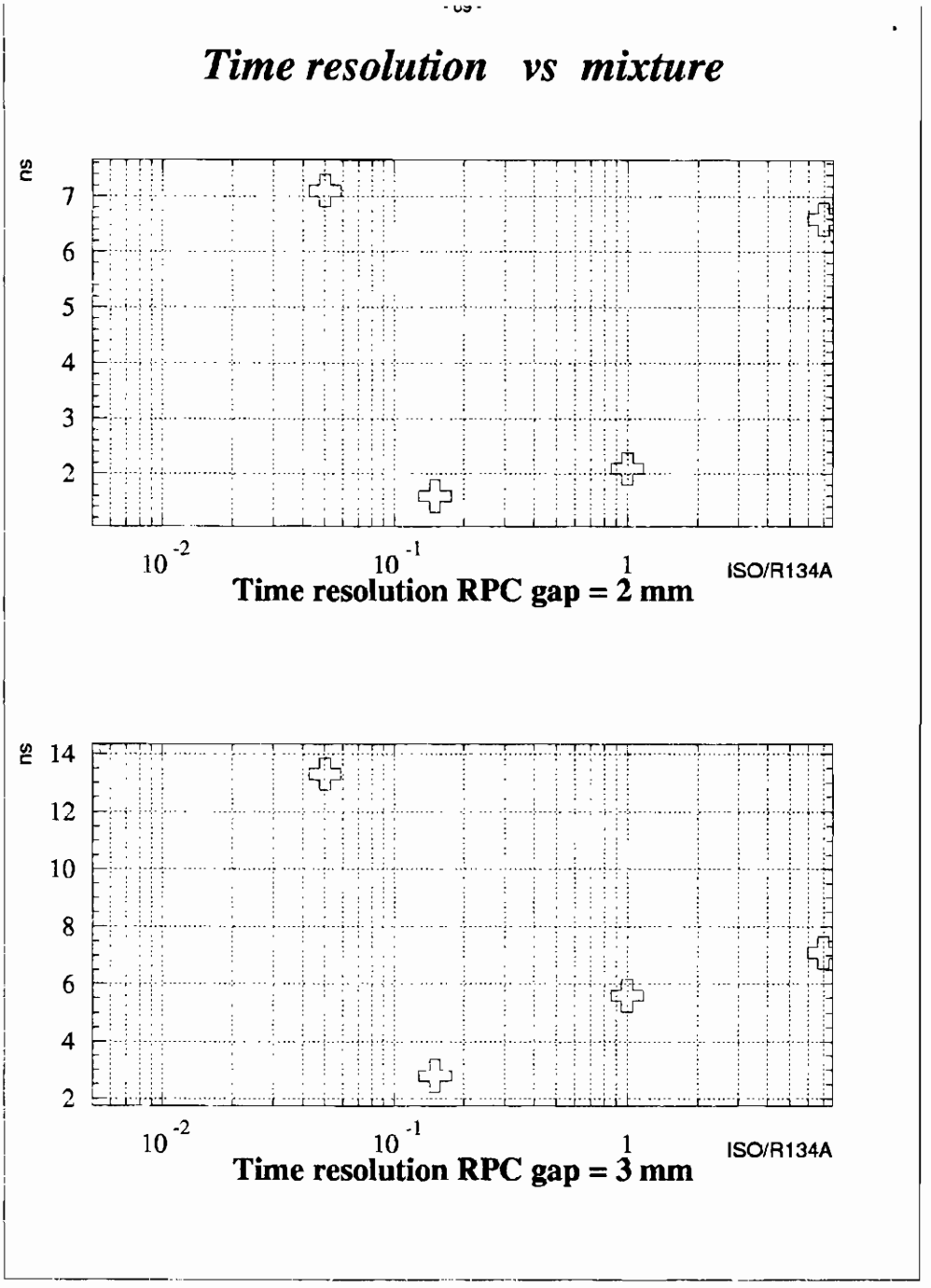


Figure 6: *Time resolution of the GSC's as a function of the Iso/R134A ratio.*

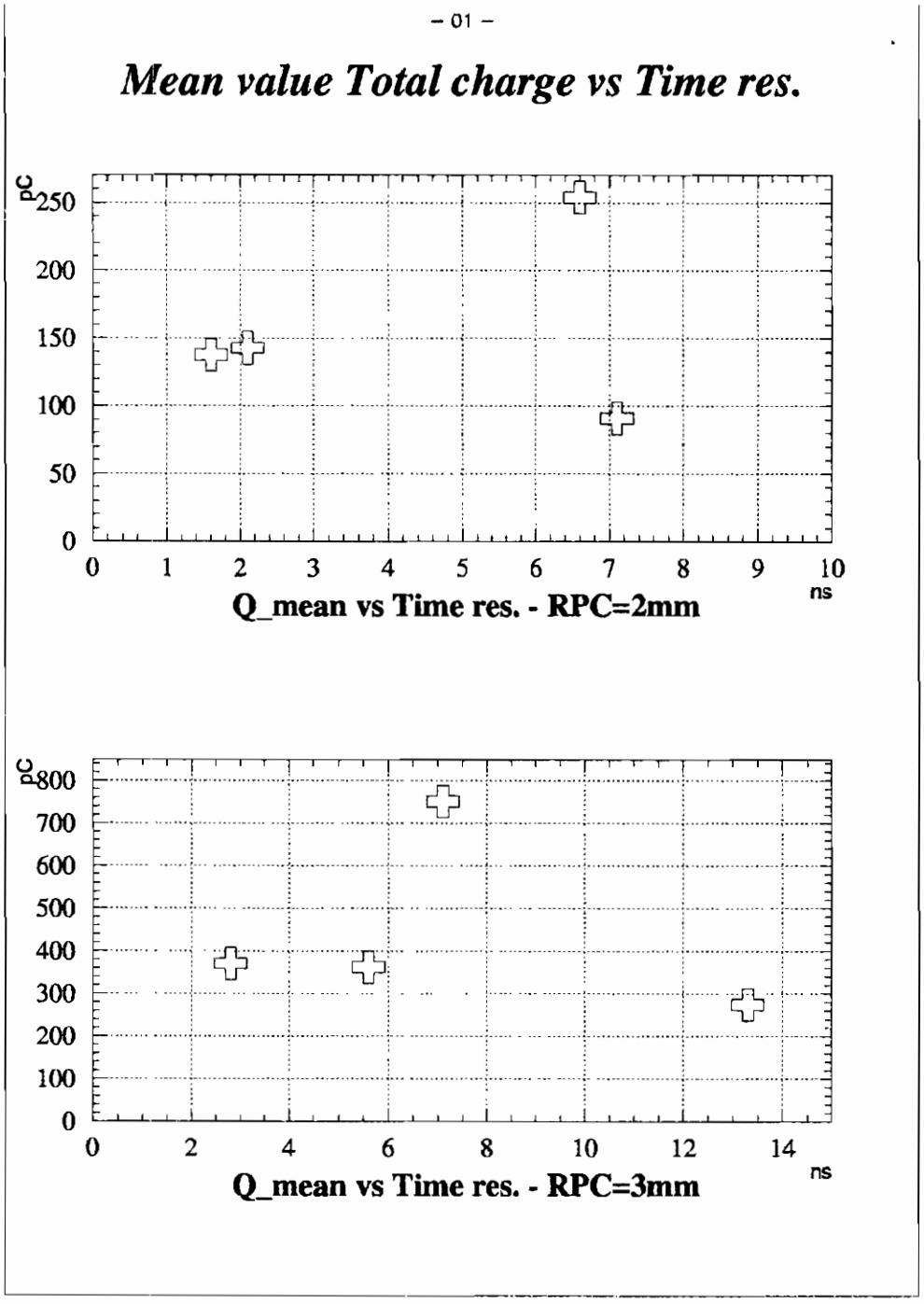


Figure 7: *Time resolution of GSC as a function of the total charge.*

the charge of the streamer. The time resolution reaches the best value for the 2 (3) mm gap chambers when a total charge of about 140 (350) pC is induced by the streamer process. A time resolution worsening occurs when the streamer charge increases, due to saturation effects. Also, when the streamer process produces a too small amount of charge, the GSC's are operating in a regime where the time jitter between the proportional signals and the saturated ones worsen the time resolution (*Cardarelli et. al. 1996*).

## 4. GSC INDUCED SIGNAL SHAPE

The GSC performance as a function of detector parameters has been studied by comparing a set of direct measurements with the results of a simulation based on the SPICE program. These measurements have been carried out at the L.N.G.S. Laboratory using a $20 \cdot 20\, cm^2$ GSC inserted in a scintillator telescope selecting cosmic ray muons in an area of $3 \cdot 3\, cm^2$. The detector parameters are: $g = 2\, mm, d' = 1.85\, mm, \epsilon_r = 5, \rho \sim 10^{12} \Omega\, cm, \sigma \sim 300 k\Omega/square$, where $g$ is the gap; $d'$ is the thickness of the electrodes; $\epsilon_r$ is the relative dielectric constant; $\rho$ is the electrode volume resistivity; $\sigma$ is the graphite surface resistivity (see fig.8). A printed circuit board (main pick-up) with copper on both faces has been used to make 8 strips, each 1 cm wide and 15 cm long, faced to the cathode plate. The signals induced on the strips are sent to a digital oscilloscope. The pick-up faced to the anode (opposite pick-up) is a 15x15 $cm^2$ printed circuit board with copper on both faces. The opposite pick-up is referred to the ground through a $50\Omega$ resistor. We define $d_1$ to be the distance between the main pick-up plane and the external surface of the cathode and $d_2$ to be the distance between the opposite pick-up plane and the detector anode (see figure 8).

The simulation treats the detector as a lattice of appropriate resistors and capacitors. The streamer is simulated with a short circuit, through a time variable resistor, between the electrodes. The simulation input parameters are the following:

- Gap value $g$
- Electrode thickness $d'$
- Electrode dielectric constant $\epsilon_r$
- Electrode volume resistivity $\rho$

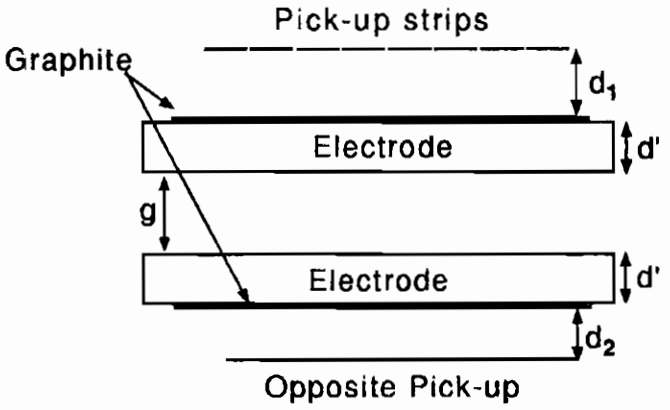


Figure 8: *Graphical definition of the parameters used for the induced pulse shape study.*

- Graphite surface resistivity $\sigma$
- Distance between the main pick-up and the cathode $d_1$
- Distance between the opposite pick-up and the cathode $d_2$
- Strip width and pitch
- Strip position with respect to the streamer location
- Lattice size and granularity

Fig.9 shows the mean induced pulse amplitude on the main read-out plane as a functions of $d = d_1 + d_2$. The data are well fitted by the formula:

$$V = V_0 \frac{g}{g + 2d'/\epsilon_r + d1 + d2} \quad (1)$$

Our data confirm that the pulse amplitude depends on $d$ alone and not on $d_1$ and $d_2$ separately. For instance, the 3 independent measurements for $d = 4mm$ (i.e. $d_1 = 4mm$ and $d_2 = 0mm$, $d_1 = d_2 = 2mm$, $d_1 = 0mm$, $d_2 = 4mm$) give the same pulse amplitude. The equation (1) is valid only if the graphite surface resistivity ensures full transparency for transient signals.

Fig. 10 shows the oscillogram of the signals induced by one streamer on consecutive strips for $d_1 = d_2 = 0.2mm$. Fig. 11 shows the corresponding simulated pulses generated by the program. The central/side

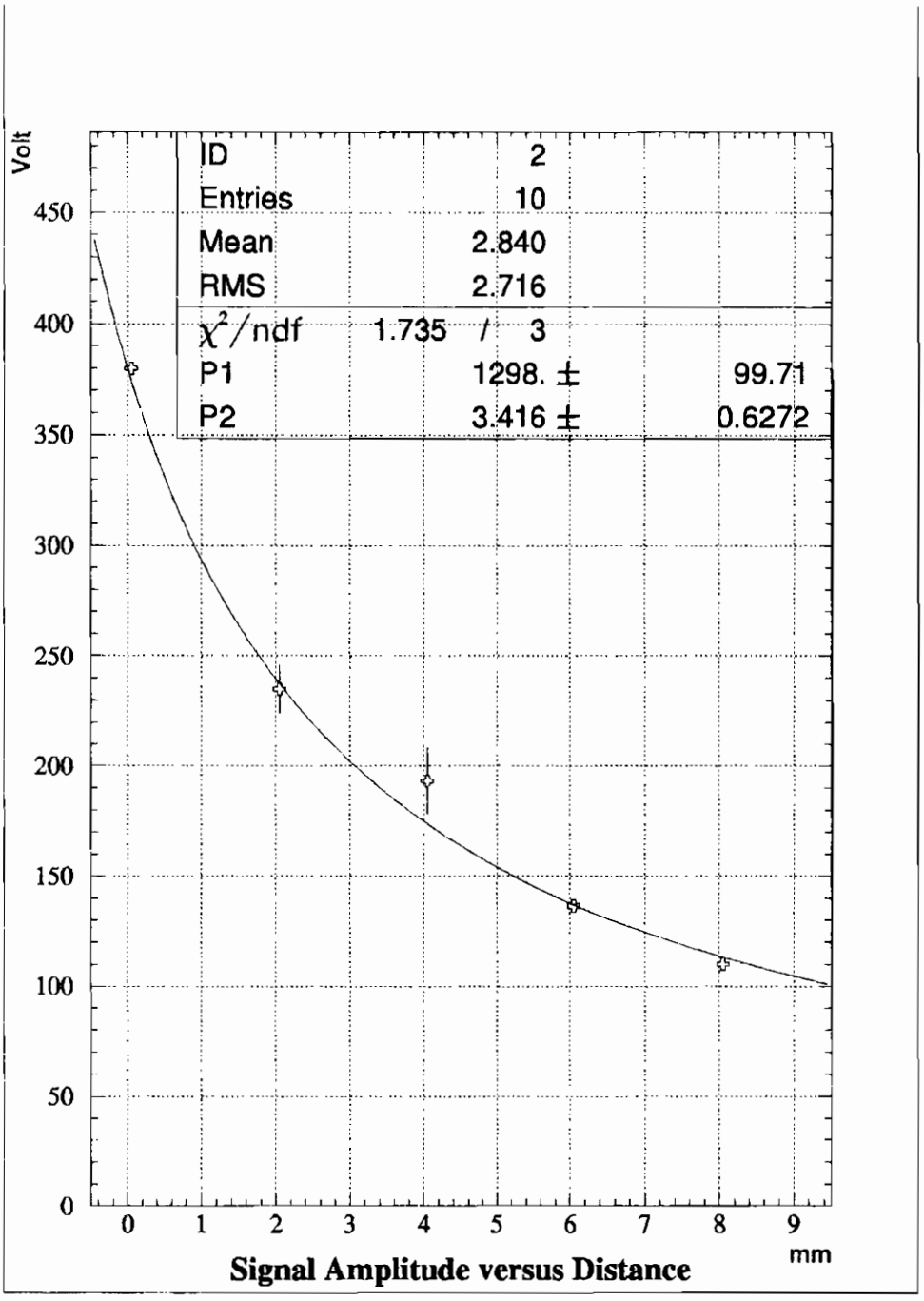


Figure 9: *Signal Amplitude as a function of* $d = d_1 + d_2$.

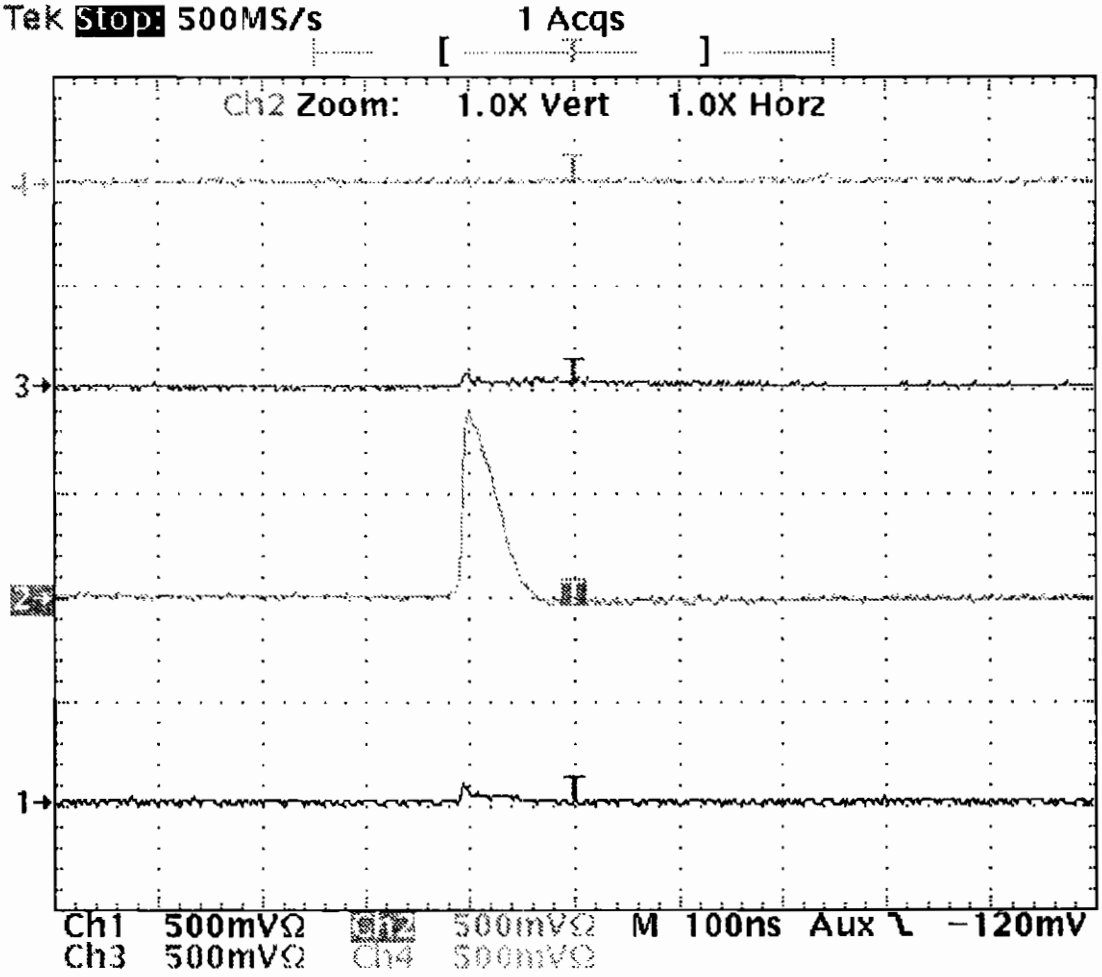


Figure 10: *Oscillogram of the induced signals on the strips* ($d_1 = d_2 = 0.2mm$.)

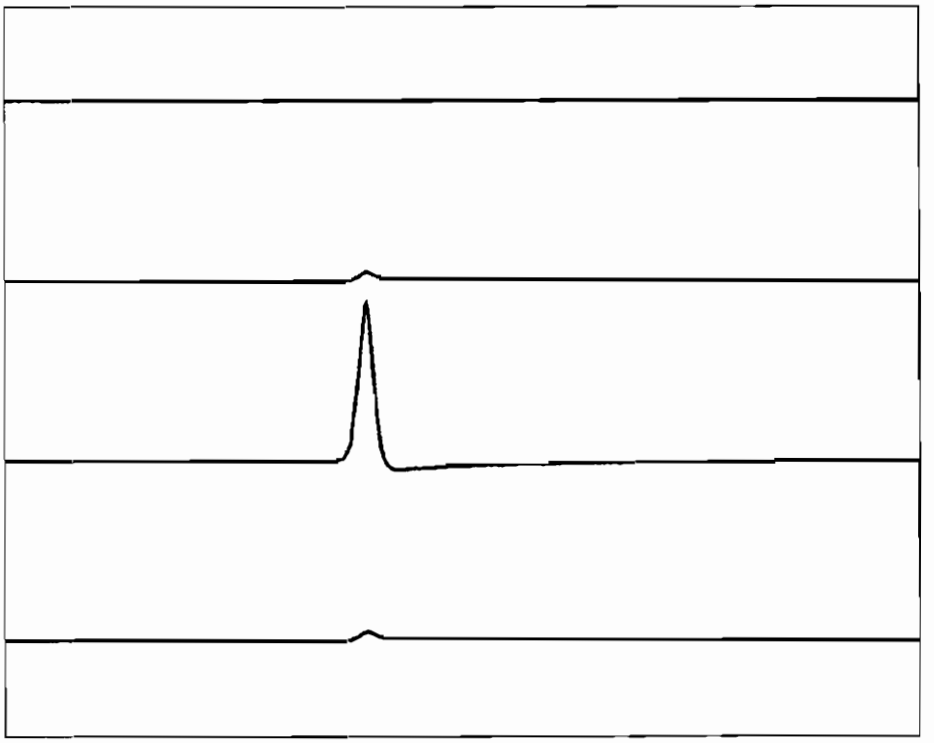

Figure 11: *Simulated induced signals on the strips* ($d_1 = d_2 = 0.2mm$). *The curves have to be compared with the oscillogram of figure 10.*

strip amplitude ratio is very large (about 10), in spite of the modest (10mm) strip width. The high multiplicity observed by some authors (see for example these proceedings) is hence not due to the direct induction on strips but most likely to the broadening of the pulses traveling on long strip elements, which depends on the strip length and on the graphite resistivity value.

Fig. 12 shows the signals induced on the strips for $d_1 = 4\ mm$ and $d_2 = 0.2\ mm$; fig. 13 shows the corresponding pulses generated by the simulation. The simulation reproduces all the interesting behaviour of the induced pulses. In particular, the simulated central/side strip amplitude ratio is in good agreement with the measured one. Furthermore, the pulse tails due to the graphite resistivity value are nicely reproduced, and can be explained as well: the signal from the central strip has an exponential negative tail after the positive pulse. In fact, the transient streamer current charges up the graphite-strip capacitance, giving a positive pulse. The negative tail is due to the capacitance discharge through the graphite, with a time constant proportional to the resistivity and to the graphite-strip capacitance. On the contrary, on the side strip, the tail following the initial pulse is positive. In this case, the positive tail is due to the extra charge coming from the discharge (through the graphite) of the central strip.

A quite unexpected pulse induction behaviour on the strips, first found by means of the simulation program and then observed with the direct measurement is shown in fig.14 and fig.15 for $d_1 = 0.2mm$ and $d_2 = 4mm$. As in the previous cases, the signal on the central strip is positive because the induced charge decreases as the electrons drift towards the anode, with a resulting positive pulse. On the contrary, this particular pick-up configuration implies an initial negligible induced charge on the side strips. However, as the electrons move away from the cathode and thus from the central strip, a small charge is induced also on the side strips, with resulting negative pulses.

## 5. CONCLUSION

We have performed an extensive study of the behaviour of the 2 mm gap and the 3 mm gap GSC's using non ozone depleting gas mixtures. Experimental data show that the 2 mm gap time resolution is always better than the 3 mm gap time resolution. Both 2 mm gap and the 3 mm gap GSC's work properly and reach high efficiency with all the

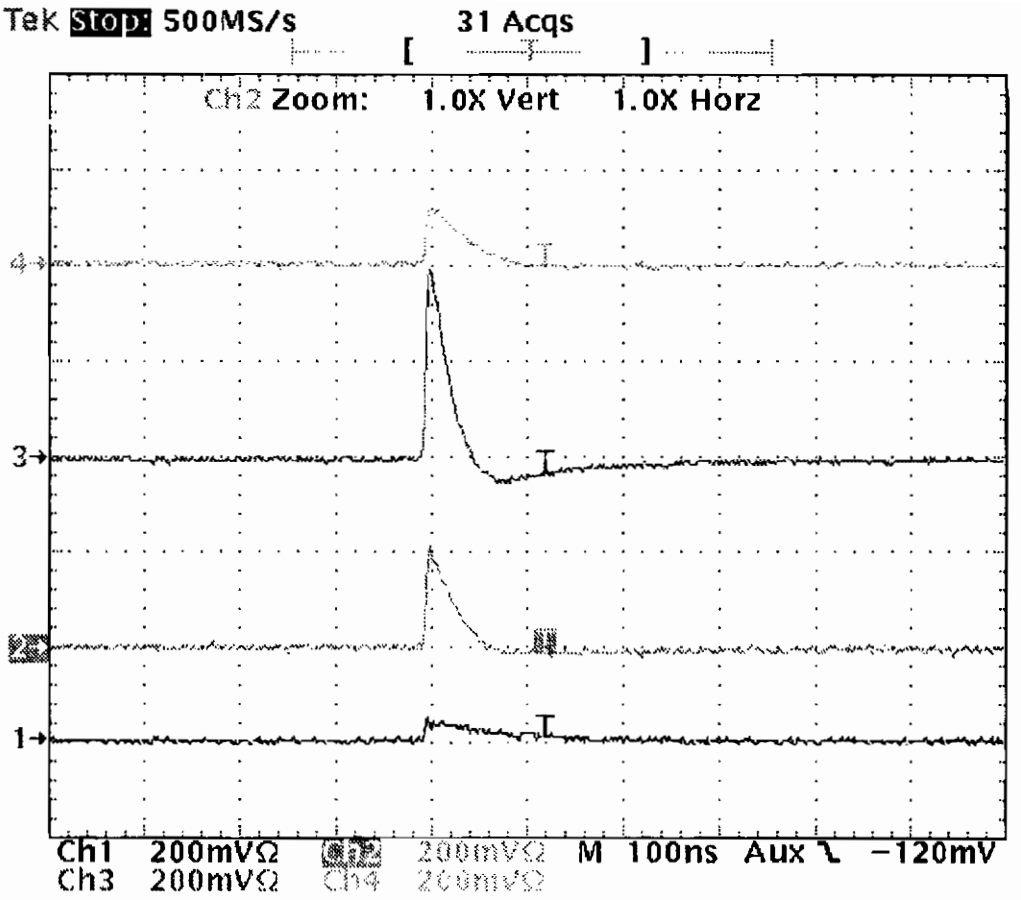


Figure 12: *Oscillogram of the induced signals on the strips* ($d_1 = 4\,mm, d_2 = 0.2\,mm$)

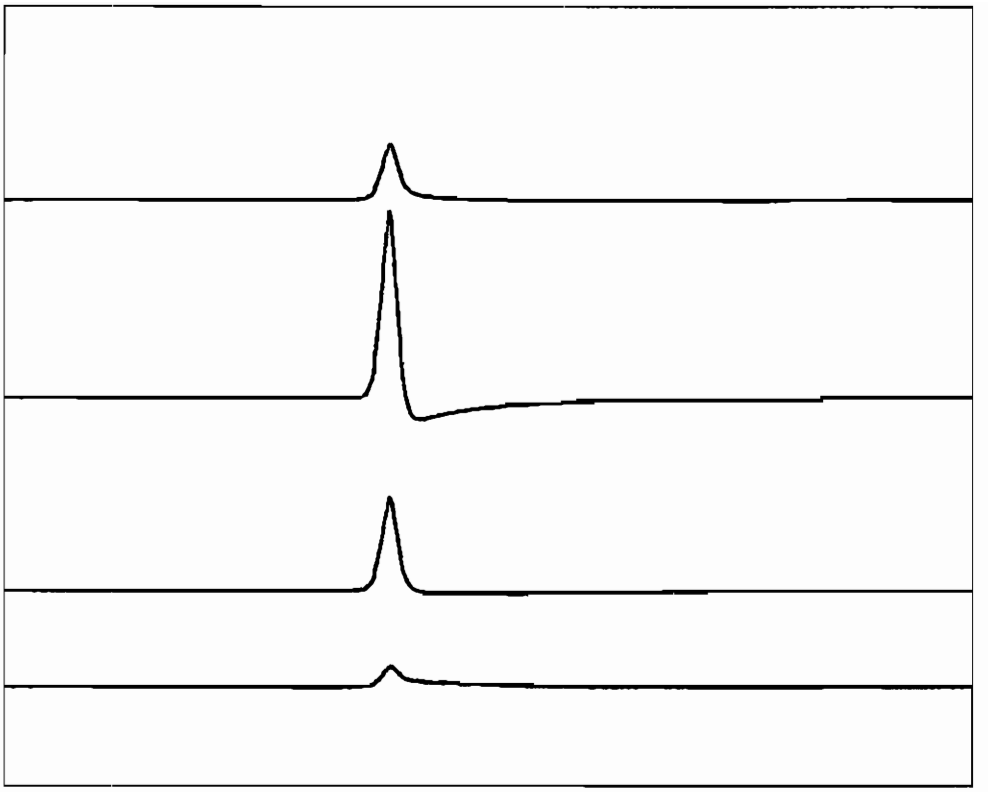

Figure 13: *Simulated induced signals on the strips* ($d_1 = 4mm, d_2 = 0.2mm$) *The curves have to be compared with the oscillogram of figure 12.*

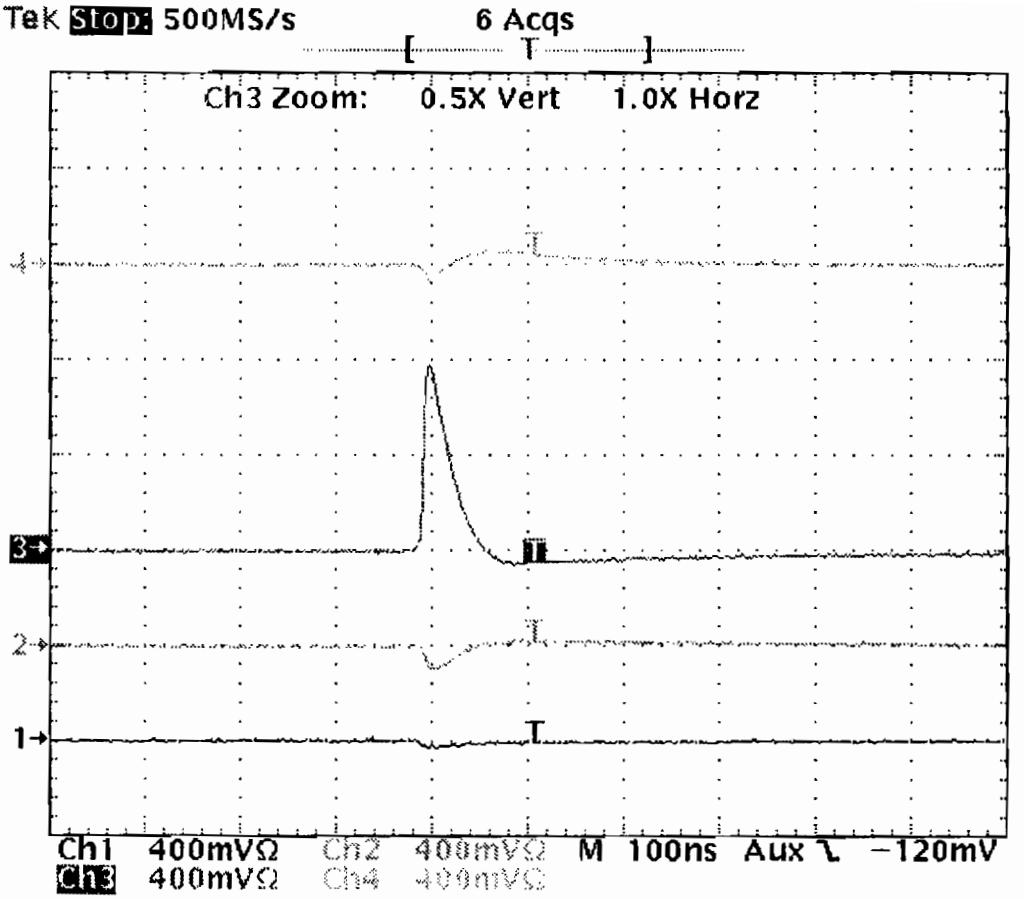


Figure 14: *Oscillogram of the induced signals on the strips* ($d_1 = 0.2mm, d_2 = 4mm$).

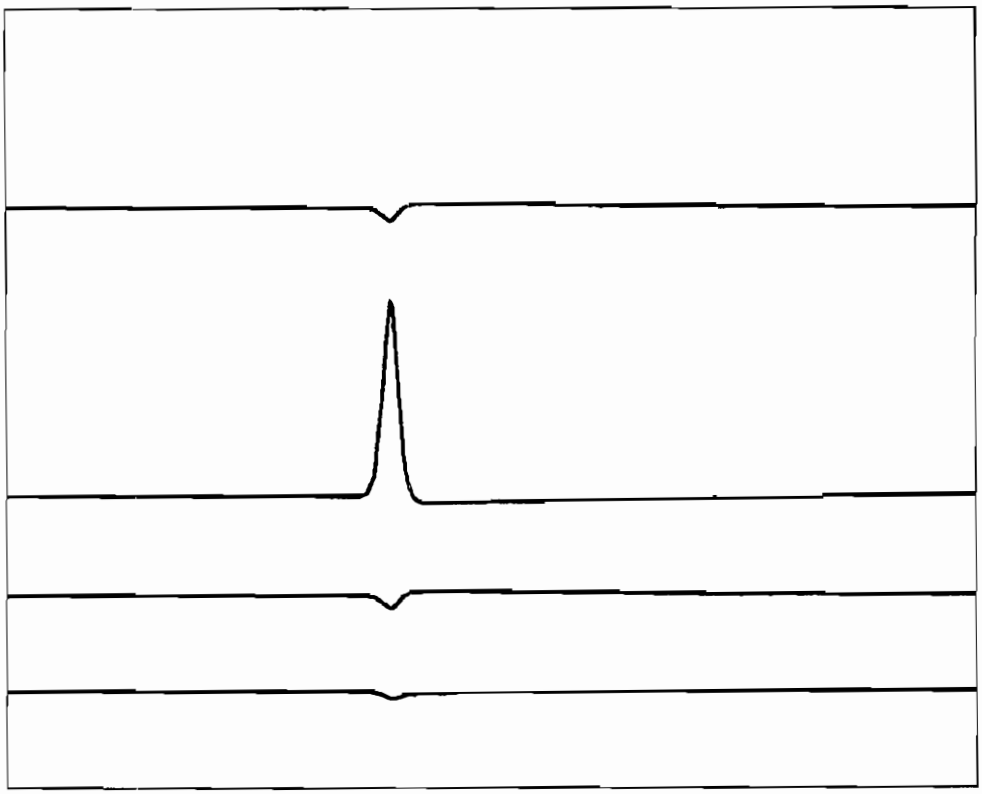

Figure 15: *Simulated induced signals on the strips* ($d_1 = 0.2mm, d_2 = 4mm$). *The curves have to be compared with the oscillogram of figure 14.*

gas mixture we used, while a good time resolution performance strongly depends on the choice of the gas mixture. The data show clearly that there is a minimum in the plot of the time resolution as a function of the Iso/R134A ratio or, equivalently, for intermediate value of the induced streamer charge.

The comparison of the measurements with our simulation program confirm the capability of the program to accurately predict the detector response. The simulation program we developed is therefore a useful tool to tailor detector parameters as a function of the experimental requirements.

## 6. AKNOWLEDGMENTS

Authors are gratefull to M. De Deo for the help in the realization of the simulation program, M. D'Incecco for the realization of the GSC front end electronics, E.Tatananni who built the detectors and G.Pellizzoni for the invaluable help in setting up the tests carried out at the RomaTre University.

## 7. REFERENCES

1. G. Bencivenni et. al. *Nucl. Instr. and Meth.* **A345** (1994) 456.
2. C. Gustavino et.al., *Scientifica Acta*, **Volume XI** (1996) 387.
3. G. Liguori et. al., *Scientifica Acta* , **Volume XI** (1996) 255.
4. R. Cardarelli et. al.,*Scientifica Acta*, **Volume XI** (1996) 11.

# DATA ACQUISITION SYSTEM FOR THE RPC DETECTOR OF BABAR EXPERIMENT

G. CROSETTI *
*Istituto Nazionale di Fisica Nucleare,*
Via Dodecaneso 33 Genova, I-16146, Italy

April 6, 1998

ABSTRACT

Resistive Plate Chamber (RPC) has been chosen as active detector to equip the Instrumented Flux Return (IFR) of the BABAR experiment. The new design of the Front-End electronics realizes a compromise between the large number of channels (50,000) and the cost of the project. The different components will be described and the results of the first prototypes presented.

*co authors : A.Palano *INFN and Un.Bari, Dipartimento di Fisica, Via Amendolia 1733,I-70126Bari, Italy* ; A.Buzzo, R.Contri, M.Lo Vetere, M.Macrí, S.Minutoli, R.Monge, M.Pallavicini, C.Patrignani, E.Robutti, A.Santroni *INFN and Un.Genova, Dipartimento di Fisica, via Dodecaneso 33, I-16146Genova* ; R.Baldini, A.Calcaterra, R.DeSangro, D.Falciai M.Piccolo, Z.Yu, A.Zallo *Lab.Nazionali di Frascati-INFN,C.P.13,I-00044 Frascati,Italy* ; F.Anulli, I.Peruzzi *INFN and Un. Perugia, Dipartimento di Fisica, via A.Pascoli,I-06123 Perugia Italy* ; G.Carlino, N.Cavallo, F.Fabozzi, C.Gatto, L.Lista, P.Paolucci, P.Parascandolo, D.Piccolo, C.Sciacca *INFN and Un.Napoli, Dipartimento di Fisica Mostra d'Oltremare, pad19, I-80125 Napoli Italy*;

## 1. Introduction

The BABAR detector has been designed to study the CP violation asymmetries in the decays of $B^0$ mesons. The experiment will be carried out at the PEP-II accelerator at Stanford Linear Accelerator Center (SLAC).

The physics program is very rich and includes also the determination of the CKM matrix elements, the $B^0$ rare decays and the Charm and Tau physics [1]. The construction of the experiment and of the beam are in advanced phase and the first collisions are foreseen in Summer 1999.

The muon detector makes use of the Flux Return of the Solenoid equipped with Resistive Plate Chambers (RPC).

The IFR group has built and installed in the detector more than 800 chambers. Before the shipment to SLAC all the chambers was tested in the INFN laboratory in Frascati for gas leaks, and HV. The measurement of HV plateau and of various efficiencies[2] were done during a cosmic rays test.

The Data Acquisition system (DAQ) is one of the key part of any high energy experiment, it must guarantee the collection of the events selected by the trigger system. It must also provide calibration, monitoring and debugging facilities. The architecture chosen by BABAR is fully pipelined in both the trigger and the data flow paths. As a result the system is nearly deadtime free at background levels up to ten times the rate give by machine simulation.

## 2. The IFR Data Acquisition System

The IFR Data Acquisition system must satisfy the requirements of the general system and, at the same time, try to realize the compromise between the large number of strips ($\sim 50,000$) used to read the RPC, and the cost of the electronic. Since the Front-End electronics is installed very close to the detector, not easily accessible, the read-out design must be also very reliable. To achieve this goal and to fulfill the BABAR requirement on the DAQ speed, a mixed parallel-serial readout has been

chosen.

A high speed clock ($59.5MHz$) will be used to synchronize the flow of data and to control, reset and throttling of data.

The IFR DAQ system, shown in Fig[1], can be divided in three parts:

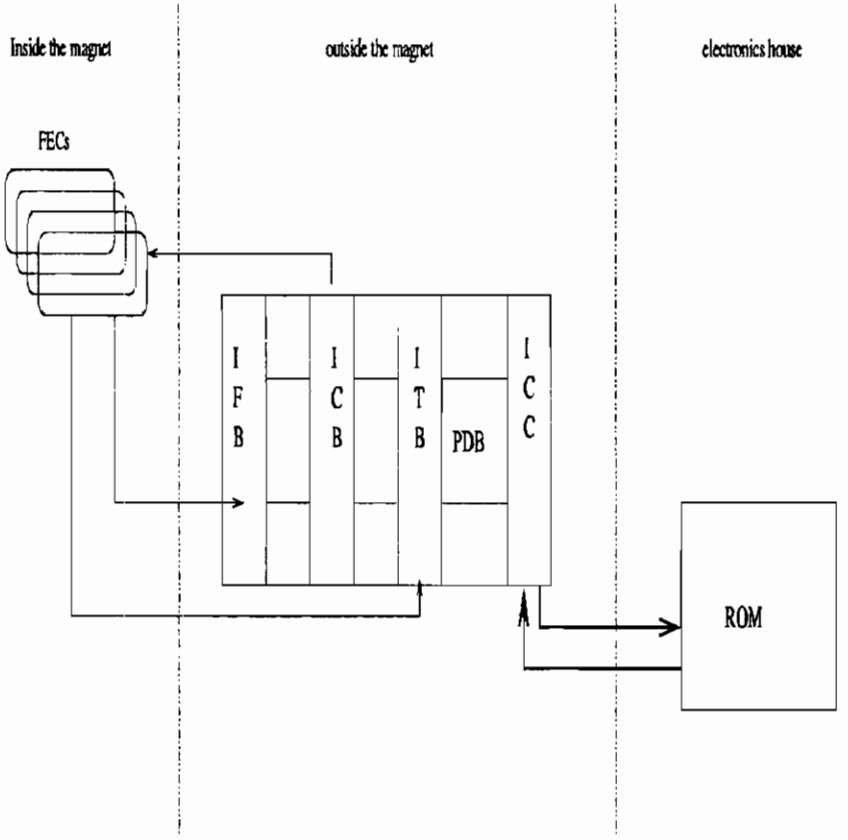


Fig. 1. IFR Data Acquisition System

- The Front End Cards (FEC) discriminate the strip signals and store the data during the trigger latency. Most of them are installed, together with the RPC, inside the iron slabs. A small part of them, when not enough space is avaliable, are hosted in special minicrate located outside the iron.

- The intermediate step is the readout crate, eight of them are distributed around the detector. In this crate there are three kinds of IFR boards, the FIFO board (IFB) where the digital strips data are kept until the DAQ is ready to read them. The TDC board

(ITB) is connected to the Fast-OR output of the 16 channels of the FEC. This signal is sent to multihit TDC and used to measure the time of RPC hits. The third board, Calibration board (ICB), is used to send test signal to the FEC input stage to check the threshold and their status.

A dedicated Crate Controller (ICC) is used to connect the crate to the Electronic House via the optical link. Inside the crate a custom point-to-point backplane (PDB) is installed, all these electronic boards have been designed to operate at the BABAR sytem frequency of $59.5 MHz$.

- The last part of the IFR DAQ system is the Readout Module (ROM). This is the standard BABAR DAQ board used by all the detectors and located in the electronic house. It is connected to the crate through an high speed data link (G_link) used to transmit data on optical fiber.

In this report the different components of the IFR DAQ system will be described and the results of the first prototype will be presented. In table[1] the total number of IFR DAQ board is shown:

Table 1. IFR DAQ boards

| | |
|---|---|
| DAQ Crate | 8 |
| ICC | 8 |
| IFB | 56 |
| ICB | 20 |
| ITB | 36 |

## 3. The Front End Card (FEC)

The RPC is a low noise detector with a good signal to noise ratio, producing fast ( rise time 2-4 ns) and hefty signals ( of the order of 300mV). These characteristics allow the use of cheap electronics with a fixed threshold. FEC input stage ( see block diagram in Fig[2]) is connected directly to the strips and operates continuously, each strip acts as a transmission line with a discriminator at the end.

The FEC takes into account also the trigger latency of $11.5 \pm .5 \mu s$, the digital signal is fed into a dual bank of monostables which enables

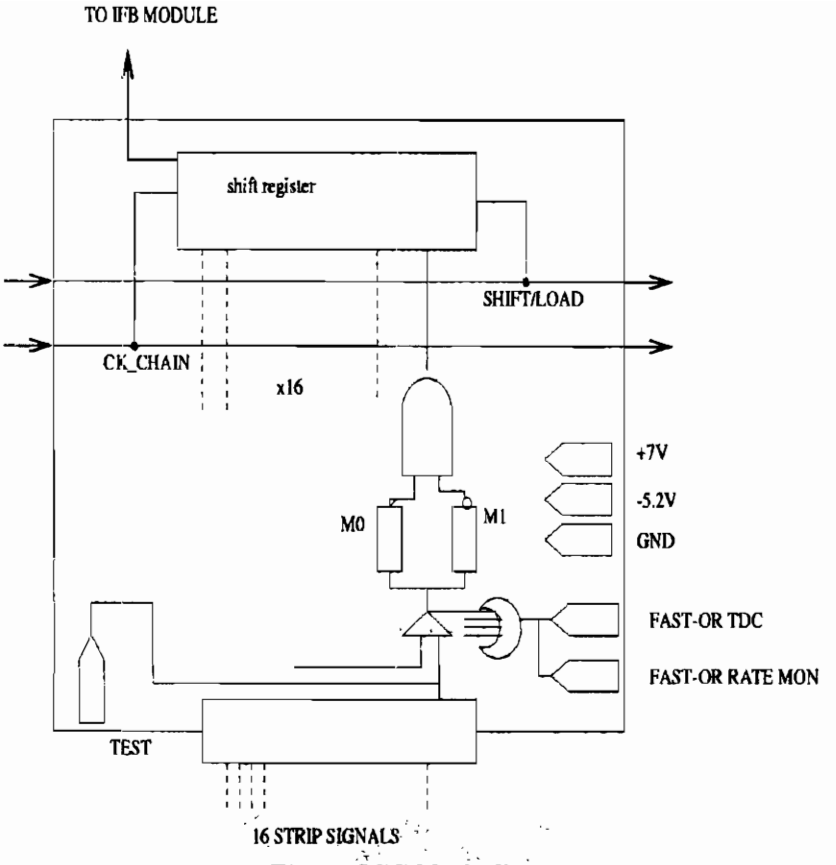

Fig. 2. ICC block diagram

the data collection only during the trigger time window of $1\mu s$. This method produces also a strong reduction of the detector noise.
On the occurrence of the trigger, a Shift/Load signal and a sequence of 16 clock pulses are sent by the IFB to the FEC. The Shift/Load signal loads the pattern into a shift register and the clock pulse shifts the 16 strips data out of the board. The FIFO board reads 64 FEC's in parallel. To test the functionality of the front end it is possible to inject a pulse into the input stage of the transistor simulating an hit on all the 16 channels.

## 4. The Point-to-Point Distribution Board (PDB)

The design of this backplane requested a special care to guarantee the delivery of signals and clock at $59.5Hz$ within the requirements of

the BABAR DAQ system. The "stripline" technology (Fig[3]), with 9 layers, was chosen after a successful test on a prototype board, all lines have controlled impedance (50Ω).
The Point-to-point Distribution board is a 21 slot backplane for standard 6U Eurocard crate, 17 of them are used by the readout boards, 4 are reserved to power IFR trigger boards. Signals are located on J2 connector, row A and C are for signals, row B is for power and ground. The first position is for the ICC. Each board is connected to the ICC via 3 lines for single-ended signals, data-in, data-out and the clock, all lines have the same length ( 14.8" ± .1") to minimize the skew between them. Line terminations on the PDB can be chosen to be resistive or AC coupled.

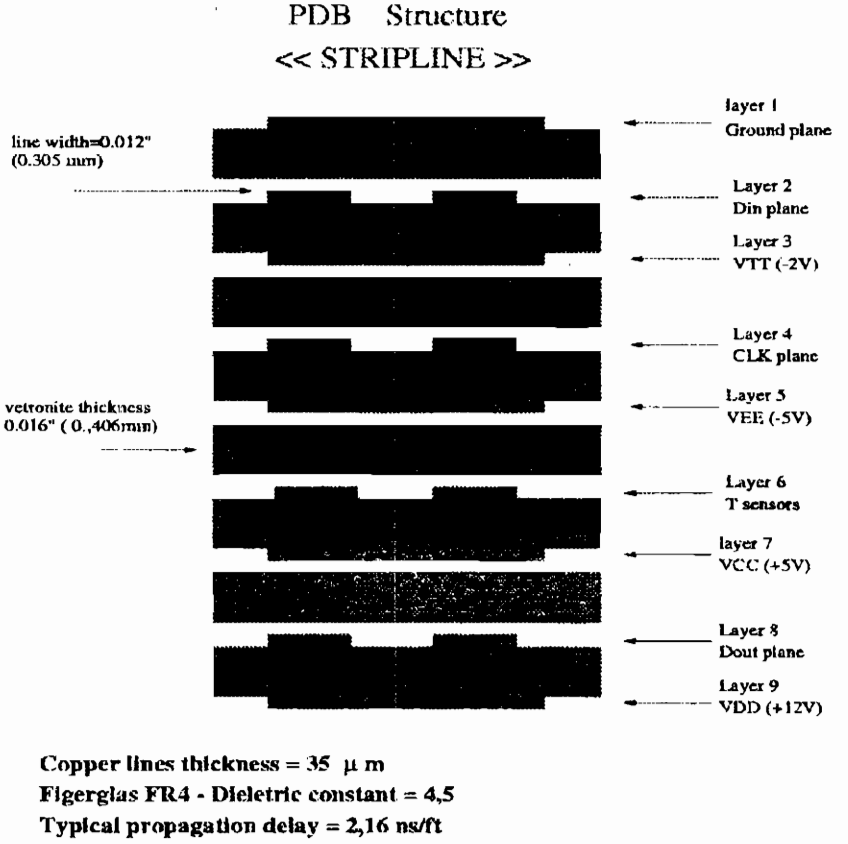


Fig. 3. Point-to-Point Distribution Board

## 5. The IFR Crate Controller (ICC)

The ICC must guarantee clock and the data delivery to the 16 boards with a jitter less than $\pm 0.5ns$. Unfortunately the use of high performance clock drivers does not guarantee free trouble operation. Only careful board layout and consideration of system noise issue can guarantee reliable clock distribution.
The block diagram of the ICC is shown in Fig[4]. The FINISAR transceiver is the physical interface with the optical link. It is a low cost and high reliability data link up to $1.5Gbits/s$ for application less than a kilometer in length.
The HP chips (HDMP-12, HDMP-14) are used to serialize/deserialize the data, they also perform clock and data recovery, frame synchronization, error recovery and link state monitor.
The clock, received at the exit of the HDMP-1014 receiver, is reshaped in a PLL and then distributed to the 16 boards after been synchronized with the data. The same clock, delayed to wait the data coming from IFR boards, is used to send back data to the ROM.
In the ICC a microntroller (MC68HCX32CFU) monitors the status of the FINISAR modules and reads the temperature inside the crate. The chips provides an external connection with the CAN bus driver, this technology has been chosen by the experiment to communicate the slow control data.

## 6. The IFR FIFO Board (IFB)

The IFB (Fig[5]) reads data from 64 FEC's, store data until DAQ is ready for the event readout.
After receiving a L1T command (Trigger), the IFB starts a serial data transfer from the FEC's (by means of Shift/Load and Clock signals). Incoming data are stored in the IFB FIFO's dimensioned to allocate up to 56 complete event fragments ( each fragment consists of 1024 bits correspondig to as many strips).
On the arrival of RDE command (Read Event) data are extracted from the FIFO and sent to the ROM. According to the BABAR protocol, two more global commands must be decoded by the boards: the SYNC command used to resynchronize the Time Stamp of the board, and the

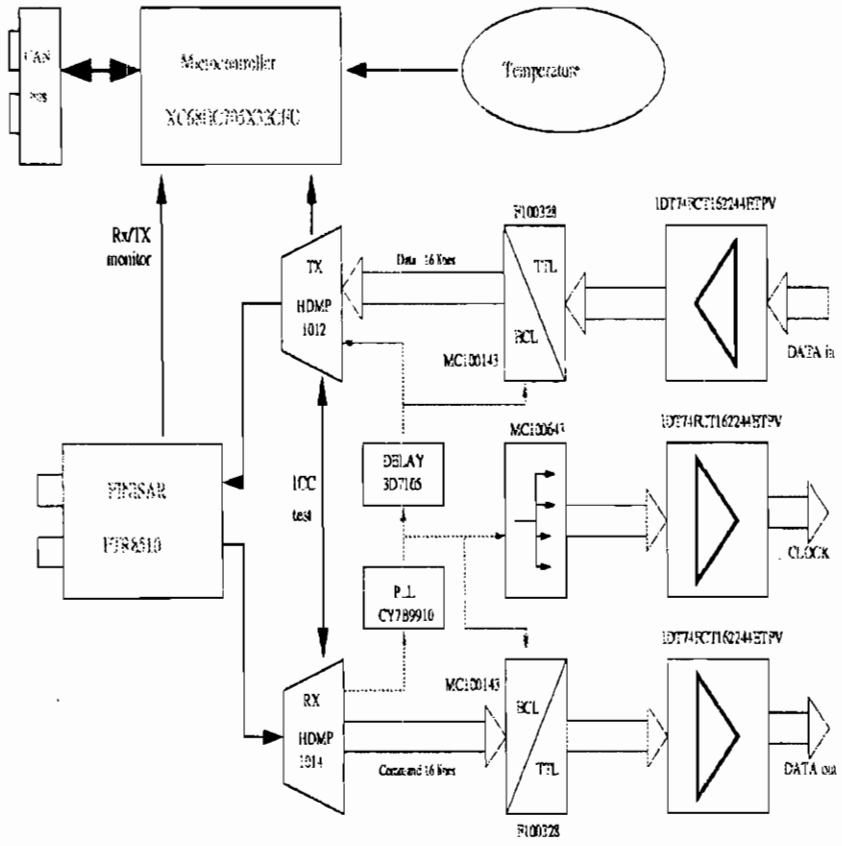


Fig. 4. ICC block diagram

CLEAR command resetting the FIFO pointers.
For debugging purpose two specific commands have been implemented to write 64 bits test pattern (WRF) in the FIFO and to read them back (RDF).

## 7. The IFR Calibration Board (ICB)

The Calibration board (Fig[6]) will be used to monitor and debug the FEC's. Each board has 96 output channels; the signal generated can be programmed both in shape and amplitude using a specific command (Write Control Register, WCR). Positive or negative polarity can be chosen using the same command.

A further specific command (Write Pattern Register, WPR), containing a 96 bit mask, selects the FEC's to be pulsed.

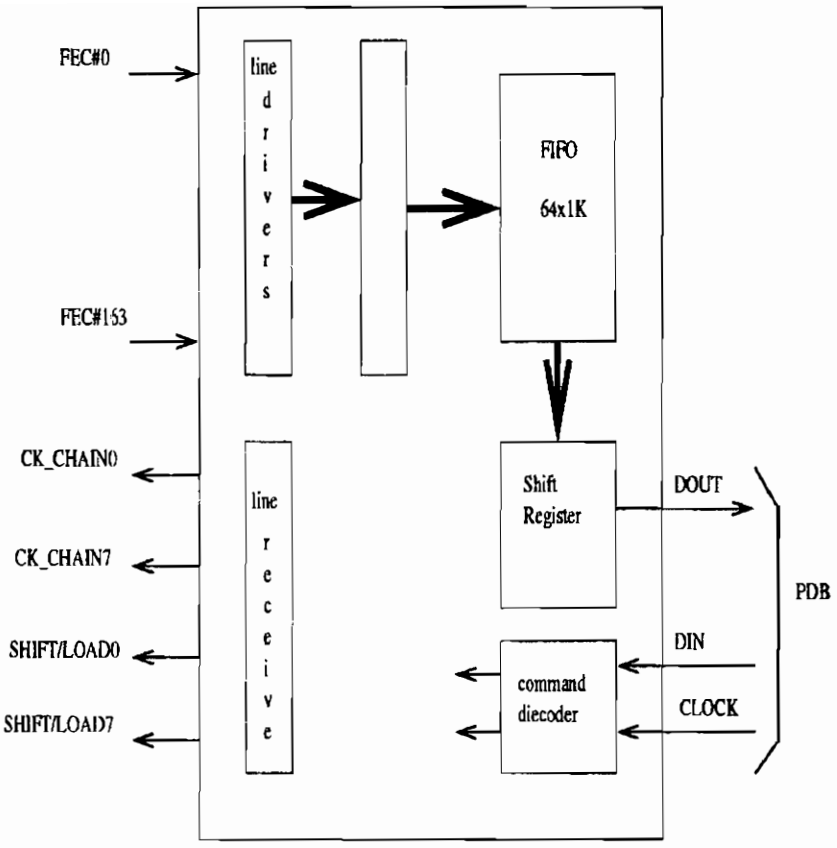


Fig. 5. IFB block diagram

Whenever a Calibration Strobe command (CAS) arrives, the ICB injects a test pulse in the Front-End electronics. The BABAR DAQ system assures a L1T command following at exact $11.5\mu s$ the CAS one. In this way the Trigger latency is preserved and the front-end electronics can be read as during normal data taking.

## 8. The IFR TDC Board

The TDC board will exploit the excellent time resolution of the RPC's to determine the bunch crossing time of the beam.
The TDC chips, designed at CERN ([3]) as general purpose converter, can operate in many different configurations. These chips have a large memory able to store the ungated input of the FEC's until the trigger arrives. The data selected according the trigger latency and its time

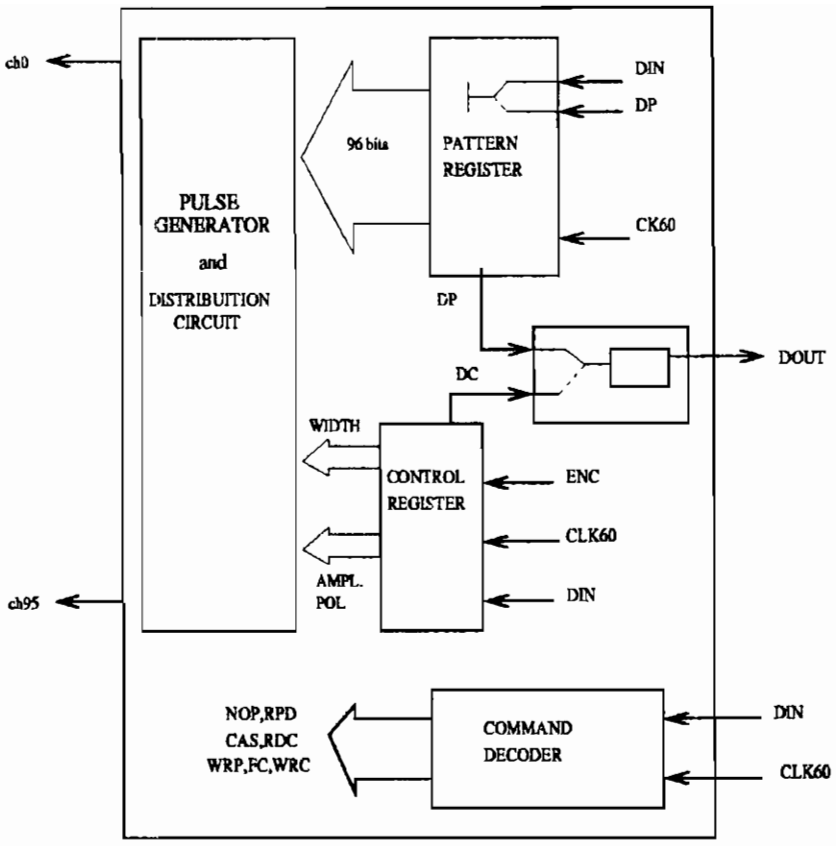


Fig. 6. ICB block diagram

window, are copied in the external large FIFO until the DAQ asks for them. A powerful programmable device (XILINX 4006) will take care of decoding the protocol global and subsystem commands. In order to deliver the system clock to the TDC chips with a jitter lower than $200ps$ and a duty cycle between 45% and 55%, the signal will be re-shaped in the PLL just after being received. The TDC configuration will be loaded (and checked) with specific command by writing (and reading) configuration registers. The block diagram is shown in Fig[7].

## 9. Results from Prototype Tests

A test bench shown in Fig[8] has been arranged and used to test the prototypes of readout boards. The same setup will be utilized to validate the final production. It consists of 4 minicrates with 16 FECs

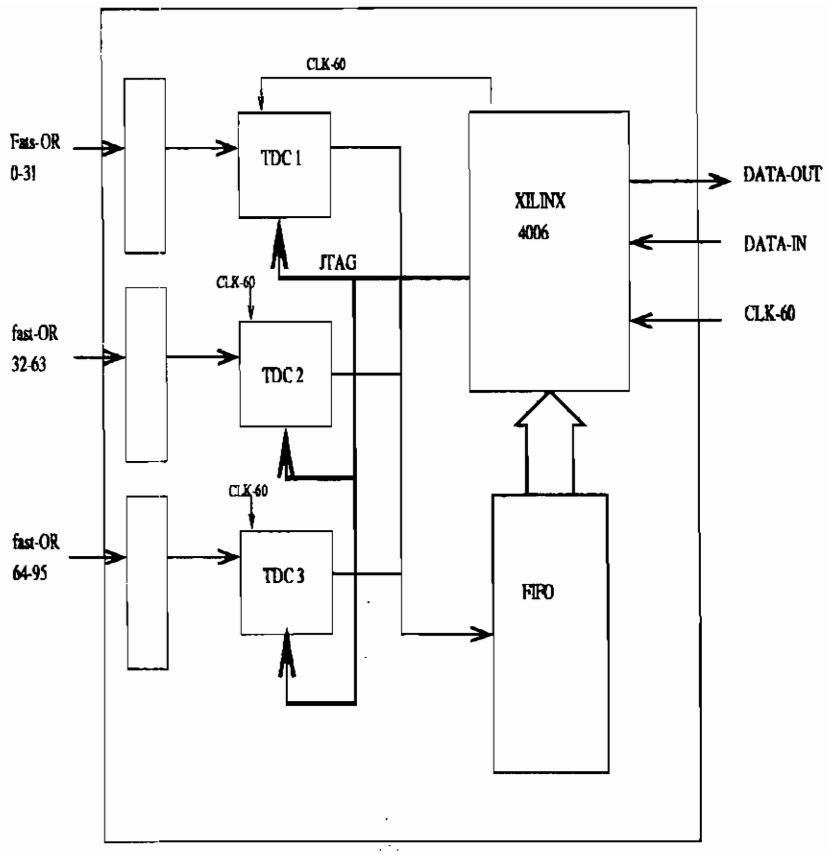


Fig. 7. ITB block diagram

each, one crate with 1 ICC, 4 IFB and 1 ICB. The data are read into the ROM via 40m optical fibre and stored in UNIX station. A second ICC is used close to the ROM, as personality board, to allow the connection with the optical link.

During normal test the calibration signal is sent from the ICB to the FEC's, after a trigger latency of $11.5\mu s$, the FEC's are read and data is sent into the IFB. The RDE command enables the transport of the data from the IFB to the ROM.

With this test it is possible to check the correct performaces of all the boards and their synchronization with the system frequency of $59.5MHz$.

Last point verified is the correct operation of the G_link in the IFR DAQ

environment.

## 10. Conclusions

The prototypes of all the IFR board needed for the data acquisition system are built. Each board has been tested in stand-alone mode to check its compatibility to the BABAR DAQ system.
In a complete test of IFR DAQ system all boards have shown no problems and the procedure to test the final production is found.

IFR DAQ electronics set-up

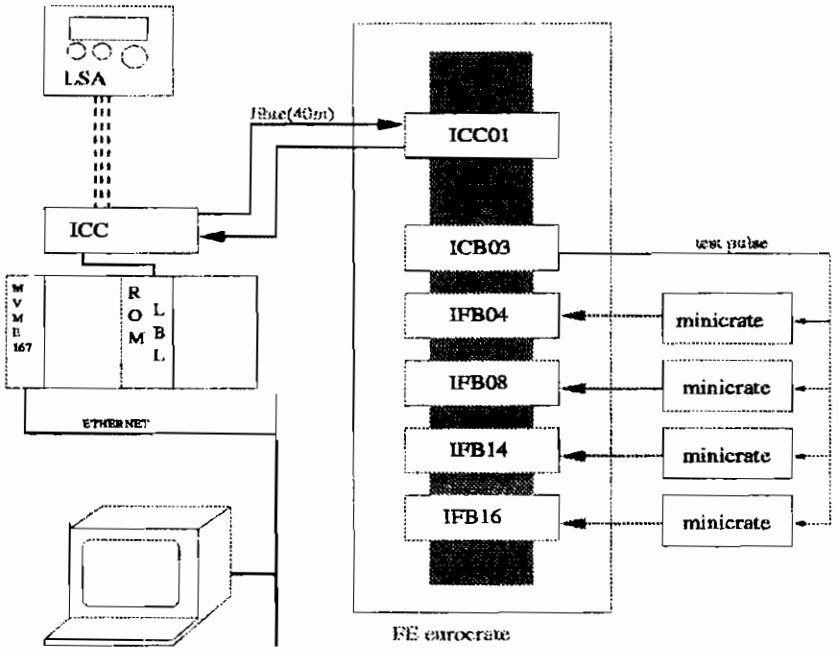


Fig. 8. DAQ IFR test bench.

## 11. Acknowledgements

We are indebted to the competent help and steady dedication of G.Barisone, L.D'Aniello, V.Masone, M.Negri and L.Parascandolo. With-

out their continuous support the IFR DAQ construction and test could not be completed in time.

## 12. References


1. Paper contributed by D. Piccolo to these proceedings.
2. Paper contributed by A. Calcaterra to these proceedings.
3. J.Cristiansen, *32 Channel general purpose Time to Digital*, CERN/ECP-MIC,http://pcvlsi5.cern.ch:80/MicDig/jorgen/tdc32_ma.pdf.

# The dimuon trigger of the ALICE–LHC experiment

Pascal Dupieux *
*Laboratoire de Physique Corpusculaire de Clermont-Fd,*
*IN2P3–CNRS–Université Blaise Pascal,*
*63177 AUBIERE Cedex, France*

January 8, 1998

ABSTRACT

We describe the trigger system of the ALICE dimuon spectrometer, based on RPC detectors. The background rate is at least one order of magnitude less in ALICE than in LHC p–p experiments due to the lower luminosity in ion running. Hence we study the possibility to operate the RPCs either in streamer or proportional mode. We report a study done with cosmic rays concerning gas mixtures for streamer mode. The aim is to minimize the streamer charge for a better flux capability of the RPC and a smaller cluster size, as needed for ALICE. We also give the results of a beam test at SPS where the RPC was placed in the vicinity of a hadron absorber, simulating the operation conditions in ALICE.

## 1. Physics Motivations

The suppression of the production rate of the $J/\Psi$ and $\Upsilon$ resonances by Debye screening effect [1] will be a signature of the Quark Gluon Plasma (QGP) formation in heavy ion collisions at LHC. In order to study this issue in the dimuon decay channel, the ALICE collaboration, devoted to heavy ion at LHC, decided recently to upgrade the

*for the ALICE Collaboration

central part of the detector by adding a muon spectrometer at forward angles [2]. This spectrometer measures the complete spectrum of heavy quark vector mesons i.e. $J/\Psi$, $\Psi'$, $\Upsilon$, $\Upsilon'$, $\Upsilon''$ via their muonic decay in p–p and ion–ion collisions. An independent normalization is obtained by measuring open charm and beauty production which are not affected by final state interactions and are not sensitive to the nature of the medium (i.e. confined or deconfined). The observables which determine the general conditions of the collision such as the centrality are provided by the central detectors [3] of ALICE.

## 2. Spectrometer Overview [2]

The main elements of the dimuon spectrometer are shown in Fig 1. The angular acceptance goes from 2° to 9° ($2.5 < \eta < 4.0$). It consists of a front absorber of low Z material starting 90 cm from the vertex, a large dipole magnet with a 3 T.m. field integral and 10 planes TC1–TC10 of high granularity tracking chambers. At the end of the spectrometer, two stations MC1–MC2 of RPCs protected by a 1.2 m iron wall (muon absorber in Fig 1) are used for muon identification and triggering. The spectrometer is shielded throughout its length by a dense absorber (small angle absorber in Fig 1) which surrounds the beam pipe.

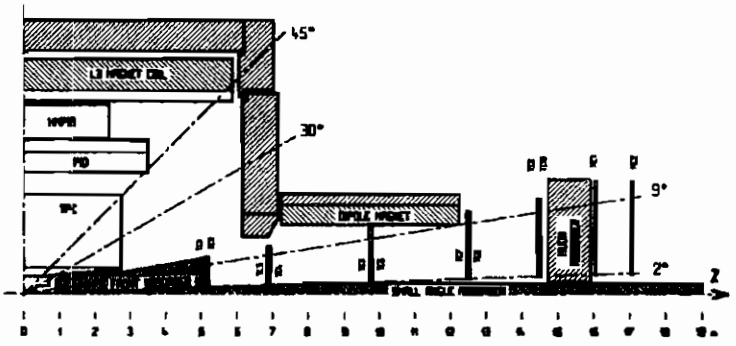


Fig. 1. Spectrometer overview

## 3. Description of the Trigger System [2]

The trigger is based on a cut in the muon transverse momentum (so-called LVL1 trigger) using the dipole deflection, taking advantage of

the high $p_t$ of the muons from resonances. A subsequent cut (LVL2) on the dimuon mass can be done.

The dimuon signal from resonances must be sorted out from the large multiplicity of background muons from pion, kaon and charm decay and soft background (mainly electrons leaking out from the beam shield and the iron wall). The heaviest system at LHC is Pb–Pb at $\sqrt{s}$ =5.5 TeV/nucleon where 4000–8000 charged particles (mainly pions and kaons) per unit of rapidity are produced in a central collison. In such events, a mean number of 12 background muons and 40 prompt soft background hits (per gas plane) are expected on the trigger. Hence, the set-up requires a high level of segmentation.

### *3.1. Trigger Set-up*

Two trigger stations MC1 and MC2 are located at 16 and 17 m from the interaction point. They cover an area of about $6 \times 6$ m$^2$ with a $0.6 \times 0.6$ m$^2$ opening in the centre to accomodate the beam pipe and shielding (Fig 2).

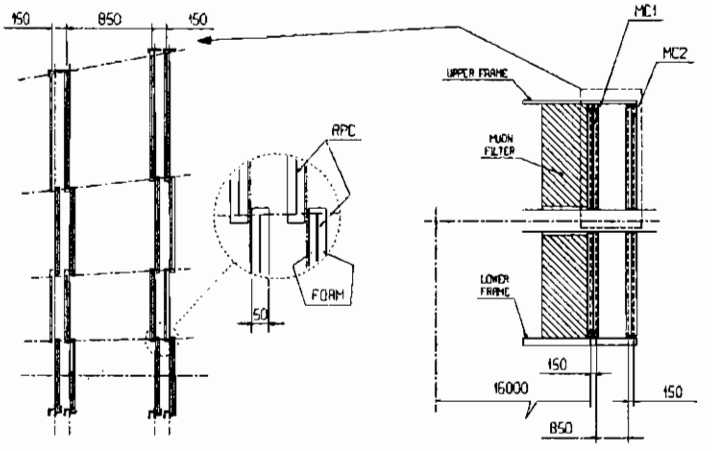


Fig. 2. Trigger set-up

Each station consists of two planes of single-gap RPCs [4] and each plane is read out on both sides of the gas gap via orthogonal strips ($x$–$y$ readout). A total of about 30k strips are needed to account for the high multiplicity in Pb–Pb collisions. We require a 3/4 majority coincidence

both in $x$ and $y$ to reject soft background hits. In the bending plane of the dipole ($x$, vertical), the strip width increases from 1 to 3 cm almost linearly with the radial distance from the beam axis and so does at first order the magnetic deviation. With this set-up, we obtain a deviation of about $\pm 4$ strips for a $p_t$=1 GeV/c muon, whatever its location on the trigger. In the non-bending plane $y$, the strip width is 2 and 3 cm (inner and outer part of the trigger respectively) and we ask the track to point back to the interaction point.

### *3.2. Trigger Electronics*

The information from the trigger chambers is treated by a dedicated trigger electronics (LVL1 electronics) to perform the cut on the single muon transverse momentum. To do that the LVL1 electronics defines "roads" between MC1 and MC2 which width corresponds to a given $p_t$ cut (a narrow "road" corresponds to a high $p_t$ cut and a small magnetic deviation and vice-versa). The "road" description is loaded in memories of the trigger chips. Two $p_t$ cuts are foreseen : $p_t > 1$ GeV/c for the "J/$\Psi$ trigger" and $p_t >$ 2-3 GeV/c for the "$\Upsilon$ trigger" at low rate.

The trigger chips give a decision on valid "roads" including the sign of the deviation for each $p_t$ threshold. The information of all the LVL1 circuits ($\sim$ 1000 circuits) is finally collected and two valid "roads" of unlike sign essentially are required to build the final dimuon trigger. These operations must be done in less than 600 ns. The LVL1 rates should not exceed 1 kHz. We aim to read out all the spectrometer plus ITS information when a LVL1 decision occurs, though some scaling is possible in case the rates are too high.

A subsequent cut on the dimuon mass can be done by fast processing within 100 $\mu$s (called LVL2 trigger). The LVL2 rate allows to read out the full ALICE barrel detectors in coincidence with the muon spectrometer which opens some interesting physics perspectives especially in Pb–Pb collisions.

### *3.3. Trigger efficiency and rates*

The trigger efficiency has been calculated with an almost complete simulation of the set-up, including the trigger detector segmentation and the treatment of the information by the LVL1 electronics.

The trigger efficiency as a function of $p_t$, for perfect ("Reference")

and segmented trigger plane ("Chambers + Strips") is represented in Fig 3 for two selected $p_t$ cuts (left part : $p_t \simeq 1$ GeV/c, right part : $p_t \simeq$ 2.3 GeV/c) at 50 % efficiency.

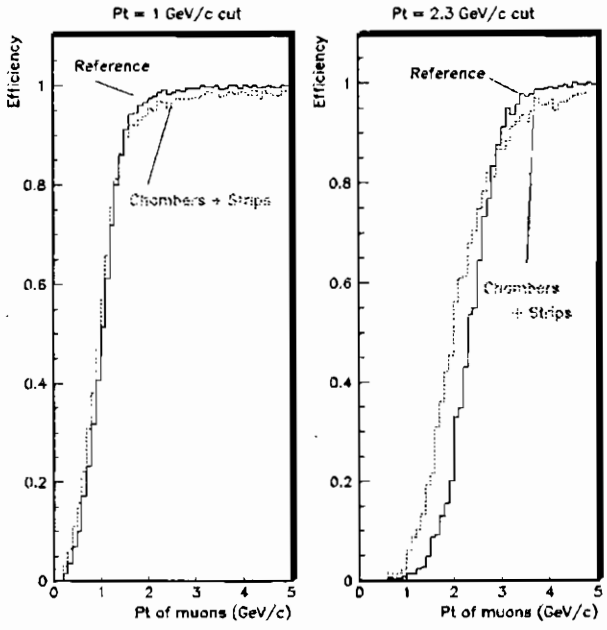


Fig. 3. LVL1 trigger efficiency versus muon $p_t$ (two $p_t$ cuts)

For the same $p_t$ cuts, the trigger efficiencies are given in Table 1 for the resonances (J/$\Psi$, $\Upsilon$), for background (pion and kaon decay into muon), charm and beauty decay [5]. The effects of the detector do not exceed a few percent.

Table 1. LVL1 trigger efficiency for signal and background

| | Efficiency : $p_t = 1$ GeV/c | Efficiency : $p_t \simeq 2.3$ GeV/c |
|---|---|---|
| J/$\Psi$ | 75% (detection) | |
| $\Upsilon$ | | 92% (detection) |
| Backgr. (sngle $\mu$) | 85% (rejection) | 97% (rejection) |
| Charm (sngle $\mu$) | 71% (rejection) | 95% (rejection) |
| Beauty (sngle $\mu$) | | 74% (rejection) |

The LVL1 trigger rates are deduced from these efficiency calculations and shown in Table 2. The trigger rates are about 1 kHz in Pb–Pb and

Ca–Ca running. The trigger chamber segmentation is sensitive in case of Pb–Pb collisions and induces for instance about 30 % increase of the LVL1 rates for the $p_t$ = 1 GeV/c cut. We give also in Table 2 the expected detection rate of resonances J/$\Psi$ and $\Upsilon$ after all cuts.

Table 2. LVL1 trigger rates (minimum bias)

| | | Pb–Pb | Ca–Ca | p–p |
|---|---|---|---|---|
| L ($cm^{-2}$ $s^{-1}$) | | $10^{27}$ | $10^{29}$ | $10^{31}$ |
| Min. Bias (Hz) | | 8000 | 3 $10^5$ | $10^6$ |
| | | Unlike sign $\mu$–$\mu$ rate at LVL1 | | |
| $p_t$ > 1 GeV/c | Tot (Hz) | 900 | 1200 | 20 |
| | J/$\Psi$ (Hz) | 1 | 2 | 1 |
| $p_t$ > 2.3 GeV/c | Tot (Hz) | 200 | 50 | 1 |
| | $\Upsilon$ (Hz) | 0.01 | 0.03 | 0.01 |

## 4. Gas mixtures for streamer mode

From FLUKA simulations [6], we estimate that the maximum rate on the ALICE trigger chambers reaches 50 Hz/cm$^2$ in Ca–Ca running (10 Hz/cm$^2$ in Pb–Pb and p–p), close to the beam shielding. Most of this background is created by soft charged particles leaking out from the beam shielding and the iron wall. The simulation accuracy has been cross-checked during two running periods at SPS in 1996 and 1997 (see Ref. [7] and last section). We have found that the experimental background yields close to a thick hadron absorber are reproduced within 50 % by the simulation. Hence, our requirement concerning the flux capability of the trigger detector is fixed to 100 Hz/cm$^2$ at present. This value is certainly the last limit of the operation in streamer mode with low resistivity RPCs (keeping also in mind that we will have at LHC a continuous irradiation on the whole surface of the chambers). Nonetheless, in the first part of our R&D program, we have started to investigate gas mixtures for streamer mode which lower the pulse charge at maximum in order to optimize the rate capability of the RPCs.

### *4.1. Cosmic ray test set-up*

We use a 50×50 cm$^2$ RPC with strips 3 cm wide terminated on a 50 $\Omega$ resistor at one end and connected to the front-end electronics (FEE)

at the other end. The trigger consists of a coincidence of 3 scintillators which matches the geometrical acceptance of one strip of the RPC (so-called "central strip"). The efficiency is defined as the ratio $N_2/N_1$ with :

- $N_1$ : coincidence counting rate of the scintillators
- $N_2$ : coincidence of scintillators and chamber (taking actually the logical OR of 5 strips centered around the "central strip")

We also record the "neighbour efficiency", removing the "central strip" when counting $N_2$ : small values of the neighbour "efficiency" are obviously correlated with a small cluster size (number of fired adjacent strips) which is an important parameter for the RPC operation at LHC.

### *4.2. Selected gas mixture*

We have tested gas mixtures of Ar, Isobutane, Forane ($C_2H_2F_4$), SF6 and CO2 in various combination percentage.

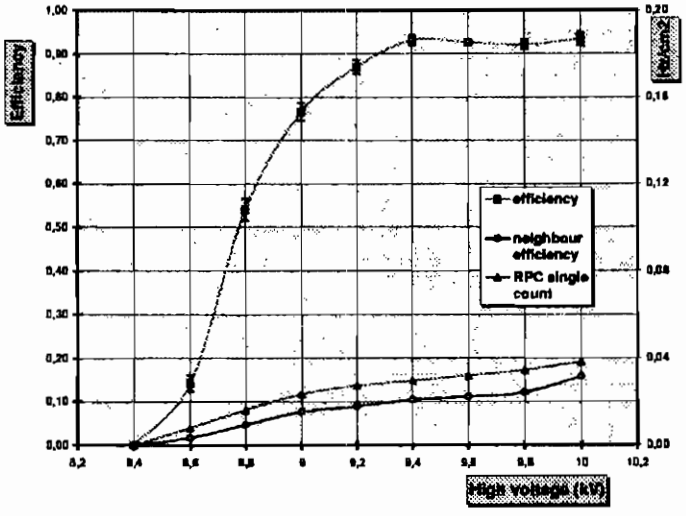


Fig. 4. RPC efficiency for the gas mixture Ar 49% Isob 7% Forane 40% $SF_6$ 4%

An example of efficiency curve is shown in Fig 4. On the same plot the "neighbour efficiency" is represented as well as the RPC single

counting rate (right scale). The discriminator thresholds in the FEE were set at 35 mV.

Some results are given in Table 3. The value of the running high voltage (HV) in Table 3 is chosen about 400 V above the "knee" of the efficiency curve and corresponds to a RPC efficiency close to 100% (apart from geometrical inefficiency).

The mixture Ar 49% , Isobutane 7% , Forane 40% , $SF_6$ 4% gives the best results i.e. good efficiency, low "neighbour efficiency", small charge, small rise time and very stable pulses.

Table 3. Parameters of various gas mixtures

| Gas mixture | H.V. | neighbour efficiency | charge (pC) | amplitude (mV) | time resol (ns) |
|---|---|---|---|---|---|
| Ar 49% Isob 7% SF6 4% For 40% | 9500 | 11 % | 48 ±25 | 113 ±44 | $\leq 2$ |
| Ar/Isob 80/20 SF6 4% | 7300 | 13 % | 70 ±40 | 144 ±51 | $\leq 2$ |
| Ar/Isob 70/20 For 10% | 6700 | 46 % | 330 ±160 | 393 ±173 | |

Two other gas mixtures usual for streamer mode are listed for comparison in Table 3. The mixture without Forane (line 2 of Table 3) gives quite good results too but the pulses exhibit a lot of secondary peaks. The characteristics of the mixture without SF6 (line 3 of Table 3) are quite different, showing the necessity of the addition of a small percentage of a very electro-negative gas like SF6 to reduce the pulse charge.

We have also found that addition of CO2 leads to rather unstable gas mixtures.

## 5. RPC operating in the vicinity of a hadron absorber

In ALICE, energetic hadrons (~100 MeV) emitted during the ion collision intercept the beam shielding and develop hadronic showers. The charged particles leaking out from this thick absorber are responsible for most of the background on the trigger.

In Aug-Sept 97 we have performed an experiment at CERN/SPS where a hadron beam of 120 GeV/c momentum was dumped in a thick lead absorber (100 cm long in the beam direction and 60×60 $cm^2$ of section) which simulates the ALICE beam shielding. A RPC (50×50

$cm^2$) was placed on the side of the lead absorber, orthogonally to the beam, at 60 cm from the beam entry face. The lateral thickness of lead between the beam axis and the the RPC was varied between 20–40 cm.

The goal of the experiment was twofold :

- Cross-check the simulation absolute yields of hits with the actual detector ones
- Operate the RPC in such "unusual" conditions : the simulations indicate for instance that the incident angle of the particles on the detector is peaked at $50^0$

The RPC was operated in streamer mode with the gas mixture described in line 1 of Table 3.

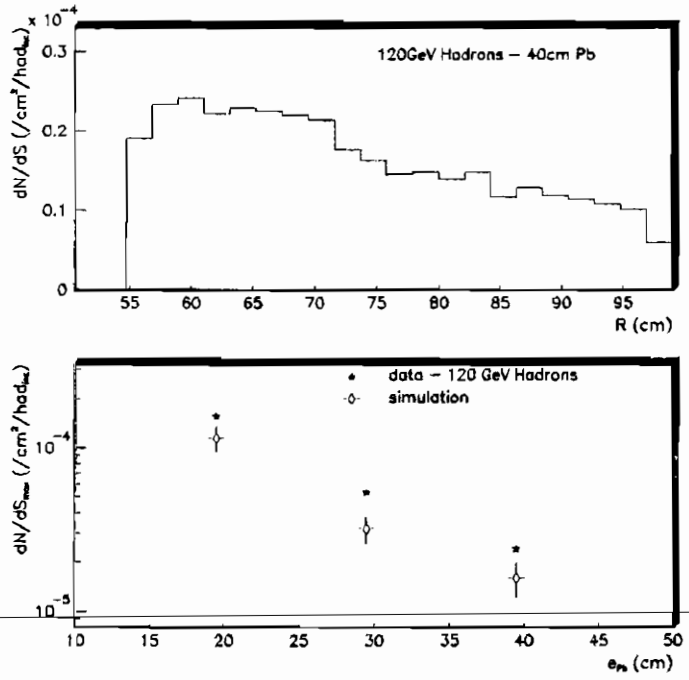


Fig. 5. Upper part : background hit radial distribution (see text)
Lower part : comparison of maximum yields to simulation results

The general behaviour of the RPC during the test was quite satisfying. We show in the upper part of Fig 5 the background radial

distribution measured with the RPC for a lateral Pb thickness of 40 cm. The experimental distribution starts at about 55 cm because the first strip of the RPC is 15 cm away from the absorber due to the mechanical support. In the lower part of Fig 5 we compare the experimental and simulated maximum yields, close to the absorber, for three values of the lateral Pb thickness. The simulation slighly underestimates the absolute yields but the radial decrease (not shown on the figure) is well reproduced. The simulation was actually performed with GEANT+FLUKA, including the MICAP interface for the treatment of low energy neutrons. FLUKA simulations are in progress.

Finally we show the experimental cluster size distribution in Fig 6, for 2 cm wide strips. We get a mean value of 1.4 strips fired which is quite satisfactory.

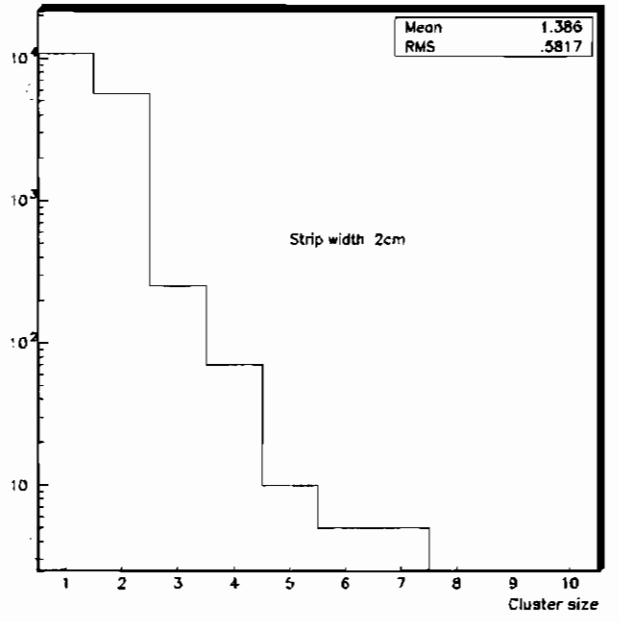


Fig. 6. Experimental cluster size distribution

During this test we have also exposed the RPC directly to the beam. In these conditions, the cluster size was about 1.2 strips. The rate capability that we have achieved is not relevant since the resistivity of the RPC was not optimized.

Similar tests are planned in 98 in streamer and proportional mode with low resistivity RPCs.

## 6. Acknowledgements

I would like to thank Prof R. Santonico and his group for their help concerning the RPC detector.

## 7. References

[1] T. Matsui and H. Satz, *Phys. Lett.* **B178** (1986) 416.
[2] ALICE collaboration, *CERN/LHCC note* **96–32** (1996)
[3] ALICE collaboration, *CERN/LHCC note* **95–71** (1995)
[4] R. Santonico and R. Cardarelli, *Nucl. Instr. and Meth.* **A263** (1981) 377.
[5] K. Eggert and A. Morsch, *ALICE note* **95–05 /phy** (1995)
A. Morsch, *ALICE note* **96–31 /phy** (1996)
[6] A. Morsch, *ALICE note* **96–29 /dim** (1996)
[7] A. Baldit et al, *ALICE note* **96–14 /dim** (1996)

# A simulation study of the RPC muon trigger for CMS

G. Bruno *
*Dipartimento Interateneo di Fisica and Sezione INFN, Bari, Italy*

December 17, 1997

ABSTRACT

This document contains new simulation results concerning the performance of the CMS muon trigger based on the Resistive Plate Chambers. Full time response of the system has been simulated taking into account the time of flight of muons, the signal propagation time along the read-out strips and the timing properties of the detectors. Trigger efficiency has been evaluated as a function of the time resolution and average efficiency of the RPCs.

## 1. Introduction

The performance of the CMS muon trigger system [1,2] based on the Resistive Plate Chambers (RPCs) [3,4] will heavily depend on the efficiency and timing properties of these detectors. The latter, in particular, will play an extremely delicate role in the trigger algorithm since individual hits have to be correctly assigned to 25 ns spaced bunch crossings. This requirement obviously imposes demanding conditions on the time resolution of RPCs. Furthermore, since the trigger needs informa-

*co authors: M. Abbrescia, A. Colaleo, G. Iaselli, G. Lamanna, M. Maggi, B. Marangelli, S. Natali, S. Nuzzo, G. Pugliese, A. Ranieri, F. Romano *Dipartimento Interateneo di Fisica and Sezione INFN, Bari, Italy*; S. Altieri, V. Arena, G. Bonomi, G. Gianini, M. Merlo, S. P. Ratti, C. Riccardi, L. Viola, P. Vitulo *Dipartimento di Fisica Nucleare e Teorica and Sezione INFN, Pavia, Italy.*

tion from several chambers it is also necessary to synchronize the signals in order to relate them to the same bunch crossing. For these reasons a realistic evaluation of the trigger performance requires the complete simulation of the time response of the system in addition to that of the trigger algorithm.

## 2. The RPC trigger for CMS

### *2.1. The basic principle*

The RPC based muon trigger for CMS relies on the 4 T strong solenoidal magnetic field of the apparatus (about 1.8 T in the iron return yoke). Assuming cylindrical coordinates with the $z$ axis along the beam line, muon tracks are bent in the $r\varphi$ plane so that one can measure the muon transverse momentum ($p_t$) from the bending of the track.

Four logical RPC planes are used for triggering both in the barrel and in the endcap region. The planes are located in the muon stations MB1-4 (barrel) and ME1-4 (endcaps). Muons with $4 < p_t < 7$ GeV/c in the barrel are not able to reach the outer muon stations MB3 and MB4, therefore, to allow the trigger action to take place also on these muons, an additional plane is inserted in each of the two inner stations MB1 and MB2. The trigger basic principle is shown in Fig. 1. A muon travelling through the apparatus produces hits on the RPC read-out strips and in this way it generates a pattern of hits that carries the information about the bending. The estimation of the $p_t$ can be accomplished by means of trigger processors that compare the observed patterns with predefined valid ones, each corresponding to a certain $p_t$ value. In the barrel there are additional low $p_t$ processors which deal with signals coming from the four inner planes.

In the absence of energy loss and multiple scattering there would be a one to one correspondence between the muon transverse momentum and the produced hit pattern. In reality, due to the two mentioned phenomena, a given pattern could be associated to $p_t$ values in a certain range; for this reason each valid pattern is assigned a maximal $p_t$ value. Because of large multiple scattering and energy losses the track shapes of low momentum muons are subject to large fluctuations that lead to a rapid increase in the number of patterns to be loaded in each trigger processor. On the other hand tracks are more bent at low momenta,

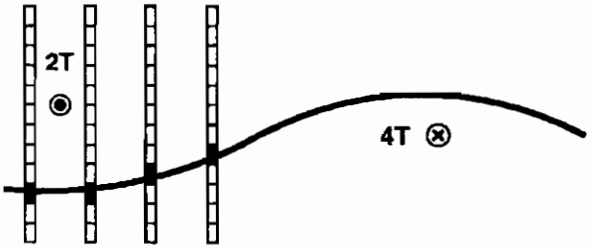


Figure 1: The basic principle of the RPC muon trigger.

therefore the number of valid patterns is reduced by OR-ing logically the strips by 2, 4 or 8, depending on the momentum. The sets of valid patterns are presently obtained from simulation, but they will be corrected later when real reconstructed muon tracks will be available. Details about the procedure followed to find the sets of valid patterns and the associated $p_t$ values can be found in [5].

*2.2. The segmentation*

The RPC trigger system is foreseen for the pseudorapidity region $|\eta| < 2.1$, but at present there are some possibilities of upgrading it to $|\eta| < 2.4$. In the barrel the muon stations are grouped in 5 wheels. The RPC planes in stations MB1, MB3 and MB4 and the upper plane in MB2 consist of 2 chambers while the lower plane in MB2 is made up of 3 chambers.[a] In the endcaps the muon stations have a trapezoidal geometry and the RPC strips run radially. The number of chambers varies from station to station.

The logical segmentation differs from the physical one. Each trigger processor is related to a *segment* which is the basic logical unit of the trigger and is defined by 8 strips in a reference RPC plane. In the barrel the reference plane is the inner one in MB2, while in the endcaps it is the one in ME2. Since every strip covers $5/16^0$ and, in the reference planes, about 0.1 in $\eta$, a segment covers $\Delta\eta \sim 0.1$ pseudorapidity units and $\Delta\varphi = 2.5^0$. Segments are grouped into 39 rings also called towers

[a]It must be noted that the simulation study has been performed with the old geometry for the RPC system in which 3 chambers make up an RPC plane in every barrel muon station.

(-19, .., 0, .., 19) whose $\eta$ limits are reported in Tab.1.

*2.3. The signal synchronization*

At LHC the time separation between two successive bunch crossings will be 25 ns. In order to achieve correct bunch crossing assignment the signals coming from the four RPC planes in a given segment need to be synchronized so that the trigger processor can deal with signals related to the same bunch crossing. The synchronization task will be performed by the so called synchronization blocks which will be located close to the RPC front-end electronics. Each block is presently assumed to serve twelve adjacent strips of a chamber. After being discriminated and shaped the signals from one of these groups of strips will be suitably shifted in time to match the LHC clock and in this way they will get the bunch crossing number before being sent to the trigger processor through an optical link. Seen in another way, the signals related to a certain bunch crossing will be correctly assigned if they reach the blocks in specific time windows. The following contributions must be taken into account to determine the time shift (or opening time of the window) to apply to each group of strips:

- Time of flight of muons from the vertex to the strips.
- Response time of RPCs and jitter due to their intrinsic time resolution.
- Signal propagation time along the strips.
- Delay and jitter due to the front-end electronics.
- Possibly, lengths of cables used to transport the signals.

The last contribution can be directly controlled whereas the others are the sources of the spread in the distribution of the arrival times of the signals. The width of the time window cannot be longer than 25 ns to allow unambiguous bunch crossing assignment. One would actually like to keep it as narrow as possible to reduce random background, but at the same time it has to be wide enough to avoid missing signals.

## 3. The underlying simulation

The simulation study has been carried out with the GEANT based

CMSIM 103 program implementing geometry version 14 for the apparatus. The CMS layout obtained with this version is shown in Fig. 2 where the RPC planes chosen for the high $p_t$ trigger algorithm are also reported. As it was previously pointed out, the low $p_t$ algorithm is based on the 4 inner planes of the barrel and is limited to towers -6, ..,6.

The simulation software for the RPC system has been extensively described elsewhere [6]. Here only the main features will be recalled. RPCs are grouped in *rolls*. Every barrel muon station is divided along $z$ in 3 identical RPCs, therefore a roll can be defined as a CMS slice containing the chambers which are located at the same z coordinate. In the endcaps a muon station is divided in RPCs assuming cylindrical geometry and fixing the inner and outer radii of the chambers. An endcap roll is a cylinder containing all the RPCs which are located between these radii. Rolls are numbered from -23 to 23 (-7, ..,7 in the barrel); their boundaries (only for rolls 0, ..,20) can be seen in Fig. 2 where they are represented by the thin dotted lines, vertical in the barrel and horizontal in the endcap. RPCs are simply represented by two 2.8 cm thick bakelite plates separated by a 2 mm thick gas layer which is the active volume of the detector. The dead space due to the spacers and to the surrounding 2.5 cm wide seal is not implemented in the present detector geometry. The RPC strips are also implemented in a rather simplified way. They are characterized by the $\varphi$ coordinate assuming the exact $5/16^0$ single strip coverage that leads to a total number of 1152 strips in a given RPC roll and plane type. Their lenght is determined by the roll they belong to: it is always equal to 83 cm in the barrel while it varies from 13 cm (roll 23) up to 100 cm (roll 8) in the endcaps.

In this simulation study the response of an RPC was assumed to take place 20 ns after the passage of a charged particle through the detector with a gaussian distributed jitter which also accounts for the contribution from the front-end electronics. In the following the r.m.s. of the jitter distribution will be referred to as the time resolution of the RPCs. The value chosen as the average response time of the RPC is only an approximate one since it also depends on the high voltage at which the detector is operated. No cluster size effects have been simulated; this means that the passage of a charged particle through an RPC causes only one strip to give rise to a signal. The signal propagation speed along the strips was fixed at 0.66c and the front-end electronics was placed at the strip end with larger $|z|$ in the barrel and larger $r$ in the endcaps. This choice allows minimizing the uncertainty on the arrival time of the

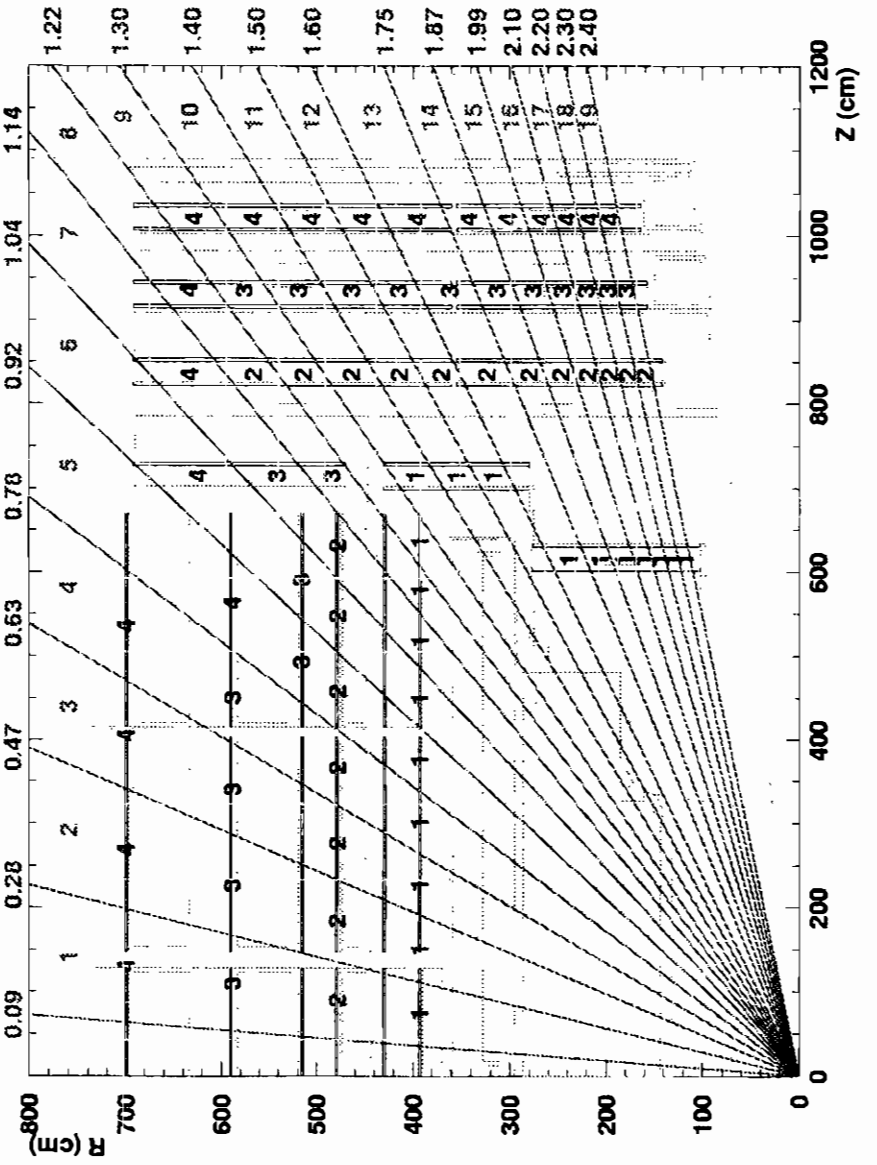


Figure 2: CMS geometry implemented in the GEANT based CMSIM program. The logical RPC planes chosen for the high $p_t$ trigger algorithm are indicated for each tower.

signals. No benefit can however be gained from any of the two possible choices in the chambers of the central roll.

Half a million muons of both signs were generated altogether. The events were divided in 50 data samples distinguished by the sign and $p_t$ range of the muons as reported in Tab.2. The adopted scale approximately reflects the expected $p_t$ distribution of the muons produced at the vertex [5]. The muons, which are flat distributed both in $\eta$ and $\varphi$, were generated in the region $0 < \varphi < 2\pi$ and $-0.25 < \eta < 2.4$. The choice of the $\eta$ interval was motivated by the simmetry of the apparatus, which allows considering only one of its halves, and by the necessity to fully include the RPCs belonging to the central roll.

## 4. Results of the simulation

The study was performed essentially in two steps. The generated events were initially used to obtain all the time distributions relative to the groups of 12 adjacent strips. Each distribution allowed the determination of the average time elapsed between the muon production at the vertex and the arrival of the signals from the corresponding group of strips.

In the second stage the events were used again to calculate the trigger efficiency in different $\eta$ and $p_t$ ranges and for several values of the cut on the transverse momentum ($p_t^{cut}$). The trigger efficiency has been calculated as a function of the average efficiency ($\epsilon_{RPC}$) and time resolution ($\sigma_{RPC}$) of the RPCs. This was done by passing to the simulation of the trigger algorithm only those hits which actually gave rise to a signal according to the assumption for $\epsilon_{RPC}$. Furthermore the signal was also required to fall within a time window whose middle point coincides with the previously obtained mean value of the time distribution relative to the group to which the strip carrying the signal belongs. The width of the time windows was set equal to 20 ns.

### *4.1. Time distributions*

The time distributions of some representative groups of 12 strips in every RPC plane of the central roll (0) are shown in Fig. 3. In this case $\sigma_{RPC}$ was set equal to 0 hence the spread is only due to the variation in time of flight and to the propagation time along the strips. Since the latter contribution is flat distributed with width equal to about 4 ns

| tower index | $\eta$ interval |
|---|---|
| 0 | -0.09 - 0.09 |
| 1 | 0.09. - 0.28 |
| 2 | 0.28 - 0.47 |
| 3 | 0.47 - 0.63 |
| 4 | 0.63 - 0.78 |
| 5 | 0.78 - 0.92 |
| 6 | 0.92 - 1.04 |
| 7 | 1.04 - 1.14 |
| 8 | 1.14 - 1.22 |
| 9 | 1.22 - 1.30 |
| 10 | 1.30 - 1.40 |
| 11 | 1.40 - 1.50 |
| 12 | 1.50 - 1.60 |
| 13 | 1.60 - 1.75 |
| 14 | 1.75 - 1.87 |
| 15 | 1.87 - 1.99 |
| 16 | 1.99 - 2.10 |
| 17 | 2.10 - 2.20 |
| 18 | 2.20 - 2.30 |
| 19 | 2.30 - 2.40 |

Table 1: $\eta$ tower limits.

| $p_t$ index | $p_t$ interval (GeV/c) |
|---|---|
| 0 | 0. - 1. |
| 1 | 1. - 1.2 |
| 2 | 1.2 - 1.5 |
| 3 | 1.5 - 2. |
| 4 | 2. - 2.5 |
| 5 | 2.5 - 3. |
| 6 | 3. - 3.5 |
| 7 | 3.5 - 4. |
| 8 | 4. - 5. |
| 9 | 5. - 6. |
| 10 | 6. - 7. |
| 11 | 7. - 8. |
| 12 | 8. - 10. |
| 13 | 10. - 12. |
| 14 | 12. - 14. |
| 15 | 14. - 17. |
| 16 | 17. - 20. |
| 17 | 20. - 25. |
| 18 | 25. - 30. |
| 19 | 30. - 35. |
| 20 | 35. - 40. |
| 21 | 40. - 50. |
| 22 | 50. - 70. |
| 23 | 70. - 100. |
| 24 | 100. - $\infty$ |

Table 2: $p_t$ division.

and the obtained distributions are always contained in 10 ns, one can conclude that the spread due only to the variation in time of flight is entirely limited within 6 ns, at least in the considered roll.

The time distributions shown in Fig. 4 are instead obtained by setting $\sigma_{RPC} = 3$ ns and refer to rolls 0, 5 and 9. They are relative to the RPC planes in station MB(E)1 (inner plane in MB1) and MB(E)4. The two distributions at the top can be compared with the corresponding ones in Fig. 3. From inspection of the r.m.s. values, it is evident that the RPC time resolution dominates on the other contributions everywhere. In particular, the distributions show that the contribution of the variation in time of flight and of the strip length to the time spread of rolls other than the central one remains within the limits indicated in Fig. 3. Since the various contributions to the time spread add up quadratically, one can conclude that the RPC time resolution is the dominant one provided it is greater than 3 ns. This result is particularly important in view of the new geometry for the barrel which is characterized by chambers with longer strips. The increased length of the strips should therefore not affect significantly the performance of the trigger system.

### *4.2. Efficiency curves*

The trigger efficiency is shown in Figs. 5 and 6 for two different combinations of $\sigma_{RPC}$ and $\epsilon_{RPC}$: 3 ns, 100 % and 5 ns, 95 % respectively. In both figures the efficiency is shown for the following $p_t^{cut}$ values: 5 , 14 , 40 and 100 GeV/c. Each bin of the histograms refers to a specific $p_t$ range and tower (see Tabs. 1 and 2) and is filled with the fraction of the muons which were generated in that bin and were asssigned a $p_t$ greater than the $p_t^{cut}$ by the trigger algorithm. These histograms can be compared with those reported in previous works [7] which anyway did not include any simulation of the time response of the apparatus and assumed full efficiency for the RPCs. While the plots in Fig. 5 do not show any relevant difference with the mentioned results, it is evident a degradation of the trigger efficiency in the histograms of Fig. 6. The worsening affects especially towers 0, .., 9, 13 and 14. The RPC system does not show full geometrical acceptance in these towers [7] and particularly in 1, ..,9; this implies that the algorithm often has to deal with hits from only three out of four logical planes and, since it needs a minimum of three planes with hits to "find" a muon, the additional

loss of some hits can cause more dramatic effects in these towers rather than in the others.

The specific dependence of the trigger efficiency on $\sigma_{RPC}$ and $\epsilon_{RPC}$ is better shown in Fig. 7 in which the values of the fixed parameters are $\epsilon_{RPC} = 100\%$ and $\sigma_{RPC} = 3$ ns respectively. The plots refer to $50 < p_t < 70$ GeV/c muons in three different towers: 0, 5 (which exhibits the lowest acceptance and efficiency) and 16. The applied $p_t^{cut}$ value is 5 GeV/c. As far as the time resolution is concerned it is evident that the trigger efficiency starts falling down at $\sigma_{RPC} = 4$ ns. This result can be safely extended to all the other towers and $p_t$ ranges since, as previously remarked, the other contributions to the time spread can be neglected for values of $\sigma_{RPC}$ greater than 3 ns. Towers 0 and 5 are clearly more sensitive than tower 16 to a worsening of the RPC time resolution. On the other hand the dependence on the RPC efficiency seems to be quite smooth in the investigated range Also in this case towers 0 and 5 exhibit a steeper fall with respect to tower 16, however, the reduction of the trigger efficiency over the considered $\epsilon_{RPC}$ range remains, in both towers, close to 10%.

Finally in Fig. 8 it is shown the effect of shifting by a given off-set all the opening times of the windows in which signals are accepted. The trigger efficiency is shown for $50 < p_t < 70$ GeV/c muons in tower 0, the $p_t^{cut}$ being 5 GeV/c. The assumed values for $\epsilon_{RPC}$ and $\sigma_{RPC}$ are 100% and 3 ns respectively. The resulting efficiency plateau is about 8 ns wide. This can give an idea of the precision with which the synchronization must be achieved.

## 5. Conclusions

The results of this study show that in order to avoid efficiency losses of the trigger greater than 5% of the value attainable with ideal detectors, RPCs are required to have an intrinsic time resolution not exceeding 4 ns and an efficiency greater than 95%. It must be underlined that the conclusions concerning the time resolution which have been presented in this paper apply to the particular value (20 ns) assumed for the width of the time windows in which signals are accepted. Smaller values will consequently impose stricter conditions on the timing performance of the RPCs and vice versa. In any case it has been shown that the trigger efficiency is significantly more sensitive to a degradation of the performance of the detectors in those regions where the system

shows poorer geometrical acceptance. This is the case of almost the entire barrel region and part of the endcap ones.

However it must be remarked that this study has to be considered a first step toward a truly realistic simulation of the RPC trigger system. Such a simulation should necessarily include the hits due to the background which are a major issue especially in the endcap regions. In addition, one also has to take into account the cluster size of the RPCs which will surely play a fundamental role in the actual capability of the trigger to estimate the muon transverse momentum. Finally, a complete realistic simulation of the trigger system should necessarily require a more detailed geometrical description of the RPC.

## 6. References


1. *The Compact Muon Solenoid - Technical Proposal*, **CERN/LHCC 94-38**.
2. M. Andlinger et al., *"Pattern Comparator Trigger (PACT) for the Muon System of the CMS Experiment"*, **CERN-PPE 94-227** and **NIM A 370 (1996) 389**.
3. M. Abbrescia et al., *"Performance of a Resistive Plate Chamber operated in avalanche mode under $^{137}Cs$ irradiation"*, **CMS Note 1997-003**; submitted to NIM for publication.
4. M. Abbrescia et al., *"Beam Test Results on Resistive Plate Chambers for the CMS experiment"*, **CMS Note 1997-062**; submitted to NIM for publication.
5. M. Konecki, J. Krolikowski and G.Wrochna, *"Simulation study of the single muon, RPC based trigger for CMS"*, **CMS TN/92-039**.
6. M. Konecki, J. Krolikowski and G.Wrochna, *"RPC Muon Trigger Software MRPC 100-102"*, CMS Note in preparation.
7. M. Konecki, J. Krolikowski and G.Wrochna, *"Parametrisation functions of the RPC based muon trigger"*, **CMS TN/96-104**.

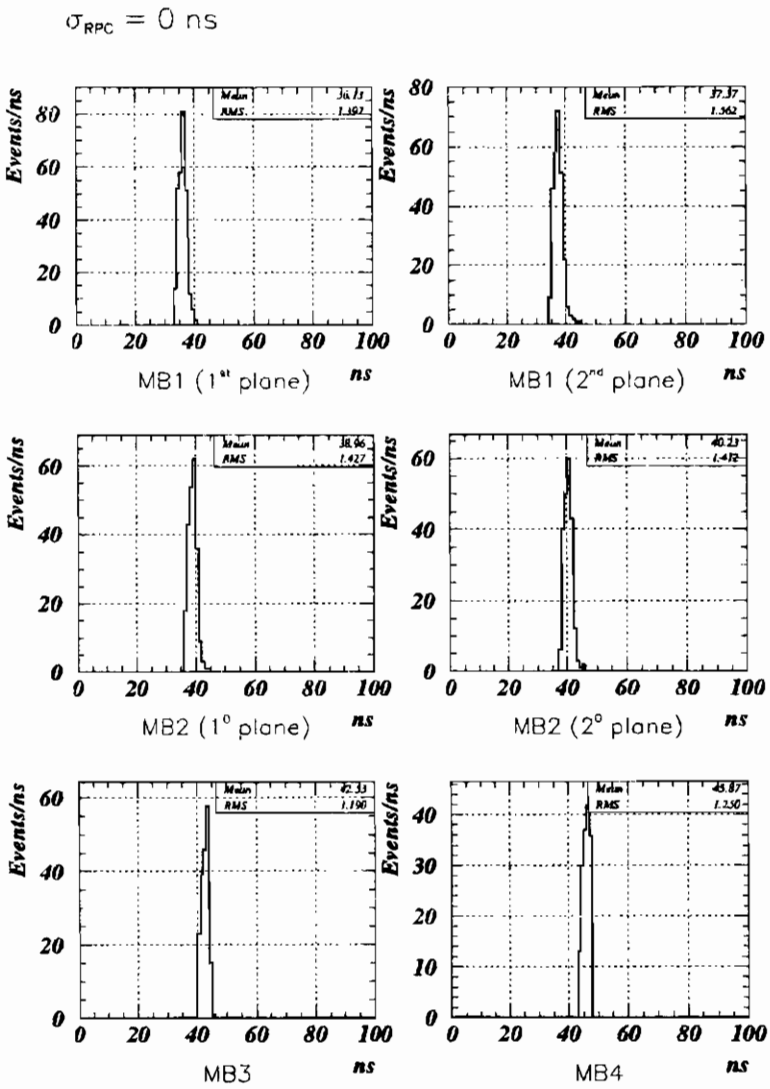


Figure 3: Distributions of the signal arrival times for some representative groups of 12 adjacent strips in every RPC plane of the central roll (0). They have been obtained assuming $\sigma_{RPC} = 0$ ns.

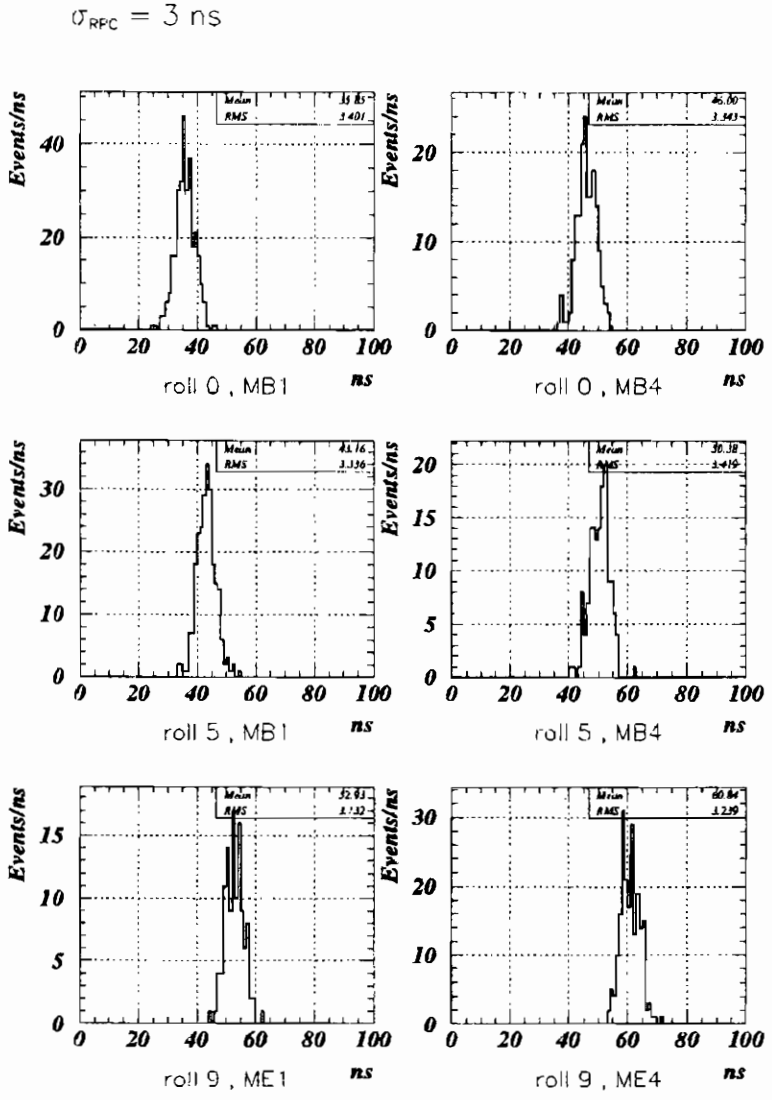


Figure 4: Distributions of the signal arrival times for some representative groups of 12 adjacent strips in three rolls of CMS. The distributions refers to groups belonging to the RPC planes in MB(E)1 (inner plane in MB1) and MB(E)4. They have been obtained assuming $\sigma_{RPC} = 3$ ns.

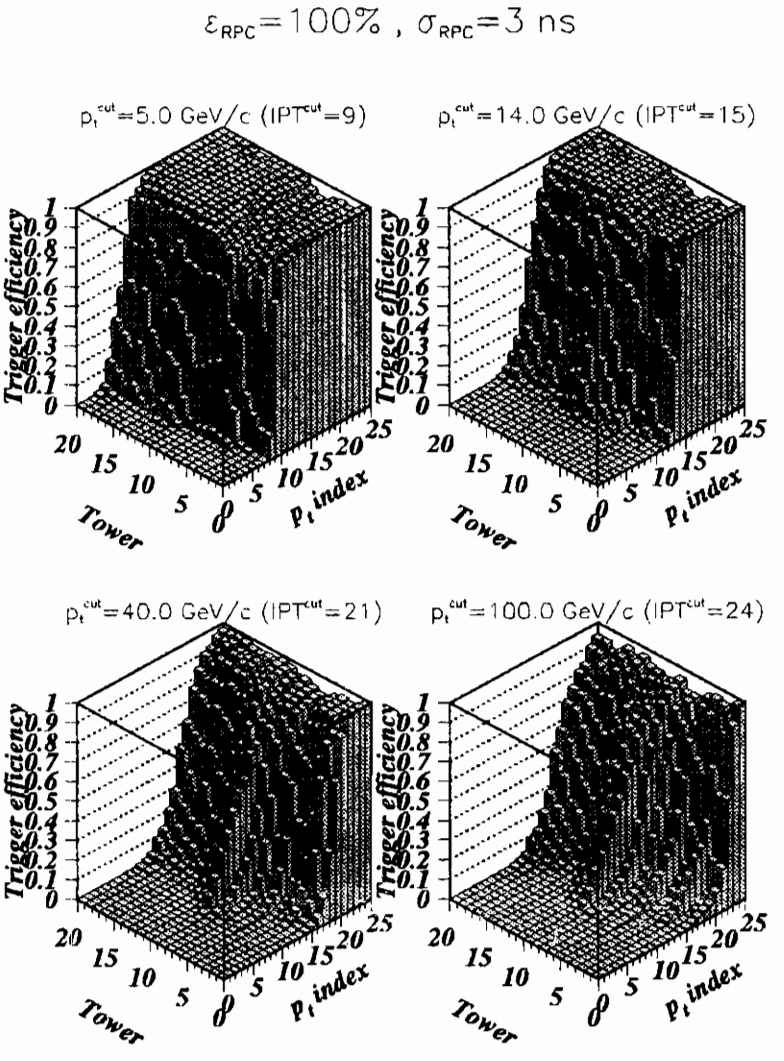


Figure 5: Trigger efficiency for some representative $p_t^{cut}$ values. Each bin of the histograms refers to a certain tower and $p_t$ range (see Tabs. 1 and 2). It has been assumed $\epsilon_{RPC} = 100$ % and $\sigma_{RPC} = 3$ ns.

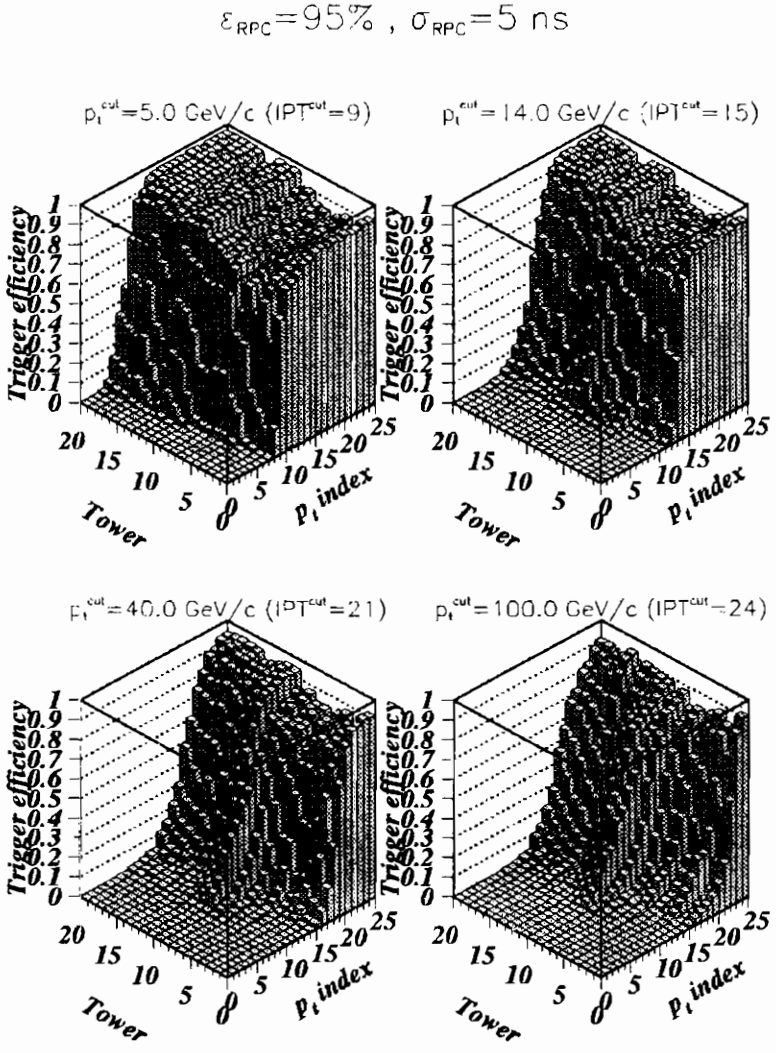


Figure 6: Trigger efficiency for some representative $p_t^{cut}$ values. Each bin of the histograms refers to a certain tower and $p_t$ range (see Tabs. 1 and 2). It has been assumed $\epsilon_{RPC} = 95$ % and $\sigma_{RPC} = 5$ ns.

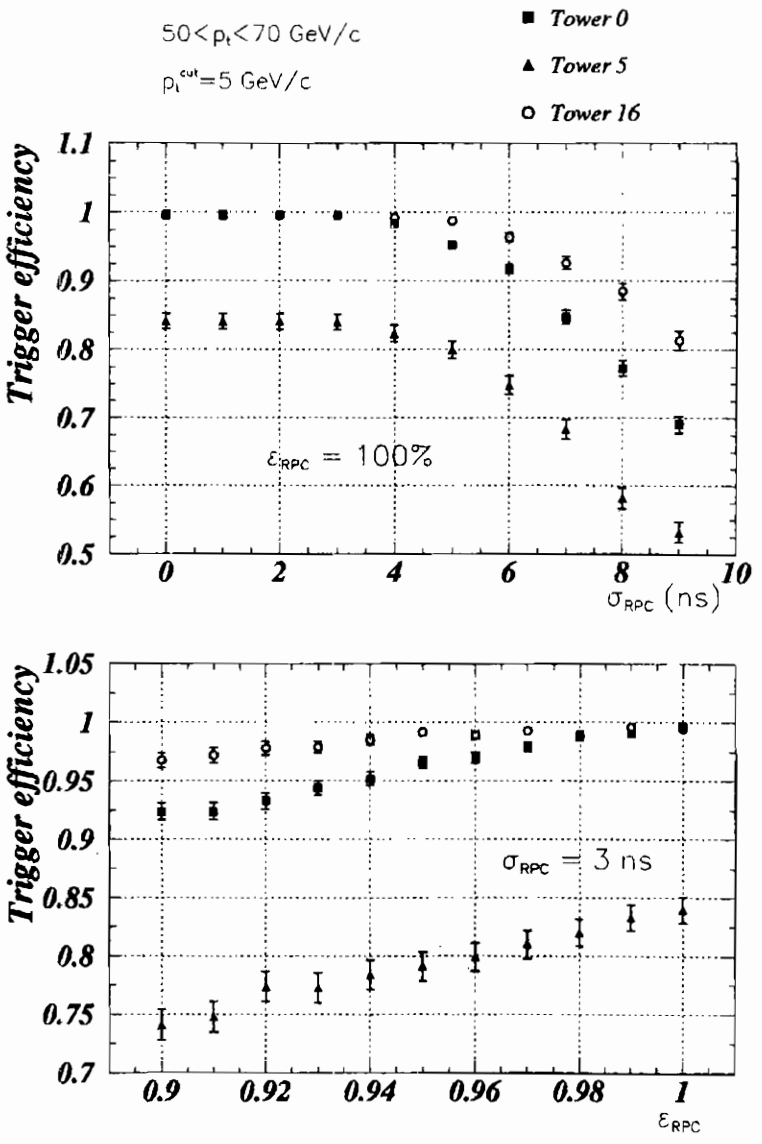


Figure 7: Dependence of the trigger efficiency on $\sigma_{RPC}$ (above) and $\epsilon_{RPC}$ (below). Trigger efficiency is shown for $50 < p_t < 70$ GeV/c muons generated in three different towers: 0, 5 and 16; the applied $p_t^{cut}$ value is 5 GeV/c. The value of the fixed parameter is $\epsilon_{RPC} = 100\%$ (above) and $\sigma_{RPC} = 3$ ns (below).

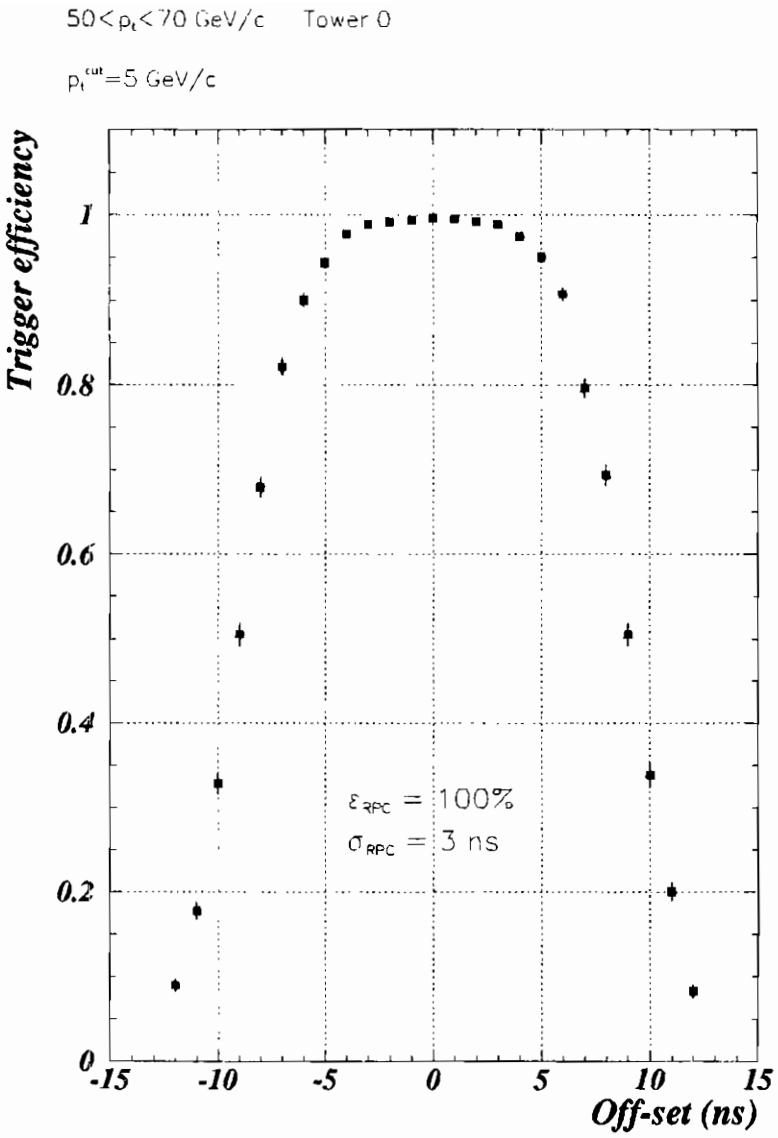


Figure 8: Efficiency plateau of the trigger. The points have been obtained after shifting all the opening times of the windows in which signals are accepted by the time off-set indicated on the x axis. The trigger efficiency is relative to muons generated in tower 0 with $50 < p_t < 70$ GeV/c and subject to a $p_t^{cut}$ value of 5 GeV/c.

# RPC97 Participant list

| | |
|---|---|
| *Marcello Abbrescia* | *Politecnico di Bari e sezione INFN di Bari - Italy* |
| *Maria Grazia Alviggi* | *Università di Napoli, Dip.to di scienze fisiche - Italy* |
| *Michelangelo Ambrosio* | *INFN Sezione di Napoli - Italy* |
| *Carla Aramo* | *Università e INFN di Catania - Italy* |
| *Walter Blum* | *CERN European Lab. for particle physics, Geneva - Switzerland* |
| *Giacomo Bruno* | *Università di Bari, Dip.to Interateneo di Fisica - Italy* |
| *Sandro Calcaterra* | *Laboratori Nazionali di Frascati - Italy* |
| *Paolo Camarri* | *INFN Sezione di Roma II - Italy* |
| *Roberto Cardarelli* | *INFN Sezione di Roma II - Italy* |
| *Gianpaolo Carlino* | *Università di Napoli, Dip.to di scienze fisiche - Italy* |
| *Sergio Catalanotti* | *Università di Napoli, Dip.to di scienze fisiche - Italy* |
| *Nicola Cavallo* | *INFN Sezione di Napoli - Italy* |
| *Guido Ciapetti* | *Università di Roma la Sapienza - Italy* |
| *Anna Colaleo* | *Università di Bari, Dip.to Interateneo di Fisica - Italy* |
| *Giovanni Crosetti* | *INFN -Genova - Italy* |
| *Benedetto D'Ettorre Piazzoli* | *Università di Napoli, Dip.to di scienze fisiche - Italy* |
| *Riccardo de Asmundis* | *INFN Sezione di Napoli - Italy* |
| *Anna Di Ciaccio* | *Università di Roma Tor Vergata - Italy* |
| *Wojtec Dominik* | *Warsaw - Polland* |
| *Pascal Dupieux* | *Laboratoire de Physique Corpusculaire de Clermont-Fd - France* |
| *Francesco Fabozzi* | *INFN Sezione di Napoli - Italy* |
| *Ercolino Fabrizi* | *General Tecnica - Italy* |
| *Jaques Fargeix* | *Laboratoire de Physique Corpusculaire de Clermont-Fd - France* |
| *Paulo Fonte* | *LIF-Coimbra - Portugal* |
| *M.Margarida Fraga* | *LIP-Coimbra - Portugal* |
| *Eduardo Gorini* | *Dip.to di Fisica Università di Lecce - Italy* |
| *Francesco Grancagnolo* | *INFN Sezione di Lecce - Italy* |
| *Donato Grassi* | *Università di Napoli, Dip.to di scienze fisiche - Italy* |
| *Giovanni Grieco* | *CAEN, Viareggio - Italy* |
| *Carlo Gustavino* | *INFN Laboratori Nazionali del Gran Sasso - Italy* |
| *Yoshimoto Hoshi* | *Tohoku Gakuin University, Dep.t of applied Physics - Japan* |
| *Michele Iacovacci* | *INFN Sezione di Napoli - Italy* |
| *Gianluca Introzzi* | *Dip.to di Fisica Nucleare e Teorica, Univ. Di Pavia - Italy* |
| *DongHee Kim* | *Kyungpook National University - Korea* |
| *Do-Won Kim* | *Departememt of Physics, Kangnung National University - Korea* |
| *Giovanni Latwnna* | *INFN Sezione di Bari - Italy* |
| *Jose Lamas* | *CERN European Lab. for particle physics, Geneva - Switzerland* |
| *Guido Lamperti* | *3M Italia - Italy* |
| *Lucia Lippi* | *General Tecnica - Italy* |
| *Luca Lista* | *INFN Sezione di Napoli - Italy* |

| | |
|---|---|
| *Flavio Loddo* | *INFN Sezione di Bari - Italy* |
| *Marcello Maggi* | *INFN Sezione di Bari - Italy* |
| *Bartolomeo Marangelli* | *INFN Sezione di Bari - Italy* |
| *Stefano Mari* | *Università di Roma - Italy* |
| *Leonardo Merola* | *Università di Napoli, Dip.to di scienze fisiche - Italy* |
| *Marco Napolitano* | *Università di Napoli, Dip.to di scienze fisiche - Italy* |
| *Salvatore Nuzzo* | *Univenità di Bari, Dip.to Interateneo di Fisica - Italy* |
| *Pierluigi Paolucci* | *Università di Napoli, Dip.to di scienze fisiche - Italy* |
| *Il Park* | *Kyungpook National University - Korea* |
| *Antonio Passeri* | *Università di Roma III - Italy* |
| *Sergio Patricelli* | *Università di Napoli, Dip.to di scienze fisiche - Italy* |
| *Ida Peruzzi* | *INFN Laboratori Nazionali di Frascati - Italy* |
| *Davide Piccolo* | *INFN Sezione di Napoli - Italy* |
| *Marcello Piccolo* | *INFN Laboratori Nazionali di Frascati - Italy* |
| *Anna Piccotti* | *Università di Torino - Italy* |
| *Edward Platner* | *CERN European Lab. for particle physics, Geneva - Switzerland* |
| *Venetios Polychronakos* | *Brookhaven National Laboratoty - U.S.A.* |
| *Ludovico Pontecorvo* | *INFN Sezione di Roma - Italy* |
| *Margherita Primavera* | *INFN Sezione di Lecce - Italy* |
| *Gabriella Pugliese* | *Università di Bari, Dip.to Interateneo di Fisica - Italy* |
| *Ernst Radermacher* | *CERN European Lab. for particle physics, Geneva - Switzerland* |
| *Antonio Ranieri* | *INFN Sezione di Bari - Italy* |
| *Teodorico Raponi* | *General Tecnica - Italy* |
| *Sergio Ratti* | *Dip.to di scienze fisiche e INFN Sezione di Pavia - Italy* |
| *Hans Reithler* | *CERN European Lab. for particle physics, Geneva - Switzerland* |
| *Raffaele Romano* | *Università di Trieste - Italy* |
| *Carl Rosenfeld* | *University of South Carolina - U.S.A.* |
| *Rinaldo Santonico* | *Università di Roma Tor Vergata - Italy* |
| *Eleuterio Spiriti* | *Università di Roma III - Italy* |
| *Yoshiki Teramoto* | *Osaka City University; Inst. for Cosmic Ray Physics - Japan* |
| *Paolo Vitulo* | *Università di Pavia - Italy* |
| *Crispin Williams* | *CERN European Lab. for particle physics, Geneva - Switzerland* |
| *Douglas Wright* | *LLNL - U.S.A.* |
| *Grzegorz Wrochna* | *CERN European Lab. for particle physics, Geneva - Switzerland* |